



biomolecules

Cholinesterase Research

Edited by

Ondrej Soukup and Jan Korabecny

Printed Edition of the Special Issue Published in *Biomolecules*

Cholinesterase Research

Cholinesterase Research

Editors

Ondrej Soukup

Jan Korabecny

MDPI • Basel • Beijing • Wuhan • Barcelona • Belgrade • Manchester • Tokyo • Cluj • Tianjin



Editors

Ondrej Soukup	Jan Korabecny
Biomedical Research Center,	Biomedical Research Center,
University Hospital	University Hospital
Hradec Kralove	Hradec Kralove
Faculty of Military Health	Faculty of Military Health
Sciences, University of Defense	Sciences, University of Defense
Hradec Kralove	Hradec Kralove
Czech Republic	Czech Republic

Editorial Office

MDPI
St. Alban-Anlage 66
4052 Basel, Switzerland

This is a reprint of articles from the Special Issue published online in the open access journal *Biomolecules* (ISSN 2218-273X) (available at: www.mdpi.com/journal/biomolecules/special_issues/Cholinesterase_Research).

For citation purposes, cite each article independently as indicated on the article page online and as indicated below:

LastName, A.A.; LastName, B.B.; LastName, C.C. Article Title. <i>Journal Name</i> Year , <i>Volume Number</i> , Page Range.
--

ISBN 978-3-0365-1798-8 (Hbk)

ISBN 978-3-0365-1797-1 (PDF)

© 2021 by the authors. Articles in this book are Open Access and distributed under the Creative Commons Attribution (CC BY) license, which allows users to download, copy and build upon published articles, as long as the author and publisher are properly credited, which ensures maximum dissemination and a wider impact of our publications.

The book as a whole is distributed by MDPI under the terms and conditions of the Creative Commons license CC BY-NC-ND.

Contents

About the Editors	vii
Preface to “Cholinesterase Research”	ix
Jan Korabecny and Ondrej Soukup Cholinesterase Research Reprinted from: <i>Biomolecules</i> 2021 , <i>11</i> , 1121, doi:10.3390/biom11081121	1
Danna De Boer, Nguyet Nguyen, Jia Mao, Jessica Moore and Eric J. Sorin A Comprehensive Review of Cholinesterase Modeling and Simulation Reprinted from: <i>Biomolecules</i> 2021 , <i>11</i> , 580, doi:10.3390/biom11040580	5
Jakub Jończyk, Jędrzej Kukułowicz, Kamil Łatka, Barbara Malawska, Young-Sik Jung, Kamil Musilek and Marek Bajda Molecular Modeling Studies on the Multistep Reactivation Process of Organophosphate-Inhibited Acetylcholinesterase and Butyrylcholinesterase Reprinted from: <i>Biomolecules</i> 2021 , <i>11</i> , 169, doi:10.3390/biom11020169	41
Sofya V. Lushchekina, Gaetan Inidjel, Nicolas Martinez, Patrick Masson, Marie Trovaslet-Leroy, Florian Nachon, Michael Marek Koza, Tilo Seydel and Judith Peters Impact of Sucrose as Osmolyte on Molecular Dynamics of Mouse Acetylcholinesterase Reprinted from: <i>Biomolecules</i> 2020 , <i>10</i> , 1664, doi:10.3390/biom10121664	63
Irina V. Zueva, Sofya V. Lushchekina, Ian R. Pottie, Sultan Darvesh and Patrick Masson 1-(3- <i>Tert</i> -Butylphenyl)-2,2,2-Trifluoroethanone as a Potent Transition-State Analogue Slow-Binding Inhibitor of Human Acetylcholinesterase: Kinetic, MD and QM/MM Studies Reprinted from: <i>Biomolecules</i> 2020 , <i>10</i> , 1608, doi:10.3390/biom10121608	83
Jan Konecny, Anna Misiachna, Martina Hrabínova, Lenka Pulkrabkova, Marketa Benkova, Lukas Prchal, Tomas Kucera, Tereza Kobrlova, Vladimir Finger, Marharyta Kolcheva, Stepan Kortus, Daniel Jun, Marian Valko, Martin Horak, Ondrej Soukup and Jan Korabecny Pursuing the Complexity of Alzheimer’s Disease: Discovery of Fluoren-9-Amines as Selective Butyrylcholinesterase Inhibitors and <i>N</i> -Methyl- γ -Aspartate Receptor Antagonists Reprinted from: <i>Biomolecules</i> 2020 , <i>11</i> , 3, doi:10.3390/biom11010003	105
André-Guilhem Calas, Anne-Sophie Hanak, Nina Jaffré, Aurélie Nervo, José Dias, Catherine Rousseau, Charlotte Courageux, Xavier Brazzolotto, Pascal Villa, Adeline Obrecht, Jean-François Goossens, Christophe Landry, Johan Hachani, Fabien Gosselet, Marie-Pierre Dehouck, Jagadeesh Yerri, Maria Kliachyna, Rachid Baati and Florian Nachon Efficacy Assessment of an Uncharged Reactivator of NOP-Inhibited Acetylcholinesterase Based on Tetrahydroacridine Pyridine-Aldoxime Hybrid in Mouse Compared to Pralidoxime Reprinted from: <i>Biomolecules</i> 2020 , <i>10</i> , 858, doi:10.3390/biom10060858	129
Hafsa Amat-ur-Rasool, Fenella Symes, David Tooth, Larissa-Nele Schaffert, Ekramy Elmorsy, Mehboob Ahmed, Shahida Hasnain and Wayne G. Carter Potential Nutraceutical Properties of Leaves from Several Commonly Cultivated Plants Reprinted from: <i>Biomolecules</i> 2020 , <i>10</i> , 1556, doi:10.3390/biom10111556	151

Abdullah Al Mamun, Jana Maříková, Daniela Hulcová, Jiří Janoušek, Marcela Šafratová, Lucie Nováková, Tomáš Kučera, Martina Hrabínová, Jiří Kuneš, Jan Korábečný and Lucie Cahlíková	
Amaryllidaceae Alkaloids of Belladine-Type from <i>Narcissus pseudonarcissus</i> cv. Carlton as New Selective Inhibitors of Butyrylcholinesterase	
Reprinted from: <i>Biomolecules</i> 2020 , <i>10</i> , 800, doi:10.3390/biom10050800	173
Gilbert Audira, Nguyen Thi Ngoc Anh, Bui Thi Ngoc Hieu, Nemi Malhotra, Petrus Siregar, Omar Villalobos, Oliver B. Villaflores, Tzong-Rong Ger, Jong-Chin Huang, Kelvin H.-C. Chen and Chung-Der Hsiao	
Evaluation of the Adverse Effects of Chronic Exposure to Donepezil (An Acetylcholinesterase Inhibitor) in Adult Zebrafish by Behavioral and Biochemical Assessments	
Reprinted from: <i>Biomolecules</i> 2020 , <i>10</i> , 1340, doi:10.3390/biom10091340	191
Faez Saleh Al-Hamed, Ola M. Maria, Jeff Phan, Ahmed Al Subaie, Qiman Gao, Alaa Mansour, Lina Abu Nada, Imane Boukhatem, Osama A. Elkashty, Simon D. Tran, Marie Lordkipanidzé, Zahi Badran and Faleh Tamimi	
Postoperative Administration of the Acetylcholinesterase Inhibitor, Donepezil, Interferes with Bone Healing and Implant Osseointegration in a Rat Model	
Reprinted from: <i>Biomolecules</i> 2020 , <i>10</i> , 1318, doi:10.3390/biom10091318	217

About the Editors

Ondrej Soukup

Ondrej is the head of the Biomedical Research Center of the University Hospital Hradec Kralove and is focused mostly on the drug development process. He became the Associate Professor in Toxicology at the University of Defence in Hradec Kralove. He also obtained the PhD title in 2011 in this field. As a postdoctoral fellow, he was responsible for the development and testing of new therapeutics for Alzheimer's disease and organophosphorus poisoning. Besides the scientific activity, Ondrej is devoted to supervising students and teaching. The research focus can be described as a screening of biological properties of the new compounds, assessment of the blood-brain-barrier penetration, interaction with the cholinergic system and the determination of their cytotoxic effects; pharmacological and toxicological profile determination in vitro and in vivo, disinfectant and decontaminant agents and their efficacy.

Jan Korabecny

Jan is the deputy head at the Biomedical Research Center of the University Hospital Hradec Kralove and is mainly involved in the early stages of drug development. In 2020, he received an Associate Professor degree from Pharmaceutical Chemistry at the Faculty of Pharmacy in Hradec Kralove (Charles University). He also obtained his PhD title in 2012 in this field. His main area of interest is the development of novel therapeutics for Alzheimer's disease, cancer, tuberculosis, and organophosphorus poisoning. Besides the scientific activity, Jan is Editor-in-Chief of Military Medical Science Letters; he is supervising pregradual and PhD students. The research area is concentrated on drug development mainly applying different in silico techniques, and synthesis of small molecules as novel pharmacological entities. He is married and has two children.

Preface to “Cholinesterase Research”

The scope of the Cholinesterase Research Special Issue was to provide a broad and updated overview of all the aspects that encompass cholinesterase research.

This collection of 10 scientific papers includes original as well as review articles focused on the cholinesterase structural aspects, drug design and development of novel cholinesterase ligands, but also contains papers focused on the natural compounds and their effect on the cholinergic system and unexplored effects of donepezil. The Special Issue is dedicated mostly to the scientific community in order to support research in the field of cholinesterases.

The editors would like to thank all authors for contribution to the special issue and for their hard everyday work in this field.

This work has been also institutionally supported by MH CZ –DRO (UHHK, 00179906) and by the Ministry of Defence of the Czech Republic “Long Term Development Plan –Medical Aspects of Weapons of Mass Destruction” of the Faculty of Military Health Sciences Hradec Kralove, University of Defence, Czech Republic.

Ondrej Soukup, Jan Korabecny
Editors

Editorial

Cholinesterase Research

Jan Korabecny^{1,2,*}  and Ondrej Soukup^{1,2,*} 

¹ Biomedical Research Center, University Hospital Hradec Kralove, Sokolska 581, 500 05 Hradec Kralove, Czech Republic

² Faculty of Military Health Sciences, University of Defence, Trebesska 1575, 500 05 Hradec Kralove, Czech Republic

* Correspondence: jan.korabecny@fnhk.cz (J.K.); ondrej.soukup@fnhk.cz (O.S.)

Cholinesterases are fundamental players in the peripheral and central nervous systems. These serine hydrolases are presented by a two-membered family, namely acetylcholinesterase (AChE, E.C. 3.1.1.7) and butyrylcholinesterase (BChE, E.C. 3.1.1.8). Under physiological conditions, AChE terminates the action of acetylcholine at synapses. AChE is also implicated in the differentiation of embryonic stem cells, neurogenesis, cell adhesion, synaptogenesis, activation of dopamine neurons, amyloid beta fiber assembly, haematopoiesis and thrombopoiesis, or regulation of glutamate-mediated hippocampal activity. Many compounds target to inhibit this enzyme in order to symptomatically counteract low cholinergic tone; however, irreversible AChE blockade may have fatal consequences. This phenomenon is typical for a class of highly toxic compounds—nerve agents and pesticides. The role of BChE is still extensively discussed; it plays an important role in cholinergic mediation, it contributes to neurogenesis, and has a detoxifying effect towards different xenobiotic drugs. It is also assumed that BChE overtakes the function of AChE in the case of malfunction or later stages of Alzheimer’s disease (AD).

Based on the abovementioned, both AChE and BChE are considered as highly relevant targets in the field of medicinal chemistry. For neurodegenerative disorders such as AD, there is a strong consensus that AChE/BChE reversible inhibitors can, at least temporarily, alleviate the symptoms associated with the disorder, and enhance the cognitive performance of individuals. Other cholinesterase ligands, namely cholinesterase reactivators, typically endowed with strong nucleophilic function, can revert the irreversible action of organophosphorus compounds (nerve agents and pesticides). However, there are many other areas of research involving AChE and BChE, for example, pesticides; inflammation; and other neuronal disorders such as Lewy body dementia, Parkinson’s disease, myasthenia gravis, and so on.

The scope of this Special Issue of *Biomolecules*, “Cholinesterase Research”, was to provide a broad and updated overview of all the aspects that encompass cholinesterase research. The collection includes cholinesterase structural aspects, drug design and development, in vitro biochemical studies, animal studies, and computational approaches, all devoted primarily to cholinesterases.

Computational studies focus mostly on the structural and dynamical aspects of cholinesterases: first of all a comprehensive review of cholinesterase modelling and simulation was provided by De Boer and colleagues [1]. It analyses AChE/BChE structure and function using computer-based modelling and simulation techniques using different models of both enzymes. It also discusses key structural similarities in the active site gorges of the two enzymes, such as flexibility, binding site location, and function, as well as differences, such as gorge volume and binding site residue composition. Catalytic studies are also described, with an emphasis on the mechanism of acetylcholine hydrolysis by each enzyme and novel mutants that increase catalytic efficiency. The review also explores the inhibitory properties of several compounds currently approved by the FDA and other experimental drugs through Monte Carlo-based docking calculations and molecular dynamics simulations.



Citation: Korabecny, J.; Soukup, O. Cholinesterase Research. *Biomolecules* **2021**, *11*, 1121. <https://doi.org/10.3390/biom11081121>

Received: 27 July 2021

Accepted: 29 July 2021

Published: 30 July 2021

Publisher’s Note: MDPI stays neutral with regard to jurisdictional claims in published maps and institutional affiliations.



Copyright: © 2021 by the authors. Licensee MDPI, Basel, Switzerland. This article is an open access article distributed under the terms and conditions of the Creative Commons Attribution (CC BY) license (<https://creativecommons.org/licenses/by/4.0/>).

The study by Jończyk and colleagues [2] explores molecular mechanisms determining the efficiency and selectivity of individual oximes to reactivate AChE/BChE blocked by sarin and tabun. The study investigated the reactivation of AChE and BChE by selected oximes using molecular docking methods. It identified amino acids essential for effective reactivation and those responsible for the selectivity of individual oximes against inhibited AChE/BChE. The observation made herein can significantly contribute to support the search for new effective reactivators.

The paper of Lushchekina et al. [3] investigated the effect of different concentrations of sucrose on the protein and water dynamics in cholinesterases. It revealed a non-linear correlation with increasing sucrose concentration, i.e., first a decrease in the dynamics at 5 wt% followed by a gain at 10 wt% sucrose. The explanation of this phenomenon is that sucrose molecules interact with the surface of the protein and the entrance of the gorge at a lower concentration through the water layer, damping the motions at the surface, but increasing them inside the gorge. When increasing the sucrose concentration more, the sucrose molecules replace some of the water molecules at the surface, permitting again more water molecules to enter the gorge and opening simultaneously new pathways, among them the hypothesized backdoor to the gorge.

The study by Zueva and colleagues [4] is a kinetic study corroborated by molecular modelling simulation of human AChE inhibition by fluorinated acetophenone derivative, namely 1-(3-*tert*-butylphenyl)-2,2,2-trifluoroethanone (TFK). TFK was found to be a competitive type inhibitor reaching steady state inhibition slowly. It is speculated that after binding, TFK acylates the active serine, forming a hemiketal; the disruption of such complex, i.e., deacylation is slow. Modelling of interactions between TFK and AChE active site by QM/MM showed that the “isomerization” step of enzyme-inhibitor complex leads to a complex similar to substrate tetrahedral intermediate, a so-called “transition state analog”, followed by a labile covalent intermediate. TFK can be classified as a slow-binding inhibitor with potential dual effect that could be of interest in palliative therapy of AD or protection of central AChE against organophosphorus compounds.

When it comes to a development of novel chemical compounds targeting cholinesterases both in the inhibitory and reactivation manner, the Special Issue contains the following experimental studies: the article by Konecny et al. [5] describes the design, synthesis and biological evaluation of a series of 15 novel fluoren-9-amine derivatives as dually active cholinesterase inhibitors and *N*-methyl-D-aspartate receptor (NMDAR) antagonists. The study builds on the concept of so-called multi-target directed ligands (MTDLs) that are believed to provide higher benefit compared to single-oriented drugs. The compounds under the study were initially *in silico* screened for CNS and oral availability, fitting all the prediction models used. Ongoing assessment of the biological profile included determination of the cholinesterase inhibition and NMDA receptor antagonism at the GluN1/GluN2A and GluN1/GluN2B subunits of NMDAR, along with a low cytotoxicity profile in the CHO-K1 cell line. Compounds were found to be highly selective BChE inhibitors with antagonistic activity on the NMDARs.

The group of Florian Nachon compared *in vitro* and *in vivo* efficacy, and toxicity of a hybrid tetrahydroacridine pyridinaldoxime reactivator, namely KM297, with pralidoxime [6]. The study revealed that blood–brain barrier crossing capacity of KM297 *in vitro* exceeds the permeability coefficient of pralidoxime twice. However, KM297 is also endowed with higher cytotoxicity, particularly on bone marrow-derived cells. Its strong cholinesterase inhibition potency seems to be correlated to its low protective efficacy in mice exposed to paraoxon. Ventilatory monitoring of KM297-treated mice by double-chamber plethysmography displayed toxic effects at the selected therapeutic dose.

Natural compounds and their effect on the cholinesterases are involved as well. Namely, the article by Amat-ur-Rasool and colleagues [7] screened methanolic extracts from seven commonly cultivated plants for their nutraceutical potential with particular emphasis on AChE/BChE inhibition and antioxidant capacity. The majority of extracts inhibited AChE and BChE, with henna and eucalyptus extracts highlighted as the most potent

ones. Moreover, all plant extracts were able to scavenge free radicals in a concentration-dependent manner, with eucalyptus being the most potent antioxidant.

The article by Al Mamun and colleagues [8] describes the isolation of thirteen known and three previously undescribed alkaloids of belladine structural type. Notably, significant human BChE inhibition was demonstrated by newly described alkaloids carltonine A and carltonine B, representing a new scaffold for generation of a novel structural type of BChE inhibitors with highly selective pattern over AChE.

Finally, the effect of clinically used donepezil has been investigated: the study of Audira and colleagues [9] is dedicated to donepezil, a currently approved drug for mild-to-moderate stages of AD. The study exploits a zebrafish model to analyze potential adverse effects of donepezil on the short-term memory, behavioral and biochemical changes. Donepezil caused a slight improvement in the short-term memory of zebrafish and induced significant elevation in aggressiveness, while the novel tank and shoaling tests revealed anxiolytic-like behavior. The latter can be ascribed to alterations associated with an elevation of oxytocin and a reduction in cortisol levels in the brain. Thus, chronic waterborne exposure to donepezil can severely induce adverse effects on normal zebrafish in a dose-dependent manner.

In another article by Al-Hamed et al. [10], postoperative administration of donepezil on bone healing was studied in the group of Sprague–Dawley rats. After two weeks of donepezil administration, rats were euthanized, and their bones were analyzed by Micro-CT and histology, with the authors concluding that bone defects and implant osseointegration were significantly reduced compared to the saline-treated rats. Histomorphometric analysis pointed to lower immune cell infiltration in bone defects as the possible culprit for disrupted bone healing.

To conclude, this Special Issue describes important findings related to cholinesterases' physiological and pathological roles, their involvement in metabolic studies, and the influence of different modulators (inhibitors, reactivators) on their activity. All these findings may broaden the knowledge and the impact on clinical and pharmacological applications of different small molecules targeted to AChE/BChE.

Funding: The work has been supported also by the Long Term Development Plan—Medical Aspects of Weapons of Mass Destruction; of the Faculty of Military Health Sciences Hradec Kralove, University of Defence, Czech Republic and University Hospital Hradec Kralove (MH CZ-DRO) (UHHK, 00179906).

Conflicts of Interest: The authors declare no conflict of interest.

References

1. De Boer, D.; Nguyen, N.; Mao, J.; Moore, J.; Sorin, E.J. A Comprehensive Review of Cholinesterase Modeling and Simulation. *Biomolecules* **2021**, *11*, 580. [[CrossRef](#)] [[PubMed](#)]
2. Jończyk, J.; Kukułowicz, J.; Łątka, K.; Malawska, B.; Jung, Y.-S.; Musilek, K.; Bajda, M. Molecular Modeling Studies on the Multistep Reactivation Process of Organophosphate-Inhibited Acetylcholinesterase and Butyrylcholinesterase. *Biomolecules* **2021**, *11*, 169. [[CrossRef](#)]
3. Lushchekina, S.V.; Inidjel, G.; Martinez, N.; Masson, P.; Trovaslet-Leroy, M.; Nachon, F.; Koza, M.M.; Seydel, T.; Peters, J. Impact of Sucrose as Osmolyte on Molecular Dynamics of Mouse Acetylcholinesterase. *Biomolecules* **2020**, *10*, 1664. [[CrossRef](#)]
4. Zueva, I.V.; Lushchekina, S.V.; Pottie, I.R.; Darvesh, S.; Masson, P. 1-(3-Tert-Butylphenyl)-2,2,2-Trifluoroethanone as a Potent Transition-State Analogue Slow-Binding Inhibitor of Human Acetylcholinesterase: Kinetic, MD and QM/MM Studies. *Biomolecules* **2020**, *10*, 1608. [[CrossRef](#)]
5. Konecny, J.; Misiachna, A.; Hrabínova, M.; Pulkrabkova, L.; Benkova, M.; Prchal, L.; Kucera, T.; Koblrova, T.; Finger, V.; Kolcheva, M.; et al. Pursuing the Complexity of Alzheimer's Disease: Discovery of Fluoren-9-Amines as Selective Butyrylcholinesterase Inhibitors and N-Methyl-d-Aspartate Receptor Antagonists. *Biomolecules* **2021**, *11*, 3. [[CrossRef](#)]
6. Calas, A.-G.; Hanak, A.-S.; Jaffré, N.; Nervo, A.; Dias, J.; Rousseau, C.; Courageux, C.; Brazzolotto, X.; Villa, P.; Obrecht, A.; et al. Efficacy Assessment of an Uncharged Reactivator of NOP-Inhibited Acetylcholinesterase Based on Tetrahydroacridine Pyridine-Aldoxime Hybrid in Mouse Compared to Pralidoxime. *Biomolecules* **2020**, *10*, 858. [[CrossRef](#)]
7. Amat-ur-Rasool, H.; Symes, F.; Tooth, D.; Schaffert, L.-N.; Elmorsy, E.; Ahmed, M.; Hasnain, S.; Carter, W.G. Potential Nutritional Properties of Leaves from Several Commonly Cultivated Plants. *Biomolecules* **2020**, *10*, 1556. [[CrossRef](#)] [[PubMed](#)]

8. Al Mamun, A.; Maříková, J.; Hulcová, D.; Janoušek, J.; Šafratová, M.; Nováková, L.; Kučera, T.; Hrabínová, M.; Kuneš, J.; Korábečný, J.; et al. Amaryllidaceae Alkaloids of Belladine-Type from *Narcissus Pseudonarcissus* Cv. Carlton as New Selective Inhibitors of Butyrylcholinesterase. *Biomolecules* **2020**, *10*, 800. [[CrossRef](#)]
9. Audira, G.; Ngoc Anh, N.T.; Ngoc Hieu, B.T.; Malhotra, N.; Siregar, P.; Villalobos, O.; Villaflores, O.B.; Ger, T.-R.; Huang, J.-C.; Chen, K.H.-C.; et al. Evaluation of the Adverse Effects of Chronic Exposure to Donepezil (An Acetylcholinesterase Inhibitor) in Adult Zebrafish by Behavioral and Biochemical Assessments. *Biomolecules* **2020**, *10*, 1340. [[CrossRef](#)] [[PubMed](#)]
10. Al-Hamed, F.S.; Maria, O.M.; Phan, J.; Al Subaie, A.; Gao, Q.; Mansour, A.; Abu Nada, L.; Boukhatem, I.; Elkashty, O.A.; Tran, S.D.; et al. Postoperative Administration of the Acetylcholinesterase Inhibitor, Donepezil, Interferes with Bone Healing and Implant Osseointegration in a Rat Model. *Biomolecules* **2020**, *10*, 1318. [[CrossRef](#)] [[PubMed](#)]

Review

A Comprehensive Review of Cholinesterase Modeling and Simulation

Danna De Boer ^{1,†}, Nguyet Nguyen ^{2,†}, Jia Mao ², Jessica Moore ³ and Eric J. Sorin ^{1,*} ¹ Department of Chemistry & Biochemistry, California State University, Long Beach, CA 90840, USA² Department of Chemical Engineering, California State University, Long Beach, CA 90840, USA³ Department of Biomedical Engineering, California State University, Long Beach, CA 90840, USA

* Correspondence: eric.sorin@csulb.edu

† Authors wish it to be known that the first two authors contributed equally to this work.

Abstract: The present article reviews published efforts to study acetylcholinesterase and butyrylcholinesterase structure and function using computer-based modeling and simulation techniques. Structures and models of both enzymes from various organisms, including rays, mice, and humans, are discussed to highlight key structural similarities in the active site gorges of the two enzymes, such as flexibility, binding site location, and function, as well as differences, such as gorge volume and binding site residue composition. Catalytic studies are also described, with an emphasis on the mechanism of acetylcholine hydrolysis by each enzyme and novel mutants that increase catalytic efficiency. The inhibitory activities of myriad compounds have been computationally assessed, primarily through Monte Carlo-based docking calculations and molecular dynamics simulations. Pharmaceutical compounds examined herein include FDA-approved therapeutics and their derivatives, as well as several other prescription drug derivatives. Cholinesterase interactions with both narcotics and organophosphate compounds are discussed, with the latter focusing primarily on molecular recognition studies of potential therapeutic value and on improving our understanding of the reactivation of cholinesterases that are bound to toxins. This review also explores the inhibitory properties of several other organic and biological moieties, as well as advancements in virtual screening methodologies with respect to these enzymes.

Keywords: acetylcholinesterase; butyrylcholinesterase; docking; molecular dynamics; hydrolysis; molecular recognition; catalysis; inhibition; reactivation



Citation: De Boer, D.; Nguyen, N.; Mao, J.; Moore, J.; Sorin, E.J. A Comprehensive Review of Cholinesterase Modeling and Simulation. *Biomolecules* **2021**, *11*, 580. <https://doi.org/10.3390/biom11040580>

Academic Editors: Jan Korabecny and Ondrej Soukup

Received: 21 March 2021

Accepted: 11 April 2021

Published: 15 April 2021

Publisher's Note: MDPI stays neutral with regard to jurisdictional claims in published maps and institutional affiliations.



Copyright: © 2021 by the authors. Licensee MDPI, Basel, Switzerland. This article is an open access article distributed under the terms and conditions of the Creative Commons Attribution (CC BY) license (<https://creativecommons.org/licenses/by/4.0/>).

1. Introduction

The cholinesterase enzyme family has but two members: acetylcholinesterase (AChE) and butyrylcholinesterase (BChE). The former's primary biological purpose is regulating acetylcholine, a neurotransmitter, via hydrolysis at neuromuscular junctions, thus proving itself to be an essential component in the maintenance and performance of nervous systems. AChE, which has also been referred to as "true cholinesterase", is created in muscle, nerve, and hematopoietic cells and is considered to be one of the most efficient enzymes due to its rapid rate of catalysis [1]. AChE's plasma analog, BChE, previously referred to as "pseudocholinesterase", is produced in the liver and, unlike AChE, has been viewed as having a much more ambiguous biological purpose, as it was long believed to be vestigial [2]. BChE has a higher concentration in plasma than AChE, is present in many vertebrates, and tolerates several mutations, which has prompted the theory that BChE evolved from AChE to be a general detoxifier while still retaining some function in the process of neurotransmission [3]. This theory seems apt given the structural similarity of their binding sites, their shared affinities for certain substrates and ligands, and their sequence homology of approximately 65% [4]. Figure 1 depicts both AChE (bottom) and BChE (top) from a gorge-centric view and after a 90° rotation.

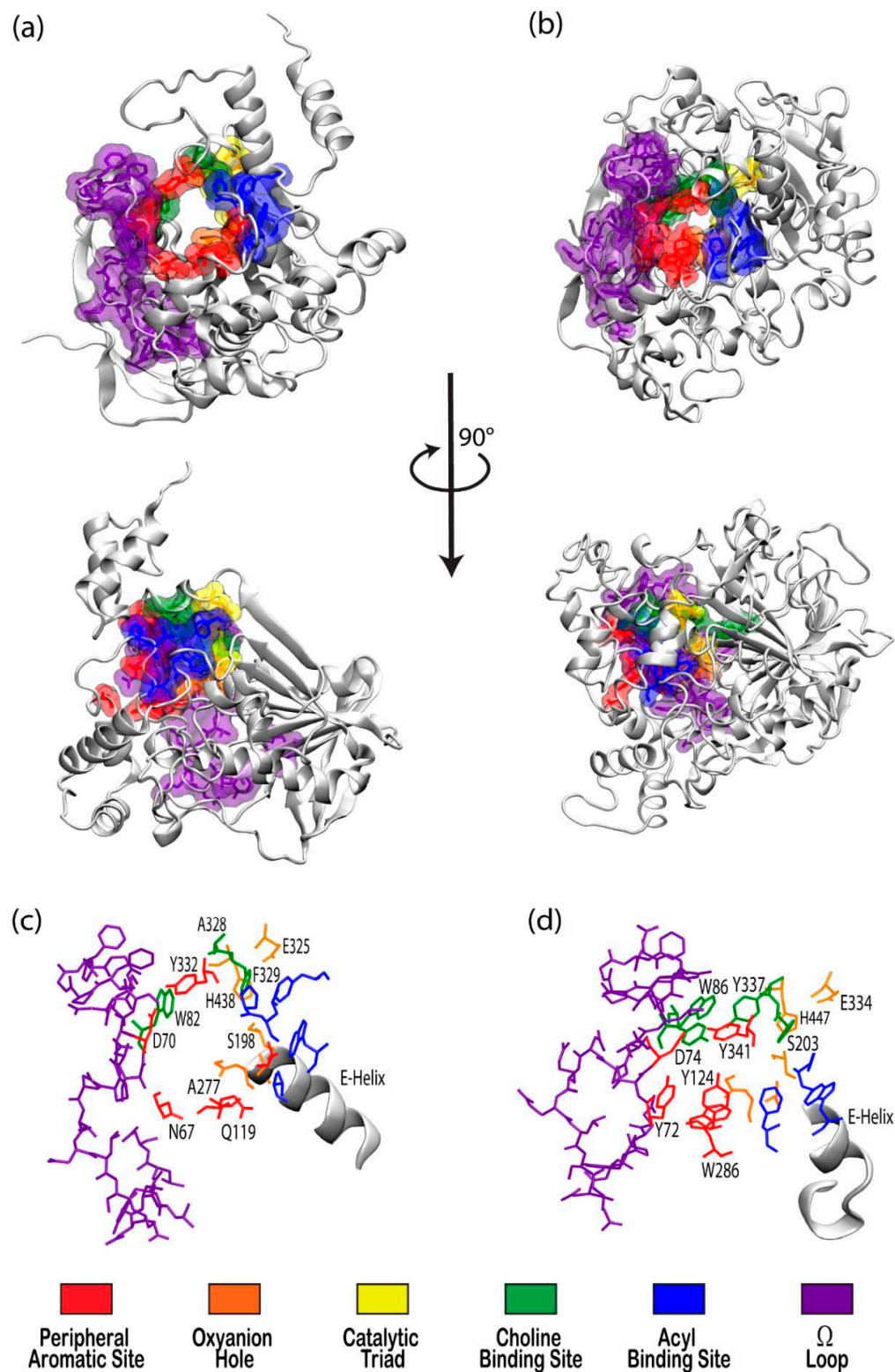


Figure 1. Visualizations of (a) butyrylcholinesterase (BChE) (PDBID 1P0I) and (b) acetylcholinesterase (AChE) (PDBID 1B41) in white ribbon mode with residues in notable binding sites shown as semi-transparent van der Waals surfaces colored according to the key. Top panels present views directly into the active site gorges with structures in the center panel rotated 90° about the vertical axis. Bottom panels present magnified views of the binding site regions of (c) BChE and (d) AChE with key residues labeled.

One difference between the two enzymes is the relative size of the binding pocket, with BChE and AChE having approximate gorge volumes of 1500 \AA^3 and 1300 \AA^3 , respectively [5]. X-ray crystallography of *Torpedo californica* (*Tc*, pacific ray) AChE revealed the enzyme to have a deep hydrophobic gorge with residues that stabilize substrates in the pocket [6], as well as a bottleneck region in the active site [7] that narrows to approximately 4 \AA in width [8]. Common models of AChE, including human, mouse, and *Torpedo californica* (*TcAChE*), demonstrate conserved active sites, save for a few residues that participate in ligand binding [9], and both have negative surface potentials that become more negative deeper within the gorge. This negative potential, which is high near the catalytic site at the “bottom” of the gorge, seems to have evolved to facilitate electrostatic attraction of positively charged choline substrates by both enzymes [8].

Although BChE is structurally similar to AChE, 6 of the 14 aromatic amino acids that line the active site gorge in AChE are substituted with aliphatic residues in BChE [10]. In particular, the substitution of Phe288 and Phe290 in *TcAChE* with the smaller Leu286 and Val288 in human BChE lead to conformational changes that result in a deeper gorge in BChE, thereby allowing BChE to interact with, and potentially hydrolyze, a much wider range of substrates and inhibitors than AChE [11]. BChE is thus characterized as the promiscuous, or non-specific, bigger sibling to the smaller and much more specific AChE.

The tremendous growth and improvement in computational resources and modeling techniques over the past few decades have led to an exponential increase in computational studies of biomolecular systems. In 2003, the Protein Data Bank (PDB) launched its online presence, thereby making myriad biomolecules and complexes available for structural and computational research, and by 2016 there were 178 AChE structures available to the public, many of those including bound substrates or inhibitors of medical and pharmacological significance [9]. In fact, some of the earliest and most significant contributions of cholinesterase models were reported by Sussman et al., who performed an X-ray analysis of AChE at 2.8 resolution in 1991 [12], and Nicolet et al., who examined several crystal structures of BChE in 2003 [13]. Modeling and simulation-based studies of the cholinesterase enzymes have advanced in tandem with this growth.

The application of molecular dynamics (MD) simulations, Monte Carlo (MC) based docking calculations, and more sophisticated quantum mechanical/molecular mechanics (QM/MM) simulations have proven highly insightful in probing cholinesterase structure and activity. Notable areas of interest include the mechanisms of cholinesterase catalysis, reversible and irreversible inhibition of both enzymes to manage Alzheimer’s Disease (AD) and other ailments, BChE-specific inhibition, and the reactivation of phosphorylated cholinesterases, a process that normally follows nerve agent attacks or pesticide poisoning [14]. Figure 2a,b depict the common paths of substrate or ligand binding and phosphorylation, respectively.

Most therapeutic treatments of AD, and other illnesses to which the cholinesterases have been linked, are reversible inhibitors that form non-covalent molecular recognition (MR) complexes with cholinesterases and can leave the active site, thus existing in an equilibrium between bound and unbound states characterized by K_I and/or IC_{50} values. The three mechanisms that reversible inhibition can follow are competitive, noncompetitive, and uncompetitive, as depicted in Figure 2a. During competitive inhibition, the substrate and inhibitor are competing for the same binding site, and the binding of a competitive inhibitor within the active site blocks entrance of the substrate, thereby hindering formation of the enzyme substrate complex. By contrast, uncompetitive inhibitors function by binding to the enzyme-substrate complex to prevent product formation, and noncompetitive inhibitors can bind to either the enzyme or the enzyme-substrate complex to regulate catalytic activity.

Many organic compounds, including organophosphates (OPs), are categorized as irreversible inhibitors, which covalently bond to residues in the gorge and thus cannot leave the active site. In the cholinesterases, OPs covalently bind to the serine residue of the catalytic triad. Irreversibly inhibited cholinesterases, however, can be reactivated via

various pathways with compounds such as oximes, as illustrated in Figure 2b. Oximes reactivate an inhibited cholinesterase to its native structure by nucleophilic substitution of the phosphorylated serine. If untreated, the inhibited enzyme can undergo the dealkylation process, also known as aging, where the loss of the second leaving group produces an oxyanion on the phosphoryl group.

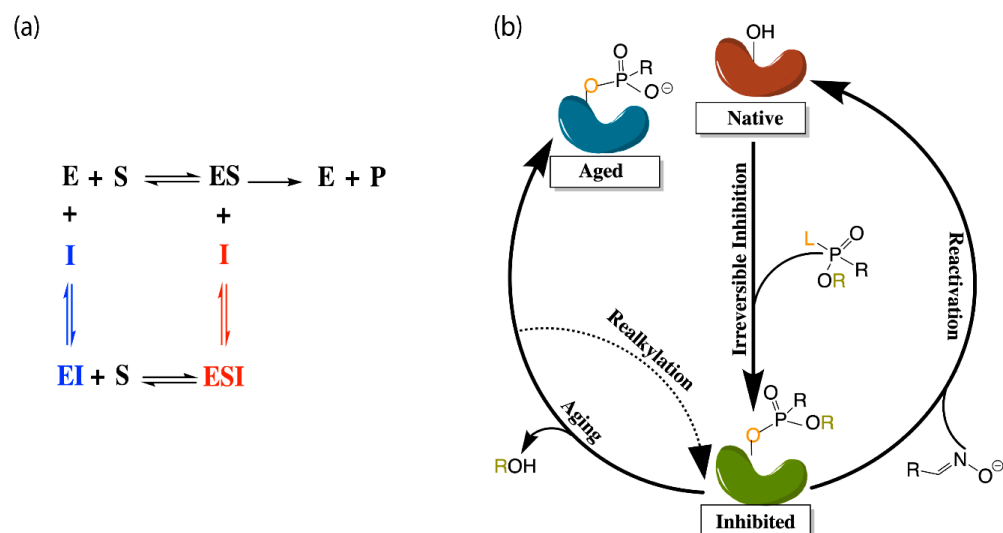


Figure 2. (a) Depiction of the enzyme catalytic mechanism (black) and reversible inhibition mechanisms including competitive inhibition (blue), uncompetitive inhibition (red), and noncompetitive inhibition (both blue and red). (b) Representation of irreversible (covalent) inhibition by organophosphorus ligands and the reactivation mechanisms to revert the aged enzyme (blue) back to the inhibited complex (green). L and R represent the first and second leaving groups of the organophosphate, respectively, following the paths of inhibition and reactivation.

Aged cholinesterase is highly stable due to the strong electrostatic interactions between the oxyanion and the positively charged catalytic histidine. Known reactivators of OP-inhibited AChE, such as oximes, are ineffectual against aged AChE [15]. Though a successful attempt to reactivate aged AChE by a class of compounds called “quinone methide precursors” (QMPs) was reported by Hadad and coworkers [16], the reaction between QMPs and aged AChE was rendered too slow to be useful [17]. The present review will examine many studies generally focusing on these areas of interest and, unless otherwise specified, all amino acid numbering used below will refer to human cholinesterase models.

2. Structure and Dynamics

While understanding the structure, function, and behavior of cholinesterase binding sites seems a practical starting point for modeling studies, early researchers initially wanted to understand how substrates and inhibitors entered the active sites of these enzymes. Molecular dynamics (MD) simulations of human BChE lasting for 5 and 10 ns indicated that inhibitors can access the binding subsites in the catalytic cavity due to the highly flexible entrance (or “mouth”) of the gorge, a portion of which is formed by the flexible omega loop (Ω -loop) region, as well as the peripheral aromatic site (PAS, formerly mistakenly called the peripheral anionic site). In these simulations, the Asp70 residue in PAS showed significant deviation from the crystal structure with root-mean-square deviation (RMSD) values of 2 to 6 Å [18]. AChE has also been shown to experience such fluctuations at the gorge entrance, with a similarly flexible Ω -loop region that is thought to increase enzyme specificity by making it more difficult for large molecules to enter the AChE gorge without hindering the productivity of the enzyme [19].

Apart from the fluctuations at the mouth of the gorge, AChE also experiences what is known as bottleneck fluctuations, with the bottleneck being the narrowest part of the

gorge. These fluctuations, which have come to be known as the “breathing” of the enzyme, can help inhibitors or substrates move from the surface to deeper regions of the gorge [20]. Cheng et al. recently defined this breathing by monitoring the varying distance between the C_{ε2} atom of Phe330 (CBS) and the O_H atom of Tyr121 (PAS) in TcAChE, which suggested that a number of subdomains within the enzyme, particularly the Ω-loop, contribute to modulating the size of the gorge bottleneck [21]. A comprehensive comparison between 47 crystal structures of AChE (in its native form and in complex with small molecules), as well as a 20 ns simulation of TcAChE, provided by Sussman and coworkers, suggested that the 14 aromatic residues lining the AChE gorge and creating over half of the gorge surface area contribute greatly to the overall flexibility of the enzyme, the observed bottleneck breathing motions, and the resulting ability to perform its catalytic function [22].

Some of these aromatic residues play significant roles in primary subsites within the cholinesterase gorges, such as the catalytic active site (CAS) and the peripheral aromatic site (PAS) [22]. While these sites, which are addressed in more detail below, are integral to cholinergic activity, cholinesterases do not only perform cholinergic functions. As discussed by Chinnadurai et al., the aryl acylamidase activity (AAA) of AChE, which also involves hydrolysis, only requires the CAS and does not interact with the PAS at all [23]. This has prompted the theory that AAA substrates enter from a side-door into the enzyme, rather than via the mouth of the gorge and, indeed, researchers have suggested that there are a number of doors through which substrates can enter the gorge including a back door [24], an Ω-loop door, and the suggested side door [23]. It was suggested that the side door may open more frequently than the other doors to mediate AAA activity, and MD simulations of side door probing emphasize the importance of hydrophobic interactions, hydrogen bonding, and water mediated interactions (“water bridges”) in moving the substrate towards the CAS [23]. To be sure, simulations of AChE in explicit solvent sans substrate [25], as well as analyses of TcAChE crystal structures in its native and several inhibited forms [26], have underscored the importance of the presence of molecular water in enzyme structure.

At higher concentrations, dimerization and the further dimerization of dimers to form tetramers is known to affect the structure and function of cholinesterase enzymes [27]. While MD simulations suggested that two of the four binding sites in tetramerized cholinesterases are sterically blocked, thereby becoming less active [28], as reflected by a 15% decrease in catalytic activity [29], a recently elucidated CryoEM structure of hBChE shows distinct structural variance from the simulated tetramer, with the active site gorges being fully solvent accessible [27]. Tetramerization, however, increases the half-life of the enzymes, which is a desirable result when cholinesterases, and BChE in particular, are being used to counteract drug overdoses. For example, the addition of proline-rich attachment domains (PRADs) to BChE increases tetramer stability, leading to an extended circulation time [30]. Interestingly, glycosylated models of BChE increase the enzyme’s flexibility and half-life without hindering its ability to bind to glycans, which cannot be said of all therapeutic protein targets [31]. On the other hand, cholinesterase phosphorylation, or the irreversible binding of organophosphate to the active site, which will be discussed in more detail in the organophosphate inhibition section below, severely restricts the flexibility of both AChE and BChE, as reported by Bennion et al. [32]. Experimental findings of AChE covalently bound to the nerve agent soman agree that OP-poisoned AChE is significantly stiffer [33].

2.1. Important Binding Sites

There has been substantial past effort to study the sites responsible for molecular recognition (MR) and binding affinity within the active site gorge of both enzymes, and it is clear that those binding sites, specific chemical subsites within each active site gorge, mirror each other and perform similar functions respective to each enzyme. While it is important to note that these binding sites have been examined experimentally with X-ray and kinetic studies, including a recent study by Rosenberry et al. [34], the present review

focuses on the unique perspective provided by computational investigations. As expected, one of the most important sites for both cholinesterases is the catalytic active site (CAS), and the peripheral aromatic site (PAS) also plays an indispensable role in cholinesterase or ligand binding, while the Ω -loop (OML), acyl binding site (ABS), and oxyanion hole (OAH) sites are more essential in contributing to binding affinity and complex stability. Alvarado et al. have provided a method of succinct graphical tabulation of BChE-ligand contacts and interactions, referred to as contact tables, that include these five sites and additional protein residues of interest [35], as discussed below. A detailed analysis of these binding sites is provided here in the same order that they are encountered by substrates and inhibitors upon entering and moving into the gorge.

2.1.1. Peripheral Aromatic Site

The peripheral aromatic site (PAS, red in Figure 1) is located near the mouth of gorge [36] and plays a prominent role in substrate and ligand binding [37]. For decades, peer-reviewed studies have used PAS to denote the “peripheral anionic site”. In recent years, however, the aromatic properties of this binding site that are vital to cholinesterase function have driven the community to instead refer to this region as the “peripheral aromatic site”. Important amino acids in the PAS of AChE include serine, tyrosine, aspartic acid, and tryptophan [36,38], while notable PAS residues in BChE include asparagine, aspartic acid, glutamine, serine, and tyrosine [35], highlighting the polar, negatively charged, and electron-rich nature of residues in this site. As previously mentioned, one distinction between the cholinesterases is the aromatic nature of the residues surrounding the PAS in AChE, which is more aliphatic in BChE [10]. The PAS makes contact with many loops and secondary structural elements at the surface of the protein, including the Ω -loop, which contributes to the needed flexibility discussed above. Although steric and electrostatic interactions may slow the catalytic efficiency of AChE, the PAS is valuable for trafficking ligands into the gorge [39], particularly positively charged species such as choline. MD simulations have emphasized the importance of cation- π interactions, which stabilize the ligand at the rim of the gorge entrance prior to entering the gorge [40], and it has been proposed that non-cholinergic activity of the PAS could include the deposition of amyloids, adhesion to cells, and outgrowth of neurites [41].

2.1.2. Acyl and Choline Binding Sites

Once a ligand has entered the gorge, the acyl and choline binding sites (ABS and CBS, shown as blue and green in Figure 1, respectively), which are located near the catalytic triad, assist in positioning the ligand for catalysis. The ABS and CBS are hydrophobic regions composed primarily of tryptophan, tyrosine, and phenylalanine in human AChE. Tyr337 in the choline binding site of AChE is replaced by Ala328 in that of BChE; Phe295 and Phe297 in the acyl binding site of AChE are replaced by Leu286 and Val288, respectively, in BChE. The replacement of aromatic residues in the ABS and CBS of BChE enable it to bind larger substrates and inhibitors than AChE [42]. In addition, the ABS and CBS are largely responsible for the specificity of these enzymes and are thus primary targets studied when synthesizing inhibitors such as imidazole or pyridine derivatives [43].

2.1.3. Catalytic Active Site

The catalytic active site (CAS, yellow in Figure 1) is located approximately 20 Å deep at the bottom of both the AChE and BChE gorges [12,24] and is made up of serine, glutamic acid, and histidine residues, prompting the name “catalytic triad” [24,35]. The CAS is surrounded by numerous aromatic and acidic residues [44] and is observed to engage in shorter hydrogen bonds in crystal and NMR structures than observed in simulation [45,46]. More importantly, the CAS is highly conserved [44], emphasizing historically vital biological roles of these enzymes and their cholinergic activities. QM/MM simulations at the MP2(6-31 + G*) level reveal a potential energy barrier of 10.5 kcal/mol, which agrees with experimental data [47], and MD simulations of AChE bound to acetylcholine (ACh)

show that ACh stabilizes the CAS and improves the binding ability of the peripheral aromatic site [48].

It has been postulated that a back-door exists in AChE, just behind the CAS and controlled by a tryptophan residue, which was theorized after a single water molecule exited the active site gorge from a direction opposite that of the gorge entrance in an MD simulation [49]. This “back door” was later thought to open three to four Å wide such that catalysis products could exit the gorge of the enzyme without blocking the gorge entrance, and thus contributing to a high catalytic rate [50]. Aromatic residues surrounding the CAS histidine also largely influence the productivity and efficiency of the enzyme [51], which decreased approximately 600-fold when disrupted or replaced by aliphatic side chains [52]. More recently, Xu et al. used MD to study TcAChE and, from 27 of their 40 trajectories, observed thiocholine to frequently exit the active site via a back-door created by cooperative motions of CAS residue Trp86 along with Val132 and Gly448 [53], for which previous experimental support was noted [54,55].

Indeed, other mutations in or near the CAS are known to have effects on the structure, and subsequent function, of the enzyme. This research has naturally focused on, and is more applicable to, BChE due to its much greater natural affinity for mutations than AChE [3]. For example, prolonged use of muscle relaxers led to the discovery of the “silent phenotype” in which an alanine is mutated to a valine near the CAS of BChE. This mutation was studied *in silico* and observed to severely disrupt interactions between the histidine and serine in the catalytic triad [56], leading to a dysfunctional CAS, regardless of the inhibitor, and increases in the volume of the enzyme, indicating that this may be a pre-denaturation state [57].

The mutation of a nearby alanine *in silico* to cystine in wild-type (WT) BChE causes the histidine in the catalytic triad to flip, an event that is largely guided by local water molecules [58]. This man-made mutation, while possibly slowing the speed of binding, ultimately still allows for substrate binding to the active site; the naturally occurring mutation of that alanine to aspartic acid, however, is claimed to be catalytically inactive due to strong disruptive interactions between aspartic acid and the CAS histidine residue [59]. Both mutations showcase the possible hysteretic behavior of BChE, or its reliance on past-states, which can likely be attributed to its toxicological and pharmaceutical functions [58,59]. For instance, a man-made mutant of BChE was recently modeled and examined by Masson and coworkers, using QM/MM and Markov state analysis, and was determined to be a template for future investigations into organophosphate hydrolase functions [60].

2.1.4. Oxyanion Hole

The oxyanion hole (OAH, orange in Figure 1), made of two glycines and one alanine [35,47], is generally a two-pronged site in many proteases and hydrolases; in the case of AChE, and subsequently BChE, the OAH is a three-pronged hole [61]. Early MD simulations of AChE phosphorylation suggested that the OAH exerts a pulling force on leaving groups during the alkylation step [45], and the OAH is known to lower the energy barrier for ACh hydrolysis in both cholinesterases [62]. QM/MM simulations exhibited consistent, tight hydrogen bonding between the OAH and the carbonyl carbon of the substrate, suggesting that the OAH facilitates stabilizing interactions in intermediate and transition states [61].

2.1.5. Ω-loop (Omega Loop)

The Ω-loop (OML, purple in Figure 1), consisting of a series of nearly 30 residues, is located along one side of the active site gorge wall. In the presence of a substrate or inhibitor, the Ω-loop plays an important role in modulating enzyme “breathing”, regulating the size of the gorge, and thereby enabling the passage of the ligand to the active site [21]. The OML undergoes conformational changes, such as gorge enlargement, through torsional motion and segmental fluctuations [63,64]. Unregulated motions and decreased electrostatic interactions, however, can significantly decrease the binding affinity of these

enzymes, such as the case of the atypical mutation from Asp70 to Gly70 in the OML of BChE, which Masson et al. reported could increase the K_m values 10- to 100-fold [65]. Moreover, the Ω -loop is speculated to facilitate an alternative entrance, the proposed side-door model noted above, to the active site of the enzyme; MD simulations performed by Wiesner et al. suggested that protonation of the AChE active site leads to conformational changes within the Ω -loop at Asn87 and Glu84 that result in the opening of this side door [66]. A similar observation was recently reported by the Rydzewski laboratory for TcAChE, where opening and closing of this side door due to the displacement of the OML favored alternative dissociate routes of the substrate and inhibitor [67]. To put these computational results into perspective, a number of experimental investigations into the omega loop and backdoor of AChE from various species have suggested that the back door opens in some cases [50,68,69], but also that this opening is likely not relevant functionally [70].

3. Catalysis

The primary catalytic function performed by AChE is hydrolysis of the neurotransmitter acetylcholine (ACh) [1], and molecular modeling and simulation studies have provided insight into this process that cannot be easily gleaned from experimental efforts. For example, MD simulations using an ab initio QM/MM potential were conducted to map the reaction mechanism of AChE with ACh, pointing to a mechanism with two main processes: acylation and deacylation. In the first step of acylation, the system must overcome the initial free energy barrier of 12.4 kcal/mol, during which the oxygen atom of Ser203 performs a nucleophilic attack at the carbonyl carbon of acetylcholine, with a synchronous proton transfer from Ser203 to His447, resulting in the first tetrahedral intermediate [71]. This intermediate is stabilized by local hydrogen bonds from the oxyanion region and electrostatic interactions with the glutamic acid in the catalytic triad [47]. The second step in acylation has an additional free energy barrier of 1.9 kcal/mol and is characterized by the proton transferring to the leaving group of ACh, resulting in bond cleavage and choline release from the pocket [71].

The next step in this process, deacylation, also occurs in two steps, the first of which includes interaction between a water molecule and the carbonyl carbon of the acetyl group in acetylcholine, leading to a second tetrahedral intermediate that is stabilized by the Gly121, Gly122, and Ala204 residues of the oxyanion hole. The proton then transfers to the acetylserine oxygen atom from His447, yielding the products acetic acid and AChE, with the initial free energy barrier of deacylation higher than that of acylation at 17.5 kcal/mol and thus predicted to be the rate-limiting step [71].

Modeling efforts by Chen et al. have shown BChE to have a similar reaction pathway for hydrolysis of ACh and acetylthiocholine, with two-step acylation and deacylation processes [72,73]. Like AChE, residues in the oxyanion hole of BChE are integral for stabilization of the intermediate and catalytic function [73]. However, the acylation and deacylation processes for BChE were predicted to have free energy barriers of 13.8 and 11.9 kcal/mol, respectively, indicating that the rate-limiting step for BChE is not the deacylation step, as predicted for AChE, but rather the acylation step [72]. Figure 3 displays free energy profiles for the hydrolysis of ACh by both AChE and BChE to allow for a side-by-side comparison [71,72] of these results.

Given the promiscuous nature of BChE and its circulation in plasma, this enzyme has a much broader natural variety of substrates than AChE [2,3]. For example, BChE is one of the primary enzymes to hydrolyze heroin and produce its most active form, 6-monoacetylmorphine. Computational efforts by Zhan and coworkers showed this process to follow the two-step acylation and deacylation scheme outlined above [74]. In contrast, work by the same group to model BChE hydrolysis of ghrelin, the hunger hormone, showed a single-step acylation process [75]. Interestingly, Suarez et al. modeled BChE hydrolysis of butyrylcholine, a synthetic molecule that mimics acetylcholine and for which BChE is named [3], and found that the presence of glycerol or another butyrylcholine

in the active site pocket stabilizes the intermediate product after transition state 2 in the deacylation step, which is a complex of BChE with butyric acid [76].

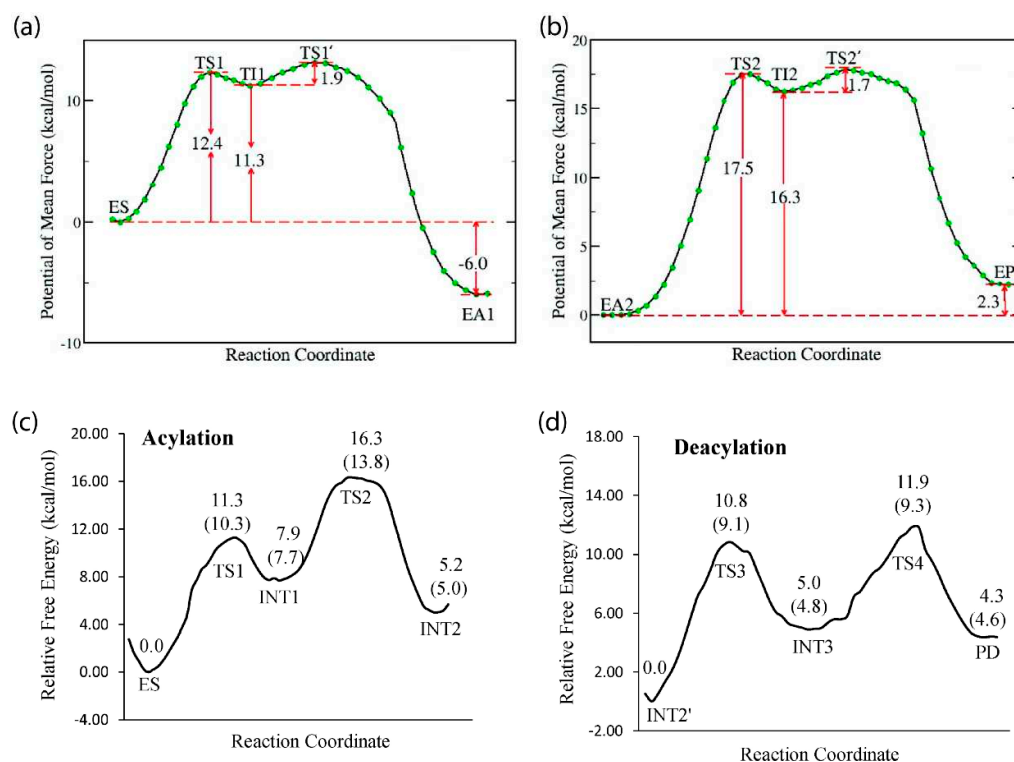


Figure 3. (Top) Free energy profiles for hydrolysis of ACh by AChE including the (a) acylation and (b) deacylation steps [71]. (Bottom) Free energy profiles for hydrolysis of ACh by BChE showing analogous (c) acylation and (d) deacylation steps [72].

Cocaine is another substrate of interest for BChE catalysis studies, as increasing the catalytic efficiency of BChE for cocaine hydrolysis can be an effective method to treat overdoses, making BChE mutants and transition states important focal points for study. Rate-determining steps can be made faster with residue mutations [77] by changing local interactions and increasing substrate stability [78]. For example, computational mutations of non-active residues in the BChE active site gorge were predicted to increase catalytic efficiency as much as 1000-fold by strengthening hydrogen bonds [61]. The Ala199Ser/Ser287Gly/Ala328Trp/Tyr332Gly BChE mutant achieves this by increasing the strength of hydrogen bonds in the first transition state of BChE-cocaine catalysis and lowering the energy barrier [79].

Free energy perturbation (FEP) simulations have allowed researchers to see the deviation in free energy barriers at transition states for different BChE mutants and led to the discovery of a mutant, Ala328Trp/Ala199Ser/Phe227Ala/Glu441Asp/Ser287Gly, that is around 1800-fold more efficient than wild-type BChE [80]. Further work by Zhan and coworkers using FEP simulations showed the Ala328Trp/Tyr332Gly/Ala199Ser BChE mutant to have the potential to greatly increase catalytic efficiency and to thus serve as a potential means for exogenous therapy [81]. Using QM/MM simulations, Zhan's team revealed two transition states for BChE-cocaine binding involving deformation of the non-prereactive complex and formation of the prereactive complex [77,82]. Indeed, efforts by the Zhan laboratory have resulted in a prodigious quantity and breadth of computational studies of cholinesterase catalysis in the 21st century.

4. Inhibition

We now turn to the area around which the majority of cholinesterase research has been dedicated over the past two decades: inhibition of one or both enzymes by various

compounds, presented below in distinct chemical groupings including pharmaceuticals, narcotics, organophosphates, other organic species, and biological agents and salts. FDA-approved pharmaceutical inhibitors and their derivatives generally serve to treat the symptoms of AD. Due to the difference in size of the two enzymes, many drugs experience a wide range of selectivity and target multiple binding sites. As previously mentioned, the biological roles that BChE plays are much more ambiguous than those of AChE. However, hydrolysis of narcotics, such as nicotine and cocaine, has been identified as a possible role of BChE and, as noted above, this enzyme has been a target to treat narcotics overdoses.

Organophosphate inhibitors have proven to have a wide field of study with myriad applications, and many phosphate-based molecules serve as potential cholinesterase inhibitors for disease management, while also being known for their highly toxic roles as irreversible inhibitors in nerve agents and pesticides. Finally, there are myriad compounds being researched, many aimed specifically at AD and other human ailments, that are still in early phases of research and not yet FDA-approved. Due to the vast number of unique inhibitors studied over the past two decades, many have been classified below under the broad category of other organic species, which are further organized according to prominent functional groups. Prior to this current effort, Anand and Singh reviewed different classes of cholinesterase inhibitors including tacrine, donepezil, rivastigmine, galantamine, xanthostigmine, para-amino-benzoic acid, coumarin, flavonoid, and pyrrolo-isoxazole analogues in their 2013 article [83]. Figure 4 presents molecular structures for many of the pharmaceuticals, narcotics, nerve agents, and related inhibitors mentioned above and detailed in the sections below.

4.1. Pharmaceuticals

4.1.1. Tacrine and Derivatives

Tacrine, or 1,2,3,4-tetrahydroacridin-9-amine, was a commonly-used drug to treat AD (under the brand name Cognex) that was the first FDA-approved cholinesterase inhibitor, but was later discontinued due to liver toxicity [84]. Given this history, it is used as a comparison for other drug studies [85], as well as the subject of study for potential chemical derivatives. Intensive 3D-QSAR (quantitative structure-activity relationship) studies, molecular docking analyses, and MD simulations of 60 tacrine-based inhibitors bound to *TcAChE* have identified key residues involved in binding to be Tyr70 (PAS), Trp84 (CBS), Tyr121 (PAS), Trp279 (PAS), and Phe330 (CBS) across various binding sites [86].

Tacrine derivatives have been investigated using docking calculations. In a survey of racemic tacrine derivatives in complex with AChE, Maalej et al. found the derivative 4-(13-amino-10,11,12,14-tetrahydro-9H-benzo[5,6]chromeno[2,3-b]quinolin-14-yl)phenol to be four times more effective in inhibitory activity than tacrine [87]. Tacrine-carbazole hybrids in complex with both AChE and BChE were also investigated via docking by Thiratmatrakul et al., who not only found these hybrids to exhibit a preference for BChE, but also showed them to have a potential for ABTS radical scavenging activity [88]. In the early 2000s, in situ click-chemistry led to the discovery of potent, femtomolar range tacrine derivatives [89], which have since been studied in complex with mouse, *Drosophila melanogaster*, and *TcAChE* through MD simulations [90]. More recently, the Richardson laboratory employed docking and quantum characterization, which revealed that tacrine derivatives with spacers, such as pentylaminopropene and pentylaminopropane, can increase inhibitor specificity to target BChE [91].

As expected, MD simulations can provide more detailed insight into tacrine-cholinesterase complexes, especially when coupled with experimental observations. For example, MD simulations allowed Decker and coworkers to explore interactions between ring-opened and ring-closed cyclohexen-like rings of tacrine derivatives [92], as well as to provide IC_{50} values for indole-3-acetic acid (IAA)-tacrine dual AChE/BChE inhibitors [93]. Other studies using only computational methodologies have focused on tacrine-cholinesterase complex dynamics. While recent QM/MM simulations of tacrine bound to AChE reported by Nascimento et al. demonstrated that van der Waals forces play

just as important a role as electrostatics in binding and stabilization of the complex [94], MD simulations of BChE in complex with tacrine reported by Wan et al. emphasize the importance of protonating Glu197 near the catalytic triad, which stabilizes participation of a localized water molecule and leads to preservation of the His438 residue [95].

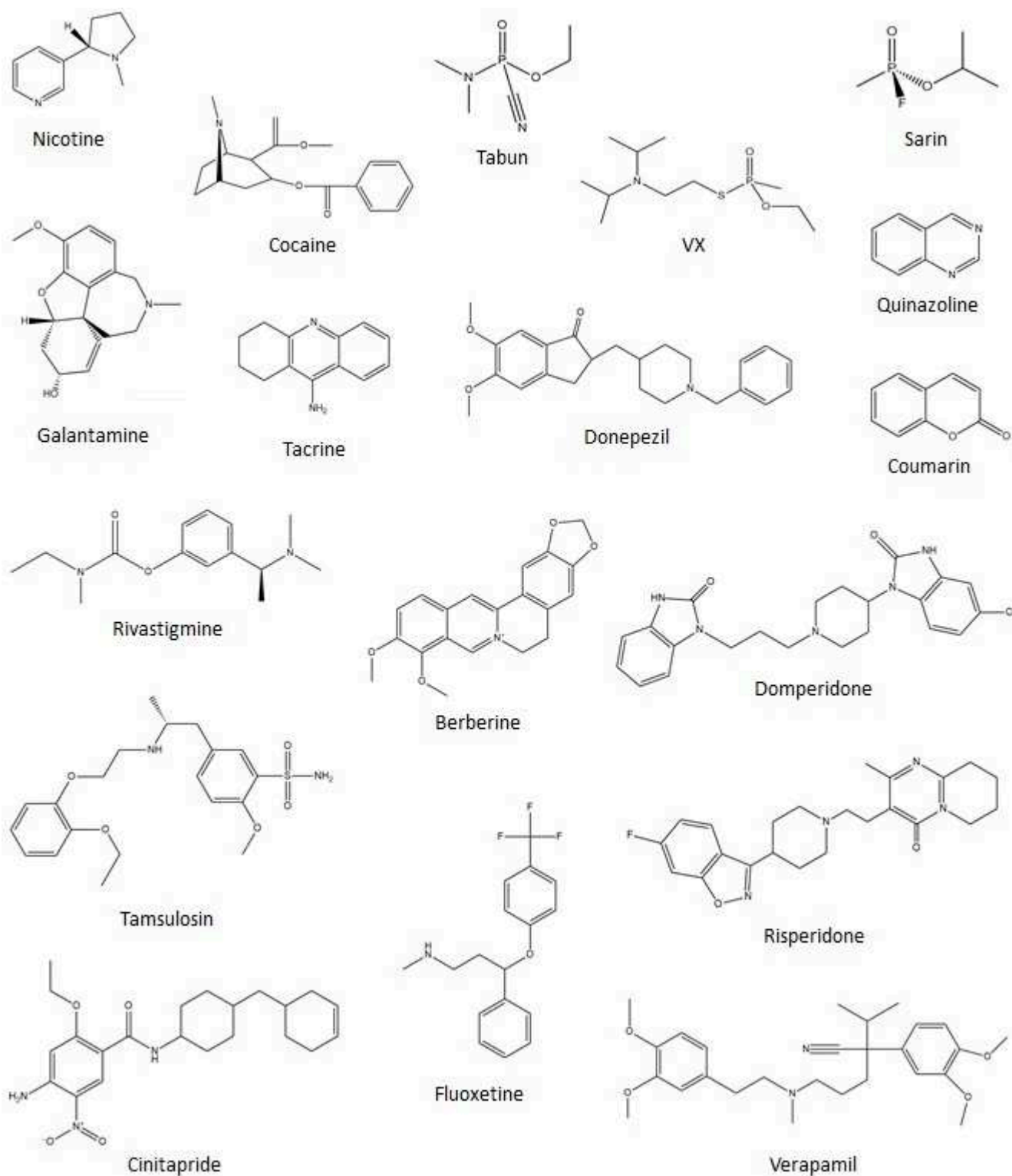


Figure 4. Chemical structures of various narcotic, nerve agent, and pharmaceutical cholinesterase inhibitors discussed in this review.

Interestingly, MD simulations of a survey of tacrine-huprine heterodimers revealed that derivatives show potential for AD and prion disease treatment because they both inhibit the PAS and CAS in AChE while reducing β -amyloid and prion peptide aggregation [96]. Other dimers that exhibit dual-site inhibitory activity with the cholinesterase enzymes are the bis(7)tacrine derivative with S-allylcysteine and cystamine, both of which can also serve as antioxidants [97,98]. The hybrid of tacrine and quercetin, dubbed Tac-Quer in a 2019 study by Habibpour et al., allows tacrine to act as an inhibitor to either AChE or BChE, while quercetin, a well-known metal scavenger, seeks Zn^{2+} , Cu^{2+} , and Fe^{2+} cations in trace quantities in brain plaque [99].

4.1.2. Galantamine and Derivatives

Galantamine, or (4aS,6R,8aS)-5,6,9,10,11,12-hexahydro-3-methoxy-11-methyl-4aH-[1]benzofuro[3a,3,2-ef][2]benzazepin-6-ol, is another pharmaceutical that targets AD, sold under the brand name Razadyne in the United States [84]. It can be isolated from the *Amaryllidaceae* family of plants [100] and, like tacrine, is used as a reference compound in drug discovery [4]. Examination of the X-ray structure of the TcAChE-galantamine complex hinted that galantamine interacts with residue Trp84 at the choline binding site and residues Phe288 and Phe290 at the acyl binding site [38]. Recent docking calculations, however, suggest that galantamine inhibits AChE at the base of the active site gorge [101], and MD simulations point to the importance of hydrogen bonds with water for inhibitor stability in the gorge [102]. While galantamine is larger than the AChE gorge entrance observed in crystal structures, a recent experimental-computational collaboration by Roca et al. illustrated that it can enter the active site pocket of the enzyme following reorientation of the PAS to traffic the ligand inside, as mentioned previously [39].

4.1.3. Donepezil and Derivatives

Donepezil, or 1-benzyl-4-[(5,6-dimethoxy-1-indanon-2-yl)methyl]piperidine, sold under the brand name Aricept [84], also serves as a reference compound in drug discovery studies [102], and was shown in a recent MD study by the Treptow laboratory to act as a mixed competitive and non-competitive inhibitor that interacts strongly with the PAS, ABS, and CAS regions of AChE [103].

QSAR examinations into cholinesterase inhibition have produced handfuls of donepezil derivatives [104,105], indicating that the parent compound is structurally favored to be an inhibitor. Docking simulations of pyridonepezil and quinolinodonepezil derivatives were performed with both cholinesterases, with quinolinodonepezil derivatives proving much less effective at inhibiting human AChE than pyridonepezil derivatives [106]. Marco-Contelles and coworkers took a multi-pronged approach to study donepezil-pyridyl hybrids, which proved to inhibit both cholinesterases at the PAS and CAS, and suggested that the N-alkyl bridge could be used to selectively enhance AChE inhibition by such pyridine-based derivatives [104]. Docking studies by Al-Rashid and Hsung further suggest that the E-ring in the donepezil-like (+)-arisugacin A compound can play a crucial role in binding to AChE [107], and Rahman et al. employed DFT and docking to demonstrate that halogenated derivatives of donepezil, including fluorine and chlorine groups, also show AChE inhibiting potential [108].

In a computational-experimental collaborative study focusing on a series of N-substituted amine derivatives [84], docking and MD simulations were performed using the AChE crystal structure from the pre-formed AChE-donepezil complex and some compounds were observed to mimic the binding pose (position and orientation) of donepezil [109]. In another more recent study, well-tempered metadynamics (WTMD) simulations of AChE in complex with donepezil by Ghosh et al. showed the protein-ligand complex to increase the ordering of water molecules around Ser203 of the CAS, which discourages ACh from interacting with the active site [110]. Hybrids of donepezil's benzylpiperidine moiety connected via an oligomethylene linker to an indolyl propargylamino moiety were examined via MD simulations and identified as dual-site binding cholinesterase inhibitors [111]. Docking and

MD simulations by Yekta et al. suggest that glycosylated-AChE (a glycine and AChE complex) poses a challenge for donepezil binding due to the rearrangement of Trp286 and Tyr341 that block this inhibitor from entering the binding cavity [112].

4.1.4. Rivastigmine and Derivatives

Exelon is the brand name for rivastigmine, or [3-[(1S)-1-(dimethylamino) ethyl]phenyl] N-ethyl-N-methylcarbamate [84]. Docking and MD simulations conducted recently by Ali et al. show that, due to the presence of rivastigmine, TcAChE undergoes carbamylation [102]. Rivastigmine and numerous conformationally restricted analogs were studied by Bolognesi et al. using Monte Carlo calculations, which suggested that the carbamic N-alkyl chain has a more negative effect on binding to AChE than BChE due to the larger acyl binding site present in BChE [113]. Another much more recent study by Wang et al. focusing on a series of chalcone-rivastigmine hybrids support this observation, with results from MD simulations showing rivastigmine hybrids to bind to BChE more easily [114].

4.1.5. Quinazoline and Derivatives

Quinazoline is another pharmaceutical that has been considered as a potential AD treatment. In fact, a number of derivatives have been FDA-approved as anti-cancer and anti-tumor drugs, including Gefitinib, Erlotinib, Vandetanib, Lapatinib, and Afatinib [115]. Although, of the two cholinesterases, quinazoline derivatives seem to bind more effectively to AChE [116], the addition of alicyclic groups to quinazoline analogs increases the binding affinity towards BChE, as these groups bind more effectively to the PAS [117]. Homobivalent quinazolinimes are also derivatives that bind more closely with BChE; here, in docking simulations, the homobivalent quinazolinimes engage with BChE with π -interactions that are absent in the AChE complex [118]. However, in a study by the Decker laboratory tricyclic and tetracyclic quinazoline derivatives led to an “inverted binding mode” with the aliphatic amine in the center [119] and Daoud et al., who used a multi-pronged computational approach to study cholinesterase inhibition, found that pyrazinamide derivatives exhibit strong hydrogen bonding with Tyr121 in TcAChE and Tyr332 in BChE, suggesting that these derivatives are ChE effective inhibitors [120].

4.1.6. Coumarin

Coumarin, or 2H-1-benzopyran-2-one, a natural product found in many plants, has been scrutinized as a potentially potent cholinesterase inhibitor comparable to tacrine. Recent molecular docking simulations by Tanoli et al. reveal that the most potent coumarin derivatives, containing both piperidinyl and ethoxyl groups, lower the binding energy with AChE by nearly 1.5-fold that of tacrine. Large substituents attached to the coumarin ring enable these inhibitors to increase molecular contact with grooves in the enzyme active site gorge including, notably, simultaneous interactions with residues from the choline binding site, the peripheral aromatic site, and the catalytic triad [121]. Coumarin-linked thiourea derivatives exhibit similar binding modes in docking calculations, forming contact with the catalytic triads of both AChE and BChE [122]. However, in this same study, the thiourea group is observed to consistently hydrogen bond with Tyr146 of AChE, with no analogous hydrogen bonding observed for BChE due to the structural differences between the two enzymes. Moreover, hydrophobic interactions appear to dominate electrostatic interactions in these docking results. Another coumarin derivative, 7-hydroxycoumarin, also displays dual binding site capability with both the PAS and CAS of both cholinesterases [123]. A recent docking and MD study conducted by the Mubarek laboratory indicates that while hydrophobic interactions are dominant in stabilizing AChE in complex with coumarin derivatives, structural stability of BChE in complex with these species is predominantly due to hydrogen bonding [124].

4.1.7. Other Pharmaceuticals

A variety of other FDA-approved drugs not intended to treat AD have been examined as possible cholinesterase inhibitors using computational methods. For example, adamantyl-based ester derivatives, which have been more widely used as acne, type 2 diabetes, and anti-viral medications, were studied in complex with both cholinesterases via docking; compounds with a methoxy substituent at position three on the phenyl ring showed the highest potential of binding strongly to both AChE and BChE [125].

Curiously, a number of marine metabolites, which show promising capabilities as pharmaceuticals, were docked with AChE and analyzed as potential treatments for AD [126]. From a database of FDA-approved drugs, Hassan et al. recently employed a screening technique that chose five drugs with higher capacity for AChE inhibition: Risperidone (for schizophrenia and bipolar disorder), Domperidone (for nausea and vomiting), Verapamil (for high blood pressure), Tamsulosin (for enlarged prostate), and Cinitapride (for nausea and ulcers); MD simulations indicated that all complexes were stable [127].

Another recent study by Ozer and coworkers employed docking calculations to understand interactions between BChE and fluoxetine, also known as Prozac, which is commonly used to treat anxiety, obsessive compulsive disorder, and anorexia [128]. Coupled with experimental kinetics measurements, fluoxetine proved to be a competitive inhibitor of BChE that binds deep in the active site gorge [128]. Previous MD and docking studies of BChE in complex with berberine derivatives, compounds found in medications for diabetes and high cholesterol, indicated that Trp82 (CBS), Gly117 (OAH), Trp231 (ABS), and Phe329 (CBS) are all important for binding [129]. Pyridoxine, commonly known as vitamin B6, is also recognized for its AChE inhibition ability: MD simulations of this complex indicate that the ligand forms a covalent bond with Ser203 of the catalytic triad, thus creating a steric barrier for acetylcholine [130].

4.2. Narcotics

Another field of inhibition centers around the interactions between narcotics and the cholinesterases, particularly BChE. As mentioned above, BChE is a promiscuous plasma enzyme, and can thus hydrolyze a variety of substrates during circulation. For example, BChE is one of the enzymes responsible for hydrolyzing, and subsequently activating, heroin, making it an ideal enzyme to target as a treatment for heroin overdose. In a recent study by Zhou et al. that addresses the need to block the activation of heroin by BChE, novel inhibitors from solanaceous alkaloid scaffolds were discovered via virtual screening, thus identifying a series of highly selective BChE inhibitors [131].

Recent docking and MD studies have also investigated cholinesterase interactions with nicotine and numerous derivatives thereof. For example, investigations into nicotine-AChE complexes using MD simulations, in tandem with experimental efforts, showed R-nicotine to more strongly disturb the secondary structure of, and to be a stronger inhibitor of, AChE than the S-nicotine analog [132]. Nicotine is the parent compound to the neonicotinoid family, which are present in commercial insecticides and, unsurprisingly, act as agonists to ACh receptors. In a 2018 study, Terali assessed the seven commercially available neonicotinoids using docking calculations, revealing different binding modes with AChE and BChE, and suggesting them to be potential compounds to treat cholinergic and non-cholinergic AD pathogenesis [133].

As discussed in the catalysis section above, cocaine is also a narcotic of interest for cholinesterase studies, and details of the catalytic mechanism of cocaine hydrolysis were discussed in that section. From MD simulations and hydrogen bonding energy (HBE) calculations, the energy barrier for hydrolysis of ACh by each enzyme was compared to the hydrolysis of (+)- and (−)-cocaine by human BChE and both of these differences were found to be approximately 3–5 kcal/mol [62]. This energy difference is attributed to the fact that only Gly117 and Ala199 in the OAH of BChE interacts with the carbonyl oxygen of cocaine, with Gly116 not participating [62,134].

A focal point in computational research of BChE-cocaine complexes is how BChE can be mutated to hydrolyze cocaine faster and remain in circulation longer as a possible treatment for cocaine overdose [30]. For example, MD simulations uncovered that mutations of Phe547, Met554, and Phe561 (in the C-terminus section of hBChE) to more hydrophobic residues may increase its circulation [30]. Circulation time of BChE may also be increased due to the introduction of more cross-subunit disulfide bonds, resulting in higher dimer stability as suggested in an MD study by Fang et al. [135].

Decreasing the activation energy for transition states, particularly for the rate-determining step, is another approach to amplify BChE catalytic efficiency. After combined computational and experimental studies revealed the rate determining step for the Ala328Trp/Tyr332Ala and Ala328Trp/Tyr332Gly BChE mutants [78,136], MD simulations and virtual screening techniques were employed to determine how these mutations could lower these energy barriers, eventually yielding a mutant that was approximately 2000-fold more catalytically efficient than WT BChE, the 5-point mutant Ala199Ser/Phe227Ala/Ser287Gly/Ala328Trp/Tyr332Gly [137]. The aforementioned Ala328Trp/Tyr332Ala and Ala328Trp/Tyr332Gly BChE mutants were identified as being more catalytically active than WT human BChE, whose binding modes with (–)- and (+)-cocaine isomers as prereactive and non-prereactive complexes are displayed in Figure 5 [138]. The Ala328Trp/Tyr332Ala/Tyr419Ser mutant studied therein lost catalytic potency, as the conformation in which cocaine binds to this mutant is not conducive to catalysis [138]. Not all BChE mutants, however, are more catalytically efficient than WT BChE. Prompted by kinetics studies [139,140], a 2015 MD study of mouse and human BChE, alongside their Ala199Ser/Ser227Ala/Ser287Gly/Ala328Trp/Tyr332Gly mutants, showed that the parent enzymes are approximately 250-fold more catalytically effective than their derivative hydrolases [141].

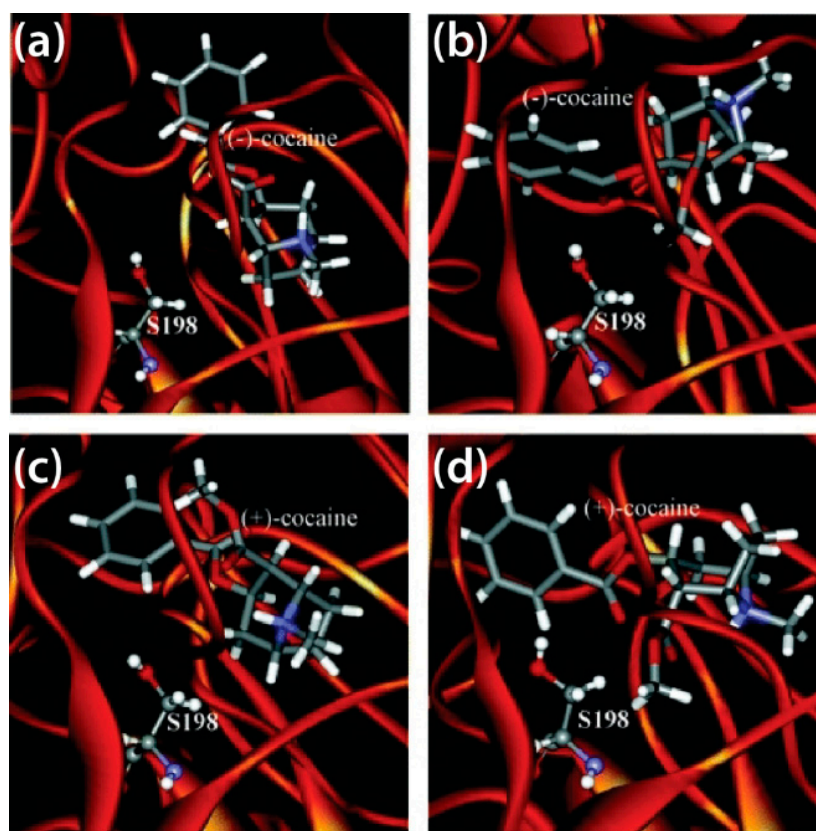


Figure 5. Wild-type BChE bound to (a) (–)-cocaine in a non-prereactive complex, (b) (–)-cocaine in a prereactive complex, (c) (+)-cocaine in a non-prereactive complex, and (d) (+)-cocaine prereactive complex [138].

4.3. Organophosphates

4.3.1. Reversible Inhibition

Many organophosphates (OPs) with good leaving groups (weak bases) bind irreversibly to both cholinesterases, and molecular recognition complexes have been examined with docking and MD simulations. Human, mouse, and housefly models of AChE, as well as horse BChE, in complex with O,O-dialkylphosphate inhibitors suggest that the amino acid at position 400, which is either valine or phenylalanine, plays a key role in determining how well the OP will bind in the pocket based on the bulkiness of that amino acid [142]. Furthermore, Lee and Barron studied insect and mouse AChE with OP inhibitors using docking/QSAR techniques, demonstrating that Leu328 in the acyl binding site of insect AChE allows for less enzyme specificity in comparison to Phe295 of mouse AChE, and emphasized the importance of interactions with the OAH [6].

Around this same time, Veselinovic et al. used Monte Carlo as part of their QSAR analysis to identify the best AChE inhibitors from a database of 278 OP compounds, with the goal of reducing cholinergic activity [143]. In recent months, Yang et al. published their combined Monte Carlo/MD study of TcAChE adsorption in charged monolayers, which revealed that binding sites in the active site gorge orient themselves toward positively charged surfaces and away from negatively charged surfaces, a somewhat intuitive result given that cholinesterases have evolved to attract and hydrolyze positively charged choline moieties, but also providing useful insight for experimentalists using AChE as a means to detect OP compounds [144]. Also reported in the last few months were docking calculations of *Electrophorus electricus* AChE in complex with the voluminous and negatively charged 12-tungstosilicic acid and 12-tungstophosphoric acid, which allowed for detection of a previously-unknown allosteric binding site that has been subsequently labeled β -AS [145].

BChE-OP molecular recognition complexes have also been investigated by the Sorin laboratory using docking and MD methods. In a collaborative 2017 study that featured experimental work, the structural basis for relative K_I values was probed via massive docking calculations for an assortment of dialkyl and aryl phosphate inhibitors in complex with BChE [146]. That same year, a massively-parallel MD study involving a very limited number of dialkyl phenyl phosphates probed the entropy change associated with binding to these OPs, and demonstrated there to be residual entropy associated with larger, more complex inhibitors that can sample from a much broader array of binding microstates (poses), thus adding to the stability of those larger and more flexible inhibitors entropically [147].

More recently, this same laboratory studied an array of dialkyl phenyl phosphate inhibitors via MD simulation, including numerous phenyl substitutions that had been previously probed via docking calculations [146] and a small set of alkyl-to-cholinyl substitutions to mimic the chemistry of the natural substrates. It was noted therein that larger R-groups increase van der Waals contact area between the enzyme and the ligand, with S-enantiomers apparently binding more strongly than their R analogs [35]. In an effort to characterize the observed modes of binding in the flexible BChE-OP complexes, contact tables such as that shown in Figure 6 were used to highlight specific interactions between portions of the inhibitor and specific binding sites and amino acids in the BChE active site gorge. Each row below the label rows at the top represents a binding mode, and every column is an amino acid residue known to participate in binding. Here, contacts are identified as chemical groups separated by 5 Å or less and the cell entries report which functional group dominates that interaction based on relative intermolecular interaction strength.

In a 2020 follow-up study, these BChE-OP were subject to massively-parallel MD simulation and then used as model systems around which to develop a methodology for accurately identifying binding modes from such rich data sets [148]. The resulting technique, brute force k -means clustering of surface-weighted interaction fingerprints (SWIFs), employs simple and intuitive statistical criteria to identify binding modes, and bypasses the heuristic nature of the k -means clustering algorithm. The contact table in Figure 6, taken from this most recent publication [148], demonstrates distinct binding

modes for the OP inhibitor that binds most strongly to BChE of those so far studied by that laboratory and their collaborators, with $K_1 = 1(\pm 0.4) \mu\text{M}$.

1000 Sims DIM5	ASN68	ASP70	GLN119	ALA277	SER287	TYR332	SER198	GLI325	HIS438	GLY116	GLY117	ALA199	TRP82	ALA328	PHE329	TRP281	PRO285	LEU286	VAL288	PHE308	ILE69	GLN71	PHE73	PRO74	GLY75	PHE76	MET81	ASN83	SER79	TYR114	GLY115	PHE118	THR120	TYR128	GLU197	ASN397	TRP490	MET497	GLY499	TYR440	ILE442	Pop (%)			
Mode	PAS			CAT			OAH			CBS			ABS			OML			Additional Protein Residues (APR)																										
0			Ph	AK1	Ph	PO4	PO4	PO4	PO4	PO4	AK1	PO4	AK2	PO4	AK1	AK2	AK1	AK1	AK1	AK1	Ph											PO4	AK1	PO4		PO4								28.7	
1			Ph	AK1	Ph	PO4	PO4	PO4	PO4	PO4	AK1	PO4	AK2	PO4	AK1	Ph	AK1	AK1	AK1	AK1	Ph								Ph		PO4	AK1	PO4		PO4									20.2	
2			Ph	AK1	Ph	PO4	PO4	PO4	PO4	PO4	AK1	PO4	AK2	PO4	AK1	Ph	AK1	AK1	AK1	AK1	Ph					Ph	AK2				PO4	AK1	PO4		PO4										18.7
3			Ph		Ph	PO4	PO4	PO4	PO4	PO4	AK1	PO4	AK2	PO4	AK1	PO4	AK1	AK1	AK1	AK1	Ph										PO4	AK1	PO4		PO4									13.2	
4			PO4	AK1	Ph	AK1				AK1	PO4	AK1	Ph	Ph	PO4	AK1	Ph	AK1	PO4	AK1	AK2										AK1	PO4		PO4									9.2		
5	Ph		PO4	AK1	AK2	PO4	AK1	PO4	AK1	PO4	AK2	PO4	AK1	PO4	AK1	AK2	AK1	AK1	AK1	AK1	AK2	Ph									PO4	AK1	PO4		PO4								6.6		
6		Ph	AK1	AK1	Ph	AK1	PO4	PO4	PO4	AK1	PO4	AK2	PO4	AK1	PO4	AK1	PO4	AK1	AK1	AK1						Ph	AK2							PO4										3.4	

Figure 6. Contact table for the DIM5 inhibitor in BChE binding pocket. SWIFs were taken post 80 ns from one thousand 110 ns MD simulations [148].

4.3.2. Irreversible Inhibition, Activation, and Reactivation

While the section above centered on reversible molecular recognition of OP inhibitors, “aged” cholinesterases are those that have undergone phosphorylation and have experienced significant structural change, thereby rendering them catalytically impotent. A survey of the energy landscape of the acyl pocket loop uncovered that the products of the reaction between AChE and diisopropyl fluorophosphate deviate significantly from the AChE crystal structure [149].

Like some narcotic and catalysis studies, researchers have focused on how BChE mutants can address and add insight to OP poisoning. For instance, Dwyer et al. found that BChE mutants Tyr332Ser, Asp340His, and Tyr332Ser/Asp340His all resist nerve agents by modifying the size of the “main door” [150]. However, in the case that the enzyme is already bound to the OP, Masson et al. focused on transition states in order to find more catalytically efficient mutants [151], and a more recent study by this same team showed that other mutations, such as Asn322Glu/Glu325Gly with an alternate Ser198, His438, Asn322Glu catalytic triad, allow complexes to self-reactivate [60].

MD simulations have also shown that minor mutations, such as replacing Gly116 in the OAH of BChE, could cause severe structural deviations [152], and simulations of the Gly117His and Gly117Asp mutants of BChE revealed the presence of a water molecule near Ser198 in the catalytic triad, which may be responsible for the reordering of water and subsequent conformational changes present in the mutants [152]. When these water molecules are replaced by glycerol molecules in cresyl saligenin phosphate-phosphorylated BChE, there is a conformational change caused by His438 leading to a less reactive intermediate complex [5]. The structure of the Gly117His BChE mutant, studied via X-ray by Nachon et al. [153], was probed by Amitay and Shurki, who identified a single conformation from a set of computationally-generated structures that would fully reproduce the acetylation of acetylthiocholine [154]. The Gly117His BChE mutant was further explored as a potential OP bioscavenger in a QM/MM study by Yao et al. that reported improved activity against sarin by reducing the rate-determining energy barrier compared to wild type hBChE [155], as demonstrated in Figure 7.

The introduction of another compound as a reactivator to aged, or phosphorylated, cholinesterase has also been considered. Many reactivation studies have centered around AChE because of its crucial role in neurotransmission, which is interrupted by the introduction of nerve agents and insecticides, but a recent structure-based study suggested that small molecules (<200 Da), such as oximes, may act as strong antidotes for OP-poisoned AChE [9]. Oximes have been widely explored as reactivators for deactivated cholinesterases, so it is no surprise that the structure-activity relationship and docking studies proposed oxime-based compounds as antidotes for cholinesterases poisoned by OPs [156,157].

Nerve agents such as VX (venomous agent) and sarin (GB, as classified by the US-American military) have also been a focal point of studies on cholinesterase reactivation. Oximes used as reactivating compounds for OP-poisoned AChE are supported by computa-

tional and experimental research [158]. The prereactive complex of the oxime HI-6 and *Mus musculus* AChE covalently inhibited by sarin was examined by Allgardson et al., whose X-ray investigations and DFT calculations provided an essential foundation for research into the reactivation mechanism of OP-poisoned AChE [159]. Monte Carlo calculations by Veselinovic et al. of AChE-sarin reactivation reiterated that pyridinium oximes are decent antidotes [160]. A more recent study of charged and uncharged oximes by de Souza et al. compared these species with VX- and GB-poisoned AChE: while charged oximes proved to outperform the uncharged oximes, it is also an unfortunate reality that charged oximes do not cross the blood-brain barrier very well, making physical intake of the better reactivator more difficult [161]. Despite this setback, oximes are generally explored in more depth compared to pre-exposure antidote carbamates because carbamates also change the AChE structure via carbamylation [162].

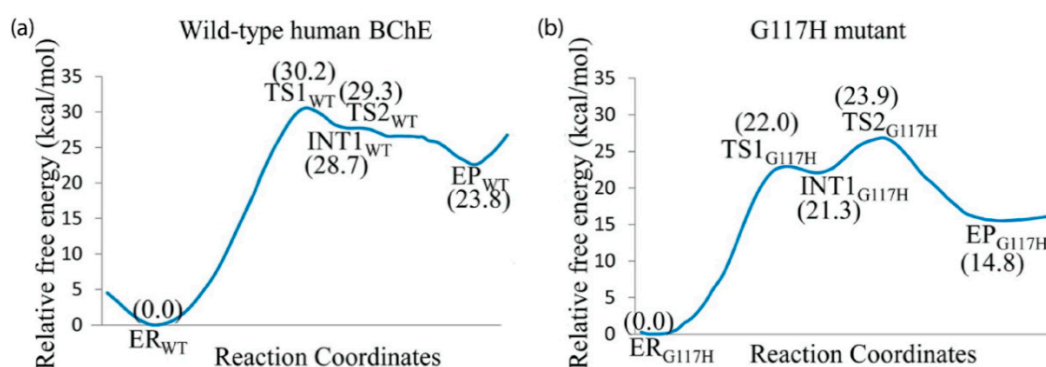


Figure 7. Free energy profiles for the reactivation of sarin-phosphorylated human BChE for (a) wild type hBChE and (b) the G117H mutant discussed in the text [155].

Tabun (GA, as designated by the US-American military) is, unlike other nerve agents, particularly resistant to oxime compounds as reactivators [163]. This resistant quality has motivated researchers to find more effective oxime derivatives for tabun-cholinesterase complex reactivators. Dimethyl(pyridin-2-yl)sulfonium based oximes were examined at the DFT M05-2X/6-31G* level and determined to be better reactivators, as they lower the energy barrier by 4.4 kcal/mol [164], and hierarchical ab initio calculations revealed that charged oxime derivatives as antidotes to tabun bound AChE are stronger than normal oxime compounds due to specific stereoelectronic characteristics [163]. Indeed, a 2014 study by Lo and Ganguly found charged oximes to be more effective than their uncharged analogs, and their QM/MM studies further suggested that N-(pyridin-2-yl)hydroxylamine is a better antidote than traditional oxime treatments and that it has a similar IC₅₀ value [165].

Treatments for general nerve agent and insecticide poisoning have utilized oxime derivatives as well. Reactivation of a VX-AChE complex using a deprotonated pralidoxime, or 2-pralidoxime (2-PAM), occurs through consecutive addition-elimination steps and shows promising results as an antidote [166]. Docking and QM/MM methods paired with experimental observations revealed that trimedoximes show potential to reactivate *Mus musculus* AChE, with the AChE-VX complex showing the best results [167], and MD simulations of 2-PAM with phosphorylated AChE support this claim [168]. The importance of protonated Glu202 in the reactivation of VX-inhibited mouse AChE was observed in QM/MM simulations performed by Driant et al. [169]. Further, symmetrical and unsymmetrical isoquinolinium-5-carbaldoximes showed strong inhibition for both cholinesterases; the weaker inhibitors were selected for additional experimental and computational investigation [170]. Interestingly, QSAR studies found that a combination compound consisting of tacrine and acryloyl acid phenylamide moieties showed potential as pre-exposure OP-poisoning antidotes [171].

4.4. Other Organic Moieties

4.4.1. Hydrocarbons

The Sepčić laboratory studied the interactions of the carbon-based nanomaterials (NM) carbon black (CB), fullerene (C₆₀), and graphene oxide (GO) in complex with AChE experimentally and with docking and MD simulations, finding that CB inhibited AChE most efficiently, while C₆₀ was least efficient and interactions with the GO surface allowed AChE to retain its native shape and activity [172].

Flavonoids are targeted as potential inhibitors that are not regulated by the FDA. Vats et al. found a number of flavonoid analogues to be novel AChE inhibitors via QSAR analysis [173]. Another sub-class of flavonoids are catechins, including hydroxyl-rich epicatechin, which has been undergoing trials as a potential therapeutic for diabetes and cancer. Of these, epicatechin 3,5-O-digallate was investigated with docking and MD simulations in complex with BChE and found to bind closely to the His484 residue of the catalytic triad with as many as six stabilizing hydrogen bonds [174].

As noted above, investigations into cholinesterase structure and function in the presence of certain toxins are of significant interest. The behavior of aflatoxin, for example, which is regulated by the FDA, not as a pharmaceutical but as a toxin, was examined by Sanson et al. in complex with AChE using MD simulations [50], which revealed that the presence of aflatoxin and its interaction with Trp84 (in the CBS) caused enlargement of the active site gorge [50]. Furthermore, a recent study by the de Almeida laboratory showed aflatoxin M1, a toxic natural compound found in contaminated dairy products, to be another potential inhibitor of AChE, which binds to the CAS region of AChE but does not bind to or inhibitor BChE [175].

Other compounds that have been considered as BChE inhibitors include derivatives of 2-phenylbenzofuran [176]. MD simulations revealed that, while these derivatives bound to the PAS and CAS sites quite well, a derivative that included a para-position hydroxy group on the phenyl moiety improved inhibition against BChE [176]. Phenyl valerate is another aromatic hydrocarbon that has been studied recently in complex with BChE by Estevez et al.: they observed via MD simulation that phenyl valerate inhibits BChE at different ends of the active site gorge, thereby inhibiting the hydrolysis of ACh; it was experimentally determined, however, that both phenyl valerate and ACh can be hydrolyzed simultaneously [177], highlighting the need for extensive simulation time with respect to complex systems and caution when interpreting the results of those simulations.

4.4.2. Nitrogenous Compounds

Amines

Amines are one of the most common functional groups occurring in nature. As a reminder, compounds are placed in this section due to the general abundance or consistent occurrence of amine groups in the inhibitor series studied in a given paper. For example, piperidine is an amine-containing compound that has been considered as a cholinesterase inhibitor in a handful of publications, including phenoxyethyl piperidine derivatives, which were studied via MD simulation in complex with electric eel AChE and horse BChE [178]. The phenoxyethyl derivatives most structurally similar to donepezil had the ability to bind to both the CAS and PAS, while many others bound only to the CAS [178]. In contrast, piperidine compounds substituted with arylaminopropanone were recently examined by Hudcova et al. via docking, MD, and QM/MM approaches and were compared to rivastigmine and galantamine [179]. In fact, our current appreciation for the role of hydrophobic active sites residues in binding is highlighted by a previous study by Khayamian and coworkers, who tested 68 piperidine and amine compounds as AChE inhibitors using docking and MD simulations, thereby confirming that hydrophobic interactions are a dominant factor in cholinesterase-inhibitor binding [180].

A handful of other amine compounds have been considered as possible cholinesterase inhibitors. Docking simulations of 4-acetoxy-plakinamine B in complex with AChE uncovered that the inhibitor binds primarily with the PAS and ABS [181]. Moreover, Shrivastava

et al. recently studied 23 *p*-aminobenzoic acid derivatives in complex with both AChE and BChE, which were compared to the binding affinity of donepezil [182], and 1*H*-benzimidazole compounds with amine substituents were shown, in a previous study, to prefer BChE in docking and MD simulations [183]. Indeed, around 85 amine-containing compounds were used as an input to a QSAR study by Abuhamdah et al., with 24 compounds exhibiting micromolar IC₅₀ values [184].

Amides, Imides, Imines, and Carbamates

Other miscellaneous but common nitrogenous functional groups and compound types are amides, imines, and carbamates. Imides are one of the least examined groups, which is acceptable given the large swath of papers with inhibitor series that have little in common with each other. A QSAR analysis of 84 *N*-aryl-monosubstituted derivatives provided 42 imide inhibitors and emphasized the importance of interactions with the Trp82 and Trp86 residues in BChE and AChE, respectively, via MD simulations [185]. Imines are close behind, with *N*-(1-(5-bromo-2-hydroxyphenyl)-ethylidene)-3,4,5-trihydroxybenzohydrazide, a Schiff base derivative and the most potent AChE inhibitor in this series of compounds, revealed via docking calculations to interact mostly with the PAS and ABS [186], as was reported above.

Amide compounds have been more widely studied as cholinesterase inhibitors, including anandamides and acylethanolamides (NAEs), commonly found in most tissues, along with oleoylethanolamide and palmitoylethanolamide, which were docked with BChE; the latter were found to be uncompetitive inhibitors of BChE, and anandamides were found to be noncompetitive [187]. Docking and MD were also utilized to study the inhibitory activity of 4-aryl-oxo-2-aminybutamides with both AChE and BChE. Although many of these compounds were ineffective towards AChE, the most potent AChE inhibitors displayed a tendency for stronger interactions between -NH moiety and the Tyr124 hydroxyl in the PAS [188]. More recently, Singh and Gupta used a multi-pronged QSAR analysis, docking, and MD approach to study a series of potential AChE inhibitors in which over half contained amide groups, reporting that inhibitors lacking amide groups received lower docking scores [189].

Carbamates are structurally similar to amides and carbamate-based inhibitors thus behave similarly to amide-based inhibitors. Recently reported RMSD calculations of carbamate-based inhibitors in complex with AChE were found to reach structural equilibrium after about 6 ns of MD simulation time and demonstrated that carbamate inhibitors with aromatic rings were more strongly drawn to AChE's binding pocket [190]. Indeed, from another recent MD-based study of thymol carbamates in complex with BChE, the importance of hydrophobic interactions with Trp82 (CBS), Gly116 (OAH), and Gly197 was emphasized in relation to MR-complex stability, as were water mediated interactions within the complex [191]. Analogously, the stability of AChE-inhibitor complexes was found to depend strongly on hydrophobic interactions with Tyr341 and Trp286 (near gorge entrance) and hydrogen bonds with Tyr124 (also near gorge entrance) and Phe295 (farther down inside the gorge) [191].

Nitrogenous Heterocyclic Rings and Derivatives

One class of molecule common to this group are indoles and indole derivatives, a number of which have been studied via docking. For example, docking calculations by Dominguez et al. with AChE revealed that meta-substituted benzylamine indole derivatives outperformed other indole cholinesterase inhibitors [192]. Dileep et al. also docked indole-3-acetic acid (IAA) and indole 3-butyric acid (IBA) derivatives with AChE; these indoles are known as auxins, or plant growth regulators, which are used in culture experiments for plant tissue [193]. Most recently, Bingul et al. docked six 4,6-dimethoxyindole based hydrazide-hydrazones that were found to bind to both AChE and BChE more strongly if they contained a phenyl group [194].

Piperine, a chemical closely associated with black pepper, has also been investigated as a potential cholinesterase inhibitor. Arylamino propanone derivatives substituted with

piperidine were docked and simulated with both cholinesterases, proving that they perform most similarly to galantamine and rivastigmine among the series of arylaminopropanone with N-phenylcarbamate moieties [179]. In another recent docking study, piperidine and curcumin, a chemical found in turmeric plants, were found to bind most closely to AChE, with binding energies of -10.5 kcal/mol and -9.6 kcal/mol, respectively [195], and it has been shown that cholinesterase binding sites most responsible for strong interactions with piperidine, as with many of the species discussed above, are the CAS and the PAS regions of the gorge [196,197].

Docking and MD simulations revealed that isoalloxazine derivatives with an ortho dimethoxybenzyl group were favorably bound to the peripheral binding site of AChE [198]. AChE-docked 4-aminopyridine semicarbazone derivatives with biphenyl rings had stronger hydrophobic interactions and overall better binding affinities than derivatives without those groups [199]. Carbazole-based stilbene derivatives were also docked with both cholinesterases, as well as the $A\beta_{1-42}$ peptide, and displayed potential as a multitarget inhibitor for AD in a 2020 study by Patel et al. [200].

One interesting potential cholinesterase inhibitor comes from the Chilean *Rhodophila* (Amaryllidaceae) plant. Docking simulations were performed on *Rhodophila* compounds with the highest alkaloid compositions, with IC_{50} values also reported from in vitro experiments [201]. The Bohorquez laboratory also studied novel N-allyl/propargyl 4-substituted 1,2,3,4-tetrahydroquinoline derivatives in complex with both AChE and BChE. Their results from docking, MM/GBSA simulations, and experimental work showed a high correlation between the calculated binding free energy and inhibitor activity for both cholinesterase targets [202]. Several years later, this same team studied tetrahydroquinoline (THQ)-isoxazole/isoxazoline compounds, which proved to have similar binding modes to galantamine [203]. Furthermore, tricyclic and tetracyclic nitrogen bridgehead compounds in complex with AChE were investigated with docking and MD simulations as potential inhibitors for AD treatment by the Decker group, with their strongest inhibitor in the tens of nanomolar regime [204].

Interestingly, numerous molecules are studied in tandem with other receptors and enzymes. For example, the Decker group effort noted above also used docking and MD to understand the high affinity of their inhibitors for the human histamine H_3 receptors [204] and Samadi et al. docked heterocyclic substituted alkyl and cycloalkyl propargyl amines to AChE, BChE, and monoamine oxidases, which are also closely linked to AD [205]. Similarly, small benzimidazole-based molecules were studied as both BChE inhibitors and as human cannabinoid receptor agonists, highlighting the possible future development of a dual-acting therapeutic to treat AD [206].

4.4.3. Organosulfates

It is noteworthy that many studies have used inhibitor series that consistently contain sulfur groups. In some cases, sulfur groups are not the intended focal point; however, since sulfur is a common element in nature, it is deserving of a sub-section. One example is a pair of recent studies by Hassan et al., who studied a series of amide and piperazine sulfonamide derivatives via docking with AChE and BChE [207,208], in which the piperazine sulfonamide derivatives with substituted alkenes proved to be the strongest BChE inhibitors [208]. Another recent example comes from the 2019 study of Yang et al., who looked at a series of inhibitors discovered from structure-based pharmacophore virtual screening and included a number of potential inhibitors containing either thiols or sulfones [209].

Phthalimide-dithiocarbamate hybrids were also recently docked with both cholinesterases, revealing binding modes that are comparable to the FDA-regulated donepezil and rivastigmine pharmaceuticals [210]. In addition, an earlier study showed 7H-thiazolo[3,2-b]-1,2,4-triazin-7-one derivatives with two substituents on the phenyl group closest to the sulfur to show promise of dual CAS and PAS binding and AChE inhibition [211]. Interestingly, a pattern of correlation was found between decreasing fluorescence intensity and increas-

ing binding activity of thioflavin-T with AChE, which was confirmed with docking and MD simulations [212].

Clearly, compounds with thiol or other sulfur-containing groups can be quite effective cholinesterase inhibitors, and early MD simulations revealed that a rivastigmine analog with a sulfur system was 192-fold more efficient at inhibiting cholinesterases reversibly than the rivastigmine parent molecule [113]. MD simulations also demonstrated that the non-competitive substrate acetylthiocholine inhibits both cholinesterases at different ends of the active site; despite the partial competition, experimental work points out that acetylthiocholine and ACh can be hydrolyzed virtually simultaneously [177]. The last compound we will mention here, benzothiazepine, was preferentially bound to BChE due to stronger hydrogen bonding, as observed in MD simulations [11].

4.5. Proteins, Nucleic Acids, and Salts

4.5.1. Protein and RNA Binding

Cholinesterase inhibition by small proteins and RNAs has also been studied computationally for a number of species. For instance, fasciculin II is a peptidic three-finger snake toxin and was observed in 5 ns MD simulations to bind to the mouth of the active site gorge in mouse AChE, effectively blocking any substrate from entering the gorge [213], as was observed in an X-ray structure from the Sussman laboratory just a few years earlier [214]. AChE was also modeled with cytochrome c (Cyt c), a heme protein generally associated with respiratory cell functions, and it was reported that AChE interactions with Cyt c play a crucial role in apoptosome formation. Macro-modeling studies reveal that Cyt c binds to the PAS of AChE, blocking gorge access a la fasciculin, and also that binding modes with AChE are similar regardless of whether the heme group in Cyt c is present (Holo) or absent (Apo) [215].

Sohail and Rashid used docking and MD simulation to study interactions between the RNA recognition motif (RRM), the most abundant RNA-binding protein domain, and BChE. While it is unclear the degree to which RRM-bound BChE would be catalytically efficient, the authors note that gaining a better understanding of these interactions in vivo could prove highly useful in therapeutic development [216]. A recent docking-based follow-up to that article reports the use of microRNA (miR-132) as a potential inhibitor of AChE, with miR-132 binding predominantly via interactions with the catalytic triad, and thus blocking access to the substrate [217].

4.5.2. Nucleobase Derivatives

Most nucleobase derivatives have focused on pyrimidine, a six-membered heterocyclic compound found in DNA and RNA. Examples of these derivatives include a series of di-phenylpyrimidine derivatives that were recently investigated as AChE inhibitors with docking and MD simulations [218,219]. The molecule labeled VB8 by Kumar et al. showed the highest activity against AChE by demonstrating additional (substituent-induced) interactions with the active site gorge [219]. Another recent docking and MD study reveals that uracil derivatives can inhibit both cholinesterases [220], and 6-methyluracil has also been recently modeled in complex with AChE and BChE, showing stronger binding than donepezil and stabilizing secondary binding to the PAS [7,221].

4.5.3. Ion and Salt Binding

Although not all salts are organic, it would be irresponsible to exclude them from this review. A 2020 docking study by Yigit et al. found amine-tethered benzimidazolium salts with a trimethyl benzyl ring to be efficient AChE inhibitors due to the close proximity and strong interaction with the CAS and the PAS [222]. Previously, 2-*N,N*-dimethylaminecyclohexyl 1-*N',N'*-dimethylcarbamate isomers and their methylsulfate salts were investigated computationally, in tandem with experimental work, as cholinesterase inhibitors, revealing that the lowest binding rate was 55% and the highest binding rate was 90% with BChE [223].

5. Virtual Screening

After exploring the multitudes of cholinesterase inhibitors that have been studied via computation, it is important to recognize progress and state-of-the-art improvements that have been made in the area of virtual screening, particularly as developed for or demonstrated on AChE and BChE. For those not familiar with the term, virtual screening is a computational method by which large libraries of small molecules can be searched for potential matches to a specific drug target. Many virtual screening methods that have been developed specifically in relation to the cholinesterase enzymes. As has been highlighted in numerous sections above, virtual screening studies are typically QSAR studies paired with docking and/or MD simulation; such studies are designed to find chemical entities and assess their potential inhibitory effectiveness [224].

As an example, Discovery Studio 2.5.5. was used to construct pharmacophore models with the goal of finding molecules that inhibit AChE and protect it from amyloid beta toxicity: from a sample of 62 compounds, only nine were found to interact favorably with AChE [225]. Some years later, the same research team used virtual screening to identify BChE-specific inhibitors from commercial databases of comprising 3.9 million compounds: virtual screening, docking, and bioassay reduced the list of possible matches to just six compounds [226]. Similar results have been reported for other virtual screening studies, including a computer-aided workflow that utilized hierarchical, structure-based screening, thereby yielding five potential cholinesterase inhibitors [227]. Furthermore, six inhibitors, three each for AChE and BChE, out of four commercial compound databases were found using structure-based pharmacophore modeling intended for AD treatment [209]. Similarly, both ZINC (zinc15.docking.org) and DrugBank (go.drugbank.com) were screened for reactivation oxime compounds [228]. As a true success story, the Gobec group developed a successful virtual screening method for BChE [229] that recently helped to realize the discovery of some of the most powerful reversible inhibitors of BChE known, with inhibitions constants in the picomolar to nanomolar range [230].

There are indications, however, that advancements in virtual screening remain to be made. For example, an early report of machine learning as a guide to virtual screening produced cholinesterase inhibitors with a wide range of IC_{50} values, suggesting that certain proposed inhibitors may be too toxic [231]. Detecting false positives would also improve virtual screening studies, an issue that was addressed when screening compounds from Maybridge.com and ChemBridge.com databases for potential BChE inhibitors, in which five ligands were chosen after ADMET calculations, Lipinski's Rule of Five, and docking simulations [232]. Accounting for inhibitor stereochemistry with respect to active site geometry is another factor to be addressed. For example, virtual screening studies of 24 chiral organophosphates revealed that S-isomers exhibited stronger inhibitory activity towards AChE than their respective R-isomers [233].

Given their pronounced gorges and well-defined binding sites, along with the extensive literature on cholinesterase studies, it is no surprise that AChE and BChE have been used as example enzymes in a number of virtual screening studies. Some methods take hands-on approaches, such as utilization of a Monte Carlo approach paired with CORAL calculations [234]. Employment of steered MD simulations that calculate the work needed to remove the ligand from the binding site proved to be more efficient than conventional MD simulations and subsequent calculations of binding energies [235]. Using docking simulations as a means of assessing ligand mobility, a factor that is considered in virtual screening, was also demonstrated on BChE [236]. Automated docking software, such as ICM-Pro [146] and AutoDock [237], has also proven insightful in recent studies.

In contrast, other researchers have developed their own virtual screening algorithms to focus solely on the cholinesterases. For example, SHAFTS (SHApe FeaTure Similarity) is a 3D similarity calculation designed for AChE ligand discovery [238] and LiSiCa (Ligand Similarity using Clique algorithm) is a virtual screening development featuring BChE [239]. Lastly, the ADAM&EVE virtual screening method was presented with a focus on AChE inhibition and identified thirteen potential compounds from an original database

of 160,000 [240]. It will indeed be exciting to see the directions in which this area grows in the years to come.

6. Conclusions

Cholinesterase structure, function, and inhibition have proven to be a source of great interest for the application of a broad spectrum of modeling and computational approaches. This review examined articles that detailed the mechanisms by which substrates and inhibitors locate and enter the gorges of AChE and BChE, how specific binding sites within the active site gorge of these enzymes respond to and interact with specific gorge binding sites, and pathways that the products of hydrolysis and other small molecules may find to enter or leave the active site. Also reviewed were computational studies of the mechanisms and thermodynamics of substrate hydrolysis by both enzymes, revealing that AChE and BChE have distinct rate-determining steps. Catalysis studies directed at BChE hydrolysis of cocaine, and the various mutations that can speed up the catalytic process, were also explored in depth.

The bulk of our findings, however, revolved around inhibition. Some major pharmaceutical compounds such as tacrine, galantamine, donepezil, rivastigmine, quinazoline, and coumarin—most of which are conventional, well-known medications for the treatment of AD and other human ailments—and their derivatives, were docked or simulated with AChE and BChE. A sizeable group of additional FDA-regulated compounds were also discussed, with the narcotic section highlighting findings regarding the cholinesterases either bound to or hydrolyzing heroin, nicotine, and cocaine. Organophosphates were heavily explored above, including: discussion of various OP compounds as potential reversible inhibitors; the irreversible binding of nerve agents such as sarin, tabun, and VX; and enzyme reactivation by molecules such as oxime derivatives. The final inhibition section, and by far the most diverse, included other organic compounds including various hydrocarbons, and nitrogenous compounds such as amines, amides, carbamates, and nitrogen heterocycles. Other organic molecules discussed were organosulfates, protein and nucleic acid derivatives, and ionic inhibitors.

Finally, advancements in virtual screening methodologies and software were discussed, with some of these methodologies specific to cholinesterases and others simply featuring them as prime applications. Although there have been hundreds of computational cholinesterase studies published in the last two decades, it is exciting to consider the many possible directions that computation will lend itself to improve our understanding of these enzymes and their function in the future, with potential real-world applications in human disease therapies, treatments for pesticide and nerve agent poisoning, and management of drug overdoses.

Author Contributions: Conceptualization, D.D.B., N.N., and E.J.S.; investigation, D.D.B., N.N., J.M. (Jia Mao), and J.M. (Jessica Moore); writing—original draft preparation, D.D.B. and N.N.; writing—review and editing, D.D.B., N.N., and E.J.S.; visualization, N.N. and E.J.S.; supervision, E.J.S. All authors have read and agreed to the published version of the manuscript.

Funding: This Review was supported by funding from the National Institute of General Medical Sciences of the National Institutes of Health under Award Numbers UL1GM118979, TL4GM118980, and RL5GM118978. The content is solely the responsibility of the authors and does not necessarily represent the official views of the National Institutes of Health.

Institutional Review Board Statement: Not applicable.

Informed Consent Statement: Not applicable.

Acknowledgments: N.N. and J.M. (Jia Mao) are grateful for undergraduate research scholarships from Women & Philanthropy. N.N. acknowledges a Boeing scholarship, and N.N. and J.M. (Jessica Moore) thank the CSULB College of Engineering for scholarship support. D.D.B., J.M. (Jessica Moore), and E.J.S. acknowledge support from the NIH BUILD program: this review was supported by funding from the National Institute of General Medical Sciences of the National Institutes of Health under Award Numbers UL1GM118979, TL4GM118980, and RL5GM118978. The content is solely the responsibility of the authors and does not necessarily represent the official views of the National Institutes of Health.

Conflicts of Interest: The authors declare no conflict of interest.

References

1. Taylor, P.; Camp, S.; Radić, Z. Acetylcholinesterase. In *Encyclopedia of Neuroscience*; Squire, L.R., Ed.; Academic Press: Oxford, UK, 2009. [\[CrossRef\]](#)
2. John, H.; Balszuweit, F.; Kehe, K.; Worek, F.; Thiermann, H. Chapter 50—Toxicokinetics of Chemical Warfare Agents: Nerve Agents and Vesicants. In *Handbook of Toxicology of Chemical Warfare Agents*; Gupta, R.C., Ed.; Academic Press: San Diego, CA, USA, 2009. [\[CrossRef\]](#)
3. Johnson, G.; Moore, S.W. Why has butyrylcholinesterase been retained? Structural and functional diversification in a duplicated gene. *Neurochem. Int.* **2012**, *61*, 783–797. [\[CrossRef\]](#)
4. Ortiz, J.E.; Pigni, N.B.; Andujar, S.A.; Roitman, G.; Suvire, F.D.; Enriz, R.D.; Tapia, A.; Bastida, J.; Feresin, G.E. Alkaloids from *Hippeastrum argentinum* and Their Cholinesterase-Inhibitory Activities: An in Vitro and in Silico Study. *J. Nat. Prod.* **2016**, *79*, 1241–1248. [\[CrossRef\]](#)
5. Masson, P.; Lushchekina, S.; Schopfer, L.M.; Lockridge, O. Effects of viscosity and osmotic stress on the reaction of human butyrylcholinesterase with cresyl saligenin phosphate, a toxicant related to aerotoxic syndrome: Kinetic and molecular dynamics studies. *Biochem. J.* **2013**, *454*, 387–399. [\[CrossRef\]](#) [\[PubMed\]](#)
6. Lee, S.; Barron, M.G. A mechanism-based 3D-QSAR approach for classification and prediction of acetylcholinesterase inhibitory potency of organophosphate and carbamate analogs. *J. Comput. Aided Mol. Des.* **2016**, *30*, 347–363. [\[CrossRef\]](#) [\[PubMed\]](#)
7. Kharlamova, A.D.; Lushchekina, S.V.; Petrov, K.A.; Kots, E.D.; Nachon, F.; Villard-Wandhammer, M.; Zueva, I.V.; Krejci, E.; Reznik, V.S.; Zobov, V.V.; et al. Slow-binding inhibition of acetylcholinesterase by an alkylammonium derivative of 6-methyluracil: Mechanism and possible advantages for myasthenia gravis treatment. *Biochem. J.* **2016**, *473*, 1225–1236. [\[CrossRef\]](#) [\[PubMed\]](#)
8. Felder, C.E.; Botti, S.A.; Lifson, S.; Silman, I.; Sussman, J.L. External and internal electrostatic potentials of cholinesterase models. *J. Mol. Graph. Model.* **1997**, *15*, 318–327. [\[CrossRef\]](#)
9. Ochoa, R.; Rodriguez, C.A.; Zuluaga, A.F. Perspectives for the structure-based design of acetylcholinesterase reactivators. *J. Mol. Graph. Model.* **2016**, *68*, 176–183. [\[CrossRef\]](#)
10. Saxena, A.; Redman, A.M.G.; Jiang, X.; Lockridge, O.; Doctor, B.P. Differences in Active Site Gorge Dimensions of Cholinesterases Revealed by Binding of Inhibitors to Human Butyrylcholinesterase. *Biochemistry* **1997**, *36*, 14642–14651. [\[CrossRef\]](#)
11. Ul-Haq, Z.; Khan, W.; Kalsoom, S.; Ansari, F.L. In silico modeling of the specific inhibitory potential of thiophene-2,3-dihydro-1,5-benzothiazepine against BChE in the formation of beta-amyloid plaques associated with Alzheimer's disease. *Theor. Biol. Med. Model.* **2010**, *7*, 26. [\[CrossRef\]](#)
12. Sussman, J.; Harel, M.; Frolow, F.; Oefner, C.; Goldman, A.; Toker, L.; Silman, I. Atomic structure of acetylcholinesterase from *Torpedo californica*: A prototypic acetylcholine-binding protein. *Science* **1991**, *253*, 872–879. [\[CrossRef\]](#)
13. Nicolet, Y.; Lockridge, O.; Masson, P.; Fontecilla-Camps, J.C.; Nachon, F. Crystal Structure of Human Butyrylcholinesterase and of Its Complexes with Substrate and Products. *J. Biol. Chem.* **2003**, *278*, 41141–41147. [\[CrossRef\]](#) [\[PubMed\]](#)
14. Dvir, H.; Silman, I.; Harel, M.; Rosenberry, T.L.; Sussman, J.L. Acetylcholinesterase: From 3D structure to function. *Chem. Biol. Interact.* **2010**, *187*, 10–22. [\[CrossRef\]](#) [\[PubMed\]](#)
15. Zhuang, Q.G.; Young, A.; Callam, C.S.; McElroy, C.A.; Ekici, O.D.; Yoder, R.J.; Hadad, C.M. Efforts toward treatments against aging of organophosphorus-inhibited acetylcholinesterase. *Ann. N. Y. Acad. Sci.* **2016**, *1374*, 94–104. [\[CrossRef\]](#) [\[PubMed\]](#)
16. Zhuang, Q.G.; Franjesevic, A.J.; Corrigan, T.S.; Coldren, W.H.; Dicken, R.; Sillart, S.; DeYong, A.; Yoshino, N.; Smith, J.; Fabry, S.; et al. Demonstration of In Vitro Resurrection of Aged Acetylcholinesterase after Exposure to Organophosphorus Chemical Nerve Agents. *J. Med. Chem.* **2018**, *61*, 7034–7042. [\[CrossRef\]](#) [\[PubMed\]](#)
17. Quinn, D.M. Resurrection Biology: Aged Acetylcholinesterase Brought Back to Life. *J. Med. Chem.* **2018**, *61*, 7032–7033. [\[CrossRef\]](#)
18. Suárez, D.; Field, M.J. Molecular dynamics simulations of human butyrylcholinesterase. *Proteins Struct. Funct. Bioinform.* **2005**, *59*, 104–117. [\[CrossRef\]](#) [\[PubMed\]](#)
19. Zhou, H.-X.; Wlodek, S.T.; McCammon, J.A. Conformation gating as a mechanism for enzyme specificity. *Proc. Natl. Acad. Sci. USA* **1998**, *95*, 9280–9283. [\[CrossRef\]](#)
20. Shen, T.; Tai, K.; Henchman, R.H.; McCammon, J.A. Molecular Dynamics of Acetylcholinesterase. *Acc. Chem. Res.* **2002**, *35*, 332–340. [\[CrossRef\]](#)
21. Cheng, S.M.; Song, W.L.; Yuan, X.J.; Xu, Y.C. Gorge Motions of Acetylcholinesterase Revealed by Microsecond Molecular Dynamics Simulations. *Sci. Rep.* **2017**, *7*, 3219. [\[CrossRef\]](#)

22. Xu, Y.; Colletier, J.-P.; Weik, M.; Jiang, H.; Moulton, J.; Silman, I.; Sussman, J.L. Flexibility of Aromatic Residues in the Active-Site Gorge of Acetylcholinesterase: X-ray versus Molecular Dynamics. *Biophys. J.* **2008**, *95*, 2500–2511. [[CrossRef](#)]
23. Chinnadurai, R.K.; Saravanaraman, P.; Boopathy, R. Understanding the molecular mechanism of aryl acylamidase activity of acetylcholinesterase—An in silico study. *Arch. Biochem. Biophys.* **2015**, *580*, 1–13. [[CrossRef](#)] [[PubMed](#)]
24. Axelsen, P.H.; Harel, M.; Silman, I.; Sussman, J.L. Structure and dynamics of the active site gorge of acetylcholinesterase: Synergistic use of molecular dynamics simulation and X-ray crystallography. *Protein Sci.* **1994**, *3*, 188–197. [[CrossRef](#)] [[PubMed](#)]
25. Henchman, R.H.; McCammon, J.A. Structural and dynamic properties of water around acetylcholinesterase. *Protein Sci.* **2002**, *11*, 2080–2090. [[CrossRef](#)] [[PubMed](#)]
26. Koellner, G.; Kryger, G.; Millard, C.B.; Silman, I.; Sussman, J.L.; Steiner, T. Active-site gorge and buried water molecules in crystal structures of acetylcholinesterase from *Torpedo californica*. *J. Mol. Biol.* **2000**, *296*, 713–735. [[CrossRef](#)]
27. Leung, M.R.; van Bezouwen, L.S.; Schopfer, L.M.; Sussman, J.L.; Silman, I.; Lockridge, O.; Zeev-Ben-Mordehaia, T. Cryo-EM structure of the native butyrylcholinesterase tetramer reveals a dimer of dimers stabilized by a superhelical assembly. *Proc. Natl. Acad. Sci. USA* **2018**, *115*, 13270–13275. [[CrossRef](#)]
28. Fang, L.; Pan, Y.; Muzyka, J.L.; Zhan, C.-G. Active Site Gating and Substrate Specificity of Butyrylcholinesterase and Acetylcholinesterase: Insights from Molecular Dynamics Simulations. *J. Phys. Chem. B* **2011**, *115*, 8797–8805. [[CrossRef](#)]
29. Gorfe, A.A.; Lu, B.Z.; Yu, Z.Y.; McCammon, J.A. Enzymatic Activity versus Structural Dynamics: The Case of Acetylcholinesterase Tetramer. *Biophys. J.* **2009**, *97*, 897–905. [[CrossRef](#)] [[PubMed](#)]
30. Pan, Y.; Muzyka, J.L.; Zhan, C.-G. Model of Human Butyrylcholinesterase Tetramer by Homology Modeling and Dynamics Simulation. *J. Phys. Chem. B* **2009**, *113*, 6543–6552. [[CrossRef](#)] [[PubMed](#)]
31. Fang, L.; Zheng, F.; Zhan, C.-G. A model of glycosylated human butyrylcholinesterase. *Mol. Biosyst.* **2014**, *10*, 348–354. [[CrossRef](#)]
32. Bennion, B.J.; Essiz, S.G.; Lau, E.Y.; Fattebert, J.-L.; Emigh, A.; Lightstone, F.C. A wrench in the works of human acetylcholinesterase: Soman induced conformational changes revealed by molecular dynamics simulations. *PLoS ONE* **2015**, *10*, e0121092. [[CrossRef](#)]
33. Peters, J.; Martinez, N.; Trovaslet, M.; Scannapieco, K.; Koza, M.M.; Masson, P.; Nachon, F. Dynamics of human acetylcholinesterase bound to non-covalent and covalent inhibitors shedding light on changes to the water network structure. *Phys. Chem. Chem. Phys.* **2016**, *18*, 12992–13001. [[CrossRef](#)] [[PubMed](#)]
34. Rosenberry, T.L.; Brazzolotto, X.; Macdonald, I.R.; Wandhammer, M.; Trovaslet-Leroy, M.; Darvesh, S.; Nachon, F. Comparison of the Binding of Reversible Inhibitors to Human Butyrylcholinesterase and Acetylcholinesterase: A Crystallographic, Kinetic and Calorimetric Study. *Molecules* **2017**, *22*, 2098. [[CrossRef](#)] [[PubMed](#)]
35. Alvarado, W.; Bremer, P.L.; Choy, A.; Dinh, H.N.; Eung, A.; Gonzalez, J.; Ly, P.; Tran, T.; Nakayama, K.; Schwans, J.P.; et al. Understanding the enzyme-ligand complex: Insights from all-atom simulations of butyrylcholinesterase inhibition. *J. Biomol. Struct. Dyn.* **2019**, *38*, 1028–1041. [[CrossRef](#)]
36. Bourne, Y.; Taylor, P.; Bougis, P.E.; Marchot, P. Crystal structure of mouse acetylcholinesterase—A peripheral site-occluding loop in a tetrameric assembly. *J. Biol. Chem.* **1999**, *274*, 2963–2970. [[CrossRef](#)] [[PubMed](#)]
37. Campiani, G.; Fattorusso, C.; Butini, S.; Gaeta, A.; Agnusdei, M.; Gemma, S.; Persico, M.; Catalanotti, B.; Savini, L.; Nacci, V.; et al. Development of molecular probes for the identification of extra interaction sites in the mid-gorge and peripheral sites of butyrylcholinesterase (BuChE). Rational design of novel, selective, and highly potent BuChE inhibitors. *J. Med. Chem.* **2005**, *48*, 1919–1929. [[CrossRef](#)]
38. Khan, M.T.H. Molecular interactions of cholinesterases inhibitors using in silico methods: Current status and future prospects. *New Biotechnol.* **2009**, *25*, 331–346. [[CrossRef](#)]
39. Roca, C.; Requena, C.; Sebastian-Perez, V.; Malhotra, S.; Radoux, C.; Perez, C.; Martinez, A.; Antonio Paez, J.; Blundell, T.L.; Campillo, N.E. Identification of new allosteric sites and modulators of AChE through computational and experimental tools. *J. Enzym. Inhib. Med. Chem.* **2018**, *33*, 1034–1047. [[CrossRef](#)]
40. Branduardi, D.; Gervasio, F.L.; Cavalli, A.; Recanatini, M.; Parrinello, M. The role of the peripheral anionic site and cation- π interactions in the ligand penetration of the human AChE gorge. *J. Am. Chem. Soc.* **2005**, *127*, 9147–9155. [[CrossRef](#)]
41. Johnson, G.; Moore, S. The peripheral anionic site of acetylcholinesterase: Structure, functions and potential role in rational drug design. *Curr. Pharm. Des.* **2006**, *12*, 217–225. [[CrossRef](#)]
42. Dighe, S.N.; Deora, G.S.; De la Mora, E.; Nachon, F.; Chan, S.; Parat, M.O.; Brazzolotto, X.; Ross, B.P. Discovery and Structure-Activity Relationships of a Highly Selective Butyrylcholinesterase Inhibitor by Structure-Based Virtual Screening. *J. Med. Chem.* **2016**, *59*, 7683–7689. [[CrossRef](#)]
43. Kwong, H.C.; Chidan Kumar, C.S.; Mah, S.H.; Mah, Y.L.; Chia, T.S.; Quah, C.K.; Lim, G.K.; Chandrāju, S. Crystal Correlation Of Heterocyclic Imidazo[1,2-a]pyridine Analogues and Their Anticholinesterase Potential Evaluation. *Sci. Rep.* **2019**, *9*, 926. [[CrossRef](#)]
44. Kumar, J.; Gill, A.; Shaikh, M.; Singh, A.; Shandilya, A.; Jameel, E.; Sharma, N.; Mrinal, N.; Hoda, N.; Jayaram, B. Pyrimidine-Triazolopyrimidine and Pyrimidine-Pyridine Hybrids as Potential Acetylcholinesterase Inhibitors for Alzheimer’s Disease. *ChemistrySelect* **2018**, *3*, 736–747. [[CrossRef](#)]
45. Bencsura, A.; Enyedy, I.Y.; Kovach, I.M. Probing the active site of acetylcholinesterase by molecular dynamics of its phosphonate ester adducts. *J. Am. Chem. Soc.* **1996**, *118*, 8531–8541. [[CrossRef](#)]

46. Viragh, C.; Harris, T.K.; Reddy, P.M.; Massiah, M.A.; Mildvan, A.S.; Kovach, I.M. NMR Evidence for a Short, Strong Hydrogen Bond at the Active Site of a Cholinesterase. *Biochemistry* **2000**, *39*, 16200–16205. [[CrossRef](#)] [[PubMed](#)]
47. Zhang, Y.K.; Kua, J.; McCammon, J.A. Role of the catalytic triad and oxyanion hole in acetylcholinesterase catalysis: An ab initio QM/MM study. *J. Am. Chem. Soc.* **2002**, *124*, 10572–10577. [[CrossRef](#)] [[PubMed](#)]
48. Kua, J.; Zhang, Y.; McCammon, J.A. Studying Enzyme Binding Specificity in Acetylcholinesterase Using a Combined Molecular Dynamics and Multiple Docking Approach. *J. Am. Chem. Soc.* **2002**, *124*, 8260–8267. [[CrossRef](#)] [[PubMed](#)]
49. Gilson, M.K.; Straatsma, T.P.; McCammon, J.A.; Ripoli, D.R.; Faerman, C.H.; Axelsen, P.H.; Silman, I.; Sussman, J.L. Open “back door” in a molecular dynamics simulation of acetylcholinesterase. *Science* **1994**, *263*, 1276–1278. [[CrossRef](#)]
50. Sanson, B.; Colletier, J.-P.; Xu, Y.; Lang, P.T.; Jiang, H.; Silman, I.; Sussman, J.L.; Weik, M. Backdoor opening mechanism in acetylcholinesterase based on X-ray crystallography and molecular dynamics simulations. *Protein Sci.* **2011**, *20*, 1114–1118. [[CrossRef](#)]
51. Kaplan, D.; Barak, D.; Ordentlich, A.; Kronman, C.; Velan, B.; Shafferman, A. Is aromaticity essential for trapping the catalytic histidine 447 in human acetylcholinesterase? *Biochemistry* **2004**, *43*, 3129–3136. [[CrossRef](#)] [[PubMed](#)]
52. Barak, D.; Kaplan, D.; Ordentlich, A.; Ariel, N.; Velan, B.; Shafferman, A. The aromatic “trapping” of the catalytic histidine is essential for efficient catalysis in acetylcholinesterase. *Biochemistry* **2002**, *41*, 8245–8252. [[CrossRef](#)] [[PubMed](#)]
53. Xu, Y.; Colletier, J.-P.; Weik, M.; Qin, G.; Jiang, H.; Silman, I.; Sussman, J.L. Long route or shortcut? A molecular dynamics study of traffic of thiocholine within the active-site gorge of acetylcholinesterase. *Biophys. J.* **2010**, *99*, 4003–4011. [[CrossRef](#)] [[PubMed](#)]
54. Colletier, J.; Royant, A.; Specht, A.; Sanson, B.; Nachon, F.; Masson, P.; Zaccai, G.; Sussman, J.; Goeldner, M.; Silman, I.; et al. Use of a ‘caged’ analogue to study the traffic of choline within acetylcholinesterase by kinetic crystallography. *Acta Crystallogr. D* **2007**, *63*, 1115–1128. [[CrossRef](#)] [[PubMed](#)]
55. Colletier, J.-P.; Bourgeois, D.; Sanson, B.; Fournier, D.; Sussman, J.L.; Silman, I.; Weik, M. Shoot-and-Trap: Use of specific X-ray damage to study structural protein dynamics by temperature-controlled cryo-crystallography. *Proc. Natl. Acad. Sci. USA* **2008**, *105*, 11742–11747. [[CrossRef](#)] [[PubMed](#)]
56. Delacour, H.; Lushchekina, S.; Mabboux, I.; Ceppia, F.; Masson, P.; Schopfer, L.M.; Lockridge, O. Characterization of a novel butyrylcholinesterase point mutation (p.Ala34Val), “silent” with mivacurium. *Biochem. Pharmacol.* **2014**, *92*, 476–483. [[CrossRef](#)] [[PubMed](#)]
57. Delacour, H.; Lushchekina, S.; Mabboux, I.; Bousquet, A.; Ceppia, F.; Schopfer, L.M.; Lockridge, O.; Masson, P. Characterization of a Novel BCHE “Silent” Allele: Point Mutation (p. Val204Asp) Causes Loss of Activity and Prolonged Apnea with Suxamethonium. *PLoS ONE* **2014**, *9*, e101552. [[CrossRef](#)]
58. Lushchekina, S.V.; Nemukhin, A.V.; Varfolomeev, S.D.; Masson, P. Molecular Modeling Evidence for His438 Flip in the Mechanism of Butyrylcholinesterase Hysteretic Behavior. *J. Mol. Neurosci.* **2014**, *52*, 434–445. [[CrossRef](#)]
59. Lushchekina, S.; Nemukhin, A.; Varfolomeev, S.; Masson, P. Understanding the non-catalytic behavior of human butyrylcholinesterase silent variants: Comparison of wild-type enzyme, catalytically active Ala328Cys mutant, and silent Ala328Asp variant. *Chem. Biol. Interact.* **2016**, *259*, 223–232. [[CrossRef](#)]
60. Grigorenko, B.L.; Novichkova, D.A.; Lushchekina, S.V.; Zueva, I.V.; Schopfer, L.M.; Nemukhin, A.V.; Varfolomeev, S.D.; Lockridge, O.; Masson, P. Computer-designed active human butyrylcholinesterase double mutant with a new catalytic triad. *Chem. Biol. Interact.* **2019**, *306*, 138–146. [[CrossRef](#)]
61. Zheng, F.; Yang, W.C.; Xue, L.; Hou, S.R.; Liu, J.J.; Zhan, C.G. Design of High-Activity Mutants of Human Butyrylcholinesterase against (-)-Cocaine: Structural and Energetic Factors Affecting the Catalytic Efficiency. *Biochemistry* **2010**, *49*, 9113–9119. [[CrossRef](#)]
62. Gao, D.; Zhan, C.-G. Modeling Effects of Oxyanion Hole on the Ester Hydrolysis Catalyzed by Human Cholinesterases. *J. Phys. Chem. B* **2005**, *109*, 23070–23076. [[CrossRef](#)] [[PubMed](#)]
63. Shi, J.X.; Tai, K.; McCammon, J.A.; Taylor, P.; Johnson, D.A. Nanosecond dynamics of the mouse acetylcholinesterase Cys(69)-Cys(96) omega loop. *J. Biol. Chem.* **2003**, *278*, 30905–30911. [[CrossRef](#)]
64. Shi, J.; Boyd, A.E.; Radic, Z.R.; Taylor, P. Reversibly Bound and Covalently Attached Ligands Induce Conformational Changes in the Omega Loop, Cys⁶⁹-Cys⁹⁶, of Mouse Acetylcholinesterase*. *J. Biol. Chem.* **2001**, *276*, 42196–42204. [[CrossRef](#)] [[PubMed](#)]
65. Masson, P.; Legrand, P.; Bartels, C.F.; Froment, M.T.; Schopfer, L.M.; Lockridge, O. Role of aspartate 70 and tryptophan 82 in binding of succinylthiocholine to human butyrylcholinesterase. *Biochemistry* **1997**, *36*, 2266–2277. [[CrossRef](#)] [[PubMed](#)]
66. Wiesner, J.; Kriz, Z.; Kuca, K.; Jun, D.; Koca, J. Influence of the Acetylcholinesterase Active Site Protonation on Omega Loop and Active Site Dynamics. *J. Biomol. Struct. Dyn.* **2010**, *28*, 393–403. [[CrossRef](#)] [[PubMed](#)]
67. Rydzewski, J.; Jakubowski, R.; Nowak, W.; Grubmuller, H. Kinetics of Huperzine A Dissociation from Acetylcholinesterase via Multiple Unbinding Pathways. *J. Chem. Theory Comput.* **2018**, *14*, 2843–2851. [[CrossRef](#)]
68. Bourne, Y.; Renault, L.; Marchot, P. Crystal Structure of Snake Venom Acetylcholinesterase in Complex with Inhibitory Antibody Fragment Fab410 Bound at the Peripheral Site evidence for open and closed states of a back door channel. *J. Biol. Chem.* **2015**, *290*, 1522–1535. [[CrossRef](#)] [[PubMed](#)]
69. Nachon, F.; Rosenberry, T.L.; Silman, I.; Sussman, J.L. A Second Look at the Crystal Structures of *Drosophila melanogaster* Acetylcholinesterase in Complex with Tacrine Derivatives Provides Insights Concerning Catalytic Intermediates and the Design of Specific Insecticides. *Molecules* **2020**, *25*, 1198. [[CrossRef](#)]
70. Nachon, F.; Stojan, J.; Fournier, D. Insights into substrate and product traffic in the *Drosophila melanogaster* acetylcholinesterase active site gorge by enlarging a back channel. *FEBS J.* **2008**, *275*, 2659–2664. [[CrossRef](#)]

71. Zhou, Y.; Wang, S.; Zhang, Y. Catalytic reaction mechanism of acetylcholinesterase determined by born-oppenheimer ab initio QM/MM molecular dynamics simulations. *J. Phys. Chem. B* **2010**, *114*, 8817–8825. [[CrossRef](#)]
72. Chen, X.; Fang, L.; Liu, J.J.; Zhan, C.G. Reaction Pathway and Free Energy Profile for Butyrylcholinesterase-Catalyzed Hydrolysis of Acetylcholine. *J. Phys. Chem. B* **2011**, *115*, 1315–1322. [[CrossRef](#)]
73. Chen, X.; Fang, L.; Liu, J.J.; Zhan, C.G. Reaction Pathway and Free Energy Profiles for Butyrylcholinesterase-Catalyzed Hydrolysis of Acetylthiocholine. *Biochemistry* **2012**, *51*, 1297–1305. [[CrossRef](#)]
74. Qiao, Y.; Han, K.; Zhan, C.-G. Fundamental Reaction Pathway and Free Energy Profile for Butyrylcholinesterase-Catalyzed Hydrolysis of Heroin. *Biochemistry* **2013**, *52*, 6467–6479. [[CrossRef](#)]
75. Yao, J.; Yuan, Y.; Zheng, F.; Zhan, C.-G. Unexpected Reaction Pathway for butyrylcholinesterase-catalyzed inactivation of “hunger hormone” ghrelin. *Sci. Rep.* **2016**, *6*, 22322. [[CrossRef](#)]
76. Suarez, D.; Diaz, N.; Fontecilla-Camps, J.; Field, M.J. A computational study of the deacylation mechanism of human butyrylcholinesterase. *Biochemistry* **2006**, *45*, 7529–7543. [[CrossRef](#)] [[PubMed](#)]
77. Huang, X.; Pan, Y.; Zheng, F.; Zhan, C.-G. Reaction Pathway and Free Energy Profile for Prechemical Reaction Step of Human Butyrylcholinesterase-Catalyzed Hydrolysis of (-)-Cocaine by Combined Targeted Molecular Dynamics and Potential of Mean Force Simulations. *J. Phys. Chem. B* **2010**, *114*, 13545–13554. [[CrossRef](#)] [[PubMed](#)]
78. Zhan, C.G.; Gao, D.Q. Catalytic mechanism and energy barriers for butyrylcholinesterase-catalyzed hydrolysis of cocaine. *Biophys. J.* **2005**, *89*, 3863–3872. [[CrossRef](#)] [[PubMed](#)]
79. Pan, Y.; Gao, D.; Yang, W.; Cho, H.; Yang, G.; Tai, H.-H.; Zhan, C.-G. Computational redesign of human butyrylcholinesterase for anticocaine medication. *Proc. Natl. Acad. Sci. USA* **2005**, *102*, 16656–16661. [[CrossRef](#)]
80. Yang, W.; Pan, Y.; Zheng, F.; Cho, H.; Tai, H.-H.; Zhan, C.-G. Free-Energy Perturbation Simulation on Transition States and Redesign of Butyrylcholinesterase. *Biophys. J.* **2009**, *96*, 1931–1938. [[CrossRef](#)]
81. Pan, Y.M.; Gao, D.Q.; Yang, W.C.; Cho, H.; Zhan, C.G. Free energy perturbation (FEP) simulation on the transition states of cocaine hydrolysis catalyzed by human butyrylcholinesterase and its mutants. *J. Am. Chem. Soc.* **2007**, *129*, 13537–13543. [[CrossRef](#)] [[PubMed](#)]
82. Huang, X.; Zheng, F.; Zhan, C.-G. Human butyrylcholinesterase-cocaine binding pathway and free energy profiles by molecular dynamics and potential of mean force simulations. *J. Phys. Chem. B* **2011**, *115*, 11254–11260. [[CrossRef](#)] [[PubMed](#)]
83. Anand, P.; Singh, B. A review on cholinesterase inhibitors for Alzheimer’s disease. *Arch. Pharmacol. Res.* **2013**, *36*, 375–399. [[CrossRef](#)] [[PubMed](#)]
84. Castellani, R.J.; Rolston, R.K.; Smith, M.A. Alzheimer Disease. *Dis. Mon.* **2010**, *56*, 484–546. [[CrossRef](#)] [[PubMed](#)]
85. Sukumaran, S.D.; Faraj, F.L.; Lee, V.S.; Othman, R.; Buckle, M.J.C. 2-Aryl-3-(arylideneamino)-1,2-dihydroquinazoline-4(3H)-ones as inhibitors of cholinesterases and self-induced beta-amyloid (Ab) aggregation: Biological evaluations and mechanistic insights from molecular dynamics simulations. *RSC Adv.* **2018**, *8*, 7818–7831. [[CrossRef](#)]
86. Zhou, A.; Hu, J.; Wang, L.; Zhong, G.; Pan, J.; Wu, Z.; Hui, A. Combined 3D-QSAR, molecular docking, and molecular dynamics study of tacrine derivatives as potential acetylcholinesterase (AChE) inhibitors of Alzheimer’s disease. *J. Mol. Modeling* **2015**, *21*. [[CrossRef](#)] [[PubMed](#)]
87. Maalej, E.; Chabchoub, F.; Samadi, A.; de los Rios, C.; Perona, A.; Morreale, A.; Marco-Contelles, J. Synthesis, biological assessment and molecular modeling of 14-aryl-10,11,12,14-tetrahydro-9H-benzo 5,6 chromeno 2,3-b quinolin-13-amines. *Bioorg. Med. Chem. Lett.* **2011**, *21*, 2384–2388. [[CrossRef](#)]
88. Thiratrakul, S.; Yenjai, C.; Waiwut, P.; Vajragupta, O.; Reubroycharoen, P.; Tohda, M.; Boonyarat, C. Synthesis, biological evaluation and molecular modeling study of novel tacrine-carbazole hybrids as potential multifunctional agents for the treatment of Alzheimer’s disease. *Eur. J. Med. Chem.* **2014**, *75*, 21–30. [[CrossRef](#)]
89. Manetsch, R.; Krasiński, A.; Radić, Z.; Raushel, J.; Taylor, P.; Sharpless, K.B.; Kolb, H.C. In Situ Click Chemistry: Enzyme Inhibitors Made to Their Own Specifications. *J. Am. Chem. Soc.* **2004**, *126*, 12809–12818. [[CrossRef](#)]
90. Zhu, X.-L.; Yu, N.-X.; Hao, G.-F.; Yang, W.-C.; Yang, G.-F. Structural basis of femtomolar inhibitors for acetylcholinesterase subtype selectivity: Insights from computational simulations. *J. Mol. Graph. Model.* **2013**, *41*, 55–60. [[CrossRef](#)]
91. Makhaeva, G.F.; Kovaleva, N.V.; Boltneva, N.P.; Lushchekina, S.V.; Rudakova, E.V.; Stupina, T.S.; Terentiev, A.A.; Serkov, I.V.; Proshin, A.N.; Radchenko, E.V.; et al. Conjugates of tacrine and 1,2,4-thiadiazole derivatives as new potential multifunctional agents for Alzheimer’s disease treatment: Synthesis, quantum-chemical characterization, molecular docking, and biological evaluation. *Bioorg. Chem.* **2020**, *94*, 103387. [[CrossRef](#)]
92. Chen, X.; Wehle, S.; Kuzmanovic, N.; Merget, B.; Holzgrabe, U.; König, B.; Sotriffer, C.A.; Decker, M. Acetylcholinesterase Inhibitors with Photoswitchable Inhibition of beta-Amyloid Aggregation. *ACS Chem. Neurosci.* **2014**, *5*, 377–389. [[CrossRef](#)]
93. Cheng, Z.Q.; Zhu, K.K.; Zhang, J.; Song, J.L.; Muehlmann, L.A.; Jiang, C.S.; Liu, C.L.; Zhang, H. Molecular-docking-guided design and synthesis of new IAA-tacrine hybrids as multifunctional AChE/BChE inhibitors. *Bioorg. Chem.* **2019**, *83*, 277–288. [[CrossRef](#)]
94. Nascimento, E.C.M.; Oliva, M.; Swiderek, K.; Martins, J.B.L.; Andres, J. Binding Analysis of Some Classical Acetylcholinesterase Inhibitors: Insights for a Rational Design Using Free Energy Perturbation Method Calculations with QM/MM MD Simulations. *J. Chem. Inf. Modeling* **2017**, *57*, 958–976. [[CrossRef](#)] [[PubMed](#)]
95. Wan, X.; Yao, Y.; Fang, L.; Liu, J.J. Unexpected protonation state of Glu197 discovered from simulations of tacrine in butyrylcholinesterase. *Phys. Chem. Chem. Phys.* **2018**, *20*, 14938–14946. [[CrossRef](#)]

96. Galdeano, C.; Viayna, E.; Sola, I.; Formosa, X.; Camps, P.; Badia, A.; Clos, M.V.; Relat, J.; Ratia, M.; Bartolini, M.; et al. Huprine-Tacrine Heterodimers as Anti-Amyloidogenic Compounds of Potential Interest against Alzheimer's and Prion Diseases. *J. Med. Chem.* **2012**, *55*, 661–669. [[CrossRef](#)] [[PubMed](#)]
97. Eslami, M.; Hashemianzadeh, S.M.; Moghaddam, K.G.; Khorsandi-Lagol, A.; Seyed Sajadi, S.A. Computational evidence to design an appropriate candidate for the treatment of Alzheimer's disease through replacement of the heptamethylene linker of bis(7)tacrine with S-allylcysteine. *RSC Adv.* **2015**, *5*, 66840–66851. [[CrossRef](#)]
98. Eslami, M.; Hashemianzadeh, S.M.; Bagherzadeh, K.; Sajadi, S.A.S. Molecular perception of interactions between bis(7)tacrine and cystamine-tacrine dimer with cholinesterases as the promising proposed agents for the treatment of Alzheimer's disease. *J. Biomol. Struct. Dyn.* **2015**, *34*, 855–869. [[CrossRef](#)]
99. Habibpour, R.; Eslami, M.; Amani, P.; Novir, S.B. Tacrine-flavonoid quercetin hybride as a MTDL ligand against alzheimer's disease with metal chelating and AChE, BChE, AChE-induced A β aggregation inhibition properties: A computational study. *Phys. Chem. Res.* **2019**, *7*, 561–579.
100. Brito, M.d.F.d.B.; Ferreira, J.V.; de Souza, L.R.; Gemaque, L.R.P.; Sousa, K.P.A.; dos Santos, C.F.; Braga, F.S.; Pernomian, L.; da Silva, C.H.T.P.; Santos, C.B.R.; et al. Computational Molecular Modeling of Compounds from Amaryllidaceae Family as Potential Acetylcholinesterase Inhibitors. *Curr. Bioact. Compd.* **2017**, *13*, 121–129. [[CrossRef](#)]
101. Gulcan, H.O.; Orhan, I.E.; Sener, B. Chemical and Molecular Aspects on Interactions of Galanthamine and Its Derivatives with Cholinesterases. *Curr. Pharm. Biotechnol.* **2015**, *16*, 252–258. [[CrossRef](#)]
102. Ali, M.R.; Sadoqi, M.; Möller, S.G.; Boutajangout, A.; Mezei, M. Assessing the binding of cholinesterase inhibitors by docking and molecular dynamics studies. *J. Mol. Graph. Model.* **2017**, *76*, 36–42. [[CrossRef](#)]
103. Silva, M.A.; Kiametis, A.S.; Treptow, W. Donepezil Inhibits Acetylcholinesterase via Multiple Binding Modes at Room Temperature. *J. Chem. Inf. Modeling* **2020**, *60*, 3463–3471. [[CrossRef](#)] [[PubMed](#)]
104. Bautista-Aguilera, O.M.; Esteban, G.; Chioua, M.; Nikolic, K.; Agbaba, D.; Moraleda, I.; Iriepa, I.; Soriano, E.; Samadi, A.; Unzeta, M.; et al. Multipotent cholinesterase/monoamine oxidase inhibitors for the treatment of Alzheimer's disease: Design, synthesis, biochemical evaluation, ADMET, molecular modeling, and QSAR analysis of novel donepezil-pyridyl hybrids. *Drug Des. Dev. Ther.* **2014**, *8*, 1893–1910.
105. Valasani, K.R.; Chaney, M.O.; Day, V.W.; Yan, S.S. Acetylcholinesterase Inhibitors: Structure Based Design, Synthesis, Pharmacophore Modeling, and Virtual Screening. *J. Chem. Inf. Modeling* **2013**, *53*, 2033–2046. [[CrossRef](#)]
106. Silva, D.; Chioua, M.; Samadi, A.; Agostinho, P.; Garcao, P.; Lajarin-Cuesta, R.; de los Rios, C.; Iriepa, I.; Moraleda, I.; Gonzalez-Lafuente, L.; et al. Synthesis, Pharmacological Assessment, and Molecular Modeling of Acetylcholinesterase/Butyrylcholinesterase Inhibitors: Effect against Amyloid-beta-Induced Neurotoxicity. *ACS Chem. Neurosci.* **2013**, *4*, 547–565. [[CrossRef](#)]
107. Al-Rashid, Z.F.; Hsung, R.P. A computational view on the significance of E-ring in binding of (+)-arisugacin A to acetylcholinesterase. *Bioorg. Med. Chem. Lett.* **2015**, *25*, 4848–4853. [[CrossRef](#)]
108. Rahman, A.; Ali, M.T.; Shawan, M.M.A.K.; Sarwar, M.G.; Khan, M.A.K.; Halim, M.A. Halogen-directed drug design for Alzheimer's disease: A combined density functional and molecular docking study. *SpringerPlus* **2016**, *5*, 1346. [[CrossRef](#)]
109. Alpan, A.S.; Parlar, S.; Carlino, L.; Tarikogullari, A.H.; Alptüzün, V.; Güneş, H.S. Synthesis, biological activity and molecular modeling studies on 1H-benzimidazole derivatives as acetylcholinesterase inhibitors. *Bioorg. Med. Chem.* **2013**, *21*, 4928–4937. [[CrossRef](#)]
110. Ghosh, S.; Jana, K.; Ganguly, B. Revealing the mechanistic pathway of cholinergic inhibition of Alzheimer's disease by donepezil: A metadynamics simulation study. *Phys. Chem. Chem. Phys.* **2019**, *21*, 13578–13589. [[CrossRef](#)]
111. Bolea, I.; Juárez-Jiménez, J.; de los Ríos, C.; Chioua, M.; Pouplana, R.; Luque, F.J.; Unzeta, M.; Marco-Contelles, J.; Samadi, A. Synthesis, Biological Evaluation, and Molecular Modeling of Donepezil and N-[(5-(Benzyloxy)-1-methyl-1H-indol-2-yl)methyl]-N-methylprop-2-yn-1-amine Hybrids as New Multipotent Cholinesterase/Monoamine Oxidase Inhibitors for the Treatment of Alzheimer's Disease. *J. Med. Chem.* **2011**, *54*, 8251–8270. [[PubMed](#)]
112. Yekta, R.; Sadeghi, L.; Dehghan, G. The inefficacy of donepezil on glycosylated-AChE inhibition: Binding affinity, complex stability and mechanism. *Int. J. Biol. Macromol.* **2020**, *160*, 35–46. [[CrossRef](#)] [[PubMed](#)]
113. Bolognesi, M.L.; Bartolini, M.; Cavalli, A.; Andrisano, V.; Rosini, M.; Minarini, A.; Melchiorre, C. Design, Synthesis, and Biological Evaluation of Conformationally Restricted Rivastigmine Analogues. *J. Med. Chem.* **2004**, *47*, 5945–5952. [[CrossRef](#)] [[PubMed](#)]
114. Wang, L.; Wang, Y.; Tian, Y.G.; Shang, J.L.; Sun, X.O.; Chen, H.Z.; Wang, H.; Tan, W. Design, synthesis, biological evaluation, and molecular modeling studies of chalcone-rivastigmine hybrids as cholinesterase inhibitors. *Bioorg. Med. Chem.* **2017**, *25*, 360–371. [[CrossRef](#)] [[PubMed](#)]
115. Hekal, M.H.; Abu El-Azm, F.S.M. New potential antitumor quinazolinones derived from dynamic 2-undecyl benzoxazinone: Synthesis and cytotoxic evaluation. *Synth. Commun.* **2018**, *48*, 2391–2402. [[CrossRef](#)]
116. Li, Z.; Wang, B.; Hou, J.Q.; Huang, S.L.; Ou, T.M.; Tan, J.H.; An, L.K.; Li, D.; Gu, L.Q.; Huang, Z.S. 2-(2-indolyl)-4(H)-quinazolines derivatives as new inhibitors of AChE: Design, synthesis, biological evaluation and molecular modelling. *J. Enzym. Inhib. Med. Chem.* **2013**, *28*, 583–592. [[CrossRef](#)] [[PubMed](#)]
117. Abdul Hameed, M.D.M.; Liu, J.; Pan, Y.; Fang, L.; Silva-Rivera, C.; Zhan, C.-G. Microscopic binding of butyrylcholinesterase with quinazolinimine derivatives and the structure-activity correlation. *Theor. Chem. Acc.* **2011**, *130*, 69–82. [[CrossRef](#)]
118. Chen, X.; Tikhonova, I.G.; Decker, M. Probing the mid-gorge of cholinesterases with spacer-modified bivalent quinazolinimines leads to highly potent and selective butyrylcholinesterase inhibitors. *Bioorg. Med. Chem.* **2011**, *19*, 1222–1235. [[CrossRef](#)]

119. Darras, F.H.; Wehle, S.; Huang, G.Z.; Sotriffer, C.A.; Decker, M. Amine substitution of quinazolinones leads to selective nanomolar AChE inhibitors with 'inverted' binding mode. *Bioorg. Med. Chem.* **2014**, *22*, 4867–4881. [[CrossRef](#)]
120. Daoud, I.; Bouarab, S.; Ghalem, S. Docking, dynamic simulation and quantum mechanics studies of pyrazinamide derivatives as novel inhibitors of Acetylcholinesterase and Butyrylcholinesterase. *Pharma Chem.* **2015**, *7*, 307–321.
121. Tanoli, N.U.; Tanoli, S.A.K.; Ferreira, A.G.; Mehmood, M.; Gul, S.; Monteiro, J.L.; Vieira, L.C.C.; Venancio, T.; Correa, A.G.; Ul-Haq, Z. Characterization of the interactions between coumarin-derivatives and acetylcholinesterase: Examination by NMR and docking simulations. *J. Mol. Modeling* **2018**, *24*, 11. [[CrossRef](#)]
122. Saeed, A.; Zaib, S.; Ashraf, S.; Iftikhar, J.; Muddassar, M.; Zhang, K.Y.J.; Iqbal, J. Synthesis, cholinesterase inhibition and molecular modelling studies of coumarin linked thiourea derivatives. *Bioorg. Chem.* **2015**, *63*, 58–63. [[CrossRef](#)] [[PubMed](#)]
123. Dominguez, J.L.; Fernandez-Nieto, F.; Brea, J.M.; Catto, M.; Paleo, M.R.; Porto, S.; Sardina, F.J.; Castro, M.; Pisani, L.; Carotti, A.; et al. 8-Aminomethyl-7-hydroxy-4-methylcoumarins as Multitarget Leads for Alzheimer's Disease. *ChemistrySelect* **2016**, *1*, 2742–2749. [[CrossRef](#)]
124. Abu-Aisheh, M.N.; Al-Aboudi, A.; Mustafa, M.S.; El-Abadelah, M.M.; Ali, S.Y.; Ul-Haq, Z.; Mubarak, M.S. Coumarin derivatives as acetyl- and butyrylcholinesterase inhibitors: An in vitro, molecular docking, and molecular dynamics simulations study. *Heliyon* **2019**, *5*, e01552. [[CrossRef](#)]
125. Kwong, H.C.; Mah, S.H.; Chia, T.S.; Quah, C.K.; Lim, G.K.; Kumar, C.S.C. Cholinesterase Inhibitory Activities of Adamantyl-Based Derivatives and Their Molecular Docking Studies. *Molecules* **2017**, *22*, 1005. [[CrossRef](#)]
126. Stoddard, S.V.; Hamann, M.T.; Wadkins, R.M. Insights and Ideas Garnered from Marine Metabolites for Development of Dual-Function Acetylcholinesterase and Amyloid-beta Aggregation Inhibitors. *Mar. Drugs* **2014**, *12*, 2114–2131. [[CrossRef](#)]
127. Hassan, M.; Raza, H.; Abbasi, M.A.; Moustafa, A.A.; Seo, S.Y. The exploration of novel Alzheimer's therapeutic agents from the pool of FDA approved medicines using drug repositioning, enzyme inhibition and kinetic mechanism approaches. *Biomed. Pharmacother.* **2019**, *109*, 2513–2526. [[CrossRef](#)] [[PubMed](#)]
128. Dalmizrak, O.; Terali, K.; Yetkin, O.; Ogus, I.H.; Ozer, N. Computational and experimental studies on the interaction between butyrylcholinesterase and fluoxetine: Implications in health and disease. *Xenobiotica* **2019**, *49*, 803–810. [[CrossRef](#)]
129. Fang, J.; Pang, X.; Wu, P.; Yan, R.; Gao, L.; Li, C.; Lian, W.; Wang, Q.; Liu, A.L.; Du, G.H. Molecular Modeling on Berberine Derivatives toward BuChE: An Integrated Study with Quantitative Structure–Activity Relationships Models, Molecular Docking, and Molecular Dynamics Simulations. *Chem. Biol. Drug Des.* **2016**, *87*, 649–663. [[CrossRef](#)] [[PubMed](#)]
130. Ayupov, R.K.; Akberova, N.I. Molecular dynamics of the pyridoxine derivative in the acetylcholinesterase active cavity. *Res. J. Pharm. Biol. Chem. Sci.* **2015**, *6*, 1717–1722.
131. Zhou, S.; Yuan, Y.X.; Zheng, F.; Zhan, C.G. Structure-based virtual screening leading to discovery of highly selective butyrylcholinesterase inhibitors with solanaceous alkaloid scaffolds. *Chem. Biol. Interact.* **2019**, *308*, 372–376. [[CrossRef](#)] [[PubMed](#)]
132. Yang, J.; Chen, Y.K.; Liu, Z.H.; Yang, L.; Tang, J.G.; Miao, M.M.; Gan, N.; Li, H. Differences between the binding modes of enantiomers S/R-nicotine to acetylcholinesterase. *RSC Adv.* **2019**, *9*, 1428–1440. [[CrossRef](#)]
133. Terali, K. An evaluation of neonicotinoids' potential to inhibit human cholinesterases: Protein-ligand docking and interaction profiling studies. *J. Mol. Graph. Model.* **2018**, *84*, 54–63. [[CrossRef](#)]
134. Gao, D.; Zhan, C.G. Modeling evolution of hydrogen bonding and stabilization of transition states in the process of cocaine hydrolysis catalyzed by human butyrylcholinesterase. *Proteins Struct. Funct. Bioinform.* **2006**, *62*, 99–110. [[CrossRef](#)] [[PubMed](#)]
135. Fang, L.; Hou, S.R.; Xue, L.; Zheng, F.; Zhan, C.G. Amino-acid mutations to extend the biological half-life of a therapeutically valuable mutant of human butyrylcholinesterase. *Chem. Biol. Interact.* **2014**, *214*, 18–25. [[CrossRef](#)] [[PubMed](#)]
136. Sun, H.; Pang, Y.-P.; Lockridge, O.; Brimijoin, S. Re-engineering Butyrylcholinesterase as a Cocaine Hydrolase. *Mol. Pharmacol.* **2002**, *62*, 220. [[CrossRef](#)]
137. Zheng, F.; Yang, W.; Ko, M.-C.; Liu, J.; Cho, H.; Gao, D.; Tong, M.; Tai, H.-H.; Woods, J.H.; Zhan, C.-G. Most Efficient Cocaine Hydrolase Designed by Virtual Screening of Transition States. *J. Am. Chem. Soc.* **2008**, *130*, 12148–12155. [[CrossRef](#)] [[PubMed](#)]
138. Hamza, A.; Cho, H.; Tai, H.-H.; Zhan, C.-G. Molecular Dynamics Simulation of Cocaine Binding with Human Butyrylcholinesterase and Its Mutants. *J. Phys. Chem. B* **2005**, *109*, 4776–4782. [[CrossRef](#)] [[PubMed](#)]
139. Xue, L.; Ko, M.-C.; Tong, M.; Yang, W.; Hou, S.; Fang, L.; Liu, J.; Zheng, F.; Woods, J.H.; Tai, H.-H.; et al. Design, preparation, and characterization of high-activity mutants of human butyrylcholinesterase specific for detoxification of cocaine. *Mol. Pharmacol.* **2011**, *79*, 290–297. [[CrossRef](#)] [[PubMed](#)]
140. Yang, G.; Elena, A.; Nan, S.; James, D.P.; Jeffry, D.W.; Stephen, B. Gene Transfer of Cocaine Hydrolase Suppresses Cardiovascular Responses to Cocaine in Rats. *Mol. Pharm.* **2005**, *67*, 204–211.
141. Chen, X.B.; Huang, X.Q.; Geng, L.Y.; Xue, L.; Hou, S.R.; Zheng, X.R.; Brimijoin, S.; Zheng, F.; Zhan, C.G. Kinetic characterization of a cocaine hydrolase engineered from mouse butyrylcholinesterase. *Biochem. J.* **2015**, *466*, 243–251. [[CrossRef](#)]
142. Moralev, S.N.; Tikhonov, D.B. Investigation of structure-activity relationships in organophosphates-cholinesterase interaction using docking analysis. *Chem. Biol. Interact.* **2010**, *187*, 153–156. [[CrossRef](#)]
143. Veselinovic, J.B.; Nikolic, G.M.; Trutic, N.V.; Zivkovic, J.V.; Veselinovic, A.M. Monte Carlo QSAR models for predicting organophosphate inhibition of acetylcholinesterase. *Sar Qsar Environ. Res.* **2015**, *26*, 449–460. [[CrossRef](#)] [[PubMed](#)]
144. Yang, S.; Liu, J.; Zheng, H.; Zhong, J.; Zhou, J. Simulated revelation of the adsorption behaviours of acetylcholinesterase on charged self-assembled monolayers. *Nanoscale* **2020**, *12*, 3701–3714. [[CrossRef](#)]

145. Bondžić, A.M.; Lazarević-Pašti, T.D.; Leskovic, A.R.; Petrović, S.Ž.; Čolović, M.B.; Parac-Vogt, T.N.; Janjić, G.V. A new acetylcholinesterase allosteric site responsible for binding voluminous negatively charged molecules—The role in the mechanism of AChE inhibition. *Eur. J. Pharm. Sci.* **2020**, *151*. [[CrossRef](#)] [[PubMed](#)]
146. Nakayama, K.; Schwans, J.P.; Sorin, E.J.; Tran, T.; Gonzalez, J.; Arteaga, E.; McCoy, S.; Alvarado, W. Synthesis, biochemical evaluation, and molecular modeling studies of aryl and arylalkyl di-n-butyl phosphates, effective butyrylcholinesterase inhibitors. *Bioorg. Med. Chem.* **2017**, *25*, 3171–3181. [[CrossRef](#)]
147. Sorin, E.J.; Alvarado, W.; Cao, S.; Radcliffe, A.; La, P.; An, Y. Ensemble molecular dynamics of a protein-ligand complex: Residual inhibitor entropy enhances drug potency in butyrylcholinesterase. *Bioenergetics* **2017**, *6*, 145. [[CrossRef](#)]
148. Bremer, P.L.; De Boer, D.; Alvarado, W.; Martinez, X.; Sorin, E.J. Overcoming the Heuristic Nature of k-Means Clustering: Identification and Characterization of Binding Modes from Simulations of Molecular Recognition Complexes. *J. Chem. Inf. Modeling* **2020**, *60*, 3081–3092. [[CrossRef](#)] [[PubMed](#)]
149. Carlucci, L.; Millard, C.B.; Olson, M.A. Conformational energy landscape of the acyl pocket loop in acetylcholinesterase: A Monte Carlo-generalized Born model study. *Biophys. Chem.* **2004**, *111*, 143–157. [[CrossRef](#)] [[PubMed](#)]
150. Dwyer, M.; Javor, S.; Ryan, D.A.; Smith, E.M.; Wang, B.; Zhang, J.; Cashman, J.R. Novel Human Butyrylcholinesterase Variants: Toward Organophosphonate Detoxication. *Biochemistry* **2014**, *53*, 4476–4487. [[CrossRef](#)] [[PubMed](#)]
151. Masson, P.; Lockridge, O. Butyrylcholinesterase for protection from organophosphorus poisons: Catalytic complexities and hysteretic behavior. *Arch. Biochem. Biophys.* **2010**, *494*, 107–120. [[CrossRef](#)] [[PubMed](#)]
152. Vyas, S.; Beck Jeremy, M.; Xia, S.; Zhang, J.; Hadad Christopher, M. Butyrylcholinesterase and G116H, G116S, G117H, G117N, E197Q and G117H/E197Q mutants: A molecular dynamics study. *Chem. Biol. Interact.* **2010**, *187*, 241–245. [[CrossRef](#)]
153. Nachon, F.; Carletti, E.; Wandhammer, M.; Nicolet, Y.; Schopfer, L.M.; Masson, P.; Lockridge, O. X-ray crystallographic snapshots of reaction intermediates in the G117H mutant of human butyrylcholinesterase, a nerve agent target engineered into a catalytic bioscavenger. *Biochem. J.* **2011**, *434*, 73–82. [[CrossRef](#)]
154. Amitay, M.; Shurki, A. The structure of G117H mutant of butyrylcholinesterase: Nerve agents scavenger. *Proteins* **2009**, *77*, 370–377. [[CrossRef](#)] [[PubMed](#)]
155. Yao, Y.; Liu, J.J.; Zhan, C.G. Why Does the G117H Mutation Considerably Improve the Activity of Human Butyrylcholinesterase against Sarin? Insights from Quantum Mechanical/Molecular Mechanical Free Energy Calculations. *Biochemistry* **2012**, *51*, 8980–8992. [[CrossRef](#)] [[PubMed](#)]
156. Gorecki, L.; Korabecny, J.; Musilek, K.; Malinak, D.; Nepovimova, E.; Dolezal, R.; Jun, D.; Soukup, O.; Kuca, K. SAR study to find optimal cholinesterase reactivator against organophosphorous nerve agents and pesticides. *Arch. Toxicol.* **2016**, *90*, 2831–2859. [[CrossRef](#)] [[PubMed](#)]
157. Giacompo, J.O.S.; Franca, T.C.C.; Kuca, K.; da Cunha, E.F.F.; Abagyan, R.; Mancini, D.T.; Ramalho, T.C. Molecular modeling and in vitro reactivation study between the oxime BI-6 and acetylcholinesterase inhibited by different nerve agents. *J. Biomol. Struct. Dyn.* **2015**, *33*, 2048–2058. [[CrossRef](#)] [[PubMed](#)]
158. Worek, F.; Aurbek, N.; Herkert, N.M.; John, H.; Eddleston, M.; Eyer, P.; Thiermann, H. Evaluation of medical countermeasures against organophosphorus compounds: The value of experimental data and computer simulations. *Chem. Biol. Interact.* **2010**, *187*, 259–264. [[CrossRef](#)]
159. Allgardsson, A.; Berg, L.; Akfur, C.; Hörnberg, A.; Worek, F.; Linusson, A.; Ekström, F.J. Structure of a prereaction complex between the nerve agent sarin, its biological target acetylcholinesterase, and the antidote HI-6. *Proc. Natl. Acad. Sci. USA* **2016**, *113*, 5514–5519. [[CrossRef](#)]
160. Veselinovic, A.M.; Veselinovic, J.B.; Toropov, A.A.; Toropov, A.P.; Nikolic, G.M. QSAR models for the reactivation of sarin inhibited acetylcholinesterase by quaternary pyridinium oximes based on Monte Carlo method. *Curr. Comput. Aided Drug Des.* **2014**, *10*, 266–273. [[CrossRef](#)]
161. de Souza, F.R.; Garcia, D.R.; Cuya, T.; Pimentel, A.S.; Goncalves, A.D.; de Alencastro, R.B.; Franca, T.C.C. Molecular Modeling Study of Uncharged Oximes Compared to HI-6 and 2-PAM Inside Human AChE Sarin and VX Conjugates. *ACS Omega* **2020**, *5*, 4490–4500. [[CrossRef](#)]
162. Musilek, K.; Roder, J.; Komloova, M.; Holas, O.; Hrabínova, M.; Pohanka, M.; Dohnal, V.; Opletalova, V.; Kuca, K.; Jung, Y.S. Preparation, in vitro screening and molecular modelling of symmetrical 4-tert-butylpyridinium cholinesterase inhibitors—Analogues of SAD-128. *Bioorg. Med. Chem. Lett.* **2011**, *21*, 150–154. [[CrossRef](#)]
163. Bhattacharjee, A.K.; Kuca, K.; Musilek, K.; Gordon, R.K. In Silico Pharmacophore Model for Tabun-Inhibited Acetylcholinesterase Reactivators: A Study of Their Stereoelectronic Properties. *Chem. Res. Toxicol.* **2010**, *23*, 26–36. [[CrossRef](#)] [[PubMed](#)]
164. Chandar, N.B.; Lo, R.; Ganguly, B. Quantum chemical and steered molecular dynamics studies for one pot solution to reactivate aged acetylcholinesterase with alkylator oxime. *Chem. Biol. Interact.* **2014**, *223*, 58–68. [[CrossRef](#)] [[PubMed](#)]
165. Lo, R.; Ganguly, B. Can hydroxylamine be a more potent nucleophile for the reactivation of tabun-inhibited AChE than prototype oxime drugs? An answer derived from quantum chemical and steered molecular dynamics studies. *Mol. Biosyst.* **2014**, *10*, 2368–2383. [[CrossRef](#)] [[PubMed](#)]
166. da Silva, J.A.V.; Pereira, A.F.; LaPlante, S.R.; Kuca, K.; Ramalho, T.C.; Franca, T.C.C. Reactivation of VX-Inhibited Human Acetylcholinesterase by Deprotonated Pralidoxime. A Complementary Quantum Mechanical Study. *Biomolecules* **2020**, *10*, 192. [[CrossRef](#)]

167. de Castro, A.A.; Polisel, D.A.; Pereira, B.T.L.; da Cunha, E.F.F.; Kuca, K.; Nepovimova, E.; Ramalho, T.C. Understanding the Interaction Modes and Reactivity of Trimedoxime toward MmAChE Inhibited by Nerve Agents: Theoretical and Experimental Aspects. *Int. J. Mol. Sci.* **2020**, *21*, 6510. [[CrossRef](#)] [[PubMed](#)]
168. Pang, Y.-P.; Kollmeyer, T.M.; Hong, F.; Lee, J.-C.; Hammond, P.I.; Haugabouk, S.P.; Brimijoin, S. Rational Design of Alkylene-Linked Bis-Pyridiniumaldoximes as Improved Acetylcholinesterase Reactivators. *Chem. Biol.* **2003**, *10*, 491–502. [[CrossRef](#)]
169. Driant, T.; Nachon, F.; Ollivier, C.; Renard, P.Y.; Derat, E. On the Influence of the Protonation States of Active Site Residues on AChE Reactivation: A QM/MM Approach. *Chembiochem* **2017**, *18*, 666–675. [[CrossRef](#)]
170. Malinak, D.; Dolezal, R.; Hepnarova, V.; Hozova, M.; Andrys, R.; Bzonek, P.; Racakova, V.; Korabecny, J.; Gorecki, L.; Mezeiova, E.; et al. Synthesis, in vitro screening and molecular docking of isoquinolinium-5-carbaldoximes as acetylcholinesterase and butyrylcholinesterase reactivators. *J. Enzym. Inhib. Med. Chem.* **2020**, *35*, 478–488. [[CrossRef](#)]
171. Vitorović-Todorović, M.D.; Worek, F.; Perdih, A.; Bauk, S.Đ.; Vujatović, T.B.; Cvijetić, I.N. The in vitro protective effects of the three novel nanomolar reversible inhibitors of human cholinesterases against irreversible inhibition by organophosphorous chemical warfare agents. *Chem. Biol. Interact.* **2019**, *309*, 108714. [[CrossRef](#)]
172. Mesarić, T.; Baweja, L.; Drasler, B.; Drobne, D.; Makovec, D.; Dusak, P.; Dhawan, A.; Sepcic, K. Effects of surface curvature and surface characteristics of carbon-based nanomaterials on the adsorption and activity of acetylcholinesterase. *Carbon* **2013**, *62*, 222–232. [[CrossRef](#)]
173. Vats, C.; Dhanjal, J.K.; Goyal, S.; Bharadvaja, N.; Grover, A. Computational design of novel flavonoid analogues as potential AChE inhibitors: Analysis using group-based QSAR, molecular docking and molecular dynamics simulations. *Struct. Chem.* **2015**, *26*, 467–476. [[CrossRef](#)]
174. Kim, J.H.; Lee, S.H.; Lee, H.W.; Sun, Y.N.; Jang, W.H.; Yang, S.Y.; Jang, H.B.; Kim, Y.H. (-)-Epicatechin derivate from *Orostachys japonicus* as potential inhibitor of the human butyrylcholinesterase. *Int. J. Biol. Macromol.* **2016**, *91*, 1033–1039. [[CrossRef](#)]
175. de Almeida, J.S.F.D.; Cavalcante, S.F.d.A.; Dolezal, R.; Kuca, K.; Musilek, K.; Jun, D.; Franca, T.C.C. Surface screening, molecular modeling and in vitro studies on the interactions of aflatoxin M1 and human enzymes acetyl- and butyrylcholinesterase. *Chem. Biol. Interact.* **2019**, *308*, 113–119. [[CrossRef](#)]
176. Delogu, G.L.; Matos, M.J.; Fanti, M.; Era, B.; Medda, R.; Pieroni, E.; Fais, A.; Kumar, A.; Pintus, F. 2-Phenylbenzofuran derivatives as butyrylcholinesterase inhibitors: Synthesis, biological activity and molecular modeling. *Bioorg. Med. Chem. Lett.* **2016**, *26*, 2308–2313. [[CrossRef](#)] [[PubMed](#)]
177. Estevez, J.; de Souza, F.R.; Romo, M.; Mangas, I.; Franca, T.C.C.; Vilanova, E. Interactions of human butyrylcholinesterase with phenylvalerate and acetylthiocholine as substrates and inhibitors: Kinetic and molecular modeling approaches. *Arch. Toxicol.* **2019**, *93*, 1281–1296. [[CrossRef](#)]
178. Pourshojaei, Y.; Abiri, A.; Eskandari, K.; Haghighijoo, Z.; Edraki, N.; Asadipour, A. Phenoxyethyl Piperidine/Morpholine Derivatives as PAS and CAS Inhibitors of Cholinesterases: Insights for Future Drug Design. *Sci. Rep.* **2019**, *9*, 19855. [[CrossRef](#)]
179. Hudcova, A.; Kroutil, A.; Kubinova, R.; Garro, A.D.; Gutierrez, L.J.; Enriz, D.; Oravec, M.; Csollei, J. Arylamino propanone Derivatives as Potential Cholinesterase Inhibitors: Synthesis, Docking Study and Biological Evaluation. *Molecules* **2020**, *25*, 1751. [[CrossRef](#)]
180. Gharaghani, S.; Khayamian, T.; Ebrahimi, M. Molecular dynamics simulation study and molecular docking descriptors in structure-based QSAR on acetylcholinesterase (AChE) inhibitors. *Sar Qsar Environ. Res.* **2013**, *24*, 773–794. [[CrossRef](#)]
181. Khan, I.; Samad, A.; Khan, A.Z.; Habtemariam, S.; Badshah, A.; Abdullah, S.M.; Ullah, N.; Khan, A.; Zia-Ul-Haq, M. Molecular interactions of 4-acetoxy-plakinamine B with peripheral anionic and other catalytic subsites of the aromatic gorge of acetylcholinesterase: Computational and structural insights. *Pharm. Biol.* **2013**, *51*, 722–727. [[CrossRef](#)] [[PubMed](#)]
182. Shrivastava, S.K.; Sinha, S.K.; Srivastava, P.; Tripathi, P.N.; Sharma, P.; Tripathi, M.K.; Tripathi, A.; Choubey, P.K.; Waiker, D.K.; Aggarwal, L.M.; et al. Design and development of novel p-aminobenzoic acid derivatives as potential cholinesterase inhibitors for the treatment of Alzheimer's disease. *Bioorg. Chem.* **2019**, *82*, 211–223. [[CrossRef](#)] [[PubMed](#)]
183. Coban, G.; Carlino, L.; Tarikogullari, A.H.; Parlar, S.; Sarikaya, G.; Alptuzun, V.; Alpan, A.S.; Gunes, H.S.; Erciyas, E. 1H-benzimidazole derivatives as butyrylcholinesterase inhibitors: Synthesis and molecular modeling studies. *Med. Chem. Res.* **2016**, *25*, 2005–2014. [[CrossRef](#)]
184. Abuhamdah, S.; Habash, M.; Taha, M. Elaborate ligand-based modeling coupled with QSAR analysis and in silico screening reveal new potent acetylcholinesterase inhibitors. *J. Comput. Aided Mol. Des.* **2013**, *27*, 1075–1092. [[CrossRef](#)]
185. Correa-Basurto, J.; Bello, M.; Rosales-Hernandez, M.C.; Hernandez-Rodriguez, M.; Nicolas-Vazquez, I.; Rojo-Dominguez, A.; Trujillo-Ferrara, J.G.; Miranda, R.; Flores-Sandoval, C.A. QSAR, docking, dynamic simulation and quantum mechanics studies to explore the recognition properties of cholinesterase binding sites. *Chem. Biol. Interact.* **2014**, *209*, 1–13. [[CrossRef](#)] [[PubMed](#)]
186. Gwaram, N.S.; Ali, H.M.; Abdulla, M.A.; Buckle, M.J.C.; Sukumaran, S.D.; Chung, L.Y.; Othman, R.; Alhadi, A.A.; Yehye, W.A.; Hadi, A.H.A.; et al. Synthesis, Characterization, X-ray Crystallography, Acetyl Cholinesterase Inhibition and Antioxidant Activities of Some Novel Ketone Derivatives of Gallic Hydrazide-Derived Schiff Bases. *Molecules* **2012**, *17*, 2408–2427. [[CrossRef](#)] [[PubMed](#)]
187. Romani, R.; Galeazzi, R.; Rosi, G.; Fiorini, R.; Pirisinu, I.; Ambrosini, A.; Zolese, G. Anandamide and its congeners inhibit human plasma butyrylcholinesterase. Possible new roles for these endocannabinoids? *Biochimie* **2011**, *93*, 1584–1591. [[CrossRef](#)] [[PubMed](#)]






188. Vitorovic-Todorovic, M.D.; Koukoulitsa, C.; Juranic, I.O.; Mandic, L.M.; Drakulic, B.J. Structural modifications of 4-aryl-4-oxo-2-aminybutanamides and their acetyl- and butyrylcholinesterase inhibitory activity. Investigation of AChE-ligand interactions by docking calculations and molecular dynamics simulations. *Eur. J. Med. Chem.* **2014**, *81*, 158–175. [[CrossRef](#)] [[PubMed](#)]
189. Singh, S.P.; Gupta, D. Discovery of potential inhibitor against human acetylcholinesterase: A molecular docking and molecular dynamics investigation. *Comput. Biol. Chem.* **2017**, *68*, 224–230. [[CrossRef](#)] [[PubMed](#)]
190. Mohammadi, T.; Ghayeb, Y. Atomic insight into designed carbamate-based derivatives as acetylcholine esterase (AChE) inhibitors: A computational study by multiple molecular docking and molecular dynamics simulation. *J. Biomol. Struct. Dyn.* **2018**, *36*, 126–138. [[CrossRef](#)] [[PubMed](#)]
191. Kurt, B.Z.; Gazioglu, I.; Dag, A.; Salmas, R.E.; Kayik, G.; Durdagi, S.; Sonmez, F. Synthesis, anticholinesterase activity and molecular modeling study of novel carbamate-substituted thymol/carvacrol derivatives. *Bioorg. Med. Chem.* **2017**, *25*, 1352–1363. [[CrossRef](#)]
192. Domínguez, J.L.; Fernández-Nieto, F.; Castro, M.; Catto, M.; Paleo, M.R.; Porto, S.; Sardina, F.J.; Brea, J.M.; Carotti, A.; Villaverde, M.C.; et al. Computer-Aided Structure-Based Design of Multitarget Leads for Alzheimer’s Disease. *J. Chem. Inf. Modeling* **2015**, *55*, 135–148. [[CrossRef](#)]
193. Dileep, K.V.; Remya, C.; Tintu, I.; Sadasivan, C. Inhibition, ADME and structure based modification of IAA and IBA against acetylcholinesterase: An attempt towards new drug development for Alzheimer’s disease. *Front. Life Sci.* **2013**, *7*, 164–173. [[CrossRef](#)]
194. Bingul, M.; Ercan, S.; Boga, M. The design of novel 4,6-dimethoxyindole based hydrazide- hydrazones: Molecular modeling, synthesis and anticholinesterase activity. *J. Mol. Struct.* **2020**, *1213*, 128202. [[CrossRef](#)]
195. Abdul Manap, A.S.; Tan, A.C.W.; Weng, H.L.; Chia, A.Y.Y.; Vijayabalan, S.; Arya, A.; Wong, E.H.; Rizwan, F.; Bindal, U.; Koshy, S.; et al. Synergistic Effects of Curcumin and Piperine as Potent Acetylcholine and Amyloidogenic Inhibitors With Significant Neuroprotective Activity in SH-SY5Y Cells via Computational Molecular Modeling and in vitro Assay. *Front. Aging Neurosci.* **2019**, *11*, 206. [[CrossRef](#)] [[PubMed](#)]
196. Meena, P.; Nemaish, V.; Khatri, M.; Manral, A.; Luthra, P.M.; Tiwari, M. Synthesis, biological evaluation and molecular docking study of novel piperidine and piperazine derivatives as multi-targeted agents to treat Alzheimer’s disease. *Bioorg. Med. Chem.* **2015**, *23*, 1135–1148. [[CrossRef](#)]
197. Tripathi, P.N.; Srivastava, P.; Sharma, P.; Tripathi, M.K.; Seth, A.; Tripathi, A.; Rai, S.N.; Singh, S.P.; Shrivastava, S.K. Biphenyl-3-oxo-1,2,4-triazine linked piperazine derivatives as potential cholinesterase inhibitors with anti-oxidant property to improve the learning and memory. *Bioorg. Chem.* **2019**, *85*, 82–96. [[CrossRef](#)] [[PubMed](#)]
198. Gurung, A.B.; Aguan, K.; Mitra, S.; Bhattacharjee, A. Identification of molecular descriptors for design of novel Isoalloxazine derivatives as potential Acetylcholinesterase inhibitors against Alzheimer’s disease. *J. Biomol. Struct. Dyn.* **2017**, *35*, 1729–1742. [[CrossRef](#)]
199. Sinha, S.K.; Shrivastava, S.K. Synthesis, evaluation and molecular dynamics study of some new 4-aminopyridine semicarbazones as an anti-amnesic and cognition enhancing agents. *Bioorg. Med. Chem.* **2013**, *21*, 5451–5460. [[CrossRef](#)] [[PubMed](#)]
200. Patel, D.V.; Patel, N.R.; Kanhed, A.M.; Teli, D.M.; Patel, K.B.; Joshi, P.D.; Patel, S.P.; Gandhi, P.M.; Chaudhary, B.N.; Prajapati, N.K.; et al. Novel carbazole-stilbene hybrids as multifunctional anti-Alzheimer agents. *Bioorg. Chem.* **2020**, *101*. [[CrossRef](#)]
201. Tallini, L.R.; Bastida, J.; Cortes, N.; Osorio, E.H.; Theoduloz, C.; Schmeda-Hirschmann, G. Cholinesterase Inhibition Activity, Alkaloid Profiling and Molecular Docking of Chilean Rhodophiala (Amaryllidaceae). *Molecules* **2018**, *23*, 1532. [[CrossRef](#)]
202. Rodriguez, Y.A.; Gutierrez, M.; Ramirez, D.; Alzate-Morales, J.; Bernal, C.C.; Guiza, F.M.; Bohorquez, A.R.R. Novel N-allyl/propargyl tetrahydroquinolines: Synthesis via Three-component Cationic Imino Diels-Alder Reaction, Binding Prediction, and Evaluation as Cholinesterase Inhibitors. *Chem. Biol. Drug Des.* **2016**, *88*, 498–510. [[CrossRef](#)]
203. Rodriguez Nunez, Y.A.; Gutierrez, M.; Alzate-Morales, J.; Adasme-Carreno, F.; Guiza, F.M.; Bernal, C.C.; Bohorquez, A.R.R. Tetrahydroquinoline-Isoxazole/Isoxazoline Hybrid Compounds as Potential Cholinesterases Inhibitors: Synthesis, Enzyme Inhibition Assays, and Molecular Modeling Studies. *Int. J. Mol. Sci.* **2020**, *21*, 5. [[CrossRef](#)] [[PubMed](#)]
204. Darras, F.H.; Pockes, S.; Huang, G.; Wehle, S.; Strasser, A.; Wittmann, H.-J.; Nimczick, M.; Sottriffer, C.A.; Decker, M. Synthesis, Biological Evaluation, and Computational Studies of Tri- and Tetracyclic Nitrogen-Bridgehead Compounds as Potent Dual-Acting AChE Inhibitors and hH3 Receptor Antagonists. *ACS Chem. Neurosci.* **2014**, *5*, 225–242. [[CrossRef](#)]
205. Samadi, A.; de los Ríos, C.; Bolea, I.; Chioua, M.; Iriepa, I.; Moraleda, I.; Bartolini, M.; Andrisano, V.; Gálvez, E.; Valderas, C.; et al. Multipotent MAO and cholinesterase inhibitors for the treatment of Alzheimer’s disease: Synthesis, pharmacological analysis and molecular modeling of heterocyclic substituted alkyl and cycloalkyl propargyl amine. *Eur. J. Med. Chem.* **2012**, *52*, 251–262. [[CrossRef](#)] [[PubMed](#)]
206. Dolles, D.; Hoffmann, M.; Gunesch, S.; Marinelli, O.; Moeller, J.; Santoni, G.; Chatonnet, A.; Lohse, M.J.; Wittmann, H.-J.; Strasser, A.; et al. Structure-Activity Relationships and Computational Investigations into the Development of Potent and Balanced Dual-Acting Butyrylcholinesterase Inhibitors and Human Cannabinoid Receptor 2 Ligands with Pro-Cognitive in Vivo Profiles. *J. Med. Chem.* **2018**, *61*, 1646–1663. [[CrossRef](#)]
207. Hassan, M.; Abbasi, M.A.; Rehman, A.U.; Siddiqui, S.Z.; Hussain, G.; Shah, S.A.A.; Shahid, M.; Seo, S.-Y. Exploration of synthetic multifunctional amides as new therapeutic agents for Alzheimer’s disease through enzyme inhibition, chemoinformatic properties, molecular docking and dynamic simulation insights. *J. Theor. Biol.* **2018**, *458*, 169–183. [[CrossRef](#)]

208. Hassan, M.; Abbasi, M.A.; Rehman, A.U.; Siddiqui, S.Z.; Shahzadi, S.; Raza, H.; Hussain, G.; Ali Shah, S.A.; Ashraf, M.; Shahid, M.; et al. Designing of promising medicinal scaffolds for Alzheimer's disease through enzyme inhibition, lead optimization, molecular docking and dynamic simulation approaches. *Bioorg. Chem.* **2019**, *91*, 103138. [[CrossRef](#)] [[PubMed](#)]
209. Yang, H.; Du, C.; Li, Q.; Chen, T.; Lu, X.; Li, Q.; Feng, F.; Chen, Y.; Liu, W.; Sun, H. Discovery, molecular dynamic simulation and biological evaluation of structurally diverse cholinesterase inhibitors with new scaffold through shape-based pharmacophore virtual screening. *Bioorg. Chem.* **2019**, *92*, 103294. [[CrossRef](#)]
210. Asadi, M.; Ebrahimi, M.; Mohammadi-Khanaposhtani, M.; Azizian, H.; Sepehri, S.; Nadri, H.; Biglar, M.; Amanlou, M.; Larijani, B.; Mirzazadeh, R.; et al. Design, synthesis, molecular docking, and cholinesterase inhibitory potential of phthalimide-dithiocarbamate hybrids as new agents for treatment of Alzheimer's disease. *Chem. Biodivers.* **2019**, *16*, e1900370. [[CrossRef](#)]
211. Liu, S.J.; Shang, R.F.; Shi, L.X.; Zhou, R.; He, J.Y.; Wan, D.C.C. Design, Synthesis, and Evaluation of 7H-thiazolo-3,2-b-1,2,4-triazin-7-one Derivatives as Dual Binding Site Acetylcholinesterase Inhibitors. *Chem. Biol. Drug Des.* **2014**, *84*, 169–174. [[CrossRef](#)]
212. Islam, M.M.; Rohman, M.A.; Gurung, A.B.; Bhattacharjee, A.; Aguan, K.; Mitra, S. Correlation of cholinergic drug induced quenching of acetylcholinesterase bound thioflavin-T fluorescence with their inhibition activity. *Spectrochim. Acta Part A Mol. Biomol. Spectrosc.* **2018**, *189*, 250–257. [[CrossRef](#)]
213. Tai, K.; Shen, T.; Henchman, R.H.; Bourne, Y.; Marchot, P.; McCammon, J.A. Mechanism of Acetylcholinesterase Inhibition by Fasciculin: A 5-ns Molecular Dynamics Simulation. *J. Am. Chem. Soc.* **2002**, *124*, 6153–6161. [[CrossRef](#)] [[PubMed](#)]
214. Harel, M.H.; Kleywegt, G.J.; Ravelli, R.B.; Silman, I.; Sussman, J.L. Crystal structure of an acetylcholinesterase-fasciculin complex: Interaction of a three-fingered toxin from snake venom with its target. *Structure* **1995**, *3*, 1355–1366. [[CrossRef](#)]
215. Kim, S.; Lee, Y.; Lazar, P.; Son, M.; Baek, A.; Thangapandian, S.; Jeong, N.Y.; Yoo, Y.H.; Lee, K.W. Binding conformation prediction between human acetylcholinesterase and cytochrome c using molecular modeling methods. *J. Mol. Graph. Model.* **2011**, *29*, 996–1005. [[CrossRef](#)] [[PubMed](#)]
216. Sohail, I.; Rashid, S. Molecular Dynamics and Regulation of Butyrylcholinesterase Cholinergic Activity by RNA Binding Proteins. *CNS Neurol. Disord. Drug Targets* **2014**, *13*, 1366–1377. [[CrossRef](#)]
217. Sohail, S. In Silico Study of miR-132 with mRNA of Acetylcholinesterase to Investigate the Binding Affinity for Interaction. *J. Mol. Imaging Dyn.* **2018**, *8*. [[CrossRef](#)]
218. Kumar, B.; Dwivedi, A.R.; Sarkar, B.; Gupta, S.K.; Krishnamurthy, S.; Mantha, A.K.; Parkash, J.; Kumar, V. 4,6-Diphenylpyrimidine Derivatives as Dual Inhibitors of Monoamine Oxidase and Acetylcholinesterase for the Treatment of Alzheimer's Disease. *ACS Chem. Neurosci.* **2019**, *10*, 252–265. [[CrossRef](#)] [[PubMed](#)]
219. Kumar, B.; Kumar, V.; Prashar, V.; Saini, S.; Dwivedi, A.R.; Bajaj, B.; Mehta, D.; Parkash, J.; Kumar, V. Dipropargyl substituted diphenylpyrimidines as dual inhibitors of monoamine oxidase and acetylcholinesterase. *Eur. J. Med. Chem.* **2019**, *177*, 221–234. [[CrossRef](#)]
220. Cavdar, H.; Senturk, M.; Guney, M.; Durdagi, S.; Kayik, G.; Supuran, C.T.; Ekinici, D. Inhibition of acetylcholinesterase and butyrylcholinesterase with uracil derivatives: Kinetic and computational studies. *J. Enzym. Inhib. Med. Chem.* **2019**, *34*, 429–437. [[CrossRef](#)] [[PubMed](#)]
221. Zueva, I.; Dias, J.; Lushchekina, S.; Semenov, V.; Mukhamedyarov, M.; Pashirova, T.; Babaev, V.; Nachon, F.; Petrova, N.; Nurullin, L.; et al. New evidence for dual binding site inhibitors of acetylcholinesterase as improved drugs for treatment of Alzheimer's disease. *Neuropharmacology* **2019**, *155*, 131–141. [[CrossRef](#)] [[PubMed](#)]
222. Yigit, M.; Yigit, B.; Taslimi, P.; Ozdemir, I.; Karaman, M.; Gulcin, I. Novel amine-functionalized benzimidazolium salts: Synthesis, characterization, bioactivity, and molecular docking studies. *J. Mol. Struct.* **2020**, *1207*, 127802. [[CrossRef](#)]
223. Bocca, C.C.; Rittner, R.; Hoehr, N.F.; Pinheiro, G.M.S.; Abiko, L.A.; Basso, E.A. Molecular modeling and biological evaluation of 2-N,N-dimethylaminocyclohexyl 1-N,N'-dimethylcarbamate isomers and their methylsulfate salts as cholinesterases inhibitors. *J. Mol. Struct.* **2010**, *983*, 194–199. [[CrossRef](#)]
224. Kumar, A.; Tiwari, A.; Sharma, A. Changing Paradigm from one Target one Ligand Towards Multi-target Directed Ligand Design for Key Drug Targets of Alzheimer Disease: An Important Role of In Silico Methods in Multi-target Directed Ligands Design. *Curr. Neuropharmacol.* **2018**, *16*, 726–739. [[CrossRef](#)] [[PubMed](#)]
225. Lu, S.H.; Wu, J.W.; Liu, H.L.; Zhao, J.H.; Liu, K.T.; Chuang, C.K.; Lin, H.Y.; Tsai, W.B.; Ho, Y. The discovery of potential acetylcholinesterase inhibitors: A combination of pharmacophore modeling, virtual screening, and molecular docking studies. *J. Biomed. Sci.* **2011**, *18*. [[CrossRef](#)] [[PubMed](#)]
226. Lu, X.; Yang, H.; Li, Q.; Chen, Y.; Li, Q.; Zhou, Y.; Feng, F.; Liu, W.; Guo, Q.; Sun, H. Expansion of the scaffold diversity for the development of highly selective butyrylcholinesterase (BChE) inhibitors: Discovery of new hits through the pharmacophore model generation, virtual screening and molecular dynamics simulation. *Bioorg. Chem.* **2019**, *85*, 117–127. [[CrossRef](#)] [[PubMed](#)]
227. Chen, Y.; Lin, H.; Yang, H.; Tan, R.; Bian, Y.; Fu, T.; Li, W.; Wu, L.; Pei, Y.; Sun, H. Discovery of new acetylcholinesterase and butyrylcholinesterase inhibitors through structure-based virtual screening. *RSC Adv.* **2017**, *7*, 3429–3438. [[CrossRef](#)]
228. Ochoa, R.; Rodriguez, C.A.; Zuluaga, A.F. Prediction of Ligands Binding Acetylcholinesterase with Potential Antidotal Activity: A Virtual Screening Approach. *Mol. Inform.* **2019**, *38*, 1800126. [[CrossRef](#)]
229. Brus, B.; Kosak, U.; Turk, S.; Pislir, A.; Coquelle, N.; Kos, J.; Stojan, J.; Colletier, J.-P.; Gobec, S. Discovery, Biological Evaluation, and Crystal Structure of a Novel Nanomolar Selective Butyrylcholinesterase Inhibitor. *J. Med. Chem.* **2014**, *57*, 8167–8179. [[CrossRef](#)]

230. Kosak, U.; Brus, B.; Knez, D.; Zakelj, S.; Trontelj, J.; Pislar, A.; Sink, R.; Jukič, M.; Zivin, M.; Podkova, A.; et al. The Magic of Crystal Structure-Based Inhibitor Optimization: Development of a Butyrylcholinesterase Inhibitor with Picomolar Affinity and in Vivo Activity. *J. Med. Chem* **2018**, *61*, 119–139. [[CrossRef](#)]
231. Fang, J.; Yang, R.; Gao, L.; Zhou, D.; Yang, S.; Liu, A.-l.; Du, G.-h. Predictions of BuChE Inhibitors Using Support Vector Machine and Naive Bayesian Classification Techniques in Drug Discovery. *J. Chem. Inf. Modeling* **2013**, *53*, 3009–3020. [[CrossRef](#)]
232. Sakkiah, S.; Lee, K.W. Pharmacophore-based virtual screening and density functional theory approach to identifying novel butyrylcholinesterase inhibitors. *Acta Pharmacol. Sin.* **2012**, *33*, 964–978. [[CrossRef](#)] [[PubMed](#)]
233. Zhang, A.Q.; Mu, Y.S.; Wu, F.C. An enantiomer-based virtual screening approach: Discovery of chiral organophosphates as acetyl cholinesterase inhibitors. *Ecotoxicol. Environ. Saf.* **2017**, *138*, 215–222. [[CrossRef](#)]
234. Toropova, M.A.; Raska, I.; Raskova, M.; Toropov, A.A. The Utilization of the Monte Carlo Technique for Rational Drug Discovery. *Comb. Chem. High Throughput Screen.* **2016**, *19*, 676–687. [[CrossRef](#)] [[PubMed](#)]
235. Thai, N.Q.; Nguyen, H.L.; Linh, H.Q.; Li, M.S. Protocol for fast screening of multi-target drug candidates: Application to Alzheimer's disease. *J. Mol. Graph. Model.* **2017**, *77*, 121–129. [[CrossRef](#)] [[PubMed](#)]
236. Vistoli, G.; Mazzolari, A.; Testa, B.; Pedretti, A. Binding Space Concept: A New Approach To Enhance the Reliability of Docking Scores and Its Application to Predicting Butyrylcholinesterase Hydrolytic Activity. *J. Chem. Inf. Modeling* **2017**, *57*, 1691–1702. [[CrossRef](#)] [[PubMed](#)]
237. Morris, G.M.; Green, L.G.; Radic, Z.; Taylor, P.; Sharpless, K.B.; Olson, A.J.; Grynszpan, F. Automated Docking with Protein Flexibility in the Design of Femtomolar “Click Chemistry” Inhibitors of Acetylcholinesterase. *J. Chem. Inf. Modeling* **2013**, *53*, 898–906. [[CrossRef](#)] [[PubMed](#)]
238. Liu, X.; Jiang, H.; Li, H. SHAFTS: A Hybrid Approach for 3D Molecular Similarity Calculation. 1. Method and Assessment of Virtual Screening. *J. Chem. Inf. Modeling* **2011**, *51*, 2372–2385. [[CrossRef](#)] [[PubMed](#)]
239. Lešnik, S.; Štular, T.; Brus, B.; Knez, D.; Gobec, S.; Janežič, D.; Konc, J. LiSiCA: A Software for Ligand-Based Virtual Screening and Its Application for the Discovery of Butyrylcholinesterase Inhibitors. *J. Chem. Inf. Modeling* **2015**, *55*, 1521–1528. [[CrossRef](#)] [[PubMed](#)]
240. Mizutani, M.Y.; Itai, A. Efficient method for high-throughput virtual screening based on flexible docking: Discovery of novel acetylcholinesterase inhibitors. *J. Med. Chem.* **2004**, *47*, 4818–4828. [[CrossRef](#)]

Article

Molecular Modeling Studies on the Multistep Reactivation Process of Organophosphate-Inhibited Acetylcholinesterase and Butyrylcholinesterase

Jakub Jończyk ¹, Jędrzej Kukułowicz ¹, Kamil Łątka ¹, Barbara Malawska ¹, Young-Sik Jung ^{2,3}, Kamil Musilek ^{4,5,*} and Marek Bajda ^{1,*}

- ¹ Department of Physicochemical Drug Analysis, Faculty of Pharmacy, Jagiellonian University Medical College, Medyczna 9, 30-688 Kraków, Poland; jakub.jonczyk@uj.edu.pl (J.J.); jedrzej.kukulowicz@doctoral.uj.edu.pl (J.K.); kamil.latka@doctoral.uj.edu.pl (K.Ł.); mfmalaws@cyf-kr.edu.pl (B.M.)
- ² Division of Bio and Drug Discovery, Korea Research Institute of Chemical Technology, Daejeon 34114, Korea; ysjung@kricr.re.kr
- ³ Department of Medicinal and Pharmaceutical Chemistry, University of Science and Technology, Daejeon 34113, Korea
- ⁴ Department of Chemistry, Faculty of Science, University of Hradec Kralove, Rokitsanskeho 62, 500 03 Hradec Kralove, Czech Republic
- ⁵ Biomedical Research Center, University Hospital in Hradec Kralove, Sokolska 581, 500 05 Hradec Kralove, Czech Republic
- * Correspondence: kamil.musilek@uhk.cz (K.M.); marek.bajda@uj.edu.pl (M.B.)



Citation: Jończyk, J.; Kukułowicz, J.; Łątka, K.; Malawska, B.; Jung, Y.-S.; Musilek, K.; Bajda, M. Molecular Modeling Studies on the Multistep Reactivation Process of Organophosphate-Inhibited Acetylcholinesterase and Butyrylcholinesterase. *Biomolecules* **2021**, *11*, 169. <https://doi.org/10.3390/biom11020169>

Academic Editor: Jan Korabecny
Received: 21 December 2020
Accepted: 22 January 2021
Published: 27 January 2021

Publisher's Note: MDPI stays neutral with regard to jurisdictional claims in published maps and institutional affiliations.



Copyright: © 2021 by the authors. Licensee MDPI, Basel, Switzerland. This article is an open access article distributed under the terms and conditions of the Creative Commons Attribution (CC BY) license (<https://creativecommons.org/licenses/by/4.0/>).

Abstract: Poisoning with organophosphorus compounds used as pesticides or misused as chemical weapons remains a serious threat to human health and life. Their toxic effects result from irreversible blockade of the enzymes acetylcholinesterase and butyrylcholinesterase, which causes overstimulation of the cholinergic system and often leads to serious injury or death. Treatment of organophosphorus poisoning involves, among other strategies, the administration of oxime compounds. Oximes reactivate cholinesterases by breaking the covalent bond between the serine residue from the enzyme active site and the phosphorus atom of the organophosphorus compound. Although the general mechanism of reactivation has been known for years, the exact molecular aspects determining the efficiency and selectivity of individual oximes are still not clear. This hinders the development of new active compounds. In our research, using relatively simple and widely available molecular docking methods, we investigated the reactivation of acetyl- and butyrylcholinesterase blocked by sarin and tabun. For the selected oximes, their binding modes at each step of the reactivation process were identified. Amino acids essential for effective reactivation and those responsible for the selectivity of individual oximes against inhibited acetyl- and butyrylcholinesterase were identified. This research broadens the knowledge about cholinesterase reactivation and demonstrates the usefulness of molecular docking in the study of this process. The presented observations and methods can be used in the future to support the search for new effective reactivators.

Keywords: molecular modeling; reactivators; reactivation process; organophosphates; docking studies; acetylcholinesterase; butyrylcholinesterase

1. Introduction

Organophosphorus compounds (OPs) have been known for years as effective pesticides used in agriculture (e.g., paraoxon and chlorpyrifos) and as chemical weapons (e.g., sarin, venomous agent X (VX), tabun, and soman) belonging to the so-called “nerve agent” class representing some of the strongest man-made poisons [1–3]. The toxic effects of OPs result from irreversible blockade of acetylcholinesterase (AChE), the enzyme responsible for the degradation of acetylcholine [1,3]. The accumulation of this neurotransmitter in

cholinergic synapses within the central and peripheral nervous system causes, among other effects, muscle tremors, spasms, cardiac dysfunction, and respiratory failure, often leading to death [4,5]. In addition to blocking AChE, OPs also have the ability to inhibit butyrylcholinesterase (BuChE), which also degrades other choline esters in addition to acetylcholine. The World Health Organization (WHO) estimates that approximately 3 million people are accidentally or intentionally intoxicated each year by OPs used as pesticides, with approximately 220,000 of them being poisoned fatally [6]. Although usage of chemical weapons is internationally banned, there are unfortunately still cases of the deliberate use of OPs, such as the terrorist attacks in the Tokyo subway in 1995, the bombing of civilians in Syria from 2013 to date, the use of a Novichok agent against Sergei and Yulia Skripal in 2018, and the recent poisoning of Alexei Navalny [7–9]. Treatment options for OP intoxication are limited. They are based on the administration of atropine, which reduces the overstimulation of muscarinic receptors, benzodiazepines that reduce convulsions, and oximes, which are specific antidotes capable of reactivating AChE [5,10]. The effectiveness of oximes depends on the type of OP and the time elapsed from poisoning. The small number of such compounds currently available for use as drugs and their often low activity result in the need to search for new reactivators. Intravenous administration of BuChE, alone or in combination with its reactivator, as a pseudocatalytic bioscavenger of OPs in the bloodstream is being considered for use as a supportive treatment that allows more rapid clearance of OPs from the patient [11,12]. However, the lack of effective BuChE reactivators currently limits the implementation of this therapeutic solution.

At the molecular level, the irreversible blockade of cholinesterases by OPs is based on the phosphorylation of serine, which is a part of the catalytic triad, also called the esteratic site, of the enzymes. This prevents the binding of the ester group of acetylcholine at this site and its further hydrolysis [1,13]. The other residues included in the catalytic triad are histidine and glutamic acid. The OP-enzyme complex may undergo an aging process. This process involves the dealkylation of an alkoxy moiety from the phosphorus atom of the OP. This process is clinically unfavorable because the aged complex is not susceptible to reactivation [14–16]. Other important structural elements of cholinesterases are the anionic site, which is responsible for binding the substrate quaternary ammonium group, and the acyl pocket, which binds the alkyl chains of acyl moieties. There is also an oxyanion hole that stabilizes the transition complex during the enzymatic reaction and a peripheral anionic site (PAS) located at the entry to the active gorge [17]. Notably, the active site in BuChE is significantly larger than that in AChE. This is due to the replacement of some of the aromatic amino acids within the acyl pocket, anionic site, and PAS in AChE with smaller aliphatic or even polar residues in BuChE. This translates into different substrate specificities of these enzymes as well as selective binding of inhibitors or reactivators [17,18].

The exact mechanism of cholinesterase reactivation by an oxime involves a nucleophilic attack of the oxime ion on the OP phosphorus atom bound to serine (SER) in the enzyme active site (Figure 1). As a result, a transient oxime-OP-SER adduct with a trigonal bipyramidal geometry is created. Subsequently, the OP-SER bond is broken, which restores the catalytic activity of cholinesterase and releases the OP-oxime complex. This complex should have low affinity for the binding enzyme pocket to quickly dissociate from it without rephosphorylation or further enzyme blockade [16,19,20].

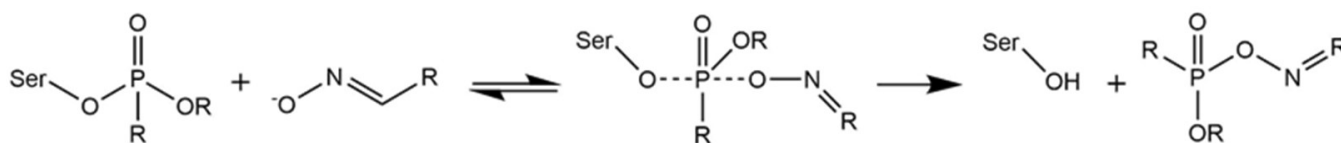


Figure 1. Mechanism of cholinesterase reactivation by oxime compounds.

Effective reactivators, in addition to a strong nucleophilic moiety such as the oxime moiety, must also have elements that allow interaction with the enzyme active site and

facilitate favorable positioning of the oxime fragment with respect to the OP phosphorus atom. These criteria are fulfilled by the strongest reactivators currently known, which are quaternary pyridinium cations with an aldoxime moiety substituted in position 2 or 4 of the pyridine ring. Due to the number of aromatic rings in the structure, they can be divided into monopyridinium and bispyridinium derivatives [21]. Examples of such reactivators are presented in Figure 2 [21–23].

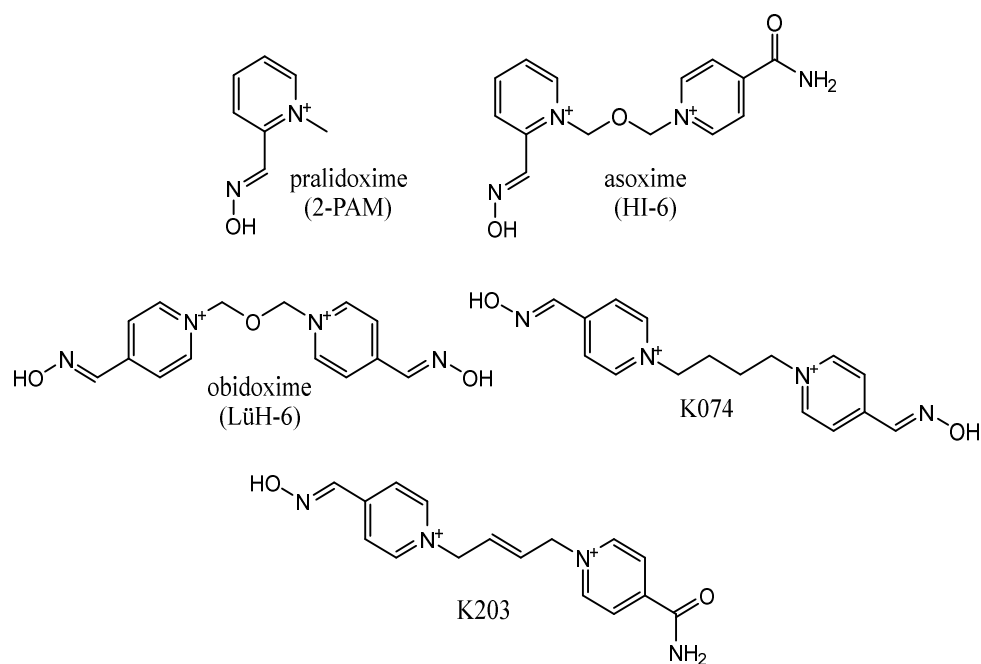


Figure 2. Structures of selected examples of cholinesterase reactivators.

Although the crystal structures of both acetyl- and butyrylcholinesterase have been known for years, only some of them present a reactivator bound to the OP-enzyme complex. In addition, in almost all cases, the ligands have conformations in which the oxime moieties are located in the opposite direction from the OP fragment or are arranged in a geometrically unfavorable position that prevents nucleophilic attack on the OP phosphorus atom [24]. Allgardsson et al. [20] named this conformation nonreactive. They also obtained one crystal structure (PDB code: 5FPP) with the preactivation conformation of the HI6 reactivator in chain A of the dimeric AChE complex inhibited by sarin. This structure presents the oxime moiety placed close to the phosphorus atom in a geometrically beneficial axial position. Interestingly, chain B obtained under the same conditions shows the nonreactivation conformation of asoxime (HI-6). It seems that the previous failures in the design of new effective reactivators may be partly caused by focusing only on the crystal structures that present reactivators in nonreactive conformations [25,26]. It is necessary to consider that an effective reactivator must be able to approach the phosphorus atom with the appropriate geometric constraints as presented by Allgardsson et al. [20]. Capturing this state by molecular modeling is not easy. It often requires the use of molecular dynamics techniques in addition to quantum methods because only they can reproduce the moment of oxime-OP bond formation [27–30]. Both molecular dynamics methods and, to an even greater extent, quantum calculations require high computational capacity, which limits their application.

In our work, we have studied the subsequent reactivation steps using relatively simple and fast molecular docking methods that are available to a wide group of researchers. In addition to the reactivation of acetylcholinesterase, we have also explored this process for butyrylcholinesterase. There is currently little research in the literature on this subject, although reactivation of BuChE appears to be beneficial from a pharmacological point of view. In addition, the presented studies consider an often overlooked state after reactivation when the OP fragment is bound to the oxime. The affinity of the oxime-OP complex to the

cholinesterase active site is important for the efficiency of the reactivation process. The present research broadens the knowledge about the cholinesterase reactivation process and provides methods and observations that can support future design of new AChE and BuChE reactivators.

2. Materials and Methods

The three-dimensional ligand structures (free oximes and oxime-OP complexes) were built with the Corina online tool (Molecular Networks GmbH, Nürnberg, Germany and Altamira, LLC, Westport, CT, USA). Free oximes were prepared in the anionic form. Sybyl-X 1.1 (Certara USA, Princeton, NJ, USA) was used for the assignment of formal and partial charges with Gasteiger-Marsili and the preparation of mol2 files with proper atom types.

All proteins used in the docking studies were prepared with Hermes 1.7 (Cambridge Crystallographic Data Centre (CCDC), Cambridge, UK) [31]. All histidine residues were protonated at N ϵ , and the hydrogen atoms were added. All complexes with modified OP conformations (5FPP-like conformation in the prereactivation state) or with OP fragments transferred from other structures (all OP-BuChE complexes) were previously optimized with the protein preparation tool from Maestro Suite (Schrödinger, New York, NY, USA) [32].

All docking experiments were performed with the Gold v5.3 program (CCDC, Cambridge, UK) [31]. A standard set of genetic algorithm parameters with a population size of 100 and a number of operations of 100,000 was applied. The binding site was always defined as all amino acid residues within 15 Å from the oxygen atom from the hydroxyl group of serine 203 (AChE) or 198 (BuChE). As a result, 10 ligand conformations were obtained and sorted according to the values of the following scoring functions: the Astex Statistical Potential (ASP), GoldScore, ChemScore and ChemPLP. All results were visualized by PyMOL 0.99rc2 [33].

Docking studies were divided into four parts.

In the first stage of this study, presenting a nonreactive conformation of oximes, ligands were docked to complexes of AChE (2Y2V and 3DL4) and BuChE (3DJY with OP transferred from AChE complexes) inhibited by sarin and tabun. No constraints were assigned to the time of docking. The optimal docking parameters identified during the tests for this stage are summarized in Supplementary Materials Table S1.

In the second stage, the previously used protein complexes were modified so that the conformations of the OP present corresponded to the sarin conformation observed in chain A of 5FPP. Sarin-AChE and sarin-BuChE complexes were obtained by transferring the sarin-bound Ser203 directly from the 5FPP complex and subsequently optimizing the structures to remove potential steric clashes. In the case of tabun-AChE, the OP was first covalently docked to the empty 3DL7 active site. Subsequently, the pose with an ethoxy substituent bent in a similar way to that of the sarin isopropoxy group from 5FPP was selected and optimized. The tabun-BuChE complex was built by replacing fragments that distinguished both organophosphates while maintaining the positions of the overlapping heavy atoms based on the 5FPP complex as a template. After transferring a serine-tabun fragment, the entire complex was optimized. To map the prereactivation position of the pyridinium oxime observed in the reference protein, substructure-based constraints were added with the oxime moiety from cocrystallization structure of asoxime with AChE (5FPP chain A). The most favorable docking parameters are summarized in Supplementary Materials Table S2.

In the third stage, all prepared oxime-OP complexes with the phosphorus atom in the trigonal bipyramidal geometry were covalently docked to the serine of the catalytic triad of each cholinesterase (AChE—PDB code: 1J06 and BuChE—PDB code: 1P0I), recreating the bond between the oxygen and phosphorus atoms. Selected docking parameters are summarized in Supplementary Materials Table S3.

During the last stage of this study, the OP-oxime (POX) complexes representing the postreactivation state (phosphorus atom in tetrahedral geometry) were docked to AChE

(PDB code: 1J06) and BuChE (PDB code: 1P0I). Docking parameters allowing to obtain the most coherent results at this stage of research are summarized in Supplementary Materials Table S4.

3. Results and Discussion

For our research, we chose tabun and sarin as model organophosphorus compounds. The processes of reactivation of AChE and BuChE were analyzed for the following selected oxime compounds: 2-PAM, HI-6, obidoxime, K074, and K203. The ability of these compounds to reactivate AChE and BuChE blocked by sarin and tabun is presented in Table 1.

Table 1. The kinetics of reactivation of sarin or tabun inhibited AChE and BuChE by the investigated oximes [34–39].

Cpd.	Sarin-AChE		Tabun-AChE		Sarin-BuChE		Tabun-BuChE	
	K_D (μM)	k_{r2} ($\text{min}^{-1} \text{M}^{-1}$)	K_D (μM)	k_{r2} ($\text{min}^{-1} \text{M}^{-1}$)	K_D (μM)	k_{r2} ($\text{min}^{-1} \text{M}^{-1}$)	K_D (μM)	k_{r2} ($\text{min}^{-1} \text{M}^{-1}$)
Pralidoxime	28.0	9300	3200	3.2	110	1500	1300	0.9
Obidoxime	31.0	30,000	1400	42.0	92.0	3500	-	-
Asoxime	50.0	14,000	-	-	1.1	18,000	1800	0.9
K074	-	-	2000	40.0	-	-	600	13.0
K203	-	-	56.0	2100	-	-	1900	4.0

K_D —phosphylated enzyme-oxime dissociation constant; k_{r2} —second-order reactivation rate constant.

While modeling the reactivation process of cholinesterases blocked by organophosphorus compounds, we assumed the existence of several states in which the ligand could be found in the active site of the enzyme (Figure 3). Allgardsson et al. [19] proposed the presence of analogous states as part of the reactivation cycle. The crystal structure of AChE inhibited by sarin presented in their work shows a prereactivation state of HI-6 consistent with the mechanism of in-line attack of the reactivator on the phosphorus atom of an organophosphorus inhibitor [40]. As it is key for the reactivation process, we considered the balance between the formation of the presented complexes, which preferably should be shifted towards the stages immediately prior to reactivation. The energy differences between the prereactivation and transition complexes should be as small as possible, and the postreactivation OP-oxime complex should be poorly fitted to the active site. Moreover, to avoid additional enzyme blocking, the oxime should not show inhibitory effects. Free oximes were investigated as anions (monoanions in the case of obidoxime and K074) according to the reaction mechanism, indicating the direct participation of these forms in binding with OP. Poor dissociation of the oxime group was often indicated as the cause of the low activity of some reactivators in this analysis.

3.1. Nonreactive Complex

First, the nonreactive complex was analyzed. This complex is commonly observed in many crystals of AChE blocked by different OPs, e.g., in complexes stored under PDB codes: 5FPP (chain B), 5HFA, and 6CQV [20,41,42]. Our simulations also showed that the nonreactive complex is the conformation most readily achieved by ligands during docking to an active site blocked by OP. The analysis of this stage seems to be important both in the context of understanding the reasons for the behavior of the tested reactivators and to assess the preferences of individual ligands to adopt a prereactivation or nonreactive conformation. The information gained from this analysis will help guide further modification by shifting the balance between the two states in favor of the path leading to reactivation. To investigate the binding mode of the studied reactivators in a nonreactivating state, we docked them to the active site of AChE inhibited by sarin or tabun.

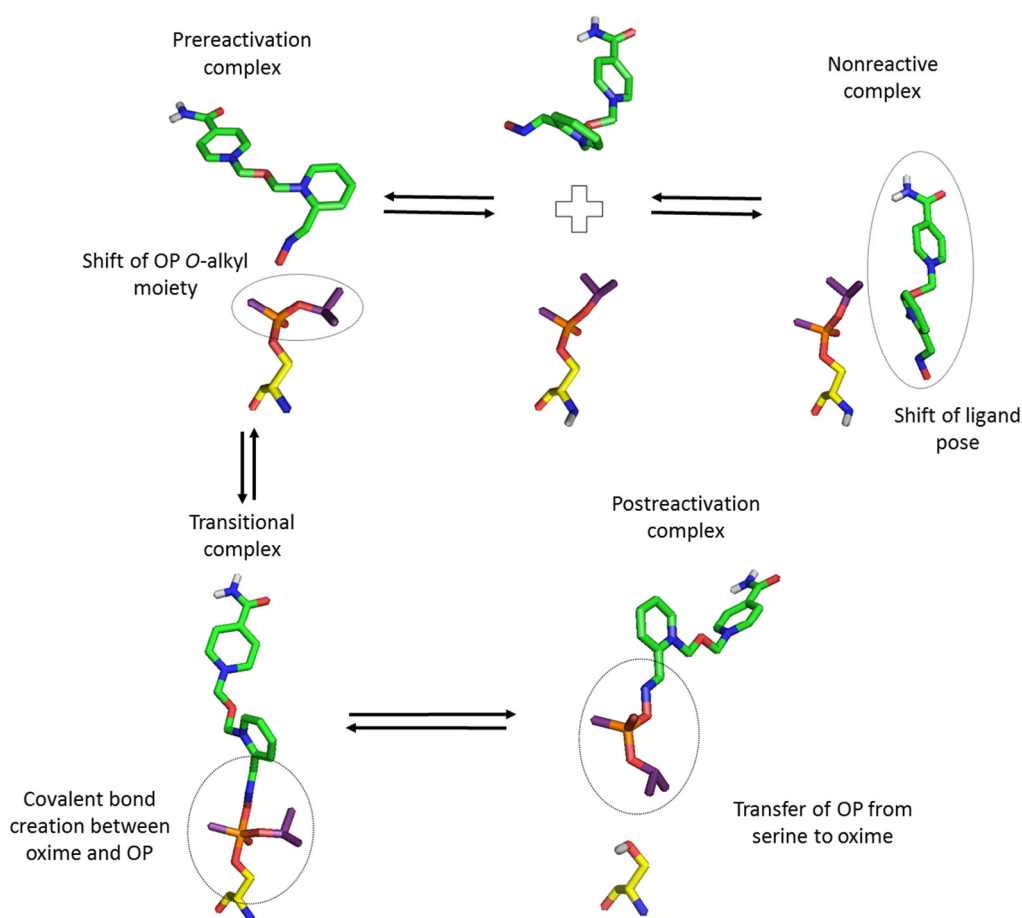


Figure 3. Multiple binding states during oxime reactivation of OP inhibited cholinesterase.

After docking to the sarin-AChE complex, most poses obtained for 2-PAM revealed conspicuous cation- π and π - π stacking interactions with Trp286 or Tyr341 (Supplementary Materials Figure S1). In the case of the tabun-AChE complex, the trend was completely different. Most of the results obtained for 2-PAM revealed a dominating arrangement in which Trp86 was involved in interactions with the pyridinium ring through π - π stacking or cation- π interactions.

Obidoxime revealed similar diversification in poses obtained for each AChE-OP complex (Supplementary Materials Figure S2). For AChE inhibited by sarin, the highest rated results showed the first pyridinium moiety interacting with Tyr124 (cation- π), Tyr337, and Tyr341 (CH- π). The other heterocyclic fragment was located in parallel with Trp286, allowing π - π stacking and cation- π interactions. AChE inhibited by tabun in most cases allowed obidoxime to interact with Trp86 by the pyridinium fragment in the parallel position while the other ring interacted with the PAS, most frequently with Trp286 and Tyr341.

Among the poses obtained for HI-6 during docking to sarin-AChE and tabun-AChE, we observed poses showing HI-6 with the amide group directed towards the catalytic site (Figure 4). A single pose for the sarin-AChE complex in a similar position to that from the 5FPP nonreactivated state was found. This dissimilarity resulted from the different conformations of Trp286, which, in our research, corresponded to the position observed in the unbound protein. Considering the above-mentioned single pose with an oxime fragment directed towards the interior of the active site of the enzyme, we observed an arrangement where the 1,2-disubstituted ring did not create any interactions, whereas oxygen belonging to the linker interacted with Tyr124 through hydrogen bond. The 1,4-disubstituted pyridinium ring interacted with Tyr341 (CH- π).

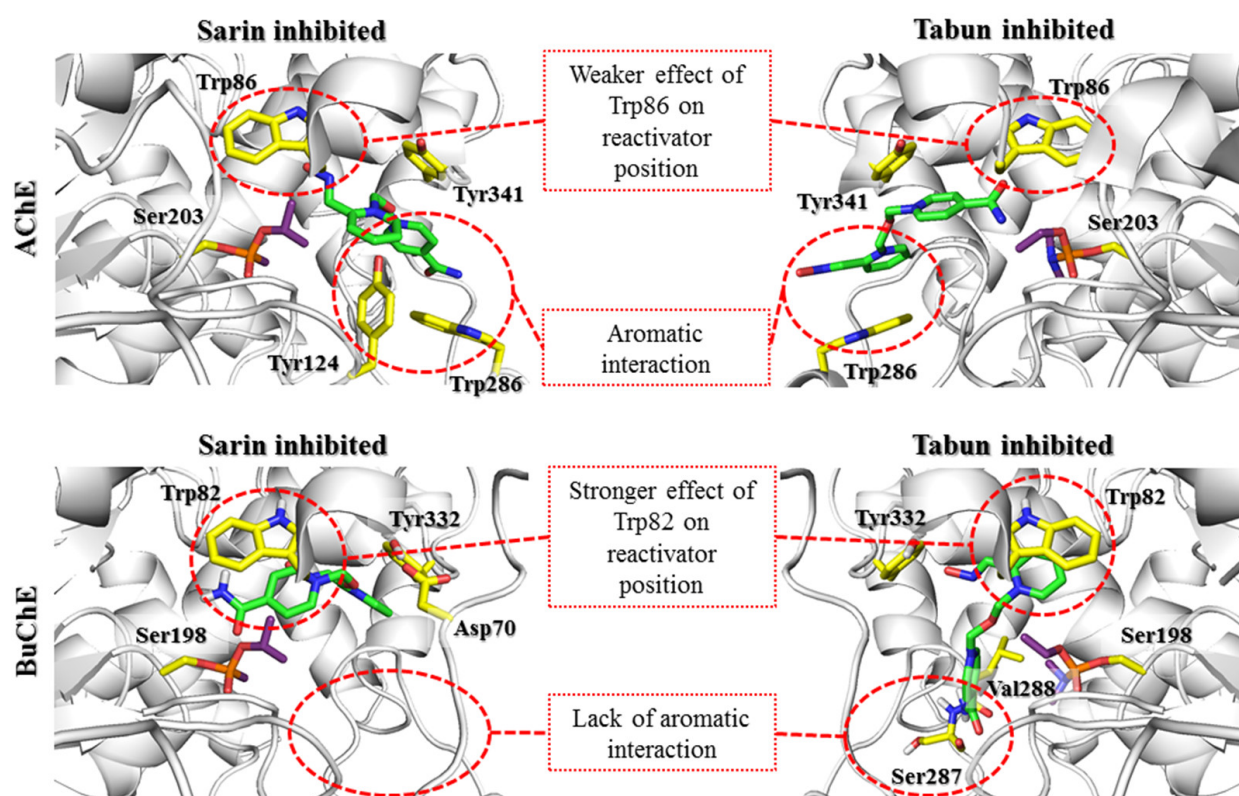


Figure 4. Docking results representing the nonreactivation conformation of the HI-6 (green) at the active site of AChE and BuChE (gray) blocked by sarin and tabun (purple). The key amino acids involved in the interactions with the reactivator are marked with yellow sticks. There is a clear difference in the binding of HI-6 in the active site of AChE and BuChE (the predominance of binding at the AChE PAS region and the BuChE anionic site).

The results for K074 and K203 coincided with those of the corresponding bispyridinium compounds obidoxime and HI-6. In the case of K074 (Supplementary Materials Figure S3), the best rated pose for AChE inhibited by sarin was arranged such that Tyr124, Tyr337, and Tyr341 were engaged in interactions with the compound. The pyridinium ring located closer to the catalytic site interacted with Tyr124 through cation- π binding, while Tyr337 created a CH- π bond. Tyr341 interacted with both pyridine rings through CH- π interactions. K074 docking to tabun-inhibited AChE revealed a binding mode close to that of obidoxime docking to tabun-inhibited AChE; the first pyridinium ring interacted with Trp86 (CH- π), while the other interacted with Tyr341 (CH- π). K203 (Supplementary Materials Figure S4) in sarin-AChE was arranged analogically to the arrangement of HI-6 docking to sarin- and tabun-inhibited AChE and was arranged in a manner in which a 1,4-disubstituted ring with an amide group was directed towards the interior of the catalytic triad, while a 1,2-disubstituted pyridinium oxime was directed towards the exit of the narrow gorge. Only a single pose of K203 in complex with AChE inhibited by tabun revealed an arrangement where the aldoxime pyridinium remained at the catalytic site; for this pose, only a CH- π interaction with Tyr341 could be distinguished.

There are currently a limited number of complexes of OP-BuChE with reactivators available in the PDB database. The structure closest to the described nonreactive state is the 4AXB crystal structure, in which 2-PAM is bound to the aged soman-BuChE complex. In docking studies, oximes easily adopt a nonreactive arrangement. This indicates a high preference for the tested compounds to occur in this conformation. It is stabilized mainly by the π - π and cation- π interactions of the pyridinium oxime moiety with Trp82. In the case of bispyridinium compounds, the other aromatic fragment created similar interactions with Tyr332.

Detailed analysis of the docking results for individual compounds revealed a very high similarity of the obtained poses both in the complex with sarin-BuChE and tabun-BuChE. In the case of 2-PAM (Supplementary Materials Figure S1), there was a slight difference in the arrangement of the pyridinium ring that directed the methyl substituent in a different direction. However, it had no significant effect on the formation of cation- π and π - π interactions with Trp82 or hydrogen bonds with the hydroxyl group of Tyr332.

Obidoxime (Supplementary Materials Figure S2) in both complexes created cation- π and π - π interactions with Trp82 and Tyr332 and hydrogen bonds between the ionized oxime moiety and Tyr128. At physiological pH, the reactivator, which has two oxime groups, was mostly present in the form in which one group was dissociated and the other was not. This allowed for the creation of an additional hydrogen bond between the nonionized oxime group and the Pro285 backbone in the sarin-BuChE complex, and, in the case of tabun-BuChE, a hydrogen bond with the carboxyl group of Glu197 was observed.

The compound HI-6 showed the greatest differences in its arrangement depending on the OP blocking the active sites of BuChE (Figure 4). In docking to sarin-BuChE, the most common and highest rated arrangement was a pose in which the pyridinium ring connected to the amide group formed cation- π and π - π interactions with Trp82. The amide group formed a hydrogen bond with Glu197. The pyridinium oxime fragment interacted with Tyr332 and was involved in the ionic bond with Asp70. The position of the oxygen atom from the linker indicates the possibility of creating hydrogen bonds with Tyr332. In the case of docking the compound HI-6 into tabun-BuChE, the results were significantly different. The pyridinium moiety with oxime substituents formed cation- π and π - π interactions with Trp82, as with most of the other examined reactivators. The oxime group was involved in creating a hydrogen bond with the hydroxyl group of Tyr332. In turn, the amide group formed a network of hydrogen bonds with the Leu286 and Ser287 main chains.

The results for compounds K074 and K203 (Supplementary Materials Figures S3 and S4) were very similar to those described for the structurally related obidoxime and HI-6. K074 at the active site of BuChE blocked by sarin created cation- π and π - π interactions with Trp82 through the ionized pyridinium oxime group. The other aromatic fragment created a CH- π interaction with Tyr332, and the oxime connected to it formed hydrogen bonds with Thr120 and the main chain of Ser287. In the tabun-BuChE complex, compound K074 was placed closer to the catalytic triad; therefore, K074 was the only tested reactivator that could form aromatic interactions with both Trp82 and His438. As in the case of obidoxime, we also observed the formation of hydrogen bonds between the ionized oxime group and Tyr128. The other aromatic ring formed cation- π and π - π interactions with Tyr332 and ionic interactions with Asp70. Compound K203 in the sarin-BuChE complex, similar to HI-6, interacted with Trp82 via a pyridinium ring with an amide substituent. Probably due to the longer linker, this fragment can be located closer to the catalytic triad so that the amide group forms hydrogen bonds with both Tyr128 and Glu197. The other pyridinium ring formed cation- π and π - π interactions with Tyr332 as well as ionic bonds with Asp70, and the oxime moiety was directed towards Thr120, forming a hydrogen bond with it.

The docking results indicate that in both AChE and BuChE, the aromatic rings of tryptophan residues greatly affect the arrangement of reactivators in the active site. In the case of AChE, the influence of Trp286 in the PAS seems to be predominant. In our research, we tried to limit the influence of amino acids that change their conformation because there is no precise research on the kinetics of these changes over time or their impact on reactivator binding. The obtained results indicate the need for further studies shedding more light on the contribution of Trp286. The change observed in the sarin-AChE complex described by Allgardsson et al. [19] significantly facilitates the positioning of the bispyridinium reactivators such that the oxime group is directed towards the interior of the active site of the enzyme. However, in BuChE, as the PAS is reduced and lacks this residue, interaction with Trp82 within the anionic site appears crucial. The interactions with the PAS that dominate in AChE enable the formation of both prereactivation and nonreactive

conformations. This indicates the ability to switch from one conformation to another. In turn, interactions with Trp82 in BuChE promote nonreactive conformations, which reduces the chance for effective reactivation of the enzyme.

3.2. Prereactivation Complex

The creation of a prereactivation complex is the first step in the process of reactivating serine blocked by an organophosphorus compound. This complex was experimentally confirmed in the 5FPP crystal structure (chain A) [19]. 5FPP represents HI-6 in the active site of sarin-inhibited AChE just before reactivation, in which the oxime group is directed towards the phosphorus atom, staying in close proximity. At the same time, this group remains in an axial relationship with the oxygen of Ser203. In addition to determining the position of the oxime at the moment of attack on the OP, a significant change in the position of the O-alkyl group is also observed. This change exposes the phosphorus atom, allowing the oxime anion to approach it.

To investigate this step of cholinesterase reactivation, modified crystal structures of AChE and BuChE inhibited by sarin or tabun were used. The modification concerned replacement of the original OP conformation with that known from 5FPP. This conformational change, which leads to exposure of the phosphorus atom to the attack of the oxime moiety, appears to be critical for obtaining the prereactivation state of the reactivator. During docking, we used constraints to obtain poses in which the oxime moiety is directed towards the OP phosphorus atom.

Visual inspection of the results obtained by docking to sarin-AChE showed two noteworthy clusters of poses. In the first cluster, the location of the oxime group resembled the one known from 5FPP, whereas the second cluster showed an aldoxime pyridinium ring shifted towards Trp86, allowing for π - π or cation- π interactions. There were also poses in which the aldoxime pyridinium ring was located at an intermediate position between those from the first and second clusters. The second cluster represented poses in which the aldoxime group did not turn towards the phosphorus atom of sarin, as the HI-6 in 5FPP also created bad contacts with the isopropoxy substituent of sarin. Accordingly, with the assumption that the oxime group remains in an axial relationship with Ser203 oxygen, we further described poses that belonged to the abovementioned first cluster of poses. In the case of 2-PAM (Supplementary Materials Figure S5), the best rated pose created cation- π and π - π stacking with Tyr341 and hydrophobic contacts with the acyl pocket. The 1,2-disubstituted ring of HI-6 (Figure 5) was slightly shifted towards Trp86 but remained between the phenol groups of Tyr124 and Tyr337, allowing cation- π stacking. In turn, the 1,4-disubstituted pyridinium moiety was parallel to Tyr341. K074 (Supplementary Materials Figure S7) interacted with Tyr341 and the acyl pocket as observed for 2-PAM. The pyridinium oxime fragment not directed towards the phosphorus atom was able to interact with Trp286 through CH- π stacking. Additionally, its oxime group interacted with the main chain amide moiety of Leu76. K203 showed π - π stacking interactions of the aldoxime pyridinium with Tyr341 and Phe338. The pyridinium ring with an amide moiety remained parallel at a close distance to Trp286. The amide group interacted with Tyr72 through hydrogen bonds. The obidoxime-binding mode (Supplementary Materials Figure S6) was the same as that for K203 (Supplementary Materials Figure S8), excluding interactions with Tyr72.

In the case of docking of reactivators to the tabun-AChE complex, for all scoring functions, the lowest rated oxime was 2-PAM (Supplementary Materials Figure S5), which also has the lowest reactivation ability. The scoring function results revealed accordance between their values and the activities of the reactivators. Oximes were arranged such that the oxime group was in axial relation with the Ser203 oxygen atom. To gain insight into pose clusters, three pose arrangements were distinguished. The first represents the group of oximes shifted towards the oxyanion hole, the second represents those shifted towards His447 and Phe338, and the third represents the intermediate position between the first and the second. Visual assessment of 2-PAM allowed us to observe interactions with Tyr124 and

Tyr337 through cation- π and π - π stacking, while the oxime group was directed towards the phosphorus atom of tabun. The results obtained for HI-6 docking showed significant differentiation of poses (Figure 5). Based on the best rated poses, the key interaction seems to be cation- π interaction of the 1,2-disubstituted pyridinium ring with Tyr124. Additional contacts were made by the 1,2-disubstituted ring with Ser125 through cation- π interactions and a 1,4-disubstituted pyridinium ring with Tyr341 through cation- π and π - π interactions. Docking of K074 (Supplementary Materials Figure S7) revealed consistent poses that represented one binding mode. For example, the best rated pose for one pyridinium ring was placed at the catalytic site, creating cation- π interactions with Tyr124, while the other aromatic fragment created π - π stacking interactions with Trp286 and Tyr341 at the edge of the narrow gorge. The ionized oxime moiety was turned towards the amide group of the main chain of Arg296. Poses obtained in docking of K203 (Supplementary Materials Figure S8) showed high cohesion representing the same binding mode. The best rated pose showed the cation- π interactions of oxime containing a pyridinium ring with Tyr124, while the second amide ring created cation- π and π - π stacking interactions with Trp286. Furthermore, the amide group interacted with the main chain of Ser293 and Phe295 through hydrogen bonds. The best rated poses for obidoxime (Supplementary Materials Figure S6) were arranged as previously described for K074. Molecular modeling of the preactivation state proved that the interaction of the pyridinium moiety with Tyr124 of AChE was crucial.

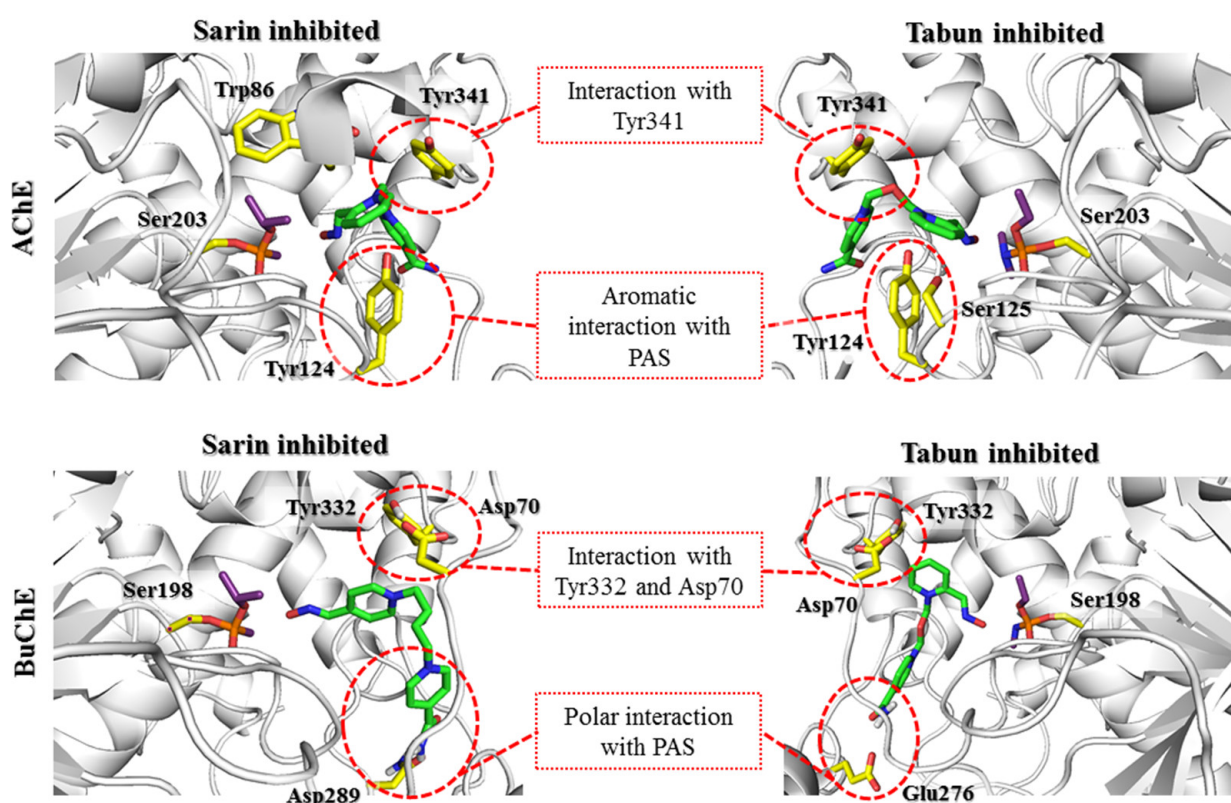


Figure 5. Docking results representing the preactivation conformations of HI-6 (green) at the active sites of AChE and BuChE (gray) blocked by sarin and tabun (purple). The key amino acids involved in the interactions with the reactivator are marked with yellow sticks. The PAS region plays a huge role in ligand binding in both AChE and BuChE, despite the clear differences in the amino acids that build PAS of AChE and BuChE. Maintaining the BuChE preactivation pose is dependent on the interaction with Tyr332 and Asp70. However, these interactions diminish during the formation of the transition state, in contrast to increasing interactions within the PAS AChE region.

After docking to BuChE, all the obtained preactivation poses of the tested oximes created cation- π , π - π , or CH- π interactions with Tyr332. The ionic bond with Asp70 was also found in most results. Therefore, it can be assumed that both amino acids are crucial in

stabilizing the pyridinium oxime reactivators in the prereactivation position. However, the structure of the PAS in BuChE is not favorable for interactions with the studied compounds in this conformation. A significant difference between AChE and BuChE is the number of aromatic amino acids located near the entrance to the enzyme. When comparing the sequences of these proteins, we noticed that the aromatic residues building the PAS in AChE were replaced by short aliphatic or even polar amino acids in BuChE. Based on the 5FPP crystal structure, it is clear that for bispyridinium reactivators, the interactions with Tyr70, Tyr121, and Trp279, which are located in the PAS, are important for binding with AChE. In BuChE, these amino acids correspond to Asn68, Gln119, and Ala277, respectively. This is the reason for the worse fit of these reactivators to BuChE in the prereactivation conformation. The prereactivation position of 2-PAM (Supplementary Materials Figure S5) was generally the same in both the sarin-BuChE and tabun-BuChE complexes. The only specific observed interactions were cation- π and CH- π interactions with Tyr332.

The prereactivation arrangement of obidoxime (Supplementary Materials Figure S6) was also very similar for both complexes. The pyridinium ring with the attached ionized oxime moiety creates cation- π interactions with Tyr332 and ionic bonds with Asp70. In turn, the other pyridinium oxime fragment forms a hydrogen bond with the Leu273 main chain through the OH moiety. The position of this group can also be stabilized by hydrogen bonds with Asn68.

The differences in the positions of compound HI-6 were more significant than those for the previously described reactivators. Although the pyridinium oxime fragment was placed near Tyr332, creating the interactions previously described for the other compounds, the further aromatic fragment exhibited a more diverse arrangement. It formed hydrogen bonds with Asn289 (sarin-BuChE) or Glu276 (tabun-BuChE) through an amide moiety (Figure 5).

The results for K074 (Supplementary Materials Figure S7) and K203 (Supplementary Materials Figure S8) were similar to those for HI-6. K074 and K203 exhibited a number of interactions with Tyr332 (cation- π) and Asp70 (ionic). The position of the second heterocyclic fragment did not show such consistency. Among the results for K074 in the sarin-BuChE complex, it was observed that this fragment was directed towards the entrance to the enzyme, where it formed a hydrogen bond with Gln71. Concerning docking to tabun-BuChE, the pyridinium moiety was located deeper and formed hydrogen bonds with Gln119 and Asn289. K203, with a double bond in the linker, had reduced conformational flexibility, which resulted in a less favorable adjustment to BuChE near the entrance to the enzyme. In the case of the sarin-BuChE complex, there was a hydrogen bond between the amide group of K203 and Asn289. In the tabun-BuChE complex, the pyridinium ring substituted by the amide moiety of K203 did not create any specific interactions.

In summary, it is worth noting the similarities in the arrangement of reactivators in the cholinesterase active sites for this step. In both AChE and BuChE, the constraint-forced position of the oxime moiety promoted ligand conformation in which the aromatic fragment not involved in binding with the OP was directed towards Trp86/Trp82 (AChE/BuChE) or, for most of the results, towards the entrance to the enzyme active site. The conserved Asp74/Asp70, Tyr341/Tyr332, and Phe338/Phe329 residues significantly facilitated the pyridinium oxime fragment to adopt a prereactivation conformation. In AChE, there were additional aromatic residues in this area that considerably reduced space and thus oriented the reactivator directly to the OP-blocked serine. The larger space of the binding site in BuChE resulted in a shift of the pyridinium oxime moiety away from the position optimal for reactivation. This indicates the need to expand this fragment of the compound to compensate for the absence of aromatic residues that restrict the arrangement of the ligand. This modification could help the reactivator accommodate the prereactivation conformation at the BuChE active site. Another observation concerns the binding of the aromatic fragment within the PAS. As previously mentioned, the PAS in BuChE is significantly reduced compared to that in AChE. As a result, the specific interactions between the aromatic fragments of the ligands and the PAS in BuChE are considerably

weakened. The interactions are usually limited to hydrogen bonds formed by the amide or oxime moiety of the reactivator. The arrangement of this part of the ligand in BuChE often corresponds to that observed in AChE. However, in the case of the latter, the presence of additional aromatic residues, especially Trp286, that can adapt to the compounds stabilizes the beneficial conformation of the entire ligand. Therefore, it appears that to increase the efficiency of BuChE reactivators, the fragment of the compound not directly involved in the reactivation process needs to be optimized to better fit the reduced PAS in BuChE.

3.3. Transitional State

The application of covalent docking allowed us to reproduce the next step of the reactivation process, i.e., the formation of transitional serine-OP-oxime complex at the cholinesterase binding sites. This is the step with the highest energy, involving and it involves the spatial reorganization of the substitutes and the creation of a covalent bond between the phosphorus atom and the oxygen atom of the oxime group with the simultaneous breaking of the phosphorus-serine bond. The serine-OP fragment changes the geometry from tetrahedral to trigonal bipyramidal with both serine and oxime oxygen atoms in one axis [19,43]. For the purpose of this step, OP-oxime complexes with the appropriate geometry were prepared. Then, they were covalently docked to AChE and BuChE with the creation of a bond between the oxygen atom of the serine from the catalytic triad and the phosphorus atom of the OP. As in the previous steps, docking was conducted using the four scoring functions available in GOLD. The criteria for selecting the best conformation included both the coherence and the reliability of the mapped poses. As the correct poses were considered, those in which the free oxygen atom from the OP interacted with the oxyanion hole and the O-alkyl and alkyl substitutes (amino-alkyl in the case of tabun) were arranged similarly to those observed in known crystal complexes.

All the scoring functions enabled us to obtain the poses of the investigated oximes with attached sarin, in which the sarin binding mode was similar to that found in 5FPP. Regarding the pyridinium oxime fragment bound to sarin, the common feature of all conjugates regardless of scoring function was interaction with the phenol group of Tyr124. Additionally, this fragment interacted with Tyr341 and Phe338 through π - π stacking. The best scored pose for HI-6-sarin, in addition to interactions with Tyr341 and Phe338, was stabilized through cation- π and π - π stacking with Tyr337 (Figure 6). The best rated poses of K074, K203 and obidoxime revealed a binding mode similar to that of HI-6 (Supplementary Materials Figures S10 and S12). The pyridinium ring of these bispyridine compounds not bound to sarin mostly interacted with Trp286, creating cation- π and π - π stacking. Moreover, the amide groups of HI-6 and K203 were involved in hydrogen bonds with the phenol moiety of Tyr72.

The transitional complex for 2-PAM docked to tabun-AChE revealed the lowest values among the conjugates for all scoring functions (Supplementary Materials Figure S9). The values for the poses of the other oximes varied among all scoring functions and did not correlate with the experimental reactivation properties. Visual inspection of the best rated poses corresponding to the transitional state of 2-PAM-tabun showed a consistent binding mode of tabun that can be observed in original tabun-AChE complexes, for example, 3DL4. The phosphoryl oxygen interacted with the oxyanion hole through hydrogen bonds, whereas the dimethylamine group was directed towards the acyl pocket. Unlike the 3DL4 complex, the alkoxy substituent in this structure was bent in a manner similar to that of the sarin isopropoxy moiety found in 5FPP. The pyridinium ring neighbored Trp286, Tyr337, and Tyr124. The best rated pose showed cation- π interactions between the pyridinium moiety and Tyr337. Poses obtained for all scoring functions were coherent, but they differed from one another due to rotation changing affinities to neighboring residues. Covalent docking of HI-6-tabun to Ser203 had an effect similar to that of the earlier docking of 2-PAM-tabun regarding the arrangement of tabun (Figure 6). Most poses appeared in similar arrangements and represented the same binding mode. The 1,2-disubstituted pyridinium ring interacted with Trp86, Tyr337, and Phe338. The oxygen atom located at the linker

fragment created a hydrogen bond with Tyr124. The 1,4-disubstituted pyridinium ring directed towards the exit of the narrow gorge was arranged between Trp286 and Tyr341. The amide group remained without any interactions.

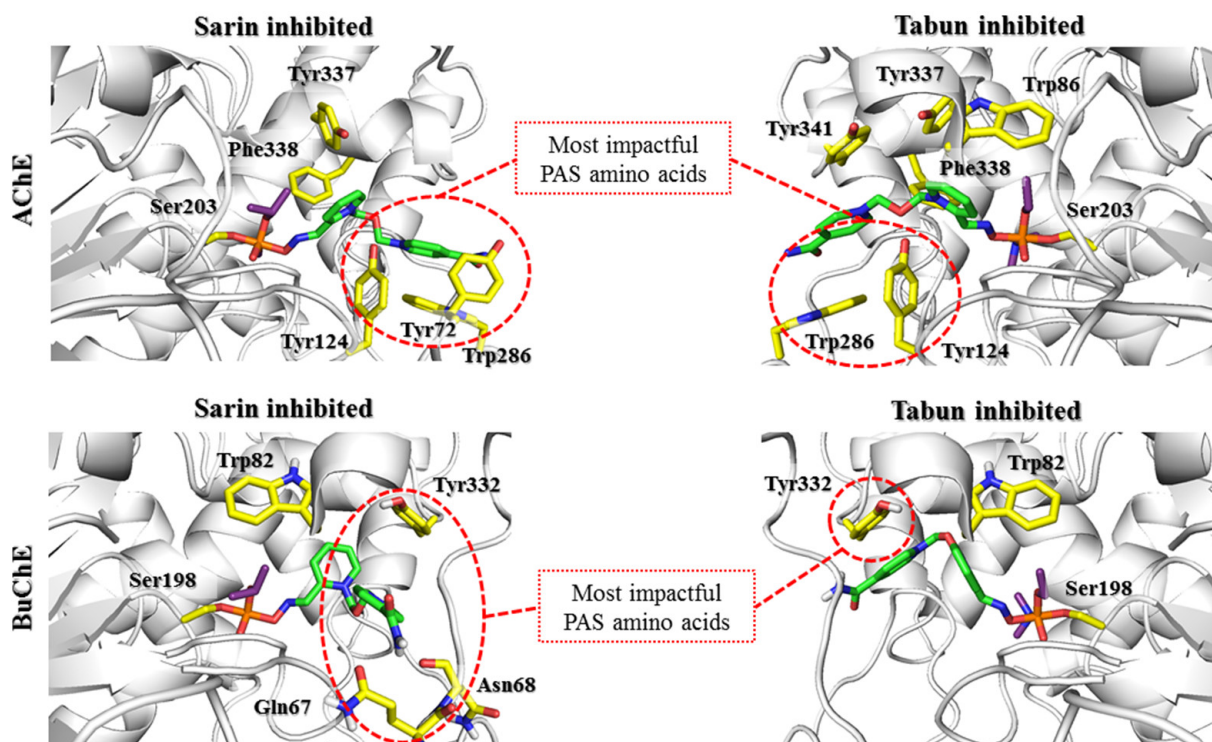


Figure 6. Docking results reflecting the formation of the transitional state by the HI-6 (green) at the active sites of AChE and BuChE (gray) blocked by sarin and tabun (purple). The key amino acids involved in the interactions with the reactivator are marked with yellow sticks. The interactions of the reactivator with AChE PAS region, observed in the prereactivation state, were further enhanced during the formation of the transitional state. In the case of BuChE, the weakening of the interactions with Tyr332 and Asp70 in the transitional state is not compensated by the PAS amino acids.

The results obtained in the covalent docking of the tabun complex with K074 and K203 showed more varied poses (Supplementary Materials Figures S11 and S12). There were notable differences regarding the tabun arrangement, which was divided into two clusters. The first cluster was consistent with the previously described position regarding the 2-PAM-tabun and HI-6-tabun complexes, while in the other cluster, we observed phosphoryl oxygen directed towards Glu202. Regarding the proximal 1,4-disubstituted pyridine ring of these oximes, it is notable that it interacts with amino acids such as Trp86 and Tyr337 and with the phenol group of Tyr124. The best rated pose of K074 showed catalytic site interactions of the pyridinium ring with Tyr337 through T-shaped stacking while the other aromatic fragment interacted with Tyr341 through parallel π - π and cation- π stacking. The oxime group not linked with tabun did not show any significant bonding. The best rated result for K203 was arranged such that one pyridinium ring linked with the phosphorus atom created T-shaped π - π stacking with Tyr337. The other pyridinium ring was parallel to Tyr341, allowing π - π and cation- π interactions. The amide group remained unbound. The investigation of obidoxime (Supplementary Materials Figure S10) revealed interesting binding modes. The phenol group of Tyr124 simultaneously interacted with both pyridinium rings. Moreover, the aromatic fragment not directly bound to the OP remained at the PAS of AChE and interacted with Tyr341.

In the case of BuChE complexes, detailed analysis of the results showed some evolution of interactions characteristic of the prereactivation complex. The interactions with Tyr332 were crucial for stabilizing the position of all tested compounds; however, they were limited to cation- π interactions, with the exception of 2-PAM, which additionally created

CH- π interactions. The movement of compounds deeper into the BuChE binding site hindered the formation of ionic bonds with Asp70. At the same time, it enabled the creation of cation- π and π - π interactions with Phe329 for most compounds. 2-PAM (Supplementary Materials Figure S9) shows the strongest interactions with Phe329 and Tyr332 in both the sarin-BuChE and tabun-BuChE complexes. The presence of equivalent amino acids in the AChE active site (Phe338 and Tyr341) might be one of the reasons for the very similar reactivation activity of 2-PAM towards AChE and BuChE.

Another analyzed compound, obidoxime (Supplementary Materials Figure S10), in addition to the previously described interactions with Phe329 and Tyr332, also created significant π - π stacking between the pyridinium oxime moiety not involved in binding the OP and Trp82 as well as a hydrogen bond between the nonionized oxime moiety and Glu197. This is a significant difference compared to the prereactivation pose, in which this pyridinium fragment was directed towards the entrance to the BuChE active site.

Compound HI-6, although similar in structure to obidoxime, did not obtain similar poses (Figure 6). The transitional complex with sarin-BuChE showed hydrogen bonds between the amide group of HI-6 and the Gln67 side chain as well as the Asn68 main chain. In turn, in a tabun-BuChE complex, asoxime was directed towards the entrance to the active site, creating a hydrogen bond with Tyr332. It is likely that changing the position of the oxime from 4- to 3- hindered the binding of the aromatic ring near Trp82.

K074 (Supplementary Materials Figure S11) in both the sarin- and tabun-blocked BuChE complexes created a transitional state in which a pyridinium oxime fragment not involved in binding the OP was directed towards the entrance to the enzyme, creating a hydrogen bond with the Gly283 main chain. The stiffening of the linker by introducing a double bond and replacing one oxime moiety with an amide group made the compound K203 the only one of the tested reactivators that did not form any specific interactions with Phe329 in any of the complexes. The K203 transitional state (Supplementary Materials Figure S12) in sarin-BuChE indicated additional cation- π interactions between the amide-bound pyridinium and Trp82. In the case of tabun-BuChE, this fragment was directed towards the entrance to the active site (in a pose analogous to that of compound K074), but no bonds that would stabilize this position were observed. It can be concluded that the ability of the pyridinium oxime moiety to create an optimal interaction with Phe329 and Tyr332 is key in the formation of the transitional complex by the studied reactivators. The substituents attached to the pyridinium ring not bound to OP should stabilize this position, as observed for obidoxime.

The results of covalent docking to the transitional state complexes of OP-AChE and OP-BuChE revealed further significant differences in the behavior of the tested reactivators. The highest rated poses for the 2-PAM transitional state with AChE and BuChE blocked by sarin or tabun presented a very similar position of the pyridinium fragment. This position created aromatic interactions with the Phe338/Phe329 and Tyr341/Tyr332 residues. In the case of AChE, an additional interaction with Tyr337 was observed. This is in accordance with the statement made in the previous step regarding the importance of interactions with these residues for the proper orientation of the pyridinium oxime fragment in a prereactivation state subsequently leading to a transitional state. Only the conformational changes of His447 and Phe338 present in the tabun-AChE complexes affected the position of the pyridinium ring, directing it towards Trp86. The results for the bispyridine compounds displayed high consistency of poses regarding docking to AChE and significant variation in the case of docking to BuChE. These discrepancies were again caused by the different structures of PAS in both enzymes. The aromatic residues of Tyr72 and Trp286 in AChE facilitated the arrangement of the aromatic fragment not directly bound to the OP within the PAS and thus positioned the entire ligand along the gorge of the enzyme. This binding mode was retained even for the 3DL4 complex, which exhibited the change in His447 and Phe338 conformations seen in tabun-AChE complexes. Moreover, the poses in which the ligand was placed over Phe338 clearly emphasize the limitations caused by this change in access to serine blocked by tabun. In the case of BuChE, the results can be divided

into two main conformations. The first conformation is similar to that observed for AChE; however, in this case, the interaction with Tyr332 is crucial. The other conformation shows the U-shaped bend of the compound so that the pyridinium fragment not connected to the OP can interact with Trp82. It appears that the type of *O*-alkyl substituent of the OP affects the conformation of the ligand to some extent. In the case of a larger *O*-isopropyl fragment of the sarin, a smaller number of poses showed interactions with Trp82. In turn, for the *O*-ethyl fragment of the tabun, this number was higher. Knowing the difference in the efficiency of the tested reactivators in relation to cholinesterases blocked by tabun and sarin, it seems that the strength of ligand interaction with Trp86/Trp82 inversely correlates with their reactivation potency. This observation is reflected in the participation of this residue in the formation of the nonreactive conformation.

3.4. Postreactivation Complex

After breaking the bond with serine, the organophosphorus fragment is transferred to the reactivator, forming a stable complex. From the point of view of the reactivation process, the OP-oxime complex (POX) should not have affinity to the binding site [19]. This would indicate a low potential of such a complex acting as an enzyme inhibitor and allow for its rapid dissociation from the binding site. For the purpose of our research, we prepared a number of oxime-OP complexes that we then docked to the AChE and BuChE active sites to examine their arrangement and possible inhibitory potential.

Among the poses obtained as a result of the docking of the sarin-oxime and tabun-oxime complexes to AChE, two clusters can be distinguished. In the first cluster, the poses were arranged such that the OP moiety remained at the catalytic site. The other cluster revealed an arrangement in which the pyridinium moiety not connected with the organophosphorus moiety was located at the catalytic site, whereas the sarin or tabun group was directed towards the outside of the narrow gorge. The best scored poses of the sarin-2-PAM conjugate belonged to the first cluster. Visual inspection showed that the phosphoryl oxygen atom of sarin was directed towards the oxyanion hole, while the pyridinium ring of 2-PAM (Supplementary Materials Figure S13) interacted with the aromatic ring of Tyr124 through cation- π and π - π stacking. The best rated results of sarin-HI-6 obtained in docking to AChE could be divided into two clusters. In the first cluster, we observed that the phosphoryl oxygen atom of sarin was adjacent to the oxyanion hole. However, the OP moiety did not create any interactions. The oxime component of the complex created cation- π and π - π stacking with Tyr341 and Trp286 via the pyridinium ring (Figure 7). Other sarin-oxime conjugates revealed coherent poses that belonged to the second cluster (Supplementary Materials Figures S14–S16).

Visual cluster analysis allowed us to notice that the organophosphorus group of tabun-oxime complexes with more active reactivators (K203, K074, and obidoxime) was preferably directed towards the exit of the narrow gorge, whereas for less potent oximes, it occurred more frequently at the catalytic site (Figure 7). The best rated pose in docking of tabun-2-PAM to AChE (Supplementary Materials Figure S13) showed an arrangement in which the phosphoryl oxygen of tabun was directed towards the oxyanion hole while the dimethylamine substituent was located near the acyl pocket. Ethoxy substituents occupied space at the exit of the catalytic pocket. The pyridinium ring of the investigated complex neighbored Tyr341 and Trp286 and also created cation- π interactions with the phenol group of Tyr124. In the case of tabun-asoxime complex, the best rated pose was arranged such that the OP moiety remained at the catalytic pocket without any significant interaction. However, the 1,2-disubstituted ring perpendicularly neighbored Tyr124, allowing for some π - π interactions. The phenol group of Tyr124 was directed towards HI-6, creating a hydrogen bond with an oxygen atom from the linker. The 1,4-disubstituted pyridinium ring was parallel to Tyr341 at a distance of 4–5 Å. The amide group of HI-6 was close to the main chains of Phe295 and Ser293, allowing hydrogen bonding. In the case of the tabun-K074 complex (Supplementary Materials Figure S15), the OP fragment remained in the catalytic site without any favorable interaction, while the 1,4-disubstituted ring

attached to the OP fragment created cation- π stacking with the phenol group of Tyr124. Free aldoxime interacted with Gly342 through hydrogen bonds. Regarding the best rated pose for tabun-K203 (Supplementary Materials Figure S16), in which the OP component remained at the catalytic site, four interactions between pyridinium rings and AChE were noted. The aromatic fragment bound to the OP interacted with Tyr124 and Tyr341 via π - π stacking, while the phenol group of Tyr124 additionally interacted through cation- π stacking. The pyridinium ring with an amide moiety was parallel to Trp286 and allowed cation- π and π - π stacking. The OP component of the investigated conjugate did not create any significant interactions. The pyridinium fragment directly connected with the OP in the obidoxime-tabun complex (Supplementary Materials Figure S14) interacted with Tyr124 and Tyr341 by cation- π and π - π stacking. Furthermore, the close distance between the free aldoxime hydrogen atom and Ser293 main chain oxygen allowed hydrogen bonding.

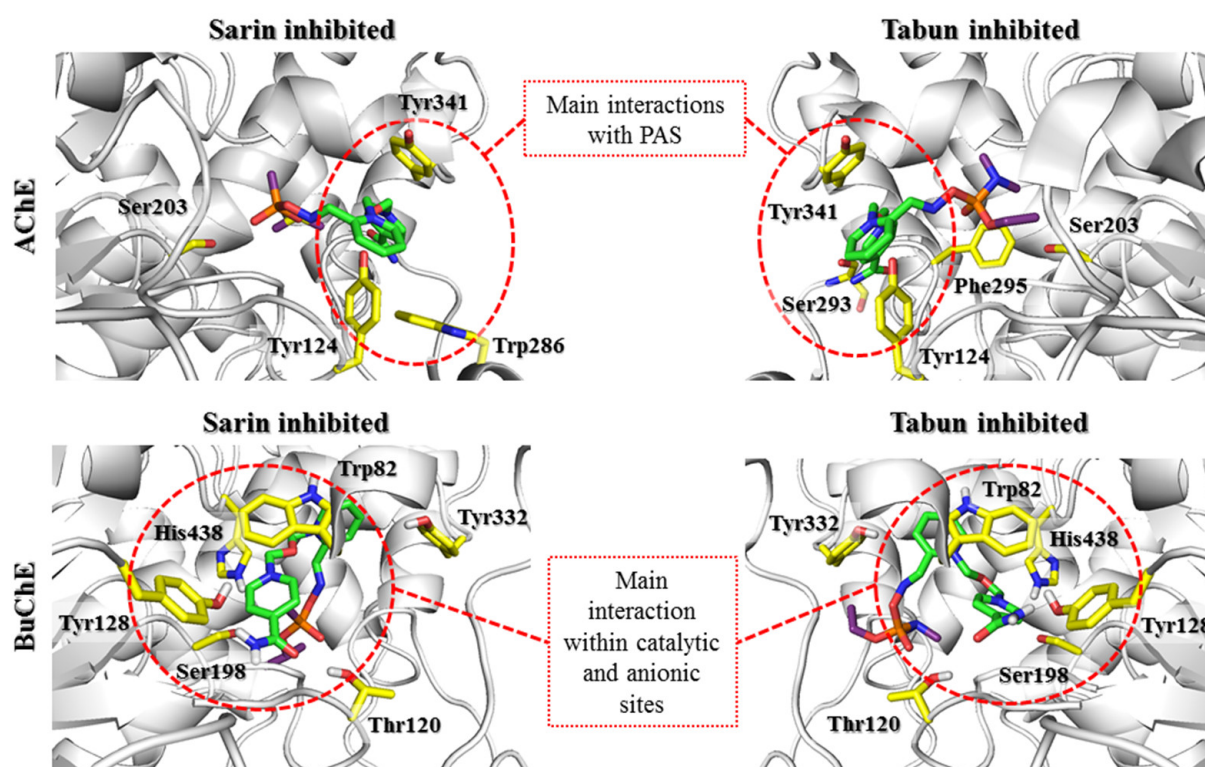


Figure 7. Docking results reflecting the behavior of the created sarin-HI-6 and tabun-HI-6 conglomerates (green) after reactivation of the active sites of AChE and BuChE (gray). The key amino acids involved in the interactions with the OP-reactivator conglomerate are marked with yellow sticks. The postreactivation complex binds more strongly at the active site of BuChE than AChE.

The results of docking to BuChE obtained for the various scoring functions were very consistent, especially for the highest rated poses. The key amino acids for binding OP-oxime complexes could be easily identified. These include Trp82, which participated in the binding of all tested postreactivation complexes, and Tyr332, which stabilized the binding mode of compounds with two pyridinium fragments (obidoxime, HI-6, K074, and K203) (Figure 7).

A significant difference in the binding mode caused by the difference in the structure of the OP attached to the reactivator was observed for pralidoxime (Supplementary Materials Figure S13). For the sarin-pralidoxime complex, the pyridinium fragment was located among the aromatic rings of Trp82, Phe329, and Tyr332, creating hydrophobic and cation- π interactions. The oxygen atom of the sarin fragment additionally formed a hydrogen bond with Ser198 or His438. For the tabun-pralidoxime complex, in the most common pose, the pyridinium fragment was located between the Trp231 and Phe329 aromatic rings and also

created hydrophobic and cation- π interactions. The oxygen atom of tabun was directed towards the oxyanion hole, but the ability to form hydrogen bonds in this position was limited.

Regarding the other reactivators, the differences caused by the type of attached OP were negligible. After binding to the OP, obidoxime (Supplementary Materials Figure S14) was arranged with a free pyridinium oxime fragment placed under the indole ring of Trp82, creating cation- π and π - π interactions. Nonreactive oxime group was in a convenient position to create hydrogen bonds with Tyr128 and Glu197. The sarin-bound pyridinium oxime fragment was placed parallel to the Tyr332 side chain, promoting cation- π and π - π interactions. This position was further stabilized by ionic bonds with Asp70. The sarin fragment facing the entrance to the active site created an additional hydrogen bond with Ser72.

The docking poses for the sarin-HI-6 and tabun-HI-6 complexes exhibited many interactions that were also observed in the previous obidoxime complexes (Figure 7). The amide-bound pyridinium ring formed cation- π and π - π interactions with Trp82. Additionally, the position of the ring allowed the creation of hydrogen bonds between the amide moiety and Thr120 and Tyr128. The main difference was the position of the sarin fragment, which was not directed towards the entrance to the active site of the enzyme but was located close to the catalytic triad. A hydrogen bond between the oxygen of the alkyloxy group and His438 was observed. A tabun fragment from an analogous complex was moved away from the catalytic triad; however, it was located deeper in the active site in this complex than in the tabun-obidoxime complex. The docking poses for the complexes of K074 and K203 (Supplementary Materials Figures S15 and S16) with both tabun and sarin were analogous to those observed for the docking of the obidoxime-OP complexes. The pyridinium ring substituted with an oxime (K074) or amide (K203) moiety was located parallel to the Trp82 side chain, forming cation- π and π - π interactions. This position was additionally stabilized by a hydrogen bond created between the oxime group and Tyr128. The second pyridinium ring was involved in cation- π and π - π interactions with Tyr332. Regardless of whether the compounds K074 and K203 formed complexes with sarin or tabun, the OP fragment was directed towards the entrance to the active site of BuChE, creating hydrogen bonds with the hydroxyl groups of the Ser72 and Gln71 main chains.

Comparing the obtained models representing the last stage of reactivation for AChE and BuChE, we observed that the differences in the trends of the arrangement of the compound depended on the structure of the reactivator and not on the type of OP or the particular cholinesterase. Both pralidoxime and HI-6 showed poor consistency of results with a slight predominance of poses in which the oxime-associated part of the postreactivation complex was directed inside the enzyme. On the other hand, reactivators such as obidoxime, K074, and K203 were arranged in a consistent manner in which the part associated with the OP was arranged within the outer part of the PAS. While the whole process of transition from the conformation in which the OP is located deep in the active site of a cholinesterase just after its bond with serine was broken to the conformation in which it is directed outwards requires further research on the molecular dynamics, it seems that stronger reactivators are characterized by this preference. It is also understood that the preference of the complex to leave the active site should positively correlate with the speed of this process and thus the restoration of the physiological functions of cholinesterase. The large number of poses in which we observed the OP-associated fragment facing outward tended to form an aromatic interaction of the pyridinium ring with Trp86/Trp82 so that the final pose was similar to the nonreactivating pose observed for the free reactivator docking.

4. Conclusions

In our study, we wanted to demonstrate the usefulness of a simple flexible molecular docking tool to model different steps in the reactivation process. We were pleased to find that by selecting various docking techniques, such as free flexible docking, flexible docking with distance constraints, and covalent docking, we obtained promising results

that allowed us to conduct a comprehensive analysis of OP–reactivator–cholinesterase interactions. Many groups involved in research on the reactivation of cholinesterases focus on an important stage in the reactivation process: the moment when the reactivator adopts a prereactivation pose [20,41,44]. Based on the reactivation cycle presented by Allgardsson et al. [20] in which the reactivator can adopt nonreactivation or prereactivation conformations at the active site of OP-blocked cholinesterase, we performed an interaction analysis for five known reactivators modeling both states at AChE and BuChE active sites blocked by sarin or tabun. For both AChE and BuChE, the nonreactive conformation was reached by the reactivator more easily, which may suggest an equilibrium shift between these positions in favor of a nonreactivating position. Analysis of interactions allowed us to identify the amino acids Phe338/Phe329 and Tyr341/Tyr332, which occur in both AChE and BuChE, as key to obtaining the prereactivation conformation. Many teams using the MD and QM/MM methods in their research have also reached similar conclusions [29,45]. Our results show that the amino acids composing the PAS of AChE are an important factor facilitating the prereactivation conformation of reactivators of this enzyme. Differences between AChE and BuChE in the structure of this fragment are the reason for the significantly lower reactivation efficacy of the tested reactivators for BuChE. The results we obtained are in line with the observations of other teams and the mapped analogous arrangements observed in the complexes available in PDB. Vyacheslav et al. [46], using the MD approach on the phosphorylated enzyme–reactivator complex, compared simulations starting from prereactivation and nonreactive positions and showed that the prereactivation (apical) position of the studied reactivators was rather stable and thus maintained over the MD trajectory, while in the nonreactive (side) position, the hydroxamic group left the active site shortly after the beginning of the simulation. Unfortunately, the small number of complexes representing some of the stages presented here, especially the prereactivation, transient and postreactivation states, makes it difficult to refer to the experimental data. This was especially troublesome when developing models for BuChE. Our study is one of the few that have conducted a comprehensive analysis of the course of reactivation of BuChE blocked by an OP. On the one hand, this limits our ability to refine the method based on the results published so far, but it is an important step towards explaining the reasons for the high resistance of OP-inhibited BuChE to known reactivators. The observed differences in the positions of the analyzed reactivators in the active sites of AChE and BuChE and the numerous similarities constitute a good starting point for proposing structural modifications to the known reactivators. Based on our observations, it seems that to improve the effectiveness of reactivators for BuChE, the key is to introduce groups that will stabilize the molecule in the PAS in a manner analogous to the interactions observed in AChE. This change could be achieved by introducing moieties that interact with the amino acids forming the acyl loop.

In summary, we believe that the protocol we have presented allows rapid and effective analysis of many important stages of the reactivation process. The presented approach may be part of advanced algorithms utilizing quantum mechanics/molecular mechanics (QM/MM) or molecular dynamics (MD) methods. After optimization of the ligand assessment process, the described method can provide an independent screening tool for predicting the potential efficacy of reactivation by new compounds.

Supplementary Materials: The following are available online at <https://www.mdpi.com/2218-273X/11/2/169/s1>, Table S1: Detailed information about the docking parameters for Nonreactivating Conformation—Free Docking, Table S2: Detailed information about the docking parameters for Prereactivation Step—Docking with Substructure Based Constraints (Oxime Moiety from Chain A of 5FPP Complex), Table S3: Detailed information about the docking parameters for Transition State—Covalent Docking, Table S4: Detailed information about the docking parameters for Postreactivation State—Free Docking, Figures S1–S16: Visualization of docking results showing nonreactivating (S1–S4), prereactivation (S5–S8), transitional (S9–S12) and postreactivation (S13,S14) poses for 2-PAM, obidoxym, K074 and K203 reactivators.

Author Contributions: Conceptualization, J.J. and M.B.; methodology, J.J., J.K. and M.B.; investigation, J.J. and J.K.; writing—original draft preparation, J.J., J.K. and K.L.; writing—review and editing, J.J., J.K., K.L., B.M., K.M., Y.-S.J. and M.B.; supervision, M.B. and B.M.; funding acquisition, B.M., Y.-S.J. and K.M. All authors have read and agreed to the published version of the manuscript.

Funding: This research was funded by Polish National Centre for Research and Development, grant number V4-Korea 3/2018, by Czech Science Foundation, grant number GA18-01734S and by University of Hradec Kralove, Faculty of Science, grant number VT2019-2021.

Institutional Review Board Statement: Not applicable.

Informed Consent Statement: Not applicable.

Data Availability Statement: Not applicable.

Acknowledgments: This research was carried out as part of the international project Visegrad Group (V4)-Korea Joint Research Program on Chemistry and Chemical Engineering.

Conflicts of Interest: The authors declare no conflict of interest.

References





- Mercey, G.; Verdelet, T.; Renou, J.; Kliachyna, M.; Baati, R.; Nachon, F.; Jean, L.; Renard, P.-Y. Reactivators of Acetylcholinesterase Inhibited by Organophosphorus Nerve Agents. *Acc. Chem. Res.* **2012**, *45*, 756–766. [[CrossRef](#)] [[PubMed](#)]
- Gunnell, D.; Eddleston, M.; Phillips, M.R.; Konradsen, F. The global distribution of fatal pesticide self-poisoning: Systematic review. *BMC Public Health* **2007**, *7*, 357. [[CrossRef](#)]
- Fukuto, T.R. Mechanism of action of organophosphorus and carbamate insecticides. *Environ. Health Perspect.* **1990**, *87*, 245–254. [[CrossRef](#)] [[PubMed](#)]
- Peter, J.V.; Sudarsan, T.; Moran, J. Clinical features of organophosphate poisoning: A review of different classification systems and approaches. *Indian J. Crit. Care Med.* **2014**, *18*, 735–745. [[CrossRef](#)]
- Jokanović, M.; Stojiljković, M.P. Current understanding of the application of pyridinium oximes as cholinesterase reactivators in treatment of organophosphate poisoning. *Eur. J. Pharmacol.* **2006**, *553*, 10–17. [[CrossRef](#)] [[PubMed](#)]
- Eddleston, M. Novel clinical toxicology and pharmacology of organophosphorus insecticide self-poisoning. *Annu. Rev. Pharmacol. Toxicol.* **2019**, *59*, 341–360. [[CrossRef](#)] [[PubMed](#)]
- Beaton, R.; Stergachis, A.; Oberle, M.; Bridges, E.; Nemuth, M.; Thomas, T. The Sarin Gas Attacks on the Tokyo Subway—10 years later/Lessons Learned. *Traumatology* **2005**, *11*, 103–119. [[CrossRef](#)]
- Chai, P.R.; Hayes, B.D.; Erickson, T.B.; Boyer, E.W. Novichok agents: A historical, current, and toxicological perspective. *Toxicol. Commun.* **2018**, *2*, 45–48. [[CrossRef](#)]
- John, H.; van der Schans, M.J.; Koller, M.; Spruit, H.E.T.; Worek, F.; Thiermann, H.; Noort, D. Fatal sarin poisoning in Syria 2013: Forensic verification within an international laboratory network. *Forensic Toxicol.* **2018**, *36*, 61–71. [[CrossRef](#)]
- Newmark, J. Therapy for Nerve Agent Poisoning. *Arch. Neurol.* **2004**, *61*, 649. [[CrossRef](#)]
- Cerasoli, D.M.; Griffiths, E.M.; Doctor, B.P.; Saxena, A.; Fedorko, J.M.; Greig, N.H.; Yu, Q.S.; Huang, Y.; Wilgus, H.; Karatzas, C.N.; et al. In vitro and in vivo characterization of recombinant human butyrylcholinesterase (Protexia™) as a potential nerve agent bioscavenger. *Chem. Biol. Interact.* **2005**, *157*, 362–365. [[CrossRef](#)] [[PubMed](#)]
- Kovarik, Z.; Katalinić, M.; Šinko, G.; Binder, J.; Holas, O.; Jung, Y.-S.; Musilova, L.; Jun, D.; Kuča, K. Pseudo-catalytic scavenging: Searching for a suitable reactivator of phosphorylated butyrylcholinesterase. *Chem. Biol. Interact.* **2010**, *187*, 167–171. [[CrossRef](#)] [[PubMed](#)]
- Sirin, G.S.; Zhang, Y. How is acetylcholinesterase phosphorylated by Soman? An ab initio QM/MM molecular dynamics study. *J. Phys. Chem. A* **2014**, *118*, 9132–9139. [[PubMed](#)]
- Carletti, E.; Li, H.; Li, B.; Ekström, F.; Nicolet, Y.; Loiodice, M.; Gillon, E.; Froment, M.T.; Lockridge, O.; Schopfer, L.M.; et al. Aging of cholinesterases phosphorylated by tabun proceeds through O-dealkylation. *J. Am. Chem. Soc.* **2008**, *130*, 16011–16020. [[CrossRef](#)] [[PubMed](#)]
- Carletti, E.; Aurbek, N.; Gillon, E.; Loiodice, M.; Nicolet, Y.; Fontecilla-Camps, J.-C.; Masson, P.; Thiermann, H.; Nachon, F.; Worek, F. Structure–activity analysis of aging and reactivation of human butyrylcholinesterase inhibited by analogues of tabun. *Biochem. J.* **2009**, *421*, 97–106. [[CrossRef](#)]
- Hörnberg, A.; Tunemalm, A.-K.; Ekström, F. Crystal Structures of Acetylcholinesterase in Complex with Organophosphorus Compounds Suggest that the Acyl Pocket Modulates the Aging Reaction by Precluding the Formation of the Trigonal Bipyramidal Transition State. *Biochemistry* **2007**, *46*, 4815–4825. [[CrossRef](#)]
- Bajda, M.; Więckowska, A.; Hebda, M.; Guzior, N.; Sotriffer, C.; Malawska, B. Structure-Based Search for New Inhibitors of Cholinesterases. *Int. J. Mol. Sci.* **2013**, *14*, 5608–5632. [[CrossRef](#)]
- Wiesner, J.; Kříž, Z.; Kuča, K.; Jun, D.; Koča, J. Why acetylcholinesterase reactivators do not work in butyrylcholinesterase. *J. Enzyme Inhib. Med. Chem.* **2010**, *25*, 318–322. [[CrossRef](#)]

19. Ashani, Y.; Bhattacharjee, A.K.; Leader, H.; Saxena, A.; Doctor, B.P. Inhibition of cholinesterases with cationic phosphonyl oximes highlights distinctive properties of the charged pyridine groups of quaternary oxime reactivators. *Biochem. Pharmacol.* **2003**, *66*, 191–202. [[CrossRef](#)]
20. Allgardsson, A.; Berg, L.; Akfur, C.; Hörnberg, A.; Worek, F.; Linusson, A.; Ekström, F.J. Structure of a pre-reaction complex between the nerve agent sarin, its biological target acetylcholinesterase, and the antidote HI-6. *Proc. Natl. Acad. Sci. USA* **2016**, *113*, 5514–5519. [[CrossRef](#)]
21. Kassa, J. Review of Oximes in the Antidotal Treatment of Poisoning by Organophosphorus Nerve Agents. *J. Toxicol. Clin. Toxicol.* **2002**, *40*, 803–816. [[CrossRef](#)] [[PubMed](#)]
22. Gorecki, L.; Soukup, O.; Kucera, T.; Malinak, D.; Jun, D.; Kuca, K.; Musilek, K.; Korabecny, J. Oxime K203: A drug candidate for the treatment of tabun intoxication. *Arch. Toxicol.* **2019**, *93*, 673–691. [[CrossRef](#)] [[PubMed](#)]
23. Kassa, J.; Jun, D.; Karasova, J.; Bajgar, J.; Kuca, K. A comparison of reactivating efficacy of newly developed oximes (K074, K075) and currently available oximes (obidoxime, HI-6) in soman, cyclosarin and tabun-poisoned rats. *Chem. Biol. Interact.* **2008**, *175*, 425–427. [[CrossRef](#)] [[PubMed](#)]
24. Ochoa, R.; Rodriguez, C.A.; Zuluaga, A.F. Perspectives for the structure-based design of acetylcholinesterase reactivators. *J. Mol. Graph. Model.* **2016**, *68*, 176–183. [[CrossRef](#)] [[PubMed](#)]
25. Iqbal, A.; Malik, S.; Nurulain, S.M.; Musilek, K.; Kuca, K.; Kalasz, H.; Fatmi, M.Q. Reactivation potency of two novel oximes (K456 and K733) against paraoxon-inhibited acetyl and butyrylcholinesterase: In silico and in vitro models. *Chem. Biol. Interact.* **2019**, *310*, 108735. [[CrossRef](#)] [[PubMed](#)]
26. Malinak, D.; Dolezal, R.; Hepnarova, V.; Hozova, M.; Andrys, R.; Bzonek, P.; Racakova, V.; Korabecny, J.; Gorecki, L.; Mezeiova, E.; et al. Synthesis, in vitro screening and molecular docking of isoquinolinium-5-carbaldoximes as acetylcholinesterase and butyrylcholinesterase reactivators. *J. Enzyme Inhib. Med. Chem.* **2020**, *35*, 478–488. [[CrossRef](#)]
27. Gerlits, O.; Kong, X.; Cheng, X.; Wymore, T.; Blumenthal, D.K.; Taylor, P.; Radić, Z.; Kovalevsky, A. Productive reorientation of a bound oxime reactivator revealed in room temperature X-ray structures of native and VX-inhibited human acetylcholinesterase. *J. Biol. Chem.* **2019**, *294*, 10607–10618. [[CrossRef](#)]
28. Lo, R.; Chandar, N.B.; Ghosh, S.; Ganguly, B. The reactivation of tabun-inhibited mutant AChE with Ortho-7: Steered molecular dynamics and quantum chemical studies. *Mol. Biosyst.* **2016**, *12*, 1224–1231. [[CrossRef](#)]
29. Da Silva, J.A.V.; Nepovimova, E.; Ramalho, T.C.; Kuca, K.; Celmar Costa França, T. Molecular modeling studies on the interactions of 7-methoxytacrine-4-pyridinealdoxime, 4-PA, 2-PAM, and obidoxime with VX-inhibited human acetylcholinesterase: A near attack conformation approach. *J. Enzyme Inhib. Med. Chem.* **2019**, *34*, 1018–1029. [[CrossRef](#)]
30. Polisel, D.A.; de Castro, A.A.; Mancini, D.T.; da Cunha, E.F.F.; França, T.C.C.; Ramalho, T.C.; Kuca, K. Slight difference in the isomeric oximes K206 and K203 makes huge difference for the reactivation of organophosphorus-inhibited AChE: Theoretical and experimental aspects. *Chem. Biol. Interact.* **2019**, *309*, 108671. [[CrossRef](#)]
31. Jones, G.; Willett, P.; Glen, R.C.; Leach, A.R.; Taylor, R.; Uk, K.B.R. Development and validation of a genetic algorithm for flexible docking. *J. Mol. Biol.* **1997**, *267*, 727–748. [[CrossRef](#)] [[PubMed](#)]
32. Madhavi Sastry, G.; Adzhigirey, M.; Day, T.; Annabhimoju, R.; Sherman, W. Protein and ligand preparation: Parameters, protocols, and influence on virtual screening enrichments. *J. Comput. Aided. Mol. Des.* **2013**, *27*, 221–234. [[CrossRef](#)] [[PubMed](#)]
33. PyMOL, version 0.99rc6; DeLano Scientific LLC: Palo Alto, CA, USA, 2006.
34. Bartling, A.; Worek, F.; Szinicz, L.; Thiermann, H. Enzyme-kinetic investigation of different sarin analogues reacting with human acetylcholinesterase and butyrylcholinesterase. *Toxicology* **2007**, *233*, 166–172. [[CrossRef](#)] [[PubMed](#)]
35. Kuca, K.; Cabal, J.; Jun, D.; Musilek, K. In vitro reactivation potency of acetylcholinesterase reactivators—K074 and K075—To reactivate tabun-inhibited human brain cholinesterases. *Neurotox. Res.* **2007**, *11*, 101–106. [[CrossRef](#)] [[PubMed](#)]
36. Kovarik, Z.; Vrdoljak, A.L.; Berend, S.; Katalinić, M.; Kuč, K.; Musilek, K.; Radić, B. Evaluation of oxime K203 as antidote in tabun poisoning. *Arh. Hig. Rada Toksikol.* **2009**, *60*, 19–26. [[CrossRef](#)]
37. Zorbaz, T.; Malinak, D.; Kuca, K.; Musilek, K.; Kovarik, Z. Butyrylcholinesterase inhibited by nerve agents is efficiently reactivated with chlorinated pyridinium oximes. *Chem. Biol. Interact.* **2019**, *307*, 16–20. [[CrossRef](#)]
38. Lucić Vrdoljak, A.; Čalić, M.; Radić, B.; Berend, S.; Jun, D.; Kuča, K.; Kovarik, Z. Pretreatment with pyridinium oximes improves antidotal therapy against tabun poisoning. *Toxicology* **2006**, *228*, 41–50. [[CrossRef](#)]
39. Kuca, K.; Musilek, K.; Jun, D.; Zdarova-Karasova, J.; Nepovimova, E.; Soukup, O.; Hrabínova, M.; Mikler, J.; Franca, T.C.C.; Da Cunha, E.F.F.; et al. A newly developed oxime K203 is the most effective reactivator of tabun-inhibited acetylcholinesterase. *BMC Pharmacol. Toxicol.* **2018**, *19*, 1–10. [[CrossRef](#)]
40. Nachon, F.; Carletti, E.; Worek, F.; Masson, P. Aging mechanism of butyrylcholinesterase inhibited by an N-methyl analogue of tabun: Implications of the trigonal-bipyramidal transition state rearrangement for the phosphorylation or reactivation of cholinesterases. *Chem. Biol. Interact.* **2010**, *187*, 44–48. [[CrossRef](#)]
41. Bester, S.M.; Guelta, M.A.; Cheung, J.; Winemiller, M.D.; Bae, S.Y.; Myslinski, J.; Pegan, S.D.; Height, J.J. Structural Insights of Stereospecific Inhibition of Human Acetylcholinesterase by VX and Subsequent Reactivation by HI-6. *Chem. Res. Toxicol.* **2018**, *31*, 1405–1417. [[CrossRef](#)]
42. Franklin, M.C.; Rudolph, M.J.; Ginter, C.; Cassidy, M.S.; Cheung, J. Structures of paraoxon-inhibited human acetylcholinesterase reveal perturbations of the acyl loop and the dimer interface. *Proteins Struct. Funct. Bioinform.* **2016**, *84*, 1246–1256. [[CrossRef](#)] [[PubMed](#)]

43. Luo, C.; Saxena, A.; Smith, M.; Garcia, G.; Radić, Z.; Taylor, P.; Doctor, B.P. Phosphoryl Oxime Inhibition of Acetylcholinesterase during Oxime Reactivation Is Prevented by Edrophonium. *Biochemistry* **1999**, *38*, 9937–9947. [[CrossRef](#)] [[PubMed](#)]
44. da Silva, J.A.V.; Pereira, A.F.; Laplante, S.R.; Kuca, K.; Ramalho, T.C.; França, T.C.C. Reactivation of VX-inhibited human acetylcholinesterase by deprotonated pralidoxime. A complementary quantum mechanical study. *Biomolecules* **2020**, *10*, 192. [[CrossRef](#)] [[PubMed](#)]
45. Ghosh, S.; Chandar, N.B.; Jana, K.; Ganguly, B. Revealing the importance of linkers in K-series oxime reactivators for tabun-inhibited AChE using quantum chemical, docking and SMD studies. *J. Comput. Aided. Mol. Des.* **2017**, *31*, 729–742. [[CrossRef](#)] [[PubMed](#)]
46. Semenov, V.E.; Zueva, I.V.; Lushchekina, S.V.; Lenina, O.A.; Gubaidullina, L.M.; Saifina, L.F.; Shulaeva, M.M.; Kayumova, R.M.; Saifina, A.F.; Gubaidullin, A.T.; et al. 6-Methyluracil derivatives as peripheral site ligand-hydroxamic acid conjugates: Reactivation for paraoxon-inhibited acetylcholinesterase. *Eur. J. Med. Chem.* **2020**, *185*, 111787. [[CrossRef](#)] [[PubMed](#)]

Article

Impact of Sucrose as Osmolyte on Molecular Dynamics of Mouse Acetylcholinesterase

Sofya V. Lushchekina ¹, Gaetan Inidjel ^{2,3}, Nicolas Martinez ^{2,3}, Patrick Masson ⁴, Marie Trovaslet-Leroy ^{5,†}, Florian Nachon ⁵, Michael Marek Koza ², Tilo Seydel ² and Judith Peters ^{2,3,*}

¹ N.M. Emanuel Institute of Biochemical Physics, Russian Academy of Sciences, 119334 Moscow, Russia; sofya.lushchekina@gmail.com

² Institut Laue Langevin, 38000 Grenoble, France; gaetan.inidjel@laposte.net (G.I.); nico100885@hotmail.com (N.M.); koza@ill.fr (M.M.K.); seydel@ill.fr (T.S.)

³ Université Grenoble Alpes, UFR PhITEM, LiPhy, CNRS, 38000 Grenoble, France

⁴ Neuropharmacology Laboratory, Kazan Federal University, Kremlevskaya str 18, 480002 Kazan, Russia; pym.masson@free.fr

⁵ Institut de Recherche Biomédicale des Armées, 91223 Brétigny sur Orge, France; mtrovaslet@hotmail.com (M.T.-L.); florian.nachon@def.gouv.fr (F.N.)

* Correspondence: jpeters@ill.fr; Tel.: +33-4-7620-7560

† In memoriam of Marie TROVASLET-LEROY.

Received: 6 November 2020; Accepted: 11 December 2020; Published: 12 December 2020



Abstract: The enzyme model, mouse acetylcholinesterase, which exhibits its active site at the bottom of a narrow gorge, was investigated in the presence of different concentrations of sucrose to shed light on the protein and water dynamics in cholinesterases. The study was conducted by incoherent neutron scattering, giving access to molecular dynamics within the time scale of sub-nano to nanoseconds, in comparison with molecular dynamics simulations. With increasing sucrose concentration, we found non-linear effects, e.g., first a decrease in the dynamics at 5 wt% followed by a gain at 10 wt% sucrose. Direct comparisons with simulations permitted us to understand the following findings: at 5 wt%, sugar molecules interact with the protein surface through water molecules and damp the motions to reduce the overall protein mobility, although the motions inside the gorge are enhanced due to water depletion. When going to 10 wt% of sucrose, some water molecules at the protein surface are replaced by sugar molecules. By penetrating the protein surface, they disrupt some of the intra-protein contacts, and induce new ones, creating new pathways for correlated motions, and therefore, increasing the dynamics. This exhaustive study allowed for an explanation of the detail interactions leading to the observed non-linear behavior.

Keywords: cholinesterase; osmotic stress; neutron scattering; molecular dynamics; MD simulations

1. Introduction

Investigations of the impact of osmotic stress on biological systems can play major role in the case of extreme environments, for instance, high salinity in oceans, the Dead Sea, and salty lakes. Osmotic stress may also be responsible for physio-pathological processes and the iatrogenic effects of injected drugs. High concentrations of osmolytes in protein solutions have important biotechnological and pharmaceutical applications. Moreover, osmotic pressure can serve as a tool to study particular parts of proteins, if access to pores or other confined regions is not possible otherwise. Such a strategy was chosen in the present case to shed light on the dynamics of the gorge of mouse acetylcholinesterase (mAChE). Acetylcholinesterase (AChE) is a key enzyme in the nervous system that terminates neurotransmission at central cholinergic synapses and at neuromuscular junctions by hydrolyzing

the neurotransmitter's acetylcholine. The structures of cholinesterases (ChE) from different species are very close to each other with, for instance, identity scores between human AChE (hAChE) and mAChE of more than 82%. Due to the interest of cholinesterases as biopharmaceuticals for pre- and post-exposure treatments of organophosphorus poisoning [1], it is important to investigate the effect of sucrose as a protein structure protectant on the molecular dynamics of a model cholinesterase.

The first solved crystalline structure of a cholinesterase was that of *Torpedo californica* AChE (TcAChE) [2]. It showed that the catalytic active site is located at the bottom of a deep (20 Å) and narrow gorge (diameter of about 5 Å at the narrowest point, called "bottle neck"). This means that the substrate hydrolysis takes place in a mostly closed space virtually isolated from the bulk solvent. Along the passageway, the channel is so narrow that substrates would have no access to the active site if the enzyme were too rigid. However, Tai et al. [3] demonstrated, by means of molecular dynamics (MD) simulations, that half of the atoms in mAChE are participating in the so-called breathing mode that is periodically opening the gorge. The groups of McCammon [4–6] and Xu [7,8] undertook simulations of mAChE over 1 ns and 20 ns, respectively. The authors analyzed the dynamics and the possible opening of a so-called backdoor and other possible side channels in detail to shed light on movements in the gorge. Water molecules and co-solutes participate as well in the transport of the substrate to the enzyme catalytic center. Finally, water is the co-substrate of AChE-catalyzed hydrolysis of acetylcholine and other esters.

The experimental study of the motions in and out of the gorge is feasible by means of incoherent neutron scattering, which is sensitive to movements mainly of the nuclei of hydrogen (H) atoms, as the incoherent neutron scattering cross section of H is much higher than for any other nucleus. However, neutron scattering does not allow for distinguishing individual particles, which means that one observes the averaged motion of the H nuclei, and of molecular subgroups to which they are bound, assuming that they are representative for the dynamics inside the protein. In principle, incoherent neutron scattering would thus highlight parts of the sample by exchanging H against its isotope deuterium (D) and follow the dynamics of H belonging to the solution only, if the protein were deuterated. However, as so far it was not possible to deuterate ChEs, such an approach had to be excluded in this instance. Instead, the idea was to expose mAChE to sucrose unplugging all molecules from the gorge, to compare such sample to a native one in pure water and to extract information about motions of the solvent molecules only.

mAChE is a very fast enzyme, especially for a serine hydrolase, functioning at a rate approaching that of a diffusion-controlled reaction. The high speed of the enzyme is essential for the rapid functioning of cholinergic synapses, with a turnover of 10^3 – 10^4 s⁻¹. Therefore, we postulate that water dynamics within the gorge could be speeded up to facilitate transport of the substrate, eventually even beyond the normal diffusion rate of bulk water molecules. Such effects were observed, for instance, when water molecules were confined within a hydrophobic matrix [9]. The gorge could certainly be assumed to resemble such a confined environment.

Recently, we measured the dynamics of hAChE under high hydrostatic pressure, and our data suggests that this enzyme enters an intermediate folded state at 1.5 kbar, before being fully denatured at 3 kbar [10]. Osmotic pressure is believed to have different effects on reactions, as already discussed theoretically [11,12] and proven for butyrylcholinesterase (BChE) [13]. By using water-cosolvent mixtures, the enzyme hydration state can be modified, and thus, also the molecular dynamics and the transfer velocity of ligands and substrates. An osmolyte added to the solvent can either modify the viscosity only, as for instance glycerol (molar mass of 92 g/mol), or have a real osmotic effect, as for instance the bigger molecule of sucrose (molar mass of 342.3 g/mol). Sucrose is not able to penetrate the active site gorge of AChE and plays therefore the role of a semi permeable membrane by pumping the water molecules from inside the enzyme. Comparing the dynamics of AChE in the presence or absence of sucrose may hence provide information about the dynamics of water inside the gorge. Such information is extremely difficult to get by any other technique. Both effects, viscosity and osmotic pressure, can possibly have a great influence on the internal dynamics as well as the global

diffusion of the protein and induce changes in enzymatic activity. Experiments with enzymes in the presence of an osmolyte would allow us to complete our understanding of how the external conditions affect AChE dynamics and the water dynamics inside the gorge.

To better understand our results, we have undertaken molecular dynamics (MD) simulations of the same system at various sucrose concentrations. MD simulations give access to time scales very similar to those probed by incoherent neutron scattering, which allows us to undertake a direct comparison of dynamics and gain a better understanding of mechanisms at the atomic level.

2. Materials and Methods

2.1. Sample Preparation

Full cDNA of mAChE were inserted into pGS vector and expressed in Chinese hamster ovary cells (CHO-K1 cells). The transfected cells were selected and maintained in BioWhittaker® Ultraculture™ medium (Lonza, Belgium) containing methionine sulfoximide (50 μ M). The enzymes secreted into the culture medium, were purified using a procainamide affinity chromatography and were concentrated as previously described [14]. The gene produces a monomer, but the enzyme dimerizes spontaneously at the concentrations used here without inter-monomeric covalent binding. In its monomeric form, mAChE has a molecular mass of 66 kDa.

Activity measurements were carried out at 25 °C according to Ellman method [15] using 1 mM acetylthiocholine (ATC) as the substrate and 0.5 mM 5-5'-dithio-bis (2-nitrobenzoic acid) (DTNB) in 0.1 M phosphate buffer pH 7.0.

The preparation of hAChE was previously described in [14]. mAChE was prepared exactly according to the same protocol. Briefly, mAChE was first dialyzed against 25 mM ammonium acetate dissolved in D₂O (pD = 7.0) and then freeze dried (12 h) at 220 K under vacuum. This salt free protein powder, placed in an appropriated aluminum sample container, was dried for 12 h at atmospheric pressure over P₂O₅ and weighed. This measured weight was the sample dry weight ($h = 0$ g D₂O/g dry powder, denoted by g/g). For neutron experiments, the sample was hydrated by vapor exchange over D₂O, at ambient temperature, in a desiccator, until a final water content of about 0.4 g/g was achieved. To verify that no loss of material had occurred, and that the hydration state was the same, the samples were weighed before and after the neutron scattering experiments and no losses were detected.

We prepared four samples of mAChE with 0%, 5%, 10%, and 15% of deuterated sucrose and hydrated them over D₂O. We have chosen deuterated sucrose from Omicron Biochemicals, Inc., USA, to avoid a significant contribution from its H atoms to the incoherent neutron scattering signal. For the same reason, we used D₂O for hydration instead of H₂O. The proportions were chosen so that the weight of sucrose corresponded to the (*w/w*)% of mass of sucrose per mass of (sample + D₂O) (see Table 1). We also prepared the buffer in D₂O with 0 and 15 (*w/w*)% sucrose, corresponding to the extreme values and interpolating the intermediate values, as this is needed for data correction.

Table 1. Sample masses used for the experiments.

(<i>w/w</i>)% Sucrose	Mass of mAChE (mg)	Mass of Sucrose (mg)	Mass of D ₂ O (mg)	Final Sample Mass (mg) after Rehydration
0	100	0	208	308
5	84	17.8	228	339.8
10	70	30.8	214	314.8
15	56	46.4	296	398.4

2.2. Elastic Incoherent Neutron Scattering

The protein was probed elastically and quasi-elastically by incoherent neutron scattering. We used three different spectrometers at the Institut Laue Langevin (ILL), France: the cold neutron time-of-flight spectrometer IN6 [16], the thermal backscattering spectrometer IN13 [17] and the high-resolution

backscattering IN16 [18]. The spectrometers give access to molecular motions within the time windows of approximately 20 ps, 100 ps, and 1 ns, respectively. The experiments were conducted consecutively using the same samples.

The elastic incoherent neutron scattering (EINS) intensity is given within the Gaussian approximation by the dynamic structure factor at zero energy exchange:

$$S_{el}(Q, \omega = 0 \pm \Delta E) \approx S_0 \exp\left(-\frac{1}{3}\langle u^2 \rangle Q^2\right) \quad (1)$$

where $\langle u^2 \rangle$ is the average atomic mean square displacement (MSD). ω and Q are the exchanged energy and momentum in units of \hbar , respectively, and ΔE is the half width half maximum (HWHM) of the instrumental energy resolution related to the time window through Heisenberg's uncertainty principle. The Gaussian approximation supposes that any atom can only undergo harmonic isotropic motions around its equilibrium position. The average MSD is related to the flexibility of the sample at a given temperature. For $Q \rightarrow 0$, the approximation is strictly valid, and it holds up to $\langle u^2 \rangle Q^2 \approx 1$. The MSD can then be obtained for each temperature by the slope of the semi-logarithmic plot of the incoherent scattering function through:

$$\langle u^2 \rangle \approx -3 \frac{d \ln S_{el}(Q, \omega = 0 \pm \Delta E)}{dQ^2} \quad (2)$$

The transmission values were measured on IN13 and were all above 0.9. Consequently, multiple scattering effects should not be taken into consideration for the data treatment. In order to obtain the scattered intensities of the sample, scattering from the empty sample holder and the buffer were subtracted. For the intermediate sucrose concentrations, we interpolated the curves of the buffer measured at 0 and 15 wt%. The data were normalized to a 2 mm thick vanadium slab, a totally incoherent scatterer, providing the relative detector efficiency and the instrumental resolution. Absorption correction was based on the correction formula of Paalman–Pings [19]. The complete data reduction was carried out using the LAMP software available at ILL [20].

Quasi-elastic neutron scattering (QENS) is the part of scattering where small amounts of energy are exchanged between the neutrons and the sample, giving rise to a broadening of the elastic peak. The quasi-elastic structure factor

$$S(Q, \omega) = e^{-\frac{1}{3}\langle u^2 \rangle Q^2} \left[A_0(Q) \delta(\omega) + \sum_i A_i(Q) L(\Gamma_i, \omega) \right] \quad (3)$$

contains the Debye–Waller factor $e^{-\frac{1}{3}\langle u^2 \rangle Q^2}$, an elastic part, proportional to a delta-function in ω and representing the particles whose motions are not resolved within the instrumental setup. Furthermore, it includes a sum over Lorentzians, L , which describe different motional contributions. In theory, the sum can be extended up to an infinite number of contributions, but in practice a few Lorentzian curves are sufficient to describe the data reasonably well without over-fitting them. Here, we used two Lorentzian curves for the buffer and two Lorentzians for the sample, as more Lorentzians did not improve the fit quality. The amplitudes $A_0(Q)$ and $A_i(Q)$ depend on the momentum transfer Q . One can demonstrate [21] that the elastic incoherent structure factor (EISF) $A_0(Q)$ is given by the elastic intensity divided by the sum of elastic and quasi-elastic intensities at $t \rightarrow \infty$. It vanishes except for $Q = 0$ if only long-range diffusive motions were present, and it is indicative of the geometry of the diffusional process otherwise. For the rotational diffusion of a particle, the EISF is unity at $Q = 0$ and falls to a minimum at a Q value which is inversely related to the radius of gyration of the rotating particle.

For data analysis, the structure factor must be convoluted with the instrumental energy resolution, which can be mimicked by a vanadium measurement:

$$S_{exp}(Q, \omega) = S(Q, \omega) \otimes S_{res}(Q, \omega) \quad (4)$$

When fitting the structure factor, it is possible to separate elastic and quasi-elastic parts. The Lorentzians are characterized by parameters of the motions, which can be extracted from their HWHM Γ_i . Indeed, the form of the HWHM as function of Q^2 informs about the movements present in the sample. A pure translational diffusion in an unrestricted homogeneous medium corresponds to Brownian motion [22], whose characteristics are a linear behavior of the HWHM in Q^2 . The structure factor in this case reads:

$$S_B(Q, \omega) = \frac{1}{\pi} \frac{D_T Q^2}{\omega^2 + (D_T Q^2)^2} \quad (5)$$

where D_T represents the translational diffusion coefficient and $\Gamma_B = D_T Q^2$ its HWHM. Such a simple relation usually does not hold in the crowded medium of a macromolecule. The atoms diffuse, for instance, through a motion called translational jump-diffusion [23], where the HWHM does not increase linearly, but deviates from such behavior at higher Q values. The atoms perform oscillatory motions around their equilibrium positions for a time τ_0 . After that they diffuse for a time τ_1 by continuous diffusion and the process is then repeated. The structure factor can be described by a single Lorentzian with the HWHM Γ_{JD} as:

$$\Gamma_{JD} = \frac{D_T Q^2}{1 + D_T Q^2 \tau_0} \quad (6)$$

At small Q -values, the slope of Γ_{JD} gives again the translational diffusion coefficient D_T and the relation reduces to Brownian's law, i.e., $\Gamma_{JD} = \Gamma_B$. At large Q -values, the HWHM tends to the asymptotic value $\Gamma_\infty = 1/\tau_0$, τ_0 being called the average residence time.

When the motions are further restricted, they can result in rotational diffusion within a confined space [24]. The structure factor describing such movements reads:

$$S_R(Q, \omega) = A_0(QR)\delta(\omega) + \frac{1}{\pi} \sum_{l=1}^{\infty} (2l+1)A_l(QR) \frac{\Gamma_l}{\omega^2 + \Gamma_l^2}, \quad (7)$$

where the diffusing atoms are limited to a sphere of radius R , $\Gamma_l = D_R l(l+1)$, D_R being the rotational diffusion coefficient. Volino and Dianoux [24] found an analytical expression for the EISF:

$$A_0(QR) = \left[\frac{3j_1(QR)}{QR} \right]^2 \quad (8)$$

where $j_1(x) = \sin x/x^2 - \cos x/x$ is the first-order spherical Bessel function. Bellissent-Funel et al. [25] expanded the model for the EISF by an immobile fraction p , where p denotes strongly bound protons. In that case, Equation (8) becomes:

$$A_0(QR) = p + (1-p) \left[\frac{3j_1(QR)}{QR} \right]^2 \quad (9)$$

Although the jump diffusion and diffusion in a confined space models were first developed for motions in fluids, such models were also successfully applied for crowded media [26].

2.3. Molecular Dynamics Simulations

The crystallographic structure of mAChE dimers PDB ID 1J06 [27] was used as a source of the protein coordinates. The missing loop 258–264 was restored using Modeller 9.14 [28], and the missing Lys496(A) and Arg493(B) side chains were reconstructed by means of a VMD *psfgen* module. Hydrogen atoms were added to construct the hydrogen bonding network by using Reduce software [29]. Water molecules recognized in the crystal structure were included in the model system and other non-protein molecules were removed. To meet experimental protein concentrations in the solution and to avoid interactions of the proteins with its copies in PBC, two dimers (four protein molecules) were

placed in solvation boxes. Clusters of sucrose molecules were built by means of VegaZZ software [30]. The total number of TIP3P water molecules and sucrose molecules added were adjusted to meet experimental concentrations. The number of molecules and sizes of the resulting systems are provided in Table S1 containing the electronic supplemental information (ESI).

MD simulations were performed with the NAMD 2.11 program [31] with CHARMM36 force field [32,33] at the Lomonosov-2 Moscow State University supercomputer center [34]. Periodic boundary conditions and PME electrostatics were applied. The systems were maintained at a constant temperature 300 K for productive runs and under pressure 1 atm (NPT ensemble) by using Langevin dynamics and Nosé-Hoover barostat. The initially prepared system underwent a 3000-step minimization.

As sucrose molecules were added to the system as a regular grid, systems with sucrose were subjected to a long pre-equilibration to optimize the solvents with 1 fs time-steps. For this, the coordinates of protein atoms and surrounding 4 Å water shells were fixed. In the first time, systems were subjected to 20 ns MD simulations at 400 K, and in the second time cooled down to 300 K during 20 ns. Then 10 ns unconstrained runs were performed for final equilibration. A radial distribution function was used to control the equilibration of the sucrose solution (see ESI, Figure S1). Then, 1 μ s productive MD-runs at 300 K with 2 fs time-steps were performed. The analysis of obtained MD trajectories was performed using VMD [35] software and custom scripts. For calculations of the number of hydrogen bonds, a distance of 3.2 Å and a 40° cutoff angle were used. The calculations of the number of atom–atom contacts involved hydrogen atoms. Mean square displacement values were calculated from MD trajectories with different lag times τ as follows:

$$\langle u^2(\tau) \rangle = [RMSF(\tau)]^2 = \langle [\bar{r}(t + \tau) - \bar{r}(t)]^2 \rangle \quad (10)$$

where *RMSF* stands for root-mean square fluctuations.

Principle component analysis (PCA) and Cartesian PCA (cPCA) were performed using ProDy software [36], dihedral angle PCA (dPCA) was performed using Carma software [37]. cPCA was performed excluding the most mobile terminal residues 1–10 and 530–543. PCA methods allow us to determine and visualize the directions in space corresponding to the axes of highest mobility.

3. Results

The experiments were performed between June and August 2013 on the instruments IN6, IN13 and IN16 (DOI:10.5291/ILL-Data.8-04-707) and we repeated one measurement in August 2014 on IN13.

3.1. Incoherent Neutron Scattering

IN13 is a backscattering spectrometer giving access to averaged local motions within the time range of about 100 ps, e.g., it mainly enables the observation of sub-molecular motions of the amino acid side chains and small rotations at the protein's surface.

The four samples were scanned elastically within the temperature range from 270 to 310 K in steps of 5 K. After correction and normalization of the raw data, we first calculated the EINS of Equation (1) summed over all available *Q*-values. Such a quantity has smaller error bars due to the increased statistics and only depends on external parameters as temperature and the sucrose concentration. In Figure 1a, we present the summed intensities as function of wt% of sucrose at all measured temperatures. Higher temperature has the expected effect of lowering the intensities. In contrast, increased intensity depicts slower dynamics as more neutrons are scattered in a way to stay within the instrumental time window. All curves show a non-linear dependence on the sucrose concentration, with a maximum of intensity around 5 wt%. At 10 wt%, the intensities drop significantly, but present a pronounced dependence on temperature. In contrast, at 15 wt% all points seem to converge. We further used Equation (2) to extract the MSD of the same data and to plot them also as function of sucrose concentration (see Figure 1b). The MSD are mainly inversely proportional to the square of the summed intensities [38], so here we find a minimum at around 5 wt%. As the data have

lower statistics, the errors are bigger and the variations higher, especially at 15 wt% where the protein quantity and therefore the data quality was below the other curves.

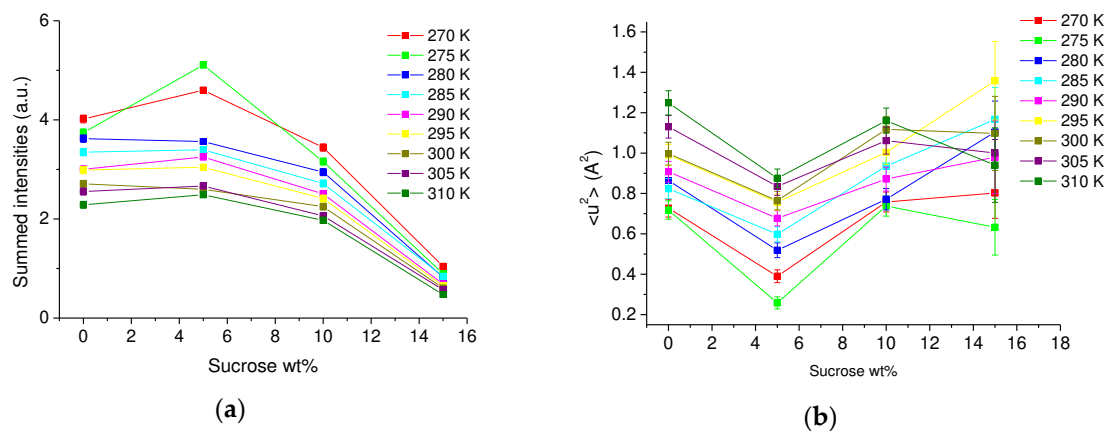


Figure 1. Samples measured as function of sucrose wt% for temperatures ranging from 270 to 310 K. (a) Summed elastic intensities. The error bars were calculated but are so small that they are within the symbols. (b) mean square displacement (MSD) extracted through Equation (2).

Figure 2 presents the same MSD extracted from IN13 data now as function of the temperature for different concentrations of sucrose. All samples follow a linear increase in temperature except the sample at the highest sucrose concentration, which presents rather high fluctuations due to low data quality. As the behavior at 5 wt% sucrose was unexpected, we reopened the sample holder, dried, and rehydrated the sample and repeated the measurement. The result is shown in the orange dashed curve, close to the red curve, except at low temperature, where we saw probably the melting of heavy water around 277 K the second time.

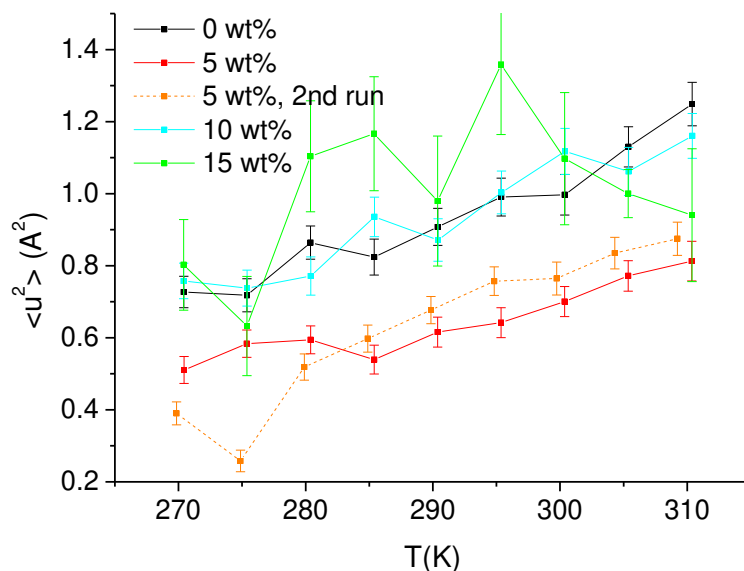


Figure 2. MSD extracted through Equation (2) from data taken on IN13 as function of temperature. The black curve corresponds to the sample with no sucrose, the red and orange curves to the sample with 5 wt% sucrose, the cyan curve to 10 wt% sucrose, and the green curve to 15 wt% sucrose.

IN6 has a time window of about 20 ps and gives access to smaller and faster motions, which are for instance directly influenced by the presence of water molecules. Here, we measured EINS and QENS spectra. Globally, the MSD are lower compared to those obtained on IN13, what is explained by

the smaller time window of IN6, but followed the same trends (see ESI, Figure S2) confirming further the non-linear behavior around 5 wt% sucrose.

QENS data were collected at 310 K, the physiological temperature of living organisms, and analyzed with the formalism described above (see Equations (3) and (4)). First, the buffer (D_2O in presence or not of sucrose) curves were fitted with two Lorentzian functions and their HWHM extracted. Water molecules can simultaneously undergo translational and rotational motions and, indeed, we obtained this type of motions. Figure 3 shows the HWHM of the first Lorentzian curve together with fits according to the jump-diffusion model described in Equation (6). The systematic dip around 2.5 \AA^{-2} can be ascribed to de Gennes narrowing consequent to coherent scattering. The second Lorentzian was about 5–6 times larger, corresponding to faster motions, and corresponded to rotational motions as identified by the absence of a Q-dependence (data not shown).

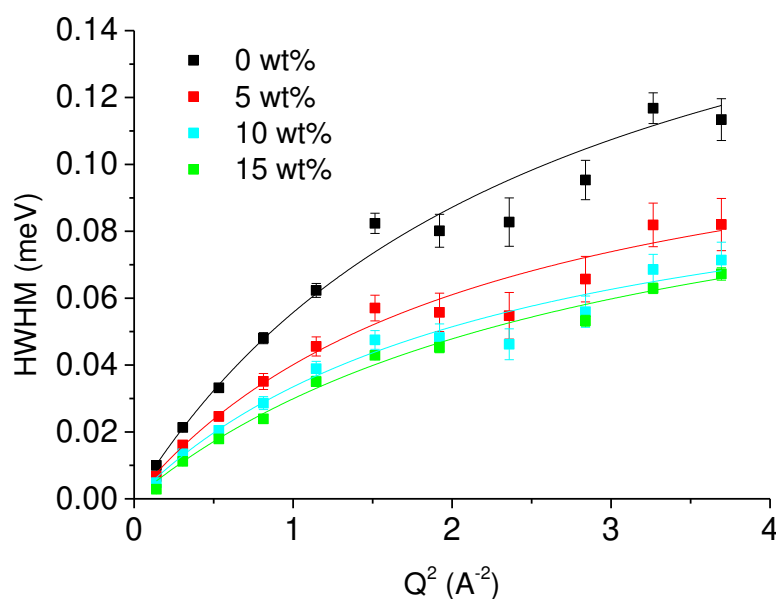


Figure 3. Half width half maximum (HWHM) Γ of the one Lorentzian curve used to fit the Quasi-elastic neutron scattering (QENS) data of D_2O in presence or not of sucrose taken on IN6 as function of Q^2 . The black curve corresponds to no sucrose, the red curve to 5 wt% sucrose and the cyan curve to 10 wt% sucrose. The lines are fits using the jump-diffusion model Equation (6).

All four samples present the typical Q-dependence of water at ambient temperature [39] and in the presence of co-solutes, corresponding to random-jump diffusion and rotations. In particular, our curves compare very well to those presented by Grimaldo et al. [40] for D_2O measured also on IN6 at the ILL, Grenoble. The addition of sucrose had the expected effect: viscosity was increased and thus the translational diffusion coefficient D_T decreased from $1.17(5)$ to $0.89(4)$, $0.73(4)$ and $0.61(3) \times 10^{-5} \text{ cm}^2/\text{s}$ with the increasing sucrose concentration. The residence times τ_0 obtained for the four cases were $3.3(3)$, $5.2(5)$, $5.9(6)$, and $5.5(5)$ ps, respectively. In comparison, pure bulk H_2O water has the characteristics $D_T = (2.5 \pm 0.1) \times 10^{-5} \text{ cm}^2/\text{s}$; and $\tau_0 = 1.1$ ps [25], which represent a higher and lower limit for these parameters. The self-diffusion in D_2O is moreover slightly below that in H_2O [41].

For the analysis of QENS data of the complete samples, we fixed then the HWHM of the two Lorentzians attributed to the buffer as well as the ratio of the absolute intensities between them, but let their absolute values vary freely together. Then, two Lorentzians were added to account for the sample. Figure 4 presents an example of such a fit of the experimental data with one elastic peak, four Lorentzian curves and a straight line to account for the background, which gives very good fit results.

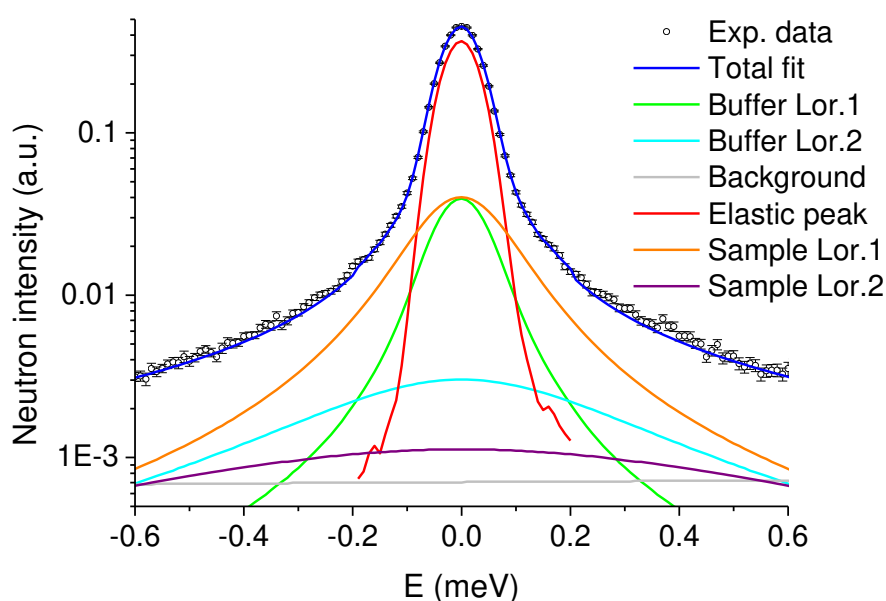


Figure 4. Logarithmic plot of an example of a fit of experimental QENS data of sample in the presence of 5 wt% sucrose for $Q = 0.9 \text{ \AA}^{-1}$ at 310 K. As described above, two Lorentzian curves were used for the buffer, two Lorentzian curves for the sample, a delta function to account for the elastic peak and a straight line for the background, resulting in a fit quality factor $\chi^2 = 1.38$.

We determined first the EISF $A_0(Q)$ for the three samples with no, 5 and 10 wt% sucrose (see Figure 5). According to the diffusion-in-a-sphere model and Equation (9), the value of the EISF at highest Q is representative for the proportion p of particles, e.g., H nuclei and molecular subgroups to which they are bound, seen as immobile within the instrumental time resolution. R is representative of the radius of the sphere delimiting the particles' motions. Both quantities are progressively increasing with sucrose concentration (see Table 2), although the radius is mainly the same for all samples within error bars. Due to the increasing viscosity of the solution in the presence of sucrose, more particles are slowed down at higher sucrose concentration.

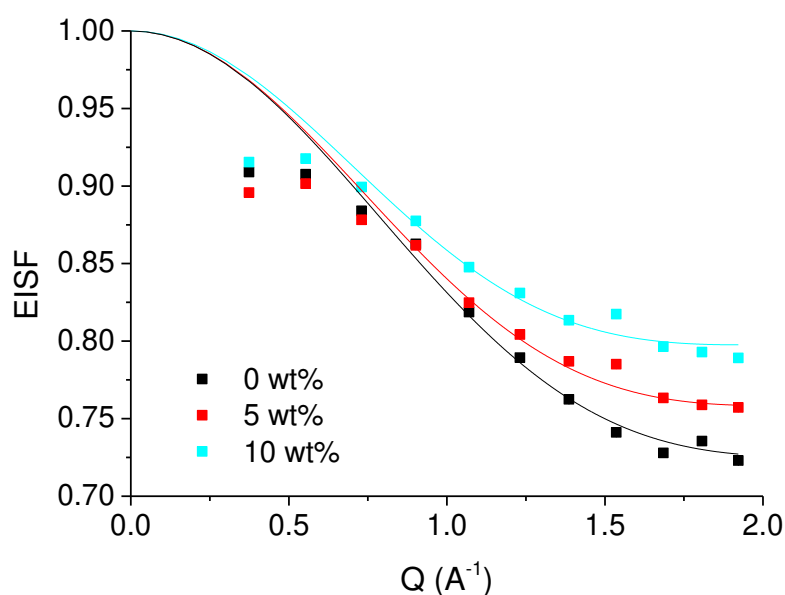


Figure 5. Elastic incoherent structure factor (EISF) of the samples with no sucrose (black curve), with 5 wt% sucrose (red curve) and with 10 wt% (cyan curve) sucrose as function of Q .

Table 2. Proportion p of particles seen as immobile and radius R of the sphere.

$(w/w)\%$ Sucrose	Proportion p	Radius R (Å)
0	72.6 (5)%	2.11 (6)
5	75.8 (3)%	2.24 (6)
10	79.8 (6)%	2.3 (1)

Further, we determined the HWHM of the Lorentzian curves of the samples (see Figures 6 and 7), plotted them as function of Q^2 and fitted them with one of the models.

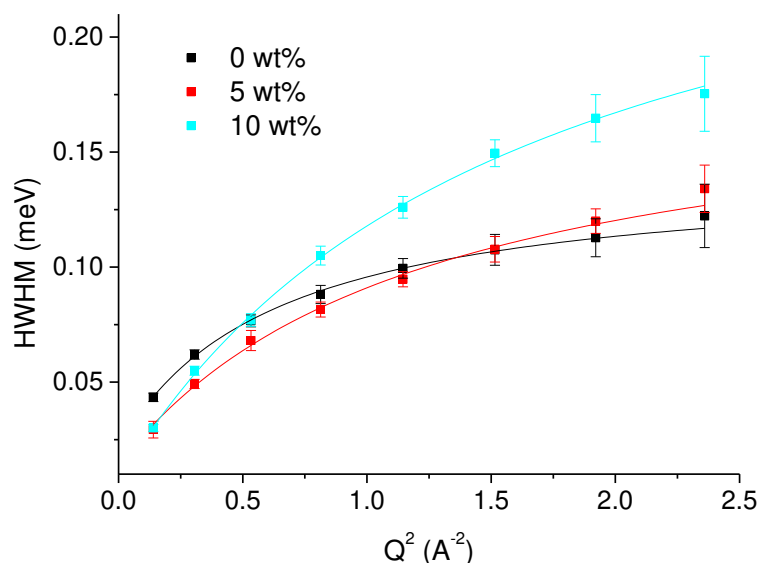


Figure 6. HWHM Γ of the narrower Lorentzian curve used to fit the QENS data of mAChE in the presence or not of sucrose taken on IN6 as function of Q^2 . The black curve corresponds to no sucrose, the red curve to 5 wt% sucrose and the cyan curve to 10 wt% sucrose. The lines are fits using the jump-diffusion model Equation (6).

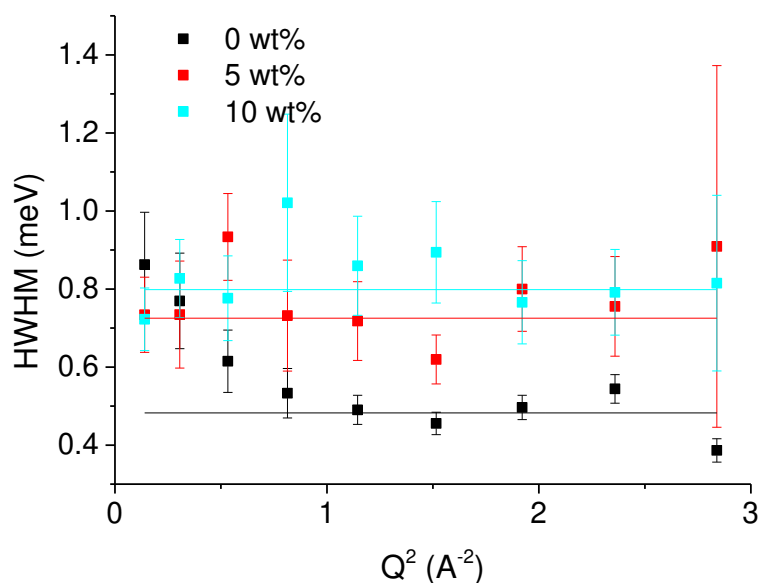


Figure 7. HWHM Γ of the broader Lorentzian curve used to fit the QENS data of mAChE in the presence or not of sucrose taken on IN6 as function of Q^2 . The black curve corresponds to no sucrose, the red curve to 5 wt% sucrose and the cyan curve to 10 wt% sucrose. The lines are fits with a constant value corresponding to rotational diffusion.

Figure 6 presents the HWHM Γ of the narrower Lorentzian function, corresponding to larger movements. We reiterate here that we are probing the internal motional diffusion of small molecular subgroups rather than global diffusion of the protein in solution, which is beyond the scope of the instrumental resolution of IN6. In this case, the tendencies are inverted with the curve at 10 wt% being clearly above the two others, which are more similar in absolute values. The Q-dependence of the HWHM still resembles jump-diffusional motions, but the slopes and curvatures differ significantly for the three samples and we notice again the non-linear behavior. The translational diffusion coefficient D_T , corresponding to the slope at small Q-values, varies from $(2.9 \pm 0.4) 10^{-5} \text{ cm}^2/\text{s}$ without sucrose to $(2.1 \pm 0.3) 10^{-5} \text{ cm}^2/\text{s}$ at 5 wt% and to $(2.7 \pm 0.2) 10^{-5} \text{ cm}^2/\text{s}$ at 10 wt% sucrose. The residence times τ_0 obtained for the three cases were now (5.5 ± 0.2) , (3.8 ± 0.2) and (2.3 ± 0.1) ps, respectively.

Figure 7 shows the HWHM of the broader Lorentzian curve, used to fit the QENS data. The obtained values are tainted with bigger error bars and do not show a systematic dependence on Q. These smaller molecular motions can be attributed to rotational diffusion, which does not depend on Q. The HWHM Γ is related to the rotational diffusion coefficient $\Gamma_R = 2D_R$ (see Equation (7)). Here, the effect of sucrose has an opposite effect: an increase of the rotational diffusional coefficient from 0 to 10 wt% yielding the values for D_R of (0.24 ± 0.02) meV, (0.36 ± 0.02) meV, and (0.4 ± 0.01) meV, respectively.

Finally, IN16 is the instrument with the highest energy resolution which thus allows us to probe motions up to about 1 ns. Such a time window might provide us with further information on local motions, however, it also includes motions of subgroups and domains. We recorded EINS data from 275 to 312 K and plotted the summed intensities (see ESI, Figure S3a) and MSD (see ESI, Figure S3b). At these longer times, the differences are becoming even more striking, but again the hierarchy between the samples is the same.

3.2. MD Simulations

Mean square displacement values $\langle u^2 \rangle$ calculated for protein over MD trajectories with different time windows (τ) showed nonlinear patterns, as it was observed experimentally: a decrease in mobility at 5 wt% sucrose, compared to 0 wt%, and an increase at 10 wt% sucrose solution (Figure 8a). This effect becomes more pronounced with the increase of τ . The per-residue RMSF distribution is ambivalent, showing increased and decreased mobility of some areas in all systems (see ESI, Figure S4).

PCA of the MD trajectories allows to separate low frequency motions and to visualize differences in mAChE mobility (Figure 8b–d). cPCA shows that in the 0 wt% sucrose sample, the most mobile segments are peripheral loops, including loop 258–264, not resolved in X-ray, and Ω -loop. In the 5 wt% sucrose solution, these movements are dampened (amplitude decreased). However, Ω -loop movements are accompanied by acyl loop movements due to the binding of sucrose molecules at the gorge entrance. In the case of 10 wt% sucrose, movements of most of α -helices and loops constituting the gorge walls (Ω -loop and acyl loop) have considerably increased their variance compared to movements in more diluted solutions, while β -sheets spanning through the protein are not affected. Other representations including network views of the cPCA results are shown in the ESI, Figure S5. dPCA free energy landscapes have distinctive local basins in case of 0 wt% and 10 wt% sucrose solutions, while for 5 wt% free energy landscape domains are more connected (ESI Figure S5).

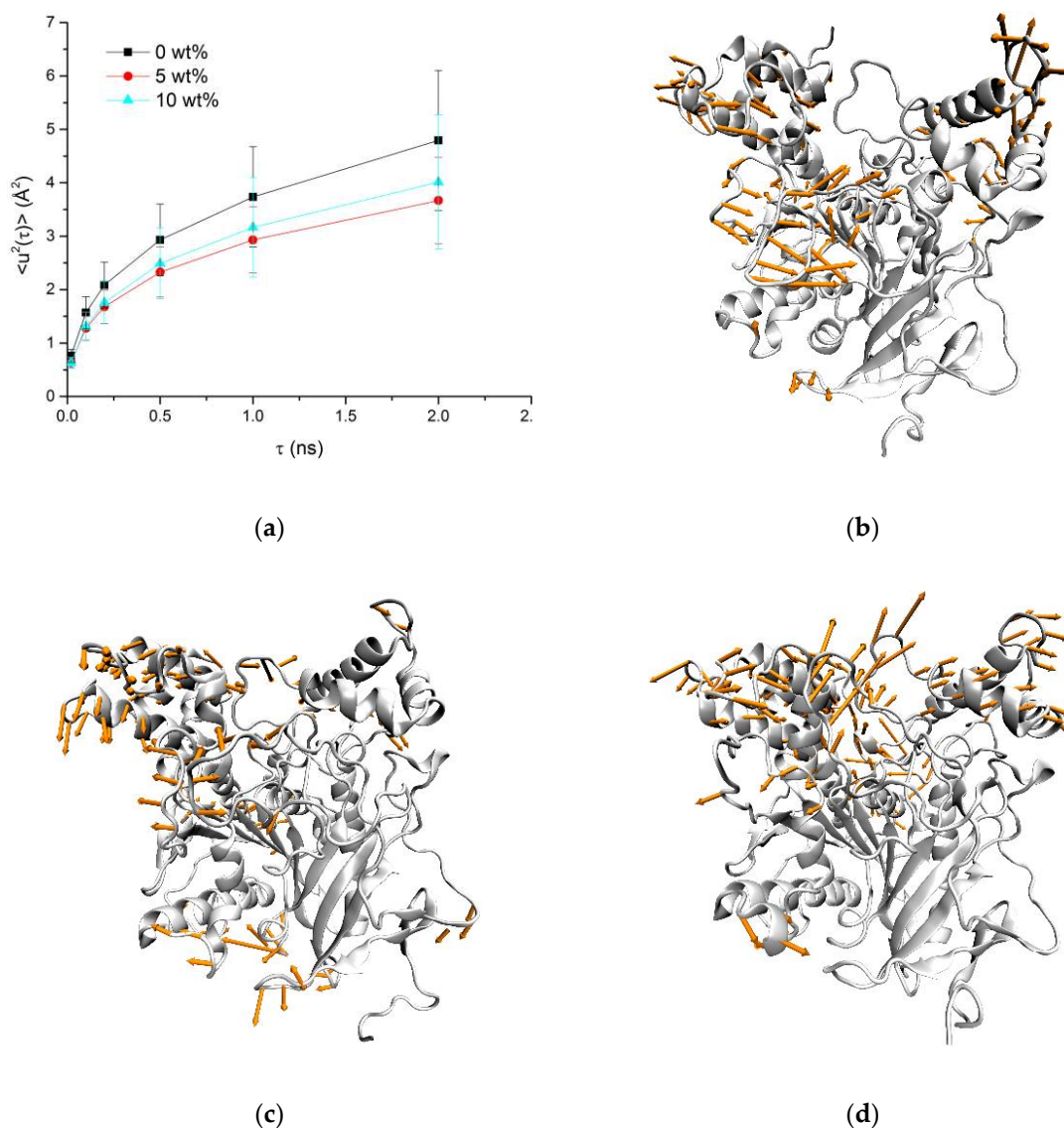


Figure 8. (a) MSD vs. τ for different sucrose concentrations. The first cPCA modes with the greatest variance and for mAChE in 0 wt% (b), 5 wt% (c) and 10 wt% (d) sucrose solutions.

mAChE conformational states corresponding to the deepest basins seen for the 10 wt% solution reflect movements of the Ω -loop, induced by interactions with the sucrose molecule. Figure 9a shows the interactions of the Ω -loop with the adjacent part of the protein. They are few: hydrogen bonds between Asp74 and Tyr341, Tyr77, and Lys348 main chain, Trp86 and Tyr449; π -cation interaction between Phe80 and Lys348 and T-stacking interaction between Phe80 and Trp439. Panel B shows that all these interactions are disrupted during MD simulation of mAChE in 10 wt% sucrose solution. Yet, the Ω -loop is only partially detached through intermittent interactions, catalytic triad remains operative, and Trp86 forms cation-binding site. Furthermore, the snapshot shows a typical situation for MD simulations of ChEs in sucrose solutions: the sucrose molecule at the entrance of the gorge interacting with the Ω -loop and acyl loop (Figure 9b and ESI Figure S6). This results in the increased mobility of the acyl loop (Figure 8) and correlated motions between the Ω -loop and acyl loop residues (ESI Figure S6).

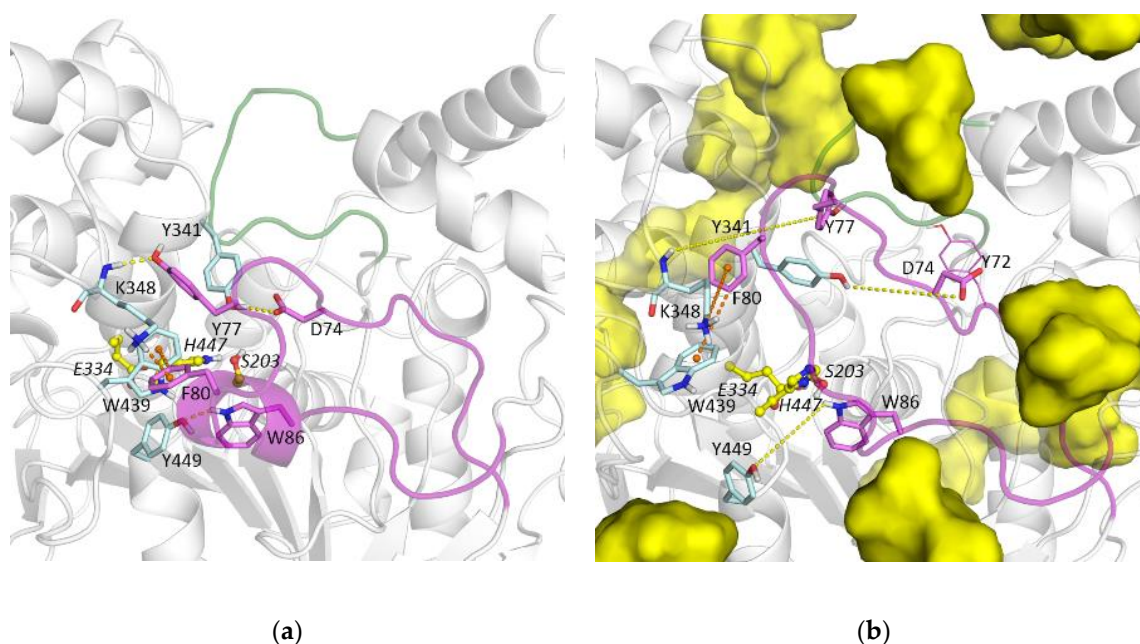


Figure 9. Ω -loop constituting the wall of the mAChE active site gorge (purple) and its interaction with the adjacent part of the protein, yellow dashes show hydrogen bonds, orange dashes show π - π and π -cation interactions, sucrose molecules are shown with yellow surface representation. (a) X-ray structure, (b) snapshot after 1 μ s MD trajectory of the 10 wt% solution system, connections between atoms shown in panel (a) as interactions are maintained. Acyl loop forming the other wall of the gorge is shown in green.

Indeed, despite the observed increase in mobility of Ω -loop and acyl loop, there is no sign of partial unfolding, induced by the increase in sucrose concentration, or change in the gyration radius R_g , or in the solvent accessible surface (SASA) (Table 3).

Table 3. Averaged parameters derived from 1 μ s MD trajectories (\pm SD).

	Water	5 wt% Sucrose	10 wt% Sucrose
SASA, \AA^2	23,991 \pm 367	23,934 \pm 273	24,047 \pm 297
R_g , \AA	23.0 \pm 0.1	23.0 \pm 0.1	23.0 \pm 0.1
Number of water molecules inside the gorge	47 \pm 4	31 \pm 4	43 \pm 5
Number of hydrogen bonds			
Protein–water	270 \pm 10	268 \pm 10	256 \pm 10
Protein–sucrose		8 \pm 3	12 \pm 4
Intra-protein	317 \pm 9	317 \pm 10	314 \pm 10
Number of atom–atom contacts (2 \AA cutoff)			
Protein–water	726 \pm 21	713 \pm 22	687 \pm 20
Protein–sucrose		19 \pm 6	33 \pm 7
Sum		732 \pm 21	720 \pm 20

The number of water molecules inside the active site gorge is decreasing in the 5 wt% system due to osmotic stress [42]. The depletion of water molecules increases the mobility of the gorge residues (ESI, Figure S4b), but cPCA shows that these are high frequency motions and the catalytic triad remains operative. In the 10 wt% sample, this number is increased due to the instability induced by sucrose molecules on the Ω -loop and acyl loop. It opens new windows including a so-called backdoor [43] and

side-door [44] for the influx of water molecules and reduces the accuracy of estimated water molecules inside the gorge (ESI Figure S6).

The averaged numbers of hydrogen bonds and atom–atom contacts have high variances; however, some tendencies could be noticed. Between the 0 wt% and 5 wt% sucrose systems, the number of protein–water interatomic contacts and hydrogen bonds slightly decreases. At the same time, the sum of the numbers of protein–water and protein–sucrose interatomic contacts and hydrogen bonds for the 5 wt% system is higher than the numbers of protein–water interatomic contacts and hydrogen bonds for the 0 wt% system. It can be interpreted as follows, when approaching the protein surface, the sucrose molecules rather interact with it through water molecules than to displace them. In addition, this could be the sign of a stiffer surrounding of the protein.

Comparing the 5 wt% and 10 wt% sucrose systems, the total number of hydrogen bonds and atom–atom interactions decreases as the percentage of sucrose is increased, and the replacement of water with sucrose molecules is more pronounced. Direct interactions of sucrose molecules with the protein surface does not lead to a significant decrease in protein intramolecular hydrogen bonding.

These differences between the nature of interactions between sucrose molecules and the protein in the 5 wt% and 10 wt% sucrose systems are illustrated by the example in Figure 10. In the 5 wt% sucrose system, the sucrose molecule interacts with mAChE residues through water molecules, on the contrary, in the 10 wt% sucrose system some interactions are through water molecules, others are direct. The salt bridge between Lys332 and Glu431 is broken, but the distant residue Asp396 is brought closer. This effect is similar to the one described above, the crosstalk between Ω -loop and acyl loop mediated by sucrose molecules. It can be seen as new contacts (correlated motions) in the network view of cPCA results (ESI Figure S5).

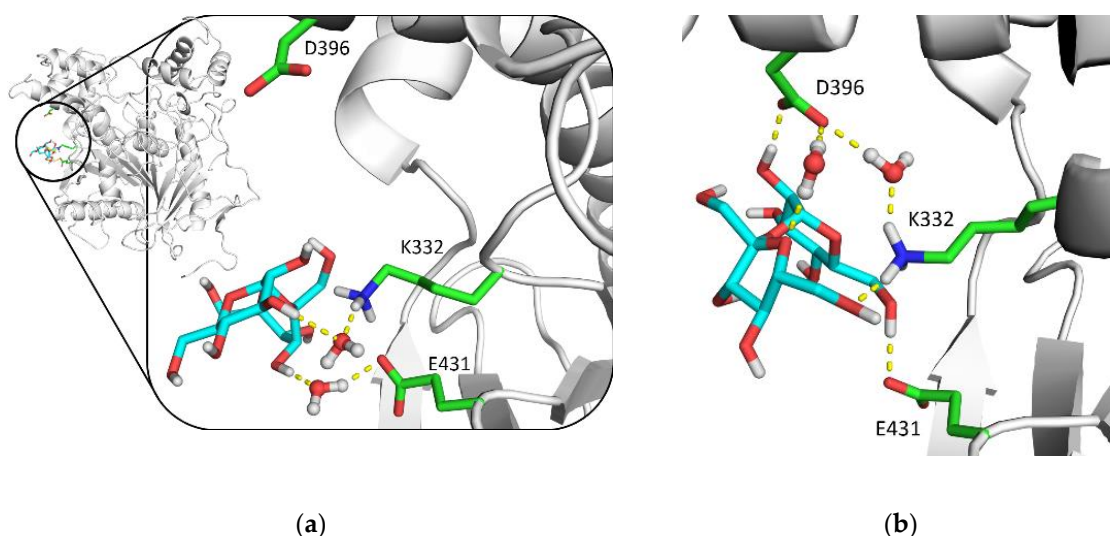


Figure 10. 5 wt% system (a) and 10 wt% system (b) snapshots after 1 μ s MD trajectory showing the interaction of sucrose molecules with the same residues.

4. Discussion

The role of viscosity on the sub-ns molecular dynamics of proteins has already been investigated in the past by means of incoherent neutron scattering and a clear impact was determined [45–47] of the presence of glycerol or glucose. As expected, co-solutes decreased the MSD of lysozyme, a small globular protein, in these cases above 150 K, but prevented the freezing even at low temperature. We were able to observe here similar behavior in the case of pure D₂O buffer, which is more and more slowed down under the effect of sucrose (see Figure 3). The corresponding translational diffusion coefficients are all below the value known from the literature for bulk H₂O [39]. In agreement with these findings, the residence times increased. The latter effect is indicative for a stronger confinement

effect [48]. The result found for the EISF of our samples points towards the same direction, as it increases at high Q values with increasing concentration of sucrose, meaning that less particles participate to the motions resolved by the instrument IN6 in the presence of the sugar although the radius of confinement is almost constant.

On the contrary, the results concerning the summed intensities and MSD extracted from three different spectrometers with increasing time window, IN6, IN13, and IN16, tell us a different story. As expected, the MSD increase with the time window, as more and more movements become visible at longer scales. The same findings hold for MD simulations as shown in Figure 8a. The MSD also increase with temperature, as the additional thermal energy permits larger amplitudes. However, the MSD equally increase with the concentration of sucrose, except for the sample at 5 wt% which presents a strong non-linear behavior. In particular, for IN6 we observe a cross-over of the curves corresponding to 0 and 5 wt% sucrose at around 290 K. Obviously, at this short time scale of 20 ps, the corresponding motions set in only at higher temperatures.

Several explanations are possible for such insights and only the MD simulations executed in parallel on the same kind of samples permitted to verify and better understand these effects:

1. When sucrose molecules are located at the entrance of the gorge, the gorge acts as semi-permeable membrane, and water can get out, but not enter due to the osmotic effect. Such an effect was previously observed with human BChE [42]. Moreover, sucrose molecules cannot enter due to their volume. At 0 wt% sucrose, there is only water inside and outside the cavity. The simulations allowed us to see that at 5 wt% sucrose, the motion of the protein's outer part is dampened, but inside the gorge motion is increased due to water depletion. Finally, at 10 wt% sucrose structural modifications seem to occur in such a way that the sugar molecules form a layer at the protein's surface and protect the water layer, which permits a higher flexibility of the enzyme. These results are reflected in the neutron scattering data through a higher stability at 5 wt% sucrose and higher mobility at 10 wt%.
2. Sugars have a small binding affinity for cholinesterases. It seems that the enzymes become more flexible in the presence of sugar. This increases both the conformational entropy and the affinity to bind, so that water molecules bound on the surface can be replaced by sugar [49].
3. Similar effects were reported earlier by Cicerone et al. [50] and Curtis et al. [51], showing that a binary glycerol–trehalose glassy matrix can stabilize a protein at a particular mass fraction of glycerol. The minimum in flexibility of the protein coincides with the lowest flexibility of trehalose in the binary glass. The authors have shown that the stabilization of the protein is due to the suppression of local fast motions in both the host matrix and the protein, although much of the important dynamics of the protein may not be coupled with viscosity of the host fluid.

QENS measurements show furthermore that not only molecular dynamics are reduced around 5 wt% of sucrose, but that the nature of the movements is also changed. Whereas the curves at 0 and 10 wt% of sucrose for the HWHM resemble to jump-diffusion motions, the curve at the intermediate sucrose concentration looks stiffer. This agrees with the fact that the modes at the protein's surface are dampened according to the simulations. The translational diffusion coefficients are indeed similar at 0 and 10 wt% but decreased in between. A re-structuration at the protein's surface and a strong coupling between the water layer and the sucrose matrix seems thus likely.

MD simulations are in good agreement with the experimental data and confirm the outstanding role of the interaction between water molecules, the sugar matrix and the protein surface. This allows us to understand the dynamics of the protein, e.g., the nonlinear behavior increasing over the time window. The analysis of MD trajectories, though partly speculative where values have high variances, allows us to suggest the following explanation: with the addition of sucrose at 5 wt%, the protein's nearest environment becomes more populated or stiff, reducing protein mobility as seen with neutron scattering. With an increase of the concentration, sucrose molecules replace more water molecules and have more direct interactions with the protein's surface. At 5 wt%, the water shell protects

the protein from sticky sucrose molecules, at 10 wt% this shell is depleted and this disturbs protein dynamics. Sucrose molecules penetrating the protein surface disrupt some of the intra-protein contacts, and induce new ones, creating new pathways for correlated motions. This effect is amplified by interactions between sucrose molecules, more frequent in more concentrated solutions.

It remains uncontested that the study of a protein in the presence of high sugar concentrations is not directly comparable to its native form. However, our observations shed light on the mechanisms of water fluxes into and out of the gorge, including the active site. Our investigations permitted us to conclude on complex dynamics of the Ω - and acyl loop. Other parts of the enzyme or polypeptide segments may also display peculiar dynamics. This opens new windows for understanding the extraordinary catalytic power of cholinesterases. In particular, the influx of water molecules across a backdoor could be addressed by MD simulations in the presence and absence of sucrose. The functionality of a backdoor as it was suggested [43] remains a puzzling issue. In the present case, simulations allowed to get information about the number of water molecules inside the gorge for the different samples. In contrast to what we expected (e.g., a continuous decrease of water molecules due to the osmotic effect and a concomitant shrinking of the gorge) maybe up to a collapse, we observed a much more subtle interplay between the different components and an increase in protein mobility at the highest sucrose concentration. The latter can be ascribed to the instability induced by sucrose molecules on Ω -loop and acyl loop, which finally results in conformational perturbation of the gorge.

5. Conclusions

In the present work, we intended to investigate the dynamics of the enzyme mAChE around its narrow gorge and of the water molecules, which move quickly into and out of the gorge. As the per-deuteration of mAChE is not possible so far, we opted for a study in D₂O solution and in the presence of increasing concentration of deuterated sucrose. The sugar exerts osmotic pressure on the water molecules in the gorge permitting to study these movements in more detail. Surprisingly, we found experimentally a non-linear behavior in the dynamics of the samples with increasing sucrose concentration, inducing first a slowing down of the dynamics at 5 wt% and then again a raise. Moreover, the nature of the dynamics was also found different at the minimum of mobility. Extensive MD simulations allowed us to study in detail the interactions of the different components leading to such behavior. Sucrose molecules interact with the surface of the protein and the entrance of the gorge at a lower concentration through the water layer, damping the motions at the surface, but increasing them inside the gorge. When increasing the sucrose concentration more, the sucrose molecules replace some of the water molecules at the surface, permitting again to more water molecules to enter the gorge and opening simultaneously new pathways, among them the hypothesized backdoor to the gorge. These multiple mutual influences and interactions permit us to explain very satisfactorily the experimental findings.

Supplementary Materials: The following are available online at <http://www.mdpi.com/2218-273X/10/12/1664/s1>, Table S1: Sample proportions used for the simulations. Figure S1: MSD extracted through Equation (2) from data taken on IN6 as function of temperature. Figure S2: Summed intensities (a) and MSD (b) extracted through Equation (2) from data taken on IN16 as function of temperature. Figure S3: Protein surface shown for the snapshot in Figure 10B. Figure S4: cPCA results presented as network view and with color-coded backbone mobility.

Author Contributions: Conceptualization, P.M., M.T.-L., F.N. and J.P.; Data curation, N.M.; Formal analysis, S.V.L., G.I. and N.M.; Funding acquisition, P.M., M.T.-L. and F.N.; Investigation, M.T.-L., F.N., M.M.K., T.S. and J.P.; Methodology, S.V.L. and J.P.; Project administration, J.P.; Software, S.V.L.; Supervision, J.P.; Writing—original draft, S.V.L. and J.P.; Writing—review & editing, J.P. All authors have read and agreed to the published version of the manuscript.

Funding: F.N and M.T. were funded by the French Ministry of Armed Forces (Direction générale de l'armement et Service de Santé des Armées) under grant BIOMDEF PDH-2-NRBC-3-C-301. P.M.'s contribution to the biochemical part was supported by the Russian Science Foundation grant # 20-14-00155.

Acknowledgments: The authors thank the ILL for attributing an internship financing to G.I. and for beamtime on the various instruments. Computer modeling was carried out using equipment from the shared research facilities of the HPC computing resources at Lomonosov Moscow State University [34]. We acknowledge the Joint Supercomputer Center of the Russian Academy of Sciences for provision of computational time.

Conflicts of Interest: The authors declare no conflict of interest.

References

1. Masson, P.; Lushchekina, S. Catalytic bioscavengers: The second generation of bioscavenger-based medical countermeasures. In *Handbook of Toxicology of Chemical Warfare Agents*; Gupta, R.C., Ed.; Academic Press: Cambridge, MA, USA, 2020; pp. 1199–1229.
2. Sussman, J.L.; Harel, M.; Frolow, F.; Oefner, C.; Goldman, A.; Toker, L.; Silman, I. Atomic structure of acetylcholinesterase from *Torpedo californica*: A prototypic acetylcholine-binding protein. *Science* **1991**, *253*, 872–879. [[CrossRef](#)] [[PubMed](#)]
3. Tai, K.; Shen, T.; Borjesson, U.; Philippopoulos, M.; McCammon, J.A. Analysis of a 10-ns molecular dynamics simulation of mouse acetylcholinesterase. *Biophys. J.* **2001**, *81*, 715–724. [[CrossRef](#)]
4. Tara, S.; Helms, V.; Straatsma, T.P.; McCammon, J.A. Molecular dynamics of mouse acetylcholinesterase complexed with huperzine A. *Biopolymers* **1999**, *50*, 347–359. [[CrossRef](#)]
5. Tara, S.; Straatsma, T.P.; McCammon, J.A. Mouse acetylcholinesterase unliganded and in complex with huperzine A: A comparison of molecular dynamics simulations. *Biopolymers* **1999**, *50*, 35–43. [[CrossRef](#)]
6. Shen, T.; Tai, K.; Henchman, R.H.; McCammon, J.A. Molecular dynamics of acetylcholinesterase. *ACC Chem. Res.* **2002**, *35*, 332–340. [[CrossRef](#)] [[PubMed](#)]
7. Xu, Y.; Shen, J.; Luo, X.; Silman, I.; Sussman, J.L.; Chen, K.; Jiang, H. How Does Huperzine A Enter and Leave the Binding Gorge of Acetylcholinesterase? Steered Molecular Dynamics Simulations. *J. Am. Chem. Soc.* **2003**, *125*, 11340–11349. [[CrossRef](#)]
8. Xu, Y.; Colletier, J.P.; Jiang, H.; Silman, I.; Sussman, J.L.; Weik, M. Induced-fit or preexisting equilibrium dynamics? Lessons from protein crystallography and MD simulations on acetylcholinesterase and implications for structure-based drug design. *Protein Sci.* **2008**, *17*, 601–605. [[CrossRef](#)]
9. Wei, M.J.; Zhou, J.; Lu, X.; Zhu, Y.; Liu, W.; Lu, L.; Zhang, L. Diffusion of water molecules confined in slits of rutile TiO₂(1 1 0) and graphite(0 0 1). *Fluid Phase Equilibria* **2011**, *302*, 316–320. [[CrossRef](#)]
10. Marion, J.; Trovaslet, M.; Martinez, N.; Masson, P.; Schweins, R.; Nachon, F.; Trapp, M.; Peters, J. Pressure-induced molten globule state of human acetylcholinesterase: Structural and dynamical changes monitored by neutron scattering. *Phys. Chem. Chem. Phys.* **2015**, *17*, 3157–3163. [[CrossRef](#)]
11. Timasheff, S.N. Thermodynamic binding and site occupancy in the light of the Schellman exchange concept. *Biophys. Chem.* **2002**, *101–102*, 99–111. [[CrossRef](#)]
12. Timasheff, S.N. Protein-solvent preferential interactions, protein hydration, and the modulation of biochemical reactions by solvent components. *Proc. Natl. Acad. Sci. USA* **2002**, *99*, 9721–9726. [[CrossRef](#)] [[PubMed](#)]
13. Masson, P.; Clery, C.; Guerra, P.; Redslob, A.; Albaret, C.; Fortier, P.L. Hydration change during the aging of phosphorylated human butyrylcholinesterase: Importance of residues aspartate-70 and glutamate-197 in the water network as probed by hydrostatic and osmotic pressures. *Biochem. J.* **1999**, *343*, 361–369. [[CrossRef](#)] [[PubMed](#)]
14. Peters, J.; Trovaslet, M.; Trapp, M.; Nachon, F.; Hill, F.; Royer, E.; Gabel, F.; van Eijck, L.; Masson, P.; Tehei, M. Activity and molecular dynamics relationship within the family of human cholinesterases. *Phys. Chem. Chem. Phys.* **2012**, *14*, 6764–6770. [[CrossRef](#)] [[PubMed](#)]
15. Ellman, G.L.; Courtney, K.D.; Andres, V., Jr.; Feather-Stone, R.M. A new and rapid colorimetric determination of acetylcholinesterase activity. *Biochem. Pharmacol.* **1961**, *7*, 88–95. [[CrossRef](#)]
16. Available online: <http://www.ill.eu/instruments-support/instruments-groups/instruments/in6/description/instrument-layout/> (accessed on 11 December 2020).
17. Natali, F.; Peters, J.; Russo, D.; Barbieri, S.; Chiapponi, C.; Cupane, A.; Deriu, A.; Di Bari, M.T.; Farhi, E.; Gerelli, Y.; et al. IN13 Backscattering Spectrometer at ILL: Looking for Motions in Biological Macromolecules and Organisms. *Neutron News* **2008**, *19*, 14–18. [[CrossRef](#)]
18. Frick, B.; Gonzalez, M. Five years operation of the second generation backscattering spectrometer IN16—a retrospective, recent developments and plans. *Phys. B Condens. Matter* **2001**, *301*, 8–19. [[CrossRef](#)]

19. Paalman, H.H.; Pings, C.J. Numerical Evaluation of X-Ray Absorption Factors for Cylindrical Samples and Annular Sample Cells. *J. Appl. Phys.* **1962**, *33*, 2635–2639. [[CrossRef](#)]
20. Richard, D.; Ferrand, M.; Kearley, G.J. Analysis and visualisation of neutron-scattering data. *J. Neutron Res.* **1996**, *4*, 33–39. [[CrossRef](#)]
21. Bée, M. *Quasielastic Neutron Scattering: Principles and Applications in Solid State Chemistry, Biology and Materials Science*; Adam Hilger: Philadelphia, PA, USA, 1988.
22. Aaboud, M.; Aad, G.; Abbott, B.; Abidinov, O.; Abeloos, B.; Abhayasinghe, D.K.; Abidi, S.H.; AbouZeid, O.S.; Abraham, N.L.; Abramowicz, H.; et al. Search for Resonant and Nonresonant Higgs Boson Pair Production in the $b\bar{b}[\text{over}]\tau^{+}\tau^{-}$ Decay Channel in pp Collisions at $\sqrt{s}=13$ TeV with the ATLAS Detector. *Phys. Rev. Lett.* **2018**, *121*, 191801. [[CrossRef](#)]
23. Singwi, K.S.; Sjölander, A. Diffusive Motions in Water and Cold Neutron Scattering. *Phys. Rev.* **1960**, *119*, 863–871. [[CrossRef](#)]
24. Volino, F.; Dianoux, A.J. Neutron Incoherent-Scattering Law for Diffusion in a Potential of Spherical-Symmetry—General Formalism and Application to Diffusion inside a Sphere. *Mol. Phys.* **1980**, *41*, 271–279. [[CrossRef](#)]
25. Bellissent-Funel, M.-C.; Teixeira, J.; Bradley, K.F.; Chen, S.H. Dynamics of hydration water in protein. *J. Phys. I Fr.* **1992**, *2*, 995–1001. [[CrossRef](#)]
26. Stadler, A.M.; Digel, I.; Embs, J.P.; Unruh, T.; Tehei, M.; Zaccai, G.; Buldt, G.; Artmann, G.M. From powder to solution: Hydration dependence of human hemoglobin dynamics correlated to body temperature. *Biophys. J.* **2009**, *96*, 5073–5081. [[CrossRef](#)] [[PubMed](#)]
27. Bourne, Y.; Taylor, P.; Radic, Z.; Marchot, P. Structural insights into ligand interactions at the acetylcholinesterase peripheral anionic site. *EMBO J.* **2003**, *22*, 1–12. [[CrossRef](#)]
28. Sali, A.; Potterton, L.; Yuan, F.; van Vlijmen, H.; Karplus, M. Evaluation of comparative protein modeling by MODELLER. *Proteins* **1995**, *23*, 318–326. [[CrossRef](#)]
29. Word, J.M.; Lovell, S.C.; Richardson, J.S.; Richardson, D.C. Asparagine and glutamine: Using hydrogen atom contacts in the choice of side-chain amide orientation. *J. Mol. Biol.* **1999**, *285*, 1735–1747. [[CrossRef](#)]
30. Pedretti, A.; Villa, L.; Vistoli, G. VEGA—An open platform to develop chemo-bio-informatics applications, using plug-in architecture and script programming. *J. Comput. Mol. Des.* **2004**, *18*, 167–173. [[CrossRef](#)]
31. Phillips, J.C.; Braun, R.; Wang, W.; Gumbart, J.; Tajkhorshid, E.; Villa, E.; Chipot, C.; Skeel, R.D.; Kale, L.; Schulten, K. Scalable molecular dynamics with NAMD. *J. Comput. Chem.* **2005**, *26*, 1781–1802. [[CrossRef](#)]
32. Best, R.B.; Zhu, X.; Shim, J.; Lopes, P.E.; Mittal, J.; Feig, M.; Mackerell, A.D., Jr. Optimization of the additive CHARMM all-atom protein force field targeting improved sampling of the backbone phi, psi and side-chain chi(1) and chi(2) dihedral angles. *J. Chem. Theory Comput.* **2012**, *8*, 3257–3273. [[CrossRef](#)]
33. Guvench, O.; Hatcher, E.R.; Venable, R.M.; Pastor, R.W.; Mackerell, A.D. CHARMM Additive All-Atom Force Field for Glycosidic Linkages between Hexopyranoses. *J. Chem. Theory Comput.* **2009**, *5*, 2353–2370. [[CrossRef](#)]
34. Voevodin, V.V.; Antonov, A.S.; Nikitenko, D.A.; Shvets, P.A.; Sobolev, S.I.; Sidorov, I.Y.; Stefanov, K.S.; Voevodin, V.V.; Zhumatyi, S.A. Supercomputer Lomonosov-2: Large Scale, Deep Monitoring and Fine Analytics for the User Community. *Supercomput. Front. Innov.* **2019**, *6*, 4–11.
35. Humphrey, W.; Dalke, A.; Schulten, K. VMD: Visual molecular dynamics. *J. Mol. Graph.* **1996**, *14*, 33–38. [[CrossRef](#)]
36. Bakan, A.; Meireles, L.M.; Bahar, I. ProDy: Protein dynamics inferred from theory and experiments. *Bioinformatics* **2011**, *27*, 1575–1577. [[CrossRef](#)] [[PubMed](#)]
37. Glykos, N.M. Software news and updates. Carma: A molecular dynamics analysis program. *J. Comput. Chem.* **2006**, *27*, 1765–1768. [[CrossRef](#)] [[PubMed](#)]
38. Zeller, D.; Telling, M.T.F.; Zamponi, M.; Garcia Sakai, V.; Peters, J. Analysis of elastic incoherent neutron scattering data beyond the Gaussian approximation. *J. Chem. Phys.* **2018**, *149*, 234908. [[CrossRef](#)]
39. Teixeira, J.; Bellissent-Funel, M.; Chen, S.H.; Dianoux, A.J. Experimental determination of the nature of diffusive motions of water molecules at low temperatures. *Phys. Rev. A Gen. Phys.* **1985**, *31*, 1913–1917. [[CrossRef](#)]
40. Grimaldo, M.; Roosen-Runge, F.; Jalarvo, N.; Zamponi, M.; Zanini, F.; Hennig, M.; Zhang, F.; Schreiber, F.; Seydel, T. High-resolution neutron spectroscopy on protein solution samples. *EPJ Web Conf.* **2015**, *83*, 02005. [[CrossRef](#)]

41. Murday, J.S.; Cotts, R.M. Self-Diffusion in Liquids: H₂O, D₂O, and Na. *J. Chem. Phys.* **1970**, *53*, 4724–4725. [[CrossRef](#)]
42. Masson, P.; Lushchekina, S.; Schopfer, L.M.; Lockridge, O. Effects of viscosity and osmotic stress on the reaction of human butyrylcholinesterase with cresyl saligenin phosphate, a toxicant related to aerotoxic syndrome: Kinetic and molecular dynamics studies. *Biochem. J.* **2013**, *454*, 387–399. [[CrossRef](#)]
43. Bourne, Y.; Renault, L.; Marchot, P. Crystal structure of snake venom acetylcholinesterase in complex with inhibitory antibody fragment Fab410 bound at the peripheral site: Evidence for open and closed states of a back door channel. *J. Biol. Chem.* **2015**, *290*, 1522–1535. [[CrossRef](#)]
44. Wiesner, J.; Kriz, Z.; Kuca, K.; Jun, D.; Koca, J. Influence of the acetylcholinesterase active site protonation on omega loop and active site dynamics. *J. Biomol. Struct. Dyn.* **2010**, *28*, 393–403. [[CrossRef](#)] [[PubMed](#)]
45. Cornicchi, E.; Marconi, M.; Onori, G.; Paciaroni, A. Controlling the protein dynamical transition with sugar-based bioprotectant matrices: A neutron scattering study. *Biophys. J.* **2006**, *91*, 289–297. [[CrossRef](#)] [[PubMed](#)]
46. Cornicchi, E.; Onori, G.; Paciaroni, A. Picosecond-Time-Scale Fluctuations of Proteins in Glassy Matrices: The Role of Viscosity. *Phys. Rev. Lett.* **2005**, *95*, 158101–158104. [[CrossRef](#)] [[PubMed](#)]
47. Paciaroni, A.; Cornicchi, E.; De Francesco, A.; Marconi, M.; Onori, G. Conditioning action of the environment on the protein dynamics studied through elastic neutron scattering. *Eur. Biophys. J. Biophys. Lett.* **2006**, *35*, 591–599. [[CrossRef](#)] [[PubMed](#)]
48. Jasnin, M.; Stadler, A.M.; Tehei, M.; Zaccai, G. Specific cellular water dynamics observed in vivo by neutron scattering and NMR. *Phys. Chem. Chem. Phys.* **2010**, *12*, 10154–10160. [[CrossRef](#)] [[PubMed](#)]
49. Levitsky, V.; Xie, W.; Froment, M.T.; Lockridge, O.; Masson, P. Polyol-induced activation by excess substrate of the D70G butyrylcholinesterase mutant. *Biochim. Biophys. Acta* **1999**, *1429*, 422–430. [[CrossRef](#)]
50. Cicerone, M.T.; Soles, C.L. Fast dynamics and stabilization of proteins: Binary glasses of trehalose and glycerol. *Biophys. J.* **2004**, *86*, 3836–3845. [[CrossRef](#)]
51. Curtis, J.E.; Dirama, T.E.; Carri, G.A.; Tobias, D.J. Inertial suppression of protein dynamics in a binary glycerol-trehalose glass. *J. Phys. Chem. B* **2006**, *110*, 22953–22956. [[CrossRef](#)]

Publisher’s Note: MDPI stays neutral with regard to jurisdictional claims in published maps and institutional affiliations.



© 2020 by the authors. Licensee MDPI, Basel, Switzerland. This article is an open access article distributed under the terms and conditions of the Creative Commons Attribution (CC BY) license (<http://creativecommons.org/licenses/by/4.0/>).

Article

1-(3-*Tert*-Butylphenyl)-2,2,2-Trifluoroethanone as a Potent Transition-State Analogue Slow-Binding Inhibitor of Human Acetylcholinesterase: Kinetic, MD and QM/MM Studies

Irina V. Zueva ¹, Sofya V. Lushchekina ² , Ian R. Pottie ^{3,4} , Sultan Darvesh ^{3,5}  and Patrick Masson ^{6,*}

¹ Arbuzov Institute of Organic and Physical Chemistry, Federal Research Center “Kazan Scientific Center of the Russian Academy of Sciences”, Arbuzov str., 8, 420088 Kazan, Russia; zueva.irina.vladimirovna@gmail.com

² Emanuel Institute of Biochemical Physics, Russian Academy of Sciences, Kosygin str. 4, 119334 Moscow, Russia; sofya.lushchekina@gmail.com

³ Department of Chemistry and Physics, Mount Saint Vincent University, Halifax, NS B3M 2J6, Canada; ian.pottie@msvu.ca (I.R.P.); sultan.darvesh@dal.ca (S.D.)

⁴ Department of Chemistry, Saint Mary’s University, Halifax, NS B3M 2J6, Canada

⁵ Department of Medicine (Neurology and Geriatric Medicine) & Medical Neuroscience, Dalhousie University, Halifax, NS B3H 4R2, Canada

⁶ Neuropharmacology Laboratory, Kazan Federal University, Kremlevskaya str. 18, 480002 Kazan, Russia

* Correspondence: pym.masson@free.fr

Received: 23 October 2020; Accepted: 24 November 2020; Published: 27 November 2020



Abstract: Kinetic studies and molecular modeling of human acetylcholinesterase (AChE) inhibition by a fluorinated acetophenone derivative, 1-(3-*tert*-butylphenyl)-2,2,2-trifluoroethanone (TFK), were performed. Fast reversible inhibition of AChE by TFK is of competitive type with $K_i = 5.15$ nM. However, steady state of inhibition is reached slowly. Kinetic analysis showed that TFK is a slow-binding inhibitor (SBI) of type B with $K_i^* = 0.53$ nM. Reversible binding of TFK provides a long residence time, $\tau = 20$ min, on AChE. After binding, TFK acylates the active serine, forming an hemiketal. Then, disruption of hemiketal (deacylation) is slow. AChE recovers full activity in approximately 40 min. Molecular docking and MD simulations depicted the different steps. It was shown that TFK binds first to the peripheral anionic site. Then, subsequent slow induced-fit step enlarged the gorge, allowing tight adjustment into the catalytic active site. Modeling of interactions between TFK and AChE active site by QM/MM showed that the “isomerization” step of enzyme-inhibitor complex leads to a complex similar to substrate tetrahedral intermediate, a so-called “transition state analog”, followed by a labile covalent intermediate. SBIs of AChE show prolonged pharmacological efficacy. Thus, this fluoroalkylketone intended for neuroimaging, could be of interest in palliative therapy of Alzheimer’s disease and protection of central AChE against organophosphorus compounds.

Keywords: acetylcholinesterase; slow-binding inhibition; transition state analog; organophosphorus

1. Introduction

Fluoroalkylketones (FAK) are potent inhibitors of acetyl cholinesterase (AChE, ES.3.1.1.7) and butyrylcholinesterase (BChE, EC.3.1.1.8) [1–4]. A characteristic of inhibition by these compounds is the slow establishment of equilibrium between enzyme and inhibitor. This process is called slow-binding inhibition (SBI). Unlike classical reversible inhibitors for which equilibrium establishes

within microseconds, in SBI, establishment of equilibrium may take seconds, minutes or hours. Three types of SBI have been described: (1) type A is characterized by a single step mechanism with slow k_{on} and k_{off} ; (2) type B is a two-step mechanism: after rapid formation of a first enzyme-inhibitor complex, a slow induced-fit step occurs; (3) type C results from the existence of several enzyme forms in slow equilibrium that determine a slow conformational selection for inhibition [5].

Kinetic analysis of AChE inhibition by 1-[3-(trimethylamino)phenyl]-2,2,2-trifluoro-1-ethanone (TMTFA) (Figure 1A) showed that this compound is a slow-binding inhibitor of type A for *Torpedo californica* AChE ($K_i = 15 \times 10^{-15}$ M; $t_{1/2}^{diss} = 2.8$ h) [3] whereas it is a slow-binding inhibitor of type B for electric eel (*Electrophorus electricus*) AChE ($K_i = 1.3 \times 10^{-15}$ M; $t_{1/2}^{diss} = 19$ h) [3,4]. Later, the X-ray structure of *Torpedo californica* AChE-TMTFA complex (PDB ID 1AMN [6]) showed that the tight interactions between the enzyme and inhibitor are similar to interactions that take place in the enzyme active center with acetylcholine in the transition state [6]. Thus, FAK, first considered as quasi-substrate inhibitors, are in fact transition state analogues.

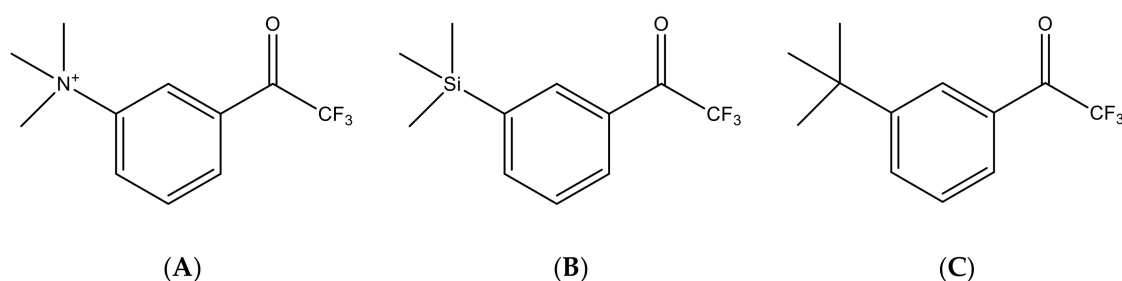


Figure 1. Chemical structure of related trifluoromethylketone molecules: (A): 1-[3-(trimethylamino)phenyl]-2,2,2-trifluoro-1-ethanone (TMTFA); (B): 2,2,2-trifluoro-1-[*m*-(trimethylsilyl)phenyl]-1-ethanone (Zifrosilone); (C): 1-(3-*tert*-butylphenyl)-2,2,2-trifluoroethanone (TFK).

In early 1990s, when AChE inhibitors started to be developed for the palliative treatment of Alzheimer disease (AD), a related silyl compound, Zifrosilone (Figure 1B) [7] was considered as a promising anti-AD symptomatic drug. Though pharmacokinetic/pharmacodynamic (PK/PD) studies were advanced, human clinical trials were discontinued in mid-90s [8–10]. Yet, incorporation of a silicone atom does not induce additional toxicity to molecules of pharmacological interest [11]. After a first report on inhibition of human cholinesterases (hChEs) by a family of ¹⁸F-acetophenones developed for PET neuroimaging [12], it was of interest to investigate thoroughly the carbon analogue of Zifrosilone (Figure 1B), 1-(3-*tert*-butylphenyl)-2,2,2-trifluoroethanone (TFK) (Figure 1C), to describe the mechanism of inhibition of hAChE by kinetics and molecular modeling approaches. Moreover, possible modulation and/or protection of AChE by TFK against OP phosphorylation was explored.

2. Materials and Methods

2.1. Chemicals

TFK was synthesized as described in [12]. Solution of TFK (0.1 M) was made in acetonitrile. Echothiophate iodide was from Biobasal AG (Basel, Switzerland). Stock solution of echothiophate (0.1 M) was made in water. Paraoxon was purchased from Sigma-Aldrich (Saint Louis, MO, USA). Stock solution of paraoxon (0.1 M) was made in EtOH. Cresylsaligenyl phosphate (CSP) was a gift from Prof O. Lockridge (UNMC, Omaha, NE, USA). Solution of CSP (0.1 M) was made in acetonitrile. Acetylthiocholine iodide was from Sigma-Aldrich (Saint Louis, MO, USA). Stock solution of ATC (0.1 M) was made in water. Stock solutions of substrate and inhibitors were stored at -20 °C.

Dithiobisnitrobenzoic acid (DTNB) was from Sigma-Aldrich (Saint Louis, MO, USA). 50 mM solution of DTNB was prepared as described in Ellman [13]. Calbiochem Probe IV (3-(7-Hydroxy-2-oxo-2H-chromen-3-ylcarbonyl) acrylic acid methylester) was from Merck Millipore (Darmstadt, Germany).

Stock solution of Probe IV (1 mM) was in DMSO and stored at $-20\text{ }^{\circ}\text{C}$. All other chemicals were of biochemical grade.

2.2. Enzymes

Recombinant human AChE monomer (MW = 70,000 Da) was expressed in CHO-K1 (Chinese-hamster ovary, ATCC) cells [14]. AChE purification was carried out as described [15]. The enzyme was concentrated to 14.7 mg/mL using a Vivaspin 6 (30,000 MW cutoff, Sartorius) and dialyzed at $4\text{ }^{\circ}\text{C}$ against 10 mM HEPES pH 7.5 buffer containing 10 mM NaCl. The active site concentration of AChE was determined by the method of residual activity according to Leuzinger [16], using echothiophate, as titrating agent. The residual activity after complete phosphorylation by each concentration of echothiophate was measured by the Ellman's method [13] in 0.1 M sodium phosphate, pH 8.0 at $25\text{ }^{\circ}\text{C}$ with 1 mM ATC as the substrate. The active site concentration of the pure rhuAChE monomer was $2.1 \times 10^{-4}\text{ M}$. The working enzyme was diluted 20,000 times in 0.1 M phosphate buffer containing 1 mg/mL BSA ($[E]_w = 1 \times 10^{-8}\text{ M}$).

2.3. Kinetic Study of Inhibition

Kinetic studies of human recombinant AChE inhibition by TFK were performed in 0.1 M sodium phosphate buffer pH 8.0 at $25\text{ }^{\circ}\text{C}$, using the Ellman's method [13] with acetylthiocholine (ATC) as the substrate. Three different concentrations of ATC were used (0.1, 0.5 and 1 mM): Assays were initiated by addition of the enzyme. The final enzyme concentration, E , was $1 \times 10^{-10}\text{ M}$.

After rapid mixing of solutions, absorbance change 412 nm was recorded for 60 min using a spectrophotometer PerkinElmer $\lambda 25$ with photodiode detector (PerkinElmer Inc., Waltham, MA, USA). The inhibition process was characterized by a slow onset before reaching steady state. This process is described by Equation (1):

$$[P]_t = v_{ss}t + \frac{(v_i - v_{ss})(1 - \exp(-k_{obs}t))}{k_{obs}} \quad (1)$$

where v_i is the initial velocity, v_{ss} the steady-state velocity and k_{obs} , the first-order rate constant associated with establishment of the steady state. The reciprocal of k_{obs} is the lag time before steady state. This is characteristic of slow binding inhibition [17–19].

The initial reversible inhibition step was analyzed from the tangents of progress curves. The general case for linear reversible inhibition is described by following rate Equation (2):

$$v_i = \frac{V_{max}[S]}{K_m[1 + ([I]/K_{ci})] + [S](1 + ([I]/K_{ui}))} \quad (2)$$

where V_{max} is the maximum velocity, $[S]$ the substrate concentration, K_m the Michaelis-Menten constant, $[I]$, the inhibitor concentration, K_{ci} , the competitive inhibition constant, and K_{ui} , the uncompetitive inhibition constant. Rearranging Equation (2) as $1/v_i$ or $[S]/v_i$ as a function of $[I]$ provides two complementary plots as described by Cornish-Bowden [20]. In the limiting case of competitive inhibition, $K_{ui} \rightarrow \infty$, while for uncompetitive inhibition, $K_{ci} \rightarrow \infty$. Non-competitive inhibition gives $K_{ci} = K_{ui}$ and mixed-type inhibition gives $K_{ci} \neq K_{ui}$. Therefore, inhibition constant and type of reversible inhibition of the fast step were determined according to the graphical methods of Cornish-Bowden [20] by building Dixon plots ($1/v_i$ vs. [TFK]) and Cornish-Bowden plots ($[ATC]/v_i$ vs. [TFK]) at 3 different ATC concentrations $[S] = 0.1; 0.5$ and 1 mM .

Diagnosis of type of SBI and binding kinetic parameters and inhibition constant corresponding to final reversible step were determined from secondary plots, k_{obs} vs. [TFK] at 3 different ATC concentration [5].

For the study of transient enzyme acylation by $2 \times 10^{-8}\text{ M}$ TFK and slow reactivation, the enzyme activity was monitored by the Ellman assay [13]. However, for analyzing slow reactivation after 10- and 1000-fold dilution of the system, because the enzyme concentration became very low

(10^{-10} and 10^{-12} M), the recovery of activity was monitored at 25 °C under the same buffer conditions by high sensitivity spectrofluorimetric assay, using the Calbiochem thiol Probe IV [21] instead of DTNB. The Calbiochem probe IV is a coumarinyl derivative that reacts with thiol-chemicals to form a highly fluorescent conjugate. It was found to be the fastest and the most sensitive thiol reagent. Assay of ChEs using this thiol reagent instead of DTNB is more than 2 orders more sensitive than the classical Ellman assay, allowing measurement of activity in media containing $<10^{-11}$ M ChE. Kinetic and molecular modeling studies showed that Probe IV does not interfere with activity measurements so that ATC-based assays using DTNB and Probe IV are correlated. The experimental conditions of assay in a Peltier thermostated spectrofluorimeter F-7100 (Hitachi Ltd., Tokyo, Japan) were previously described [21,22].

2.4. Modulation of AChE Phosphorylation Following Enzyme Preincubation in the Presence of TFK

Two OPs were selected, CSP and paraoxon. Inhibition of hAChE by CSP (0.21 μ M) was performed in 0.1 M phosphate buffer, pH 8.0 after different pre-incubation times ranging from 5 to 120 min in the presence of various concentrations of TFK (0.1–10 nM). We investigated the effect of pre-incubation by TFK (1–10 nM) on inhibition of huAChE by 50 nM paraoxon under the same conditions.

2.5. Molecular Modeling

2.5.1. Molecular Docking

Molecular docking was performed using as targets several structures of hAChE co-crystallized with different non-covalent inhibitors (PDB ID 4EY4-4EY8 [15]) and one covalently bound to an organophosphorus adduct (human AChE phosphorylated by sarin, PDB ID 5FPQ, [23]). These structures are missing peripheral loop fragments 259–264 and 495–497. These were inserted from another hAChE X-ray structure (PDB ID 4BDT [24]). Inhibitors, ions and water molecules were removed prior docking. Hydrogen atoms were added with respect of hydrogen bonding network by Reduce software [25]. Molecular docking with a Lamarckian Genetic Algorithm (LGA) [26], was performed with Autodock 4.2.6 [27] software. Grid box for docking of 30 Å \times 30 Å \times 30 Å included the whole gorge from the mouth to the active site, including PAS. In spite of low number of torsion degrees of freedom of the inhibitor, number of docking runs was increased to analyze cauterization (2 Å tolerance). The main of selected LGA parameters were as follows: 2000 runs, 25×10^6 evaluations, 27×10^4 generations and population size 300.

2.5.2. Molecular Dynamics

For the preparation of the model systems and further analysis of MD trajectories, VMD software [28] was used.

Ligand parameterization: For TFK and TMTFA molecules parameters were taken from Charmm General Force Field [29] through CGenFF interface (<https://cgenff.umaryland.edu/>), missing parameters were adjusted with the help of *ffTK* plugin of VMD [30,31].

System setup: For MD simulations, complexes of hAChE with the inhibitors (TFK and TMTFA) obtained from molecular docking (X-ray structure PDB ID 4EY7 as a target, binding pose with inhibitors in the active site) were chosen. TIP3P water box was added with boundaries in at least 10 Å from protein and ligand atoms. Sodium and chloride ions were added to final concentration of 0.15 M. Final size of both systems was 67,804 atoms, 84.6 Å \times 85.8 Å \times 95.4 Å.

For all MD simulations, NAMD 2.11 software [32] with CHARMM36 force field [33] was used in NPT ensemble (298 K, 1 atm) with periodical boundary conditions. MD simulations were run at the Lomonosov Moscow State University supercomputer [34].

For pre-optimization, coordinates of all atoms present in X-ray structure were fixed. Positions of all added atoms were minimized in 5000 steps and subjected 5 ns MD simulation to optimize water box

and added loops. Then, all atoms were minimized in 5000 steps. This structure was used as reference and starting point for targeted molecular dynamics (TMD) and QM/MM calculations.

To create starting points for umbrella-sampling free energy calculations, pathways of pulling the inhibitors inside hAChE active site gorge and outside the protein, were obtained by means of targeted molecular dynamics with initial structure as a reference (see Supplementary Materials for details).

Umbrella sampling (US): Pathways obtained by TMD were divided into 240 windows separated by 0.25 Å. State in each window was sampled during 1 ns simulations with harmonic restraining force 50 kcal/mol·Å², with RMSD of trifluoroacetophenone part of the inhibitors as a collective variable. These parameters were adjusted in series of test runs and provided good overlapping of histograms. To construct PMF weighted histogram analysis method (WHAM) [35,36] in A. Grossfield implementation, v. 2.0.9 (<http://membrane.urmc.rochester.edu/content/wham>) was used.

Replica exchange molecular dynamics (REMD-US): To ensure better sampling, after analysis of PMF obtained by US, 168 of US windows were used as initial coordinates of REMD-US replicas [37,38] with the same other parameters. All replicas were simulated concurrently having Hamiltonians with different biasing potentials. Every 100 steps replicas of the system underwent exchange performed using the Metropolis Monte Carlo criterion. Simulations were performed until full convergence during 10 ns for each replica.

2.5.3. QM/MM Calculations

Initial systems of hAChE-TFK/TMTFA complexes were taken after MD optimization. First solvation shell (water molecules within 2 Å from the protein) was kept. QM/MM calculations were performed with the NwChem 6.6 software [39]. The density functional theory approach with Grimme empirical dispersion correction [40] PBE0-D3/cc-pvdz was used in QM part. The MM subsystem was modeled with the AMBER force field [41]. Quantum sub-system includes the whole inhibitor molecule and active site residues: the catalytic triad Ser203, His447, Glu334; oxyanion hole Gly121, Gly122, Ala204; other principal residues forming hydrogen-bonding network around the catalytic residues, Glu202, Ser229, Glu450 and three water molecules between them, 129 atoms total, including link atoms. Total size of the system was ~11,500 atoms. For the reactivation process, distance between the inhibitor carbonyl atom and Ser203 O^γ atoms was increased using harmonic constraints. Unconstrained optimization was performed for obtained reactivation pathway points.

3. Results and Discussion

3.1. Slow-Binding Inhibition Kinetics of rhAChE by TFK

Inhibition kinetics of hAChE by TFK ranging from 0.1 to 50 nM was recorded for 60 min in the presence of ATC (0.1, 0.5 and 1 mM). Kinetic analysis of inhibition progress curves showed that there is a slow onset of inhibition before reaching the equilibrium in less than 4 min (Figure 2). This is in agreement with what was previously reported [12]. The steady state was established in less than 35 min. The dependence of the first order rate constant (k_{obs}), the reciprocal of the lag time, of the pre-steady state phase on TFK concentration was analyzed according to the formalism of slow binding inhibition (SBI) [5].

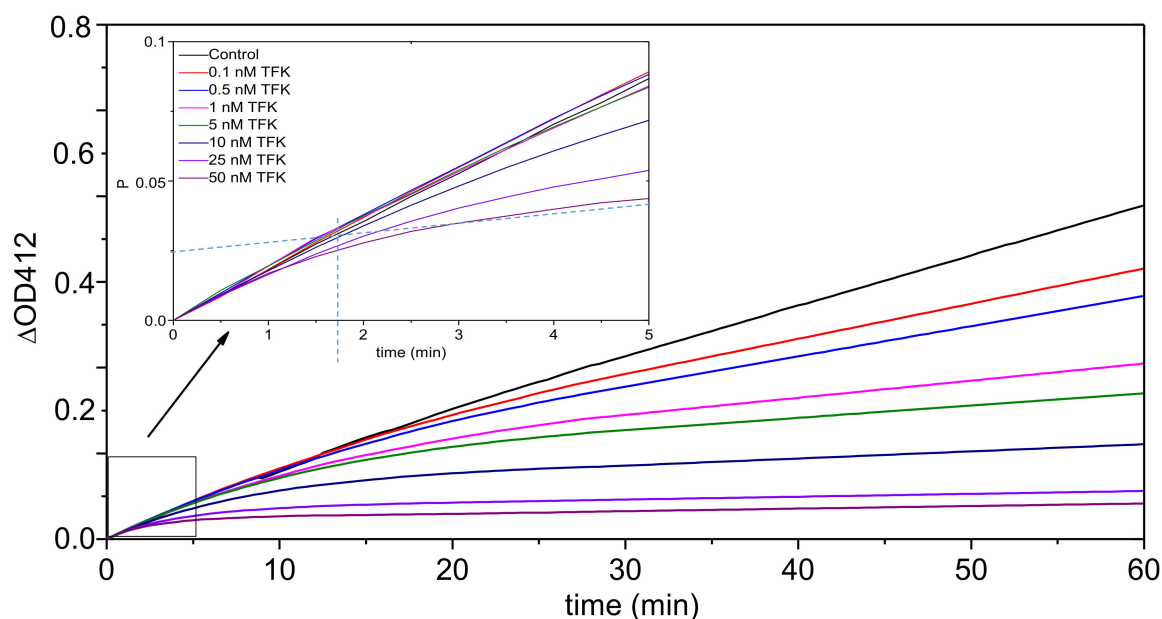


Figure 2. Typical progress curves (without treatment for smoothing noise) for slow-binding inhibition of AChE by TFK. $[E] = 0.08 \text{ nM}$, $[ATC] = 0.1 \text{ mM}$ and $[TFK]$ ranged from 0.1 to 50 nM. ΔOD_{412} is the concentration of ATC hydrolysis product (in Equation (1), $[P] = \text{thiocholine} = \text{thionitrobenzoate}$), expressed as the absorbance increase at 412 nm. The reciprocal of k_{obs} is the lag time (vertical dotted line at $t = 1.75 \text{ min}$ for 50 nM TFK) before steady state. Progress curves fit to Equation (1).

Initial fast inhibition type and inhibition constant ($K_i = k_{-3}/k_{+3}$) for the first binding step (formation of EI) were determined from tangents to progress curves k_{obs} vs. time (Figure 2), Dixon and Cornish-Bowden plots (Figure 3). Three different concentrations of ATC were used (0.1; 0.5 and 1 mM). Panels A and B in Figure 3 provide evidence that fast reversible inhibition step is competitive (Dixon plots are intersecting at $-[TFK] = K_{ci}$ and Cornish-Bowden plots are parallel) with $K_{ci} = K_i = 5.15 \pm 0.36 \text{ nM}$.

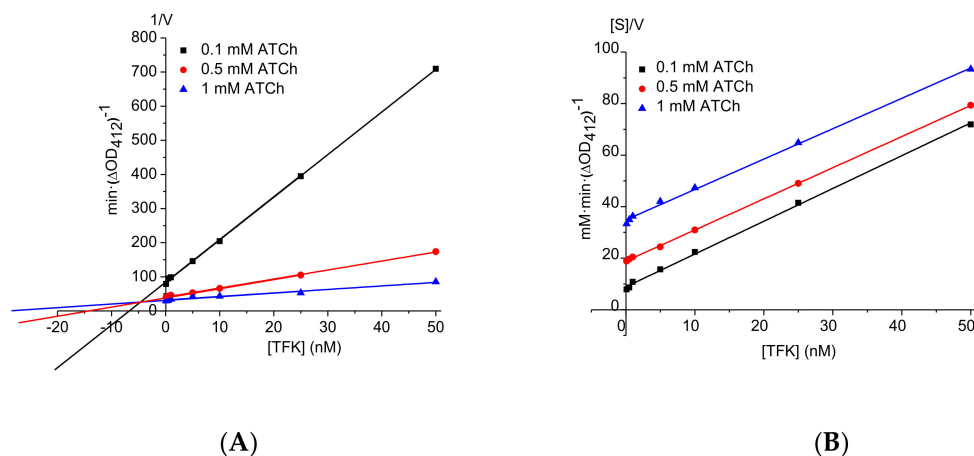


Figure 3. Dixon plot (A) and Cornish-Bowden plot (B) for determination of fast reversible inhibition constant.

The plots of k_{obs} vs. $[TFK]$ were built for each ATC concentration (Figure 4). This diagnosis plot established the type of SBI.

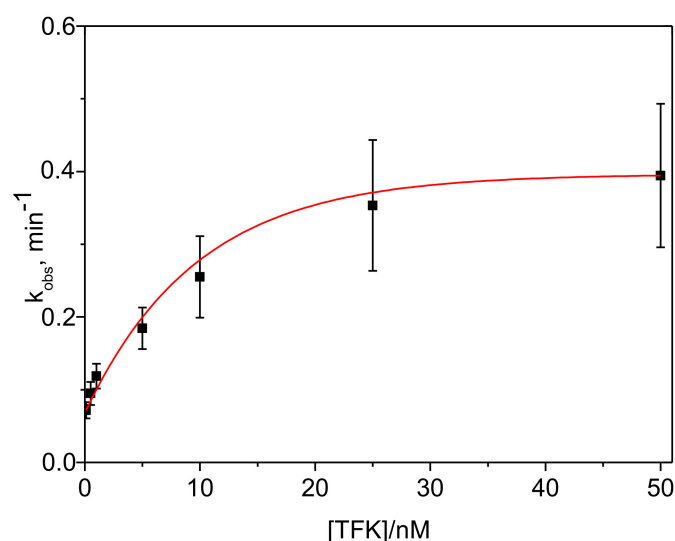


Figure 4. Typical dependence of k_{obs} as a function of TFK concentration for inhibition in the presence of 0.1 mM ATC. The k_{obs} values were determined from nonlinear fitting of progress curves in Figure 2 at three substrate concentrations. Data were fitted to Equation (3): ordinate is k_{-4} and asymptote is $k_{-4} + k_{+4}$ in Scheme of Figure 5.

Plots of k_{obs} vs. [TFK] are upward hyperboles (Figure 4). This is characteristic of SBI of type B (Figure 5). Equation (3) describes the dependence of k_{obs} on inhibitor concentration, [I], in SBI of type B.

$$k_{obs} = k_{-4} + \frac{k_{+4}[I]}{K_I(1 + [S]/K_M) + [I]} \quad (3)$$

Accordingly, after rapid formation of a first complex EI, characterized by an inhibition constant K_i , the enzyme undergoes a slow «isomerization», leading to a second complex EI* characterized by a stronger ligand binding affinity ($K_i^* < K_i$).

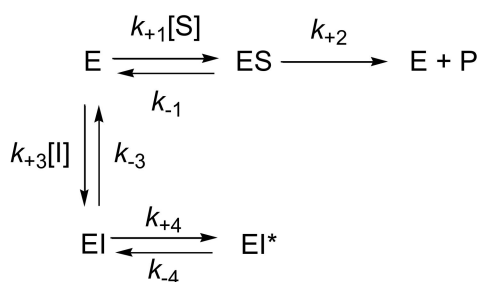


Figure 5. Slow-binding inhibition model of type B.

The binding kinetic parameters were determined from non-linear curve fitting of secondary plots k_{obs} vs. [TFK] (Figure 4) obtained for inhibition in the presence of 0.1, 0.5 and 1 mM ATC. In Figure 4 the ordinate intercept is k_{-4} and the asymptote is $k_{-4} + k_{+4}$. The constants k_{-4} and k_{+4} were found to be independent on ATC concentration, as expected for SBI of type B. Thus, their averages values are $k_{-4} = 0.054 \pm 0.006 \text{ min}^{-1}$ and $k_{+4} = 0.456 \pm 0.095 \text{ min}^{-1}$. Then, the inhibition constant corresponding to formation of EI*, $K_i^* = 0.53 \text{ nM}$, was determined as follows: $K_i^* = K_i k_{-4} / (k_{-4} + k_{+4}) = 0.53 \pm 0.07 \text{ nM}$. This value is in agreement with values previously determined by two different methods (0.4 and 0.56 nM) in the presence of 5 mM ATC in 0.1 phosphate buffer pH 7.4 after 70 min incubation at 23 °C [12].

Other important binding kinetic parameters are the residence time on AChE (the reciprocal of the overall k_{off} rate constant, $\tau = 1/k_{off}$) and the fractional occupancy of AChE (FO_t) [42]. These parameters were derived from elementary kinetic constants (Equations (4) and (5)):

$$\tau = \frac{(k_{-3} + k_{+4} + k_{-4})}{k_{-3}k_{-4}} \quad (4)$$

$$FO_t = \frac{[I]_t}{[I]_t + (k_{-3}/(k_{+3} + (k_{+3}k_{+4})/k_{-4}))} \quad (5)$$

However, as seen in Equations (4) and (5), estimation of τ and FO_t implies knowledge of k_{-3} , and k_{on} , the second-order rate constant for the initial binding step to hAChE. This constant is not known for TFK in hAChE. However, apparent values of k_{on} of several trifluoroketones for binding to different AChE were reported. These constants were determined assuming a single binding step process. For binding of neutral aliphatic trifluoroketones to electric eel AChE, $k_{on} = 1\text{--}5 \times 10^9 \text{ M}^{-1} \text{ min}^{-1}$ [2]. For binding of TFK to mouse AChE, k_{on} was similar, $3 \times 10^9 \text{ M}^{-1} \text{ min}^{-1}$ [43]. On the other hand, for the charged counterpart of TFK, TMTFA (Figure 1), an SBI of type A (a single slow step corresponding to formation of EI), k_{on} is slower, $6 \times 10^6 \text{ M}^{-1} \text{ min}^{-1}$ for electric eel AChE [3], while for the neutral silylated homologue, Zifrosilone (Figure 1), $k_{on} = 6 \times 10^6 \text{ M}^{-1} \text{ min}^{-1}$ for electric eel AChE [7]. The k_{on} values for binding of neutral trifluoroketones, are of the order of the values reported for binding of small drugs to biological targets, 6×10^7 to $6 \times 10^9 \text{ M}^{-1} \text{ min}^{-1}$ [44]. Thus, it may be assumed that the second order association rate constant of TFK in hAChE (k_{+3}) is close to the k_{on} value for mouse AChE. Thus, taking $k_{+3} \approx 3 \times 10^9 \text{ M}^{-1} \text{ min}^{-1}$, with $\langle K_i \rangle = 5.15 \text{ nM}$, it follows that $k_{-3} \approx 15.45 \text{ min}^{-1}$. This leads to an overall $k_{off} \approx 0.052 \text{ min}^{-1}$ and $\tau = 19 \pm 2 \text{ min}$. The half-time for dissociation of reversibly bound TFK is $t_{1/2} = \ln 2/k_{off} \approx 13 \text{ min}$. The silylated homologue displays a much longer residence time of about 70 h for rat brain AChE, although its affinity is close to that of TFK ($K_i = 0.26 \text{ nM}$) [7].

Because both the concentration of drug in the target compartment and the residence time on physiological target as a function of time, determine the duration of action of a drug in the body, the pharmacological efficacy of a drug depends on the fractional occupancy of the enzyme as a function of time (FO_t) [42,44]. Then, FO_t depends on both the pharmacokinetic profile of considered drug, i.e., its concentration in the central compartment (the blood circulation) as a function of time, and the binding kinetic parameters on target(s). FO_t change with time is therefore a useful theoretical parameter for estimating the potential pharmacological interest of drugs with long residence times on the target. For TFK, as a SBI of type B, FO_t , for different $[I]_t$ can be calculated from Equation (5). Assuming that the initial concentration of TFK in blood is $4.3 \mu\text{M}$ at time 0 (e.g., after intravenous injection to mice of a dose of 1 mg/kg), it follows that $FO_{t_0} = 99.9\%$. After a certain time (t') when concentration in blood has dropped to 4.3 nM , $FO_{t_0} = 88.7\%$. If after time t'' , the concentration has decreased by another order of magnitude (4.3 pM), then $FO_{t_0} = 7.3\%$. Thus, it is clear that with a residence time on AChE of about 20 min, the potential pharmacological efficacy of TFK could be maintained at a high level even though the drug concentration in blood has decreased to a very low value.

3.2. Transient Acylation of AChE by TFK and Subsequent Enzyme Reactivation

Binding of a transition state analogue, like acetophenone, to ChEs, the formation of a transient hemiketal conjugate mimicking the acetyl tetrahedral intermediate was observed or hypothesized in some cases [6,43]. Thus experiments were performed to study enzyme spontaneous reactivation.

The reaction process was performed under pseudo-first order conditions to reach complete inhibition of enzyme by $2 \times 10^{-8} \text{ M}$ TFK. Then, the enzyme activity was monitored up to 180 min, far beyond establishment of reversible steady-state equilibrium. During this second step, the recovery of enzyme activity was monitored without dilution or after dilution in order to drop TFK concentration in the medium. As seen in Figure 6 red curve, after formation of the second reversible complex EI^* , the enzyme activity progressively started to increase. This suggested, that after formation

of EI* the enzyme was transiently acylated, and then slowly deacylated. However, during the putative deacylation process, the enzyme could have been re-inhibited by the excess of TFK present in the medium. Thus, after 20 min inhibition, the system was diluted 10- and 1000-fold to drop TFK concentration, and the enzyme activity was monitored as a function of time. Because after dilution, the enzyme activity became very low for accurate monitoring of activity vs. time, instead of the classical Ellman assay, the activity was monitored using a new method with the fluorescent thiol probe (Calbiochem Probe IV) instead of DTNB [21,22]. Results showed that dilution of TFK speeded up the deacylation process (blue and green curves in Figure 6, showing faster recovery of enzyme activity). In the presence of non-inhibitory TFK concentration (2×10^{-11} M), enzyme reactivation was completed in 40 min with $k_{react} \approx 0.05 \text{ min}^{-1}$; $t_{1/2} \approx 14 \text{ min}$ (Figure 6, green curve) instead of more than 3 h in the presence of 2×10^{-8} M TFK (Figure 6, red curve).

The slow enzyme reactivation process was interpreted as spontaneous slow deacylation of bound TFK from AChE active center. Molecular modeling (see next section) confirmed the occurrence of transient acylation of AChE active site serine after TFK binding and shed light on molecular interactions involved in these acylation and deacylation steps. Then, considering that the residence time (τ) on AChE calculated from reversible SBI is 20 min, the subsequent acylation and deacylation processes provide an overall residence time of about 60 min.

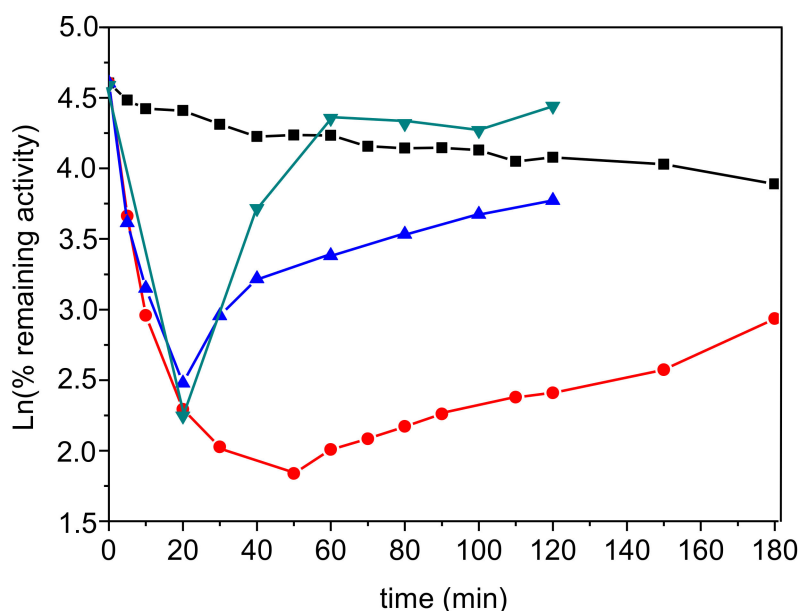


Figure 6. SBI and subsequent acylation of 2×10^{-9} M AChE by 2×10^{-8} M TFK, followed by slow deacylation. Activity was assayed with 1 mM ATC with DTNB as the thiol probe (black, blue, red curves) and with Probe IV as the thiol probe (green curve). The black curve is enzyme activity (control) in the presence of 2% acetonitrile; the red curve is enzyme activity monitored up to 180 min in the presence of 2×10^{-8} M TFK. Blue curve: after steady-state SBI, the system was diluted 10 times, so that TFK dropped to 2×10^{-9} M after $t = 20$ min. Green curve: after steady-state SBI, the system was diluted 1000 times, then TFK final concentration dropped to 2×10^{-11} M after $t = 20$ min. The first-order rate constant of deacylation (k_{reac}) was estimated from the slope of Ln increase in activity vs. time.

The slow recovery of enzyme activity depends on the TFK concentration present in the medium. In the presence of remaining 0.02 nM TFK (green curve), it takes less than 40 min to regain an activity similar to that of control enzyme at $t = 60$ min.

3.3. Molecular Modeling of Interaction between TFK and AChE

Molecular modeling was used to depict in terms of molecular events the different steps of TFK interactions with huAChE. Preliminary results about interaction between TFK and AChE were recently reported [45].

In majority of docking results, TFK was found in the peripheral anionic site (PAS) or bottleneck area (Figure S1). The dominating poses (red clusters in Figure S1) were stabilized by C-Hal ... π interactions of $-CF_3$ group with Trp286 ring (Figure S2A). In another pose within cluster making up the red structures, the trifluoro moiety produces hydrogen bonds with the peptide backbone of Phe295, Arg296 (Figure S2B) in a way, similar to interactions in the oxyanion hole. In the next less populated clusters (orange and yellow structures) there were other poses with the same binding pattern (Figure S2C), showing interactions with Ser293 peptide backbone and possible hydrogen bond between the trifluoro moiety and side chain hydroxyl group (Figure S2D). In general in PAS, trifluoroketo-group interacts with the acyl-binding loop as with a huge oxyanion hole, trapping it near entrance to the gorge. Among complexes of AChEs with inhibitors, containing a trifluoro moiety, the majority of them are structures of non-hydrolysable substrate analogues covalently bound to the catalytic serine, and will be discussed below. However, one X-ray structure shows a non-covalent inhibitor, N-(2-diethylamino-ethyl)-3-trifluoromethyl-benzenesulfonamide (PDB ID: 4B84, [46]) with the trifluoro moiety bound in the PAS in the similar fashion (Figure S3), oriented by interactions with acyl-loop main chain NH group.

Binding poses of TFK suitable for covalent interactions with the catalytic triad were found only for X-ray structures PDB ID: 4EY7 and PDB ID: 5FPQ as targets in minor clusters. 4EY7 co-crystallized with donepezil has a wider gorge than the other X-ray structures due to rotation of Tyr337. In many cases this allows to better accommodate bulky inhibitors [47]. In this case, rotation of the catalytic serine side chain, forming hydrogen bond with Glu202, not His447 as usual, gives space for TFK to enter in the active site. Though this is not enough, carbonyl oxygen atom is slightly displaced from the oxyanion hole in these cases, indicating that Trp86 side chain has to move a bit for better fit. Following QM/MM optimization provided necessary expansion of the active site and full accommodation of the inhibitor. X-ray structure 5FPQ is the non-aged covalent conjugate of AChE with sarin. The methyl isopropoxy phosphonyl adduct expands the active site. In particular, Trp86 side chain is moved a bit (Figure S4). These displacements provide enough space for TFK, though between two possible poses, one has *tert*-butyl moiety outside cation-binding site Trp86 and Glu202 (Figure S5A, PDB ID: 4EY7 as a target), and in the other pose, the phenyl ring is out of plane of the trifluoroketo-group (Figure S5B, PDB ID: 5FPQ as a target).

The TFK pose at the bottom of the gorge but outside the active site (Figure S5C) is interesting. Indeed, such a pose was observed only in docking with X-ray structure PDB ID: 4EY8 (complex between AChE and Fasciculin-2) as a target. This provides an additional evidence for Fasciculin-induced conformational changes of AChE, widely discussed previously [48,49].

Generalizing docking results, 3 major binding poses can be outlined: in the PAS, at the area of bottleneck and in the active site (Figure 7A). For comparison, docking results for TMTEFA were less diverse, and binding at the area of bottleneck was dominating, while binding to the PAS was negligible. Binding to the active site is similar to TFK, with the trimethyl ammonium group slightly closer to Glu202 due to electrostatic attraction (Figure 7B).

Potential of mean force (PMF) profiles for binding of TFK and TMTEFA to hAChE calculated using REMD-US method are in agreement with docking results (Figure 7C). For TFK, two close minima at level 9 and 12 Å, corresponding to binding in the PAS and bottleneck are seen, while for TMTEFA only one global minimum at level 9 Å, corresponding to binding in the area of the bottleneck was observed. Transition from these favorable positions in the middle of the gorge to the active site is associated with energy barriers. For TMTEFA of 15 kcal/mol, and for TFK it is much higher, more than 20 kcal/mol.

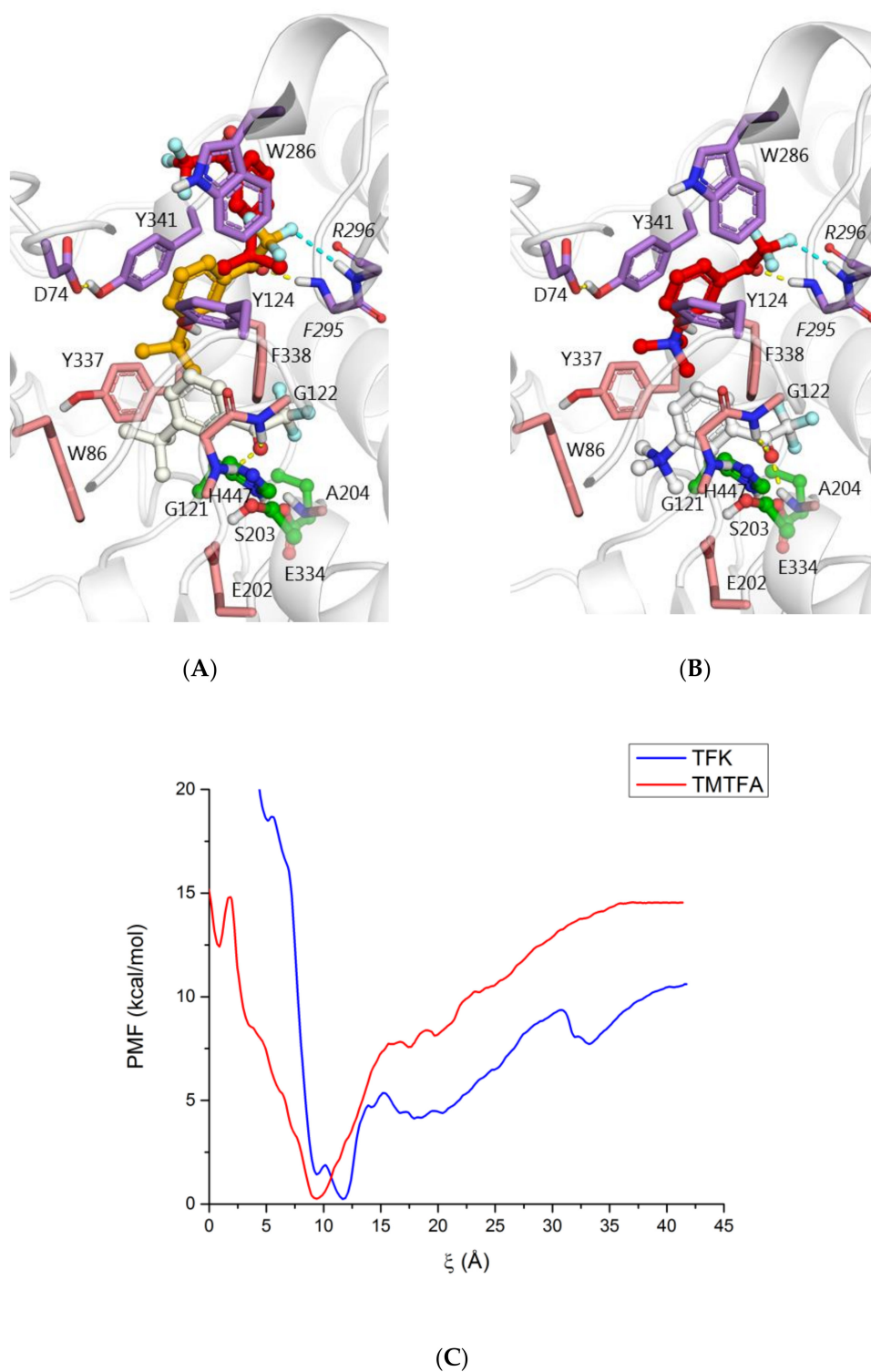


Figure 7. Binding of TFK to AChE: (A) main docked poses in the gorge: in the PAS (most populated cluster, carbon atoms colored red), at the gorge rim partly blocking the bottleneck (carbon atoms orange), and in the active site ready to react with the catalytic serine (least populated cluster, carbon atoms are colored white) compared to the main binding poses of TMTFA (B). Docking results with X-ray structure PDB ID: 4EY7 as a target are shown. (C) Free energy (PMF) profile of the binding process calculated with REMD-US method. Process coordinate ξ is the distance between the TFK/TMTFA trifluoroketone group and the active site, oxyanion hole and catalytic serine hydroxyl-group.

In addition to the two distinctive positions inside the gorge, PMF for TFK allows to assume non-specific interactions on the protein surface (local minima valleys in area 17–18 Å and 33–34 Å from the gorge bottom, Figure S6), additionally slowing down the inhibition process. In contrast, TMTFa slides directly into the gorge. This is an illustration of the effect of the positive charge and the role of AChE as a macro-dipole [50,51]. This electrostatic effect acts as a driving force for trafficking of the inhibitor down the gorge and its incorporation in the active site, as it was previously discussed [51–54].

QM/MM optimization of non-covalent complex of hAChE with TFK in the active site obtained by molecular docking leads to size expansion of the active site necessary to accommodate the inhibitor and lower energy barrier for formation of covalent adduct. Traditionally, resulting hemiketals are called “transition state analogs”, though practically they are rather analogs of tetrahedral intermediate of AChE-catalyzed ester hydrolysis [55,56]. Hemiketal configuration is very close for TFK and TMTFa, with the only difference that trimethyl ammonium group of TMTFa is 0.6 Å closer to Glu202 than *tert*-butyl moiety of TMTFa. Accordingly, it is similar to configuration X-ray structure of TMTFa bound to *Mus musculus* (PDB ID: 2H9Y [53]) and *Torpedo californica* (PDB ID: 1AMN [6]) AChE (Figure 8A).

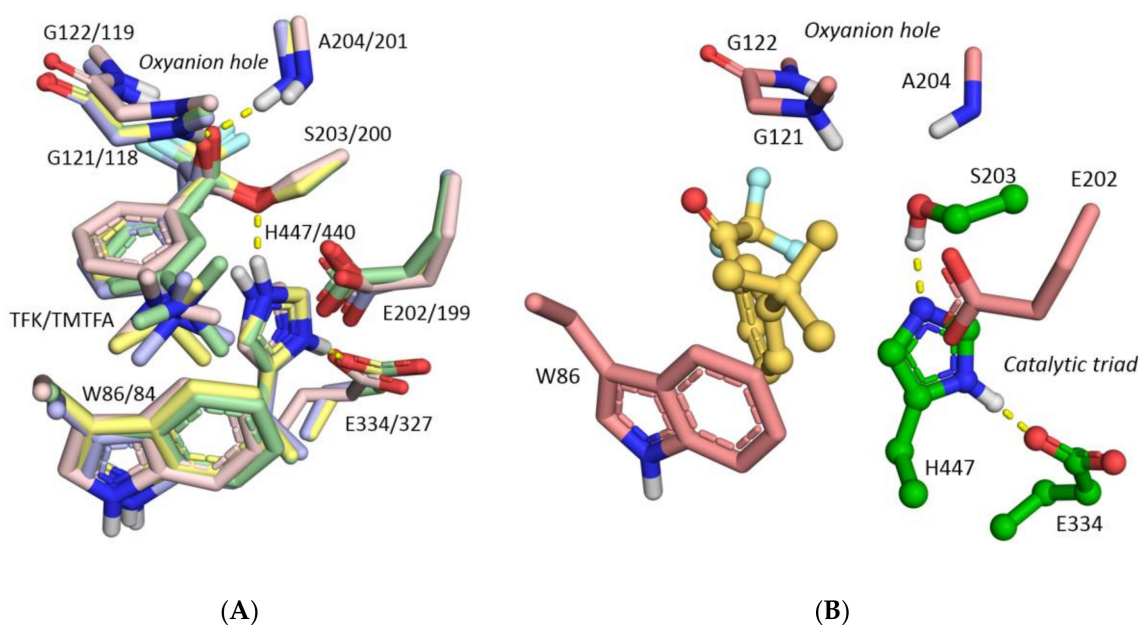


Figure 8. (A) Tetrahedral adducts for reaction between TFK (carbon atoms shown in yellow) and TMTFa (carbon atoms shown in green) and hAChE obtained by QM/MM calculations overlaid with X-ray structures of conjugates of TMTFa with *Mus musculus* (PDB ID: 2H9Y [53], carbon atoms shown in blue) and *Torpedo californica* (PDB ID: 1AMN [6], carbon atoms shown in pink). Double hAChE/TcAChE numbering is provided; (B) Non-covalent complex between TFK and hAChE, stable product resulting from the tetrahedral adduct reactivation process.

Energy scan for reactivation process shows that while inhibitor is inside the active site, i.e., carbonyl oxygen atom is within the oxyanion hole, formation of the tetrahedral adduct occurs spontaneously. Stable noncovalent complex was obtained only when the TFK group left the oxyanion hole (Figure 8B).

Though reaction itself occurs barrier-less, it has associated energy barrier for incorporation of the TFK group into the oxyanion hole, estimated with QM/MM method as 19.3 kcal/mol for TFK and 13.0 kcal/mol for TMTFa. Energy barrier for TMTFa estimated with QM/MM method corresponds to values obtained with REMD-US (Figure 7C, free energy profile, 15 kcal/mol energy barrier between position in the gorge at 9 Å and local minima at 1 Å, corresponding to position in the active site), while for TFK, barrier calculated with classical methods was overestimated, probably due to lack of polarizability in classical molecular dynamics.

Molecular modeling results suggest that binding of TFK to hAChE is slow due to non-specific interactions on the protein surface, multiple binding poses inside the gorge (EI*), and high energy barrier associated with induced-fit entrance of the inhibitor into the active site. Absence of positive charge additionally slows down this process compared to positively charged analogs.

3.4. Modulation of AChE Phosphorylation by Pre-Incubation with TFK

Then, we investigated the possible modulating or protecting effect of TFK on AChE phosphorylation by two different OPs. The first OP was cresylsaligenyl phosphate (CSP), the active metabolite of tricresylphosphate. CSP is a strong phosphorylating agent of ChEs [57,58]. Inhibition of ChEs by CSP under first order conditions is biphasic. This atypical phosphorylation process has been reported with other OPs and carbamates [45], and was interpreted it in terms of SBI of type C. Accordingly, the enzyme exists as two forms, E and E' in slow equilibrium, each form reacting at different rates with the agent I (Equations (6)–(9) and Figure 9) [57,58].

$$[E_{\text{tot}}] = [E_0] + [E'_0] \tag{6}$$

$$[E_t] = [E_0] \exp(-k_{\text{obs}}t) + [E'_0] \exp(-k'_{\text{obs}}t) \tag{7}$$

$$k_{\text{obs}} = \frac{k_p [I]}{K_I + [I]} \tag{8}$$

$$k'_{\text{obs}} = \frac{k'_p [I]}{K'_I + [I]} \tag{9}$$

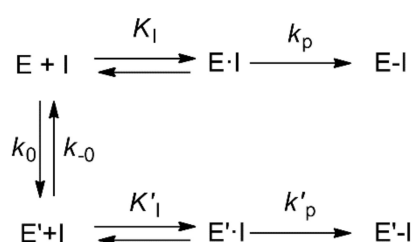


Figure 9. Slow-binding inhibition of type C with a subsequent covalent step, enzyme phosphorylation (k_p) in the present case.

This type of SBI followed by a covalent step, i.e., phosphorylation, is related to enzyme hysteresis [59]. These mechanisms have been thoroughly investigated [60,61]. Thus, we hypothesized that TFK could affect the phosphorylation process by preferential binding to one or both enzyme forms.

Inhibition of hAChE by CSP (0.21 μM) performed after different pre-incubation times in the presence of various concentrations of TFK (0.1–1 nM) showed that the biphasic progressive inhibition process of the enzyme is affected by TFK. The biphasic progressive inhibition was analyzed as a function of pre-incubation time and concentration in TFK.

It was found that pre-incubation of AChE with TFK increased the observed rate of the fast process of phosphorylation but has no significant effect on the slow process (Figure 10). The effects of pre-incubation duration and TFK concentration on the rate of inhibition was directly quantified from the slope of \ln (residual Activity) vs time of the fast phosphorylation process and pre-incubation duration the residual activity increased as pre-incubation duration and TFK concentration increased. The deleterious effect of TFK was maximum for 10 nM TFK (Figure 11) and reached a plateau after 120 min pre-incubation (Figure 12).

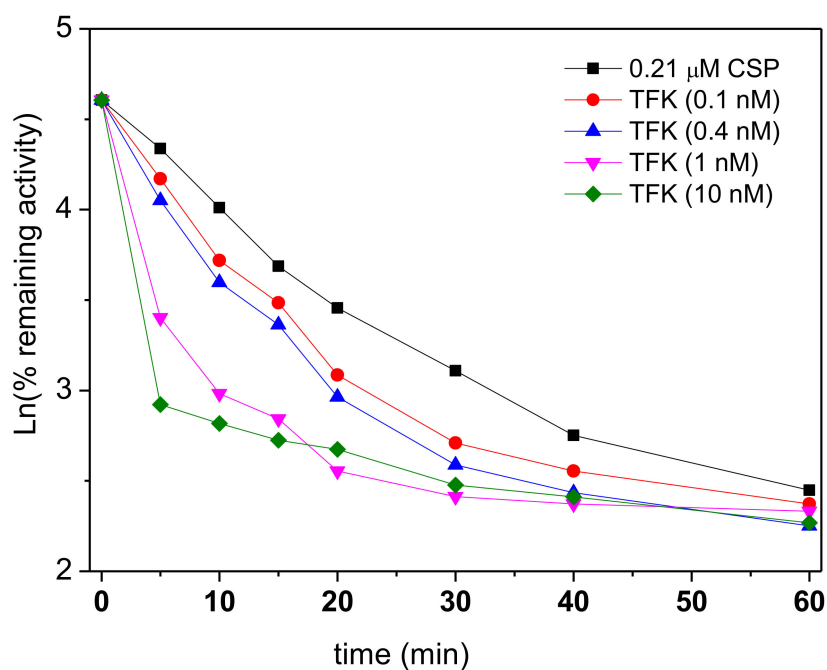


Figure 10. Modulation of progressive biphasic inhibition of hAChE by CBDP CSP (0.21 μ M) after pre-incubation of the enzyme for 120 min in the presence of TFK (0.1–10 nM).

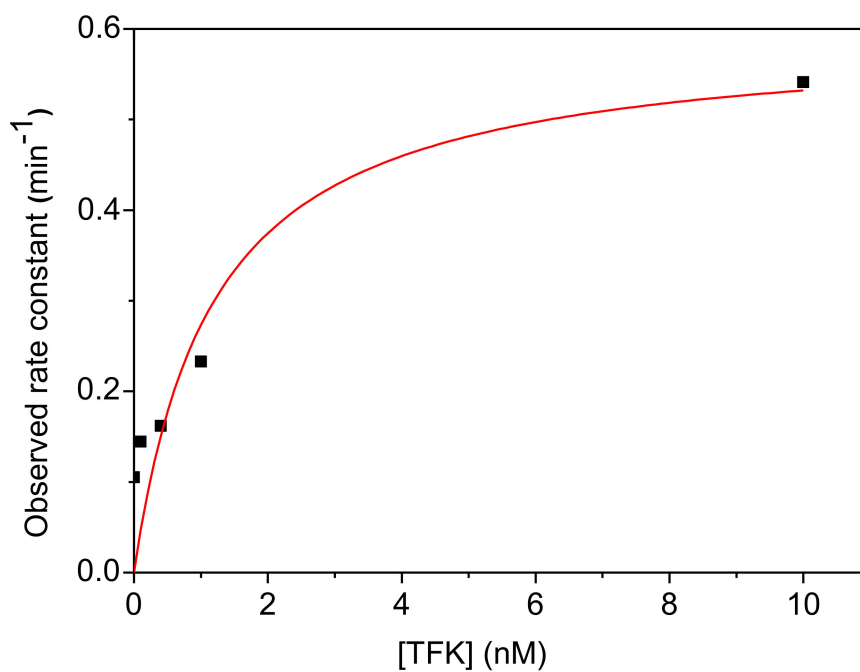


Figure 11. Dependence of $k_{\text{obs,max}}$ (fast process, see Equations (7) and (8)) of hAChE phosphorylation by CSP as a function of TFK concentration (after 120 min pre-incubation).

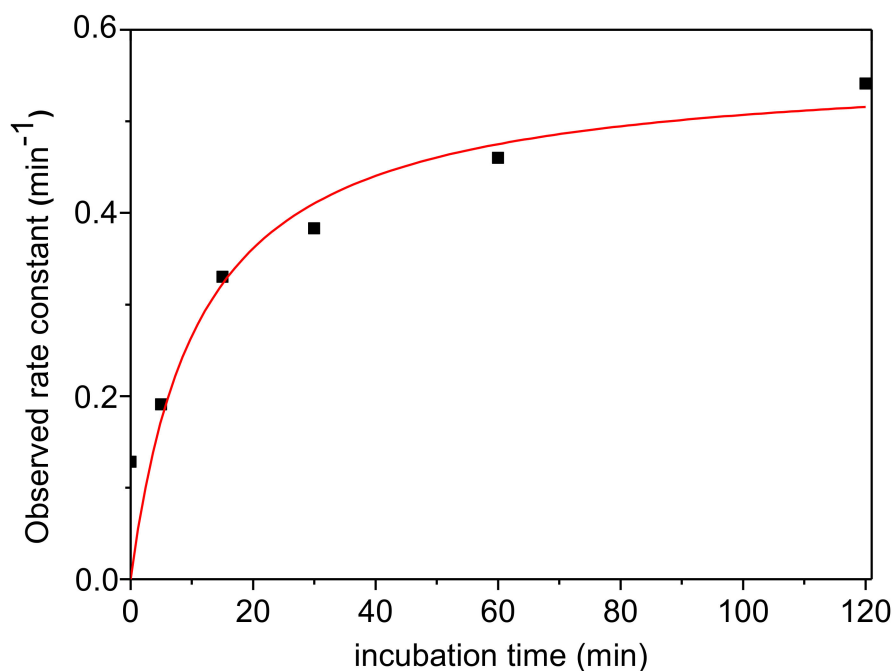


Figure 12. Observed first process (fast process) phosphorylation rate constant of hAChE by 0.21 μM CSP as a function of enzyme pre-incubation time in the presence of 10 mM TFK.

Because of the hysteretic behavior of AChE with CSP as a phosphorylating agent, the modulating effect of enzyme pre-incubation in the presence of TFK, makes the enzyme form E more susceptible to phosphorylation by CSP, and accelerates the overall phosphorylation rate of the enzyme system.

Then, we investigated the effect of TFK (1–10 nM) on AChE phosphorylation by 50 nM paraoxon. Unlike progressive inhibition of AChE by CSP, first order inhibition of the enzyme by paraoxon is linear as with most OPs. It was found that pre-incubation of AChE with TFK decreased the observed rate of phosphorylation. Thus, the effects of pre-incubation duration and TFK concentration on the rate of inhibition was directly quantified from the slope of \ln (residual Activity) vs time and pre-incubation duration the residual activity increased as pre-incubation duration and TFK concentration increased. The protective effect was maximum for 10 nM TFK (Figure 13) and reached a plateau after 40 min pre-incubation (Figure 14).

A recent *in vivo* work provided evidence that the slow-binding inhibitor C-547 has a long protective action, up to 3 days, on peripheral AChE against inhibition by paraoxon with no side effects [62]. This suggests that C-547 could be used in pre-treatment of OP-poisoning for long-term protection of the peripheral cholinergic system. However, in the case of TFK, the opposite effect on phosphorylation observed between CSP and paraoxon, makes it difficult to predict whether all SBIs can be protectant or anti-protectant of ChEs against all types of OPs. However, it may be hypothesized that the anti-protective effect on AChE reflects the enzyme hysteretic behavior with certain OPs, and results from preferential phosphorylation of the E form that kept memory of SBI binding. A conclusive answer needs further investigation with different SBIs and OPs.

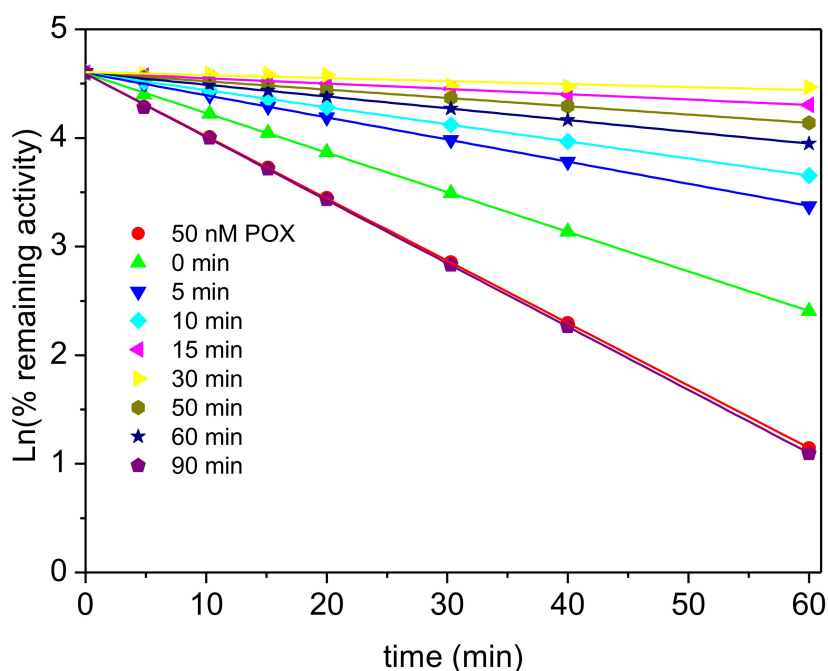


Figure 13. First-order inhibition of AChE by 50 nM paraoxon after pre-incubation of the enzyme in the presence of 10 nM TFK up to 90 min, pH 8.0, 25 °C.

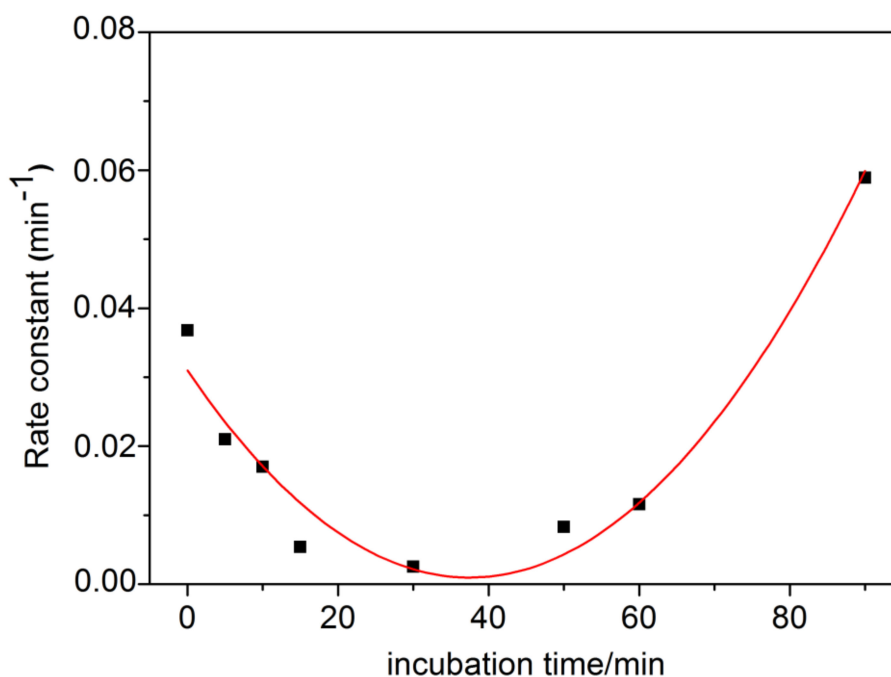


Figure 14. Observed phosphorylation rate constant of hAChE by 50 nM paraoxon as a function of enzyme pre-incubation time (from 0 to 90 min) in the presence of 10 nM TFK.

4. Conclusions

Kinetic analysis and molecular modeling of hAChE inhibition by TFK showed that this ligand is a SBI of type B. Moreover, after formation of the final complex, a transiently stabilized tetrahedral conjugate is formed, and then slowly dissociates. The existence of covalent and stable acyl tetrahedral intermediates in ChEs [6,63,64] is not completely understood. It is, however, one of the puzzling features of the catalytic power of these enzymes that deserves further studies.

TFK as an SBI of type B capable of binding to human AChE with high affinity, could be of pharmacological interest. It is already the subject of clinical investigations for neuroimaging of neurodegenerative diseases [12]. The related silyl compound, Zifrosilone, a slow tight binding inhibitor of type A with a long residence time $\tau = 70$ h and $K_i = 0.26$ nM for rat brain AChE [7] was promising for symptomatic treatment of AD [7,8,10]. However, human clinical trials were discontinued likely because of its longer residence time on AChE target. Thus, TFK with a much shorter residence time ($\tau \approx 20$ min for reversible binding and overall residence time of about 1 h for full recovery of activity after transient acylation and deacylation of huAChE active serine) appears to be more suitable for further research as an effective and safe pharmacological drug for palliative treatment of AD.

Other possible pharmacological applications may be considered. In particular, research of new molecules for protection of ChEs against phosphorylation by OPs is an active field. At the moment, the currently used molecules for pre-treatment of OP poisoning have limited and short protective actions and may induce behavioral and locomotor side effects [65]. Certain SBIs, e.g., huperzine A, galantamine, donepezil have been successfully tested (review in [45]). Novel SBIs may be of interest to expand the duration of AChE protection prior and after exposure to OPs. For example, a recent work from our group provided evidence that the AChE slow-binding inhibitor of type B, C-547, a bulky methyluracil derivative (1,3-bis[5-(diethyl-*o*-nitrobenzylammonium)pentyl]-6-methyluracil dibromide) [45,66] has a long protective action, up to 3 days, on peripheral AChE against its phosphorylation by paraoxon with no side effects [62]. Thus, the low toxicity of TFK in rodents and its protective action on central and peripheral AChEs against toxicity of paraoxon make this compound also of interest for protection of both central and peripheral AChE against OP poisoning (Zueva et al., unpublished).

Supplementary Materials: Supplementary Materials: The following are available online at <http://www.mdpi.com/2218-273X/10/12/1608/s1>, Supplementary materials to the Methods section and supplementary figures. Figure S1. Major binding poses found by molecular docking with structures 4EY4-4EY7, 5FPQ as target, clustered together. Representatives of the clusters are colored according to their population from red (most populated) to white (least populated). Figure S2. Individual binding poses of TFK in the PAS from the most populated clusters. Yellow dashes show ordinary hydrogen bonds, cyan dashes show halogen interactions (hydrogen bonds and C-Hal ... π interactions), and orange dashes show π - π interactions. Figure S3. Overlay of binding pose of TFK in the PAS shown in details in Figure S2-B (here, TFK molecule is highlighted in magenta) with X-ray structures of mAChE in complex with N-(2-Diethylamino-ethyl)-3-trifluoromethyl-benzenesulfonamide (PDB ID: 4B84, carbon atoms are shown green). Figure S4. Overlay of X-ray structures of hAChE in apo-state (PDB ID: 4EY4, carbon atoms are shown blue) and covalent conjugate with sarin (PDB ID: 5FPQ, carbon atoms are shown green, Ser203-sarin conjugate atoms are shown as spheres). Figure S5. Individual binding poses of TFK in the catalytic active site. Based on docking results with X-ray structures PDB ID 4EY7 (A), 5FPQ (B) and 4EY8 (C) used as a target. Figure S6. Binding of TFK to AChE surface, corresponding to local minima valleys in area 17-18 Å (colored green) and 33-34 Å (colored magenta) from the gorge bottom (see Figure 7, C, blue line for TFK).

Author Contributions: I.V.Z. performed kinetic studies; S.V.L. performed molecular modeling studies; I.R.P. and S.D. synthesized and developed TFK as a neuroimaging agent; P.M. wrote the manuscript. All authors have read and agreed to the published version of the manuscript.

Funding: This study was funded by Russian Science Foundation grant # 20-14-00155 to P.M.

Acknowledgments: The authors are grateful to J. Dias (IRBA, Brétoche, France) for providing rhuAChE, and Oksana Lockridge (UNMC, Omaha, NE, USA) for the gift of CSP. Computer modeling was carried out using equipment from the shared research facilities of the HPC computing resources at Lomonosov Moscow State University. We acknowledge the Joint Supercomputer Center of the Russian Academy of Sciences for provision of computational time.

Conflicts of Interest: The authors declare no conflict of interest.

References

1. Brodbeck, U.; Schweikert, K.; Gentinetta, R.; Rottenberg, M. Fluorinated aldehydes and ketones acting as quasi-substrate inhibitors of acetylcholinesterase. *Biochim. Biophys. Acta (BBA) Enzym.* **1979**, *567*, 357–369. [CrossRef]
2. Allen, K.N.; Abeles, R.H. Inhibition kinetics of acetylcholinesterase with fluoromethyl ketones. *Biochemistry* **1989**, *28*, 8466–8473. [CrossRef]

3. Nair, H.K.; Lee, K.; Quinn, D.M. m-(N,N,N-Trimethylammonio)trifluoroacetophenone: A femtomolar inhibitor of acetylcholinesterase. *J. Am. Chem. Soc.* **1993**, *115*, 9939–9941. [[CrossRef](#)]
4. Nair, H.K.; Seravalli, J.; Arbuckle, T.; Quinn, D.M. Molecular Recognition in Acetylcholinesterase Catalysis: Free-Energy Correlations for Substrate Turnover and Inhibition by Trifluoro Ketone Transition-State Analogs. *Biochemistry* **1994**, *33*, 8566–8576. [[CrossRef](#)]
5. Masson, P.; Lushchekina, S.V. Slow-binding inhibition of cholinesterases, pharmacological and toxicological relevance. *Arch. Biochem. Biophys.* **2016**, *593*, 60–68. [[CrossRef](#)]
6. Harel, M.; Quinn, D.M.; Nair, H.K.; Silman, I.; Sussman, J.L. The X-ray Structure of a Transition State Analog Complex Reveals the Molecular Origins of the Catalytic Power and Substrate Specificity of Acetylcholinesterase. *J. Am. Chem. Soc.* **1996**, *118*, 2340–2346. [[CrossRef](#)]
7. Hornsperger, J.-M.; Collard, J.-N.; Heydt, J.-G.; Giacobini, E.; Funes, S.; Dow, J.; Schirlin, D. Trimethylsilylated trifluoromethyl ketones, a novel class of acetylcholinesterase inhibitors: Biochemical and pharmacological profile of MDL 73,745. *Biochem. Soc. Trans.* **1994**, *22*, 758–763. [[CrossRef](#)]
8. Dow, J.; Dulery, B.D.; Hornsperger, J.M.; Di Francesco, G.F.; Keshary, P.; Haegele, K.D. Pharmacokinetics and pharmacodynamics of the acetylcholinesterase inhibitor 2,2,2-trifluoro-1-(3-trimethylsilylphenyl) ethanone in dog. Potential for transdermal patch delivery. *Arzneimittelforschung* **1995**, *45*, 1245–1252.
9. Zhu, X.-D.; Giacobini, E.; Hornsperger, J.-M. Effect of MDL 73,745 on acetylcholine and biogenic amine levels in rat cortex. *Eur. J. Pharmacol.* **1995**, *276*, 93–99. [[CrossRef](#)]
10. Cutler, N.R.; Seifert, R.D.; Schleman, M.M.; Sramek, J.; Szyllayko, O.J.; Howard, D.R.; Barchowsky, A.; Wardle, T.S.; Brass, E.P. Acetylcholinesterase inhibition by zifrosilone: Pharmacokinetics and pharmacodynamics*. *Clin. Pharmacol. Ther.* **1995**, *58*, 54–61. [[CrossRef](#)]
11. Ramesh, R.; Reddy, D.S. Quest for Novel Chemical Entities through Incorporation of Silicon in Drug Scaffolds. *J. Med. Chem.* **2018**, *61*, 3779–3798. [[CrossRef](#)]
12. Jollymore-Hughes, C.T.; Pottier, I.R.; Martin, E.; Rosenberry, T.L.; Darvesh, S. Development of acetophenone ligands as potential neuroimaging agents for cholinesterases. *Bioorg. Med. Chem.* **2016**, *24*, 5270–5279. [[CrossRef](#)]
13. Ellman, G.L.; Courtney, K.; Andres, V.; Featherstone, R.M. A new and rapid colorimetric determination of acetylcholinesterase activity. *Biochem. Pharmacol.* **1961**, *7*, 88–95. [[CrossRef](#)]
14. Carletti, E.; Li, H.; Li, B.; Ekström, F.; Nicolet, Y.; Loiodice, M.; Gillon, E.; Froment, M.T.; Lockridge, O.; Schopfer, L.M.; et al. Aging of Cholinesterases Phosphorylated by Tabun Proceeds through O-Dealkylation. *J. Am. Chem. Soc.* **2008**, *130*, 16011–16020. [[CrossRef](#)]
15. Cheung, J.; Rudolph, M.J.; Burshteyn, F.; Cassidy, M.S.; Gary, E.N.; Love, J.; Franklin, M.C.; Height, J.J. Structures of Human Acetylcholinesterase in Complex with Pharmacologically Important Ligands. *J. Med. Chem.* **2012**, *55*, 10282–10286. [[CrossRef](#)]
16. Leuzinger, W. The number of catalytic sites in acetylcholinesterase. *Biochem. J.* **1971**, *123*, 139–141. [[CrossRef](#)]
17. Morrison, J.F.; Stone, S.R. Approaches to the study and analysis of the inhibition of enzymes by slow- and tight-binding inhibitors. *Comments Mol. Cell. Biophys.* **1985**, *2*, 347–368.
18. Sculley, M.J.; Morrison, J.F.; Cleland, W. Slow-binding inhibition: The general case. *Biochim. Biophys. Acta (BBA) Protein Struct. Mol. Enzym.* **1996**, *1298*, 78–86. [[CrossRef](#)]
19. Solo, C.G.-D.; Garcia-Canovas, F.; Havsteen, B.H.; Castellanos, R.V. Kinetic analysis of enzyme reactions with slow-binding inhibition. *Biosystems* **1999**, *51*, 169–180. [[CrossRef](#)]
20. Cornish-Bowden, A. A simple graphical method for determining the inhibition constants of mixed, uncompetitive and non-competitive inhibitors (Short Communication). *Biochem. J.* **1974**, *137*, 143–144. [[CrossRef](#)]
21. Mukhametgalieva, A.R.; Zueva, I.V.; Aglyamova, A.R.; Lushchekina, S.V.; Masson, P. A new sensitive spectrofluorimetric method for measurement of activity and kinetic study of cholinesterases. *Biochim. Biophys. Acta (BBA) Proteins Proteom.* **2020**, *1868*, 140270. [[CrossRef](#)]
22. Zueva, I.; Lushchekina, S.V.; Daudé, D.; Chabrière, E.; Masson, P. Steady-State Kinetics of Enzyme-Catalyzed Hydrolysis of Echothiophate, a P-S Bonded Organophosphorus as Monitored by Spectrofluorimetry. *Molecules* **2020**, *25*, 1371. [[CrossRef](#)]
23. Allgardsson, A.; Berg, L.; Akfur, C.; Hörnberg, A.; Worek, F.; Linusson, A.; Ekström, F.J. Structure of a prereaction complex between the nerve agent sarin, its biological target acetylcholinesterase, and the antidote HI-6. *Proc. Natl. Acad. Sci. USA* **2016**, *113*, 5514–5519. [[CrossRef](#)]

24. Nachon, F.; Carletti, E.; Ronco, C.; Trovaslet, M.; Nicolet, Y.; Jean, L.; Renard, P.-Y. Crystal structures of human cholinesterases in complex with huprine W and tacrine: Elements of specificity for anti-Alzheimer's drugs targeting acetyl- and butyryl-cholinesterase. *Biochem. J.* **2013**, *453*, 393–399. [[CrossRef](#)]
25. Worda, J.M.; Lovell, S.C.; Richardson, J.S.; Richardson, D.C. Asparagine and glutamine: Using hydrogen atom contacts in the choice of side-chain amide orientation 1 Edited by J. Thornton. *J. Mol. Biol.* **1999**, *285*, 1735–1747. [[CrossRef](#)]
26. Morris, G.M.; Goodsell, D.S.; Halliday, R.S.; Huey, R.; Hart, W.E.; Belew, R.K.; Olson, A.J. Automated docking using a Lamarckian genetic algorithm and an empirical binding free energy function. *J. Comput. Chem.* **1998**, *19*, 1639–1662. [[CrossRef](#)]
27. Morris, G.M.; Ruth, H.; Lindstrom, W.; Sanner, M.F.; Belew, R.K.; Goodsell, D.S.; Olson, A.J. AutoDock4 and AutoDockTools4: Automated docking with selective receptor flexibility. *J. Comput. Chem.* **2009**, *30*, 2785–2791. [[CrossRef](#)]
28. Humphrey, W.; Dalke, A.; Schulten, K. VMD: Visual molecular dynamics. *J. Mol. Graph.* **1996**, *14*, 33–38. [[CrossRef](#)]
29. Vanommeslaeghe, K.; Hatcher, E.; Acharya, C.; Kundu, S.; Zhong, S.; Shim, J.; Darian, E.; Guvench, O.; Lopes, P.; Vorobyov, I.; et al. CHARMM general force field: A force field for drug-like molecules compatible with the CHARMM all-atom additive biological force fields. *J. Comput. Chem.* **2009**, *31*, 671–690. [[CrossRef](#)]
30. Zhu, X.; Lopes, P.E.M.; MacKerell, A.D., Jr. Recent developments and applications of the CHARMM force fields. *Wiley Interdiscip. Rev. Comput. Mol. Sci.* **2012**, *2*, 167–185. [[CrossRef](#)]
31. Mayne, C.G.; Saam, J.; Schulten, K.; Tajkhorshid, E.; Gumbart, J.C. Rapid parameterization of small molecules using the force field toolkit. *J. Comput. Chem.* **2013**, *34*, 2757–2770. [[CrossRef](#)]
32. Phillips, J.C.; Braun, R.; Wang, W.; Gumbart, J.; Tajkhorshid, E.; Villa, E.; Chipot, C.; Skeel, R.D.; Kalé, L.; Schulten, K. Scalable molecular dynamics with NAMD. *J. Comput. Chem.* **2005**, *26*, 1781–1802. [[CrossRef](#)]
33. Best, R.B.; Zhu, X.; Shim, J.; Lopes, P.E.M.; Mittal, J.; Feig, M.; MacKerell, J.A.D. Optimization of the Additive CHARMM All-Atom Protein Force Field Targeting Improved Sampling of the Backbone ϕ , ψ and Side-Chain χ_1 and χ_2 Dihedral Angles. *J. Chem. Theory Comput.* **2012**, *8*, 3257–3273. [[CrossRef](#)]
34. Supercomputer Lomonosov-2: Large Scale, Deep Monitoring and Fine Analytics for the User Community. *Supercomput. Front. Innov.* **2019**, *6*, 4–11. [[CrossRef](#)]
35. Gumbart, J.C.; Roux, B.; Chipot, C. Efficient Determination of Protein–Protein Standard Binding Free Energies from First Principles. *J. Chem. Theory Comput.* **2013**, *9*, 3789–3798. [[CrossRef](#)]
36. Roux, B. The calculation of the potential of mean force using computer simulations. *Comput. Phys. Commun.* **1995**, *91*, 275–282. [[CrossRef](#)]
37. Gumbart, J.C.; Roux, B.; Chipot, C. Standard binding free energies from computer simulations: What is the best strategy? *J. Chem. Theory Comput.* **2013**, *9*, 794–802. [[CrossRef](#)]
38. Zhou, R. Replica exchange molecular dynamics method for protein folding simulation. *Adv. Struct. Saf. Stud.* **2007**, *350*, 205–224. [[CrossRef](#)]
39. Valiev, M.; Bylaska, E.; Govind, N.; Kowalski, K.; Straatsma, T.; Van Dam, H.; Wang, D.; Nieplocha, J.; Apra, E.; Windus, T.; et al. NWChem: A comprehensive and scalable open-source solution for large scale molecular simulations. *Comput. Phys. Commun.* **2010**, *181*, 1477–1489. [[CrossRef](#)]
40. Grimme, S.; Antony, J.; Ehrlich, S.; Krieg, H. A consistent and accurate ab initio parametrization of density functional dispersion correction (DFT-D) for the 94 elements H-Pu. *J. Chem. Phys.* **2010**, *132*, 154104. [[CrossRef](#)]
41. Case, D.A.; Iii, T.E.C.; Darden, T.; Gohlke, H.; Luo, R.; Merz, K.M.M., Jr.; Onufriev, A.; Simmerling, C.; Wang, B.; Woods, R.J. The Amber biomolecular simulation programs. *J. Comput. Chem.* **2005**, *26*, 1668–1688. [[CrossRef](#)]
42. Tummino, P.J.; Copeland, R.A. Residence Time of Receptor–Ligand Complexes and Its Effect on Biological Function. *Biochemistry* **2008**, *47*, 5481–5492. [[CrossRef](#)]
43. Radić, Z.; Quinn, D.M.; Vellom, D.C.; Camp, S.; Taylor, P. Allosteric Control of Acetylcholinesterase Catalysis by Fasciculin. *J. Biol. Chem.* **1995**, *270*, 20391–20399. [[CrossRef](#)]
44. Copeland, R.A. *Evaluation of Enzyme Inhibitors in Drug Discovery: A Guide for Medicinal Chemists and Pharmacologists*, 2nd ed.; Wiley: Hoboken, NJ, USA, 2013.
45. Lushchekina, S.V.; Masson, P. Slow-binding inhibitors of acetylcholinesterase of medical interest. *Neuropharmacology* **2020**, *177*, 108236. [[CrossRef](#)]

46. Andersson, C.D.; Forsgren, N.; Akfur, C.; Allgardsson, A.; Berg, L.; Engdahl, C.; Qian, W.; Ekström, F.; Linusson, A. Divergent Structure–Activity Relationships of Structurally Similar Acetylcholinesterase Inhibitors. *J. Med. Chem.* **2013**, *56*, 7615–7624. [[CrossRef](#)]
47. Lushchekina, S.V.; Makhaeva, G.F.; Novichkova, D.A.; Zueva, I.V.; Kovaleva, N.V.; Richardson, R.R. Supercomputer Modeling of Dual-Site Acetylcholinesterase (AChE) Inhibition. *Supercomput. Front. Innov.* **2018**, *5*, 89–97. [[CrossRef](#)]
48. Bourne, Y.; Taylor, P.; Marchot, P. Acetylcholinesterase inhibition by fasciculin: Crystal structure of the complex. *Cell* **1995**, *83*, 503–512. [[CrossRef](#)]
49. Tai, K.; Shen, T.; Henchman, R.H.; Bourne, Y.; Marchot, P.; McCammon, J.A. Mechanism of Acetylcholinesterase Inhibition by Fasciculin: A 5-ns Molecular Dynamics Simulation. *J. Am. Chem. Soc.* **2002**, *124*, 6153–6161. [[CrossRef](#)]
50. Sussman, J.L.; Harel, M.; Frolow, F.; Oefner, C.; Goldman, A.; Toker, L.; Silman, I. Atomic structure of acetylcholinesterase from *Torpedo californica*: A prototypic acetylcholine-binding protein. *Science* **1991**, *253*, 872–879. [[CrossRef](#)]
51. Wlodek, S.T.; Clark, T.W.; Scott, L.R.; McCammon, J.A. Molecular Dynamics of Acetylcholinesterase Dimer Complexed with Tacrine. *J. Am. Chem. Soc.* **1997**, *119*, 9513–9522. [[CrossRef](#)]
52. Ripoll, D.R.; Faerman, C.H.; Axelsen, P.H.; Silman, I.; Sussman, J.L. An electrostatic mechanism for substrate guidance down the aromatic gorge of acetylcholinesterase. *Proc. Natl. Acad. Sci. USA* **1993**, *90*, 5128–5132. [[CrossRef](#)]
53. Bourne, Y.; Radić, Z.; Sulzenbacher, G.; Kim, E.; Taylor, P.; Marchot, P. Substrate and Product Trafficking through the Active Center Gorge of Acetylcholinesterase Analyzed by Crystallography and Equilibrium Binding. *J. Biol. Chem.* **2006**, *281*, 29256–29267. [[CrossRef](#)]
54. Colletier, J.-P.; Fournier, D.; Greenblatt, H.M.; Stojan, J.; Sussman, J.L.; Zaccari, G.; Silman, I.; Weik, M. Structural insights into substrate traffic and inhibition in acetylcholinesterase. *EMBO J.* **2006**, *25*, 2746–2756. [[CrossRef](#)]
55. Ngo, P.D.; Mansoorabadi, S.O.; Frey, P.A. Serine Protease Catalysis: A Computational Study of Tetrahedral Intermediates and Inhibitory Adducts. *J. Phys. Chem. B* **2016**, *120*, 7353–7359. [[CrossRef](#)]
56. Makhaeva, G.F.; Elkina, N.A.; Shchegolkov, E.V.; Boltneva, N.P.; Lushchekina, S.V.; Serebryakova, O.G.; Rudakova, E.V.; Kovaleva, N.V.; Radchenko, E.V.; Palyulin, V.A.; et al. Synthesis, molecular docking, and biological evaluation of 3-oxo-2-tolylhydrazinylidene-4,4,4-trifluorobutanoates bearing higher and natural alcohol moieties as new selective carboxylesterase inhibitors. *Bioorg. Chem.* **2019**, *91*, 103097. [[CrossRef](#)]
57. Carletti, E.; Schopfer, L.M.; Colletier, J.-P.; Froment, M.-T.; Nachon, F.; Weik, M.; Lockridge, O.; Masson, P. Reaction of Cresyl Saligenin Phosphate, the Organophosphorus Agent Implicated in Aerotoxic Syndrome, with Human Cholinesterases: Mechanistic Studies Employing Kinetics, Mass Spectrometry, and X-ray Structure Analysis. *Chem. Res. Toxicol.* **2011**, *24*, 797–808. [[CrossRef](#)]
58. Carletti, E.; Colletier, J.-P.; Schopfer, L.M.; Santoni, G.; Masson, P.; Lockridge, O.; Nachon, F.; Weik, M. Inhibition Pathways of the Potent Organophosphate CBDP with Cholinesterases Revealed by X-ray Crystallographic Snapshots and Mass Spectrometry. *Chem. Res. Toxicol.* **2013**, *26*, 280–289. [[CrossRef](#)]
59. Frieden, C. Slow Transitions and Hysteretic Behavior in Enzymes. *Annu. Rev. Biochem.* **1979**, *48*, 471–489. [[CrossRef](#)]
60. Masson, P. Time-dependent kinetic complexities in cholinesterase-catalyzed reactions. *Biochemistry (Moscow)* **2012**, *77*, 1147–1161. [[CrossRef](#)]
61. Baici, A. *Kinetics of Enzyme-Modifier Interactions*; Springer Science and Business Media LLC: Vienna, Austria, 2015.
62. Lenina, O.A.; Zueva, I.V.; Zobov, V.V.; Semenov, V.E.; Masson, P.; Petrov, K.A. Slow-binding reversible inhibitor of acetylcholinesterase with long-lasting action for prophylaxis of organophosphate poisoning. *Sci. Rep.* **2020**, *10*, 1–12. [[CrossRef](#)]
63. Nicolet, Y.; Lockridge, O.; Masson, P.; Fontecilla-Camps, J.C.; Nachon, F. Crystal Structure of Human Butyrylcholinesterase and of Its Complexes with Substrate and Products. *J. Biol. Chem.* **2003**, *278*, 41141–41147. [[CrossRef](#)]
64. Tormos, J.R.; Wiley, K.L.; Seravalli, J.; Nachon, F.; Masson, P.; Nicolet, Y.; Quinn, D.M. The Reactant State for Substrate-Activated Turnover of Acetylthiocholine by Butyrylcholinesterase is a Tetrahedral Intermediate. *J. Am. Chem. Soc.* **2005**, *127*, 14538–14539. [[CrossRef](#)]

65. Masson, P. Novel approaches in prophylaxis/pretreatment and treatment of organophosphorus poisoning. *Phosphorus Sulfur Silicon Relat. Elem.* **2016**, *191*, 1433–1443. [[CrossRef](#)]
66. Kharlamova, A.D.; Lushchekina, S.V.; Petrov, K.A.; Kots, E.D.; Nachon, F.V.; Villard-Wandhammer, M.; Zueva, I.V.; Krejci, E.; Reznik, V.S.; Zobov, V.V.; et al. Slow-binding inhibition of acetylcholinesterase by an alkylammonium derivative of 6-methyluracil: Mechanism and possible advantages for myasthenia gravis treatment. *Biochem. J.* **2016**, *473*, 1225–1236. [[CrossRef](#)]



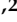


Publisher’s Note: MDPI stays neutral with regard to jurisdictional claims in published maps and institutional affiliations.



© 2020 by the authors. Licensee MDPI, Basel, Switzerland. This article is an open access article distributed under the terms and conditions of the Creative Commons Attribution (CC BY) license (<http://creativecommons.org/licenses/by/4.0/>).

Article

Pursuing the Complexity of Alzheimer's Disease: Discovery of Fluoren-9-Amines as Selective Butyrylcholinesterase Inhibitors and *N*-Methyl-D-Aspartate Receptor Antagonists

Jan Konecny ^{1,2,†}, Anna Misiachna ^{3,4,5,†}, Martina Hrabnova ^{1,2} , Lenka Pulkrabkova ^{1,2}, Marketa Benkova ², Lukas Prchal ², Tomas Kucera ^{1,2} , Tereza Kobrlova ², Vladimir Finger ^{2,6}, Marharyta Kolcheva ^{3,4}, Stepan Kortus ^{3,4}, Daniel Jun ^{1,2} , Marian Valko ⁷, Martin Horak ^{3,4}, Ondrej Soukup ^{1,2,*}  and Jan Korabecny ^{1,2,*} 

- ¹ Department of Toxicology and Military Pharmacy, Faculty of Military Health Sciences, Trebesska 1575, 500 01 Hradec Kralove, Czech Republic; jan.konecny@unob.cz (J.K.); martina.hrabnova@unob.cz (M.H.); lenka.pulkrabkova@fnhk.cz (L.P.); tomas.kucera2@unob.cz (T.K.); daniel.jun@unob.cz (D.J.)
- ² Biomedical Research Centre, University Hospital Hradec Kralove, Sokolska 581, 500 05 Hradec Kralove, Czech Republic; Marketa.Benkova@fnhk.cz (M.B.); lukas.prchal@fnhk.cz (L.P.); tereza.kobrlova@fnhk.cz (T.K.); fingerv@faf.cuni.cz (V.F.)
- ³ Institute of Experimental Medicine of the Czech Academy of Sciences, Videnska 1083, 142 20 Prague, Czech Republic; anna.misiachna@iem.cas.cz (A.M.); marharyta.kolcheva@iem.cas.cz (M.K.); stepan.kortus@iem.cas.cz (S.K.); martin.horak@iem.cas.cz (M.H.)
- ⁴ Institute of Physiology of the Czech Academy of Sciences, Videnska 1083, 142 20 Prague, Czech Republic
- ⁵ Department of Physiology, Faculty of Science, Charles University in Prague, Albertov 6, 128 43 Prague, Czech Republic
- ⁶ Department of Organic and Bioorganic Chemistry, Faculty of Pharmacy in Hradec Kralove, Charles University, Akademia Heyrovskeho 1203, 500 05 Hradec Kralove, Czech Republic
- ⁷ Faculty of Chemical and Food Technology, Slovak University of Technology, Radlinskeho 9, 812 37 Bratislava, Slovakia; marian.valko@stuba.sk
- * Correspondence: ondrej.soukup@fnhk.cz (O.S.); jan.korabecny@fnhk.cz (J.K.); Tel.: +420-495-833-447 (O.S. & J.K.)
- † These authors contributed equally to this paper.



Citation: Konecny, J.; Misiachna, A.; Hrabnova, M.; Pulkrabkova, L.; Benkova, M.; Prchal, L.; Kucera, T.; Kobrlova, T.; Finger, V.; Kolcheva, M.; Kortus, S.; et al. Pursuing the Complexity of Alzheimer's Disease: Discovery of Fluoren-9-Amines as Selective Butyrylcholinesterase Inhibitors and *N*-Methyl-D-Aspartate Receptor Antagonists. *Biomolecules* **2021**, *11*, 3. <https://dx.doi.org/10.3390/biom11010003>

Received: 25 November 2020

Accepted: 18 December 2020

Published: 22 December 2020

Publisher's Note: MDPI stays neutral with regard to jurisdictional claims in published maps and institutional affiliations.



Copyright: © 2020 by the authors. Licensee MDPI, Basel, Switzerland. This article is an open access article distributed under the terms and conditions of the Creative Commons Attribution (CC BY) license (<https://creativecommons.org/licenses/by/4.0/>).

Abstract: Alzheimer's disease (AD) is a complex disorder with unknown etiology. Currently, only symptomatic therapy of AD is available, comprising cholinesterase inhibitors and *N*-methyl-D-aspartate (NMDA) receptor antagonists. Drugs targeting only one pathological condition have generated only limited efficacy. Thus, combining two or more therapeutic interventions into one molecule is believed to provide higher benefit for the treatment of AD. In the presented study, we designed, synthesized, and biologically evaluated 15 novel fluoren-9-amine derivatives. The *in silico* prediction suggested both the oral availability and permeation through the blood–brain barrier (BBB). An initial assessment of the biological profile included determination of the cholinesterase inhibition and NMDA receptor antagonism at the GluN1/GluN2A and GluN1/GluN2B subunits, along with a low cytotoxicity profile in the CHO-K1 cell line. Interestingly, compounds revealed a selective butyrylcholinesterase (BChE) inhibition pattern with antagonistic activity on the NMDARs. Their interaction with butyrylcholinesterase was elucidated by studying enzyme kinetics for compound **3c** in tandem with the *in silico* docking simulation. The docking study showed the interaction of the tricyclic core of new derivatives with Trp82 within the anionic site of the enzyme in a similar way as the template drug tacrine. From the kinetic analysis, it is apparent that **3c** is a competitive inhibitor of BChE.

Keywords: acetylcholinesterase; Alzheimer's disease; butyrylcholinesterase; fluorene; *in vitro*; *in silico*; multi-target directed ligands; *N*-methyl-D-aspartate receptor

1. Introduction

Alzheimer's disease (AD) is a debilitating neurodegenerative disorder that manifests as progressive memory loss leading to dementia [1,2]. AD not only represents a serious health burden, but it also imposes social and economic issues [3–6]. Worldwide, nearly 50 million people have developed AD, and it is expected that the number will double within the next 20 years [7]. An effective cure able to halt or slow down the disease progression still does not exist, mainly because of our limited knowledge about AD pathophysiology. However, mechanisms resulting in the clinical symptoms of AD are well-established [8,9]. Among them, amyloid- β ($A\beta$) and tau proteins are considered as major contributors to AD, forming extracellular aggregates [10,11] and intracellular neurofibrillary tangles, respectively [12–14]. So far, the therapy is only palliative, either enhancing the cholinergic neurotransmission or modulating the synaptic excitotoxicity via *N*-methyl-D-aspartate (NMDA) receptors [15–18]. Oxidative stress [19,20], metal ion imbalance [21], or neuroinflammation [22] are other crucial players in AD pathophysiology.

Currently, AD is treated by acetylcholinesterase (AChE, E.C. 3.1.1.7) inhibitors to restore the physiological levels of acetylcholine (ACh) and the NMDA receptor antagonist, which reduce the excitotoxicity by mitigating the excessive glutamate stimulation of the receptors [23,24]. Donepezil, galantamine, and rivastigmine represent the marketed drugs from the group of AChE inhibitors; memantine acts as a noncompetitive NMDA receptor antagonist, blocking the overstimulation of the respective receptors. Since AChE inhibitors are administered in mild-to-moderate stages of AD, memantine is indicated for severe stages of the disease [25]. It is worth mentioning that the combination of donepezil and memantine into one capsule, known as Namzaric, was approved in 2014. Such a combination offers an improved efficacy compared to single-agent administration with a good pharmacokinetic profile, safety, and tolerability [26,27].

Given the complexity of AD and the high failure rate of single-targeted drug candidates from clinical trials in the last few years, the idea of multitarget directed ligands (MTDLs) has emerged as a new approach to tackle the disease [28–31]. Accordingly, the design of these molecules is oriented towards the modulation of different pathological pathways simultaneously [29,32]. Recently, we have critically pointed out that not all the combined effects are suitable to be amalgamated into a single molecule to achieve the highest therapeutic effect [29]. Indeed, AD is a long-term condition with progressive brain changes occurring 20 years before the AD outbreak into the symptomatic phase [33]. With respect to the combination of therapeutic targets of interest and to achieve maximum synergy, the ideal drugs should be designed by following the timescale for specific pathological cascades. Within this study, we have focused on the symptomatic stage of AD, in which $A\beta$ plaques and neurofibrillary tangles of paired helical filaments are ubiquitous, and their clearance has no effect on improving cognitive functions. This is well-documented, for instance, by the insufficient efficacy of β -secretase inhibitors in phase III clinical trials [34]. With this in mind, we turned our attention to impaired neurotransmission, which is the most critically affected at the later stages of AD, thus pursuing the two most pronounced systems, namely cholinergic and glutamatergic ones [35,36].

Tacrine (THA), an AChE inhibitor, was the first drug approved for AD treatment in 1993. Hepatotoxicity and gastrointestinal discomfort are the culprits responsible for its withdrawal in 2013 [37]. THA acts not only as AChE inhibitor but, also, via the antagonism of NMDA receptors, which might contribute to its pharmacological effects [38]. Indeed, THA inhibits NMDA receptor responses with high specificity in a concentration-dependent manner with an $IC_{50} = 20 \mu\text{M}$ at -60 mV and much higher values at positive membrane potentials [39]. Mechanistically, the THA action at NMDA receptors can be classified as reversible, blocking the channel's open state with binding in the proximity of the channel entrance [40,41]. Likewise, other THA derivatives emerged as interesting drugs with a potential applicability for AD treatment due to the pharmacological behavior of both cholinesterases and the NMDA receptor [39,42]. Based on this, our goal was to design

a series of novel multipotent agents, which, in one molecule, shows a representative cholinesterase inhibition together with NMDA antagonist activity.

In a recent work, we developed novel molecules building on a fluorene moiety. The compounds are structurally related to other tricyclic congeners like THA or carbazole, known for their cholinesterase inhibition and/or neuroprotective properties (Figure 1) [43–45]. We took advantage of the above-mentioned and designed novel molecules substituted at the C9 position by various primary or secondary amines, generating 15 novel compounds (**3a–o**; Figure 1) as potential cholinesterase inhibitors and NMDA receptor antagonists. Importantly, since several techniques on how to construct MTDLs exist, we applied the so-called merging approach in this study. This approach best corresponds to the drug-likeness of the final molecule compared to the linking or fusing strategies [28,29,32]. Furthermore, the design of the novel family was envisaged in parallel with their physicochemical properties, presuming both oral and central bioavailability. The biological profile includes the assessment of AChE, butyrylcholinesterase (BChE; E.C. 3.1.1.8), and NMDA receptor affinities, with the cytotoxicity and BBB permeation being evaluated as well.

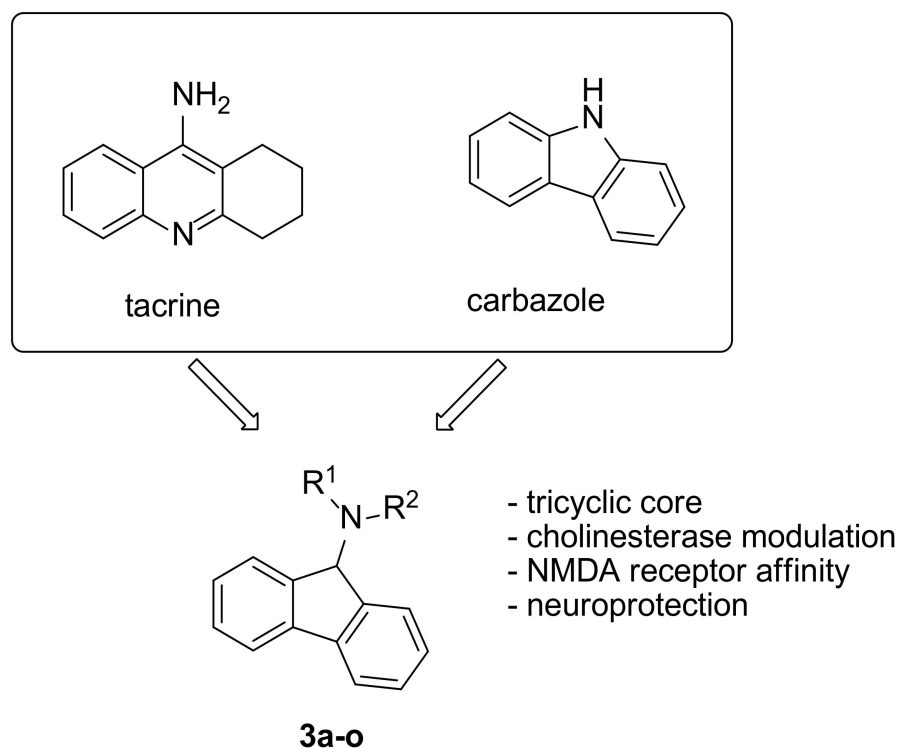


Figure 1. Design of a novel 9-aminofluorene overlapping the tacrine (THA) and carbazole moieties. NMDA: *N*-methyl-*D*-aspartate.

2. Materials and Methods

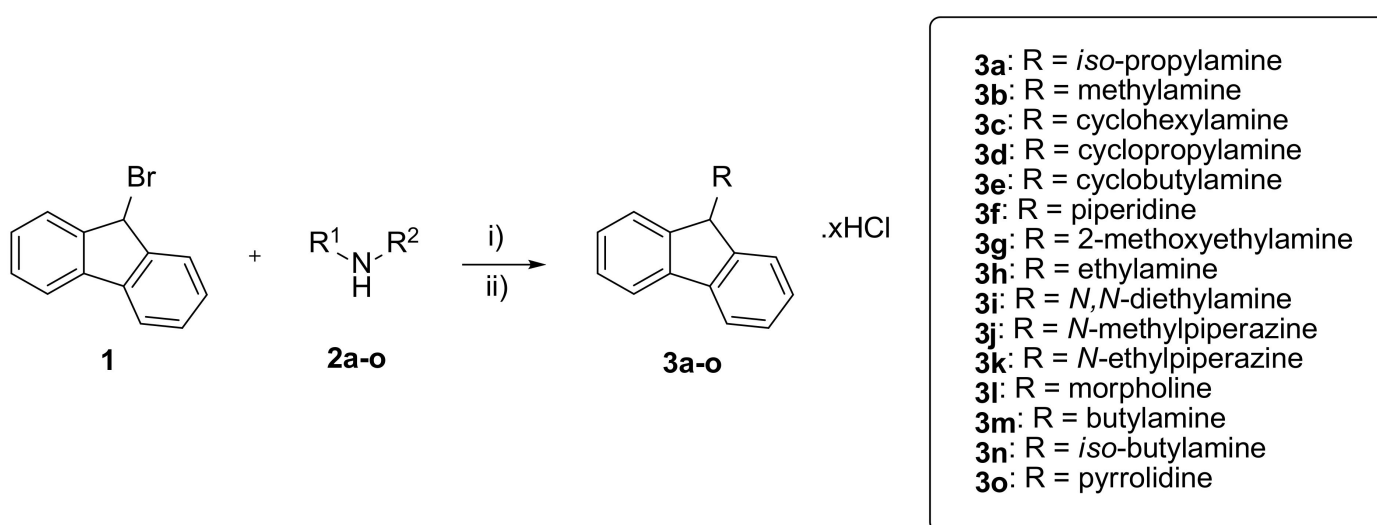
2.1. Chemistry

All chemical solvents and reagents were used in the highest available purity without further purification, and they were purchased from Sigma-Aldrich (Prague, Czech Republic) or FluoroChem (Hadfield, UK). The reactions were monitored by thin-layer chromatography (TLC) on silica gel plates (60 F254, Merck, Prague, Czech Republic), and the spots were visualized by ultraviolet light (254 nm). Purification of crude products was carried out using a PuriFlash Gen5 column, 5.250 (Interchim, Montluçon, France) (silica gel 100, 60 Å, 230–400-mesh ASTM, Sigma-Aldrich, Prague, Czech Republic). NMR spectra were recorded in deuterated chloroform (CDCl₃) and deuterated dimethyl sulfoxide (DMSO-*d*₆) on a Bruker Avance NEO 500 MHz spectrometer (499.87 MHz for ¹H-NMR and 125.71 MHz for ¹³C-NMR; Vienna, Austria). Chemical shifts are reported in parts per millions (ppm), and spin multiplicities are given as broad singlet (bs), doublet (d), doublet

of doublet (dd), triplet (t), doublet of triplet (dt), quartet (q), pentet (p), or multiplet (m). Coupling constants (J) are reported in Hz. Recorded NMR spectra are available in the Supplementary Materials. Melting points were measured using an automated melting point recorder M-565 (Büchi, Flawil, Switzerland). The synthesized compounds were analyzed by an LC-MS system consisting of UHPLC Dionex Ultimate 3000 RS coupled with a Q Exactive Plus orbitrap mass spectrometer to obtain high-resolution mass spectra (Thermo Fisher Scientific, Bremen, Germany) (see Supplementary Materials). The samples were dissolved in DMSO/methanol 50/50 (*v/v*). Reverse-phase C18 column Kinetex EVO (Phenomenex, Torrance, CA, USA) was used as a stationary phase, and purified water with 0.1% formic acid (mobile phase A) and LC-MS grade acetonitrile with 0.1% formic acid (mobile phase B) were used as the mobile phases. Gradient elution was used to determine purities and mass spectra. Method started with 5% B for 0.3 min, then the gradient rose to 100% B in the third min and was at 100% B for 0.7 min and then went back to 5% B and was equilibrated for 3.5 min. Total run time of the method was 7.5 min. Column was tempered to 27 °C, the flow of the mobile phase was 0.5 mL/min, and the injection volume was 1 µL. Gradient LC analysis with UV detection (254 nm) confirmed a >97% purity. High-resolution mass spectra were collected from the total ion current in the scan range 105–1000 *m/z*, with the resolution set to 140,000.

2.2. General Procedure for the Preparation of 9-Bromofluorene hydrochlorides (3a–o)

Appropriate primary or secondary amine (Scheme 1) was dissolved in 10 mL of dry MeCN under argon atmosphere and stirred vigorously at 40 °C for 15 min. 9-Bromofluorene (Scheme 1) was dissolved in 5 mL of dry MeCN and added dropwise to the reaction mixture. The reaction was maintained with stirring at 40 °C for 3 h. After cooling, the solvent was evaporated under reduced pressure, and the crude material was purified on a FlashChrom column (eluent dichloromethane/methanol (DCM/MeOH) with 1% of NH₃, gradient 95:5 → 90:10) to get the appropriate products as a free base. These were converted into hydrochloride salts by the treatment with 1 mL of concentrated aqueous solution of HCl (35%) in 5 mL of MeOH, starting from 0 °C to room temperature for 1 h. The solvent was removed in vacuo, and the residual water was distilled via azeotropic distillation with absolute EtOH three times. The solid product was washed by ice-cold acetone, resulting in hydrochloride salt as a white solid.



Scheme 1. Synthetic procedure for the preparation of substituted fluoren-9-amines 3a–o. Reaction conditions: (i) MeCN, 40 °C, 3 h and (ii) HCl (aq.), MeOH, RT, 1 h.

2.2.1. *N*-Propan-2-yl-9*H*-fluoren-9-amine hydrochloride (**3a**)

Yield 43% as a white solid. Melting point (m.p.): decomposed at 238.5 °C. ¹H-NMR (500 MHz, DMSO-*d*₆) δ 10.17 (bs, *J* = 5.6 Hz, 2H), 8.12 (dd, *J* = 7.6, 1.0 Hz, 2H), 7.95 (dt, *J* = 7.6, 1.0 Hz, 2H), 7.54 (td, *J* = 7.6, 1.0 Hz, 2H), 7.42 (td, *J* = 7.6, 1.0 Hz, 2H), 5.61–5.57 (m, 1H), 3.27–3.17 (m, 1H), 1.18 (d, *J* = 6.5 Hz, 6H). ¹³C-NMR (126 MHz, dmso) δ 141.41, 138.60, 130.43, 128.33, 127.35, 121.21, 58.25, 48.44, 20.18. HRMS (ESI⁺): [M + H]⁺: calculated for C₁₆H₁₈N⁺ (*m/z*): 224.14392; found: 224.14343. LC-MS purity 99%.

2.2.2. *N*-Methyl-9*H*-fluoren-9-amine hydrochloride (**3b**)

Yield 13% as a white solid. M.p.: decomposed at 205.9 °C. ¹H-NMR (500 MHz, DMSO-*d*₆) δ 10.52 (bs, 2H), 8.07 (dd, *J* = 7.6, 1.0 Hz, 2H), 7.94 (dd, *J* = 7.6, 1.0 Hz, 2H), 7.53 (td, *J* = 7.6, 1.0 Hz, 2H), 7.42 (td, *J* = 7.6, 1.0 Hz, 2H), 5.64 (s, 1H), 2.12 (s, 3H). ¹³C-NMR (126 MHz, dmso) δ 141.42, 137.56, 130.25, 128.20, 126.62, 120.94, 59.75, 27.06. HRMS (ESI⁺): [M + H]⁺: calculated for C₁₄H₁₄N⁺ (*m/z*): 196.11262; found: 196.11229. LC-MS purity 100%.

2.2.3. *N*-Cyclohexyl-9*H*-fluoren-9-amine hydrochloride (**3c**)

Yield 43% as a white solid. M.p. 267.3–269.6 °C. ¹H-NMR (500 MHz, DMSO-*d*₆) δ 10.17 (bs, 2H), 8.10 (dd, *J* = 7.6, 1.0 Hz, 2H), 7.95 (dd, *J* = 7.6, 1.0 Hz, 2H), 7.54 (td, *J* = 7.6, 1.0 Hz, 2H), 7.42 (td, *J* = 7.6, 1.0 Hz, 2H), 5.60 (s, 1H), 2.84 (t, *J* = 11.5 Hz, 1H), 1.81–1.71 (m, 2H), 1.68–1.59 (m, 2H), 1.50 (m, *J* = 15.0, 5.3, 4.4 Hz, 3H), 1.13–1.00 (m, 3H). ¹³C-NMR (126 MHz, dmso) δ 141.09, 138.37, 130.15, 128.09, 127.00, 120.94, 57.68, 54.59, 29.72, 24.68, 23.99. HRMS (ESI⁺): [M + H]⁺: calculated for C₁₉H₂₂N⁺ (*m/z*): 264.17522; found: 264.17465. LC-MS purity 99%.

2.2.4. *N*-Cyclopropyl-9*H*-fluoren-9-amine hydrochloride (**3d**)

Yield 57% as a white solid. M.p.: decomposed at 233.1 °C. ¹H-NMR (500 MHz, DMSO-*d*₆) δ 10.63 (bs, 2H), 8.13 (dd, *J* = 7.6, 1.0 Hz, 2H), 7.94 (dd, *J* = 7.6, 1.0 Hz, 2H), 7.53 (td, *J* = 7.6, 1.0 Hz, 2H), 7.41 (td, *J* = 7.6, 1.0 Hz, 2H), 5.63 (s, 1H), 2.25–2.15 (m, 1H), 0.85–0.76 (m, 2H), 0.55–0.46 (m, 2H). ¹³C-NMR (126 MHz, dmso) δ 141.38, 138.07, 130.14, 127.95, 127.08, 120.82, 60.17, 26.24, 3.50. HRMS (ESI⁺): [M + H]⁺: calculated for C₁₆H₁₆N⁺ (*m/z*): 222.12827; found: 222.12776. LC-MS purity 99%.

2.2.5. *N*-Cyclobutyl-9*H*-fluoren-9-amine hydrochloride (**3e**)

Yield 51% as a white solid. M.p.: decomposed at 271.6 °C. ¹H-NMR (500 MHz, DMSO-*d*₆) δ 10.77 (bs, 2H), 8.10 (dd, *J* = 7.6, 1.0 Hz, 2H), 7.92 (dd, *J* = 7.6, 1.0 Hz, 2H), 7.52 (td, *J* = 7.6, 1.0 Hz, 2H), 7.40 (td, *J* = 7.6, 1.0 Hz, 2H), 5.57 (s, 1H), 3.12 (p, *J* = 9.1, 8.6 Hz, 1H), 2.22–2.10 (m, 2H), 1.62–1.41 (m, 4H). ¹³C-NMR (126 MHz, dmso) δ 141.23, 137.87, 130.16, 127.97, 126.96, 120.84, 58.50, 47.72, 27.67, 15.64. HRMS (ESI⁺): [M + H]⁺: calculated for C₁₇H₁₈N⁺ (*m/z*): 236.14392; found: 236.14333. LC-MS purity 99%.

2.2.6. 1-(9*H*-fluoren-9-yl)piperidine hydrochloride (**3f**)

Yield 45% as a white solid. M.p.: decomposed at 251.4 °C. ¹H-NMR (500 MHz, DMSO-*d*₆) δ 11.79 (bs, 1H), 8.24 (dd, *J* = 7.6, 1.0 Hz, 2H), 7.94 (dd, *J* = 7.6, 1.0 Hz, 2H), 7.55 (td, *J* = 7.6, 1.0 Hz, 2H), 7.42 (td, *J* = 7.6, 1.0 Hz, 2H), 5.72 (s, 1H), 3.23 (d, *J* = 11.7 Hz, 2H), 2.79 (q, *J* = 11.7 Hz, 2H), 2.07 (q, *J* = 12.6, 11.7 Hz, 2H), 1.67 (d, *J* = 12.6 Hz, 3H), 1.34–1.20 (m, 1H). ¹³C-NMR (126 MHz, dmso) δ 141.83, 135.94, 130.66, 128.29, 128.17, 120.91, 67.23, 49.46, 22.29, 21.67. HRMS (ESI⁺): [M + H]⁺: calculated for C₁₈H₂₀N⁺ (*m/z*): 250.15957; found: 250.15875. LC-MS purity 98%.

2.2.7. *N*-(2-methoxyethyl)-9*H*-fluoren-9-amine hydrochloride (**3g**)

Yield 11% as a white solid. M.p.: 183.4–185.1 °C. ¹H-NMR (500 MHz, DMSO-*d*₆) δ 10.60 (bs, 2H), 8.15 (dd, *J* = 7.6, 1.0 Hz, 2H), 7.93 (dd, *J* = 7.6, 1.0 Hz, 2H), 7.53 (td, *J* = 7.6, 1.0 Hz, 2H), 7.42 (td, *J* = 7.6, 1.0 Hz, 2H), 5.59 (s, 1H), 3.47 (t, *J* = 5.2 Hz, 2H), 3.19 (s, 3H), 2.47–2.40 (m, 2H). ¹³C-NMR (126 MHz, dmso) δ 141.42, 137.56, 130.27, 128.26, 126.69,

120.93, 67.03, 59.32, 58.16, 40.87. HRMS (ESI⁺): [M + H]⁺: calculated for C₁₆H₁₈NO⁺ (*m/z*): 240.13884; found: 240.13831. LC-MS purity 99%.

2.2.8. *N*-Ethyl-9*H*-fluoren-9-amine hydrochloride (**3h**)

Yield 36% as a white solid. M.p.: decomposed at 264.8 °C. ¹H-NMR (500 MHz, DMSO-*d*₆) δ 10.46 (bs, *J* = 9.3 Hz, 2H), 8.12 (dd, *J* = 7.6, 1.0 Hz, 2H), 7.94 (dd, *J* = 7.6, 1.0 Hz, 2H), 7.53 (td, *J* = 7.6, 1.0 Hz, 2H), 7.42 (td, *J* = 7.6, 1.0 Hz, 2H), 5.61 (d, *J* = 3.5 Hz, 1H), 2.51–2.48 (m, 2H), 1.14 (t, *J* = 7.2 Hz, 3H). ¹³C-NMR (126 MHz, dms) δ 141.29, 137.89, 130.19, 128.18, 126.72, 120.91, 59.17, 37.35, 11.53. HRMS (ESI⁺): [M + H]⁺: calculated for C₁₅H₁₆N⁺ (*m/z*): 210.12827; found: 210.12784. LC-MS purity 99%.

2.2.9. *N,N*-Diethyl-9*H*-fluoren-9-amine hydrochloride (**3i**)

Yield 7% as a white solid. M.p.: 166.2–167.9 °C. ¹H-NMR (500 MHz, DMSO-*d*₆) δ 11.66 (bs, 1H), 8.15 (dd, *J* = 7.6, 1.0 Hz, 2H), 7.98 (dd, *J* = 7.6, 1.0 Hz, 2H), 7.57 (td, *J* = 7.6, 1.0 Hz, 2H), 7.44 (td, *J* = 7.6, 1.0 Hz, 2H), 5.85 (s, 1H), 3.12–3.02 (m, 1H), 3.02–2.94 (m, 1H), 1.30 (t, *J* = 7.2 Hz, 6H). ¹³C-NMR (126 MHz, dms) δ 141.62, 136.45, 130.54, 128.37, 127.49, 121.07, 63.15, 46.29, 10.32. HRMS (ESI⁺): [M + H]⁺: calculated for C₁₇H₂₀N⁺ (*m/z*): 238.15957; found: 238.15903. LC-MS purity 99%.

2.2.10. 1-(9*H*-fluorene-9-yl)-4-methylpiperazine dihydrochloride (**3j**)

Yield 7% as a white solid. M.p.: decomposed at 206.4 °C. ¹H-NMR (500 MHz, DMSO-*d*₆) δ 10.80 (bs, 1H), 7.85 (dd, *J* = 7.6, 1.0 Hz, 2H), 7.59 (dd, *J* = 7.6, 1.0 Hz, 2H), 7.42 (td, *J* = 7.6, 1.0 Hz, 2H), 7.34 (td, *J* = 7.6, 1.0 Hz, 2H), 5.03 (s, 1H), 3.31–2.71 (m, 8H), 2.68 (s, 3H). ¹³C-NMR (126 MHz, dms) δ 143.00, 140.64, 128.64, 127.51, 125.88, 120.36, 68.65, 53.41, 45.50, 42.34. HRMS (ESI⁺): [M + H]⁺: calculated for C₁₈H₂₁N₂⁺ (*m/z*): 265.17047; found: 265.16974. LC-MS purity 99%.

2.2.11. 1-(9*H*-fluorene-9-yl)-4-ethylpiperazine dihydrochloride (**3k**)

Yield 25% as a white solid. M.p.: decomposed at 233.6 °C. ¹H-NMR (500 MHz, DMSO-*d*₆) δ 10.75 (bs, 1H), 7.85 (dd, *J* = 7.6, 1.0 Hz, 2H), 7.59 (dd, *J* = 7.6, 1.0 Hz, 2H), 7.42 (td, *J* = 7.6, 1.0 Hz, 2H), 7.33 (td, *J* = 7.6, 1.0 Hz, 2H), 5.03 (s, 1H), 3.02 (q, *J* = 7.3 Hz, 2H), 2.99–2.61 (m, 8H), 1.19 (t, *J* = 7.3 Hz, 3H). ¹³C-NMR (126 MHz, dms) δ 143.05, 140.63, 128.62, 127.49, 125.90, 120.34, 68.67, 51.28, 50.79, 45.45, 9.01. HRMS (ESI⁺): [M + H]⁺: calculated for C₁₉H₂₄N₂⁺ (*m/z*): 279.18612; found: 279.18555. LC-MS purity 99%.

2.2.12. 4-(9*H*-fluorene-9-yl)morpholine hydrochloride (**3l**)

Yield 50% as a white solid. M.p.: decomposed at 239.8 °C. ¹H-NMR (500 MHz, DMSO-*d*₆) δ 12.66 (bs, 1H), 8.21 (dd, *J* = 7.6, 1.0 Hz, 2H), 7.96 (dd, *J* = 7.6, 1.0 Hz, 2H), 7.58 (td, *J* = 7.6, 1.0 Hz, 2H), 7.45 (td, *J* = 7.6, 1.0 Hz, 2H), 5.81 (s, 1H), 4.18–3.93 (m, 2H), 3.94–3.75 (m, 2H), 3.31–3.09 (m, 2H), 3.09–2.87 (m, 2H). ¹³C-NMR (126 MHz, DMSO) δ 142.19, 131.09, 128.60, 128.46, 121.30, 67.38, 63.41, 48.58. HRMS (ESI⁺): [M + H]⁺: calculated for C₁₇H₁₈NO⁺ (*m/z*): 252.13884; found: 252.13837. LC-MS purity 99%.

2.2.13. *N*-Butyl-9*H*-fluoren-9-amine hydrochloride (**3m**)

Yield 12% as a white solid. M.p.: decomposed at 201.3 °C. ¹H-NMR (500 MHz, DMSO-*d*₆) δ 10.13 (bs, 2H), 8.10 (dd, *J* = 7.6, 1.0 Hz, 2H), 7.93 (dd, *J* = 7.6, 1.0 Hz, 2H), 7.52 (td, *J* = 7.6, 1.0 Hz, 2H), 7.42 (td, *J* = 7.6, 1.0 Hz, 2H), 5.54 (s, 1H), 2.33 (t, 2H), 1.58–1.47 (m, 2H), 1.25–1.14 (m, 2H), 0.74 (t, *J* = 7.3 Hz, 3H). ¹³C-NMR (126 MHz, DMSO) δ 141.52, 130.26, 128.40, 126.78, 121.12, 59.98, 41.80, 28.70, 19.70, 13.86. HRMS (ESI⁺): [M + H]⁺: calculated for C₁₇H₂₀N⁺ (*m/z*): 238.15957; found: 238.15912. LC-MS purity 97%.

2.2.14. *N*-(2-methylpropyl)-9*H*-fluoren-9-amine hydrochloride (**3n**)

Yield 34% as a white solid. M.p.: 254.8–256.1 °C. ¹H-NMR (500 MHz, DMSO-*d*₆) δ 10.52 (bs, 2H), 8.19 (dd, *J* = 7.6, 1.0 Hz, 2H), 7.94 (dd, *J* = 7.6, 1.0 Hz, 2H), 7.54 (td, *J* = 7.6,

1.0 Hz, 2H), 7.44 (td, $J = 7.6$, 1.0 Hz, 2H), 5.62 (s, 1H), 2.13–2.03 (m, 2H), 1.98–1.85 (m, 1H), 0.82 (d, $J = 6.7$ Hz, 6H). ^{13}C -NMR (126 MHz, DMSO) δ 141.72, 137.87, 130.54, 128.56, 126.89, 121.22, 59.76, 48.58, 26.03, 20.52. HRMS (ESI⁺): [M + H]⁺: calculated for C₁₇H₂₀N⁺ (m/z): 238.15957; found: 238.15903. LC-MS purity 97%.

2.2.15. 1-(9H-fluoren-9-yl)pyrrolidine hydrochloride (3o)

Yield 30% as a white solid. M.p.: decomposed at 239.3 °C. ^1H -NMR (500 MHz, DMSO-*d*₆) δ 12.31 (bs, 1H), 8.14 (dd, $J = 7.6$, 1.0 Hz, 2H), 7.96 (dd, $J = 7.6$, 1.0 Hz, 2H), 7.56 (td, $J = 7.6$, 1.0 Hz, 2H), 7.43 (td, $J = 7.6$, 1.0 Hz, 2H), 5.84 (s, 1H), 3.49–3.27 (m, 2H; signal overlapped with residual DMSO), 3.13–2.92 (m, 2H), 1.97–1.72 (m, 4H). ^{13}C -NMR (126 MHz, DMSO) δ 141.85, 130.84, 128.57, 127.78, 121.22, 64.49, 50.55, 23.96. HRMS (ESI⁺): [M + H]⁺: calculated for C₁₇H₁₈N⁺ (m/z): 236.14392; detected: 236.14328. LC-MS purity 99%.

2.3. In Vitro Anti-ChE Assay

The human AChE/human BChE (*hAChE/hBChE*) inhibitory activity of the tested derivatives was determined using Ellman's method [46–48] and is expressed as IC₅₀, i.e., a concentration that reduces the cholinesterase activity by 50%. The human recombinant BChE and AChE were prepared at the Department of Toxicology and Military Pharmacy (Faculty of Military Health Sciences, Hradec Kralove, Czech Republic). 5,5'-dithiobis(2-nitrobenzoic acid) (Ellman's reagent, DTNB), phosphate buffer (PB, pH 7.4), acetylthiocholine (ATC), and butyrylthiocholine (BTC) were purchased from Sigma-Aldrich, Prague, Czech Republic. For measuring purposes, polystyrene Nunc 96-well microplates with a flat bottom shape (Thermo Fisher Scientific, Waltham, MA, USA) were utilized. All the assays were carried out in 0.1-M KH₂PO₄/K₂HPO₄ buffer, pH 7.4. Enzyme solutions were prepared at 2.0 units/mL in 2-mL aliquots. The assay medium (100 μL) consisted of 40 μL of 0.1-M phosphate buffer (pH 7.4), 20 μL of 0.01-M DTNB, 10 μL of the enzyme, and 20 μL of 0.01-M substrate (ATC/BTC iodide solution). Inhibitor solutions in the concentration range 10⁻³–10⁻¹¹ M were prepared, and IC₅₀ values were calculated. Tested compounds were preincubated for 5 min. The reaction was started by the immediate addition of 20 μL of the substrate. The activity was determined by measuring the increase in absorbance at 412 for *hAChE/hBChE* at 37 °C at 2 min intervals using a multimode microplate reader Synergy 2 (BioTek Instruments, Inc., Winooski, VT, USA). Each concentration was assayed in triplicate. Software GraphPad Prism 5 (San Diego, CA, USA) was used for the statistical data evaluation.

2.4. Kinetic Study of hBChE Inhibition

The kinetic study of *hBChE* was performed by using the above-mentioned modified Ellman's method. The values of V_{max} and K_m of the Michaelis-Menten kinetics, as well as the value of K_i , were calculated by nonlinear regression from the substrate velocity curves. Linear regression was used for calculation of the Cornish-Bowden plots. All calculations were performed using GraphPad Prism software version 6.07 for Windows (San Diego, CA, USA).

2.5. Antagonist Activity Towards the NMDA receptor

2.5.1. HEK293 Cell Culture and Transfection

Human embryonic kidney 293 (HEK293) cells were cultured in Opti-MEM I containing 5% fetal bovine serum (FBS; both from Thermo Fisher Scientific) [49]. The cells grown in a 24-well plate were put in Opti-MEM I media containing a mixture of 0.9 μL of MATra-A Reagent (IBA) and 900 ng of DNA vectors carrying the human versions of the GluN1-1a (GluN1), GluN2A, or GluN2B subunits and green fluorescent protein (GFP; all vectors were added in equal ratio) [39,50,51]. The cells were placed on a strong magnet plate for 30 min and then trypsinized; resuspended in Opti-MEM I containing 1% FBS, 20-mM MgCl₂, and 3-mM kynurenic acid (to inhibit the NMDAR-induced excitotoxicity); and plated on

poly-L-lysine-coated glass coverslips. The electrophysiological experiments were executed 24–48 h after transfection [52].

2.5.2. Electrophysiology

Whole-cell patch-clamp recordings were conducted at room temperature on the GFP-positive HEK293 cells using an Axopatch 200B amplifier (Molecular Devices, San Jose, CA, USA); the series resistance compensation was >80% for all cells [39]. The recorded currents were filtered at 2 kHz with an eight-pole low-pass Bessel filter and digitized at 5 kHz with Digidata 1322A and pClamp 10 software (Molecular Devices). The WAS02 application system, which can reach the solution exchange time around the recorded cell of 10–20 ms, was used to apply the extracellular solution (ECS) [53]. The ECS contained (in mM): 160 NaCl, 2.5 KCl, 10 HEPES, 10 glucose, 0.2 EDTA, and 0.7 CaCl₂ (pH adjusted to 7.3 with NaOH) and was supplemented with the saturating concentrations of co-agonists glycine (50 μM) and agonist glutamate (1 mM; both from Merck). The stock solutions of **3a–o** (10 mM) were prepared freshly before each experiment in dimethylsulfoxide (DMSO; Merck), and the background concentration of DMSO was kept equal in each ECS. The borosilicate glass pipettes with a tip resistance ~4–7 MΩ were made using a P-1000 micropipette puller (Sutter Instrument Co., Novato, CA, USA) and were filled with an intracellular solution (in mM: 125 gluconic acid, 15 CsCl, 5 EGTA, 10 HEPES, 3 MgCl₂, 0.5 CaCl₂, and 2 ATP-Mg salt (pH adjusted to 7.2 with CsOH)). Data were analyzed using SigmaPlot 14.0 (Systat Software, Inc., Chicago, IL, USA), and the dose-response curves were built using Equation (1): $I = 1 / (1 + ([\text{compound}] / IC_{50})^h)$, where IC₅₀ is the concentration of the compound that produces a 50% inhibition of the glutamate-evoked current, [compound] is the concentration of the studied compound, and h is the apparent Hill coefficient [54].

2.6. In Vitro Cell Viability Assessment

Standard MTT assay (3-(4,5-dimethylthiazol-2-yl)-2,5-diphenyltetrazolium bromide; Sigma Aldrich, Prague, Czech Republic) was used according to the manufacturer's protocols on the CHO-K1 (Chinese hamster ovary, ECACC, Salisbury, UK) and hCMEC/D3 (Sigma Aldrich, St. Louis, MO, USA). The cells were cultured according to recommended conditions and seeded in a density of 8000 cells per well, as described previously [55]. Briefly, the tested compounds were dissolved in dimethyl sulfoxide (DMSO; Sigma Aldrich, St. Louis, MO, USA) and subsequently diluted in the nutrient mixture F-12 ham growth medium (Sigma Aldrich, St. Louis, MO, USA), supplemented with 10% fetal bovine serum and 1% penicillin-streptomycin (both Sigma Aldrich, St. Louis, MO, USA), so that the final concentration of DMSO did not exceed 0.5% (v/v). CHO-K1 cells were exposed to serially diluted tested compounds for 24 h. Then, the medium was replaced by a fresh medium containing 0.5 mg/mL of MTT, and the cells were allowed to produce formazan for another approximately 3 h under surveillance. Thereafter, the medium with MTT was removed, and crystals of formazan were dissolved in DMSO (100 μL/well; PENTA s.r.o., Prague, Czech Republic). Cell viability was assessed spectrophotometrically by the amount of formazan produced. The absorbance was measured at 570 nm with a 650-nm reference wavelength on Synergy HT (BioTek, Winooski, VT, USA). The IC₅₀ value (half-maximal inhibitory concentration) was calculated from the control-subtracted triplicates using nonlinear regression (four parameters) by GraphPad Prism 7.03 software (GraphPad Software Inc., San Diego, CA, USA) for the CHO-K1 cell line, and for hCMEC/D3 cells, the cell viability was expressed as the % relative to the untreated control. Final IC₅₀ and SEM (standard error of the mean) values were obtained as a mean of three independent measurements.

2.7. Determination of In Vitro BBB Permeation

The D3 assay evaluates the ability of compounds to diffuse from the donor compartment through the D3/hCMEC cell membrane into the acceptor compartment. The D3 cells

were seeded on a PET membrane (area 1.12 cm²) with 3- μ m pores of the 12-well plates with 12-mm inserts. The tested compounds were dissolved in DMSO and then diluted with Opti-MEM to reach final a concentration of 30 μ M for **3m** and 50 μ M for others; the concentration of DMSO did not exceed 0.5% (*v/v*). The donor solution (750 μ L) was added to the donor compartment (insert), and the same volume of Opti-MEM was added into the acceptor. The concentration of the drug in both compartments was measured by UV-VIS spectrophotometry in 5, 15, 30, and 60 min of incubation in triplicates. The apparent permeability coefficient (P_{app}) was calculated from the concentration ratios. Tightness of the D3 monolayer was conducted by the fluorescein isothiocyanate (FITC) test after each experiment. The accepted values of FITC (fluorescein isothiocyanate) in 0.4 mg/mL in the acceptor compartment after 30 min of incubation must not exceed 1.5% of the initial donor concentration.

$$P_{app} = \left(\frac{dC}{dt} \right) \times \frac{V_r}{(A \times C_0)} \quad (1)$$

A: area of the well/cell monolayer,

dC/dt: amount in the receiver compartment in given time,

V_r : volume of the receiver compartment, and

C_0 : the initial concentration of tested compounds.

2.8. Molecular Modeling Studies

The model of hBChE (Protein Data Bank (PDB) ID: 4BDS, resolution: 2.10 Å) was downloaded from the RCSB Protein Data Bank (<https://rcsb.org>) and prepared for flexible molecular docking by MGL Tools [56,57]. The preparation of these receptors involved removal of the inhibitor, water molecules and nonbonded co-crystallized compounds, and the addition of polar hydrogens. Default Gasteiger charges were assigned to all atoms. Flexible parts of the enzymes were set based on previous experiences [58,59]. The rotatable bonds in the flexible residues were detected automatically by AutoDock Tools 1.5.4. The flexible receptor parts contained 39 residues. The studied ligands were firstly drawn in HyperChem 8.0, then manually protonated, as suggested by MarvinSketch 18.24.0 software (<http://www.chemaxon.com>), geometrically optimized by software Avogadro, and stored as pdb files. The structures of the ligands were processed for docking by the AutoDock Tools 1.5.4 program. Molecular docking was carried out by the software AutoDock Vina 1.1.2 utilizing computer resources of the Czech National Grid Infrastructure MetaCentrum. The search algorithm of AutoDock Vina efficiently combines a Markov chain Monte Carlo-like method for the global search and a Broyden-Fletcher-Goldfarb-Shano gradient approach for the local search [60]. It is a type of memetic algorithm based on interleaving stochastic and deterministic calculations [61]. Each docking task was repeated 20 times with the exhaustiveness parameter set to 8, employing 8 CPUs in parallel multithreading. From the obtained results, the solutions reaching the minimum docking score were taken as the top-scoring modes. The graphical representations of the docked poses were shown in PyMOL (The PyMOL Molecular Graphics System, Version 2.0.6. Schrödinger, LLC, New York, NY, USA). 2D diagrams were generated using Maestro 12.3 (Schrödinger Release, Schrödinger, LLC, New York, NY, USA).

2.9. In Silico Pharmacokinetics and Drug-Likeness Prediction

SwissADME, web tool was used to predict gastrointestinal absorption, BBB permeation and bioavailability [62]. Physicochemical properties (pK_a , $ClogP$, HBA, HBD, and TPSA) were predicted by MarvinSketch 20.4.0, ChemAxon Ltd. (Budapest, Hungary; see Table S1, Supplementary Materials). BBB scores were calculated by the BBB calculator available at the ACS website [63].

3. Results and Discussion

3.1. In Silico Prediction of the CNS and Oral Availability

All the newly designed compounds were initially screened in silico to predict their peroral and CNS availability. Indeed, both of these features are essential in the drug discovery process of small molecules as potential anti-AD therapeutics and should be estimated before synthesis. To this end, the in silico pharmacokinetics; drug-likeness; and ADME (absorption, distribution, metabolism, and excretion) prediction was applied to compounds **3a–o** using a web-based tool SwissADME [62,64,65]. THA and memantine were used as references with known CNS statuses and pharmacokinetic profiles [42,66,67]. Data are presented in Figures 2 and 3 and Table 1 and Table S1.

Table 1. Summary of the in silico absorption, distribution, metabolism, and excretion (ADME) and drug-likeness of derivatives **3a–o** with tacrine (THA) and memantine using various prediction models.

Compound	GIA ^a	BBB ^b	BBB Score ^c	Lipinski ^d	Bio. Score ^e
3a	High	Yes	5.63	Yes	0.55
3b	High	Yes	5.63	Yes	0.55
3c	High	Yes	5.59	Yes	0.55
3d	High	Yes	5.64	Yes	0.55
3e	High	Yes	5.93	Yes	0.55
3f	High	Yes	5.15	Yes	0.55
3g	High	Yes	5.68	Yes	0.55
3h	High	Yes	5.63	Yes	0.55
3i	High	Yes	5.17	Yes	0.55
3j	High	Yes	5.67	Yes	0.55
3k	High	Yes	5.86	Yes	0.55
3l	High	Yes	5.55	Yes	0.55
3m	High	Yes	5.62	Yes	0.55
3n	High	Yes	5.62	Yes	0.55
3o	High	Yes	5.72	Yes	0.55
THA	High	Yes	5.38	Yes	0.55
Memantine	High	Yes	4.61	Yes	0.55

^a GIA = gastrointestinal absorption, ^b BBB = blood–brain barrier permeation, ^c Reference [63],

^d Reference [68], and ^e Bio. Score = bioavailability score [69].

The pink middle area (Figures 2 and 3) represents the optimum range for bioavailability. It is a sum of the lipophilicity (LIPO), size, polarity (POLAR), solubility (INSOLU), saturation (INSATU), and flexibility (FLEX). The red lines show the predicted state for the designed compounds [62,64,65]. The calculated parameters for all the compounds, except for **3b** and **3h**, are situated inside the pink area, suggesting their high oral bioavailability [69]. A positive correlation for the bioavailability was also supported by the BOILED-Egg method [70], proposing high gastrointestinal adsorption and penetration through the BBB [70]. The BBB score, a new predictive model for CNS availability, was also calculated for all the derivatives fitting the range between 5 and 6, indicating a high probability to permeate through the BBB (estimated physicochemical parameters are shown in Table S1, Supplementary Materials) [63]. Besides, all compounds also fulfill the drug-likeness rules of pharmacological models defined by pharmaceutical companies like Veber's (GSK) [71], Lipinski's (Pfizer) [72], Egan's (Pharmacopeia) [73], Ghose's (Amgen) [74], and Muegge's (Bayer) [75] (Table S2, Supplementary Materials). In summary, derivatives **3a–o** unambiguously show high predictive peroral bioavailability, BBB permeation, and acceptable pharmacokinetic profiles, making the compounds prospective candidates for the treatment of CNS disorders, including AD.

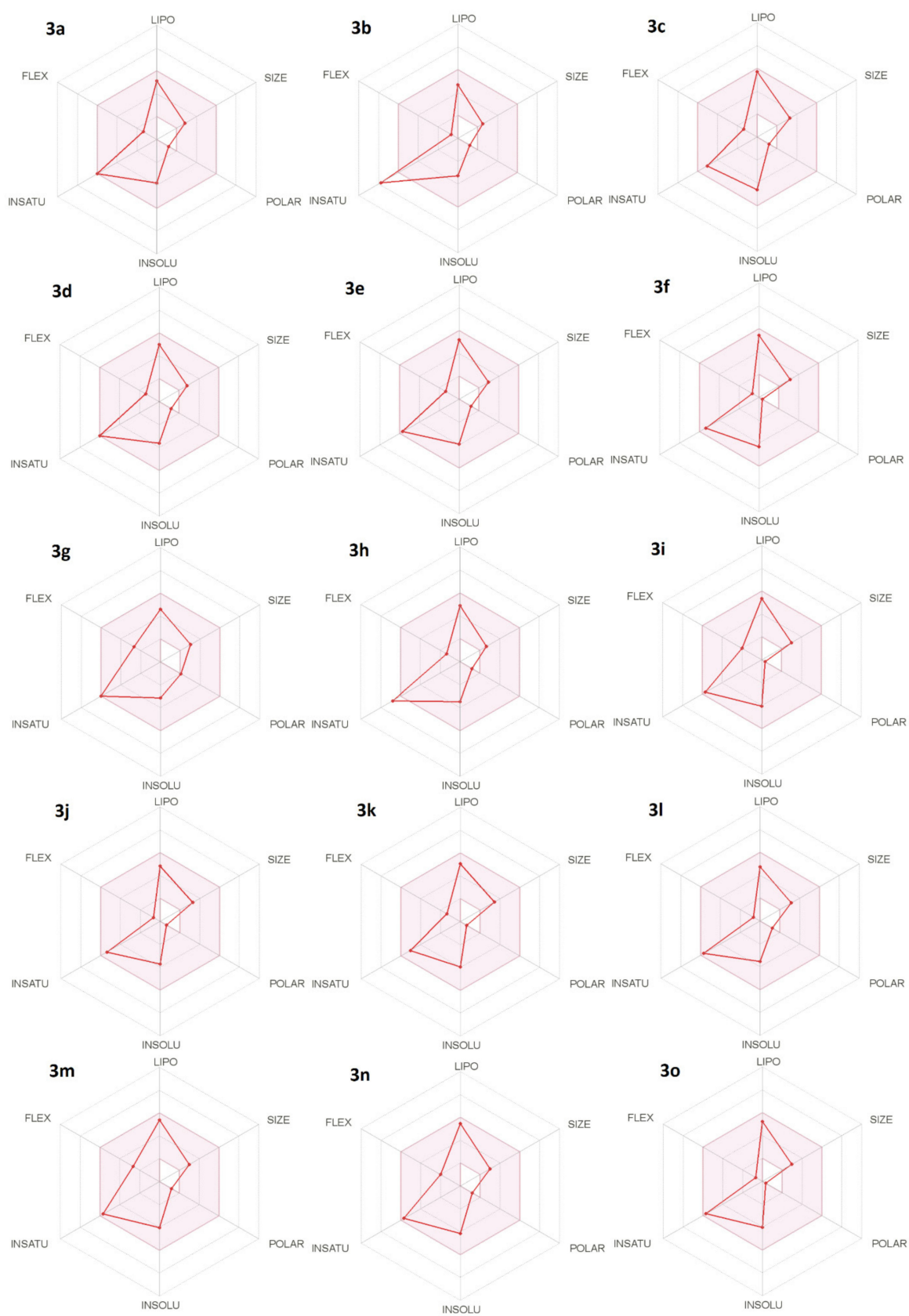


Figure 2. The bioavailability radar chart of the designed fluorene-9-amines **3a–o**.

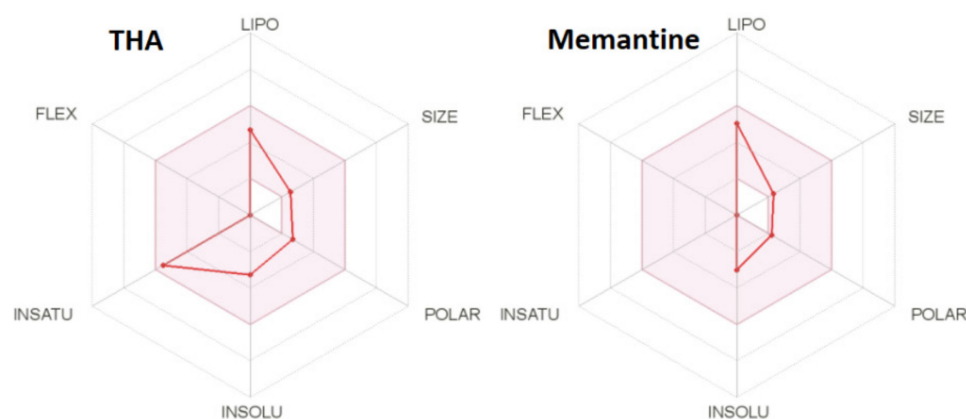


Figure 3. The bioavailability radar chart for the standards THA and memantine (please see detailed description in the text).

3.2. Synthesis

Fluoren-9-amines were prepared in a one-step procedure from commercially available 9-bromofluorene (**1**) with an excess of various primary or secondary amines (**2a–o**) in dry acetonitrile (Scheme 1). This reaction afforded the formation of fluoren-9-amines (**3a–o**) in high yields (80–95%). The free bases were then converted to the respective hydrochloride salts. The final products were characterized by ^1H , ^{13}C -NMR spectra, melting points, and HRMS analysis. LC analysis confirmed the purity for all the derivatives > 97% (Supplementary Materials).

3.3. Evaluation of Cholinesterase Inhibitory Activity

Fluoren-9-amines were tested for their inhibitory potential against human AChE (*hAChE*) and human BChE (*hBChE*) enzymes using the modified spectrophotometric method of Ellman et al. [46,48,76]. THA was used as a reference compound. The IC_{50} values of all tested compounds and their selectivity indexes (SI) for *hBChE* are summarized in Table 2. All tested derivatives showed a preferential inhibition of *hBChE* (usually in the single-digit micromolar range), whereas only compounds **3c** and **3m** showed weak inhibitory activity for *hAChE* at 13.98 and 49.91 μM , respectively. The *hBChE* inhibition ranged between 0.47–54.65 μM . According to the *hBChE* inhibition potency, the top-ranked derivative from all the derivatives under the study was **3c** ($\text{IC}_{50} = 0.47 \mu\text{M}$), being 20 times less active compared to THA. However, the relatively unique selectivity to BChE is of immense interest. Indeed, the selectivity profile for the ChE drugs potentially useful in AD treatment is extensively discussed [77]. The currently used ChE inhibitors are AChE-selective (donepezil) or possess more or less nonselective patterns of inhibition (rivastigmine and galantamine) [25]. It was proven that the levels of BChE in the brain of AD patients are elevated with age, while the levels of AChE are suppressed. This finding underlines the importance of selective-BChE inhibitors in the treatment of the later stages of AD [77,78].

3.4. Kinetic Study of *hBChE* Inhibition

To determine the inhibition pattern of **3c**, a kinetic study was performed to elucidate the interaction mechanism of the compound with *hBChE*. The kinetics of the inhibition were revealed from velocity curves measured at several concentrations of **3c** and the *hBChE* substrate butyrylthiocholine. The type of enzyme inhibition and appropriate affinity parameter (K_i) were determined using nonlinear regression analysis. The results for each type of model of inhibition (competitive, noncompetitive, uncompetitive, and mixed) were compared by the sum-of-squares *F*-test. A statistical analysis showed a competitive type of inhibition for *hBChE* ($p < 0.05$) that was in line with the Cornish–Bowden plot used for visualization of the obtained data (Figure 4).

Table 2. The inhibitory activities of compounds **3a–o** for human acetylcholinesterase (*hAChE*) and human butyrylcholinesterase (*hBChE*).

Compound	IC ₅₀ ± SEM (μM) ^a		SI for BChE ^b
	<i>hAChE</i>	<i>hBChE</i>	
3a	n.a.	2.95 ± 0.09	-
3b	n.a.	8.91 ± 0.31	-
3c	13.98 ± 0.35	0.47 ± 0.01	29.7
3d	n.a.	6.42 ± 0.22	-
3e	n.a.	2.03 ± 0.08	-
3f	n.a.	2.13 ± 0.06	-
3g	n.a.	2.56 ± 0.11	-
3h	n.a.	6.58 ± 0.19	-
3i	n.a.	5.38 ± 0.11	-
3j	n.a.	23.5 ± 0.8	-
3k	n.a.	12.8 ± 0.3	-
3l	n.a.	54.7 ± 1.9	-
3m	49.91 ± 3.05	1.02 ± 0.03	48.9
3n	n.a.	0.90 ± 0.02	-
3o	n.a.	1.80 ± 0.06	-
THA ^c	0.50 ± 0.10 ^c	0.023 ± 0.003 ^c	21.7

^a Results are expressed as the mean of at least three experiments ± SEM. n.a. stands for not active at the tested concentration scale. ^b SI = selectivity index; the selectivity for *hBChE* is determined as a ratio of the half-maximal inhibitory concentration (IC₅₀)(*hAChE*)/IC₅₀(*hBChE*). ^c Data taken from Reference [79].

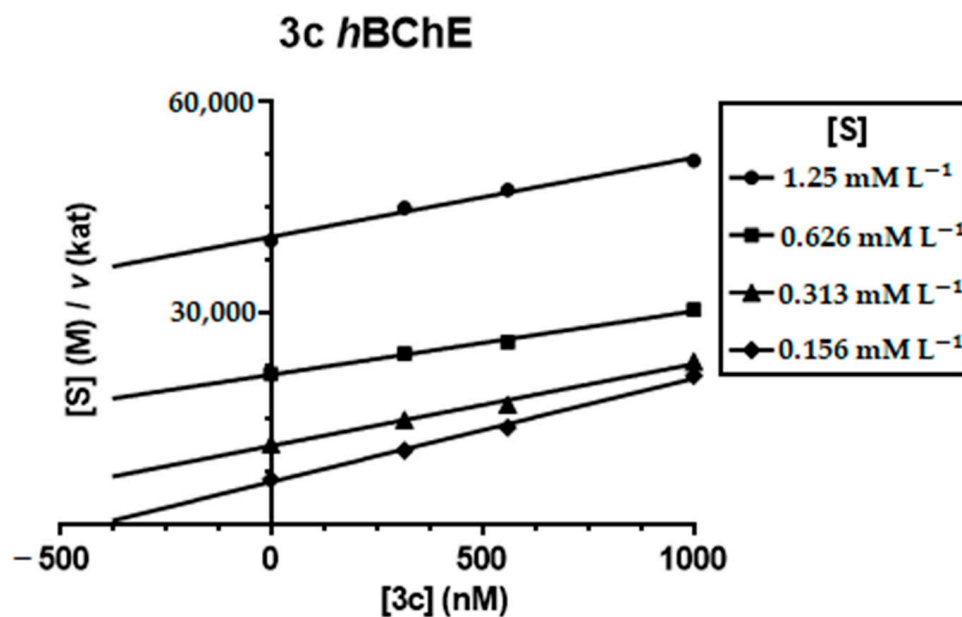


Figure 4. Steady-state inhibition of the *hBChE* substrate (human butyrylthiocholine) hydrolysis by compound **3c** at different concentrations. Cornish–Bowden plots of (S)/*v* against the (I) of the initial velocity at increasing substrate concentrations (2.5–20.0 mM) are presented. Lines were derived from the linear regression of the data points. Each point is the average of three determinations.

The parallel lines indicate a competitive inhibition of *hBChE* by **3c**, which means a reversible binding mode to the active site of the enzyme. With the increasing concentration of the inhibitor, the apparent V_{\max} remained unchanged and K_m increased. A K_i value of 173 ± 25 nM was determined for **3c** on *hBChE*.

3.5. Evaluation of Antagonist Activity towards the NMDA Receptor

Further, we aimed to examine the effects of all synthesized compounds (**3a–o**) at both the GluN1/GluN2A and GluN1/GluN2B receptors. First, we held the transfected cells at a membrane potential of -60 mV, and we assessed the relative inhibitory effect of each compound at a $10\text{-}\mu\text{M}$ concentration upon its application with the (co-)agonists (Figure 4). These experiments showed that all studied compounds exhibited an inhibitory effect ranging from $\sim 7\%$ to $\sim 52\%$ at both studied NMDAR combinations (Table 3). Interestingly, we revealed that **3e** was the most potent compound at the GluN1/GluN2A receptors, while **3m** was at the GluN1/GluN2B receptors. Subsequently, we generated concentration-response curves for **3e** and **3m** ($1\text{--}300\ \mu\text{M}$) for both the GluN1/GluN2A and GluN1/GluN2B receptors at the negative (-60 mV) and positive (40 mV) membrane potentials (Figure 5). Our analysis showed that both compounds exhibited a more profound inhibitory effect at the negative membrane potential (IC_{50} values ranged from $\sim 9\ \mu\text{M}$ to $\sim 15\ \mu\text{M}$), while they were much less potent at the positive membrane potential (IC_{50} values ranged from $\sim 83\ \mu\text{M}$ to $\sim 221\ \mu\text{M}$); the results are summarized in Table 4. Together, our data show that both **3e** and **3m** act as potent voltage-dependent inhibitors of the NMDARs, suggesting that they act as open-channel blockers of NMDARs. Interestingly, the IC_{50} values for both **3e** and **3m** at the GluN1/GluN2A and GluN1/GluN2B receptors were in a similar range to those previously obtained with THA (Table 4) [39]. However, both **3e** and **3m** were less potent than memantine under the studied conditions (Table 4).

3.6. In Vitro Cell Viability Assessment

The in vitro cytotoxicity evaluation on mammalian cells served as a preliminary toxicity indicator for the newly developed compounds (Table 5). In our previous work, we observed a correlation between the calculated $\log P$ (ClogP) values (MarvinSketch software, v. 18.24.0; Table 5) and the toxicity; however, our results within the presented study showed no clear relationship [80]. For instance, one of the most lipophilic compounds (**3f**) yielded as the least toxic, whereas other more hydrophilic fluoren-9-amines were regarded as low-toxic (e.g., **3g** as the most hydrophilic compound) agents as well. The least cytotoxic compound can be classified as **3f** with an attached piperidine moiety. At the pole separation, the most cytotoxic agents were **3c**, **3m**, and **3e**. Importantly, some of the new derivatives were less cytotoxic than THA.

Table 3. The inhibitory effect of the derivatives **3a–o** at the GluN1/GluN2A and GluN1/GluN2B receptors.

Compound	GluN1/GluN2A		GluN1/GluN2B	
	RI ^a (%) \pm SEM	n	RI ^a (%) \pm SEM	n
3a	33.29 \pm 1.66	4	25.00 \pm 1.82	4
3b	36.16 \pm 2.16	4	18.01 \pm 0.78	4
3c	41.02 \pm 3.56	5	17.24 \pm 2.39	4
3d	26.56 \pm 0.85	5	14.26 \pm 0.35	5
3e	52.30 \pm 4.18	5	44.79 \pm 3.43	5
3f	33.01 \pm 1.96	5	19.35 \pm 2.65	5
3g	18.68 \pm 1.98	5	6.76 \pm 1.00	4
3h	26.90 \pm 2.14	5	17.48 \pm 2.46	5
3i	25.66 \pm 1.92	5	20.12 \pm 2.82	5
3j	29.15 \pm 2.85	4	21.88 \pm 2.10	4
3k	32.08 \pm 1.01	4	19.12 \pm 1.48	6
3l	14.89 \pm 1.76	4	11.64 \pm 0.52	5
3m	36.23 \pm 3.73	6	51.22 \pm 3.24	5
3n	37.87 \pm 2.43	6	49.71 \pm 1.72	5
3o	27.80 \pm 1.74	5	32.39 \pm 2.99	5

^a The relative inhibition (RI) was calculated as the ratio of the steady-state currents in the presence and absence of $10\ \mu\text{M}$ of the compound (multiplied by 100) at the membrane potential of -60 mV (see text for more details). Data are shown as mean \pm SEM; n = number of recorded cells (see Figure 5).

Table 4. The activity of derivatives **3e** and **3m** at the *N*-methyl-D-aspartate (NMDA) receptors at different membrane potentials compared to THA and memantine (Mem).

	GluN1/GluN2A ^a					GluN1/GluN2B ^a				
	IC ₅₀ −60 mV	<i>h</i> −60 mV	IC ₅₀ 40 mV	<i>h</i> 40 mV	<i>n</i> (−60/ 40 mV)	IC ₅₀ −60 mV	<i>h</i> −60 mV	IC ₅₀ 40 mV	<i>h</i> 40 mV	<i>n</i> (−60/ 40 mV)
3e	8.85 ± 1.21	1.07 ± 0.05	82.62 ± 14.17	1.28 ± 0.12	8/5	15.27 ± 2.38	1.17 ± 0.05	156.40 ± 14.94	1.10 ± 0.08	12/7
3m	14.21 ± 1.60	1.19 ± 0.14	113.99 ± 26.63	1.23 ± 0.13	5/4	11.67 ± 1.72	1.12 ± 0.05	220.78 ± 12.24	0.97 ± 0.10	9/6
THA ^b	9.1 ± 0.5	1.7 ± 0.0	84.6 ± 1.6	1.6 ± 0.1	8/4	19.7 ± 1.8	1.8 ± 0.1	168.8 ± 9.3	1.4 ± 0.1	9/6
Mem ^b	1.34 ± 0.08	1.04 ± 0.06	27.04 ± 1.19	1.16 ± 0.05	6/7	0.78 ± 0.09	1.04 ± 0.03	10.57 ± 0.63	0.84 ± 0.04	5/6

^a The experimental data obtained using six concentrations of each compound (1, 3, 10, 30, 100, and 300 μM) were fitted by Equation (1) (see Section 2.5.2); the values of the IC₅₀ (in μM), Hill coefficient (*h*), and numbers of analyzed cells (*n*) obtained from the membrane potentials of −60 mV or 40 mV are shown as mean ± SEM. Dose-response relationships of the inhibitory effects of **3e** or **3m** at the GluN1/GluN2A and GluN1/GluN2B receptors (see Figure 6). ^b THA values were published by our group recently [39]. Mem corresponds to memantine.

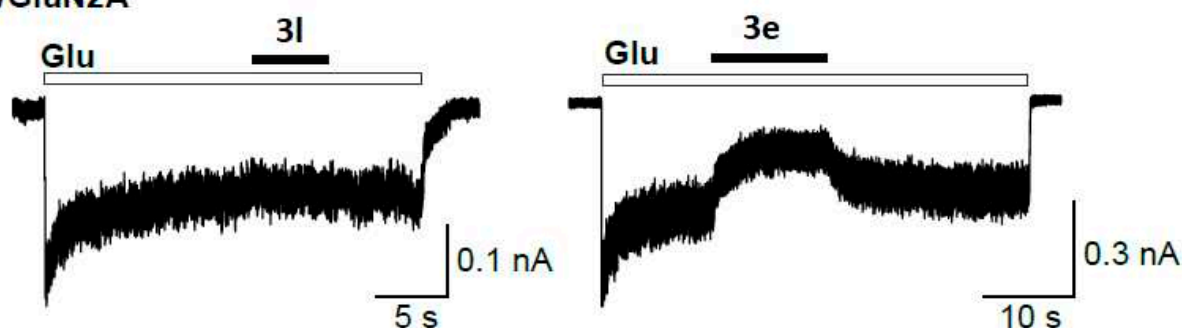
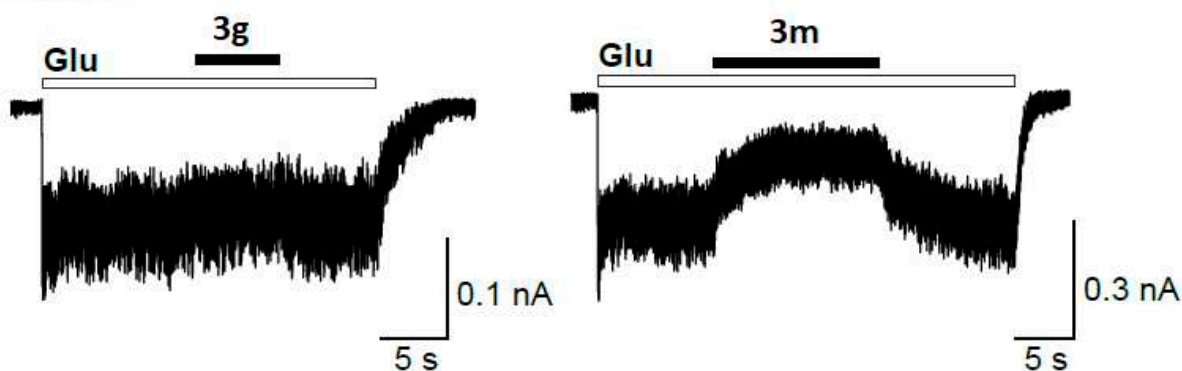
A GluN1/GluN2A**B GluN1/GluN2B**

Figure 5. The examples of the most (**3e** and **3m**) and least (**3l** and **3g**) potent compounds from all tested fluoren-9-amines at the NMDARs. Representative whole-cell currents induced by 1 mM of glutamate (Glu) and 50 μM of glycine at the negative (−60 mV) membrane potential with (A) the least potent compounds: **3l** measured at GluN1/GluN2A and **3g** at GluN1/GluN2B NMDARs and (B) the most potent compounds: **3e** measured at GluN1/GluN2A and **3m** at GluN1/GluN2B NMDA receptor (see Table 3).

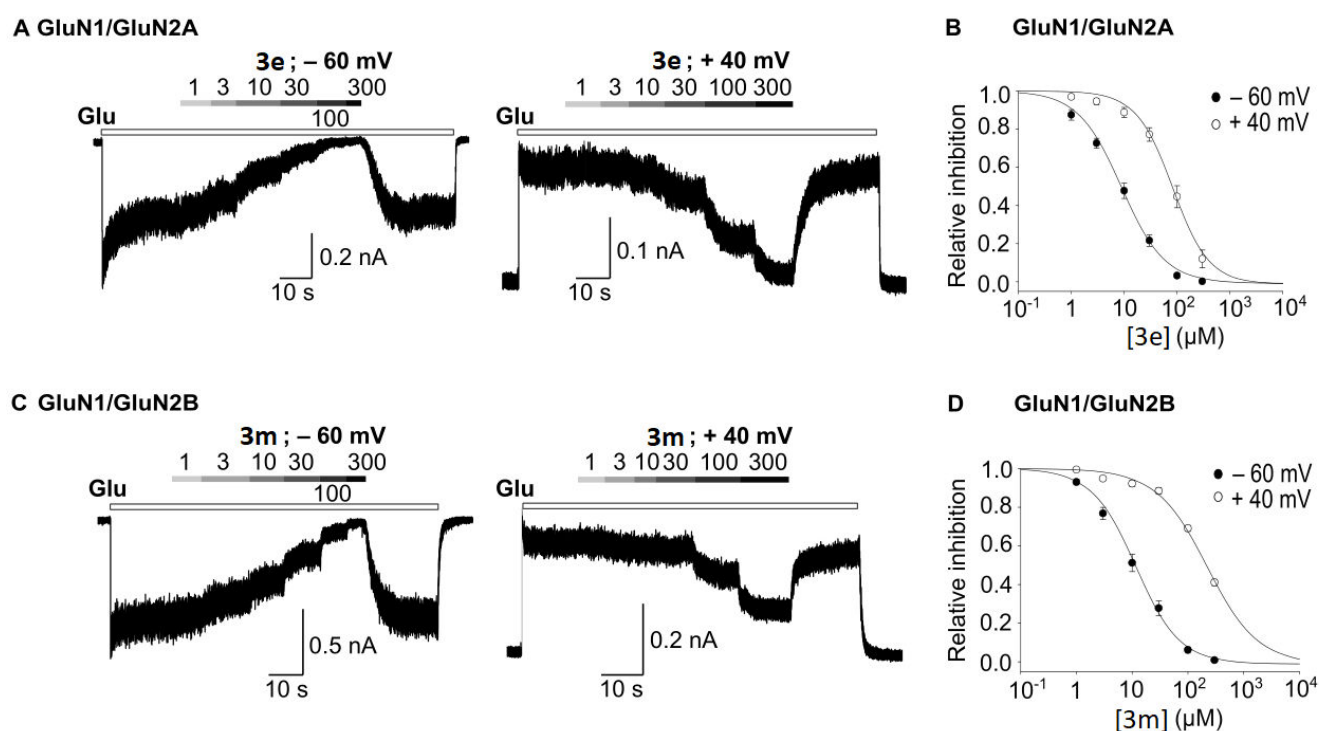


Figure 6. The most potent inhibitory compounds **3e** and **3m** acting at the GluN1/GluN2A and GluN1/GluN2B receptors. (A) Whole-cell representative currents of the GluN1/GluN2A receptors showing the inhibitory effects of **3e** (1–300 μM) at membrane potentials –60 mV and +40 mV. (C) Representative currents of the GluN1/GluN2B receptors inhibited by **3m** (1–300 μM) at membrane potentials –60 mV and +40 mV. (B,D) Dose-response inhibitory curves at two membrane potentials (–60 and +40 mV) at the GluN1/GluN2A receptors for **3e** (B) and at the GluN1/GluN2B receptors for **3m** (D). The inhibition dose-response curves were fitted by Equation (1) (see Section 2.5.2); the resulting values are shown in Table 4.

Table 5. The effects of the tested compounds on the CHO-K1 cell viability.

Compound.	IC ₅₀ ± SEM (μM) ^a	ClogP
3a	387 ± 32	3.76
3b	427 ± 12	2.99
3c	111 ± 10	4.79
3d	353 ± 32	3.46
3e	192 ± 3	3.90
3f	872 ± 10	4.22
3g	738 ± 1	2.94
3h	417 ± 16	3.35
3i	266 ± 3	4.09
3j	259 ± 12	3.22
3k	239 ± 35	3.58
3l	>800 ^b	3.15
3m	140 ± 15	4.31
3n	236 ± 24	4.29
3o	413 ± 15	3.78
THA	248 ± 11 ^c	2.63

^a Values are expressed as the mean of three independent measurements. ^b Determined at the maximum solubility of the compound. ^c Data taken from Reference [81]. ClogP: calculated logP.

3.7. In Vitro BBB Permeation

The top-ranked BChE inhibitors and NMDA receptor antagonists were selected (i.e., **3e**, **3n**, **3c**, and **3m**) to evaluate their ability to cross the BBB. For this reason, we used the human brain microvascular endothelial cell line hCMEC/D3 as a suitable model for the

normal human BBB [82]. Before that, we investigated whether the applied concentration (50 μ M) of the tested compound negatively influenced the cell viability in the monolayer. Despite the relatively low toxicity of the CHO-K1 model, we investigated the effects on the cell viability of the hCMEC/D3 line using MTT at 100 and 50 μ M (Table S3). We found that all tested compounds at 50 μ M did not substantially reduce the cell viability (>90% of viable cells), except **3m**, which reduced the cell viability to approx. 82% at 50 μ M. Due to this fact, a concentration of 30 μ M was used for the BBB permeation test for **3m**.

To investigate the potential of the BBB permeation, we used a panel of reference drugs for which the BBB permeation in vivo is known and correlated the P_{app} values to them. Thus, our measurements predict that the compounds **3c**, **3e**, and **3n** have a low potential to passively pass the BBB. On the other hand, the P_{app} value for **3m** corresponds to those of standard drugs with high CNS permeability (Table 6).

Table 6. Prediction of the BBB penetration of drugs expressed as the apparent permeability coefficient (P_{app}) \pm SEM.

Compound	$P_{app} \pm \text{SEM} (\times 10^{-6} \text{ cm s}^{-1})$	CNS (+/−) ^a	N ^b
3e	13.51 \pm 1.54	CNS −	3
3n	14.61 \pm 1.88	CNS −	3
3c	12.28 \pm 2.33	CNS −	3
3m	18.48 \pm 2.37	CNS +	4
THA	22.29 \pm 2.01	CNS +	4
Donepezil	24.19 \pm 2.83	CNS +	4
Rivastigmine	28.63 \pm 4.64	CNS +	5
Propranolol	23.06 \pm 2.06	CNS +	5
Antipyrine	17.19 \pm 1.82	CNS +	3
Furosemide	13.89 \pm 0.92	CNS −	3
Obidoxime	14.35 \pm 0.52	CNS −	4

^a CNS+ and CNS− represent the final predictions of the compound capability to cross or not to cross the BBB, respectively. ^b n stands for the number of independent experiments.

3.8. In Silico Studies

To better understand the inhibition mechanism between hBChE with **3c** (Figure 7A,B) and **3n** (Figure 7C,D), respectively, as the top-ranked inhibitors of the respective enzyme, we performed a molecular modeling simulation. The crystal structure of the THA-hBChE complex (Figure 7E,F; PDB ID: 4BDS) was used for comparative purposes [56]. In line with the compounds' designs, both of the inspected fluoren-9-amines **3c** and **3n** adopted a similar arrangement to that of THA within the hBChE active site. The crucial observation is that the tricyclic cores of both new molecules interact with Trp82 via parallel π - π stacking in the anionic site of the enzyme. The protonated amino group enabled hydrogen bond formation to carboxylic oxygen from Asp70 (**3c** and **3n**) and the hydroxyl group from Tyr332 (**3n**). In the case of THA, this type of interaction is replaced by two water bridges with the primary amino group. From the catalytic triad residues (His438, Glu197, and Ser198), only His438 is involved in hydrophobic contact with **3c** and **3n**, whereas THA is involved in direct hydrogen contact with this residue. The docking results also highlighted the importance of the attached appendages. Both aliphatic parts, either the cyclohexyl (**3c**) or *iso*-butyl (**3n**) moiety, are engaged in hydrophobic contacts with the Tyr332, Phe329, and Ala328 residues. The cyclohexyl moiety of **3c** seems to deliver another hydrophobic contact to Pro285 and Gly78 that presumably mediates a slightly higher inhibition potency. Contrary to THA anchoring, missing cation- π contacts in the **3c**- and **3n**-hBChE complexes can be denoted as the culprit responsible for the slightly decreased affinity of these two agents.

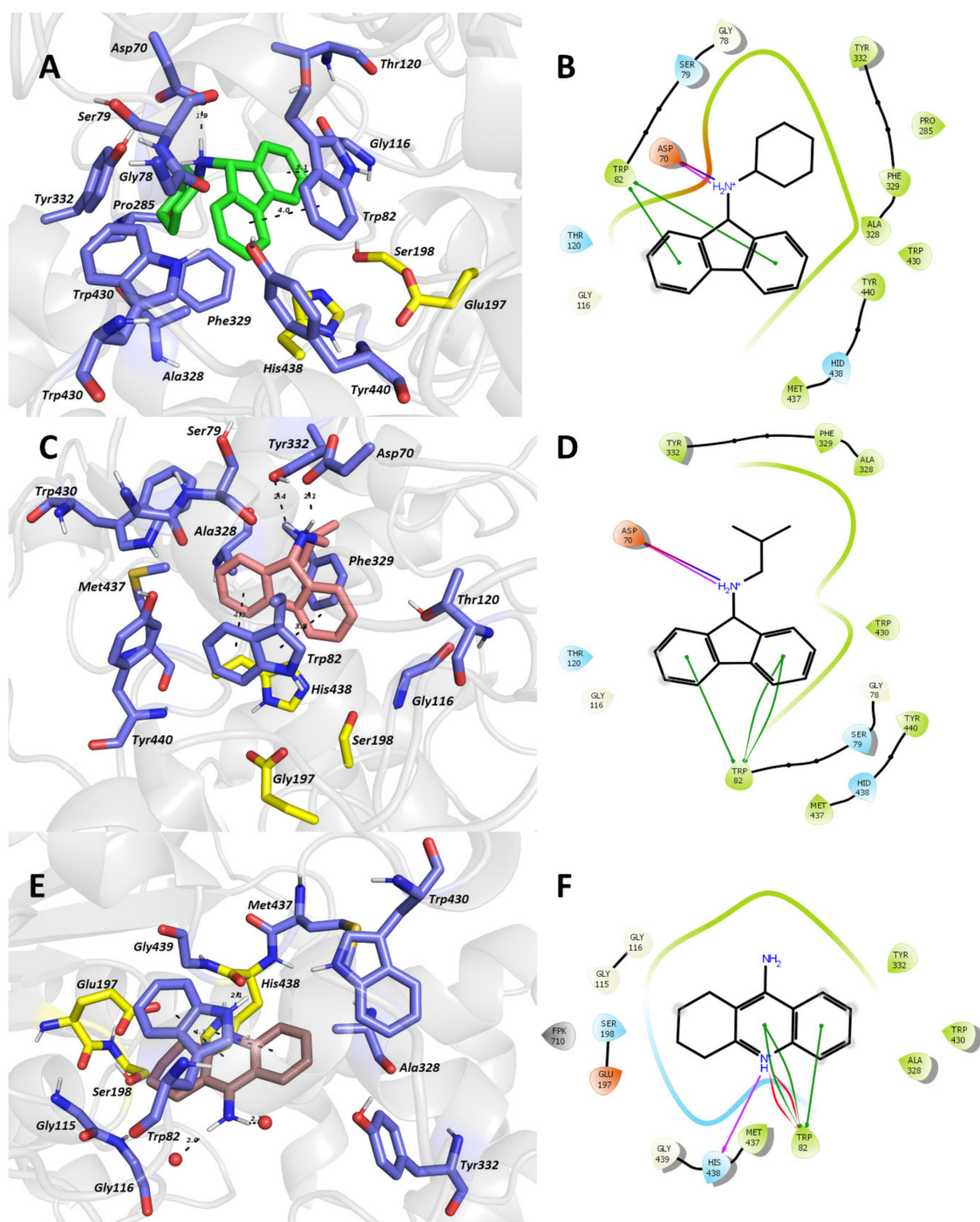


Figure 7. Top-scored docking poses of **3c** (A,B), **3n** (C,D), and the crystal structure of **THA** (E,F) within the *h*BChE active site (Protein Data Bank (PDB) ID: 4BDS) [56]. Ligands are displayed in green (A), salmon (C), and brown (E) for **3c**, **3n**, and **THA**, respectively. Important amino acid residues involved in the enzyme-ligand interaction are shown in dark-blue, and the catalytic triad is rendered in yellow. Distances are colored as dashed lines, and the distance is measured in Å (A,C,E). 3D figures were created by using PyMOL 2.0.6 viewer. 2D diagrams were generated with Maestro 12.3 (Schrödinger Release, Schrödinger, LLC., New York, NY, USA).

4. Conclusions

Since the cholinergic hypothesis was first postulated [15], five decades of intensive research have generated a few marketed drugs for symptomatic relief only. The proper and in-depth elucidation of the disease biology imposes challenging tasks that remain

to be resolved by delivering the drugs in the right stage of the disorder [29]. So far, the attempts to approve any drugs have continuously failed, with memantine receiving the final approval in 2003. A glimmer of hope emerged in 2019 when sodium oligomannate (GV-971) was approved in China, acting in a completely different way to other marketed drugs. Indeed, GV-971 suppresses gut dysbiosis, mitigates neuroinflammation, and reverses cognition impairment [83]. Designing MTDLs is an interesting approach that has generated several preclinical candidates for the therapy of AD. However, most of these newly developed agents suffer from limitations, as disclosed recently [29]. Our study was inspired by the appealing combination of donepezil and memantine into one capsule that resulted in a higher therapeutic benefit than the single-agent administrations [27]. Herewith, pursuing the symptomatic stage of AD by modulating the cholinergic and glutamatergic systems, we developed a series of 15 molecules with fluorene tricyclic scaffolds substituted with secondary or tertiary amines at C9. Prior to the synthesis, we took the compound's predicted physicochemical parameters and calculated their oral and CNS availability. Indeed, all the compounds adhered to these criteria. Under in vitro conditions, we demonstrated that the compounds can interact with both NMDAR and BChE while having only a marginal effect on AChE. We also showed that they have a relatively low cytotoxic profile, as determined using CHO-K1 cell lines, and for one compound (**3m**) out of the four selected candidates, a BBB permeation ability was confirmed. The obtained data herein warrant future research with this class of compounds; however, we may state that we found low-toxic BChE-selective compounds with antagonistic activity on the NMDARs that potentially permeate the BBB.

Supplementary Materials: The following are available online at <https://www.mdpi.com/2218-273X/11/1/3/s1>, Table S1. Physicochemical parameters of compounds **3a–o**, THA and Memantine.; Table S2. Drug-likeness of derivatives **3a–o**, THA and memantine.; Table S3. Effect of tested compounds on the cell viability of the hCMEC/D3 cells.; ¹H and ¹³C NMR spectra; HRMS, and HPLC records of compounds.

Author Contributions: J.K. (Jan Konecny), chemical synthesis, data interpretation, and manuscript writing; M.H. (Martina Hrabinoval), in vitro measurement of cholinesterase activity; L.P. (Lenka Pulkrabkova) and M.B., cytotoxicity evaluation and BBB permeation; L.P. (Lukas Prchal), HRMS analysis; T.K. (Tereza Kobrlova), BBB permeation; T.K. (Tomas Kucera), in silico calculations; V.F., design of the compounds; D.J., enzyme kinetic analysis; A.M., S.K., M.K., and M.H. (Martin Horak), NMDA receptor measurements; M.V.; manuscript writing; O.S., design of the study, BBB permeation, and manuscript writing; and J.K. (Jan Korabecny), design of the study, data interpretation, docking studies, and manuscript writing. All authors have read and agreed to the published version of the manuscript.

Funding: This project was supported by the Czech Health Research Council (No. NU20-08-00296), by the faculty of Military Health Sciences, University of Defence (SV project FVZ201803, Long-term development plan), by MH CZ—DRO (University Hospital Hradec Kralove, No. 00179906), by the European Regional Development Fund: Project “PharmaBrain” (no. CZ.02.1.01/0.0/0.0/16_025/0007444), and by the project “e-Infrastruktura CZ” (e-INFRA LM2018140) provided within the program Projects of Large Research, Development and Innovations Infrastructures. V.F. acknowledges the support of Charles University (SVV 260 547).

Data Availability Statement: Data is contained within the article or Supplementary Materials.

Acknowledgments: The authors would like to acknowledge the skillful assistance of Barbora Hejtmankova during the BChE enzyme kinetic evaluation.

Conflicts of Interest: The authors declare no conflict of interest.

References

1. Ferri, C.P.; Prince, M.; Brayne, C.; Brodaty, H.; Fratiglioni, L.; Ganguli, M.; Hall, K.; Hasegawa, K.; Hendrie, H.; Huang, Y.; et al. Global Prevalence of Dementia: A Delphi Consensus Study. *Lancet* **2005**, *366*, 2112–2117. [[CrossRef](#)]
2. Bondi, M.W.; Edmonds, E.C.; Salmon, D.P. Alzheimer's Disease: Past, Present, and Future. *J. Int. Neuropsychol. Soc.* **2017**, *23*, 818–831. [[CrossRef](#)] [[PubMed](#)]

3. Kirova, A.-M.; Bays, R.B.; Lagalwar, S. Working Memory and Executive Function Decline across Normal Aging, Mild Cognitive Impairment, and Alzheimer's Disease. *Biomed. Res. Int.* **2015**, *2015*, 748212. [[CrossRef](#)] [[PubMed](#)]
4. Lyketsos, C.G.; Carrillo, M.C.; Ryan, J.M.; Khachaturian, A.S.; Trzepacz, P.; Amatniek, J.; Cedarbaum, J.; Brashear, R.; Miller, D.S. Neuropsychiatric Symptoms in Alzheimer's Disease. *Alzheimers Dement* **2011**, *7*, 532–539. [[CrossRef](#)]
5. Weller, J.; Budson, A. Current Understanding of Alzheimer's Disease Diagnosis and Treatment. *F1000Res* **2018**, *7*. [[CrossRef](#)]
6. Schachter, A.S.; Davis, K.L. Alzheimer's Disease. *Dialogues Clin. Neurosci.* **2000**, *2*, 91–100. [[CrossRef](#)]
7. 2020 Alzheimer's Disease Facts and Figures. *Alzheimer's Dement.* **2020**, *16*, 391–460. [[CrossRef](#)]
8. Vaz, M.; Silvestre, S. Alzheimer's Disease: Recent Treatment Strategies. *Eur. J. Pharm.* **2020**, *887*, 173554. [[CrossRef](#)]
9. Abeysinghe, A.A.D.T.; Deshapriya, R.D.U.S.; Udawatte, C. Alzheimer's Disease; a Review of the Pathophysiological Basis and Therapeutic Interventions. *Life Sci.* **2020**, *256*, 117996. [[CrossRef](#)]
10. Goedert, M.; Crowther, R.A. Amyloid Plaques, Neurofibrillary Tangles and Their Relevance for the Study of Alzheimer's Disease. *Neurobiol. Aging* **1989**, *10*, 405–406; discussion 412–414. [[CrossRef](#)]
11. Lewis, D.A.; Higgins, G.A.; Young, W.G.; Goldgaber, D.; Gajdusek, D.C.; Wilson, M.C.; Morrison, J.H. Distribution of Precursor Amyloid-Beta-Protein Messenger RNA in Human Cerebral Cortex: Relationship to Neurofibrillary Tangles and Neuritic Plaques. *Proc. Natl. Acad. Sci. USA* **1988**, *85*, 1691–1695. [[CrossRef](#)] [[PubMed](#)]
12. Mondragón-Rodríguez, S.; Basurto-Islas, G.; Santa-Maria, I.; Mena, R.; Binder, L.I.; Avila, J.; Smith, M.A.; Perry, G.; García-Sierra, F. Cleavage and Conformational Changes of Tau Protein Follow Phosphorylation during Alzheimer's Disease. *Int. J. Exp. Pathol.* **2008**, *89*, 81–90. [[CrossRef](#)] [[PubMed](#)]
13. Mondragón-Rodríguez, S.; Mena, R.; Binder, L.I.; Smith, M.A.; Perry, G.; García-Sierra, F. Conformational Changes and Cleavage of Tau in Pick Bodies Parallel the Early Processing of Tau Found in Alzheimer Pathology. *Neuropathol. Appl. Neurobiol.* **2008**, *34*, 62–75. [[CrossRef](#)] [[PubMed](#)]
14. Mondragón-Rodríguez, S.; Perry, G.; Luna-Muñoz, J.; Acevedo-Aquino, M.C.; Williams, S. Phosphorylation of Tau Protein at Sites Ser(396-404) Is One of the Earliest Events in Alzheimer's Disease and Down Syndrome. *Neuropathol. Appl. Neurobiol.* **2014**, *40*, 121–135. [[CrossRef](#)] [[PubMed](#)]
15. Davies, P.; Maloney, A.J. Selective Loss of Central Cholinergic Neurons in Alzheimer's Disease. *Lancet* **1976**, *2*, 1403. [[CrossRef](#)]
16. Sarter, M.; Bruno, J.P. Cognitive Functions of Cortical Acetylcholine: Toward a Unifying Hypothesis. *Brain Res. Brain Res. Rev.* **1997**, *23*, 28–46. [[CrossRef](#)]
17. Hasselmo, M.E.; Anderson, B.P.; Bower, J.M. Cholinergic Modulation of Cortical Associative Memory Function. *J. Neurophysiol.* **1992**, *67*, 1230–1246. [[CrossRef](#)]
18. Wang, R.; Reddy, P.H. Role of Glutamate and NMDA Receptors in Alzheimer's Disease. *J. Alzheimers Dis.* **2017**, *57*, 1041–1048. [[CrossRef](#)]
19. Cheignon, C.; Tomas, M.; Bonnefont-Rousselot, D.; Faller, P.; Hureau, C.; Collin, F. Oxidative Stress and the Amyloid Beta Peptide in Alzheimer's Disease. *Redox Biol.* **2018**, *14*, 450–464. [[CrossRef](#)]
20. Butterfield, D.A.; Lauderback, C.M. Lipid Peroxidation and Protein Oxidation in Alzheimer's Disease Brain: Potential Causes and Consequences Involving Amyloid Beta-Peptide-Associated Free Radical Oxidative Stress. *Free Radic. Biol. Med.* **2002**, *32*, 1050–1060. [[CrossRef](#)]
21. Bush, A.I.; Pettingell, W.H.; Multhaup, G.; Paradis, M.d.; Vonsattel, J.P.; Gusella, J.F.; Beyreuther, K.; Masters, C.L.; Tanzi, R.E. Rapid Induction of Alzheimer A Beta Amyloid Formation by Zinc. *Science* **1994**, *265*, 1464–1467. [[CrossRef](#)] [[PubMed](#)]
22. Bolós, M.; Perea, J.R.; Avila, J. Alzheimer's Disease as an Inflammatory Disease. *Biomol. Concepts* **2017**, *8*, 37–43. [[CrossRef](#)] [[PubMed](#)]
23. Cummings, J.L.; Tong, G.; Ballard, C. Treatment Combinations for Alzheimer's Disease: Current and Future Pharmacotherapy Options. *J. Alzheimers Dis.* **2019**, *67*, 779–794. [[CrossRef](#)] [[PubMed](#)]
24. Joe, E.; Ringman, J.M. Cognitive Symptoms of Alzheimer's Disease: Clinical Management and Prevention. *BMJ* **2019**, *367*, l6217. [[CrossRef](#)]
25. Zemek, F.; Drtinova, L.; Nepovimova, E.; Sepsova, V.; Korabecny, J.; Klimes, J.; Kuca, K. Outcomes of Alzheimer's Disease Therapy with Acetylcholinesterase Inhibitors and Memantine. *Expert Opin. Drug Saf.* **2014**, *13*, 759–774. [[CrossRef](#)]
26. Owen, R.T. Memantine and Donepezil: A Fixed Drug Combination for the Treatment of Moderate to Severe Alzheimer's Dementia. *Drugs Today* **2016**, *52*, 239–248. [[CrossRef](#)]
27. Calhoun, A.; King, C.; Khoury, R.; Grossberg, G.T. An Evaluation of Memantine ER + Donepezil for the Treatment of Alzheimer's Disease. *Expert Opin. Pharm.* **2018**, *19*, 1711–1717. [[CrossRef](#)]
28. Cavalli, A.; Bolognesi, M.L.; Minarini, A.; Rosini, M.; Tumiatti, V.; Recanatini, M.; Melchiorre, C. Multi-Target-Directed Ligands to Combat Neurodegenerative Diseases. *J. Med. Chem.* **2008**, *51*, 347–372. [[CrossRef](#)]
29. Benek, O.; Korabecny, J.; Soukup, O. A Perspective on Multi-Target Drugs for Alzheimer's Disease. *Trends Pharmacol. Sci.* **2020**, *41*, 434–445. [[CrossRef](#)]
30. Cummings, J.L.; Morstorf, T.; Zhong, K. Alzheimer's Disease Drug-Development Pipeline: Few Candidates, Frequent Failures. *Alzheimer's Res. Ther.* **2014**, *6*, 37. [[CrossRef](#)]
31. Morphy, R.; Kay, C.; Rankovic, Z. From Magic Bullets to Designed Multiple Ligands. *Drug Discov. Today* **2004**, *9*, 641–651. [[CrossRef](#)]





32. Proschak, E.; Stark, H.; Merk, D. Polypharmacology by Design: A Medicinal Chemist's Perspective on Multitargeting Compounds. *J. Med. Chem.* **2019**, *62*, 420–444. [[CrossRef](#)] [[PubMed](#)]
33. Jack, C.R.; Knopman, D.S.; Jagust, W.J.; Petersen, R.C.; Weiner, M.W.; Aisen, P.S.; Shaw, L.M.; Vemuri, P.; Wiste, H.J.; Weigand, S.D.; et al. Tracking Pathophysiological Processes in Alzheimer's Disease: An Updated Hypothetical Model of Dynamic Biomarkers. *Lancet Neurol.* **2013**, *12*, 207–216. [[CrossRef](#)]
34. Panza, F.; Lozupone, M.; Watling, M.; Imbimbo, B.P. Do BACE Inhibitor Failures in Alzheimer Patients Challenge the Amyloid Hypothesis of the Disease? *Expert Rev. Neurother.* **2019**, *19*, 599–602. [[CrossRef](#)]
35. Kandimalla, R.; Reddy, P.H. Therapeutics of Neurotransmitters in Alzheimer's Disease. *J. Alzheimers Dis.* **2017**, *57*, 1049–1069. [[CrossRef](#)]
36. Fitzpatrick-Lewis, D.; Warren, R.; Ali, M.U.; Sherifali, D.; Raina, P. Treatment for Mild Cognitive Impairment: A Systematic Review and Meta-Analysis. *CMAJ Open* **2015**, *3*, E419–E427. [[CrossRef](#)]
37. Watkins, P.B.; Zimmerman, H.J.; Knapp, M.J.; Gracon, S.I.; Lewis, K.W. Hepatotoxic Effects of Tacrine Administration in Patients With Alzheimer's Disease. *JAMA* **1994**, *271*, 992–998. [[CrossRef](#)]
38. Horak, M.; Holubova, K.; Nepovimova, E.; Krusek, J.; Kaniakova, M.; Korabecny, J.; Vyklicky, L.; Kuca, K.; Stuchlik, A.; Ricny, J.; et al. The Pharmacology of Tacrine at N-Methyl-d-Aspartate Receptors. *Prog. Neuropsychopharmacol. Biol. Psychiatry* **2017**, *75*, 54–62. [[CrossRef](#)]
39. Kaniakova, M.; Kleteckova, L.; Lichnerova, K.; Holubova, K.; Skrenkova, K.; Korinek, M.; Krusek, J.; Smejkalova, T.; Korabecny, J.; Vales, K.; et al. 7-Methoxyderivative of Tacrine Is a "foot-in-the-Door" Open-Channel Blocker of GluN1/GluN2 and GluN1/GluN3 NMDA Receptors with Neuroprotective Activity in Vivo. *Neuropharmacology* **2018**, *140*, 217–232. [[CrossRef](#)]
40. Vorobjev, V.S.; Sharonova, I.N. Tetrahydroaminoacridine Blocks and Prolongs NMDA Receptor-Mediated Responses in a Voltage-Dependent Manner. *Eur. J. Pharmacol.* **1994**, *253*, 1–8. [[CrossRef](#)]
41. Nelson, M.E.; Albuquerque, E.X. 9-Aminoacridines Act at a Site Different from That for Mg²⁺ in Blockade of the N-Methyl-D-Aspartate Receptor Channel. *Mol. Pharmacol.* **1994**, *46*, 151–160. [[PubMed](#)]
42. Soukup, O.; Jun, D.; Zdarova-Karasova, J.; Patocka, J.; Musilek, K.; Korabecny, J.; Krusek, J.; Kaniakova, M.; Sepsova, V.; Mandikova, J.; et al. A Resurrection of 7-MEOTA: A Comparison with Tacrine. *Curr. Alzheimer Res.* **2013**, *10*, 893–906. [[CrossRef](#)] [[PubMed](#)]
43. Choubdar, N.; Golshani, M.; Jalili-Baleh, L.; Nadri, H.; Küçükilinc, T.T.; Ayazgök, B.; Moradi, A.; Moghadam, F.H.; Abdolahi, Z.; Ameri, A.; et al. New Classes of Carbazoles as Potential Multi-Functional Anti-Alzheimer's Agents. *Bioorg. Chem.* **2019**, *91*, 103164. [[CrossRef](#)] [[PubMed](#)]
44. Zhu, D.; Chen, M.; Li, M.; Luo, B.; Zhao, Y.; Huang, P.; Xue, F.; Rapposelli, S.; Pi, R.; Wen, S. Discovery of Novel N-Substituted Carbazoles as Neuroprotective Agents with Potent Anti-Oxidative Activity. *Eur. J. Med. Chem.* **2013**, *68*, 81–88. [[CrossRef](#)]
45. Crismon, M.L. Tacrine: First Drug Approved for Alzheimer's Disease. *Ann. Pharm.* **1994**, *28*, 744–751. [[CrossRef](#)]
46. Ellman, G.L.; Courtney, K.D.; Andres, V.; Feather-Stone, R.M. A New and Rapid Colorimetric Determination of Acetylcholinesterase Activity. *Biochem. Pharm.* **1961**, *7*, 88–95. [[CrossRef](#)]
47. Pohanka, M.; Jun, D.; Kuca, K. Improvement of Acetylcholinesterase-Based Assay for Organophosphates in Way of Identification by Reactivators. *Talanta* **2008**, *77*, 451–454. [[CrossRef](#)]
48. Sepsova, V.; Karasova, J.Z.; Korabecny, J.; Dolezal, R.; Zemek, F.; Bennion, B.J.; Kuca, K. Oximes: Inhibitors of Human Recombinant Acetylcholinesterase. A Structure-Activity Relationship (SAR) Study. *Int. J. Mol. Sci.* **2013**, *14*, 16882–16900. [[CrossRef](#)]
49. Skrenkova, K.; Hemelikova, K.; Kolcheva, M.; Kortus, S.; Kaniakova, M.; Krausova, B.; Horak, M. Structural Features in the Glycine-Binding Sites of the GluN1 and GluN3A Subunits Regulate the Surface Delivery of NMDA Receptors. *Sci. Rep.* **2019**, *9*, 12303. [[CrossRef](#)]
50. Kaniakova, M.; Lichnerova, K.; Vyklicky, L.; Horak, M. Single Amino Acid Residue in the M4 Domain of GluN1 Subunit Regulates the Surface Delivery of NMDA Receptors. *J. Neurochem.* **2012**, *123*, 385–395. [[CrossRef](#)]
51. Vyklicky, V.; Krausova, B.; Cerny, J.; Ladislav, M.; Smejkalova, T.; Kysilov, B.; Korinek, M.; Danacikova, S.; Horak, M.; Choudounska, H.; et al. Surface Expression, Function, and Pharmacology of Disease-Associated Mutations in the Membrane Domain of the Human GluN2B Subunit. *Front. Mol. Neurosci.* **2018**, *11*, 110. [[CrossRef](#)] [[PubMed](#)]
52. Gazova, Z.; Soukup, O.; Sepsova, V.; Siposova, K.; Drtinova, L.; Jost, P.; Spilovska, K.; Korabecny, J.; Nepovimova, E.; Fedunova, D.; et al. Multi-Target-Directed Therapeutic Potential of 7-Methoxytacrine-Adamantylamine Heterodimers in the Alzheimer's Disease Treatment. *Biochim. Et Biophys. Acta (BBA) Mol. Basis Dis.* **2017**, *1863*, 607–619. [[CrossRef](#)] [[PubMed](#)]
53. Hemelíková, K.; Kolcheva, M.; Skrenkova, K.; Kaniaková, M.; Horák, M. Lectins Modulate the Functional Properties of GluN1/GluN3-Containing NMDA Receptors. *Neuropharmacology* **2019**. [[CrossRef](#)] [[PubMed](#)]
54. Kaniakova, M.; Nepovimova, E.; Kleteckova, L.; Skrenkova, K.; Holubova, K.; Chrienova, Z.; Hepnarova, V.; Kucera, T.; Koblrova, T.; Vales, K.; et al. Combination of Memantine and 6-Chlorotacrine as Novel Multi-Target Compound against Alzheimer's Disease. *Curr. Alzheimer Res.* **2019**, *16*, 821–833. [[CrossRef](#)] [[PubMed](#)]
55. Soukup, O.; Benkova, M.; Dolezal, R.; Sleha, R.; Malinak, D.; Salajkova, S.; Markova, A.; Hympanova, M.; Prchal, L.; Ryskova, L.; et al. The Wide-Spectrum Antimicrobial Effect of Novel N-Alkyl Monoquaternary Ammonium Salts and Their Mixtures; the QSAR Study against Bacteria. *Eur. J. Med. Chem.* **2020**, *206*, 112584. [[CrossRef](#)]

56. Nachon, F.; Carletti, E.; Ronco, C.; Trovaslet, M.; Nicolet, Y.; Jean, L.; Renard, P.-Y. Crystal Structures of Human Cholinesterases in Complex with Huprine W and Tacrine: Elements of Specificity for Anti-Alzheimer's Drugs Targeting Acetyl- and Butyryl-Cholinesterase. *Biochem. J.* **2013**, *453*, 393–399. [[CrossRef](#)]
57. Cheung, J.; Rudolph, M.J.; Burshteyn, F.; Cassidy, M.S.; Gary, E.N.; Love, J.; Franklin, M.C.; Height, J.J. Structures of Human Acetylcholinesterase in Complex with Pharmacologically Important Ligands. *J. Med. Chem.* **2012**, *55*, 10282–10286. [[CrossRef](#)]
58. Spilovska, K.; Korabecny, J.; Sepsova, V.; Jun, D.; Hrabnova, M.; Jost, P.; Muckova, L.; Soukup, O.; Janockova, J.; Kucera, T.; et al. Novel Tacrine-Scutellarin Hybrids as Multipotent Anti-Alzheimer's Agents: Design, Synthesis and Biological Evaluation. *Molecules* **2017**, *22*, 1006. [[CrossRef](#)]
59. Mezeiova, E.; Korabecny, J.; Sepsova, V.; Hrabnova, M.; Jost, P.; Muckova, L.; Kucera, T.; Dolezal, R.; Misik, J.; Spilovska, K.; et al. Development of 2-Methoxyhuprine as Novel Lead for Alzheimer's Disease Therapy. *Molecules* **2017**, *22*, 1265. [[CrossRef](#)]
60. Trott, O.; Olson, A.J. AutoDock Vina: Improving the Speed and Accuracy of Docking with a New Scoring Function, Efficient Optimization and Multithreading. *J. Comput. Chem.* **2010**, *31*, 455–461. [[CrossRef](#)]
61. Liu, B.; Wang, L.; Jin, Y.-H. An Effective PSO-Based Memetic Algorithm for Flow Shop Scheduling. *IEEE Trans. Syst. Man Cybern. Part B (Cybern.)* **2007**, *37*, 18–27. [[CrossRef](#)] [[PubMed](#)]
62. Daina, A.; Michielin, O.; Zoete, V. SwissADME: A Free Web Tool to Evaluate Pharmacokinetics, Drug-Likeness and Medicinal Chemistry Friendliness of Small Molecules. *Sci. Rep.* **2017**, *7*, 42717. [[CrossRef](#)] [[PubMed](#)]
63. Gupta, M.; Lee, H.J.; Barden, C.J.; Weaver, D.F. The Blood-Brain Barrier (BBB) Score. *J. Med. Chem.* **2019**, *62*, 9824–9836. [[CrossRef](#)] [[PubMed](#)]
64. Daina, A.; Michielin, O.; Zoete, V. ILOGP: A Simple, Robust, and Efficient Description of n-Octanol/Water Partition Coefficient for Drug Design Using the GB/SA Approach. *J. Chem. Inf. Model.* **2014**, *54*, 3284–3301. [[CrossRef](#)] [[PubMed](#)]
65. Naz, A.; Iqtadar, R.; Siddiqui, F.A.; Ul-Haq, Z. Degradation Kinetics of Fluvoxamine in Buffer Solutions: In Silico ADMET Profiling and Identification of Degradation Products by LC-MS/ESI. *Arab. J. Chem.* **2020**, *13*, 4134–4146. [[CrossRef](#)]
66. Madden, S.; Spaldin, V.; Park, B.K. Clinical Pharmacokinetics of Tacrine. *Clin. Pharm.* **1995**, *28*, 449–457. [[CrossRef](#)]
67. Liu, M.-Y.; Meng, S.-N.; Wu, H.-Z.; Wang, S.; Wei, M.-J. Pharmacokinetics of Single-Dose and Multiple-Dose Memantine in Healthy Chinese Volunteers Using an Analytic Method of Liquid Chromatography-Tandem Mass Spectrometry. *Clin. Ther.* **2008**, *30*, 641–653. [[CrossRef](#)]
68. Lipinski, C.A. Lead- and Drug-like Compounds: The Rule-of-Five Revolution. *Drug Discov. Today Technol.* **2004**, *1*, 337–341. [[CrossRef](#)]
69. Martin, Y.C. A Bioavailability Score. *J. Med. Chem.* **2005**, *48*, 3164–3170. [[CrossRef](#)]
70. Daina, A.; Zoete, V. A BOILED-Egg to Predict Gastrointestinal Absorption and Brain Penetration of Small Molecules. *ChemMedChem* **2016**, *11*, 1117–1121. [[CrossRef](#)]
71. Veber, D.F.; Johnson, S.R.; Cheng, H.-Y.; Smith, B.R.; Ward, K.W.; Kopple, K.D. Molecular Properties That Influence the Oral Bioavailability of Drug Candidates. *J. Med. Chem.* **2002**, *45*, 2615–2623. [[CrossRef](#)] [[PubMed](#)]
72. Bade, R.; Chan, H.-F.; Reynisson, J. Characteristics of Known Drug Space. Natural Products, Their Derivatives and Synthetic Drugs. *Eur. J. Med. Chem.* **2010**, *45*, 5646–5652. [[CrossRef](#)] [[PubMed](#)]
73. Egan, W.J.; Merz, K.M.; Baldwin, J.J. Prediction of Drug Absorption Using Multivariate Statistics. *J. Med. Chem.* **2000**, *43*, 3867–3877. [[CrossRef](#)] [[PubMed](#)]
74. Ghose, A.K.; Viswanadhan, V.N.; Wendoloski, J.J. A Knowledge-Based Approach in Designing Combinatorial or Medicinal Chemistry Libraries for Drug Discovery. 1. A Qualitative and Quantitative Characterization of Known Drug Databases. *J. Comb. Chem.* **1999**, *1*, 55–68. [[CrossRef](#)]
75. Muegge, I.; Heald, S.L.; Brittelli, D. Simple Selection Criteria for Drug-like Chemical Matter. *J. Med. Chem.* **2001**, *44*, 1841–1846. [[CrossRef](#)]
76. Pohanka, M.; Karasova, J.Z.; Kuca, K.; Pikula, J.; Holas, O.; Korabecny, J.; Cabal, J. Colorimetric Dipstick for Assay of Organophosphate Pesticides and Nerve Agents Represented by Paraoxon, Sarin and VX. *Talanta* **2010**, *81*, 621–624. [[CrossRef](#)]
77. Nordberg, A.; Ballard, C.; Bullock, R.; Darreh-Shori, T.; Somogyi, M. A Review of Butyrylcholinesterase as a Therapeutic Target in the Treatment of Alzheimer's Disease. *Prim. Care Companion CNS Disord.* **2013**, *15*. [[CrossRef](#)]
78. Greig, N.H.; Utsuki, T.; Ingram, D.K.; Wang, Y.; Pepeu, G.; Scali, C.; Yu, Q.-S.; Mamczarz, J.; Holloway, H.W.; Giordano, T.; et al. Selective Butyrylcholinesterase Inhibition Elevates Brain Acetylcholine, Augments Learning and Lowers Alzheimer Beta-Amyloid Peptide in Rodent. *Proc. Natl. Acad. Sci. USA* **2005**, *102*, 17213–17218. [[CrossRef](#)]
79. Nepovimova, E.; Korabecny, J.; Dolezal, R.; Babkova, K.; Ondrejicek, A.; Jun, D.; Sepsova, V.; Horova, A.; Hrabnova, M.; Soukup, O.; et al. Tacrine-Trolox Hybrids: A Novel Class of Centrally Active, Nonhepatotoxic Multi-Target-Directed Ligands Exerting Anticholinesterase and Antioxidant Activities with Low In Vivo Toxicity. *J. Med. Chem.* **2015**, *58*, 8985–9003. [[CrossRef](#)]
80. Sobolova, K.; Hrabnova, M.; Hepnarova, V.; Kucera, T.; Kobrlova, T.; Benkova, M.; Janockova, J.; Dolezal, R.; Prchal, L.; Benek, O.; et al. Discovery of Novel Berberine Derivatives with Balanced Cholinesterase and Prolyl Oligopeptidase Inhibition Profile. *Eur. J. Med. Chem.* **2020**, *203*, 112593. [[CrossRef](#)]
81. Chalupova, K.; Korabecny, J.; Bartolini, M.; Monti, B.; Lamba, D.; Caliandro, R.; Pesaresi, A.; Brazzolotto, X.; Gastellier, A.-J.; Nachon, F.; et al. Novel Tacrine-Tryptophan Hybrids: Multi-Target Directed Ligands as Potential Treatment for Alzheimer's Disease. *Eur. J. Med. Chem.* **2019**, *168*, 491–514. [[CrossRef](#)] [[PubMed](#)]

82. Weksler, B.; Romero, I.A.; Couraud, P.-O. The HCMEC/D3 Cell Line as a Model of the Human Blood Brain Barrier. *Fluids Barriers CNS* **2013**, *10*, 16. [[CrossRef](#)] [[PubMed](#)]
83. Wang, X.; Sun, G.; Feng, T.; Zhang, J.; Huang, X.; Wang, T.; Xie, Z.; Chu, X.; Yang, J.; Wang, H.; et al. Sodium Oligomannate Therapeutically Remodels Gut Microbiota and Suppresses Gut Bacterial Amino Acids-Shaped Neuroinflammation to Inhibit Alzheimer's Disease Progression. *Cell Res.* **2019**, *29*, 787–803. [[CrossRef](#)] [[PubMed](#)]

Article

Efficacy Assessment of an Uncharged Reactivator of NOP-Inhibited Acetylcholinesterase Based on Tetrahydroacridine Pyridine-Aldoxime Hybrid in Mouse Compared to Pralidoxime

André-Guilhem Calas ^{1,2,*}, Anne-Sophie Hanak ^{1,2}, Nina Jaffré ^{1,2}, Aurélie Nervo ^{1,2}, José Dias ¹, Catherine Rousseau ^{1,2}, Charlotte Courageux ¹, Xavier Brazzolotto ¹ , Pascal Villa ^{3,4} , Adeline Obrecht ^{3,4}, Jean-François Goossens ⁵, Christophe Landry ⁶, Johan Hachani ⁶, Fabien Gosselet ⁶ , Marie-Pierre Dehouck ⁶, Jagadeesh Yerri ⁷, Maria Kliachyna ⁷, Rachid Baati ⁷ and Florian Nachon ¹ 

¹ Département de Toxicologie et Risques Chimiques, Institut de Recherche Biomédicale des Armées, F-91220 Brétigny-sur-Orge, France; anne-sophie.hanak@def.gouv.fr (A.-S.H.); nina.jaffre@def.gouv.fr (N.J.); aurelie.nervo@def.gouv.fr (A.N.); jose.dias@def.gouv.fr (J.D.); catherine.delage@def.gouv.fr (C.R.); charlotte.courageux@def.gouv.fr (C.C.); xavier.brazzolotto@def.gouv.fr (X.B.); florian.nachon@def.gouv.fr (F.N.)

² COGNition and ACtion Group, UMR 8257, CNRS-MD-UPV, Centre universitaire des Saints-Pères, F-75006 Paris, France

³ CNRS, Université de Strasbourg, PCBIS Plate-forme de Chimie Biologique Intégrative de Strasbourg UMS 3286, F-67412 Illkirch, France; pvilla@unistra.fr (P.V.); aobrecht@unistra.fr (A.O.)

⁴ Labex MEDALIS, F-67000 Strasbourg, France

⁵ Université de Lille, ULR-7365—GRITA Groupe de Recherche sur les Formes Injectables et Technologies Associées, F-59000, Lille, France; jean-francois.goossens@univ-lille2.fr

⁶ Université d'Artois (UArtois), UR 2465, LBHE Laboratoire de la Barrière Hémato-Encéphalique, F-62307 Lens, France; christophe.landry@univ-artois.fr (C.L.); johan.hachani@univ-artois.fr (J.H.); fabien.gosselet@univ-artois.fr (F.G.); mpierre.dehouck@univ-artois.fr (M.-P.D.)

⁷ UMR CNRS 7515, ICPEES Institut de Chimie et Procédés pour l'Énergie, l'Environnement et la Santé, F-67087 Strasbourg, France; jagadeesh.yerri@gmail.com (J.Y.); kliachyna.maria@gmail.com (M.K.); rachid.baati@unistra.fr (R.B.)

* Correspondence: guilhem.calas@def.gouv.fr; Tel.: +33-1-78-65-13-95

Received: 7 May 2020; Accepted: 3 June 2020; Published: 4 June 2020



Abstract: (1) Background: Human exposure to organophosphorus compounds employed as pesticides or as chemical warfare agents induces deleterious effects due to cholinesterase inhibition. One therapeutic approach is the reactivation of inhibited acetylcholinesterase by oximes. While currently available oximes are unable to reach the central nervous system to reactivate cholinesterases or to display a wide spectrum of action against the variety of organophosphorus compounds, we aim to identify new reactivators without such drawbacks. (2) Methods: This study gathers an exhaustive work to assess in vitro and in vivo efficacy, and toxicity of a hybrid tetrahydroacridine pyridinaldoxime reactivator, KM297, compared to pralidoxime. (3) Results: Blood–brain barrier crossing assay carried out on a human in vitro model established that KM297 has an endothelial permeability coefficient twice that of pralidoxime. It also presents higher cytotoxicity, particularly on bone marrow-derived cells. Its strong cholinesterase inhibition potency seems to be correlated to its low protective efficacy in mice exposed to paraoxon. Ventilatory monitoring of KM297-treated mice by double-chamber plethysmography shows toxic effects at the selected therapeutic dose. This breathing assessment could help define the No Observed Adverse Effect Level (NOAEL) dose of new oximes which would have a maximum therapeutic effect without any toxic side effects.

Keywords: organophosphorus nerve agents; oxime; cholinesterase; reactivation; ventilation; pharmacodynamics; blood-brain barrier crossing

1. Introduction

The organophosphorus compounds (OP) family includes molecules like parathion used as pesticides, plasticizer, flame retardants, anti-wear additives in jet engine lubricants such as tricresyl phosphate (TCP), as well as highly toxic chemical warfare nerve agents such as VX or sarin. Each year, self-poisonings by OP insecticides lead to around 100,000 deaths worldwide [1]. Recently, attacks were perpetrated with nerve agents in Syria (2013 and 2017) [2,3], Malaysia (2017) [4], and also in the United Kingdom (2018) [5]. The toxic action of these agents is characterized by symptoms such as headache, nausea with vomiting and/or diarrhea, fasciculations progressing to paralysis, loss of consciousness, seizures, and apnea [6]; eventually leading to death. These toxic effects come from the irreversible inhibition of primarily acetylcholinesterase (AChE, E.C. 3.1.1.7) and butyrylcholinesterase (BChE, E.C. 3.1.1.8). Their inhibition results in high concentrations of the acetylcholine neurotransmitter, which leads to the over-stimulation and/or the desensitization of cholinergic receptors located in the synaptic cleft of peripheral and central synapses.

AChE irreversibly inhibited by OP can be reactivated by oximes reactivators (for a review see [7]). Such reactivators associated with an antimuscarinic drug (atropine) and an anticonvulsant (diazepam) form the current emergency treatment in the event of OP poisoning. However, currently marketed oximes do not readily cross the blood–brain barrier (BBB) due to their permanent positive charge. They are, consequently, poorly active in the central nervous system (CNS). Moreover, despite 60 years of research, none of them display an extensive broad spectrum of reactivation [8].

Here we present a toxicological study on human cell lines and a comparative *in vivo* study in Swiss mice of pralidoxime (2-PAM) with a hybrid tetrahydroacridine pyridinaldoxime reactivator, KM297 (Figure 1), designed to readily cross the BBB and which has shown promising reactivation properties *in vitro* [9].

Blood clearance of 2-PAM and KM297 as a free base and as various salts are monitored by an established pharmacodynamic method and blood AChE and BChE activity is followed after KM297 chlorhydrate (HCl) injection. Cytotoxicity of 2-PAM and KM297 HCl is assessed on 6 different cell lines. The penetration of both oximes through the BBB is measured using a human *in vitro* model named brain-like endothelial cells (BLECs) [10]: briefly, their cell toxicity is evaluated using a monolayer integrity marker followed by a permeability test on the BLEC monolayer. Protective efficacy of the oximes without atropine co-treatment is assessed *in vivo* by 24 h-long-surviving tests in VX-challenged and paraoxon-challenged mice using the up-and-down method; paraoxon being the active and toxic metabolite of parathion. Finally, the toxicity of this novel reactivator is assessed by following the potential of KM297 HCl to alter the breathing pattern of mice.

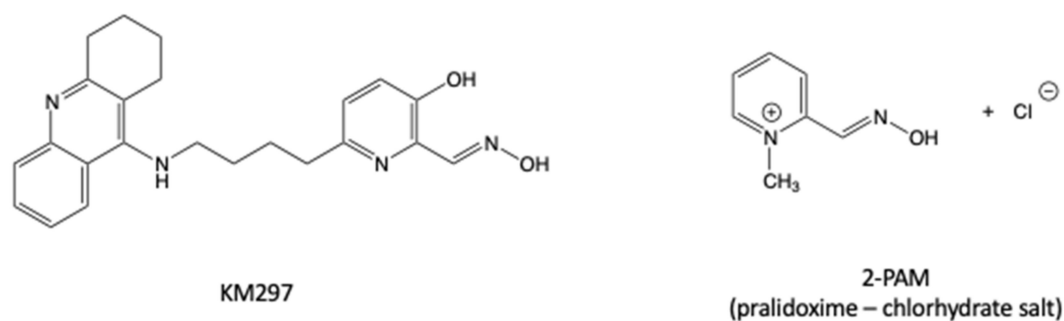


Figure 1. Chemical structures of the oximes used in this study, the reference oxime 2-PAM, and the novel α -hydroxypyridine oxime KM297.

2. Materials and Methods

2.1. Animals

We used 8- to 10-week-old male Swiss mice (Janvier, Le Genest-Saint-Isle, France), weighing 37–43 g at the experimentation time. The animals (3–4/cage) were housed for 7–14 days before the experiments in an environment maintained at 23 °C with controlled humidity on a 12 h dark/light cycle with light provided between 7 a.m. and 7 p.m. They were given food and tap water ad libitum. All experiments were carried out in compliance with the European Directive on the protection of animals used for scientific purposes (2010/63/UE) and were approved by our Institutional Animal Care and Research Advisory Committees (2012/22.0 and 12-98).

2.2. Chemicals

VX was obtained from DGA maîtrise NRBC (Vert le Petit, France), 2-PAM from Pharmacie Centrale des Armées (Orléans, France), KM297 from UMR CNRS 7515 ICPEES (Strasbourg, France). Heparine, Cremophor-EL, DMSO, iso-OMPA, DTNB, acetylthiocholine, and butyrylthiocholine were purchased from Sigma-Aldrich.

Excluding the cytotoxic study, 2-PAM (chlorhydrate salt) was directly dissolved into physiological serum (0.9% NaCl) to obtain the desired concentration (see protocol of each experiment). KM297 free base was first dissolved into DMSO. The solution was then 10-fold-diluted into Cremophor-EL with a final 10-fold dilution into 0.9% NaCl to obtain the final concentration of 1 % *v/v* DMSO (see protocol of each experiment). The three different salts of KM297, namely chlorhydrate (KM297 HCl), acetate (KM297 AcOH) and methylsulfonate (KM297 MSA) were directly dissolved into 0.9 % saline solution apart from cytotoxic study.

2.3. Inhibition of AChE by OP Agents

2.3.1. Inhibition of Human AChE (hAChE) by VX

Recombinant hAChE was produced and purified as previously described [11]. The stock solution of VX was 5 mM in isopropanol. Inhibition of purified hAChE at 120 μ M [12] was achieved with a 5-fold excess of VX (10-fold for standard reactivation curves) in sodium phosphate buffer (0.1 M, pH 7.4, 0.1% BSA) at 25 °C. Complete inhibition of hAChE was monitored by measuring the residual activity as previously described [13]. After a 20 min-incubation, excess VX was removed by desalting on a PD-10 column (GE Healthcare, Uppsala, Sweden) in the same sodium phosphate buffer.

2.3.2. Inhibition of Murine AChE (mAChE) by Paraoxon

Recombinant mAChE was produced and purified as hAChE. The stock solution of paraoxon was 100 μ M in DMSO. Inhibition of purified mAChE at 113 μ M [14] was achieved with a 10-fold excess of paraoxon in sodium phosphate buffer (0.1 M, pH 7.4, 0.1% BSA) at 25 °C. Complete inhibition of mAChE was monitored by measuring the residual activity as previously described [13]. After a 15 min-incubation, excess paraoxon was removed by desalting on a PD-10 column (GE Healthcare) in the same sodium phosphate buffer.

2.4. Plasma Test Protocols

2.4.1. Monitoring of the reactivability of blood samples

This protocol has been previously fully described [15].

Standard Curves of Reactivation

Briefly, VX-inhibited hAChE or paraoxon-inhibited mAChE solution in sodium phosphate buffer was incubated for 30 min at 37 °C in the presence of different concentrations of oximes diluted in

heat-inactivated mice plasma (0, 1, 5, 10, 50, 100, 150, and 250 μM). Ten-microliter aliquots of each sample were transferred to cuvettes containing 1 mM acetylthiocholine in 1 mL Ellman's buffer (sodium phosphate 0.1 M, pH 7.4, 0.5 mM DTNB, 25 °C) for monitoring AChE activity at 412 nm. The percentage of reactivated enzyme (% E_{react}) (either VX-inhibited hAChE or paraoxon-inhibited mAChE) was calculated as the ratio of the recovered OP-inhibited AChE activity and HI-6 reactivated hAChE activity, which is considered as maximal reactivation (i.e., % $E_{\text{react}} = 100\%$). HI-6 reactivation was achieved by incubating VX-inhibited hAChE with 200 μM HI-6 diluted in heat-inactivated plasma. Three independent experiments were carried out for each oxime.

Standard curves were fitted with GraphPad Prism software using a standard asymptotic/exponential time-dependent reactivation equation giving % E_{react} in the function of the oxime concentration ([Ox]):

$$\% E_{\text{react}} = 100 \times \left(1 - e^{-k_{r2} \times [\text{Ox}] \times t}\right) \frac{IC_{50}^n}{IC_{50}^n + [\text{Ox}]^n} \quad (1)$$

where k_{r2} is the apparent bimolecular rate constant ($\mu\text{M}^{-1} \cdot \text{min}^{-1}$) and $t = 30$ min for these series of experiments, $IC_{50} = 0.25$ μM and n , the Hill coefficient.

Blood Sampling

At least 24 h before the experiment, mice were anesthetized with isoflurane gas (Vetflurane[®], Virbac, France) allowing their hind limbs to be shaved using a 3-min-long application of commercial depilatory cream. Mice were returned to their cages to allow recovery and complete anesthesia washout. On the day of experimentation, mice received intraperitoneal (i.p.) injection of oxime at 23.3 $\mu\text{mol/kg}$, which corresponds to the highest dose of the soluble free base or 100 $\mu\text{mol/kg}$ analogous with our previous studies [15]. At various time-points (0, 2, 5, 10, 15, 30, 60, and 180 min after oxime injection), the saphenous vein was drilled with a needle and approximately 15 μL of blood was collected with a heparinized capillary tube and deposited in a collection tube containing 2 μL of sodium heparin (Choay[®], Sanofi, France). Plasma was next isolated from erythrocytes by centrifugation at 4 °C, 3000 g for 10 min. Plasma samples were then heated 30 min at 56 °C and treated as previously described in chapter 2.4.1.1. to obtain the percentage of the reactivated enzyme (% E_{react}) with a one-compartment model. T_{max} corresponds to the time when the curve reaches a peak of % E_{react} . The areas under the percentage of reactivation curve (AUC) and the first-moment curve (AUMC) were calculated using the trapezoidal rule. Mean residence time (MRT) was calculated as the ratio of AUMC to AUC [16].

2.4.2. Follow-up of Endogenous Blood AChE and BChE Activity

As in paragraph 2.4.1.2., mice were prepared for blood collection at the same time-points after KM297 HCl i.p. injection at 100 $\mu\text{mol/kg}$. Whole blood samples were diluted 100-fold in sodium phosphate buffer (0.1 M, pH 7.4, 0.1% BSA). Eighteen-microliter aliquots of each sample were transferred to a 96-well plate containing 10 mM acetylthiocholine or butyrylthiocholine in Ellman's buffer with or without iso-OMPA, a BChE inhibitor [17], for a 40-min measurement with a 10 s time-interval at room temperature for AChE or BChE activity respectively.

2.5. IC_{50} of Cholinesterase (ChE) Activity by KM297 HCl

IC_{50} is the concentration of KM297 HCl that inhibits half of hAChE, mAChE, or human BChE (hBChE) activity. Recombinant hBChE was produced in eukaryotic cells as described earlier [18] and the protein purified by BChE specific affinity (Hupresin; CHEMFORASE, Rouen, France) followed by size exclusion chromatography (Superdex 200, GE Healthcare), as previously described [19]. Briefly, hAChE, mAChE, or hBChE diluted in sodium phosphate buffer was incubated for 1 min at room temperature with KM297 HCl in Ellman's buffer. Acetylthiocholine or butyrylthiocholine diluted in Ellman's buffer was added to the previous solution and the resulting cholinesterase (ChE) activity was immediately measured using a microplate reader (SPARK, Tecan) at 412 nm for 1 min.

2.6. Cytotoxicity

2.6.1. Cell Lines

Cell lines were purchased from ATTC (Manassas, VA, USA), grown in their respective media and stored as master cell banks and working cell banks. New aliquots were thawed and grown for each experiment. The following cell lines were used:

HEK293 (ATCC CRL-1573): human kidney embryonic epithelial cells

HeLa (ATCC CCL-2): human cervix epithelioid carcinoma cells

MCF-7 (ATCC HTB-22): human breast adenocarcinoma cells

HepG2 (ATCC HB-8065): human liver hepatocellular cells

Caco-2 (ATCC HTB-37): human colon adenocarcinoma cells

HL-60 (ATCC CCL-240): human promyelocytic leukemia cells

2.6.2. Cell Culture

For HEK293, MCF-7, HeLa and HepG2 cells, EMEM (Sigma, St-Quentin Falavier, France, M5650) was used supplemented with 10 % FBS (Invitrogen 10270-106) and the following compounds: 2 mM L-glutamine (PAA-GE-Healthcare, Velizy-Villacoublay, France M11-004), 100 U/mL penicillin/100 µg/mL streptomycin (Sigma P0781) and 1 mM sodium pyruvate (Invitrogen-Fisher Scientific, Illkirch, France 11360-039). The same medium was employed for Caco-2 cells, but with an increase to 20% for the FBS (Invitrogen 10270-106).

HL-60 cells were grown in Iscove's Modified Dulbecco's Medium (Sigma 51471C) with 20% FBS (Invitrogen 10270-106) and 100 U/mL penicillin/100 µg/mL streptomycin (Sigma P0781).

Cells were seeded at different concentrations into microtiter plates (Greiner Bio-One, Courtaboeuf, France, 655090) according to cell type using automated multidrop seeder (Thermo Fisher Scientific, Courtaboeuf, France): 5×10^4 cells/well for HeLa and Caco-2 cells, 10^5 cells/well for HEK293 cells, 2×10^5 cells/well for MCF-7 and HepG2 cells, 2.5×10^5 cells/well for HL-60 cells in a volume of 50 µL/well.

2.6.3. Treatment

KM297 HCl and 2-PAM were dissolved in DMSO at a final concentration of 0.1 M. Aliquots were prepared and frozen at -20 °C before use. An internal control of cytotoxicity with 50 µM chlorpromazine (Sigma C8138) was included in all experiments [20]. After 24 h of incubation (cell incubator, 37 °C, 5% CO₂), cells were treated by adding 50 µL of medium containing KM297 HCl or 2-PAM (or controls) at twice the final concentration. The dose-response curves were built using the following final concentrations: 100, 30, 10, 3, 1, and 0.3 µM. All treatments were done using a fully automated robotized platform (Beckman Coulter, Villepinte, France). DMSO concentration was the same in all wells (0.5% final).

2.6.4. Cell Viability Assay

Cell viability assays were performed 48 h after treatment. Cell viability was measured using the WST-1 assay (Ozyme, Saint-Quentin-en-Yvelines, France) according to the manufacturer's protocol as described by Houel et al. [21]. Briefly, WST-1-containing medium was added to cells and cell viability was determined by measuring absorbance at 450 nm using an Envision reader (Perkin Elmer, Villebon-sur-Yvette, France) 1 h after incubating at 37 °C and 5% CO₂. Each measurement was performed in triplicate and results were expressed as means of three independent experiments.

Statistical calculation of Z' [22] was performed in all experiments. A $Z' > 0.5$ confirms that the results were significant and the assay is robust.

$$Z' = 1 - 3 \times \frac{(SD_+ + SD_-)}{(Mean_+ - Mean_-)} \quad (2)$$

where SD_+ = standard deviation of DMSO-treated cells, SD_- = standard deviation of cytotoxic active control (chlorpromazine), $Mean_+$ = mean of DMSO-treated cells, $Mean_-$ = mean of cytotoxic active control.

2.7. Transport Experiments Across the Human *in vitro* BBB Model

2.7.1. Design of the Human *In Vitro* BBB Model

The *in vitro* model was set up using stem cells as described previously [10]. Endothelial cells were derived from human umbilical cord blood CD34⁺-cells. In accordance with French legislation, the infant's parents signed informed consent. The collection protocol was approved by the French Ministry of Higher Education and Research (CODECOH number DC2011-1321).

Briefly, CD34⁺-hematopoietic stem cells were isolated and differentiated into endothelial cells as described by Pedroso et al., [23]. Then these endothelial cells were seeded onto matrigel (BD Biosciences, Franklin Lakes, NJ, USA, 354230) coated Transwell inserts (Corning, NY, USA, 3401). Endothelial cells (8×10^4 cells/cm²) were seeded onto the insert and cultured in the presence of 5×10^4 cells/cm² bovine brain pericytes seeded at bottom of a well (12-well format). The medium of this co-culture [ECM-5 composed of ECM basal medium (Sciencell, Carlsbad, CA, USA) supplemented with 5% (*v/v*) fetal calf serum, 1% (*v/v*) EC growth supplement (Sciencell) and 50 µg/mL gentamycin (Biochrom AG, Berlin, Germany)] was renewed every 2 days. After 6 days of co-culture with pericytes, the endothelial cells differentiated into BBB endothelial cells and were ready for experiments. This model named BLECs reproduces several features of the *in vivo* BBB [24–26].

2.7.2. Endothelial Permeability Measurement

Endothelial permeability coefficients were determined as described by Dehouck et al., [27]. The inserts, containing an endothelial cell monolayer or only coated with matrigel, were transferred into 12-well plates containing 1.5 mL of Ringer-HEPES (RH) buffer saline (150 mM NaCl, 5.2 mM KCl, 2.2 mM CaCl₂, 0.2 mM MgCl₂·6H₂O, 0.6 mM NaHCO₃, 5 mM HEPES, pH 7.4) per well, thus constituting the abluminal compartment. Then, 0.5 mL of RH buffer saline containing 5 µM or 50 µM of the compound to be tested (2-PAM, KM297 HCl or diazepam, which easily crosses the BBB and was used as the positive control) was added to the upper (luminal) compartment, in place of the culture medium in contact with the BBB endothelial cells. After different time-points (20, 40, and 60 min), filters were transferred into a new well containing RH buffer saline. All incubations were performed at 37 °C. After 60 min, the concentration of the molecules tested was determined in the upper and lower compartments.

To assess the toxicity of the molecules on the BLECs, Lucifer yellow (LY) (Sigma-Aldrich, L0259) that poorly crosses the BBB, was used as the monolayer integrity marker. Diffusion of 50 µM LY was tested alone (control) or incubated with KM297 HCl or 2-PAM, as described above. At 60 min, a 200 µL aliquot from a lower compartment at each time point and a 20 µL aliquot of the initial solution placed in the upper compartment were put in a fluorimeter (Synergy H1; BioTek, Winooski, VT, USA) for LY concentration measurements or a liquid scintillation counter (Perkin Elmer, Courtabœuf, France) for ³H-diazepam measurements, while the concentrations of 2-PAM and KM297 HCl were determined by mass-spectrometry in the solutions from the upper and lower compartments [28].

The endothelial permeability coefficients (P_e) to LY, 2-PAM, KM297 HCl, and diazepam were calculated using the clearance principle to generate a concentration-independent parameter as described by Siflinger-Birnboim et al., [29]. First, the volumes cleared were plotted versus time (20, 40, 60 min) and

the slopes were estimated by linear regression for both insert only coated with matrigel (PSf) and for insert coated with matrigel and seeded with cells (PSt). PSe was calculated according to the following formula: $1/PSe = 1/PSt - 1/PSf$ where "S" represented the surface area of the porous membrane of the insert. PSe was divided by the membrane surface (1.12 cm^2) to generate the endothelial permeability coefficients (Pe) to the studied molecules expressed in cm/min.

2.7.3. LC-MS/MS Analysis

The molecules (2-PAM and KM297 HCl) were analyzed by an LC-MS/MS system consisted of a Thermo Scientific™ TSQ Vantage™ Triple Quadrupole mass spectrometer outfitted with a Thermo Accela™ LC System. The separation was carried out on a Synergi™ Hydro-RP 80 Å reverse phase column ($3 \times 150 \text{ mm}$, particle size $4 \mu\text{m}$) in isocratic mode using a mixture of water (A)/acetonitrile (B), both solutions containing 0.1% formic acid. The mobile phase was delivered through the column (temperature maintained at $35 \text{ }^\circ\text{C}$) at a flow rate of 0.7 mL/min , whereas the temperature of the autosampler was kept at $8 \text{ }^\circ\text{C}$ with an injection volume of $10 \mu\text{L}$. Chromatographic conditions are summarized in Table 1. The detection was performed in liquid chromatography-tandem mass spectrometry with a source operating in positive ion mode. The mass spectrometer was used in the multiple reaction monitoring mode (MRM). The precursor/product ion transitions with the highest intensity and/or specificity were selected to give the maximum sensitivity and selectivity for each analyte (Table 2). The acquired MRM data were processed and quantified with Xcalibur™ software. Each experiment was repeated at least three times.

Table 1. Chromatographic conditions for LC-MS/MS analysis.

	KM297 HCl	2-PAM
Column	Synergi Hydro-RP column ($4 \mu\text{m}$, $3 \text{ mm I.D.} \times 150 \text{ mm}$)	
Mobile phases	A: water + 0.1% formic acid, B: acetonitrile + 0.1% formic acid	
Isocratic mode	A: 35% - B: 65%	A: 99% - B: 1%
Flow rate	0.7 mL/min	
Injection volume	$10 \mu\text{L}$	
Total runtime	8 min	

Table 2. Multiple reaction monitoring (MRM) transitions and retention times. amu = atomic mass unit.

Compounds	m/z (amu) Q1	m/z (amu) Q3 Quantifier	m/z (amu) Q3 Qualifier	Retention Time (min)
KM297 HCl	391.3	199.1	373.3	1.5
2-PAM	137.0	119.1	93.0	2.2

2.8. LD₅₀ Estimation and Protective Index Using the Up-and-Down Method

LD₅₀ was estimated using the improved method of Dixon's up-and-down procedure described by Rispin et al., [30]. This method uses an iterative dose-selection algorithm. It consists of a single ordered dose progression in which mice are dosed, one at a time, at 24 h intervals. The first animal receives a dose a step below the level of the best estimate of the LD₅₀. If the mouse survives, the dose for the next animal has increased by 1.1-fold the original dose; if it dies, the dose for the next animal is decreased by the same factor. In our particular conditions, the testing stops when one of the following criteria is met: (1) three consecutive animals survive at the highest dose (which is normally 2000 mg/kg); (2) five reversals occur in any six consecutive animals tested; (3) at least four animals have followed the first reversal and the specified likelihood-ratios which compare the maximum likelihood estimate for LD₅₀ with LD₅₀ values above and below exceed the critical value of 2.5. Profile likelihood methods are used to estimate confidence intervals. In practice, the stopping criteria, the resulting LD₅₀, and the corresponding confidence interval were determined using the AOT 425 Pgm software as recommended by OECD [31]. The antidotal efficacy of the oximes is expressed as a protective index (PI) with 95% confidence interval. The PI corresponds to the ratio of LD₅₀ of the studied OP agent (either VX or

paraoxon) combined with oxime treatment on LD₅₀ of OP alone. LD₅₀(VX) was previously established with a value of 15.4 µg/kg [15].

2.9. Ventilatory Effect Measurement Using Double-Chamber Plethysmography

Ventilatory parameters were recorded in a double-chamber plethysmograph (DCP, EMKA Technologies, Paris, France) according to the method described and validated by Nervo et al., [32]. Briefly, this system consists of two interconnected Plexiglas chambers, the head chamber, and the body chamber. The awake mouse is maintained in a conical tube with a small opening to allow the animal's muzzle to pass through. This restrainer is placed into the body chamber, the mouse's muzzle being in the head chamber so that there is no airflow between the two compartments. Each chamber is equipped with a pneumotachograph and a differential pressure transducer. The pneumotachograph ensures the air passages with the outside, while the differential pressure transducer measures the pressure differences between the atmosphere and the relevant compartment. There is a linear relationship between airflow and pressure difference. The mouse breathing leads to two distinct air flows which are simultaneously recorded: i-the nasal flow generated by the airflow in and out of the muzzle; and ii-the thoracic flow generated by compression and expansion of air when the thorax rises and falls. Both chambers are connected to a ventilation pump that removes carbon dioxide and moisture formed inside the chamber.

On the day of the experiment, DCP calibration was performed on two points, high value and a low value by injection of 20 mL and 0 mL of air (corresponding to no flow), respectively. The range of measures had to be included between ± 280 and ± 420 mL/s. The mouse was then placed in the device for a 5–10 min habituation session. Once its spontaneous breathing was calm and regular, the recording was started. The inspiratory time, the expiratory time, the tidal volume, the peak inspiratory flow, the peak expiratory flow, the duration of end-inspiratory pauses and end-expiratory pauses, and the specific airway resistance were continuously measured for 45–50 min using Iox[®] software (EMKA Technologies, Paris, France) and stored on a computer for subsequent analysis and calculation of additional parameters including the breathing frequency and the minute volume. The first 15 min of the recording corresponded to the physiological breathing of the mouse and were considered as an internal control. The mouse was then gently removed from the plethysmograph to receive an i.p. injection of KM297 HCl and replaced thereafter in the device for the 30-min remaining measurements. Since two experiments were performed in parallel, the KM297 HCl administration was delayed by 5 min between the first and the second mouse.

We adapted the up-and-down method previously described in chapter 2.8 to determine the KM297 HCl dose considered as the “no observed adverse effect level” (NOAEL). Thus, the first group of mice received 100 µmol/kg KM297 HCl. A 1.1-fold lower dose was then administered to the next animal. This process was repeated until reaching the dose for which no ventilatory effect was visually observed on the plethysmography traces by the experimenter. At the end of the experiment, the mouse was euthanized by an i.p. lethal injection of sodium pentobarbital (Doléthal[®], Vétéquinol SA, France).

2.10. Data Analysis

Results are expressed as mean \pm SEM.

For the cell viability assays: The IC₅₀ values were calculated using 4 parametric nonlinear regressions by Prism software (version 6.07, GraphPad Software, Inc., San Diego, CA, USA) from the logarithmic dose-response curve.

For transport measurements through the BBB model: Statistical comparisons of the endothelial permeability were performed between KM297 HCl and 2-PAM or diazepam by nonparametric Mann-Whitney test.

For DCP analysis: To study the time-course of ventilatory parameters, the values obtained after KM297 HCl injection were compared to the baseline values at T₋₅–T₀ time period using Friedman ANOVA followed by multiple comparison tests using Dunn's correction. Thereafter the analysis was

carried out on a 5-min recording period free of movements of the mouse selected at the peak of the ventilatory effects, i.e., between 10 and 15 min after the KM297 HCl injection using LabChart software (ADIInstruments, Paris, France). For each ventilatory parameter, the normality of data distribution was verified using the Shapiro–Wilk test. The differences between the KM297 HCl pre-injection and post-injection data were compared using a paired Student's *t*-tests in case of Gaussian distribution or non-Gaussian Wilcoxon tests. All tests were performed using Prism version 7.0 (GraphPad Software, Inc., San Diego, CA, USA).

For all tests, statistical differences were considered significant when $p < 0.05$.

3. Results

3.1. Pharmacodynamic Measurements

3.1.1. Based on the Reactivability of OP-Inhibited AChE

Relying on the method previously reported [15], we established standard curves of 2-PAM and KM297 HCl. While a pralidoxime concentration higher than 200 μM allowed to fully reactivate hAChE and increasing pralidoxime concentrations was correlated with increasing mAChE reactivation, KM297 HCl effect on both inhibited hAChE and mAChE was only visible at low concentrations. For concentrations higher than 20 μM , the enzyme reactivation was counterbalanced by a strong inhibition effect (Figure 2). This particular profile of KM297 did not allow us to convert an in situ percentage of AChE reactivation in a unique oxime concentration since a single measured percentage could correspond to two different concentrations, either before or after the reactivation percentage peak.

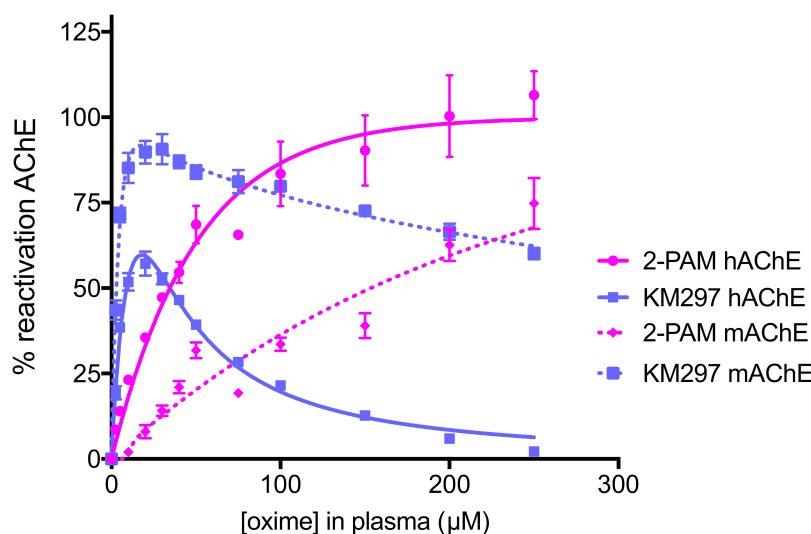


Figure 2. Standard curves of concentration-dependent reactivation of VX-inhibited hAChE and paraoxon-inhibited mAChE by two oximes. VX-inhibited hAChE and paraoxon-inhibited mAChE were incubated with 0–250 μM of oximes (2-PAM or KM297 HCl) diluted in heat-inactivated mice plasma. The recovered activity was determined after 30 min incubation at 37 °C. The best-fit curves and apparent bimolecular rate constants k_{r2} were calculated by nonlinear regression using the equation described in part 2.4.1.1 and GraphPad Prism software. Three independent experiments were performed for each oxime and each inhibited enzyme. Values are presented as mean \pm SEM.

In situ clearance of this reactivator followed by in vitro VX-inhibited hAChE reactivation showed that at the same molar concentration (i.e., 23.3 $\mu\text{mol}/\text{kg}$ or 10 mg/kg of KM297 as the free base, which corresponded to its highest concentration completely soluble in 0.9% NaCl) the four galenic forms of the studied oxime presented different pharmacodynamic properties; mainly due to their different reactivation percentage peak. The less soluble free base of the oxime predictably showed

the lowest maximal reactivation in mice plasma (React max = 5.1 ± 1.1 %), whereas the chlorhydrate salt showed a higher value (23.0 ± 2.3 %) than the two other salts (15.8 ± 2.9 % for the methylsulfonate vs. 18.6 ± 2.6 % for the acetate). The time to reach the peak of hAChE reactivation in plasma was around 5 min for the different salt forms of KM297 (from 3.5 to 6.5 ± 0.5 min). The last parameter established by the reactivability kinetic profile, the mean residence time (MRT), showed that the hAChE reactivability potential of KM297 salts was eliminated from plasma within 23 min compared to 31.0 ± 3.0 min for the free base (Figure 3a and Table 3). As the KM297 chlorhydrate salt appeared to be the galenic form with the best pharmacodynamic properties, i.e., with the highest hAChE reactivation peak together with a long mean residence time, this salt was selected for the subsequent studies. In particular, its pharmacodynamic profile was compared to pralidoxime at the same therapeutic dose of $100 \mu\text{mol/kg}$. In these conditions, KM297 HCl and 2-PAM showed a similar peak of reactivation (57.9 ± 4.3 % vs. 50.6 ± 1.7 % respectively), but 2-PAM reached its peak later than KM297 HCl (4.5 ± 0.5 min vs. 0.5 min respectively) which was consistent with a longer persistence in mice plasma (30.8 ± 2.8 min vs. 19.5 ± 1.1 min for the MRT respectively) (Figure 3b and Table 3).

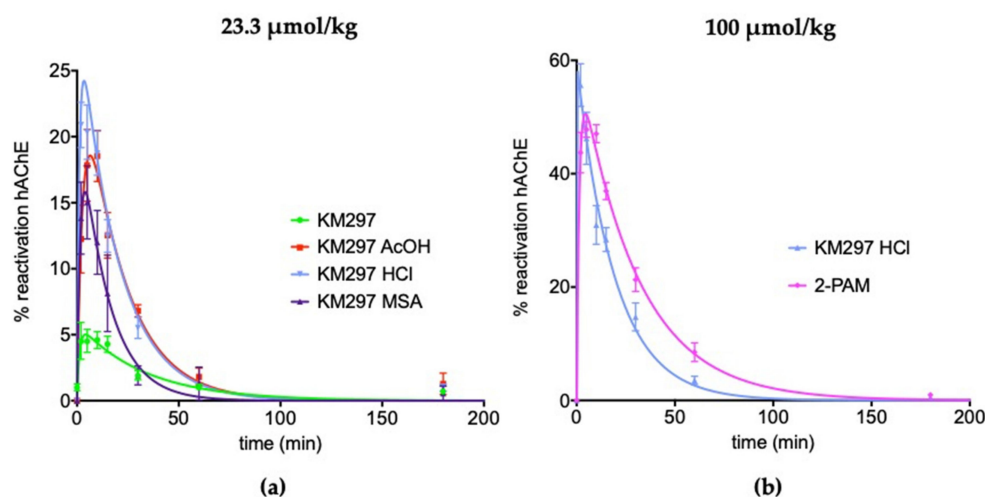


Figure 3. The reactivability of VX-inhibited hAChE by KM297 as free base and salts, and 2-PAM in mice plasma. **(a)** The same dose of $23.3 \mu\text{mol/kg}$ of KM297 free base and salts: acetate (AcOH), chlorhydrate (HCl) and methylsulfonate (MSA) was administered intraperitoneally to mice ($n = 8$). **(b)** The same dose of $100 \mu\text{mol/kg}$ of KM297 HCl and 2-PAM was administered intraperitoneally to mice ($n = 8$ – 10). Blood samples were drawn at various time points (0, 2, 5, 10, 15, 30, 60 and 180 min) after treatment, and the levels of reactivation of VX-inhibited hAChE were determined. Values are presented as percentages of maximum reactivation and points are means \pm SEM. Fitting was performed on GraphPad Prism software.

Table 3. MRT: mean residence time, t_{max} and React max respectively x and y coordinates of the peak of reactivability of VX-inhibited hAChE by KM297 as free base and salts, and 2-PAM in mice plasma presented in Figure 3.

Dose ($\mu\text{mol/kg}$)	Oxime	MRT (min)	t_{max} (min)	React Max (%)
23.3	KM297	31.0 ± 3.0	5.5 ± 1.0	5.1 ± 1.1
23.3	KM297 MSA	15.1 ± 2.7	4.0	15.8 ± 2.9
23.3	KM297 AcOH	22.4 ± 0.2	6.5 ± 0.5	18.6 ± 2.6
23.3	KM297 HCl	20.2 ± 0.5	3.5	23.0 ± 2.3
100	KM297 HCl	19.5 ± 1.1	0.5	57.9 ± 4.3
100	2-PAM	30.8 ± 2.8	4.5 ± 0.5	50.6 ± 1.7

3.1.2. Based on Blood AChE and BChE Activities

The follow-up of mice blood AChE and BChE activities showed a rapid and significant decrease of plasma BChE activity as early as 2 min after KM297 HCl injection that reached a minimum of 63% of the initial activity at 10 min and a slow recovery. Erythrocyte AChE activity decreased more slowly, reached a minimum at 1 h, and remained stable during the 3 h experiment (Figure 4).

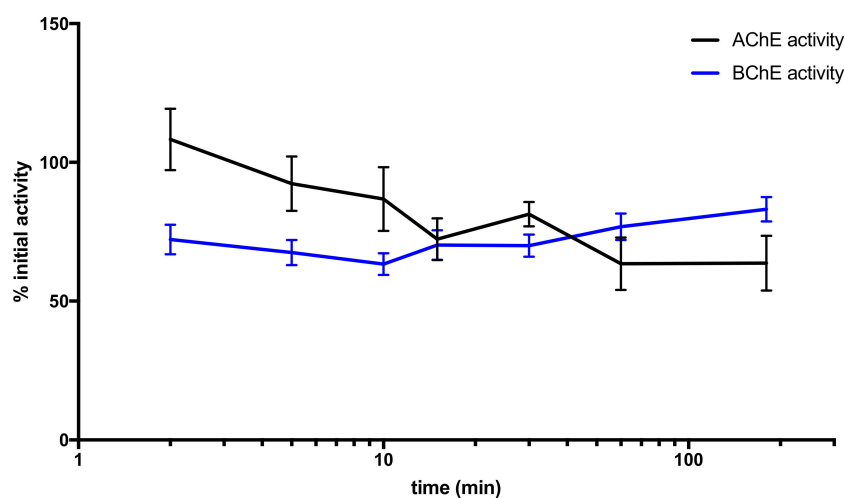


Figure 4. Mice blood AChE and BChE activity follow-up after an i.p. administration of 100 µmol/kg KM297 HCl ($n = 8-10$). Blood samples were drawn at various time points (0, 2, 5, 10, 15, 30, 60, and 180 min) after treatment, and AChE and BChE activity levels were measured. Values are presented as percentages of corresponding initial activity and points are means \pm SEM.

3.2. IC_{50} Measurements of ChE (hAChE, mAChE, and hBChE) Activity

An in vitro determination of the half-maximal inhibitory concentration (IC_{50}) value of KM297 HCl was performed on recombinant hAChE, mAChE, and hBChE to assess its ChE inhibitor potency. It showed that this oxime induced a 10-fold higher inhibition of hAChE ($0.25 \pm 0.01 \mu\text{M}$) than of mAChE ($2.5 \pm 0.1 \mu\text{M}$). It is also noteworthy that KM297 is a powerful inhibitor of hBChE ($11.2 \pm 0.2 \text{ nM}$) (Figure 5).

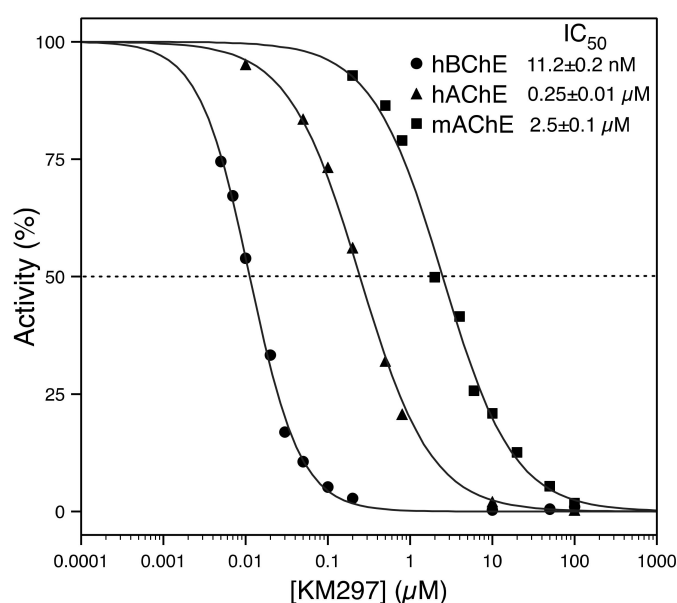


Figure 5. In vitro IC_{50} determination of KM297 HCl for hAChE, mAChE, and hBChE.

3.3. Cytotoxicity

First of all, it is noteworthy that WST-1 assay does not allow to differentiate proliferation decrease and cell viability. However, a cellular confluency-based assay (imaging assay using Incucyte[®] apparatus from Sartorius) performed in parallel (data not shown) showed that the cells were dying. Thus, we can affirm that, in our study, the WST-1 assay measured a decrease in cell viability.

While 2-PAM exposure did not induce any deleterious effect on each 6 cell line tested from 0.3 to 100 μM of oxime, KM297 HCl exposure induced a decrease of cell viability on each of them at the dose of 100 μM . Calculated IC_{50} values in each studied cell line are presented in Table 4. It should be noted that each calculated Z' result reached the ≥ 0.5 value that demonstrates the significance and robustness of the assay. HL60 cells seemed to be the most sensitive to KM297 HCl exposure with an IC_{50} value of 13.1 μM . In the HEK293 cell line, the IC_{50} value was calculated as 45.5 μM while in the other cell lines i.e., HeLa, MCF-7, HepG2, and Caco-2 cells, the IC_{50} was determined to be 75.4, 74.3, 61.9, and 65.3 μM , respectively (Figure 6 and Table 4).

Table 4. IC_{50} values of cell viability WST-1 assay, their respective 95% confidence interval and calculated Z' value following KM297 HCl exposure of each cell line.

Cell Line	IC_{50} (μM)	95 % Confidence Interval	Z' Value WST-1/ Positive Control Chlorpromazine
HEK293	45.5	[38.0; 54.4]	0.66
HeLa	75.4	[34.4; 165.5]	0.74
MCF-7	74.3	[65.3; 84.4]	0.55
HepG2	61.9	[50.4; 75.9]	0.68
Caco-2	65.3	[58.9; 72.3]	0.51
HL60	13.1	[9.4; 18.4]	0.64

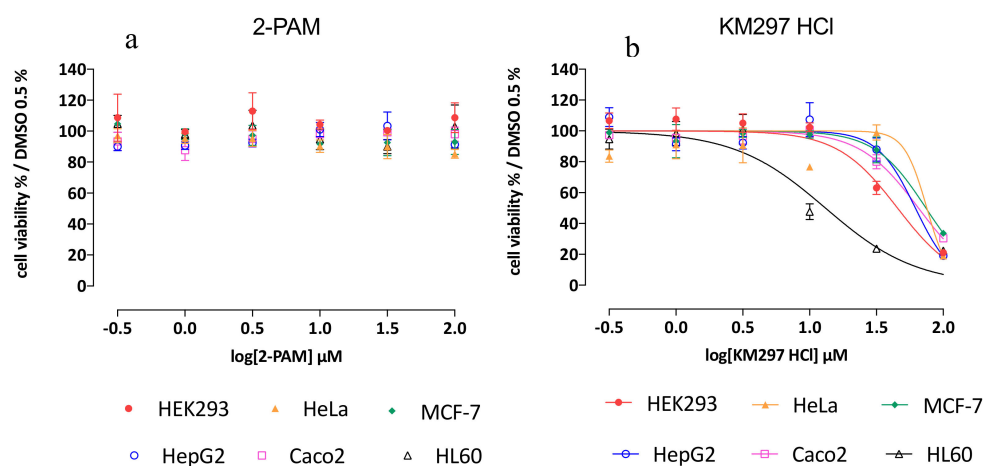


Figure 6. Cell viability WST-1 assay on 6 various cell lines (HEK293, HeLa, MCF-7, HepG2, Caco-2, and HL60 cells) after (a) 2-PAM and (b) KM297 HCl exposure. All experiments were carried out in triplicate and means \pm SEM determined.

3.4. Transport Assessment Across the Human *In Vitro* BBB Model

Before measuring transportation, the toxicity of 2-PAM and KM297 HCl was tested in the human *in vitro* BBB model. To this extent, the P_e of LY, the small hydrophilic molecule used as BBB integrity marker, incubated with the oximes during the experiment was measured in the presence and absence of oximes. At the dose of 5 and 50 μM , $P_{e\text{LY}}$ values were equivalent to that obtained for LY incubated alone ($P_{e\text{LY}} = 0.57 \times 10^{-3} \pm 0.04 \text{ cm/min}$), confirming the absence of toxicity of these compounds on the endothelial cell monolayer.

The passage of 2-PAM and KM297 HCl across BLEC monolayer was assessed using the human in vitro model (Figure 7). The Pe of KM297 HCl was 2- and 1.5-fold greater than that of 2-PAM at the dose of 5 μM and 50 μM , respectively ($\text{Pe}_{\text{KM297}, 5 \mu\text{M}} = 2.36 \times 10^{-3} \pm 0.49 \text{ cm/min}$ vs. $\text{Pe}_{\text{2-PAM}, 5 \mu\text{M}} = 1.16 \times 10^{-3} \pm 0.18 \text{ cm/min}$, $p = 0.001$ and $\text{Pe}_{\text{KM297}, 50 \mu\text{M}} = 5.35 \times 10^{-3} \pm 0.53 \text{ cm/min}$ vs. $\text{Pe}_{\text{2-PAM}, 50 \mu\text{M}} = 2.89 \times 10^{-3} \pm 1.81 \text{ cm/min}$, $p = 0.036$).

As brain penetration of a drug such as diazepam is known to be relatively high, Pe values of KM297 HCl were compared with those of diazepam as a positive control. The Pe of 50 μM KM297 HCl remained significantly lower than that of diazepam ($\text{Pe}_{\text{KM297}, 50 \mu\text{M}} = 5.35 \times 10^{-3} \pm 0.53 \text{ cm/min}$ vs. $\text{Pe}_{\text{diazepam}, 50 \mu\text{M}} = 7.54 \times 10^{-3} \pm 0.95 \text{ cm/min}$, $p = 0.024$).

Transport of 2-PAM and KM297 HCl across the human in vitro BBB was concentration-dependent at the dose of 5 and 50 μM as endothelial permeability increased with the oximes concentration whereas that of diazepam did not (Table 5).

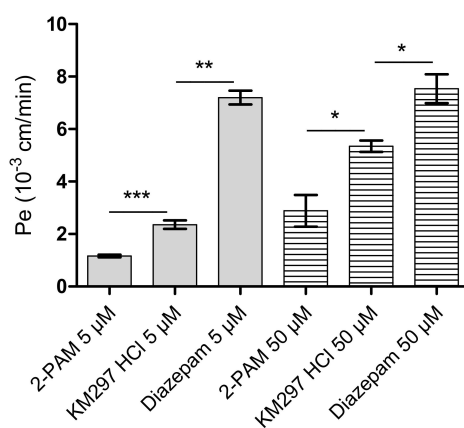


Figure 7. Endothelial permeability coefficient (Pe) of 2-PAM, KM297 HCl, and diazepam measured in the human in vitro BBB model at 5 and 50 μM . Values are presented as mean \pm SEM, $n = 3\text{--}12$. Comparisons were performed using Mann–Whitney test between KM297 HCl and 2-PAM or diazepam. * $p < 0.05$, ** $p < 0.01$, *** $p \leq 0.001$.

Table 5. The statistical comparison performed by a nonparametric Mann–Whitney test of the Pe values at 5 and 50 μM for 2-PAM, KM297 HCl, and diazepam.

2-PAM	<i>p</i> -Value
5 μM vs. 50 μM	0.0076 (**)
KM297 HCl	
5 μM vs. 50 μM	0.0004 (***)
Diazepam	
5 μM vs. 50 μM	0.7 (ns)

3.5. In Vivo Protective Index Assessment

Experiments of the up-and-down procedure performed on VX and paraoxon exposure are presented in Tables 6 and 7, respectively. $\text{LD}_{50}(\text{VX})$ was already established previously with a value of 15.4 $\mu\text{g/kg}$ [15]. Intraperitoneal injection of the KM297 free base at the dose of 10 mg/kg did not show any protection after the VX challenge as demonstrated by the PI equal to 1 (Table 6). LD_{50} of paraoxon was established to be 796 $\mu\text{g/kg}$. Alone, 100 $\mu\text{mol/kg}$ of 2-PAM induced higher protective efficacy than the same dose of KM297 HCl (PI value of 2.58 and 1.18, respectively). Intraperitoneal treatment with less than a two-thirds dose of KM297 HCl (i.e., 62 $\mu\text{mol/kg}$) increased its efficacy after subcutaneous paraoxon challenge (PI = 1.94) (Table 7). LD_{50} of i.p. injection of KM297 HCl was also assessed by the up-and-down method and achieved a value of 300 $\mu\text{mol/kg}$ (Table 8).

Table 6. LD₅₀ estimation using the up-and-down method for intraperitoneally injected mice at the dose of 10 mg/kg (i.e., 23.3 μmol/kg) of KM297 free base one minute after VX subcutaneous challenge.

	KM297			Assumed LD ₅₀ = 1.1 × LD ₅₀ (VX)	
VX Dose (× LD ₅₀ (VX))	0.91	1.0	1.1	All	
Survival	1/1	1/3	0/1	2/5	
LD ₅₀ = 1 × LD ₅₀ (VX); 95% confidence interval [0; +∞[

An LD₅₀ value is initially assumed at the beginning of each experiment with sigma = 0.0414 (= log 1.1). The LD₅₀ value was calculated using the AOT 425 Pgm software.

Table 7. LD₅₀ estimation using the up-and-down method for untreated mice or injected intraperitoneally at the dose of 100 μmol/kg of 2-PAM or KM297 HCl and 62 μmol/kg of KM297 HCl one minute after paraoxon subcutaneous challenge. An LD₅₀ value is initially assumed at the beginning of each experiment with sigma = 0.0414 (= log 1.1). The LD₅₀ values were calculated using the AOT 425 Pgm software.

	No Treatment		Assumed LD ₅₀ = 964 μg/kg						
Paraoxon dose (μg/kg)	724	796	876	All					
Survival	1/1	1/2	0/2	2/5					
LD ₅₀ = 796 μg/kg; 95% Confidence Interval [283; 904]									
2-PAM 100 μmol/kg		Assumed LD ₅₀ = 1.6 × LD ₅₀ (Paraoxon)							
Paraoxon dose (× LD ₅₀ (paraoxon))	1.45	1.60	1.76	1.94	2.13	2.34	2.58	2.83	All
Survival	1/1	1/1	1/1	1/1	1/1	1/1	2/3	0/2	8/11
LD ₅₀ = 2.58 × LD ₅₀ (paraoxon); 95% Confidence Interval [2.40; 2.92]									
KM297 HCl 100 μmol/kg		Assumed LD ₅₀ = 1.2 × LD ₅₀ (Paraoxon)							
Paraoxon dose (× LD ₅₀ (paraoxon))	0.99	1.09	1.2	All					
Survival	1/1	2/3	1/2	4/6					
LD ₅₀ = 1.18 × LD ₅₀ (paraoxon); 95% Confidence Interval [0; +∞[
KM297 HCl 62 μmol/kg		Assumed LD ₅₀ = 2.13 × LD ₅₀ (paraoxon)							
Paraoxon dose (× LD ₅₀ (paraoxon))	1.76	1.94	2.13	All					
Survival	1/1	2/3	0/2	3/6					
LD ₅₀ = 1.94 × LD ₅₀ (paraoxon); 95% Confidence Interval [1.73; 2.25]									

Table 8. LD₅₀ estimation of KM297 HCl using the up-and-down method for injected intraperitoneally mice. An LD₅₀ value of 200 μmol/kg is initially assumed at the beginning of the experiment with sigma = 0.0176 (= log 1.5). The LD₅₀ value was calculated using the AOT 425 Pgm software.

	No Treatment		Assumed LD ₅₀ = 200 μmol/kg		
KM297 HCl dose (μmol/kg)	133	200	300	450	All
Survival	1/1	2/2	1/2	0/1	4/6
LD ₅₀ = 300 μmol/kg; 95% Confidence Interval [206; 961]					

3.6. Ventilatory Effect Measurements in Mice

Thanks to the accurate monitoring of mice ventilation with the DCP system, a NOAEL dose has been determined. This NOAEL corresponds to the highest i.p. injected dose of KM297 HCl without any observable toxic effects as described below. From the symptomatic dose of 100 μmol/kg, we iteratively decreased the dose of the treatment by the same factor of 1.1. This process was continued

down to the dose of 62 $\mu\text{mol/kg}$ for which no ventilatory alteration was visually observed by the experimenter. Six different animals were treated at this dose to confirm the lack of visual effect on breathing. As a result, the observed NOAEL is equivalent to approximately one-fifth of the LD_{50} of KM297 HCl (300 $\mu\text{mol/kg}$).

Samples of plethysmography recording are presented in Figure 8. For all ventilatory parameters, no significant difference was noticed between both treated groups before KM297 HCl injection (at the dose of 100 $\mu\text{mol/kg}$ and 62 $\mu\text{mol/kg}$ respectively). However, the minute volume was significantly decreased (peak effect: 18.88 ± 2.80 vs. 26.67 ± 3.70 mL, $p < 0.0001$; Figure 9a) probably due to an increase of end-inspiratory pauses duration (peak effect: 40.13 ± 10.85 vs. 15.32 ± 8.48 ms, $p < 0.01$; Figure 9b) for 100 $\mu\text{mol/kg}$ KM297 HCl-treated mice compared to the same mice before treatment, (i.e., at the T_{-5} – T_0 reference period). These ventilatory effects started as early as the 5th minute following KM297 HCl injection, peaked between 10- and 15-min after, for up to 20 min, then gradually decreased over time while remaining present. From these kinetics, the set of ventilatory parameters was then analyzed at the peak of the effects, i.e., at the T_{10} – T_{15} time period.

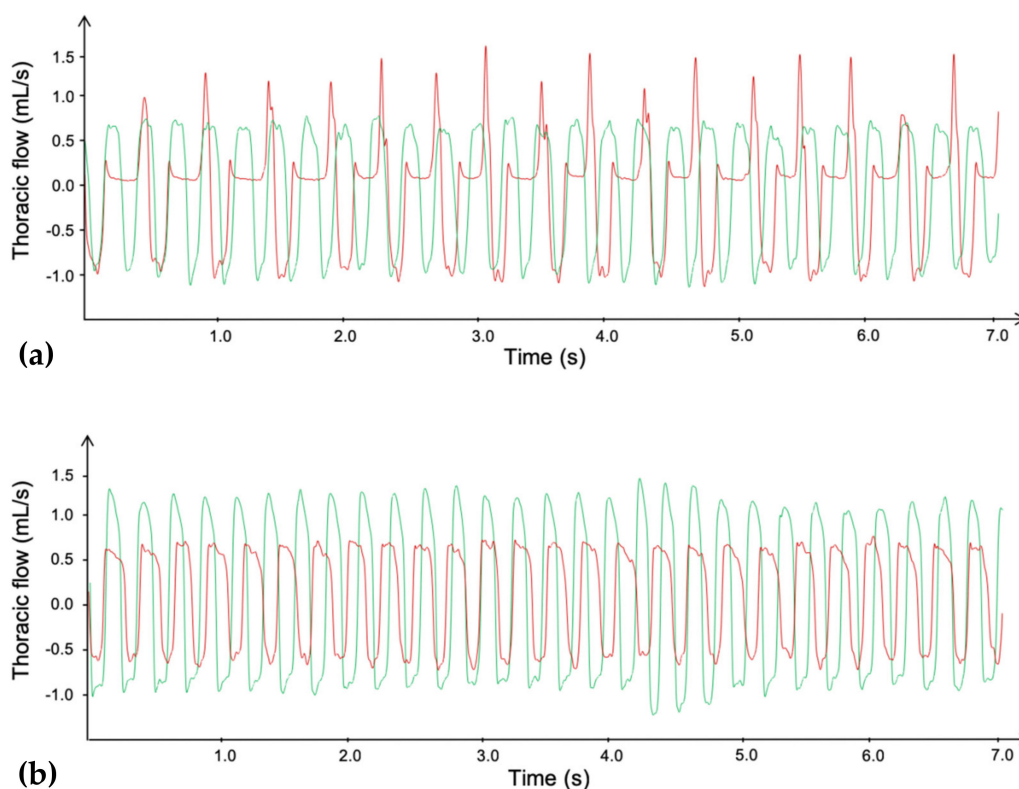


Figure 8. Plethysmography traces of the thoracic flow before (green line) and after (red line) i.p. injection of a dose of 100 $\mu\text{mol/kg}$ (a) or 62 $\mu\text{mol/kg}$ (b) of KM297 HCl in mice. Traces were selected at the peak of the ventilatory effects, i.e., between 10 and 15 min after the KM297 HCl administration.

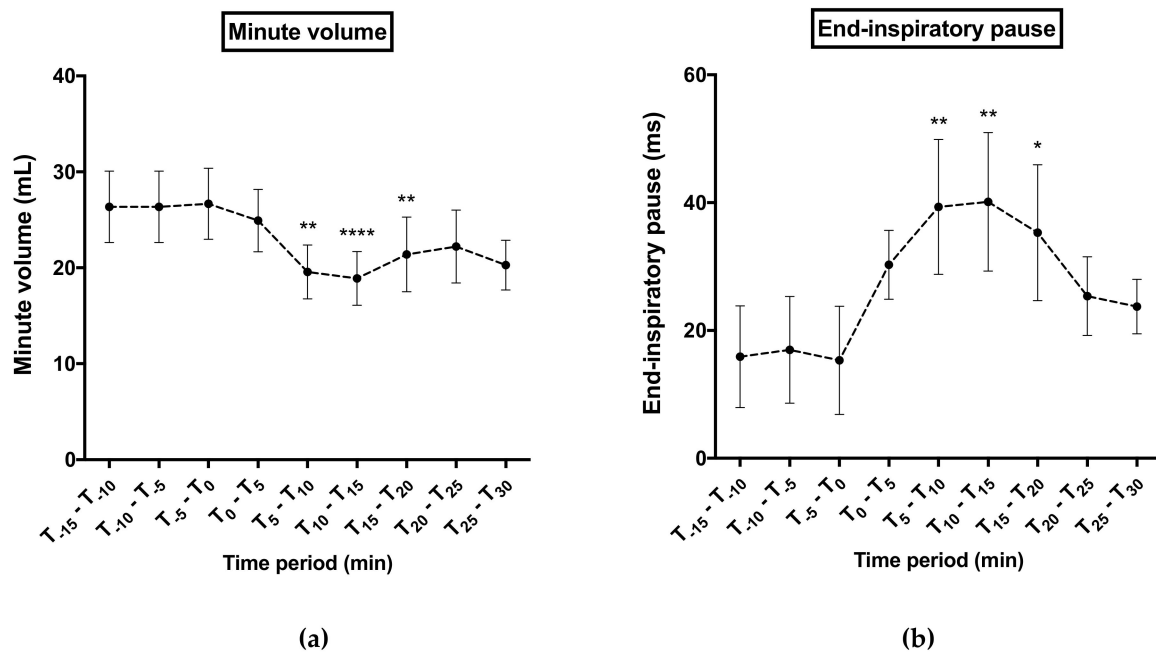


Figure 9. Time course of minute volume (a) and end-inspiratory pause (b) 15 minutes before 100 $\mu\text{mol/kg}$ KM297 HCl injection up to 30 min later. Results are presented as the mean of 5 min-means of recordings \pm SEM, $n = 10$. Comparisons were performed using Friedman ANOVA followed by multiple tests using Dunn's correction with T_{-5} – T_0 time period considered as the reference period. * $p < 0.05$, ** $p < 0.01$, **** $p < 0.0001$.

The inspiratory time ($p = 0.0323$, Figure 10a) as well as the end-inspiratory pauses duration ($p = 0.0371$, Figure 10c) were significantly increased following 100 $\mu\text{mol/kg}$ KM297 HCl injection in comparison to pre-injection data, while there was no significant difference following 62 $\mu\text{mol/kg}$ KM297 HCl administration. In contrast, the peak inspiratory flow ($p = 0.0002$, Figure 10e) and the resulting ventilatory amplitude ($p = 0.0098$, Figure 10f) were significantly decreased following 100 $\mu\text{mol/kg}$ KM297 HCl administration, while no difference was observed regarding the peak inspiratory flow after 62 $\mu\text{mol/kg}$ KM297 HCl injection. With this latter dose the ventilatory amplitude remained reduced ($p = 0.0353$), but with a lower intensity than that of the dose of 100 $\mu\text{mol/kg}$ (5.6% vs. 19.8% respectively). A marked reduction in the tidal volume ($p = 0.0020$, Figure 10d) and the resulting minute volume ($p = 0.0002$, Figure 10b) was also noticed following 100 $\mu\text{mol/kg}$ KM297 HCl injection, and persisted with a lower intensity after the administration of the dose of 62 $\mu\text{mol/kg}$ (20.4% vs. 10% respectively for the tidal volume, $p = 0.0435$; 29% vs. 11.4% respectively for the minute volume, $p = 0.0129$). Other ventilatory parameters remained unchanged (data not shown).

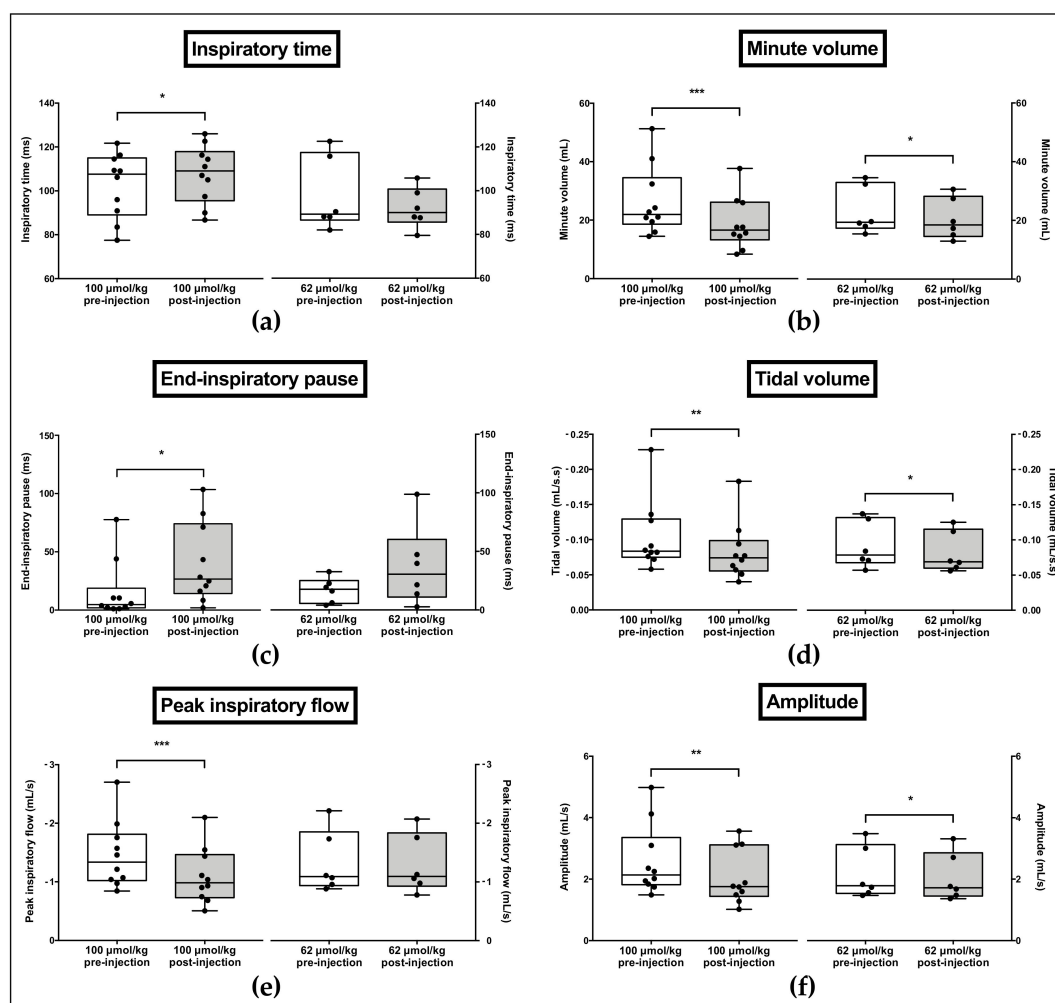


Figure 10. Effects of i.p. administration of 100 $\mu\text{mol/kg}$ or 62 $\mu\text{mol/kg}$ KM297 HCl on ventilatory parameters recorded by double-chamber plethysmography: inspiratory time (a), minute volume (b), end-inspiratory pause (c), tidal volume (d), peak inspiratory flow (e) and amplitude (f). $n = 6\text{--}10$. The line in the middle of the box is plotted at the median. Each individual value is represented as black circles. Whiskers range from the maximum value to minimum value. Comparisons were performed using paired t-tests for normally distributed variables or Wilcoxon tests in case of non-Gaussian distribution. * $p < 0.05$, ** $p < 0.01$, *** $p < 0.001$.

4. Discussion

KM297 is an uncharged reactivator of OP-inhibited AChE based on tetrahydroacridine pyridine-aldoxime hybrids [9,33]. Its tacrine scaffold has been recently identified as relevant against an OP pesticide poisoning [34]. Designed to cross the BBB, the high lipophilicity of the free base leads to poor solubility [35]: 10 mg/kg (i.e., 23.3 $\mu\text{mol/kg}$) is the highest achievable concentration in 1% DMSO, 10% Cremophor-EL, 0.9% NaCl. Unfavorable pharmacodynamics of the free base (React-max = $5.1 \pm 1.1\%$) is coherent with an absence of in vivo protection against a VX challenge (PI = 1). This is in agreement with the correlation between pharmacodynamic data and protective efficacy reported earlier [15].

New formulations with higher solubility in water such as MSA, AcOH, or HCl salts have been assessed. They present at least 3-fold higher maximal reactivation of VX-inhibited hAChE at their respective t_{max} (React-max value equals to $15.8\% \pm 2.9\%$, $18.6\% \pm 2.6\%$ and $23.0\% \pm 2.3\%$, respectively) when injected at the same dose of 23.3 $\mu\text{mol/kg}$. Due to its more favorable pharmacodynamic profile, the HCl salt was selected for further assessments.

We have shown that the strong reversible inhibition of AChE by KM297 HCl prevents the correlation between pharmacodynamics and pharmacokinetics since one percentage of reactivation could correspond to two oxime concentrations in the standard curve of reactivation. The paraoxon-inhibited mAChE reactivation curve by KM297 HCl presents a similar pharmacodynamic profile which is consistent with the 10-fold higher IC_{50} value measured with mAChE as compared to the one from hAChE. It is worth noting that the 20-fold lower calculated IC_{50} value with hBChE versus hAChE prevents BChE from playing a back-up role in acetylcholine hydrolysis in the case of AChE inhibition. Interestingly, the inhibition property of KM297 could be used as an alternative for reactivation to estimate its plasma concentration. The IC_{50} curve could then allow the correlation of a percentage of inhibition of AChE to a concentration of oxime.

However, *in vivo* protective efficacy of KM297 HCl after paraoxon challenge seems to be completely uncorrelated to its maximal percentage of reactivation. Indeed, the same therapeutic dose fixed at 100 $\mu\text{mol/kg}$ KM297 HCl shows a similar pharmacodynamic profile to that of 2-PAM but a different protective index: respectively 1.18 and 2.58. We can reject that this disparity is due to the lack of cerebral effect since our *in vitro* BBB model established that, as with 2-PAM, KM297 HCl does not affect BBB integrity, though at the same high dose (i.e., 50 μM) KM297 HCl induces cytotoxic effect on several cell lines. This apparent discrepancy can be explained by the huge temporal difference between both observations: endothelial cell monolayer integrity is assessed only 60 min after KM297 HCl exposure while cell line toxicity is measured 48 h post-exposure. Second, this model established that the permeability of KM297 HCl is 2-fold higher than 2-PAM, although lower than the positive control diazepam. Furthermore, 2-PAM and KM297 HCl cross the *in vitro* BBB in a dose-dependent manner, as already described for 2-PAM using *in vivo* rat brain microdialysis technique [36].

The potential cytotoxicity and/or systemic toxicity of KM297 could eventually explain its low protective efficacy against OP exposure. Cytotoxicity was evaluated in 6 different human cell lines, each related to different organs: HEK293 to the kidney, HeLa to the uterus, MCF-7 to the breast, HepG2 to the liver, Caco-2 to the colon, HL-60 to the bone marrow. Whereas 2-PAM does not seem to induce any cytotoxicity regardless of the cell line and the concentration of oxime considered, KM297 HCl appears most cytotoxic to HL-60 cells with an IC_{50} of 13.1 μM , followed by HEK293 and then to the four other cell lines: HeLa, HepG2, Caco-2 and MCF-7 cells with similar IC_{50} values greater than 61 μM . By contrast, the IC_{50} of 2-PAM in the HepG2 cell line was 22.8 mM [37]. KM297 HCl appears to be almost 400-fold more cytotoxic than the reference oxime. Bone marrow and consequently blood cells seem to be the most sensitive cells to KM297 HCl. Other tacrine-derived oximes show similar toxicity on HepG2 cells than tacrine [34]. The tacrine scaffold has also been shown, among others, to play a role in hepatotoxicity [38] even if by way of a metabolite [39].

We evaluated the systemic toxicity of KM297 HCl through *i.p.* injection by measuring the LD_{50} at 24 h with the up-and-down procedure. With an LD_{50} at 300 $\mu\text{mol/kg}$, KM297 HCl is 3-fold more toxic than 2-PAM delivered intramuscularly in the same Swiss male mice ($LD_{50}(2\text{-PAM}) = 1 \text{ mmol/kg}$) [40]. In other words, the therapeutic dose of 100 $\mu\text{mol/kg}$ chosen to compare the protective efficacy of various oximes is 1/3rd of the $LD_{50}(\text{KM297 HCl})$ whereas it is only 1/10th of $LD_{50}(2\text{-PAM})$.

In addition, mice that received an *i.p.* injection of KM297 HCl at the dose of 100 $\mu\text{mol/kg}$ showed some characteristic preliminary symptoms related to ChE inhibition such as hypotonia (data not shown). To estimate the level of AChE and BChE inhibition after *i.p.* injection of KM297 HCl in mice in the absence of OP exposure, we monitored blood AChE and BChE activities. We expected that the time at maximal inhibition of erythrocyte AChE and plasma BChE activities would match that of maximal reactivability seen in the pharmacodynamic curve, as both measurements are proxies of the actual concentration of circulating KM297 HCl. Yet blood AChE activity reached a minima of 60 min after KM297 HCl injection, and plasma BChE activity reached a minima of 10 min after injection, whereas maximal reactivation of VX-inhibited hAChE peaks only 30 s after the injection. However, the dual reactivation/inhibition activity of KM297 HCl could hamper the correct estimation of the time at the peak of reactivation as larger concentrations induce strong inhibition that cancels out the recovery of

activity due to reactivation. A longer persistence of this oxime and a delayed peak of concentration of KM297 HCl in the blood compartment could explain this incongruity.

Either method, pharmacodynamics based on reactivability power or inhibition, reports the blood compartment time-evolution of different states of the oxime: bound to ChE for the inhibition method or free oxime for the reactivability method. Consequently, by gathering these results and by taking into account the inhibition potency of KM297 HCl in the reactivability pharmacodynamic data, it is established that this oxime penetrates rapidly into the blood compartment and has a sufficiently low clearance to inhibit a significant portion of circulating AChE and BChE for hours. This long lifetime is corroborated by DCP results, which show a persistence of ventilatory alterations, thought to be related to ChE inhibition (see below), beyond the mean residence time in blood measured as measured by the reactivability method (20 min). Naturally, it must be considered that the DCP results and blood pharmacokinetic data do not show the inhibition of the same compartment i.e., lung vs. blood. Nevertheless, the difference between these two proxy-based estimates of the actual circulating concentration of oximes confirms the main deficiency of the reactivability assay which lies in its inability to take into account the intrinsic inhibition potency of the oxime. In this case, a chemical analytical method to directly measure the concentration of oximes is necessary.

ChE inhibitors such as OP compounds or carbamates may provoke death by respiratory arrest. Breath monitoring with a DCP system confirms that a dose of 100 $\mu\text{mol/kg}$ of KM297 HCl i.p. alters ventilation. In particular, this dose of KM297 HCl induces a significant increase in inspiratory time correlated to the appearance of end-inspiratory pauses. These alterations have previously been established on the breathing of mice challenged with paraoxon and physostigmine, a carbamate inhibitor of AChE [32]. These breathing alterations after administration of a dose of 100 $\mu\text{mol/kg}$ KM297 HCl can be correlated to its potency to inhibit ChE. Indeed, significant differences of minute volume and end-inspiratory pauses duration appear around 10 min after oxime injection, when the inhibition of plasmatic BChE activity is the highest, which means when BChE is no longer able to protect the ventilatory system from the toxic effects of a high circulating acetylcholine concentration [32]. Moreover, we determined the NOAEL at 62 $\mu\text{mol/kg}$ or approximately one-fifth of the LD_{50} of KM297 HCl (300 $\mu\text{mol/kg}$).

It is more relevant to treat OP-exposed animals with an equitoxic dose of reactivator as reported earlier [41,42], rather than use an equimolar dose of reactivator. But instead of applying an arbitrary factor of LD_{50} to determine the equitoxic dose, we determine the NOAEL dose for each reactivator, based on the alteration of ventilatory parameters relevant to ChE inhibition. Regarding the criteria for establishing the NOAEL dose, even if ventilatory parameters such as inspiratory time and end-inspiratory pause duration increase or peak inspiratory flow decrease are no longer noticeable, other parameter modifications persist such as tidal volume and minute volume and amplitude decrease. The latter are, however, lower than those measured at the dose of 100 $\mu\text{mol/kg}$. It seems that the visual assessment of ventilation cycle alterations does not appear to be completely accurate in comparison to the calculation of all the different breathing parameters. It seems sufficient to establish a more effective therapeutic dose since there is a significant increase of the protection brought by the KM297 HCl treatment: PI increases from 1.18 at 100 $\mu\text{mol/kg}$ to 1.94 at 62 $\mu\text{mol/kg}$. A higher protective efficacy with a lower dose has previously been described with other oximes [41]. This result combined with cytotoxic data attests to the narrowness of the therapeutic window of KM297 HCl.

5. Conclusions

We improved the solubility and bioavailability of KM297 with salt derivatives, the most favorable being the chlorhydrate salt. As performed here with KM297 HCl, inhibition potency of oximes could be identified by using the DCP system, which proves its ability to accurately detect minute ventilatory alterations related to ChE inhibition. This system also allows the establishment of a suitable therapeutic dose: we hypothesize that 20% ($\text{LD}_{50}(\text{oxime})$) would correspond to its NOAEL value, which should be used as a therapeutic dose in follow-on studies.

Finally, even if the strong ChE inhibition induced by KM297 HCl should disqualify it as a drug for emergency treatment, its potency in temporarily masking ChE sites from nerve agents, associated with its ability to cross BBB to reach the CNS targets as huperzine does [43], as well as its long-lasting persistence as a reversible adduct with ChE in at least the blood compartment, and of course, its ability to reactivate OP-inhibited ChE could conversely qualify it as an efficient prophylactic treatment for OP nerve agents.

Author Contributions: Conceptualization, A.-G.C. and F.N.; KM297 synthesis, M.K., J.Y., and R.B.; cytotoxicity experiments, A.O. and P.V.; in vivo pharmacokinetic and pharmacodynamic experiments C.R., C.C., and A.-G.C.; IC₅₀ measurement C.C., X.B., F.N., and J.D.; LD₅₀ and protective index estimation A.-G.C., C.R., and C.C.; transport experiments across human in vitro BBB model, J.-F.G., C.L., J.H., F.G., and M.-P.D., ventilatory effect measurements A.-S.H., A.N., and N.J.; writing—original draft preparation, A.-G.C.; writing—review and editing, C.C., A.-S.H., A.N., J.D., C.R., A.O., P.V., J.-F.G., C.L., J.H., F.G., M.-P.D., J.Y., M.K., R.B., X.B., N.J., and F.N.; supervision, F.N.; project administration, F.N., A.-G.C., and J.D. All authors have read and agreed to the published version of the manuscript.

Funding: This research was funded by the French Ministry of Armed Forces (Direction Générale de l'Armement and Service de Santé des Armées) under contracts PDH-2-NRBC-4-C-4203 and NBC-5-C-4210 and by ANR under contract CNS-Antidote (ANR-17-CE39-0012). Cytotoxicity: This work has benefited from an Investissement d'Avenir grant of the ANR (LABEX ANR-10-LABX-0034_Medalis).

Acknowledgments: CNRS and the University of Strasbourg are acknowledged for support. The authors are grateful to Joseph Kononchik for his critical reading and editing of the manuscript.

Conflicts of Interest: The authors declare no conflict of interest.

References

1. Eddleston, M. Novel Clinical Toxicology and Pharmacology of Organophosphorus Insecticide Self-Poisoning. *Annu. Rev. Pharmacol. Toxicol.* **2019**, *59*, 341–360. [CrossRef]
2. John, H.; Van Der Schans, M.J.; Koller, M.; Spruit, H.E.T.; Worek, F.; Thiermann, H.; Noort, D. Fatal sarin poisoning in Syria 2013: Forensic verification within an international laboratory network. *Forensic Toxicol.* **2017**, *36*, 61–71. [CrossRef] [PubMed]
3. OPCW.org. OPCW Confirms Use of Sarin and Chlorine in Ltamenah, Syria, on 24 and 25 March 2017. Available online: <https://www.opcw.org/media-centre/news/2018/06/opcw-confirms-use-sarin-and-chlorine-ltamenah-syria-24-and-25-march-2017> (accessed on 13 June 2018).
4. Patočka, J. What killed Kim Jong-Nam? Was it the agent VX? *Mil. Med. Sci. Lett.* **2017**, *86*, 86–89. [CrossRef]
5. Carlsen, L. After Salisbury Nerve Agents Revisited. *Mol. Informatics* **2018**, *38*, 8–9. [CrossRef]
6. Cannard, K. The acute treatment of nerve agent exposure. *J. Neurol. Sci.* **2006**, *249*, 86–94. [CrossRef]
7. Mercey, G.; Verdelet, T.; Renou, J.; Kliachyna, M.; Baati, R.; Nachon, F.; Jean, L.; Renard, P.-Y. Reactivators of Acetylcholinesterase Inhibited by Organophosphorus Nerve Agents. *Accounts Chem. Res.* **2012**, *45*, 756–766. [CrossRef]
8. Worek, F.; Thiermann, H.; Wille, T. Oximes in organophosphate poisoning: 60 years of hope and despair. *Chem. Interactions* **2016**, *259*, 93–98. [CrossRef]
9. Kliachyna, M.; Santoni, G.; Nussbaum, V.; Renou, J.; Sanson, B.; Colletier, J.-P.; Arboléas, M.; Loiodice, M.; Weik, M.; Jean, L.; et al. Design, synthesis and biological evaluation of novel tetrahydroacridine pyridine-aldoxime and -amidoxime hybrids as efficient uncharged reactivators of nerve agent-inhibited human acetylcholinesterase. *Eur. J. Med. Chem.* **2014**, *78*, 455–467. [CrossRef] [PubMed]
10. Cecchelli, R.; Aday, S.; Sevin, E.; Almeida, C.; Culot, M.; Dehouck, L.; Coisne, C.; Engelhardt, B.; Dehouck, M.-P.; Ferreira, L. A Stable and Reproducible Human Blood-Brain Barrier Model Derived from Hematopoietic Stem Cells. *PLoS ONE* **2014**, *9*, e99733. [CrossRef]
11. Zueva, I.; Dias, J.; Lushchekina, S.V.; Semenov, V.; Mukhamedyarov, M.; Pashirova, T.; Babaev, V.; Nachon, F.; Petrova, N.; Nurullin, L.; et al. New evidence for dual binding site inhibitors of acetylcholinesterase as improved drugs for treatment of Alzheimer's disease. *Neuropharmacol.* **2019**, *155*, 131–141. [CrossRef]
12. Carletti, E.; Li, H.; Li, B.; Ekström, F.; Nicolet, Y.; Loiodice, M.; Gillon, E.; Froment, M.T.; Lockridge, O.; Schopfer, L.M.; et al. Aging of Cholinesterases Phosphorylated by Tabun Proceeds through O-Dealkylation. *J. Am. Chem. Soc.* **2008**, *130*, 16011–16020. [CrossRef] [PubMed]

13. Ellman, G.L.; Courtney, K.; Andres, V.; Featherstone, R.M. A new and rapid colorimetric determination of acetylcholinesterase activity. *Biochem. Pharmacol.* **1961**, *7*, 88–95. [[CrossRef](#)]
14. Ronco, C.; Carletti, E.; Colletier, J.-P.; Weik, M.; Nachon, F.; Jean, L.; Renard, P.-Y. Huprine Derivatives as Sub-Nanomolar Human Acetylcholinesterase Inhibitors: From Rational Design to Validation by X-ray Crystallography. *ChemMedChem* **2011**, *7*, 400–405. [[CrossRef](#)] [[PubMed](#)]
15. Calas, A.-G.; Dias, J.; Rousseau, C.; Arboléas, M.; Touvrey-Loiodice, M.; Mercey, G.; Jean, L.; Renard, P.-Y.; Nachon, F. An easy method for the determination of active concentrations of cholinesterase reactivators in blood samples: Application to the efficacy assessment of non quaternary reactivators compared to HI-6 and pralidoxime in VX-poisoned mice. *Chem. Interactions* **2017**, *267*, 11–16. [[CrossRef](#)]
16. Kwon, Y. *Handbook of Essential Pharmacokinetics, Pharmacodynamics and Drug Metabolism for Industrial Scientists*; Springer: Boston, MA, USA, 2007; p 1 online resource; 302p.
17. Dingova, D.; Leroy, J.; Check, A.; Garaj, V.; Krejci, E.; Hrabovska, A. Optimal detection of cholinesterase activity in biological samples: Modifications to the standard Ellman’s assay. *Anal. Biochem.* **2014**, *462*, 67–75. [[CrossRef](#)]
18. Nachon, F.; Nicolet, Y.; Viguié, N.; Masson, P.; Fontecilla-Camps, J.-C.; Lockridge, O. Engineering of a monomeric and low-glycosylated form of human butyrylcholinesterase. *JBIC J. Boil. Inorg. Chem.* **2002**, *269*, 630–637. [[CrossRef](#)]
19. Brazzolotto, X.; Wandhammer, M.; Ronco, C.; Trovaslet, M.; Jean, L.; Lockridge, O.; Renard, P.-Y.; Nachon, F. Human butyrylcholinesterase produced in insect cells: Huprine-based affinity purification and crystal structure. *FEBS J.* **2012**, *279*, 2905–2916. [[CrossRef](#)]
20. Dudani, A.K.; Gupta, R.S. Effect of chlorpromazine and trifluoperazine on cytoskeletal components and mitochondria in cultured mammalian cells. *Tissue Cell* **1987**, *19*, 183–196. [[CrossRef](#)]
21. Houël, E.; Fleury, M.; Odonne, G.; Nardella, F.; Bourdy, G.; Vonthron-Sénécheau, C.; Villa, P.; Obrecht, A.; Eparvier, V.; Deharo, E.; et al. Antiplasmodial and anti-inflammatory effects of an antimalarial remedy from the Wayana Amerindians, French Guiana: Takamalaimë (*Psidium acutangulum* Mart. ex DC., Myrtaceae). *J. Ethnopharmacol.* **2015**, *166*, 279–285. [[CrossRef](#)]
22. Zhang, J.-H.; Chung, T.D.Y.; Oldenburg, K.R. A Simple Statistical Parameter for Use in Evaluation and Validation of High Throughput Screening Assays. *J. Biomol. Screen.* **1999**, *4*, 67–73. [[CrossRef](#)]
23. Pedroso, D.; Tellechea, A.; Moura, L.; Carvalho, I.F.; Duarte, J.; Carvalho, E.; Ferreira, L. Improved Survival, Vascular Differentiation and Wound Healing Potential of Stem Cells Co-Cultured with Endothelial Cells. *PLoS ONE* **2011**, *6*, e16114. [[CrossRef](#)] [[PubMed](#)]
24. Zhang, Y.; García-Gabilondo, M.; Grayston, A.; Feiner, I.V.J.; Anton-Sales, I.; Loiola, R.A.; Llop, J.; Ramos-Cabrer, P.; Barba, I.; Garcia-Dorado, D.; et al. PLGA protein nanocarriers with tailor-made fluorescence/MRI/PET imaging modalities. *Nanoscale* **2020**, *12*, 4988–5002. [[CrossRef](#)] [[PubMed](#)]
25. Nishihara, H.; Soldati, S.; Mossu, A.; Rosito, M.; Rudolph, H.; Muller, W.A.; Latorre, D.; Sallusto, F.; Sospedra, M.; Martin, R.; et al. Human CD4+ T cell subsets differ in their abilities to cross endothelial and epithelial brain barriers in vitro. *Fluids Barriers CNS* **2020**, *17*, 3–18. [[CrossRef](#)] [[PubMed](#)]
26. Viswanathan, G.K.; Shwartz, D.; Losev, Y.; Arad, E.; Shemesh, C.; Pichinuk, E.; Engel, H.; Raveh, A.; Jelinek, R.; Cooper, I.; et al. Purpurin modulates Tau-derived VQIVYK fibrillization and ameliorates Alzheimer’s disease-like symptoms in animal model. *Cell Mol. Life Sci* **2019**. [[CrossRef](#)] [[PubMed](#)]
27. Dehouck, M.-P.; Bree, F.; Fruchart, J.-C.; Cecchelli, R.; Tillement, J.-P.; Jolliet-Riant, P. Drug Transfer Across the Blood-Brain Barrier: Correlation Between In Vitro and In Vivo Models. *J. Neurochem.* **1992**, *58*, 1790–1797. [[CrossRef](#)]
28. Descat, A.; Lecoœur, M.; Kouach, M.; Goossens, L.; Thelliez, A.; Odou, P.; Decaudin, B.; Goossens, J.-F. Simultaneous determination of di(2-ethylhexyl) phthalate and diisononylcyclohexane-1,2-dicarboxylate and their monoester metabolites in four labile blood products by liquid chromatography tandem mass spectrometry. *J. Pharm. Biomed. Anal.* **2020**, *181*, 113063. [[CrossRef](#)]
29. Siflinger-Birnboim, A.; Del Vecchio, P.J.; Cooper, J.A.; Blumenstock, F.A.; Shepard, J.M.; Malik, A.B. Molecular sieving characteristics of the cultured endothelial monolayer. *J. Cell. Physiol.* **1987**, *132*, 111–117. [[CrossRef](#)]
30. Rispin, A.; Farrar, D.; Margosches, E.; Gupta, K.; Stitzel, K.; Carr, G.; Greene, M.; Meyer, W.; McCall, D. Alternative methods for the median lethal dose (LD(50)) test: The up-and-down procedure for acute oral toxicity. *ILAR J.* **2002**, *43*, 233–243. [[CrossRef](#)]





31. Organisation for Economic Co-Operation and Development. Guidance document on acute oral toxicity testing. In OECD Environment, Health and Safety Publications Series on Testing and Assessment n°24, Paris, France. June 2001; 1–24.
32. Nervo, A.; Calas, A.-G.; Nachon, F.; Krejci, E. Respiratory failure triggered by cholinesterase inhibitors may involve activation of a reflex sensory pathway by acetylcholine spillover. *Toxicology* **2019**, *424*, 152232. [[CrossRef](#)]
33. Santoni, G.; De Sousa, J.; De La Mora, E.; Dias, J.; Jean, L.; Sussman, J.L.; Silman, I.; Renard, P.-Y.; Brown, R.C.D.; Weik, M.; et al. Structure-Based Optimization of Nonquaternary Reactivators of Acetylcholinesterase Inhibited by Organophosphorus Nerve Agents. *J. Med. Chem.* **2018**, *61*, 7630–7639. [[CrossRef](#)]
34. Gorecki, L.; Junova, L.; Kucera, T.; Hepnarova, V.; Prchal, L.; Koblrova, T.; Múčková, L.; Soukup, O.; Korábečný, J. Tacroximes: Novel unique compounds for the recovery of organophosphorus-inhibited acetylcholinesterase. *Futur. Med. Chem.* **2019**, *11*, 2625–2634. [[CrossRef](#)] [[PubMed](#)]
35. Koblrová, T.; Korábečný, J.; Soukup, O. Current approaches to enhancing oxime reactivator delivery into the brain. *Toxicol.* **2019**, *423*, 75–83. [[CrossRef](#)] [[PubMed](#)]
36. Sakurada, K.; Matsubara, K.; Shimizu, K.; Shiono, H.; Seto, Y.; Tsuge, K.; Yoshino, M.; Sakai, I.; Mukoyama, H.; Takatori, T. Pralidoxime Iodide (2-PAM) Penetrates Across the Blood-Brain Barrier. *Neurochem. Res.* **2003**, *28*, 1401–1407. [[CrossRef](#)] [[PubMed](#)]
37. Múčková, L.; Pejchal, J.; Jošt, P.; Vanova, N.; Herman, D.; Jun, D. Cytotoxicity of acetylcholinesterase reactivators evaluated in vitro and its relation to their structure. *Drug Chem. Toxicol.* **2018**, *42*, 252–256. [[CrossRef](#)]
38. Blackard, W.G.; Sood, G.K.; Crowe, D.R.; Fallon, M.B. Tacrine. *J. Clin. Gastroenterol.* **1998**, *26*, 57–59. [[CrossRef](#)] [[PubMed](#)]
39. Patocka, J.; Jun, D.; Kuca, K. Possible role of hydroxylated metabolites of tacrine in drug toxicity and therapy of Alzheimer's disease. *Curr. Drug Metab.* **2008**, *9*, 332–335. [[CrossRef](#)] [[PubMed](#)]
40. Dos Santos, A.A.; Dos Santos, D.B.; Ribeiro, R.P.; Colle, D.; Peres, K.C.; Hermes, J.; Barbosa, A.M.; Dafre, A.L.; De Bem, A.F.; Kuca, K.; et al. Effects of K074 and pralidoxime on antioxidant and acetylcholinesterase response in malathion-poisoned mice. *NeuroToxicology* **2011**, *32*, 888–895. [[CrossRef](#)]
41. Žunec, S.; Radić, B.; Musilek, K.; Musilek, K.; Vrdoljak, A.L. Comparative determination of the efficacy of bispyridinium oximes in paraoxon poisoning / Usporedno određivanje učinkovitosti bispiridinijevih oksima pri trovanju paraoksonom. *Arch. Ind. Hyg. Toxicol.* **2015**, *66*, 129–134. [[CrossRef](#)]
42. Kovarik, Z.; Čalić, M.; Šinko, G.; Bosak, A.; Berend, S.; Vrdoljak, A.L.; Radić, B. Oximes: Reactivators of phosphorylated acetylcholinesterase and antidotes in therapy against tabun poisoning. *Chem. Interactions* **2008**, *175*, 173–179. [[CrossRef](#)]
43. Lallement, G.; Baille, V.; Baubichon, D.; Carpentier, P.; Collombet, J.-M.; Filliat, P.; Foquin, A.; Four, E.; Masqueliez, C.; Testylier, G.; et al. Review of the value of huperzine as pretreatment of organophosphate poisoning. *NeuroToxicology* **2002**, *23*, 1–5. [[CrossRef](#)]



© 2020 by the authors. Licensee MDPI, Basel, Switzerland. This article is an open access article distributed under the terms and conditions of the Creative Commons Attribution (CC BY) license (<http://creativecommons.org/licenses/by/4.0/>).

Article

Potential Nutraceutical Properties of Leaves from Several Commonly Cultivated Plants

Hafsa Amat-ur-Rasool ^{1,2}, Fenella Symes ³, David Tooth ⁴, Larissa-Nele Schaffert ¹, Ekramy Elmorsy ^{1,5}, Mehboob Ahmed ², Shahida Hasnain ² and Wayne G. Carter ^{1,*}

¹ School of Medicine, University of Nottingham, Royal Derby Hospital Centre, Derby DE22 3DT, UK; hafsa.phd.mmg@pu.edu.pk (H.A.-u.-R.); mzyls6@exmail.nottingham.ac.uk (L.-N.S.); ekramyelmorsy@mans.edu.eg (E.E.)

² Department of Microbiology and Molecular Genetics, University of the Punjab, Lahore 54590, Pakistan; mehboob.mmg@pu.edu.pk (M.A.); Shahida.mmg@pu.edu.pk (S.H.)

³ School of Pharmacy, University of Nottingham, Nottingham NG7 2UH, UK; fenellasymes@googlemail.com

⁴ School of Life Sciences, University of Nottingham, Nottingham NG7 2UH, UK; David.tooth@nottingham.ac.uk

⁵ Department of Forensic Medicine and Clinical Toxicology, Faculty of Medicine, Mansoura University, Mansoura 35516, Egypt

* Correspondence: Wayne.carter@nottingham.ac.uk; Tel.: +44-0-1332-724-738

Received: 15 October 2020; Accepted: 13 November 2020; Published: 15 November 2020



Abstract: Chronic dietary ingestion of suitable phytochemicals may assist with limiting or negating neurodegenerative decline. Current therapeutics used to treat Alzheimer disease elicit broad adverse drug reactions, and alternative sources of cholinesterase inhibitors (ChEIs) are required. Herein, we screened methanolic extracts from seven commonly cultivated plants for their nutraceutical potential; ability to inhibit acetylcholinesterase (AChE) and butyryl-cholinesterase (BuChE), and provision of antioxidant activity through their 2,2-diphenyl-1-picryl-hydrazyl-hydrate (DPPH) free radical scavenging capabilities. Potential neurotoxicity of plant extracts was examined via application to SHSY-5Y neuroblastoma cells and quantitation of cell viability. Methanolic extracts of *Citrus limon* (Lemon), *Bombax ceiba* (Red silk-cotton), *Lawsonia inermis* (Henna), *Eucalyptus globulus* (Eucalyptus), *Ocimum basilicum* (Basil), *Citrus reticulata* (Mandarin orange), and *Mentha spicata* (Spearmint) all displayed concentration-dependent inhibition of AChE and BuChE. The majority of extracts inhibited AChE and BuChE to near equipotency, with Henna and Eucalyptus extracts the two most potent ChEIs. All plant extracts were able to scavenge free radicals in a concentration-dependent manner, with Eucalyptus the most potent antioxidant. Toxicity of plant extracts to neuronal cells was concentration dependent, with Eucalyptus also the most toxic extract. Fractionation of plant extracts and analysis by mass spectrometry identified a number of plant polyphenols that might have contributed to the cholinesterase inhibition: 3-caffeoylquinic acid, methyl 4-caffeoylquinic acid, kaempferol-acetyl-glycoside, quercetin 3-rutinoside, quercetin-acetyl-glycoside, kaempferol 3-O-glucoside, and quercetin 3-O-glucoside. In silico molecular modeling of these polyphenols demonstrated their improved AChE and BuChE binding affinities compared to the current FDA-approved dual ChEI, galantamine. Collectively, all the plant extracts contained nutraceutical agents as antioxidants and ChEIs and, therefore, their chronic consumption may prove beneficial to combat the pathological deficits that accrue in Alzheimer disease.

Keywords: Alzheimer disease; acetylcholinesterase inhibitors; antioxidants; butyrylcholinesterase inhibitors; molecular modelling; nutraceuticals; phytochemicals

1. Introduction

Globally, we are living longer and with a demographic shift such that the proportion of the population over 60 has grown dramatically, estimated to be approximately 1 billion in 2017 but expected to double by 2050 [1]. As a consequence of population growth, the number of people living with dementia doubled between 1990 and 2016 to approximately 44 million [2] and the current number of approximately 50 million sufferers is expected to triple by 2050 [3].

Age itself represents the greatest risk factor for dementia and associated disability-adjusted life years [4]. Hence, living longer does not guarantee living healthier.

Additionally, there are other risk factors for dementia and Alzheimer disease (AD) including genetic predispositions [5] and environmental exposures [6], as well as lifestyle factors including smoking [4], excessive consumption of alcohol [7], and diet, such as levels of dietary fats [8].

The benefits of diets rich in fruits and vegetables as well as a low consumption of alcohol have been purported to contribute to reduced dementia risk and the health and longevity associated with a 'Mediterranean lifestyle' [9–14]. One of the proposed mechanisms responsible for the health benefits of certain foods and supplements is the provision of natural antioxidants that may balance age-related oxidative damage and limit the pathological changes associated with neurodegeneration [15–17].

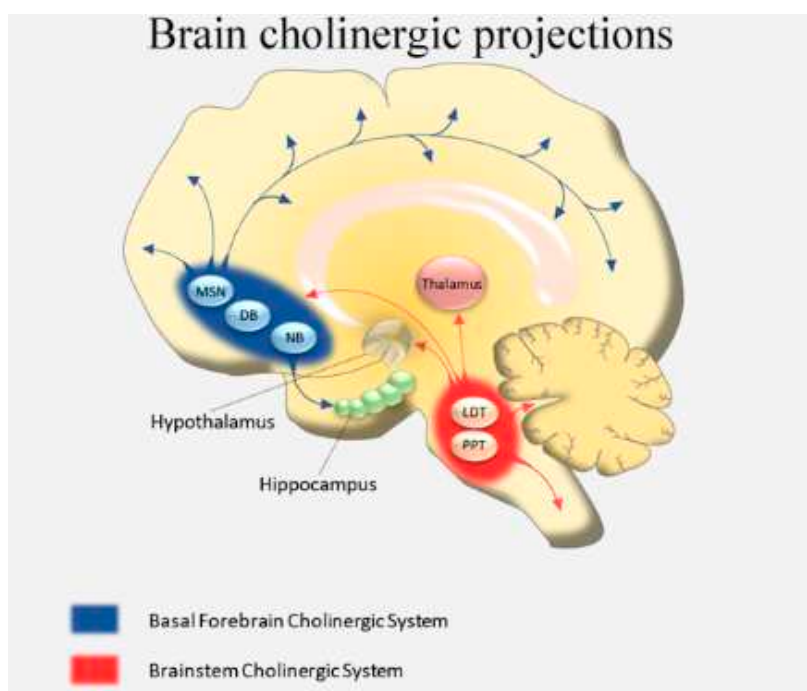
The neuropathic characterization of the major neurodegenerative disease, AD, is via the deposition of extracellular amyloid plaques of aggregated A β , and intracellular neurofibrillary tangles composed of the microtubule-associated protein (MAP) tau, which becomes extensively post-translationally modified (hyperphosphorylated) and aggregated within protein deposits [18,19]. These peptide (A β) and protein (tau) aggregates are thought to be toxic and contribute to the loss of neuronal number and cognitive ability, most notably within the frontotemporal lobes, including the entorhinal cortex and hippocampal regions of the brain [18,20]. Induction of oxidative stress and neuro-inflammation have also been proposed to contribute to brain damage in AD [21,22]. The cognitive decline experienced by AD patients is exacerbated by reduced functionality of the cholinergic pathways [22,23] (Figure 1a).

Cholinergic signaling is mediated by the transport of the neurotransmitter, acetylcholine (ACh), across the synaptic cleft to initiate post-synaptic transmission at nerves or at the neuromuscular junction. Acetylcholinesterase (AChE) is tethered to the post-synaptic membrane and is able to rapidly cleave ACh into acetate and choline and, thereby, terminate ACh stimulation (Figure 1b). The ability to sustain ACh levels through inhibition of AChE is the current mainstay of treatment for mild to moderate AD and is the primary mode of action for the FDA-approved drugs: donepezil, rivastigmine, and galantamine [24,25].

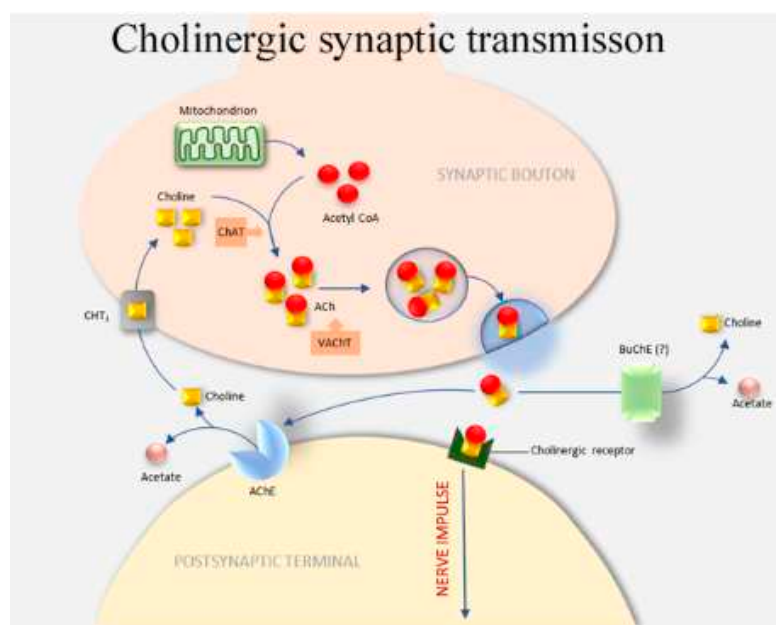
Emerging scientific evidence supports the potential use of dual (acetyl- and butyryl-) cholinesterase inhibitors (ChEIs) [26]. Indeed, the efficacy of rivastigmine may, in part, relate to its dual inhibitor ability [24]. The discovery of plant alkaloids as the source of the ChEIs, rivastigmine and galantamine, has prompted an ongoing search for phytochemicals with anti-cholinesterase activities. Phytochemicals and plant extracts may also possess a range of secondary metabolites with antioxidant activity and low target cell toxicity.

To this end, we investigated the nutraceutical potential of leaves from seven commonly cultivated plants: Lemon (*Citrus limon*), Red silk-cotton (*Bombax ceiba*), Henna (*Lawsonia inermis*), Eucalyptus (*Eucalyptus globulus*), Basil (*Ocimum basilicum*), Mandarin Orange (*Citrus reticulata*), and Spearmint (*Mentha spicata*). These plants were chosen on the basis of their availability, use within folk medicine (including within Pakistan), and previously reported phytochemicals with potential anti-cholinergic activity (Supplementary Table S1).

Citrus limon (family Rutaceae) is a small, evergreen tree native to South Asia and grown in regions with temperate summers. The tree is harvested for production of lemons (edible fruit) and lemon juice (harnessed for use in the drinks industry), as well as production of essential oils from lemon peel [27]. Plant leaves are also utilized and extoled for their health benefits when consumed as a tea [28].



(a)



(b)

Figure 1. The cholinergic system and cholinergic synapse. (a) Overview of the cholinergic system: DB, diagonal band of Broca; LDT, laterodorsal pontine tegmentum; MSN, medial septal nucleus; NB, nucleus basalis; PPT, pedunculopontine tegmental nucleus. (b) The cholinergic synapse: ACh, acetylcholine; AChE, acetylcholinesterase; BuChE, butyrylcholinesterase; ChAT, choline acetyltransferase; CHT₁, choline transporter; VACHT, vesicular acetylcholine transporter.

Bombax ceiba (family Bombacaceae) is a deciduous tree located within tropical and subtropical Asia. The flowers and flower buds are used in cooking and the production of tea, and other tree parts including roots and leaves have been utilized in traditional medicines [29,30].

Lawsonia inermis (family Lythraceae) more commonly known as Henna, is a branched, glabrous shrub or small tree commonly located within Africa, Asia, and Australia. Henna leaves contain a broad number of phytochemicals, including lawsone, and have been used historically for temporary skin staining and as a hair dye. Henna has been cultivated for its leaves, flowers, seeds, stem bark, and roots, from which extractions have been used in traditional medicine to treat a broad number of conditions [31–34].

Eucalyptus globulus (family Myrtaceae) is a member of the expansive Eucalyptus genus, native to Australia, and usually distributed within tropical and subtropical regions. Extracts and essential oils from the leaves of Eucalyptus plants including *E. globulus* have been exploited as a traditional medicine for their beneficial pharmacological activities [35,36].

Ocimum basilicum (family Lamiaceae) is native to Southeast Asia and Africa. It is extensively cultivated for its leaves, utilized as a culinary herb, and essential oil. Plant seeds and flower buds can also be harvested for food or added to drinks. *O. basilicum* (basil) has been utilized for traditional medicines with plant leaves and seeds rich in polyphenols, such as phenolic acids, with antioxidant potential [37,38].

Citrus reticulata (family Rutaceae) is another member of the Citrus genus and is believed to be native to Southeast Asia. *C. reticulata* is grown and harvested for its edible, soft, citrus fruit and peel utilized for essential oil and traditional medicines [27].

Mentha spicata (family Lamiaceae) is a gastronomic herb native to Europe and Southern Asia, with leaves cultivated for use in foods and teas, and utilized as a flavoring and aromatic oil. Plant extracts have also been traditionally utilized for their medicinal properties throughout the Mediterranean [39].

2. Materials and Methods

2.1. Plant Samples and Chemicals

Acetylcholinesterase (AChE) (EC 3.1.1.7), butyrylcholinesterase (BuChE) (EC 3.1.1.8), acetylthiocholine iodide (ATCI), 5,5'-dithiobis-(2-nitrobenzoic acid) (DTNB), galantamine hydrobromide ($C_{17}H_{21}NO_3 \cdot HBr$; 368.27 g/mol), 2,2-diphenyl-1-picrylhydrazyl (DPPH), α -tocopherol (Vitamin E), thiazolyl blue tetrazolium bromide (MTT), isopropanol, and dimethyl sulfoxide (DMSO) were purchased from Sigma Aldrich (Poole, UK). Dulbecco's Modified Eagle's Medium (DMEM), fetal bovine serum albumin (FBS), and poly-d-lysine (PDL) were purchased from Gibco (Loughborough, UK). Seven plants of purported medicinal benefit were collected from the Quaid-e-Azam Campus, University of the Punjab, Lahore, and further processed according to botanical standards. Voucher specimens were deposited in the Herbarium of the Botany Department, Abdul Wali Khan University, Mardan, Pakistan, to obtain their respective voucher numbers. The plant leaves studied were from *Citrus limon* (AWKUM.Bot.132.3.6.p21), *Bombax ceiba* (AWKUM.Bot.119.1.1.p1), *Lawsonia inermis* (AWKUM.Bot.78.3.1.p5), *Eucalyptus globulus* (AWKUM.Bot.FOC.1.18.p323), *Ocimum basilicum* (AWKUM.Bot.192.59.2.p294), *Citrus reticulata* (AWKUM.Bot.132.3.4.p25), and *Mentha spicata* (AWKUM.Bot.192.48.6.p262).

The phenological stages of the plants were as follows: *Citrus limon*, fruit development; *Bombax ceiba*, senescence; *Lawsonia inermis*, fruit development; *Eucalyptus globulus*, fruit development; *Ocimum basilicum*, flowering; *Citrus reticulata*, fruit development; and *Mentha spicata*, flowering.

2.2. Preparation of Plant Extracts

Plant leaves were air-dried and ground to a fine powder using an electric grinder (Cambridge Food Processor, FP 235, Cambridge Electric Company, Cambridge, UK). Powdered plant material (50 g) was wrapped in Whatman filter paper and fixed in the extractor glass tube of a Soxhelt apparatus. Methanol (500 mL) was used as the extraction solvent and poured into the round-bottomed flask of the apparatus. The apparatus was run at 60 °C, with running water used as cooling agent for the condenser. The plant material-to-solvent ratio was kept as 1:10 (*w/v*). Extraction was run for five cycles

for a total of 4 h. Crude extract collected within the round-bottomed flask at the end of extraction was cooled to room temperature and sieved through Whatman filter paper by funneling into a conical flask. The volume of methanol solvent was reduced using a Rotary Evaporator (4000 Efficient, Heidolph Instruments, Schwabach, Germany). The extracts were then freeze-dried (Alpha 2–4 LD Lyophilizer, Martin Christ, Osterode am Harz, Germany) after adding 50% celite (*w/w*) (Sigma-Aldrich, Poole, UK) to generate a fine powder. The extracted (lyophilized) compounds were used for experimentation.

2.3. AChE and BuChE Inhibitory Activity

Measurements of inhibition of AChE or BuChE were determined by a modified Ellman's procedure [40], adapted for a 96-well plate. Within each well, 40 μ L of 0.01 M DTNB, 46 μ L of 0.1 M (pH 8.0) phosphate buffer, 2 μ L of 0.075 M substrate, and 10 μ L of sample extract were mixed. The enzymatic reaction was initiated by the addition of 2 μ L of 0.5 U/mL AChE or BuChE and then monitored at 412 nm using a spectrophotometer (Multiskan Spectrum, Thermo Electron Corporation, Vantaa, Finland). Plant extracts were assayed across a concentration range of 0.16, 0.31, 0.63, 1.25, and 2.5 mg/mL, and the percentage of inhibition of AChE or BuChE was calculated relative to no inhibitor controls. All assays were performed in duplicates, with negative controls (no enzyme) values subtracted from all data points. Galantamine was used as a positive control for inhibition of either AChE or BuChE. The concentration of plant extract that inhibited 50% of the cholinesterase activity (IC_{50}) was calculated by nonlinear regression using GraphPad Prism V.7 (San Diego, CA, USA; <https://www.graphpad.com/scientific-software/prism/>).

2.4. Antioxidant Activity

Antioxidant activity of the plant extracts was determined using a 2,2-diphenyl-1-picryl-hydrazyl-hydrate (DPPH) free radical scavenging assay. Plant extracts, over a concentration range of 12.5, 25, 50, 100, and 200 μ g/mL, were prepared in 20 μ L of methanol and mixed with 180 μ L of 0.1 mM DPPH in 80% (*v/v*) methanol in a 96-well microtiter plate. The plate was incubated at 37 °C for 40 min and then optical density of the solution was measured at 517 nm using a spectrophotometer (Multiskan Spectrum, Thermo Electron Corporation), as described in a previous publication [41]. The percentage DPPH radical scavenging (antioxidant) activity was calculated relative to α -tocopherol (vitamin E) used as a positive control. All data points were performed in duplicates, with the absorbance values from negative controls subtracted.

2.5. Cytotoxicity Assays

Human neuroblastoma (SH-SY5Y) cells were purchased from the European Collection of Authenticated Cell Culture (ECACC) (ECACC-94030304). SH-SY5Y cells were grown in a culture medium of 43.5% Eagle's Minimum Essential Medium (EMEM) (M4655, Sigma, Poole, UK) supplemented with 43.5% Ham's F12 nut mix (217665-029, Gibco, Waltham, MA, USA), 10% heat-inactivated fetal bovine serum (FBS) (F9665, Sigma), 1% MEM Non-Essential Amino Acid Solution (RNBF3937, Sigma), 2 mM glutamine, and 1% penicillin-streptomycin solution containing 10,000 IU penicillium and 10 mg/mL streptomycin (P4333, Sigma) in T₂₅ flasks (130189, Thermofisher Scientific, Rochester, UK) at 37 °C within an atmosphere of 5% CO₂ and 95% humidity. SH-SY5Y cells (passage 15) were seeded in 96-well plates at 3×10^4 cells/well and grown until 80–90% confluence before treatment with plant extracts at 156, 312, 625, 1250, or 2500 μ g/mL. After 48 h, cell culture media was removed and replaced with 0.5% (*w/v*) thiazolyl blue tetrazolium bromide (MTT) reagent containing growth media. Plates were incubated at 37 °C for 4 h before removal of media and replacement with 1:1 (*v/v*) isopropanol:DMSO, and absorbance was recorded at 570 nm using a spectrophotometer (Multiskan Spectrum, Thermo Electron Corporation). The effect of different concentrations of plant extracts was determined by comparing the viability of treated cells with untreated control cells, and the plant concentration able to inhibit cell viability by 50% (IC_{50}) was calculated by nonlinear regression using GraphPad Prism V.7.

2.6. Liquid-Chromatography Mass-Spectrometry (LC-MS)

Plant extracts were analyzed using reversed-phase (Phenomenex; Jupiter C18; 4.6 × 250mm, 5 μm 300 Å) (Agilent, Cheshire, UK) high-pressure liquid chromatography with a 5–60% (*v/v*) gradient of acetonitrile in 0.1% (*v/v*) formic acid chromatographed at 1.0 mL.min⁻¹, with 90% of flow directed to a microplate fraction collector (Dionex; Foxy Jr, Themofisher, Loughborough, UK). Mass spectrometry (QToF Premier, Waters, UK) was performed in negative ion electrospray mode, with instrument control and externally calibrated (sodium iodide; similar to 10 ppm), and data processed using MassLynx 4.1 software (Waters, UK).

2.7. In Silico Molecular Docking Studies

The 3D structures of human AChE (PDB ID: 4EY5) and BuChE (PDB ID: 6I0C) enzymes were downloaded from RCSB-Protein Data Bank (PDB) (<https://www.rcsb.org/>). The 3D structures of the potential ChEIs identified by LC-MS/MS were downloaded from the National Center for Biotechnology Information PubChem database (<https://pubchem.ncbi.nlm.nih.gov/>). The 3D structures of these potential ligands were docked with the target enzymes AChE and BuChE separately using AutoDock Vina software and MGL tools (The Scripps Research Institute, La Jolla, CA, USA) [42]. Molecular docking results were visually analyzed using PyMOL v2.4. (Schrödinger) and the ligands ranked with regards to their binding affinities to the target enzymes.

2.8. Statistical Analysis

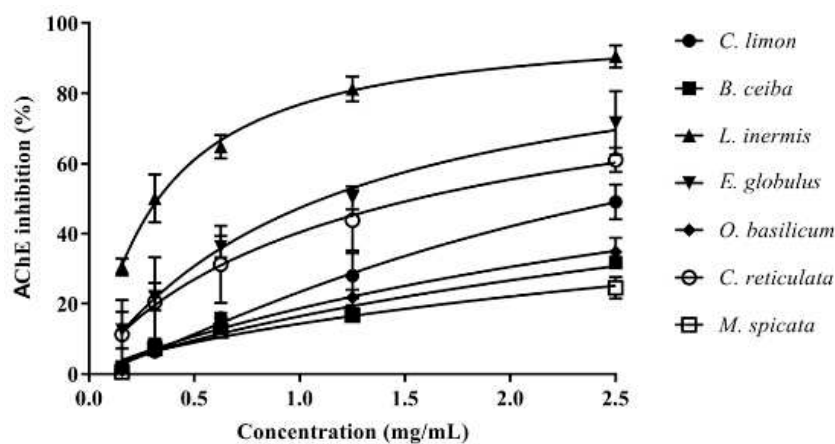
Statistical analysis was performed using GraphPad Prism V.7. Determination of IC₅₀ values were obtained by nonlinear regression (inhibitor vs. normalized response-variable slope) based on a best-fit model from at least four data points. Comparison between groups was performed using a one-way analysis of variance (ANOVA). A Spearman rank-order correlation coefficient was used to quantify the relationship between the studied parameters. A *p* value of below 0.05 was considered significant.

3. Results

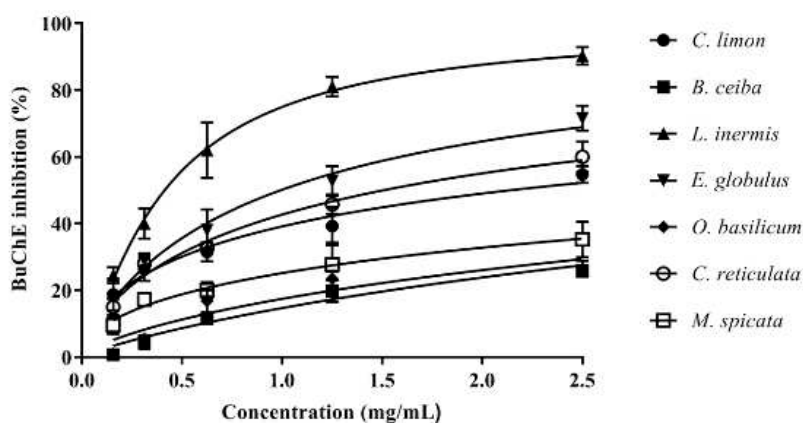
3.1. Assessment of Plant Extract AChE and BuChE Inhibitory Activity

Plant extracts were scrutinized across a concentration range of 0.16–2.5 mg/mL for their ability to inhibit AChE or BuChE using a modified Ellman's spectrophotometric assay. Plant extracts inhibited the cholinesterases in a concentration-dependent manner (Figure 2a,b). The actual or extrapolated concentration able to produce 50% inhibition (IC₅₀) of AChE or BuChE was calculated by nonlinear regression (Table 1). The anti-cholinesterase drug, galantamine, was used to provide a comparison of AChE and BuChE inhibitory activity. Galantamine inhibitor-response curves for AChE and BuChE are included in Figure 2c. From nonlinear regression, IC₅₀ values for galantamine vs. AChE and BuChE were calculated as 0.19 μg/mL (0.51 μM) and 0.49 μg/mL (1.3 μM), respectively (Supplementary Figure S1), and are included in Table 1.

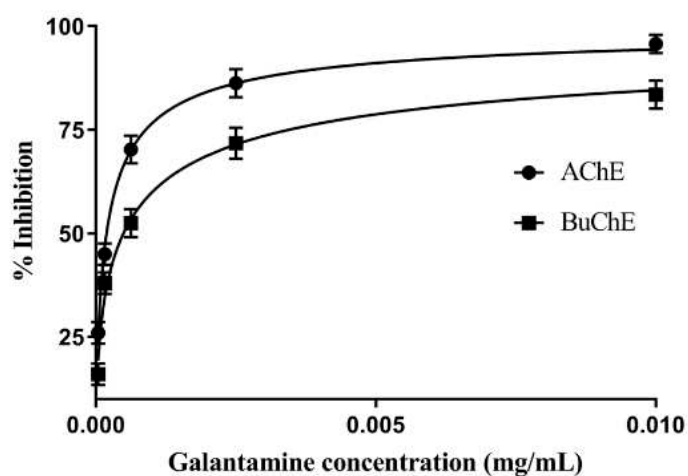
Henna (*Lawsonia inermis*) leaf extract was the most potent plant inhibitor of both AChE and BuChE, with IC₅₀ values of 0.33 and 0.41 mg/mL, respectively (Table 1). Interestingly, the majority of these plant extracts were equipotent inhibitors of AChE and BuChE (Figure 3 and Table 1). Galantamine inhibited AChE and BuChE close to maximal levels, as did the methanolic extract of *L. inermis* (Figure 3). AChE inhibitory potency for the plant extracts was in the order *L. inermis* > *E. globulus* > *C. reticulata* > *C. limon* > *O. basilicum* > *B. ceiba* > *M. spicata*. BuChE inhibitory potency was similar in order for the first four extracts: *L. inermis* > *E. globulus* > *C. reticulata* > *C. limon* > *M. spicata* > *O. basilicum* > *B. ceiba* (Figure 3 and Table 1).



(a)



(b)

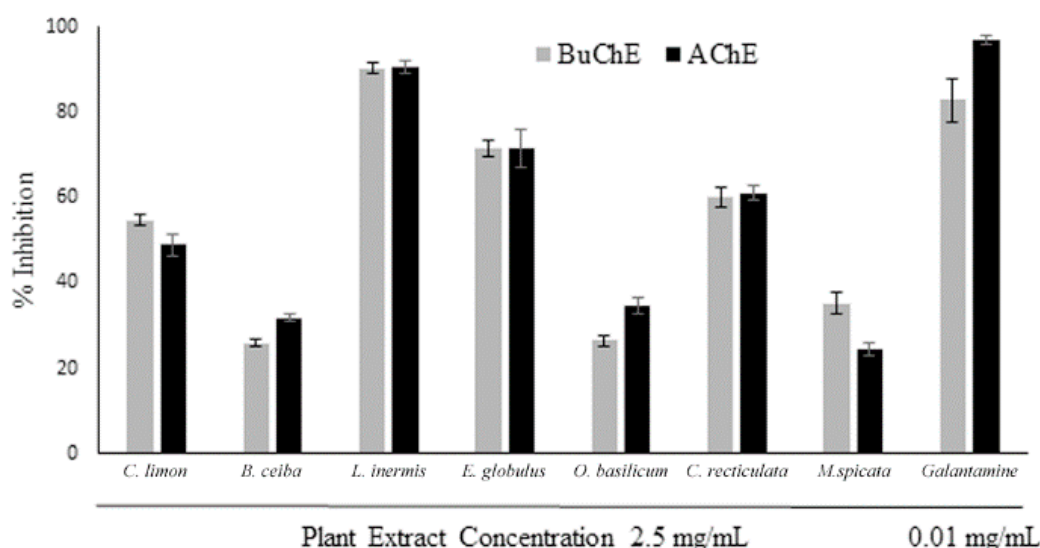


(c)

Figure 2. Assessment of the ability of plant extracts and galantamine to inhibit AChE and BuChE. (a) Inhibition of AChE by plant extracts. (b) Inhibition of BuChE by plant extracts. (c) Inhibition of AChE and BuChE by galantamine. Assays were performed using modified Ellman’s assay [40]. Results are expressed as means \pm SEM, for an n -number of 4.

Table 1. AChE and BuChE inhibitory capacity, DPPH radical scavenging, and cell viability assessment (MTT assay) of plant extracts.

Agent	Alternative or Common Name	IC ₅₀ (mg/mL)		ED ₅₀ (μg/mL)	IC ₅₀ (mg/mL)
		AChE	BuChE	DPPH	MTT
<i>Citrus limon</i>	Lemon	2.59 ± 0.14	1.82 ± 0.10	839.40 ± 135.2	1.77 ± 0.03
<i>Bombax ceiba</i>	Red silk-cotton	6.26 ± 0.72	7.38 ± 0.96	69.69 ± 3.01	1.51 ± 0.08
<i>Lawsonia inermis</i>	Henna	0.33 ± 0.02	0.41 ± 0.02	33.68 ± 1.04	0.58 ± 0.02
<i>Eucalyptus globulus</i>	Eucalyptus	1.11 ± 0.07	0.99 ± 0.05	22.15 ± 1.23	0.40 ± 0.01
<i>Ocimum basilicum</i>	Basil	4.84 ± 0.47	5.90 ± 0.81	56.13 ± 2.01	0.98 ± 0.03
<i>Citrus reticulata</i>	Mandarin	1.56 ± 0.20	1.51 ± 0.09	359.30 ± 31.64	0.68 ± 0.03
<i>Mentha spicata</i>	Spearmint	10.49 ± 2.06	5.82 ± 0.77	28.94 ± 0.96	1.12 ± 0.03
Galantamine	Galanthamine	0.00019	0.00049	ND	3.53 ± 0.21
Vitamin E	α-tocopherol	ND	ND	7.73 ± 0.66	ND

**Figure 3.** Comparison of BuChE and AChE inhibitory activity for plant extracts. The ability of plant extracts at 2.5 mg/mL to inhibit BuChE and AChE was compared with that for galantamine at 0.01 mg/mL. Results are expressed as means ± SEM, for an *n*-number of 4.

3.2. Assessment of Plant Extract Antioxidant Activity

Intrinsic antioxidant activity for the plant extracts was assessed via the ability to scavenge free radicals using a DPPH assay. All plant extracts displayed free radical scavenging (antioxidant) ability that was extract concentration dependent (Figure 4). The antioxidant capacity of the plant extracts was *E. globulus* > *M. spicata* > *L. inermis* > *O. basilicum* > *B. ceiba*, generating similar hyperbolic curves (Supplementary Figure S2). By comparison, the antioxidant capability was relatively low for the citrus fruits, *C. limon* and *C. reticulata*, and increased linearly with extract concentration (Supplementary Figure S2). At the higher concentrations examined (50–200 μg/mL), radical scavenging was to a similar level as the antioxidant vitamin E for several of the extracts (Figure 4). The concentration of extract able to produce a 50% effect (ED₅₀) was determined by nonlinear regression (Supplementary Figure S1), with values included in Table 1.

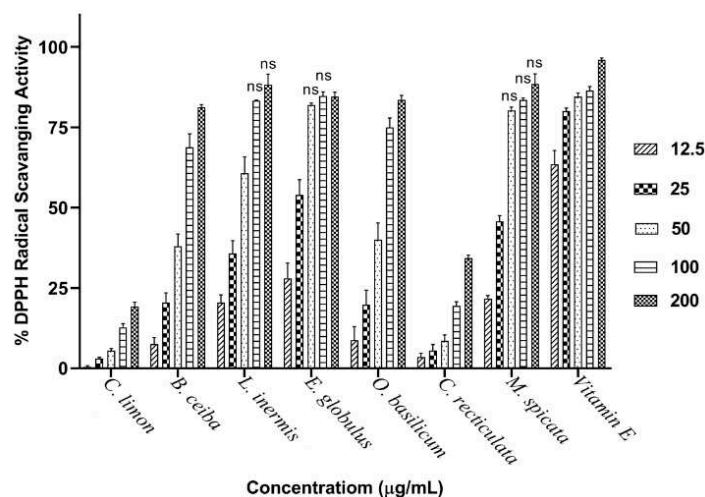


Figure 4. DPPH radical scavenging activity of plant extracts. The ability of plant extracts across a concentration range of 12.5–200 µg/mL to scavenge the DPPH• was assessed spectrophotometrically and compared with Vitamin E. Histograms represent means ± SEM for an n-number of 4; ns = nonsignificant differences from Vitamin E.

3.3. Assessment of Plant Extract Neuronal Toxicity

Plant extracts were applied to cultured neuronal (SH-SY5Y) cells over a concentration range of 0.16–2.5 mg/mL to assess neurotoxicity. Toxicity of plant extracts was concentration dependent (Figure 5). At the lowest concentrations applied to cells (0.16 mg/mL) the majority of plant extracts were nontoxic, with no significant reduction in cell viability (Figure 5). From inhibitor-response curves of cell viability (Supplementary Figure S3), IC₅₀ concentrations were calculated (Table 1). Toxicity to neuronal cells was in the order *E. globulus* > *L. inermis* > *C. reticulata* > *O. basilicum* > *M. spicata* > *B. ceiba* > *C. limon*. Eucalyptus plant extract was the most toxic (lowest IC₅₀) and reduced cell viability by 11.5% at the lowest concentration examined (0.16 mg/mL). In contrast, the pure drug, galantamine, only induced significant toxicity to neuronal cells (reduced viability of 17%) from a concentration of 1.25 mg/mL. The inhibitor-response curve for galantamine toxicity approached 50% at the highest concentration examined (2.5 mg/mL), with a predicted IC₅₀ of 3.53 mg/mL (12.2 mM) (refer to Table 1).

3.4. Assessment of Associations between Cholinesterase Inhibition, Radical Scavenging, and Cell Toxicity

To establish if there were any correlations between the studied parameters, a Spearman rank-order correlation coefficient analysis was performed to examine the relationship between AChE and BuChE inhibitory potency (Figure 6A), DPPH radical scavenging ability and cholinesterase inhibition (Figure 6B,C), cell viability and cholinesterase inhibition (Figure 6D,E), and cell viability and DPPH radical scavenging ability (Figure 6F). There was a positive and significant correlation between potency of plant extracts to inhibit AChE and BuChE (Figure 6A). Radical scavenging ability was negatively correlated with either acetyl- or butyryl-cholinesterase inhibitory potency, although not significantly (Figure 6B,C). Cell viability (measured as MTT assays) was positively correlated with AChE inhibitory potency and negatively correlated with BuChE inhibitory potency (Figure 6D,E). Cell viability was positively correlated with radical scavenging potency, but not significantly (Figure 6F).

3.5. Liquid-Chromatography Mass-Spectrometry (LC-MS)

Chemical analyses of the plant extracts were performed using LC-MS/MS, using separation conditions optimized for *Moringa oleifera* [43,44]. This revealed several molecular masses present within all plant extracts, such as rutin (quercetin-3-O-rutinoside) and kaempferol 3-O-glucoside, as well as others, including 3-caffeoylquinic acid, only present within the two most powerful cholinesterase-inhibiting plant extracts: *L. inermis* and *E. globulus* (refer to Table 2).

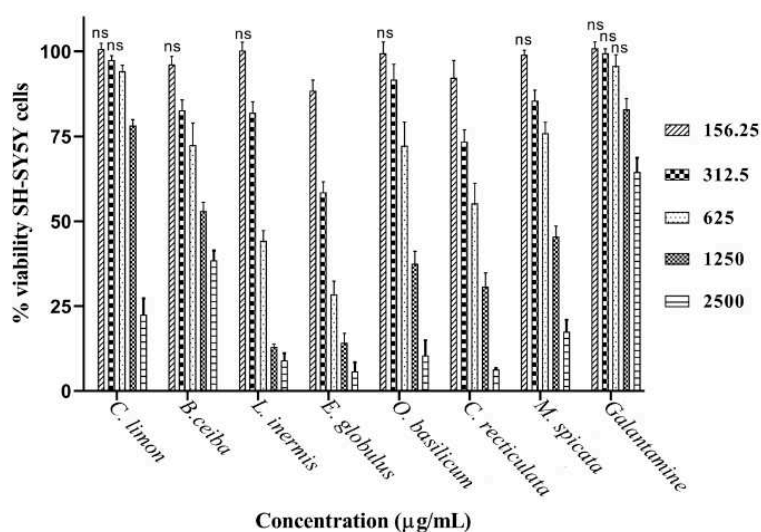


Figure 5. Toxicity of plant extracts to SH-SY5Y neuroblastoma cells. Cultured SH-SY5Y cells were exposed to plant extracts over a concentration range of 156–2500 µg/mL and for 48 h. Toxicity was evaluated by a MTT assay. Histograms represent cell viability as means ± SEM for an n-number of 4; ns = nonsignificant differences from control values.

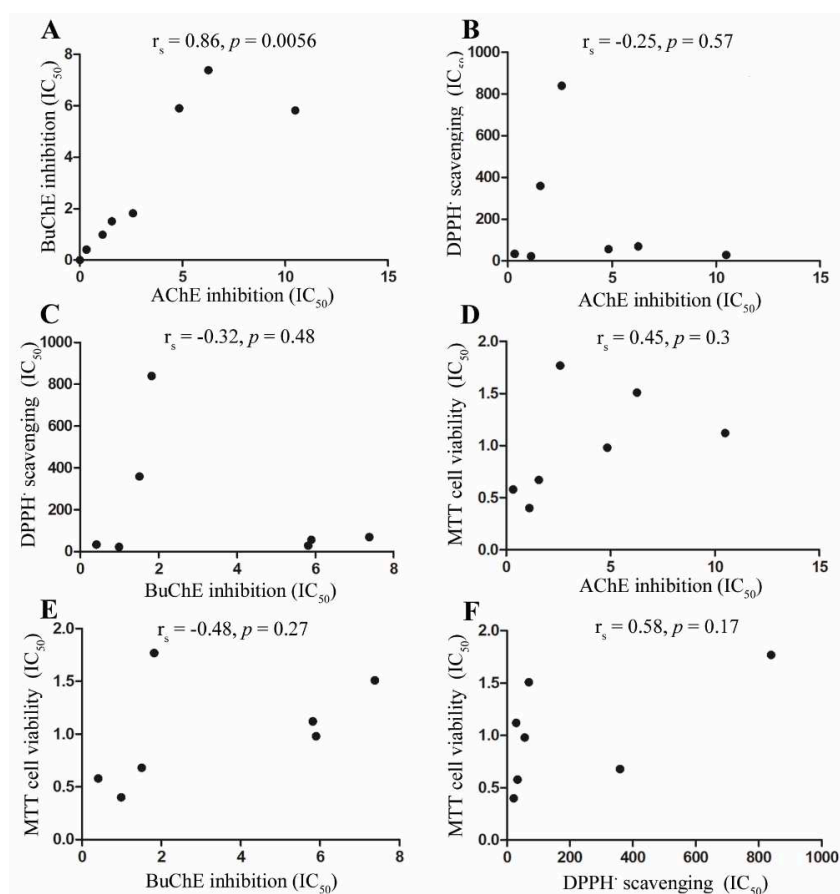


Figure 6. Correlation analysis between anti-cholinesterase activities, DPPH radical scavenging, and cell viability for plant extracts. (A) Correlation between BuChE and AChE potency. (B) Correlation between DPPH radical scavenging and AChE inhibition. (C) Correlation between DPPH radical scavenging and BuChE inhibition. (D) Correlation between cell viability and AChE inhibition. (E) Correlation between cell viability and BuChE inhibition. (F) Correlation between cell viability and DPPH radical scavenging.

Table 2. LC-MS/MS identification of plant phytochemicals.

Peak #	[M-H]	Putative Molecular Formula	Putative Identification	<i>M. oleifera</i> *	<i>C. lemon</i>	<i>B. ceiba</i>	<i>L. inermis</i>	<i>E. globulus</i>	<i>O. basilicum</i>	<i>C. reticulata</i>	<i>M. spicata</i>
1	665	C ₂₄ H ₄₂ O ₂₁	Cellotetraose	x	665.17	x	x	x	x	665.17	x
3	341	C ₁₂ H ₂₂ O ₁₁	Sucrose	341.11	341.11	341.11	341.10	341.09	341.11	341.09	x
4	503	C ₁₈ H ₃₂ O ₁₆	Cellotriose	503.15	503.17	503.17	x	503.14	x	x	503.14
2	367	C ₁₇ H ₂₀ O ₉	Methyl 4-caffeoylquininate	367.10	367.14	367.16	x	x	x	x	x
5	278	C ₁₄ H ₁₇ NO ₅	Niazirin	278.07	x	x	x	x	x	x	x
6	191	C ₇ H ₁₂ O ₆	Quinic acid isomer 1	191.06	191.06	191.04	x	191.05	x	191.05	x
10	191	C ₇ H ₁₂ O ₆	Quinic acid isomer 2	191.02	x	191.02	x	x	x	x	x
7	586	C ₂₀ H ₂₉ NO ₁₅ S ₂	3-Hydroxy-4-(α -l-rhamnopyranosyloxy) benzyl glucosinolate	586.09	x	x	x	x	x	x	x
8	570	C ₂₀ H ₂₉ NO ₁₄ S ₂	Glucomoringin	570.07	x	x	x	x	x	x	x
11	408	C ₁₄ H ₁₉ NO ₉ S ₂	Glucotropaeolin	x	x	x	x	x	x	x	408.12
12	612	C ₂₂ H ₃₁ NO ₁₅ S ₂	Acetyl-4-(α -l-rhamnopyranosyloxy) benzyl glucosinolate	612.07	x	x	x	x	x	x	x
9	353	C ₁₆ H ₁₈ O ₉	3-Caffeoylquinic acid	353.08	x	x	353.08	353.07	x	x	353.06
13	609	C ₂₇ H ₃₀ O ₁₆	Rutin (quercetin-3-O-rutinoside)	609.14	609.14	609.14	609.14	609.13	609.12	609.14	609.13
14	463	C ₂₁ H ₂₀ O ₁₂	Quercetin 3-O-glucoside	463.08	x	463.08	463.09	463.07	463.07	x	x
15	505	C ₂₃ H ₂₂ O ₁₃	Quercetin-acetyl-glycoside	505.13	x	505.26	x	505.11	505.11	505.25	x
16	447	C ₂₁ H ₂₀ O ₁₁	Kaempferol 3-O-glucoside	447.08	447.09	447.09	447.07	447.07	447.07	447.06	447.06
17	489	C ₂₃ H ₂₂ O ₁₂	Kaempferol-acetyl-glycoside	489.10	x	x	489.09	489.08	x	489.07	489.13

* *M. oleifera* was used as a reference extract for peak generation according to Xu et al. [44]. x denotes that the compound was not detected in that peak fraction.

3.6. Molecular Docking of Potential ChEIs

The cleaned 3D structures of AChE (PDB ID: 4EY5) and BuChE (PDB ID: 6I0C) were used as virtual targets for binding by the identified phytochemicals: methyl 4-caffeoylquininate (peak #2), 3-caffeoylquinic acid (peak #9), rutin (peak #13), quercetin 3-*O*-glucoside (peak #14), quercetin-acetyl-glycoside (peak #15), kaempferol 3-*O*-glucoside (peak #16), and kaempferol-acetyl-glycoside (peak #17) (refer to Table 2). The potential ChEIs were ranked according to their respective binding affinities to AChE and BuChE. The 3-caffeoylquinic acid displayed the strongest binding affinity for AChE, and rutin the strongest for BuChE, with binding energies of -9.2 and -11.0 kcal/mol, respectively (Table 3). All these phytochemicals displayed relatively strong binding affinities to AChE and BuChE compared to the commercial ChEI, galantamine (Table 3). Indeed, galantamine was only superior to one of the phytochemicals, quercetin 3-*O*-glucoside, for binding strength to AChE and to one other phytochemical, 3-caffeoylquinic acid, for binding to BuChE (Table 3).

For the most potent putative AChE inhibitor, 3-caffeoylquinic acid, modeling of its binding to AChE was undertaken. Figure 7a represents the binding pose of 3-caffeoylquinic acid looking down the catalytic gorge of AChE. Figure 7b provides a closer inspection of the binding of 3-caffeoylquinic acid with the active site residues of AChE, demonstrating the hydrogen bonding between the ligand and target enzyme.

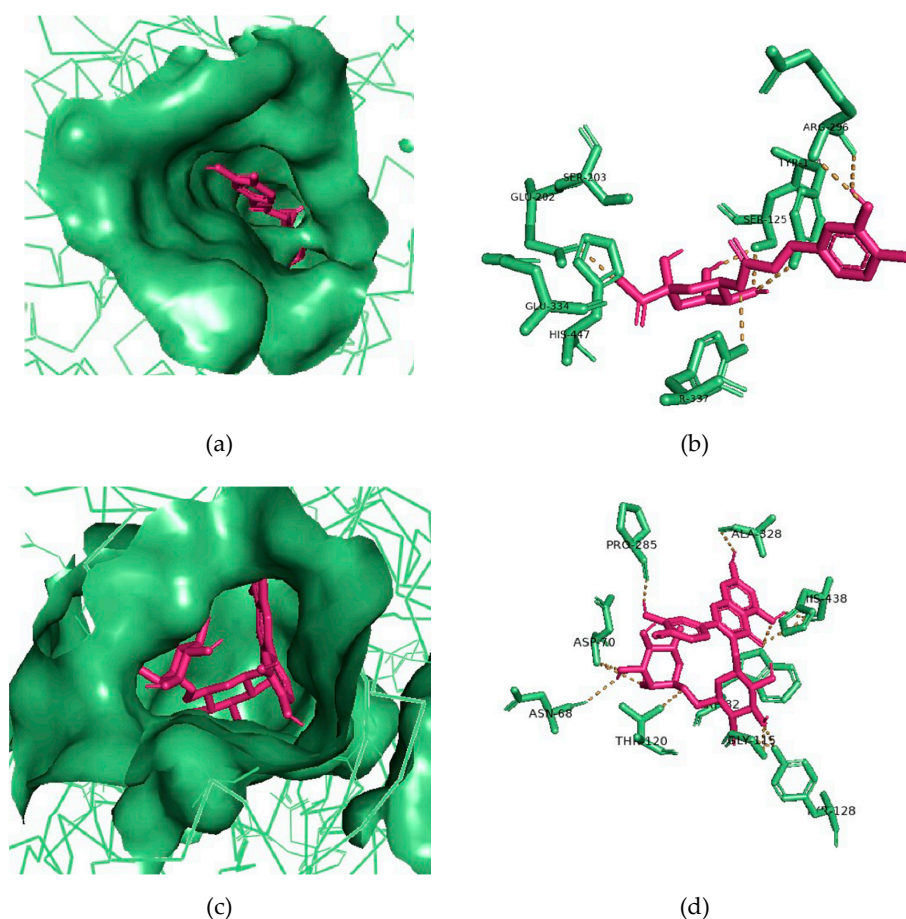


Figure 7. Molecular docking of potential ChEIs. (a) Binding pose of 3-caffeoylquinic acid (pink-colored sticks) looking down the gorge of AChE (green-colored surface representation). (b) The 3-caffeoylquinic acid (pink-colored sticks) docked with binding site residues of AChE (green-colored sticks). (c) Binding pose of rutin (pink-colored sticks) looking down the gorge of BuChE (green-colored surface representation). (d) Rutin (pink-colored sticks) docked with binding site residues of BuChE (green-colored sticks). Hydrogen bonding represented by yellow lines.

Table 3. AChE and BuChE binding characteristics of the plant phytochemicals.

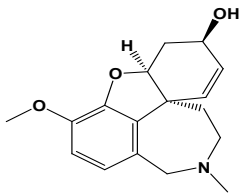
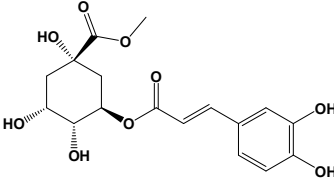
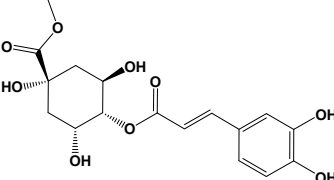
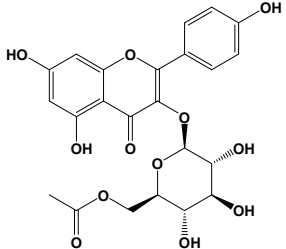
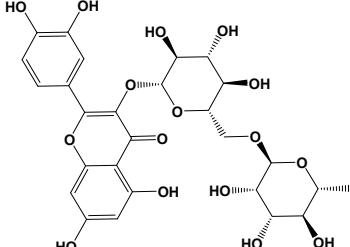
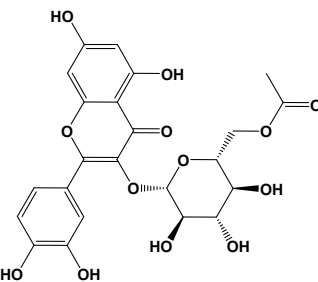
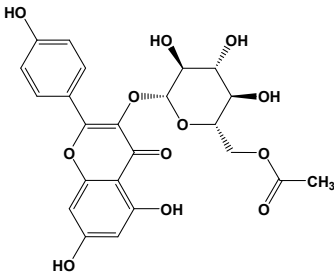
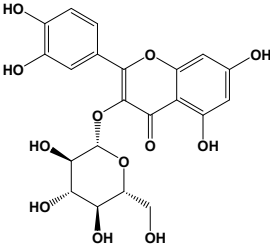
Ligand	2D Structures	Binding Affinity (kcal/mol)	
		AChE	BuChE
Galantamine		-7.7	-8.7
3-Caffeoylquinic acid		-9.2	-8.6
Methyl 4-caffeoylquininate		-8.8	-8.9
Kaempferol-acetyl-glycoside		-8.4	-10.4
Quercetin 3-rutinoside (Rutin)		-8.3	-11.0
Quercetin-acetyl-glycoside		-8.0	-10.4

Table 3. Cont.

Ligand	2D Structures	Binding Affinity (kcal/mol)	
		AChE	BuChE
Kaempferol 3-O-glucoside (Astragalín)		-7.9	-9.7
Quercetin 3-O-glucoside (Isoquercitrín)		-7.6	-9.5

Similarly, for the most potent putative BuChE inhibitor, rutin, virtual binding looking down the gorge of BuChE enzyme was performed (Figure 7c), as well as docking of rutin with the active site residues of BuChE (Figure 7d).

4. Discussion

Neurodegenerative decline, especially dementia, is a social and economic public health pandemic. Patients suffering from AD represent the greatest number of dementia cases, and deployment of ChEIs are the first-line drugs to abate the cholinergic deficit that contributes to impaired cognition [45]. Phytochemicals with ChEI and antioxidant activities may prove beneficial at both treatment and prophylactic levels. Hence, herein, we scrutinized the ability of leaf extracts from commonly cultivated plants for their nutraceutical efficacy as anti-cholinesterases and antioxidants and considered their toxicity to neuronal cells.

All the plant extracts examined displayed both AChE and BuChE inhibitory ability, but with broad potency: with an efficacy range of 32-fold for inhibition of AChE and 18-fold for BuChE. *L. inermis* (Henna) leaf extract was the most potent AChE and BuChE inhibitor: with IC_{50} values of 0.33 and 0.41 mg/mL, respectively. Henna (also commonly known as Mhendi) leaves have historically been utilized as a stain and dye, but a comprehensive range of pharmacologically active phytochemicals with desirable health benefits have been reported for leaves and other plant parts [31–34]. This includes the ability to inhibit AChE: An aqueous leaf extract displayed approximately half of the potency of the methanolic extract reported herein ($IC_{50} = 0.749$ mg/mL) [46] and other methanolic extracts with relatively weak activity have been described, but without a determination of an IC_{50} [47]. Hence, to date, our results appear to be the first determination of an IC_{50} for a methanolic extract from Henna. Furthermore, this is the first report of BuChE inhibitory activity from Henna leaf extract and, moreover, with comparable inhibitory potency to that against AChE.

The biological roles of BuChE have not been fully delineated. Serum BuChE activity has functional effects upon drug detoxification [48]. BuChE activity also influences lipid metabolism and affects appetite through modification of ghrelin [49,50]. BChE-deficient mice do not display signs of ill health and, similarly, humans devoid of active BChE activity have no reduction in longevity [51,52]. Nevertheless, BuChE is able to substitute for AChE, with AChE mice viable [53]. Furthermore, in AD, BuChE levels increase, presumably to compensate for dwindling ACh functionality [23,54,55]. Hence,

there may be additional benefit to the development and utilization of dual transient inhibitors of both cholinesterases to prolong cholinergic signaling [26,56]. For Henna, it is noteworthy that nootropic benefits have already been reported in vivo [57]. So, further development of Henna extracts could provide suitable AD-modifying agents.

For the Henna methanolic leaf extract, we also confirmed the presence of antioxidants using a free radical scavenging spectrophotometric assay. This technique employs the commercially available 1,1-diphenyl-2-picrylhydrazyl free radical (DPPH[•]), which displays a characterized UV-visible spectrum with absorbance maxima at approximately 515 nm in methanol. The provision of an antioxidant, such as a polyphenol, results in a decrease of absorbance that is proportional to the concentration and antioxidant activity of the compound itself [58,59]. In keeping with our results, other independent studies have similarly highlighted the presence of a range of Henna phytochemicals able to act as antioxidants [46,60].

E. globulus (Eucalyptus) was the next most potent inhibitor of both cholinesterases. Specific reports of anti-AChE or anti-BuChE activities from extracts of *E. globulus* are absent in the literature. However, anti-AChE activity has been demonstrated for *E. globulus* essential oil both in vitro [61] and in vivo [62]. Essential oils differ from the solvent extracts utilized for our study, since they are generated primarily through hydrodistillation and via steam or dry distillation processes. Nevertheless, it is pertinent to consider that certain essential oils are a source of agents with potential beneficial effects on cognition [63], responses that could, in part, reflect phytochemicals capable of modifying cholinesterase activities.

For the plants examined, *E. globulus* displayed the best antioxidant potency. This ability to provide useful antioxidant and free radical scavenging was also observed for a water extract from *E. globulus* leaves, with an IC₅₀ for DPPH of 12 µg/mL, in keeping with our data [64]. This water extract was also able to scavenge free radicals including those from reactive oxygen species (ROS) and reactive nitrogen species (RNS), properties proposed to align with the plant's therapeutic activities [64]. Notable antioxidant properties from Eucalyptus leaf extracts (as a food additive) [65] and essential oils [66] have also been reported.

The two citrus fruits, *C. reticulata* and then *C. limon*, were the next most powerful inhibitors of both AChE and BuChE. To our knowledge, our results constitute the first report of anti-AChE and anti-BChE activity for *C. reticulata*. Other studies have highlighted potent anti-AChE of *C. limon* [67] that may relate to the abundance of flavonoids within citrus fruit [68,69]. Furthermore, *C. limon* essential oils also contain anti-cholinesterase activities [70] and were recently shown to ameliorate age-associated cognitive decline in a mouse model of AD [71].

In contrast to their useful anti-cholinesterase activities, both citrus fruit extracts were weak antioxidants. Likewise, only low to moderate antioxidant properties have been reported for *C. reticulata* and *C. limon* peel essential oils [61,72]. Nevertheless, irrespective of their relatively weak antioxidant activity, the multitude of phytochemicals from citrus fruits may contribute to their purported neuroprotective properties [73].

O. basilicum displayed intermediate anti-cholinesterase activity, as well as antioxidant potential. Our results for anti-AChE potency of a methanolic leaf extract compare well with those from Farag et al. (2006) [74], with an IC₅₀ calculated at 6.6 mg/mL. To date, we have not encountered any other published reports of anti-BuChE activity from *O. basilicum*. The antioxidant properties of basil are thought to arise, at least in part, from a rich blend of polyphenolic compounds including phenolic acids and flavonoids [37,38,75,76]. These *O. basilicum* phytochemicals may also contribute to memory enhancement and anti-cholinesterase activity [77,78].

A methanolic leaf extract from *B. ceiba* displayed relatively weak anti-AChE activity, was the weakest anti-BuChE inhibitor, and had intermediate antioxidant potential. Similarly, a methanolic extract from *B. ceiba* flowers had comparable radical scavenging to our data (EC₅₀ = 87 µg/mL) [79]. Other solvent extracts (ethanolic and hexane) from *B. ceiba* flowers also retain useful anti-AChE

inhibition and free radical scavenging abilities [80]. These *B. ceiba* flower extracts and a methanolic leaf extract have also displayed neuroprotective potential in vivo [81,82].

Our results show that *M. spicata* was a strong antioxidant but only a weak cholinesterase inhibitor, although potent AChE inhibition by *Mentha* essential oils, including *M. spicata* ($IC_{50} = 0.088$ mg/mL), has been demonstrated [83]. In keeping with our results, *M. spicata*'s potency as an antioxidant was also demonstrated for a water and, to a lesser extent, an ethanolic extract (IC_{50} of 5.7 and 65.2 μ g/mL, respectively), with both extracts only exhibiting moderate anti-AChE activity [84].

This inverse relationship between DPPH radical scavenging and ability to inhibit cholinesterases exhibited by *M. spicata* extracts was also confirmed as a collective for the seven plant extracts (Figure 6B,C), such that stronger antioxidant potential correlated with weaker cholinesterase inhibition, although this did not reach significance.

The toxicity of the plant extracts to neuroblastoma cells was examined using the universally utilized MTT assay. This assay relies upon the reduction of MTT to formazan by non-mitochondrial and mitochondrial oxidoreductase enzymes. The color change produced directly correlates with cellular metabolic activity and thereby acts as a surrogate of cell viability or proliferation [85,86] and generates inhibitor-response curves that invariably follow those for other markers of cell viability such as ATP depletion or lactate dehydrogenase (LDH) release [87,88].

The inhibitor-response curves for the plant extracts revealed a toxicity range of 4.4-fold from the least toxic, *Citrus limon*, to the most toxic, *Eucalyptus globulus*, with all extracts more toxic than the single drug treatment of galantamine. Nevertheless, although such partially pure extracts displayed toxicity to neuronal cells, this was at concentrations significantly higher than that for radical scavenging. Indeed, functional antioxidant activity was at concentrations at least one order of magnitude below those that induced toxicity, except for the citrus fruit extracts (*C. limon* and *C. reticulata*). In contrast, anti-cholinesterase activity of the plant extracts was at concentrations more comparable to those able to induce neuronal toxicity. The exception was the Henna extract that not only contained the most potent anti-cholinesterases but was also an active inhibitor at concentrations below those able to induce toxicity.

Cellular toxicity and cell death can be induced as a consequence of irreversible inhibition of acetyl-cholinesterase, such as through organophosphate binding, with induction of redox stress [89,90]. By contrast, the current anti-AD medication elicits less toxicity than organophosphate compounds due to only transient inhibition of cholinesterases [24,25]. Our correlation analyses showed that toxicity and loss of cell viability was positively correlated to AChE inhibition, but this did not reach significance (Figure 6D). Cell viability was also negatively correlated with BuChE inhibition, indicating that the most potent BuChE inhibitors may be well tolerated.

Correlation analysis also demonstrated a significant positive association between AChE inhibition and BuChE inhibition. Thus, phytochemicals present in the plant extracts could potentially include desirable dual cholinesterase inhibitors [26] or mixtures of anti-AChE and anti-BuChE agents. It is also possible that these different plants contain a number of anti-cholinesterases or the same agent(s) but at differing concentrations.

Lastly, correlation analysis between cell viability and radical scavenging demonstrated a positive relationship, although this did not reach significance (Figure 6F). A positive correlation suggests that, at least for some of the plant extracts, higher (desirable) radical scavenging is associated with more (undesirable) toxicity. Indeed, beneficial antioxidants could suppress elevation of reactive radicals liberated in response to phytochemical redox stress. Certainly, there is a need to be mindful that some polyphenols, including certain flavonoids, are cytotoxic in vitro [91] and, if consumed in excess, may be toxic in vivo [92]. Thus, plant extracts can be double-edged, with a trade-off between provision of both beneficial and refractory polyphenols.

To investigate further the phytochemical composition of the plant extracts, we performed LC-MS/MS. This revealed several molecular masses that were present in all the plant extracts, such as rutin (quercetin-3-O-rutinoside) and kaempferol 3-O-glucoside, as well as others, including

3-caffeoylquinic acid, only detected within the two most powerful cholinesterase-inhibiting plant extracts: *L. inermis* and *E. globulus* (refer to Table 2). Consistent with our studies, 3-caffeoylquinic acid was recently demonstrated to exhibit both AChE and BuChE inhibitory capabilities [93,94]. Furthermore, other flavonoids, including rutin, are also capable of inhibiting AChE [95]. Hence, these plant extracts likely retain a range of ChEIs of polyphenol origin. Furthermore, from an in silico molecular modeling approach (Table 3 and Figure 7) [96], an assessment of their potency as ChEIs was undertaken and compared to the current FDA-approved drug, galantamine. However, it is appreciated that these plant extracts and phytochemicals will require further evaluation of their therapeutic potential in vivo.

5. Conclusions

In conclusion, we demonstrated that certain commonly harvested plants retain functional and potentially beneficial dual cholinesterase inhibitors as well as substantive antioxidant properties. From further purification and characterization of resident phytochemicals that retain beneficial pharmacology and with reduced adverse drug reactions, suitable agents may be isolated to provide nutraceuticals able to stave off the cognitive decline experienced with age and by AD patients.

Supplementary Materials: The following are available online at <http://www.mdpi.com/2218-273X/10/11/1556/s1>. Figure S1: Inhibition of AChE and BuChE by galantamine. Figure S2: DPPH radical scavenging activity of plant extracts. Figure S3: Toxicity of plant extracts to neuronal cells. Table S1: Reported phytochemicals with anti-cholinergic activity.

Author Contributions: Conceptualization, H.A.-u.-R., M.A., S.H. and W.G.C.; methodology, H.A.R., F.S. and D.T.; software, H.A.-u.-R., L.-N.S. and E.E.; validation, H.A.-u.-R., E.E. and W.G.C.; formal analysis, H.A.-u.-R., M.A. and W.G.C.; investigation, H.A.-u.-R., F.S. and D.T.; resources, H.A.-u.-R., D.T., M.A., S.H. and W.G.C.; data curation, H.A.-u.-R., E.E. and W.G.C.; writing-original draft preparation, H.A.R. and W.G.C.; writing-review and editing, H.A.-u.-R., M.A. and W.G.C.; visualization, H.A.-u.-R., M.A., S.H. and W.G.C.; supervision, M.A., S.H. and W.G.C.; project administration, H.A.-u.-R., M.A., S.H. and W.G.C.; funding acquisition, M.A., S.H. and W.G.C. All authors have read and agreed to the published version of the manuscript.

Funding: This research was funded by The Higher Education Commission (HEC) of Pakistan to H.A.R. for her PhD studies (Indigenous PhD scholarship; PIN No. 315–78152BS3–096). HEC Pakistan also provided funding to H.A.R. (IRSIP No. 1–8/HEC/HRD/2018/8570) to undertake research at the University of Nottingham, Nottingham, UK. This work was also funded by the HEC Pakistan under the National Research Programme for Universities (NRPU Grant 8288). Funding was also provided by The Commonwealth Scholarship Commission as split-site PhD funding to H.A.R. (PKCN-2018–267) to conduct part of her PhD studies at the University of Nottingham, Nottingham, UK.

Conflicts of Interest: The authors declare no conflict of interest. The funders had no role in the design of the study; in the collection, analyses, or interpretation of data; in the writing of the manuscript; or in the decision to publish the results.

References

1. United Nations Department of Economic and Social Affairs, Population Division. World Population Ageing 2017—Highlights (ST/ESA/SER.A/397). Available online: https://www.un.org/en/development/desa/population/publications/pdf/ageing/WPA2017_Highlights.pdf (accessed on 14 November 2020).
2. GBD 2016 Dementia Collaborators. Global, regional, and national burden of Alzheimer’s disease and other dementias, 1990–2016: A systematic analysis for the Global Burden of Disease Study 2016. *Lancet Neurol.* **2019**, *18*, 88–106. [CrossRef]
3. WHO. 10 Facts on Dementia. WHO Media Centre, 2016. Available online: <https://www.who.int/features/factfiles/dementia/en/> (accessed on 28 September 2020).
4. Launer, L.J.; Andersen, K.; Dewey, M.E.; Letenneur, L.; Ott, A.; Amaducci, L.A.; Brayne, C.E.; Copeland, J.R.M.; Dartigues, J.F.; Kragh-Sorensen, P.; et al. Rates and risk factors for dementia and Alzheimer’s disease: Results from EURODEM pooled analyses. *Neurology* **1999**, *52*, 78. [CrossRef] [PubMed]
5. Paulson, H.; Igo, I. Genetics of Dementia. *Semin. Neurol.* **2011**, *31*, 449–460. [CrossRef] [PubMed]
6. Killin, L.O.J.; Starr, J.M.; Shiue, I.J.; Russ, T.C. Environmental risk factors for dementia: A systematic review. *BMC Geriatr.* **2016**, *16*, 175. [CrossRef]

7. Sabia, S.; Elbaz, A.; Britton, A.; Bell, S.; Dugravot, A.; Shipley, M.; Kivimaki, M.; Singh-Manoux, A. Alcohol consumption and cognitive decline in early old age. *Neurology* **2014**, *82*, 332–339. [[CrossRef](#)]
8. Morris, M.C.; Tangney, C.C. Dietary fat composition and dementia risk. *Neurobiol. Aging* **2014**, *35*, S59–S64. [[CrossRef](#)]
9. Anstey, K.J.; Mack, H.A.; Cherbuin, N. Alcohol Consumption as a Risk Factor for Dementia and Cognitive Decline: Meta-Analysis of Prospective Studies. *Am. J. Geriatr. Psychiatry* **2009**, *17*, 542–555. [[CrossRef](#)]
10. Martínez-Lapiscina, E.H.; Clavero, P.; Toledo, E.; Estruch, R.; Salas-Salvadó, J.; Julián, B.S.; Sanchez-Tainta, A.; Ros, E.; Valls-Pedret, C.; Martínez-Gonzalez, M.Á. Mediterranean diet improves cognition: The PREDIMED-NAVARRA randomised trial. *J. Neurol. Neurosurg. Psychiatry* **2013**, *84*, 1318–1325. [[CrossRef](#)]
11. Hardman, R.J.; Kennedy, G.; MacPherson, H.; Scholey, A.B.; Pipingas, A. Adherence to a Mediterranean-Style Diet and Effects on Cognition in Adults: A Qualitative Evaluation and Systematic Review of Longitudinal and Prospective Trials. *Front. Nutr.* **2016**, *3*, 22. [[CrossRef](#)]
12. Loughrey, D.G.; Lavecchia, S.; Brennan, S.; Lawlor, B.A.; Kelly, M.E. The Impact of the Mediterranean Diet on the Cognitive Functioning of Healthy Older Adults: A Systematic Review and Meta-Analysis. *Adv. Nutr.* **2017**, *8*, 571–586. [[CrossRef](#)]
13. Rehm, J.; Gmel, G.E., Sr.; Gmel, G.; Hasan, O.S.M.; Imtiaz, S.; Popova, S.; Probst, C.; Roerecke, M.; Room, R.; Samokhvalov, A.V.; et al. The relationship between different dimensions of alcohol use and the burden of disease—An update. *Addiction* **2017**, *112*, 968–1001. [[CrossRef](#)] [[PubMed](#)]
14. Gardener, H.; Caunca, M.R. Mediterranean Diet in Preventing Neurodegenerative Diseases. *Curr. Nutr. Rep.* **2018**, *7*, 10–20. [[CrossRef](#)] [[PubMed](#)]
15. Dadhania, V.P.; Trivedi, P.P.; Vikram, A.; Tripathi, D.N. Nutraceuticals against Neurodegeneration: A Mechanistic Insight. *Curr. Neuropharmacol.* **2016**, *14*, 627–640. [[CrossRef](#)] [[PubMed](#)]
16. Sadhukhan, P.; Saha, S.; Dutta, S.; Mahalanobish, S.; Sil, P.C. Nutraceuticals: An emerging therapeutic approach against the pathogenesis of Alzheimer’s disease. *Pharmacol. Res.* **2018**, *129*, 100–114. [[CrossRef](#)]
17. Nwidu, L.L.; Alikwe, P.C.N.; Elmorsy, E.; Carter, W.G. An Investigation of Potential Sources of Nutraceuticals from the Niger Delta Areas, Nigeria for Attenuating Oxidative Stress. *Medicines* **2019**, *6*, 15. [[CrossRef](#)]
18. Perl, D.P. Neuropathology of Alzheimer’s Disease. *Mt. Sinai J. Med. J. Transl. Pers. Med.* **2010**, *77*, 32–42. [[CrossRef](#)]
19. Schaffert, L.-N.; Carter, W.G. Do Post-Translational Modifications Influence Protein Aggregation in Neurodegenerative Diseases: A Systematic Review. *Brain Sci.* **2020**, *10*, 232. [[CrossRef](#)]
20. Dugger, B.N.; Dickson, D.W. Pathology of Neurodegenerative Diseases. *Cold Spring Harb. Perspect. Biol.* **2017**, *9*, a028035. [[CrossRef](#)]
21. Agostinho, P.; Cunha, R.A.; Oliveira, C. Neuroinflammation, Oxidative Stress and the Pathogenesis of Alzheimers Disease. *Curr. Pharm. Des.* **2010**, *16*, 2766–2778. [[CrossRef](#)]
22. Du, X.; Wang, X.; Geng, M. Alzheimer’s disease hypothesis and related therapies. *Transl. Neurodegener.* **2018**, *7*, 1–7. [[CrossRef](#)]
23. Arendt, T.; Brückner, M.K.; Lange, M.; Bigl, V. Changes in acetylcholinesterase and butyrylcholinesterase in Alzheimer’s disease resemble embryonic development—A study of molecular forms. *Neurochem. Int.* **1992**, *21*, 381–396. [[CrossRef](#)]
24. Grossberg, G.T. Cholinesterase Inhibitors for the Treatment of Alzheimer’s Disease: Getting on and staying on. *Curr. Ther. Res.* **2003**, *64*, 216–235. [[CrossRef](#)]
25. Colović, M.; Krstić, D.; Lazarević-Pašti, T.D.; Bondžić, A.M.; Vasić, V.M. Acetylcholinesterase Inhibitors: Pharmacology and Toxicology. *Curr. Neuropharmacol.* **2013**, *11*, 315–335. [[CrossRef](#)] [[PubMed](#)]
26. Nordberg, A.; Ballard, C.; Bullock, R.; Darreh-Shori, T.; Somogyi, M. A Review of Butyrylcholinesterase as a Therapeutic Target in the Treatment of Alzheimer’s Disease. *Prim. Care Companion CNS Disord.* **2013**, *15*. [[CrossRef](#)] [[PubMed](#)]
27. Dosoky, N.S.; Setzer, W.N. Biological Activities and Safety of Citrus spp. Essential Oils. *Int. J. Mol. Sci.* **2018**, *19*, 1966. [[CrossRef](#)] [[PubMed](#)]
28. Del Río, J.A.; Fuster, M.D.; Gómez, P.; Porras, I.; García-Lidón, A.; Ortuño, A. Citrus limon: A source of flavonoids of pharmaceutical interest. *Food Chem.* **2004**, *84*, 457–461. [[CrossRef](#)]
29. Jain, V.; Verma, S.K.; Katewa, S.S. Myths, traditions and fate of multipurpose Bombax ceiba L.—An appraisal. *Indian J. Tradit. Knowl.* **2009**, *8*, 638–644.

30. Rameshwar, V.; Kishor, D.; Tushar, G.; Siddharth, G.; Sudarshan, G. A pharmacognostic and pharmacological overview on *Bombax ceiba*. *Sch. Acad. J. Pharm.* **2014**, *3*, 100–107.
31. Chaudhary, G.; Goyal, S.; Poonia, P. *Lawsonia inermis* Linnaeus: A phytopharmacological review. *Int. J. Pharm. Sci. Drug Res.* **2010**, *2*, 91–98.
32. Borade, A.S.; Kale, B.N.; Shete, R.V. A phytopharmacological review on *Lawsonia inermis* (Linn.). *Int. J. Pharm. Life Sci.* **2011**, *2*, 536–541.
33. Semwal, R.B.; Semwal, D.K.; Combrinck, S.; Cartwright-Jones, C.; Viljoen, A. *Lawsonia inermis* L. (henna): Ethnobotanical, phytochemical and pharmacological aspects. *J. Ethnopharmacol.* **2014**, *155*, 80–103. [[CrossRef](#)] [[PubMed](#)]
34. Patel, K.M.; Patel, P.R. Review on *Lawsonia inermis* Linn.: An Update. *Asian J. Pharm. Technol.* **2017**, *7*, 237. [[CrossRef](#)]
35. Luís, Â.; Duarte, A.; Gominho, J.; Domingues, F.; Duarte, A.P. Chemical composition, antioxidant, antibacterial and anti-quorum sensing activities of *Eucalyptus globulus* and *Eucalyptus radiata* essential oils. *Ind. Crops Prod.* **2016**, *79*, 274–282. [[CrossRef](#)]
36. Pan, M.; Lei, Q.; Zang, N.; Zhang, H. A Strategy Based on GC-MS/MS, UPLC-MS/MS and Virtual Molecular Docking for Analysis and Prediction of Bioactive Compounds in *Eucalyptus Globulus* Leaves. *Int. J. Mol. Sci.* **2019**, *20*, 3875. [[CrossRef](#)] [[PubMed](#)]
37. Javanmardi, J.; Khalighi, A.; Kashi, A.; Bais, H.P.; Vivanco, J.M. Chemical Characterization of Basil (*Ocimum basilicum* L.) Found in Local Accessions and Used in Traditional Medicines in Iran. *J. Agric. Food Chem.* **2002**, *50*, 5878–5883. [[CrossRef](#)]
38. Yanishlieva, N.V.; Marinova, E.; Pokorný, J. Natural antioxidants from herbs and spices. *Eur. J. Lipid Sci. Technol.* **2006**, *108*, 776–793. [[CrossRef](#)]
39. Karousou, R.; Balta, M.; Hanlidou, E.; Kokkini, S. “Mints”, smells and traditional uses in Thessaloniki (Greece) and other Mediterranean countries. *J. Ethnopharmacol.* **2007**, *109*, 248–257. [[CrossRef](#)]
40. Ellman, G.L.; Courtney, K.D.; Andres, V., Jr.; Feather-Stone, R.M. A new and rapid colorimetric determination of acetylcholinesterase activity. *Biochem. Pharmacol.* **1961**, *7*, 88–95. [[CrossRef](#)]
41. Nwidu, L.L.; Elmorsy, E.; Thornton, J.; Wijamunige, B.; Wijesekara, A.; Tarbox, R.; Warren, A.; Carter, W.G. Anti-acetylcholinesterase activity and antioxidant properties of extracts and fractions of *Carpolobia leuca*. *Pharm. Biol.* **2017**, *55*, 1875–1883. [[CrossRef](#)]
42. Trott, O.; Olson, A.J. AutoDock Vina: Improving the speed and accuracy of docking with a new scoring function, efficient optimization, and multithreading. *J. Comput. Chem.* **2009**, *31*, 455–461. [[CrossRef](#)]
43. Nwidu, L.L.; Elmorsy, E.; Aprioku, J.S.; Siminialayi, I.; Carter, W.G. In Vitro Anti-Cholinesterase and Antioxidant Activity of Extracts of *Moringa oleifera* Plants from Rivers State, Niger Delta, Nigeria. *Medicines* **2018**, *5*, 71. [[CrossRef](#)] [[PubMed](#)]
44. Xu, Y.-B.; Chen, G.-L.; Guo, M. Antioxidant and Anti-Inflammatory Activities of the Crude Extracts of *Moringa oleifera* from Kenya and Their Correlations with Flavonoids. *Antioxidants* **2019**, *8*, 296. [[CrossRef](#)] [[PubMed](#)]
45. Pentón-Rol, G.; Cervantes-Llanos, M. Report on the Symposium “Molecular Mechanisms Involved in Neurodegeneration”. *Behav. Sci.* **2018**, *8*, 16. [[CrossRef](#)] [[PubMed](#)]
46. Wiem, A.; Smail, A.; Wissem, M.; Faleiro, M.L.; Miguel, M. Antioxidant, anti-inflammatory and anti-acetylcholinesterase activities of leaf, flower and seed aqueous extracts of *Lawsonia inermis* from Tunisia. *Int. J. Pharm. Pharm. Sci.* **2014**, *6*, 445–452.
47. Gholamhoseinian, A.; Moradi, M.; Sharifi-Far, F. Screening the methanol extracts of some Iranian plants for acetylcholinesterase inhibitory activity. *Res. Pharm. Sci.* **2009**, *4*, 105–112. [[PubMed](#)]
48. Lynch, T.J.; Mattes, C.E.; Singh, A.; Bradley, R.M.; Brady, R.O.; Dretchen, K.L. Cocaine Detoxification by Human Plasma Butyrylcholinesterase. *Toxicol. Appl. Pharmacol.* **1997**, *145*, 363–371. [[CrossRef](#)]
49. Chen, V.P.; Gao, Y.; Geng, L.; Brimijoin, S. Butyrylcholinesterase regulates central ghrelin signaling and has an impact on food intake and glucose homeostasis. *Int. J. Obes.* **2017**, *41*, 1413–1419. [[CrossRef](#)]
50. Dorling, J.L.; Clayton, D.J.; Jones, J.; Carter, W.G.; Thackray, A.E.; King, J.A.; Pucci, A.; Batterham, R.L.; Stensel, D.J. A randomized crossover trial assessing the effects of acute exercise on appetite, circulating ghrelin concentrations, and butyrylcholinesterase activity in normal-weight males with variants of the obesity-linked FTO rs9939609 polymorphism. *Am. J. Clin. Nutr.* **2019**, *110*, 1055–1066. [[CrossRef](#)]

51. Manoharan, I.; Boopathy, R.; Darvesh, S.; Lockridge, O. A medical health report on individuals with silent butyrylcholinesterase in the Vysya community of India. *Clin. Chim. Acta* **2007**, *378*, 128–135. [[CrossRef](#)]
52. Lockridge, O. Review of human butyrylcholinesterase structure, function, genetic variants, history of use in the clinic, and potential therapeutic uses. *Pharmacol. Ther.* **2015**, *148*, 34–46. [[CrossRef](#)]
53. Mesulam, M.; Guillozet, A.; Shaw, P.; Quinn, B. Widely Spread Butyrylcholinesterase Can Hydrolyze Acetylcholine in the Normal and Alzheimer Brain. *Neurobiol. Dis.* **2002**, *9*, 88–93. [[CrossRef](#)] [[PubMed](#)]
54. Reinikainen, K.J.; Riekkinen, P.J.; Paljärvi, L.; Soininen, H.; Helkala, E.L.; Jolkkonen, J.; Laakso, M. Cholinergic deficit in Alzheimer's disease: A study based on CSF and autopsy data. *Neurochem. Res.* **1988**, *13*, 135–146. [[CrossRef](#)]
55. Mushtaq, G.; Greig, N.H.; Khan, J.A.; Kamal, M.A. Status of Acetylcholinesterase and Butyrylcholinesterase in Alzheimer's Disease and Type 2 Diabetes Mellitus. *CNS Neurol. Disord. Drug Targets* **2014**, *13*, 1432–1439. [[CrossRef](#)] [[PubMed](#)]
56. Giacobini, E. Selective Inhibitors of Butyrylcholinesterase: A valid alternative for therapy of Alzheimer's disease? *Drugs Aging* **2001**, *18*, 891–898. [[CrossRef](#)] [[PubMed](#)]
57. Iyer, M.R.; Pal, S.C.; Kasture, V.S.; Kasture, S.B. Effect of Lawsonia inermis on memory and behaviour mediated via monoamine neurotransmitters. *Indian J. Pharmacol.* **1998**, *30*, 181–185.
58. Brand-Williams, W.; Cuvelier, M.E.; Berset, C. Use of a free radical method to evaluate antioxidant activity. *LWT Food Sci. Technol.* **1995**, *28*, 25–30. [[CrossRef](#)]
59. Villaño, D.; Fernández-Pachón, M.S.; Moyá, M.L.; Troncoso, A.M.; García-Parrilla, M.C. Radical scavenging ability of polyphenolic compounds towards DPPH free radical. *Talanta* **2007**, *71*, 230–235. [[CrossRef](#)]
60. Hsouna, A.B.; Trigui, M.; Culioli, G.; Blache, Y.; Jaoua, S. Antioxidant constituents from Lawsonia inermis leaves: Isolation, structure elucidation and antioxidative capacity. *Food Chem.* **2011**, *125*, 193–200. [[CrossRef](#)]
61. Aazza, S.; Lyoussi, B.; Miguel, M.G. Antioxidant and Antiacetylcholinesterase Activities of Some Commercial Essential Oils and Their Major Compounds. *Molecules* **2011**, *16*, 7672–7690. [[CrossRef](#)]
62. Yadav, M.; Jindal, D.K.; Parle, M.; Kumar, A.; Dhingra, S. Targeting oxidative stress, acetylcholinesterase, proinflammatory cytokine, dopamine and GABA by eucalyptus oil (*Eucalyptus globulus*) to alleviate ketamine-induced psychosis in rats. *Inflammopharmacology* **2018**, *27*, 301–311. [[CrossRef](#)]
63. Ayaz, M.; Sadiq, A.; Junaid, M.; Ullah, F.; Subhan, F.; Ahmed, J. Neuroprotective and Anti-Aging Potentials of Essential Oils from Aromatic and Medicinal Plants. *Front. Aging Neurosci.* **2017**, *9*, 168. [[CrossRef](#)] [[PubMed](#)]
64. Almeida, I.F.; Fernandes, E.; Lima, J.L.F.C.; Valentão, P.; Andrade, P.B.; Seabra, R.M.; Costa, P.C.; Bahia, M. Oxygen and Nitrogen Reactive Species Are Effectively Scavenged by *Eucalyptus globulus* Leaf Water Extract. *J. Med. Food* **2009**, *12*, 175–183. [[CrossRef](#)] [[PubMed](#)]
65. Amakura, Y.; Umino, Y.; Tsuji, S.; Ito, H.; Hatano, T.; Yoshida, T.; Tonogai, Y. Constituents and their antioxidative effects in eucalyptus leaf extract used as a natural food additive. *Food Chem.* **2002**, *77*, 47–56. [[CrossRef](#)]
66. Dessì, M.A.; Deiana, M.; Rosa, A.; Piredda, M.; Cottiglia, F.; Bonsignore, L.; Deidda, D.; Pompei, R.; Corongiu, F.P. Antioxidant activity of extracts from plants growing in Sardinia. *Phytotherapy Res.* **2001**, *15*, 511–518. [[CrossRef](#)]
67. Castro, V.T.N.D.A.E.; Sobrinho, T.J.D.S.P.; Corrêa, A.J.C.; Araújo, T.A.D.S.; Da Silva, T.G.; De Amorim, E.L.C. The anticholinesterase properties of plants from the northeast of Brazil selected by an ethnopharmacological study for disorders relating to the nervous system. *Pharmacogn. Mag.* **2016**, *12*, 195–200. [[CrossRef](#)]
68. Cirmi, S.; Ferlazzo, N.; Lombardo, G.E.; Ventura-Spagnolo, E.; Gangemi, S.; Calapai, G.; Navarra, M. Neurodegenerative Diseases: Might Citrus Flavonoids Play a Protective Role? *Molecules* **2016**, *21*, 1312. [[CrossRef](#)]
69. Lee, S.; Youn, K.; Lim, G.; Lee, J.; Jun, M. In Silico Docking and In Vitro Approaches towards BACE1 and Cholinesterases Inhibitory Effect of Citrus Flavanones. *Molecules* **2018**, *23*, 1509. [[CrossRef](#)]
70. Obboh, G.; Olasehinde, T.A.; Ademosun, A.O. Essential Oil from Lemon Peels Inhibit Key Enzymes Linked to Neurodegenerative Conditions and Pro-oxidant Induced Lipid Peroxidation. *J. Oleo Sci.* **2014**, *63*, 373–381. [[CrossRef](#)]
71. Liu, B.; Kou, J.; Li, F.; Huo, D.; Xu, J.; Zhou, X.; Meng, D.; Ghulam, M.; Artyom, B.; Gao, X.; et al. Lemon essential oil ameliorates age-associated cognitive dysfunction via modulating hippocampal synaptic density and inhibiting acetylcholinesterase. *Aging* **2020**, *12*, 8622–8639. [[CrossRef](#)]

72. Kamal, M.; Ashraf, M.Y.; Hussain, A.U.; Shahzadi, A.; Chughtai, M.I. Antioxidant potential of peel essential oils of three Pakistani citrus species: *Citrus reticulata*, *Citrus sinensis* and *Citrus paradisi*. *Pak. J. Bot.* **2013**, *45*, 1449–1454.
73. Tan, S.J.; Ismail, I.S. Potency of Selected Berries, Grapes, and Citrus Fruit as Neuroprotective Agents. *Evid. Based Complement. Altern. Med.* **2020**, *2020*, 3582947. [[CrossRef](#)] [[PubMed](#)]
74. Farag, M.A.; Ezzat, S.M.; Salama, M.M.; Tadros, M.G. Anti-acetylcholinesterase potential and metabolome classification of 4 *Ocimum* species as determined via UPLC/qTOF/MS and chemometric tools. *J. Pharm. Biomed. Anal.* **2016**, *125*, 292–302. [[CrossRef](#)] [[PubMed](#)]
75. Kivilompolo, M.; Hyötyläinen, T. Comprehensive two-dimensional liquid chromatography in analysis of Lamiaceae herbs: Characterisation and quantification of antioxidant phenolic acids. *J. Chromatogr. A* **2007**, *1145*, 155–164. [[CrossRef](#)] [[PubMed](#)]
76. Nguyen, P.M.; Niemeyer, E.D. Effects of Nitrogen Fertilization on the Phenolic Composition and Antioxidant Properties of Basil (*Ocimum basilicum* L.). *J. Agric. Food Chem.* **2008**, *56*, 8685–8691. [[CrossRef](#)] [[PubMed](#)]
77. Sarahroodi, S.; Esmaeili, S.; Hemmati, Z.; Mikaili, P.; Saberi, Y. The effects of green *Ocimum basilicum* hydroalcoholic extract on retention and retrieval of memory in mice. *Anc. Sci. Life* **2012**, *31*, 185–189. [[CrossRef](#)] [[PubMed](#)]
78. Jabir, N.R.; Khan, F.R.; Tabrez, S. Cholinesterase targeting by polyphenols: A therapeutic approach for the treatment of Alzheimer’s disease. *CNS Neurosci. Ther.* **2018**, *24*, 753–762. [[CrossRef](#)] [[PubMed](#)]
79. Vieira, T.O.; Said, A.; Aboutabl, E.; Azzam, M.; Creczynski-Pasa, T.B. Antioxidant activity of methanolic extract of *Bombax ceiba*. *Redox Rep.* **2009**, *14*, 41–46. [[CrossRef](#)]
80. Sinha, S.; Kumar, B.; Singh, D.K.; Luqman, S.; Singh, M.; Singh, A. Antioxidant and Choline Esterase Inhibitory Activity of Phenolic Rich Extracts from *Bombax ceiba* L. Flowers. *Free Radic. Antioxid.* **2018**, *8*, 135–140. [[CrossRef](#)]
81. Mostafa, N.M. β -Amyrin Rich *Bombax ceiba* Leaf Extract with Potential Neuroprotective Activity against Scopolamine-Induced Memory Impairment in Rats. *Rec. Nat. Prod.* **2018**, *12*, 480–492. [[CrossRef](#)]
82. Sinha, S.; Kumar, B.; Luqman, S.; Singh, D. Neuroprotective potential of *Cucurbita maxima* Duchesne ex Poir, *Caesalpinia bunduc* (L.) Roxb and *Bombax ceiba* Linn extracts. *S. Afr. J. Bot.* **2019**, *120*, 319–325. [[CrossRef](#)]
83. Miyazawa, M.; Watanabe, H.; Umemoto, K.; Kameoka, H. Inhibition of Acetylcholinesterase Activity by Essential Oils of *Mentha* Species. *J. Agric. Food Chem.* **1998**, *46*, 3431–3434. [[CrossRef](#)]
84. Mata, A.; Proença, C.; Ferreira, A.R.; Serralheiro, M.L.M.; Nogueira, J.M.F.; Araújo, M.E.M. Antioxidant and antiacetylcholinesterase activities of five plants used as Portuguese food spices. *Food Chem.* **2007**, *103*, 778–786. [[CrossRef](#)]
85. Bernas, T.; Dobrucki, J. Mitochondrial and nonmitochondrial reduction of MTT: Interaction of MTT with TMRE, JC-1, and NAO mitochondrial fluorescent probes. *Cytometry* **2002**, *47*, 236–242. [[CrossRef](#)] [[PubMed](#)]
86. Riss, T.L.; Moravec, R.A.; Niles, A.L.; Duellman, S.; Benink, H.A.; Worzella, T.J.; Minor, L.; Markossian, S.; Sittampalam, G.S.; Grossman, A.; et al. Cell viability assays. In *Assay Guidance Manual*; Markossian, S., Sittampalam, G.S., Grossman, A., Brimacombe, K., Arkin, M., Auld, D., Austin, C.P., Baell, J., Caaveiro, J.M.M., Chung, T.D.Y., et al., Eds.; Eli Lilly & Company and the National Centre for Advancing Translational Sciences: Bethesda, MD, USA, 2013; updated 2016.
87. Elmorsy, E.; Al-Ghafari, A.; Almutairi, F.M.; Aggour, A.M.; Carter, W.G. Antidepressants are cytotoxic to rat primary blood brain barrier endothelial cells at high therapeutic concentrations. *Toxicol. Vitro.* **2017**, *44*, 154–163. [[CrossRef](#)]
88. Al-Ghafari, A.; Elmorsy, E.; Fikry, E.; Alrowaili, M.; Carter, W.G. The heavy metals lead and cadmium are cytotoxic to human bone osteoblasts via induction of redox stress. *PLoS ONE* **2019**, *14*, e0225341. [[CrossRef](#)]
89. Banerjee, B.D.; Seth, V.; Ahmed, R. Pesticide-Induced Oxidative Stress: Perspective and Trends. *Rev. Environ. Health* **2001**, *16*, 1–40. [[CrossRef](#)]
90. Carter, W.G.; Tarhoni, M.; Rathbone, A.J.; Ray, D.E. Differential protein adduction by seven organophosphorus pesticides in both brain and thymus. *Hum. Exp. Toxicol.* **2007**, *26*, 347–354. [[CrossRef](#)]
91. Matsuo, M.; Sasaki, N.; Saga, K.; Kaneko, T. Cytotoxicity of Flavonoids toward Cultured Normal Human Cells. *Biol. Pharm. Bull.* **2005**, *28*, 253–259. [[CrossRef](#)]
92. Skibola, C.F.; Smith, M.T. Potential health impacts of excessive flavonoid intake. *Free. Radic. Biol. Med.* **2000**, *29*, 375–383. [[CrossRef](#)]

93. Budryn, G.; Grzelczyk, J.; Jaśkiewicz, A.; Żyżelewicz, D.; Pérez-Sánchez, H.; Cerón-Carrasco, J.P. Evaluation of butyrylcholinesterase inhibitory activity by chlorogenic acids and coffee extracts assed in ITC and docking simulation models. *Food Res. Int.* **2018**, *109*, 268–277. [[CrossRef](#)]
94. Grzelczyk, J.; Budryn, G. Analysis of the activity of hydroxycinnamic acids from green and roasted coffee extracts as acetylcholinesterase inhibitors using an isothermal method of titration calorimetry. *Folia Pomeranae Univ. Technol. Stetin. Agric. Aliment. Piscaria Zootech.* **2019**, *349*, 15–24. [[CrossRef](#)]
95. Khan, H.; Marya; Amin, S.; Kamal, M.A.; Patel, S. Flavonoids as acetylcholinesterase inhibitors: Current therapeutic standing and future prospects. *Biomed. Pharmacother.* **2018**, *101*, 860–870. [[CrossRef](#)] [[PubMed](#)]
96. Amat-Ur-Rasool, H.; Ahmed, M. Designing Second Generation Anti-Alzheimer Compounds as Inhibitors of Human Acetylcholinesterase: Computational Screening of Synthetic Molecules and Dietary Phytochemicals. *PLoS ONE* **2015**, *10*, e0136509. [[CrossRef](#)] [[PubMed](#)]

Publisher's Note: MDPI stays neutral with regard to jurisdictional claims in published maps and institutional affiliations.



© 2020 by the authors. Licensee MDPI, Basel, Switzerland. This article is an open access article distributed under the terms and conditions of the Creative Commons Attribution (CC BY) license (<http://creativecommons.org/licenses/by/4.0/>).

Article

Amaryllidaceae Alkaloids of Belladine-Type from *Narcissus pseudonarcissus* cv. Carlton as New Selective Inhibitors of Butyrylcholinesterase

Abdullah Al Mamun ¹, Jana Maříková ², Daniela Hulcová ^{1,3}, Jiří Janoušek ^{1,3},
Marcela Šafratová ^{1,3}, Lucie Nováková ⁴, Tomáš Kučera ⁵, Martina Hrabínová ^{6,7}, Jiří Kuneš ²,
Jan Korábečný ^{6,7,*} and Lucie Cahlíková ^{1,*}

¹ ADINACO Research Group, Department of Pharmaceutical Botany, Faculty of Pharmacy, Charles University, Heyrovského 1203, 500 05 Hradec Králové, Czech Republic; almamuna@faf.cuni.cz (A.A.M.); hulcovd@faf.cuni.cz (D.H.); janousj2@faf.cuni.cz (J.J.); safratom@faf.cuni.cz (M.Š.)

² Department of Organic and Bioorganic Chemistry, Faculty of Pharmacy, Charles University, Heyrovského 1203, 500 05 Hradec Králové, Czech Republic; marikoj2@faf.cuni.cz (J.M.); kunes@faf.cuni.cz (J.K.)

³ Department of Pharmacognosy, Faculty of Pharmacy, Charles University, Heyrovského 1203, 500 05 Hradec Králové, Czech Republic

⁴ Department of Analytical Chemistry, Faculty of Pharmacy, Charles University, Heyrovského 1203, 500 05 Hradec Králové, Czech Republic; novakoval@faf.cuni.cz

⁵ Department of Military Medical Service Organisation and Management, Faculty of Military Health Sciences, University of Defence, Třebešská 1575, 500 05 Hradec Králové, Czech Republic; kucera-t@email.cz

⁶ Department of Toxicology and Military Pharmacy, Faculty of Military Health Sciences, University of Defence, Třebešská 1575, 500 05 Hradec Králové, Czech Republic; hrabinova@pmfhk.cz

⁷ Biomedical Research Centre, University Hospital Hradec Kralove, Sokolska 581, 500 05 Hradec Kralove, Czech Republic

* Correspondence: jan.korabecny@fnhk.cz (J.K.); cahlikova@faf.cuni.cz (L.C.);
Tel.: +420-495-067-311 (L.C.); +420-495-833-447 (J.K.)

Received: 30 April 2020; Accepted: 19 May 2020; Published: 22 May 2020



Abstract: Thirteen known (**1–12** and **16**) and three previously undescribed Amaryllidaceae alkaloids of belladine structural type, named carltonine A–C (**13–15**), were isolated from bulbs of *Narcissus pseudonarcissus* cv. Carlton (Amaryllidaceae) by standard chromatographic methods. Compounds isolated in sufficient amounts, and not tested previously, were evaluated for their in vitro acetylcholinesterase (AChE; E.C. 3.1.1.7), butyrylcholinesterase (BuChE; E.C. 3.1.1.8) and prolyl oligopeptidase (POP; E.C. 3.4.21.26) inhibition activities. Significant human BuChE (*h*BuChE) inhibitory activity was demonstrated by newly described alkaloids carltonine A (**13**) and carltonine B (**14**) with IC₅₀ values of 913 ± 20 nM and 31 ± 1 nM, respectively. Both compounds displayed a selective inhibition pattern for *h*BuChE with an outstanding selectivity profile over AChE inhibition, higher than 100. The in vitro data were further supported by in silico studies of the active alkaloids **13** and **14** in the active site of *h*BuChE.

Keywords: Amaryllidaceae; *Narcissus pseudonarcissus* cv. Carlton; alkaloids; carltonine A–C; Alzheimer’s disease; butyrylcholinesterase; docking studies

1. Introduction

Alzheimer’s disease (AD), a progressive neurodegenerative brain disorder featuring memory loss and cognitive impairments, has been named after German psychiatrist Alois Alzheimer. AD is the most common type of dementia among the elderly, generally diagnosed in individuals over the age of

65 years [1]. Considering population aging and increased life expectancy, the number of AD patients is predicted to increase enormously. About 4.6 million new cases are diagnosed every year throughout the world, and the World Health Organization (WHO) estimates that by 2050 over 131 million patients will suffer from AD [2]. Additionally, the current cost of dementia is about a trillion US dollars per year, and it should rise to 2 trillion US dollars by 2030 [3]. Thus, AD starts to be one of the greatest public health problems with severe impact on patients, their families and care workers.

Although the exact pathogenesis of AD remains elusive, it is currently conceived as a multifactorial disease. The main pathological hallmarks of AD are the deposits of β -amyloid peptide ($A\beta$) in senile plaques and neurofibrillary tangles (NFTs) formed by hyperphosphorylated τ -protein [4]. In addition to them, inflammation and oxidative stress processes also extensively contribute to the loss of synaptic integrity and neurodegeneration.

The current treatment is only symptomatic and mainly involves restoring of acetylcholine (ACh) levels through AChE inhibition [5]. Three AChE inhibitors, namely donepezil, galanthamine and rivastigmine, are currently used as the main therapeutic option for AD treatment [6]. BuChE is another serine hydrolase homologous to AChE that is encoded by a different gene and can be found ubiquitously throughout the body [6]. The role of BuChE has recently gained enormous interest, and not only in the field of AD research [7]. Regarding AD, it is well-documented that AChE activity is downregulated by up to 33–45% of normal values, while the activity of BuChE is escalated by up to 40–90% [8]. This dramatic switch between the AChE/BuChE ratio highlighted the supportive role of BuChE in hydrolysing the excess of ACh. Moreover, several lines of evidence also indicate that both cholinesterases play an important role in $A\beta$ aggregation and maturation to oligomers, fibrils and plaques [9].

POP, a cytosolic serine peptidase, has gained interest as a target for the treatment of neuropsychiatric and neurodegenerative diseases like schizophrenia, bipolar affective disorder, Parkinson's disease and AD [10]. POP is expressed in several brain regions, and catalyses with high specificity the cleavage of short peptides containing proline at its carboxyl site [11]. POP is responsible for the degradation of neurotransmitters, such as substance P, arginine vasopressin–oxytocin, and neurotensin, which in turn reduce the possibility of generation of toxic $A\beta$ peptides. Generally, POP can be regarded as one of the active players in the processes of learning and memory. In fact, some POP inhibitors have been experimentally found to act as antidementia drugs [10].

Natural products represent an important source of clinical drugs, especially for their structural diversity and wide range of biological activities [12]. Alkaloids are, without a doubt, the most intriguing templates of natural origin [13]. The family Amaryllidaceae comprises about 1100 species in 85 genera, which are distributed worldwide through the tropics and warm regions [14]. Some of the species are cultivated as ornamental plants for their beautiful flowers and fragrant essences. Different types of plant extracts from this family have been long used in traditional medicine for the treatment of cancer by the ancient Greeks, as well as by Africans, Asians, and Polynesian communities for the treatment of various diseases [15,16]. The medicinal value of the Amaryllidaceae species is attributed to the presence of tyrosine-derived alkaloids, typically named as Amaryllidaceae alkaloids (AAs), that are produced exclusively by this family. These alkaloids exhibit a wide range of biological activities, including AChE inhibition, antitumor, antiviral, antimalarial, analgesic antibacterial, and cytotoxic properties. One successful example of an Amaryllidaceae alkaloid is exemplified by galanthamine, a drug indicated for the treatment of mild to moderate vascular dementia and AD [17].

Narcissus L. is the most common genus of the Amaryllidaceae family comprising 80–100 wild species, mainly distributed in Southwestern Europe and North Africa, with some populations in the Balkans, Italy and France. Plants of the genus *Narcissus* L. have been used in traditional medicine worldwide in cancer therapy [18–21]. Most of the species can hybridize, thus, a large number of cultivars have been developed for ornamental purposes. Interestingly, some intersectional hybrids and cultivars have also been reported as potential sources of galanthamine and other Amaryllidaceae alkaloids [22,23]. The cultivar Carlton is cultivated for the commercial extraction of galanthamine,

because of its relatively high concentration in the bulbs, the large bulb size, and their availability in large volumes. Galanthamine is reported as the major alkaloid of *Narcissus pseudonarcissus*, followed by haemanthamine. Haemanthamine also has interesting biological activities including inhibition of protein synthesis, antimalarial and antiretroviral activity, as well as cytotoxicity against various cancer cell lines [24–26]. Recently, some semi-synthetic derivatives of haemanthamine have been published as promising candidates for AD therapy [27].

As a part of our ongoing research on Amaryllidaceae alkaloids with implication to AD, this work reports the isolation of several such alkaloids from fresh bulbs of *Narcissus pseudonarcissus* cv. Carlton. The isolated alkaloids that had not been previously studied were submitted for biological evaluation to reveal their inhibition potential towards *hAChE*, *hBuChE*, and POP. In vitro data were further supported by investigating the compound's putative binding modes in the active site of *hBuChE* to display crucial interaction.

2. Results and Discussion

2.1. Phytochemical Study of *Narcissus pseudonarcissus* cv. Carlton

Thirteen known (1–12 and 16) and three novel AAs (13–15) were isolated from bulbs of *Narcissus pseudonarcissus* cv. Carlton (Amaryllidaceae) by common chromatographic methods, as described in the Experimental section. The compounds were identified by MS, ESI-HRMS, 1D and 2D NMR spectroscopic analyses and by comparison of the obtained data with the literature (Figure 1). These techniques led to the identification of lycosinine B (1) [28], trisphaeridine (2) [29], 3,4-anhydrogalanthamine (3) [30], oduline (4) [31], masonine (5) [32], galanthamine (6) [33], galanthine (7) [34], lycorenine (8) [33], lycoramine (9) [33], homolycorine (10) [31], haemanthamine (11) [20], vittatine (12) [35], and 9-*O*-demethylhomolycorine (16) [31]. The isolated alkaloids belong to the galanthindole (1), narciclasine (2), galanthamine (3, 6, 9), homolycorine (4, 5, 8, 10, 16), lycorine (7) and haemanthamine (11, 12) structural types; newly isolated alkaloids 13–15 belong to the beladinne-type of AAs.

The new compound 13, named carltonine A, was obtained as a pale yellow oil. The HRMS of 13 showed a protonated molecular ion peak $[M + H]^+$ at m/z 433.2488, corresponding to the molecular formula $C_{27}H_{32}N_2O_3$ (433.2486 calcd for $C_{27}H_{33}N_2O_3^+$). The 1H NMR spectrum exhibited resonances associated with nine aromatic protons from which the presence of a *p*-substituted benzene ring (δ_H 7.00–6.96; 6.72–6.68), a 1,2,4,5-tetrasubstituted benzene ring (δ_H 7.10, 6.76) and a 1,2,3-trisubstituted benzene ring (δ_H 7.09, 6.82, 6.72) were obvious. The high-field part of the 1H NMR spectrum contained one singlet corresponding to two methoxy groups (δ_H 3.34), two doublets (δ_H 3.45, 3.29), two doublets of triplets (δ_H 3.32, dt, overlap, $J = 17.3, 8.8$ Hz; 3.20, dt, $J = 17.3, 8.8$ Hz), two triplets (δ_H 2.98, t, $J = 8.8$ Hz; 2.65, t, $J = 7.4$ Hz) and two singlets of *N*-methyl groups (δ_H 2.21, 2.20). The ^{13}C and HSQC data revealed signals of four deshielded sp^2 carbons (δ_C 154.0, 150.4, 148.1, 146.9), five nonprotonated sp^2 carbons (δ_C 132.5, 132.1, 131.2, 130.1, 123.0), seven aromatic methines (δ_C 130.5, 129.8 (2C), 123.3, 117.9, 115.1 (2C), 113.2, 111.1), three deshielded methylenes (δ_C 59.2, 58.5, 57.1), two methoxy groups (δ_C 55.9, 55.8), two *N*-methyls (δ_C 42.3, 38.6) and two aliphatic methylene groups (δ_C 32.8, 28.6). The COSY spectrum, supported by H2BC correlations, showed cross-peaks for the H-1/H-2, H-2''/H-3'', H-4''/H-5''/H-6'' and AA'BB' spin systems. Moreover, these assignments corresponded to the spin-spin splitting of signals in the 1H spectrum. HMBC correlation from H-2 to the sp^2 carbons at δ_C 129.8 revealed the fact that the *p*-substituted benzene ring was attached to the aminoethyl group. The nitrogen from this substructural fragment bore a methyl at δ_C 42.3 and a benzylic methylene at δ_C 58.5. The 1,2,4,5-tetrasubstituted aromatic ring was determined by HMBC correlations from H-4' and H-7'. This experiment also revealed the conjunction of this fragment with the methylene C-1' by C-2'. The HMBC cross-peaks of δ_H 6.76 to δ_C 123.0 and δ_H 6.82 to δ_C 132.1 indicated the attachment of nonprotonated carbons C-3' and C-7''. This sp^2 quaternary carbon belonged to the remaining 1,2,3-trisubstituted aromatic ring which was a part of the *N*-methylindoline moiety. This was proven by correlation of its protons to the related

carbons. Therefore, the structure of **13** was established as depicted (Figure 2). The assigned atoms are shown in Table 1.

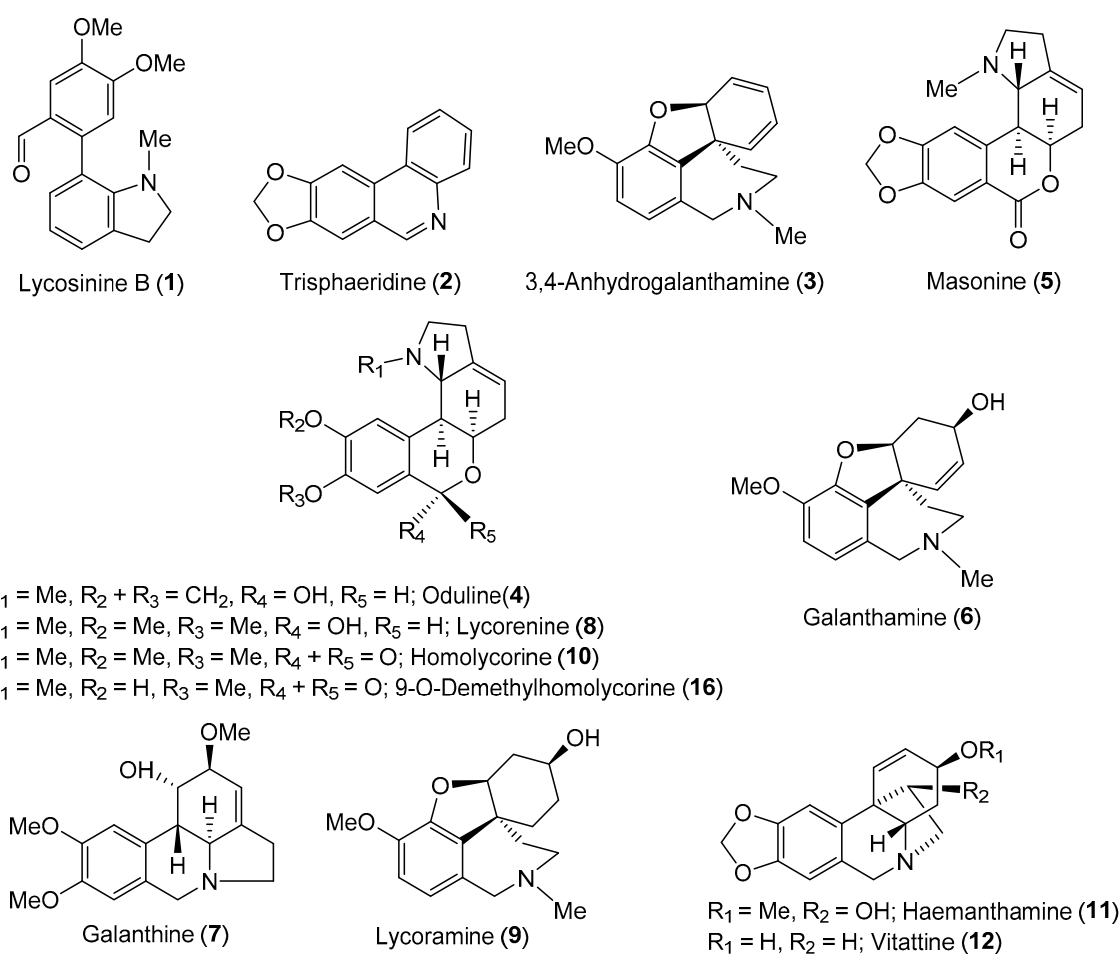


Figure 1. Structures of isolated alkaloids from *Narcissus pseudonarcissus* cv. Carlton.

Carltonine B (**14**) was obtained as a pale yellow oil. The molecular formula was determined to be $\text{C}_{26}\text{H}_{28}\text{N}_2\text{O}_3$ from the protonated molecular ion peak $[\text{M} + \text{H}]^+$ found at m/z 417.2172 (417.2173 calcd for $\text{C}_{26}\text{H}_{29}\text{N}_2\text{O}_3^+$) in the positive-ion HRMS. Due to the small quantity of sample, the ^1H NMR spectrum had poor resolution, but it looked similar to that of **13**. In addition, the ^{13}C spectrum was in accordance with this observation (see Table 1). The only difference was the absence of signals assigned to two methoxy groups of the 1,2,4,5-tetrasubstituted aromatic fragment, which were replaced by signals corresponding to a strongly deshielded methylene group of a 1,3-dioxole moiety in the 1D spectra. The key correlations are presented in Figure 2.

Another new compound, carltonine C (**15**), was obtained as a yellowish amorphous solid. The 1D NMR spectrum, as well as the 2D NMR spectra of **15** and **13**, were quite similar; however, the ^{13}C NMR data showed doubling of most carbon resonances and the absence of the *N*-methyl group of the central tertiary nitrogen. Moreover, the molecular formula was determined to be $\text{C}_{44}\text{H}_{49}\text{N}_3\text{O}_5$ from the protonated molecular ion peak $[\text{M} + \text{H}]^+$ found at m/z 700.3743 (700.3745 calcd for $\text{C}_{44}\text{H}_{50}\text{N}_3\text{O}_5^+$). These prerequisites led to the identification of the structure shown in Figure 2. The framed substituents of the central tertiary nitrogen are identical; therefore, there is no reason for doubling the signals, as appeared in the 1D NMR data. Due to the steric hindrance of these two fragments, atropisomerism has been estimated as the reason for the doubling of some signals. The analysis was performed at ambient temperature and at 50 °C. The acquired results proved the suitability of this assumption. At ambient temperature, some signals were divided into two lines that broaden with temperature increase and

eventually merge into a single line (see Supplementary Material). Unfortunately, the spectrum also revealed the signals of decomposition of this molecule.

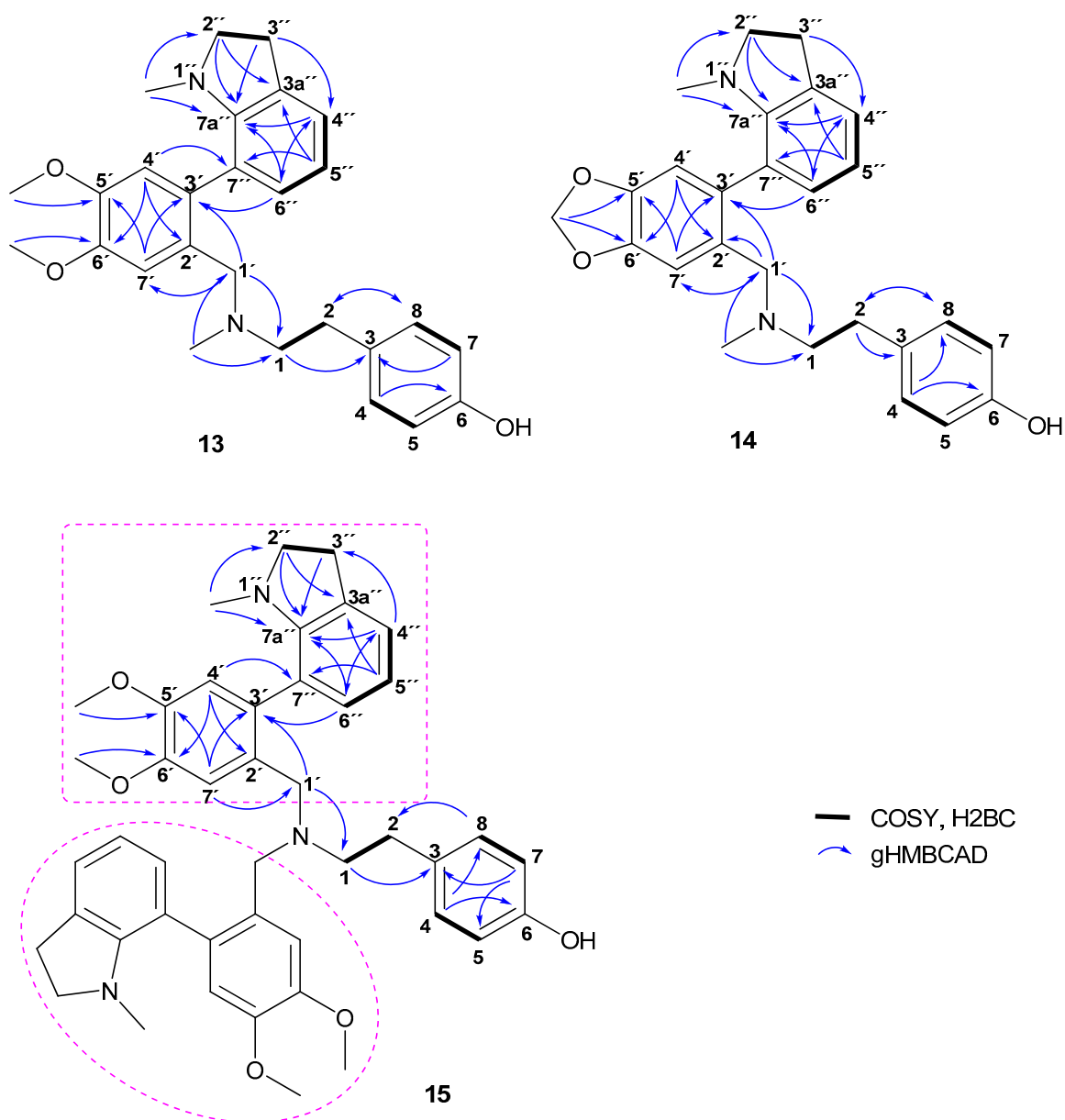


Figure 2. Key 2D NMR correlations of compounds 13–15.

Table 1. ^1H NMR (500 MHz) and ^{13}C NMR (125.7 MHz) data for **13**–**15** in CDCl_3 (δ in ppm and J in Hz).

Position	Carltonine A (13)		Carltonine B (14)		Carltonine C (15)	
	δ_{C}	δ_{H}	δ_{C}	δ_{H}	δ_{C}	δ_{H}
1	59.2	2.58–2.46, m	59.3	2.56–2.45, m	55.2; 55.4	2.66–2.42, m
2	32.8	2.65, t (7.4)	32.7	2.66–2.58, m	32.7; 32.8	2.66–2.42, m
3	132.5		132.2		132.8	
4	129.8	7.00–6.96, m	129.7	7.00–6.94, m	129.9	6.93–6.86, m
5	115.1	6.72–6.68, m	115.2	6.75–6.72, m	114.9	6.71–6.65, m
6	154.0		153.9		153.7	
7	115.1	6.72–6.68, m	115.2	6.75–6.72, m	114.9	6.71–6.65, m
8	129.8	7.00–6.96, m	129.7	7.00–6.94, m	129.9	6.93–6.86, m
1'	58.5	3.45, d (14.0) 3.29, d, overlap (14.0)	58.3	3.46, d (13.2) 3.27, d (13.2)	55.1; 55.0	3.43, d (14.5); 3.29, d (14.5); 3.37, s
2'	130.1		130.6		131.2; 131.0	
3'	132.1		133.3		131.9; 131.8	
4'	113.2	6.76, s	110.2	6.75–6.72, m	113.23; 113.15	6.74, s
5'	146.9		145.9		146.7	
6'	148.1		147.0		147.9	
7'	111.1	7.10, s, overlap	108.6	7.07, s, overlap	110.6; 110.5	7.15, s; 7.14, s
2''	57.1	3.32, dt, overlap (17.3, 8.8) 3.20, dt (17.3, 8.8)	57.1	3.35, dt (17.5, 8.7) 3.16, dt (17.5, 8.7)	57.1; 57.0	3.27–3.17, m
3''	28.6	2.98, t (8.8)	28.6	3.00–2.93, m	28.6	2.99–2.91, m
3a''	131.2		131.2		131.1	
4''	123.3	7.09, dd, overlap (7.4, 1.0)	123.4	7.08, d, overlap (7.4)	123.3	7.07, d (7.4)
5''	117.9	6.72, t, overlap (7.4)	118.1	6.70, t, overlap (7.4)	117.9; 117.8	6.71–6.65, m
6''	130.5	6.82, dd (7.4, 1.0)	130.4	6.79, d (7.4)	130.3; 130.4	6.77, d (7.4)
7''	123.0		122.9		122.8	
7a''	150.4		150.4		150.3; 150.2	
N-Me	42.3	2.20, s	41.9	2.18, s	-	-
N1''-Me	38.6	2.21, s	38.8	2.23, s	38.51; 38.48	2.14, s; 2.12, s
5'-OMe	55.8 or 55.9	3.34, s	-	-	55.9	3.84, s
6'-OMe	55.8 or 55.9	3.34, s	-	-	55.6	3.82, s; 3.81, s
-OCH ₂ O-	-	-	101.0	5.99, s 5.98, s	-	-

2.2. Biological Activity Determination of Isolated Alkaloids

All the isolated compounds that had not been studied previously for their inhibition potential of cholinesterases, and which were obtained in sufficient amounts, were screened for their *hAChE/hBuChE* inhibition potency using a modified spectrophotometric method of Ellman et al. [36]. Furthermore, *hAChE/hBuChE*-active AAs were also studied for their ability to inhibit POP enzyme. Galanthamine and eserine were used as positive controls in the *hAChE/hBuChE* assays. Berberine was selected as a positive control when measuring POP inhibition. The results are summarized in Table 2. Moreover, the in vitro data are justified by docking studies proposing orientation of the top-ranked ligands within the *hBuChE* gorge.

The *hAChE/hBuChE* inhibitory activity of the AAs was initially screened at a concentration of 100 μM . Compounds displaying inhibition ability >50% against one or both cholinesterases at the screening concentration were selected for the determination of their IC_{50} values (Table 2).

In the *hAChE* assay, all studied AAs displayed marginal inhibition potency (Table 2). On the other hand, all newly isolated belladine-type alkaloids (**13**–**15**) demonstrated promising inhibition activity towards *hBuChE* (Table 2; Figure 3). Indeed, compounds **13** and **14** displayed IC_{50} values in the nanomolar range (*hBuChE* IC_{50} = 910 nM and 31 nM, for **13** and **14**, respectively).

From the structural perspective, both AAs are endowed with the same core structure, differing only in the substitution at positions C-5' and C-6', respectively (Figure 2). The presence of a 1,3-dioxolane

ring in **14** compared with its opened dimethoxybenzene analogue **13** is plausibly responsible for the almost 30 times drop in *h*BuChE inhibition activity. Both compounds showed a *h*BuChE selective inhibition pattern with outstanding selectivity index (SI) values higher than 100 (Table 2).

Table 2. In vitro results of *h*AChE, *h*BuChE and POP inhibition of selected AAs isolated from *Narcissus pseudonarcissus* cv. Carlton.

Compound	%Inhibition <i>h</i> AChE \pm SD ^a	<i>h</i> AChE IC ₅₀ \pm SD (μ M) ^b	% inhibition <i>h</i> BuChE \pm SD ^a	<i>h</i> BuChE IC ₅₀ \pm SD (μ M) ^b	SI for <i>h</i> BuChE ^c	POP IC ₅₀ \pm SD (μ M) ^b
Lycosinine B (1)	28 \pm 1	>100	42 \pm 1	>100	nc	258 \pm 14
Trispheridine (2)	6 \pm 1	>100	13 \pm 1	>100	nc	nm
3,4-Anhydrogalanthamine (3)	4 \pm 0	>100	28 \pm 1	>100	nc	nm
Carltonine A (13)	2 \pm 0	>100	98 \pm 1	0.91 \pm 0.02	>110	143 \pm 12
Carltonine B (14)	40 \pm 1	>100	99 \pm 1	0.031 \pm 0.001	>3226	nm
Carltonine C (15)	9 \pm 0	>100	78 \pm 1	14.8 \pm 1.1	>7	nm
Galanthamine ^d	nm	1.72 \pm 0.12	nm	42 \pm 1	0.04	nm
Eserine ^d	nm	0.063 \pm 0.005	nm	0.13 \pm 0.01	0.48	nm
Berberine ^d	nm	0.72 \pm 0.11	nm	31 \pm 4	0.02	142 \pm 21

^a Tested at 100 μ M compound concentration; ^b Compound concentration required to decrease enzyme activity by 50%; the values are the mean values \pm standard deviations (SD) of three independent measurements, each performed in triplicate; ^c Selectivity index (SI) for *h*BuChE is determined as ratio *h*AChE IC₅₀/*h*BuChE IC₅₀; ^d Reference compound; nc stands for not calculated; nm stands for not measured.

Our group has previously isolated similar compounds from fresh bulbs of *Nerine bowdenii*: 6-*O*-demethylbelladine (**13**) and 4'-*O*-demethylbelladine (**14**) (Figure 3) [37]. However, neither of these two alkaloids are substituted at position C-7', and differ from each other by the absence of one methoxy group (Figure 3) [37]. 4'-*O*-demethylbelladine (IC₅₀ = 30.7 \pm 4.0 μ M) displayed slightly better in vitro inhibition activity of *h*BuChE compared with galanthamine (IC₅₀ = 42 \pm 1 μ M). On the other hand, the compounds isolated within this study are more than 30 to 100 more potent *h*BuChE inhibitors, yielding a new structural lead scaffold that may be pursued in AD research.

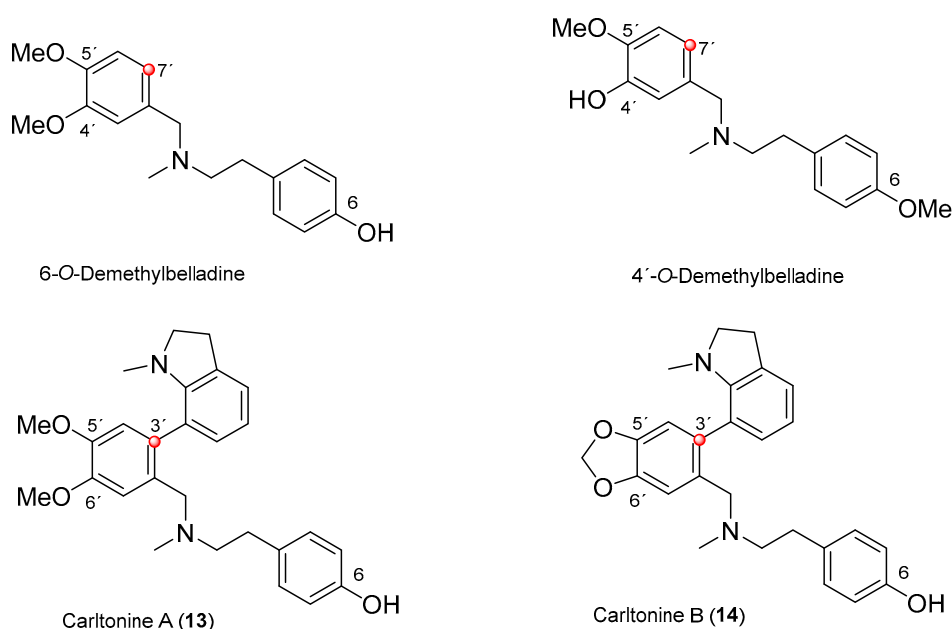


Figure 3. Structures of newly isolated (**13** and **14**) and recently reported belladine-type AAs 6-*O*-demethylbelladine and 4'-*O*-demethylbelladine [37].

Since some of the alkaloids were only isolated on a small scale, only two (**1** and **13**) were able to be tested for POP inhibition. Alkaloid **13** demonstrated POP inhibition in the same range as berberine (Table 2) [38].

The biological profiles of the other AAs (Figure 1) have already been determined within previous studies on Amaryllidaceae plants [21,39–41].

2.3. Docking Study of Carltonine A (**13**) and Carltonine B (**14**)

To reveal fundamental interactions for **13** and **14** within the *h*BuChE active site (PDB ID: 4BDS) [42], molecular docking studies were carried out, enabling better insight into the structural requirements for inhibition. Since both **13** and **14** are tertiary amines, which are protonated at physiological pH, they behave as *pseudo*-enantiomers. In this study, we attempted to predict more bioactive conformers of **13** and **14** based on their energy score and their topology within *h*BChE. To gain a more in-depth outlook into the overall ligand-enzyme complex, we are also displaying several comparative structure overlay between (*R*)-**13**-(*R*)-**14** (Figure S4A), (*S*)-**13**-(*R*)-**13** (Figure S4B), (*S*)-**13**-(*S*)-**14** (Figure S4C), and (*S*)-**14**-(*R*)-**14** (Figure S4D) *pseudo*-enantiomers (see Supplementary Material).

Carltonine A (**13**) with a central amino moiety in (*R*) (Figure 4A,B) and (*S*) (Figure 4C,D) conformations displayed completely different binding modes, even though their estimated energetic balances were equipotent (−10.6 kcal/mol for both). For the (*R*)-**13** *pseudo*-enantiomer-*h*BuChE complex (Figure 5A,B), the *N*-methylindoline moiety occupies the vicinity of the catalytic triad with a T-shaped π - π interaction close to Phe329 (5.0 Å, distance measured from ring-to-ring center). Trp82 faces the dimethoxybenzene ring by displacing π - π interaction, whereas the phenolic appendage is left somewhat vacant. In the (*S*)-**13** *pseudo*-enantiomer-*h*BuChE complex (Figure 4C,D), the *N*-methylindoline moiety is engaged in parallel π - π stacking with Trp82 (3.7 Å). Contrary to the vacant occupancy of the phenolic appendage in the (*R*)-**13** *pseudo*-enantiomer, in the case of the (*S*)-**13** *pseudo*-enantiomer, Phe329 (4.9 Å) and Trp231 (5.5 Å) anchor this moiety. The dimethoxybenzene ring is stabilized by π -anion contact to Asp70.

The top-ranked docking poses for (*R*)-**14** and (*S*)-**14** *pseudo*-enantiomers in *h*BuChE active site are depicted in Figure 5A–D, respectively. In this case, binding energies differ favoring the (*R*)-**14** *pseudo*-enantiomer (−11.6 kcal/mol) over the (*S*)-**14** one (−10.9 kcal/mol). Similarly to the (*R*)-**13** *pseudo*-enantiomer-*h*BuChE complex, *N*-methylindoline is stabilized by T-shaped π - π interaction with Phe329 (5.0 Å) and by cation- π formation with the central nitrogen atom of (*R*)-**14** (Figure 5A,B). The protonated amino-group of (*R*)-**14** orchestrates the ligand-enzyme contact by other cation- π interactions with Tyr332 (5.3 Å) and Trp82 (4.5 Å). The latter amino acid residue is in close vicinity to 2*H*-1,3-benzodioxole displaying T-shaped π - π stacking (4.8 Å), and additionally to the phenolic moiety of the ligand via parallel π - π stacking (3.8 Å). Likewise, the same applies for the (*S*)-**14** *pseudo*-enantiomer in *h*BuChE (Figure 5C,D) when observing the central protonated amine of the ligand, i.e., cation- π contact with Tyr332 (5.5 Å) and Phe329 (5.4 Å), but not with Trp82. In this case, Trp82 revealed only an apparently parallel π - π interaction with the *N*-methylindoline moiety (3.7 Å).

Taken together from all the *in silico* observations above, it can be deduced that the higher inhibition potency of **14** over **13** might be attributed to the presence of the 2*H*-1,3-benzodioxole moiety for its “extended” aromatic properties that, especially in the (*R*)-**14** *pseudo*-enantiomer, broaden the range of hydrophobic interactions between the ligand and enzyme (Table 3).

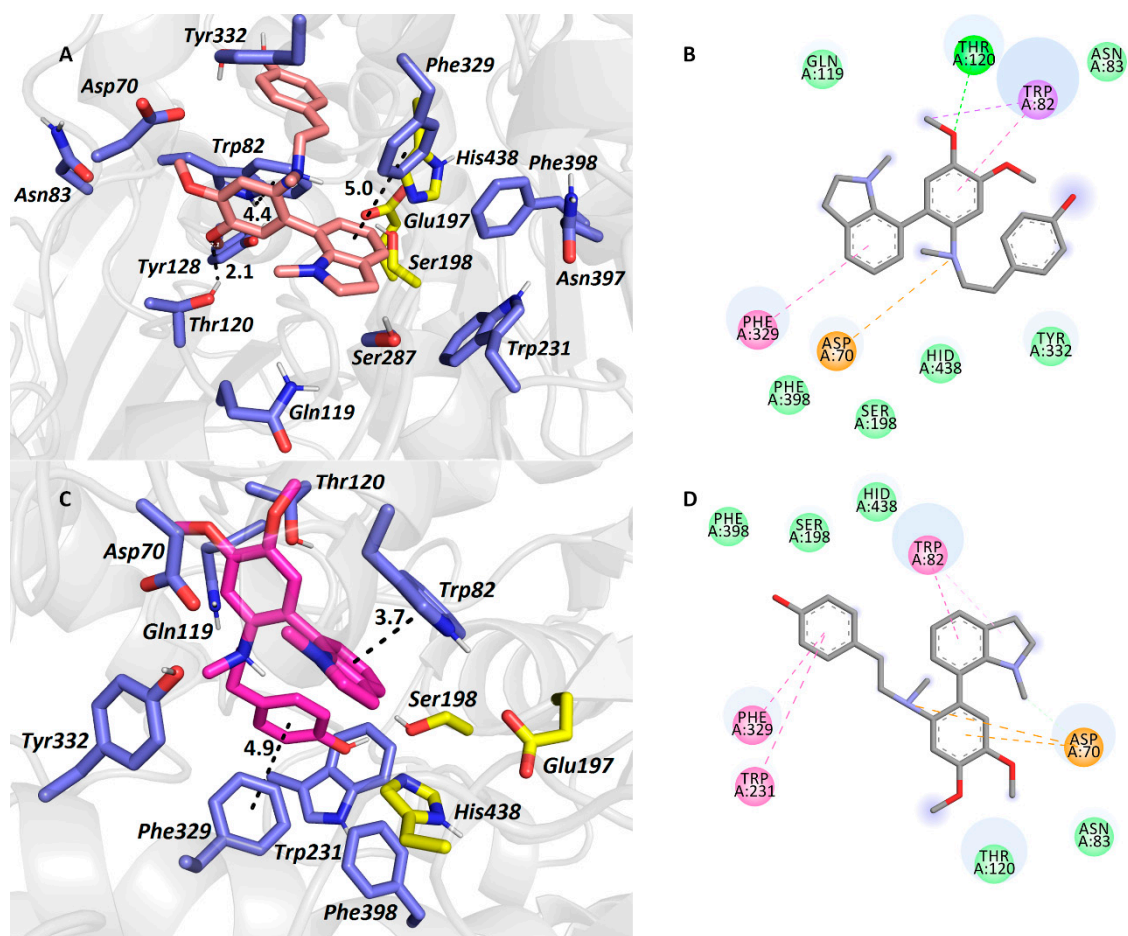


Figure 4. The *h*BuChE active site in complex with (*R*)-13 (in salmon, A,B) and (*S*)-13 (in purple, C,D) *pseudo*-enantiomers. All the amino acids exhibiting in the vicinity of the ligands up-to 6.0 Å are rendered. Hydrogen atoms of amino acids are omitted for clarity. Catalytic triad residues are shown in yellow, and amino acid residues in blue (A,C). In 2D diagrams (B,D), crucial amino acid residues are displayed in different colours depending on the nature of the interaction (e.g., purple for π - π , orange for anion- π , dark green for van der Waals contact, and light green for conventional hydrogen bond).

Table 3. The best obtained calculated binding energies with Autodock Vina software for the carltonine derivatives under the *in silico* study within *h*BuChE enzyme.

Carltonine Enantiomer	Calculated Binding Energy (kcal/mol)
(<i>R</i>)-13	−10.6
(<i>S</i>)-13	−10.6
(<i>R</i>)-14	−11.6
(<i>S</i>)-14	−10.9

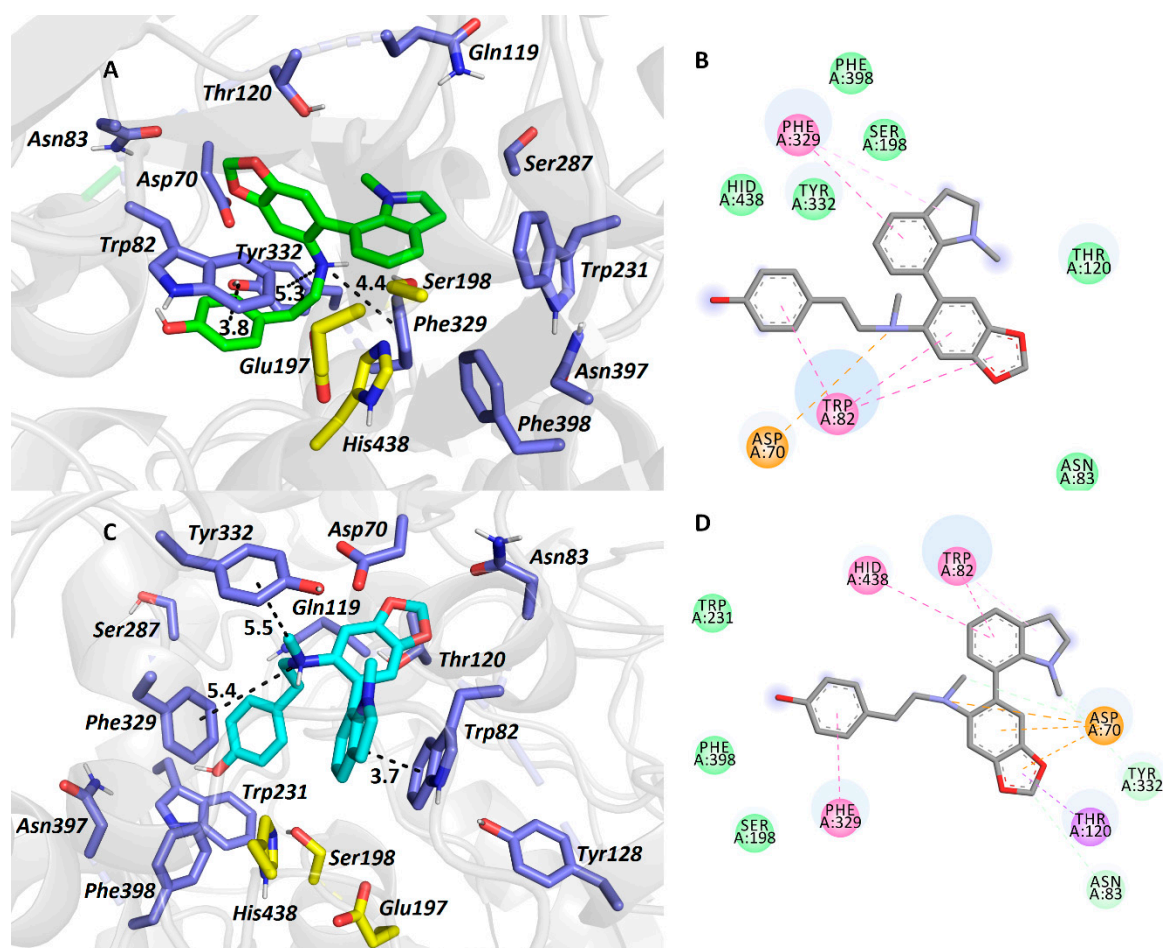


Figure 5. *h*BuChE active site in complex with (*R*)-14 (in green, **A,B**) and (*S*)-14 (in light-blue, **C,D**) *pseudo*-enantiomers. All the amino acids exhibiting in the vicinity of the ligands up-to 6.0 Å are rendered. Hydrogen atoms of amino acids are omitted for clarity. Catalytic triad residues are shown in yellow and amino acid residues in blue (**A,C**). In 2D diagrams (**B,D**), crucial amino acid residues are displayed in different colours depending on the nature of the interaction (e.g., purple for π - π , orange for anion- π , dark green for van der Waals contact, light green for conventional hydrogen bond).

3. Experimental

3.1. General Experimental Procedures

All solvents were treated using standard techniques before use. All reagents and catalysts were purchased from Sigma Aldrich, Czech Republic and used without purification. The NMR spectra were obtained in CDCl_3 and CD_3OD at ambient temperature on a VNMR S500 (Varian, Palo Alto, CA, USA) spectrometer operating at 500 MHz for ^1H and 125.7 MHz for ^{13}C . Chemical shifts were recorded as δ values in parts per million (ppm) and were indirectly referenced to tetramethylsilane (TMS) via the solvent signal (CDCl_3 —7.26 ppm for ^1H and 77.0 ppm for ^{13}C ; CD_3OD —3.30 ppm for ^1H and 49.0 ppm for ^{13}C). Coupling constants (J) are given in Hz. For unambiguous assignment of ^1H and ^{13}C signals, 2D NMR experiments, namely gCOSY, gHSQC, gHMBC and NOESY, were measured using standard parameter settings and standard pulse programs provided by the producer of the spectrometer. ESI-HRMS were obtained with a Waters Synapt G2-Si hybrid mass analyzer of a quadrupole-time-of-flight (Q-TOF) type, coupled to a Waters Acquity I-Class UHPLC system. The EI-MS were obtained on an Agilent 7890A GC 5975 inert MSD operating in EI mode at 70 eV (Agilent Technologies, Santa Clara, CA, USA). A DB-5 column (30 m \times 0.25 mm \times 0.25 μm , Agilent Technologies, USA) was used with a temperature program: 100–180 $^\circ\text{C}$ at 15 $^\circ\text{C}/\text{min}$, 1 min hold at

180 °C, and 180–300 °C at 5 °C/min and 5 min hold at 300 °C; and detection range m/z 40–600. The injector temperature was 280 °C. The flow-rate of carrier gas (helium) was 0.8 mL/min. A split ratio of 1:15 was used. TLC was carried out on Merck precoated silica gel 60 F254 plates. Compounds on the plate were observed under UV light (254 and 366 nm) and visualized by spraying with Dragendorff's reagent.

3.2. Plant Material

The fresh bulbs of *Narcissus pseudonarcissus* cv. Carlton were obtained from the herbal dealer Lukon Glads (Sadská, Czech Republic). Botanical identification was performed by Prof. L. Opletal. A voucher specimen is deposited in the Herbarium of the Faculty of Pharmacy in Hradec Králové under number: CUFPH-16130/AL-654.

3.3. Extraction and Isolation of Alkaloids

Fresh bulbs (30 kg) were minced and completely extracted with ethanol (EtOH) (96%, *v/v*, 3×) by boiling for 30 min under reflux; the combined extract was filtered and evaporated to dryness under reduced pressure. The crude extract (485 g) was acidified to pH 1–2 with 2% hydrochloric acid (HCl; 1 L) and the volume of the suspension was made up to 5 L with water. The suspension was filtered; the filtrate was defatted by diethyl ether (Et₂O, 3 × 1.5 L), alkalized to pH 9–10 with a 10% solution of sodium carbonate (Na₂CO₃) and extracted with ethyl acetate (EtOAc; 3 × 1.5L). The organic layer was evaporated to give 245 g of dark brown fluid residue. The alkaloid summary extract was again dissolved in 2% HCl (1000 mL), washed with Et₂O (3 × 300 mL) and alkalized to pH 9–10 with 10% Na₂CO₃. The water layer was extracted with Et₂O (4 × 350 mL) and chloroform (CHCl₃; 4 × 350 mL). Both Dragendorff positive parts were evaporated and pooled. A concentrated alkaloid extract (187 g) in the form of brown syrup was obtained.

The alkaloid extract was further fractionated by column chromatography on aluminum oxide (Al₂O₃; 5800 g), eluting with light petrol gradually enriched with CHCl₃ (1:1, 2:3, 1:4; each 5000 mL), followed by CHCl₃ (3000 mL) and finally by CHCl₃ enriched with EtOH (99:1, 49:1, 97:3, 12:1, 1:1; 0:100 each 3000 mL). Fractions were collected in amounts of 1000 mL and monitored by TLC. Finally, 423 fractions were collected, combined into 25 fractions, and analyzed by GC-MS. Fractions with similar profile were pooled together to give nine final fractions (I–IX).

Fraction I (650 mg) was recrystallized from an ethanol/chloroform mixture (1:1, 100 mL) to give lycosinine B (**1**, 48 mg). Preparative TLC of the mother liquor (To: cHx: Et₂NH, 60:40:5, 1×) led to the isolation of trispheridine (**2**, 5 mg). Repeated preparative TLC of the mother liquor gave 3,4-anhydrogalanthamine (**3**, 5 mg).

Fraction II (500 mg) was fractionated by preparative TLC (cHx: Me₂CO: NH₃; 30: 60: 1; 1×). Three subfractions were obtained (IIa–c). Repeated preparative TLC of subfraction IIb (cHx: Me₂CO: NH₃, 30: 60: 1; 2×) led to the isolation of oduline (**4**; 11 mg). Additional preparative TLC of subfraction IIc gave masonine (**5**; 44 mg).

Fraction III (16.3 g) was crystallized and recrystallized from EtOH and, finally, 6.39 g of galanthamine (**6**) was obtained.

Fraction IV (1.7 g) was further chromatographed by preparative TLC (To: cHx: Et₂NH, 10:10:2, 2×) to obtain subfractions IVa–b. Repeated preparative TLC of IVa (320 mg; cHx: Et₂NH, 9:1; 2×) led to the isolation of galanthine (**7**; 120 mg).

Fraction V (3.05 g) was crystallized and recrystallized three times from EtOH to give lycorenine (**9**; 981 mg).

Fraction VI (950 mg) was subjected to preparative TLC (To: cHx: Et₂NH, 50:50: 5; 2×) to obtain four subfractions VIa–d. Subfraction VIa (120 mg) was treated by preparative TLC (cHx: Me₂CO: NH₃, 20:80:1; 2×) to give lycoramine (**9**; 20 mg). Subfraction VIb (150 mg) was subjected to preparative TLC (To: cHx: Et₂NH; 40: 60: 5; 2×), crystallized from EtOH, and 45 mg of homolycorine (**10**) was obtained.

Fraction **VII** (25 g) was dissolved in hot EtOH and crystallized. Crude haemanthamine (**11**; 14.5 g) was obtained. This was repetitively (3×) recrystallized from hot EtOH to give 10.5 g of pure haemanthamine.

Repetitive preparative TLC (EtOAc: cHx: Et₂NH; 70: 20: 10; 3×) of fraction **VIII** (3.25 g) led to the isolation of five subfractions (**VIIIa-e**). Subfraction **VIIIa** (545 mg) was subjected to preparative TLC (CH₃CN: MeOH: NH₃; 70: 20: 0.3; 2×) to give vitattine (**12**; 150 mg). Subfraction **VIIIc** (550 mg) was chromatographed by preparative TLC (EtOAc: cHx: NH₃; 40: 24: 0.6; 2×) to give carltonine A (**13**; 70 mg) and subfraction **VIIIc/1**. Subfraction **VIIIc/1** (80 mg) was subjected to preparative TLC (EtOAc: cHx: NH₃; 40: 24: 0.6; 1×) and carltonine B (**14**; 6 mg) was obtained. Subfraction **VIII d** (75 mg) was further treated by preparative TLC (EtOAc: Chx: NH₃; 40: 24: 0.6; 2×) to yield carltonine C (**15**; 7 mg).

Fraction **IX** (1.65 g) was subjected to preparative TLC (To: Me₂CO: MeOH: NH₃; 50:60: 10:1; 1×) to give two subfractions **IXa-b**. Subfraction **IXa** (320 mg) was recrystallized from hot EtOH and separated by preparative TLC (To: Me₂CO: NH₃; 40:60:1; 2×) to give 9-*O*-demethylhomolycorine (**16**; 35 mg).

Carltonine A (13): pale yellow oil; for ¹H and ¹³C NMR data see Table 1; HRMS *m/z* 433.2488 [M + H]⁺ (calculated for C₂₇H₃₃N₂O₃⁺, 433.2486).

Carltonine B (14): pale yellow oil; for ¹H and ¹³C NMR data see Table 1; HRMS *m/z* 417.2172 [M + H]⁺ (calculated for C₂₆H₂₉N₂O₃⁺, 417.2173).

Carltonine C (15): yellowish amorphous solid; for ¹H and ¹³C NMR data see Table 1; HRMS *m/z* 700.3743 [M + H]⁺ (calculated for C₄₄H₅₀N₃O₅⁺, 700.3745).

3.4. Biological Assays

3.4.1. hAChE and hBuChE Inhibition Assay

The *hAChE* and *hBuChE* activities were determined using a modified method of Ellman, as described [36,43,44]. Briefly, *hAChE* and *hBuChE* activities were determined using a modified method of Ellman, with acetylthiocholine iodide (ATChI) and butyrylthiocholine iodide (BuTChI) as substrates, respectively. Briefly, 8.3 μL of either blood cell lysate or plasma dilutions (at least six different concentrations), 283 μL of 5 mM 5,5'-dithiobis-2-nitrobenzoic acid (DTNB) and 8.3 μL of the sample dilution in dimethyl sulfoxide (DMSO) (40 mM, 10 mM, 4 mM, 1 mM, 0.4 mM, and 0 mM) were added to the semi-micro cuvette. The reaction was initiated by addition of 33.3 μL 10 mM substrate (ATChI or BuTChI). The final proportion of DTNB and substrate was 1:1. The increase of absorbance (ΔA) at 436 nm for AChE and 412 nm for BuChE was measured for 1 min at 37 °C using a spectrophotometer (Synergy™ HT Multi-Detection Microplate Reader). Each measurement was repeated six times for every concentration of enzyme preparation. The % inhibition was calculated according to the following formula:

$$\% I = 100 - \left(100 \times \frac{\Delta A_{Bl}}{\Delta A_{Sa}} \right), \quad (1)$$

where ΔA_{Bl} is the increase of absorbance of the blank sample and ΔA_{Sa} is the increase of absorbance of the measured sample. Inhibition potency of the tested compounds was expressed as an IC₅₀ value (concentration of inhibitor, which causes 50% cholinesterase inhibition).

3.4.2. POP Inhibition Assay

POP (EC 3.4.21.26) was dissolved in phosphate-buffered saline (PBS; 0.01 M Na/K phosphate buffer, pH 7.4, containing 137 mM NaCl and 2.7 mM KCl); the specific activity of the enzyme was 0.2 U/mL. The assay was performed in standard polystyrene 96-well microplates with a flat and clear bottom. Stock solutions of tested compounds were prepared in DMSO (10 mM). Dilutions (10⁻³ to 10⁻⁷ M) were prepared from the stock solution with deionized H₂O; the control was performed with the same DMSO concentration. POP substrate, (*Z*)-Gly-Pro-p-nitroanilide, was dissolved in 50% 1,4-dioxane (5 mM). For each reaction, PBS (170 μL), tested compound (5 μL), and POP (5 μL) were incubated

for 5 min at 37 °C. Then, substrate (20 µL) was added, and the microplate was incubated for 30 min at 37 °C. The formation of p-nitroanilide, directly proportional to the POP activity, was measured spectrophotometrically at 405 nm using a microplate ELISA reader (multimode microplate reader Synergy 2, BioTek Instruments, Winooski, VT, USA). The inhibition potency of tested compounds was calculated by nonlinear regression analysis and was expressed as an IC₅₀ value (concentration of inhibitor which causes 50% POP inhibition). All calculations were performed using GraphPad Prism software version 7.03 for Windows (GraphPad Software Inc., San Diego, California, USA) [44].

3.4.3. Molecular Modelling Studies

Two structures of *hAChE* and *hBuChE* were gained from RCSB Protein Data Bank—PDB ID: 4EY6 (crystal structure of *hAChE*) and 4BDS (crystal structure of *hBuChE*) [42,45]. All receptor structures were prepared by DockPrep function of UCSF Chimera (v. 1.4) and converted to pdbqt-files by AutodockTools (v. 1.5.6) [46,47]. Flexible residues selection was based on previous experience with either *hAChE*, *hBuChE* or the spherical region around the binding cavity [48–50]. Three-dimensional structures of ligands were built by Open Babel (v. 2.3.1), minimized by Avogadro (v 1.1.0) and converted to pdbqt-file format by AutodockTools [51]. The docking calculations were made by Autodock Vina (v. 1.1.2) with the exhaustiveness of 8 [52]. Calculation was repeated 20 times for each ligand and receptor and the best-scored result was selected for manual inspection. The visualization of enzyme-ligand interactions was prepared using The PyMOL Molecular Graphics System (Version 2.0, Schrödinger, LLC, Mannheim, Germany). 2D diagrams were created with Dassault Systèmes BIOVIA, Discovery Studio Visualizer (v 17.2.0.16349, Dassault Systèmes, 2016, San Diego, CA, USA).

4. Conclusions

The phytochemical study of the alkaloidal extract of *Narcissus pseudonarcissus* cv. Carlton resulted in the isolation of thirteen previously described AAs, and three new AAs of belladine-type, named carltonine A–C (13–15). Their structures were elucidated using a combination of NMR and MS analysis. Compounds isolated in sufficient quantity and not previously tested for their biological activities in relation to AD, were screened for their potential to inhibit *hAChE*, *hBuChE* and POP. Significant and selective *hBuChE* inhibitory activity was demonstrated by the newly described alkaloids carltonine A (13) and carltonine B (14) with IC₅₀ values of 0.91 ± 0.02 µM and 0.031 ± 0.001 µM, respectively. The in vitro results were justified by computational studies predicting plausible binding modes of compounds 13 and 14 in the active site of *hBuChE*. The new compounds exerted an interesting biological profile deserving further lead-optimization. The next step will be the development of an appropriate synthetic route leading to carltonine derivatives with follow-up preparation of semi-synthetic derivatives.

Supplementary Materials: The following are available online at <http://www.mdpi.com/2218-273X/10/5/800/s1>, Figure S1-1: ESI-HRMS spectrum of carltonine A (13); Figure S1-2: ¹H NMR spectrum of carltonine A (13) in CDCl₃; Figure S1-3: ¹³C NMR spectrum of carltonine A (13) in CDCl₃; Figure S1-4: gCOSY spectrum of carltonine A (13) in CDCl₃; Figure S1-5: gHSQC spectrum of carltonine A (13) in CDCl₃; Figure S1-6: gHMBCAD spectrum of carltonine A (13) in CDCl₃; Figure S1-7: gH2BC spectrum of carltonine A (13) in CDCl₃; Figure S2-1: ESI-HRMS spectrum of carltonine B (14); Figure S2-2: ¹H NMR spectrum of carltonine B (14) in CDCl₃; Figure S2-3: ¹³C NMR spectrum of carltonine B (14) in CDCl₃; Figure S2-4: gCOSY spectrum of carltonine B (14) in CDCl₃; Figure S2-5: gHSQC spectrum of carltonine B (14) in CDCl₃; Figure S2-6: gHMBCAD spectrum of carltonine B (14) in CDCl₃; Figure S2-7: gH2BC spectrum of carltonine B (14) in CDCl₃; Figure S3-1: ESI-HRMS spectrum of carltonine C (15); Figure S3-2: ¹H NMR spectrum of carltonine C (15) in CDCl₃; Figure S3-3: ¹³C NMR spectrum of carltonine C (15) in CDCl₃; Figure S3-4: gCOSY spectrum of carltonine C (15) in CDCl₃; Figure S3-5: gHSQC spectrum of carltonine C (15) in CDCl₃; Figure S3-6: gHMBCAD spectrum of carltonine C (15) in CDCl₃; Figure S3-7: gH2BC spectrum of carltonine C (15) in CDCl₃; Figure S3-8: ¹H NMR spectrum of carltonine C (15) in CDCl₃ at 50 °C; Figure S3-9: ¹³C NMR spectrum of carltonine C (15) in CDCl₃ at 50 °C; Figure S4: Overlapped *pseudo*-enantiomers in the *hBuChE* active site and their topology difference.

Author Contributions: A.A.M., M.Š. contributed to the isolation of Amaryllidaceae alkaloids. J.M., J.K. (Jiří Kuneš), L.N. and M.Š. contributed to the identification of isolated alkaloids (such as MS, NMR). D.H., J.J. and M.H. were involved with the measurement of various biological activities of all isolated compounds. J.K. (Jan Korábečný), T.K. carried out the docking studies. L.C. and J.K. (Jan Korábečný) designed the study, supervised the laboratory work and contributed to critical reading of the manuscript. All authors have read and agreed to the published version of the manuscript.

Funding: This project was supported by Charles University grants (GA UK no. 178518, SVV UK 260 412, 260 401; Progres/UK Q40 and Q42), by MH CZ—DRO (University Hospital Hradec Kralove, no. 00179906), by the Czech Science Foundation (project no. 20-29633), by the Long-term Development Plan (Faculty of Military Health Sciences), and by EFSA-CDN (no. CZ.02.1.01/0.0/0.0/16_019/0000841) co-funded by ERDF and by MICU (grant no. SAF2016-76693-R to A.M.). Computational resources were provided by CESNET LM2015042 and the CERIT Scientific Cloud LM2015085, provided under the program “Projects of Large Research, Development, and Innovations Infrastructures”.

Acknowledgments: The authors wish to thank Gerald Blunden for critical reading of the manuscript and English corrections.

Conflicts of Interest: The authors declare no conflict of interest.

References

1. Burns, A.; Jacoby, R.; Levy, R. Psychiatric phenomena in Alzheimer’s disease. I: Disorders of thought content. *Br. J. Psychiatry J. Ment. Sci.* **1990**, *157*, 72–76, 92–94. [[CrossRef](#)] [[PubMed](#)]
2. Nichols, E.; Szoek, C.E.I.; Vollset, S.E.; Abbasi, N.; Abd-Allah, F.; Abdela, J.; Aichour, M.T.E.; Akinyemi, R.O.; Alahdab, F.; Asgedom, S.W.; et al. Global, regional, and national burden of Alzheimer’s disease and other dementias, 1990–2016: A systematic analysis for the Global Burden of Disease Study 2016. *Lancet Neurol.* **2019**, *18*, 88–106. [[CrossRef](#)]
3. Cimler, R.; Maresova, P.; Kuhnova, J.; Kuca, K. Predictions of Alzheimer’s disease treatment and care costs in European countries. *PLoS ONE* **2019**, *14*, e0210958. [[CrossRef](#)] [[PubMed](#)]
4. Kumar, A.; Singh, A.; Ekavali. A review on Alzheimer’s disease pathophysiology and its management: An update. *Pharmacol. Rep. PR* **2015**, *67*, 195–203. [[CrossRef](#)]
5. Hampel, H.; Mesulam, M.-M.; Cuello, A.C.; Farlow, M.R.; Giacobini, E.; Grossberg, G.T.; Khachaturian, A.S.; Vergallo, A.; Cavedo, E.; Snyder, P.J.; et al. The cholinergic system in the pathophysiology and treatment of Alzheimer’s disease. *Brain J. Neurol.* **2018**, *141*, 1917–1933. [[CrossRef](#)]
6. Zemek, F.; Drtinova, L.; Nepovimova, E.; Sepsova, V.; Korabecny, J.; Klimes, J.; Kuca, K. Outcomes of Alzheimer’s disease therapy with acetylcholinesterase inhibitors and memantine. *Expert Opin. Drug Saf.* **2014**, *13*, 759–774. [[CrossRef](#)]
7. Nachon, F.; Brazzolotto, X.; Trovaslet, M.; Masson, P. Progress in the development of enzyme-based nerve agent bioscavengers. *Chem. Biol. Interact.* **2013**, *206*, 536–544. [[CrossRef](#)]
8. Nordberg, A.; Ballard, C.; Bullock, R.; Darreh-Shori, T.; Somogyi, M. A Review of Butyrylcholinesterase as a Therapeutic Target in the Treatment of Alzheimer’s Disease. *Prim. Care Companion CNS Disord.* **2013**, *15*. [[CrossRef](#)]
9. Inestrosa, N.C.; Alvarez, A.; Pérez, C.A.; Moreno, R.D.; Vicente, M.; Linker, C.; Casanueva, O.I.; Soto, C.; Garrido, J. Acetylcholinesterase accelerates assembly of amyloid-beta-peptides into Alzheimer’s fibrils: Possible role of the peripheral site of the enzyme. *Neuron* **1996**, *16*, 881–891. [[CrossRef](#)]
10. Babkova, K.; Korabecny, J.; Soukup, O.; Nepovimova, E.; Jun, D.; Kuca, K. Prolyl oligopeptidase and its role in the organism: Attention to the most promising and clinically relevant inhibitors. *Future Med. Chem.* **2017**, *9*, 1015–1038. [[CrossRef](#)]
11. Szeltner, Z.; Polgár, L. Structure, function and biological relevance of prolyl oligopeptidase. *Curr. Protein Pept. Sci.* **2008**, *9*, 96–107. [[CrossRef](#)] [[PubMed](#)]
12. Wang, S.; Dong, G.; Sheng, C. Structural Simplification of Natural Products. *Chem. Rev.* **2019**, *119*, 4180–4220. [[CrossRef](#)] [[PubMed](#)]
13. Iranshahi, M.; Quinn, R.J.; Iranshahi, M. Biologically active isoquinoline alkaloids with drug-like properties from the genus *Corydalis*. *RSC Adv.* **2014**, *4*, 15900–15913. [[CrossRef](#)]
14. Nair, J.J.; van Staden, J. Pharmacological and toxicological insights to the South African Amaryllidaceae. *Food Chem. Toxicol. Int. J. Publ. Br. Ind. Biol. Res. Assoc.* **2013**, *62*, 262–275. [[CrossRef](#)]

15. Goietsenoven, G.V.; Mathieu, V.; Lefranc, F.; Kornienko, A.; Evidente, A.; Kiss, R. Narciclasine as well as other Amaryllidaceae Isocarboxtyrils are Promising GTP-ase Targeting Agents against Brain Cancers. *Med. Res. Rev.* **2013**, *33*, 439–455. [[CrossRef](#)]
16. Stafford, G.I.; Pedersen, M.E.; van Staden, J.; Jäger, A.K. Review on plants with CNS-effects used in traditional South African medicine against mental diseases. *J. Ethnopharmacol.* **2008**, *119*, 513–537. [[CrossRef](#)]
17. Olin, J.; Schneider, L. Galantamine for Alzheimer’s disease. *Cochrane Database Syst. Rev.* **2002**, CD001747. [[CrossRef](#)]
18. Bastida, J.; Viladomat, F.; Codina, C. Narcissus alkaloids. In *Studies in Natural Products Chemistry*; Atta-ur-Rahman, Ed.; Structure and Chemistry (Part F); Elsevier: Amsterdam, The Netherlands, 1997; Volume 20, pp. 323–405.
19. Nair, J.J.; Rárová, L.; Strnad, M.; Bastida, J.; van Staden, J. Mechanistic insights to the cytotoxicity of Amaryllidaceae alkaloids. *Nat. Prod. Commun.* **2015**, *10*, 171–182. [[CrossRef](#)]
20. Bastida, J.; Lavilla, R.; Viladomat, F. Chemical and biological aspects of Narcissus alkaloids. *Alkaloids Chem. Biol.* **2006**, *63*, 87–179. [[CrossRef](#)]
21. Hulcová, D.; Maříková, J.; Korábečný, J.; Hošťálková, A.; Jun, D.; Kuneš, J.; Chlebek, J.; Opletal, L.; De Simone, A.; Nováková, L.; et al. Amaryllidaceae alkaloids from *Narcissus pseudonarcissus* L. cv. Dutch Master as potential drugs in treatment of Alzheimer’s disease. *Phytochemistry* **2019**, *165*, 112055. [[CrossRef](#)]
22. Torras-Claveria, L.; Berkov, S.; Codina, C.; Viladomat, F.; Bastida, J. Daffodils as potential crops of galanthamine. Assessment of more than 100 ornamental varieties for their alkaloid content and acetylcholinesterase inhibitory activity. *Ind. Crops Prod.* **2013**, *43*, 237–244. [[CrossRef](#)]
23. Breiterová, K.; Ločárek, M.; Kohelová, E.; Talácková, M.; Hulcová, D.; Opletal, L.; Cahlíková, L. Daffodils as Potential Crops of Biologically-active Compounds: Assessment of 40 Ornamental Taxa for their Alkaloid Profile and Cholinesterases Inhibition Activity. *Nat. Prod. Commun.* **2018**, *13*. [[CrossRef](#)]
24. Pellegrino, S.; Meyer, M.; Zorbas, C.; Bouchta, S.A.; Saraf, K.; Pelly, S.C.; Yusupova, G.; Evidente, A.; Mathieu, V.; Kornienko, A.; et al. The Amaryllidaceae Alkaloid Haemanthamine Binds the Eukaryotic Ribosome to Repress Cancer Cell Growth. *Structure* **2018**, *26*, 416–425. [[CrossRef](#)]
25. Sener, B.; Orhan, I.; Satayavivad, J. Antimalarial activity screening of some alkaloids and the plant extracts from Amaryllidaceae. *Phytother. Res. PTR* **2003**, *17*, 1220–1223. [[CrossRef](#)] [[PubMed](#)]
26. Havelek, R.; Seifrtova, M.; Kralovec, K.; Bruckova, L.; Cahlikova, L.; Dalecka, M.; Vavrova, J.; Rezacova, M.; Opletal, L.; Bilkova, Z. The effect of Amaryllidaceae alkaloids haemanthamine and haemanthidine on cell cycle progression and apoptosis in p53-negative human leukemic Jurkat cells. *Phytomedicine Int. J. Phytother. Phytopharm.* **2014**, *21*, 479–490. [[CrossRef](#)] [[PubMed](#)]
27. Kohelová, E.; Peřinová, R.; Maafi, N.; Korábečný, J.; Hulcová, D.; Maříková, J.; Kučera, T.; Martínez González, L.; Hrabínova, M.; Vorčáková, K.; et al. Derivatives of the β -Crinane Amaryllidaceae Alkaloid Haemanthamine as Multi-Target Directed Ligands for Alzheimer’s Disease. *Molecules* **2019**, *24*, 1307. [[CrossRef](#)] [[PubMed](#)]
28. Yang, Y.; Huang, S.-X.; Zhao, Y.-M.; Zhao, Q.-S.; Sun, H.-D. Alkaloids from the Bulbs of *Lycoris aurea*. *Helv. Chim. Acta* **2005**, *88*, 2550–2553. [[CrossRef](#)]
29. Fan-Chiang, T.-T.; Wang, H.-K.; Hsieh, J.-C. Synthesis of phenanthridine skeletal Amaryllidaceae alkaloids. *Tetrahedron* **2016**, *72*, 5640–5645. [[CrossRef](#)]
30. Bozkurt, B.; Çoban, G.; Kaya, G.; Onur, M.; Unver-Somer, N. Alkaloid profiling, anticholinesterase activity and molecular modeling study of *Galanthus elwesii*. *South Afr. J. Bot.* **2017**. [[CrossRef](#)]
31. Huang, S.-D.; Zhang, Y.; He, H.-P.; Li, S.-F.; Tang, G.-H.; Chen, D.-Z.; Cao, M.-M.; Di, Y.-T.; Hao, X.-J. A new Amaryllidaceae alkaloid from the bulbs of *Lycoris radiata*. *Chin. J. Nat. Med.* **2013**, *11*, 406–410. [[CrossRef](#)]
32. Pigni, N.B.; Ríos-Ruiz, S.; Martínez-Francés, V.; Nair, J.J.; Viladomat, F.; Codina, C.; Bastida, J. Alkaloids from *Narcissus serotinus*. *J. Nat. Prod.* **2012**, *75*, 1643–1647. [[CrossRef](#)] [[PubMed](#)]
33. Chen, J.-Q.; Xie, J.-H.; Bao, D.-H.; Liu, S.; Zhou, Q.-L. Total Synthesis of (–)-Galanthamine and (–)-Lycoramine via Catalytic Asymmetric Hydrogenation and Intramolecular Reductive Heck Cyclization. *Org. Lett.* **2012**, *14*, 2714–2717. [[CrossRef](#)] [[PubMed](#)]

34. Berkov, S.; Bastida, J.; Sidjimova, B.; Viladomat, F.; Codina, C. Phytochemical differentiation of *Galanthus nivalis* and *Galanthus elwesii* (Amaryllidaceae): A case study. *Biochem. Syst. Ecol.* **2008**, *8*, 638–645. [[CrossRef](#)]
35. Bohno, M.; Sugie, K.; Imase, H.; Yusof, Y.B.; Oishi, T.; Chida, N. Total synthesis of Amaryllidaceae alkaloids, (+)-vittatine and (+)-haemanthamine, starting from d-glucose. *Tetrahedron* **2007**, *63*, 6977–6989. [[CrossRef](#)]
36. Ellman, G.L.; Courtney, K.D.; Andres, V.; Feather-Stone, R.M. A new and rapid colorimetric determination of acetylcholinesterase activity. *Biochem. Pharmacol.* **1961**, *7*, 88–95. [[CrossRef](#)]
37. Vaněčková, N.; Hošťálková, A.; Šafratová, M.; Kuneš, J.; Hulcová, D.; Hrabínová, M.; Doskočil, I.; Štěpánková, Š.; Opletal, L.; Nováková, L.; et al. Isolation of Amaryllidaceae alkaloids from *Nerine bowdenii* W. Watson and their biological activities. *RSC Adv.* **2016**, *6*, 80114–80120. [[CrossRef](#)]
38. Tarrago, T.; Kichik, N.; Seguí, J.; Giralt, E. The Natural Product Berberine is a Human Prolyl Oligopeptidase Inhibitor. *ChemMedChem* **2007**, *2*, 354–359. [[CrossRef](#)]
39. Breiterová, K.; Koutová, D.; Maříková, J.; Havelek, R.; Kuneš, J.; Majorošová, M.; Opletal, L.; Hošťálková, A.; Jenčo, J.; Řezáčová, M.; et al. Amaryllidaceae Alkaloids of Different Structural Types from *Narcissus L.* cv. Professor Einstein and Their Cytotoxic Activity. *Plants Basel Switz.* **2020**, *9*, 137. [[CrossRef](#)]
40. Cahlíková, L.; Hrabínová, M.; Kulhánková, A.; Benesová, N.; Chlebek, J.; Jun, D.; Novák, Z.; Macáková, K.; Kunes, J.; Kuca, K.; et al. Alkaloids from *Chlidanthus fragrans* and their acetylcholinesterase, butyrylcholinesterase and prolyl oligopeptidase activities. *Nat. Prod. Commun.* **2013**, *8*, 1541–1544. [[CrossRef](#)]
41. Šafratová, M.; Hošťálková, A.; Hulcová, D.; Breiterová, K.; Hrabcová, V.; Machado, M.; Fontinha, D.; Prudêncio, M.; Kuneš, J.; Chlebek, J.; et al. Alkaloids from *Narcissus poeticus* cv. Pink Parasol of various structural types and their biological activity. *Arch. Pharm. Res.* **2018**, *41*, 208–218. [[CrossRef](#)]
42. Nachon, F.; Carletti, E.; Ronco, C.; Trovaslet, M.; Nicolet, Y.; Jean, L.; Renard, P.-Y. Crystal structures of human cholinesterases in complex with huprine W and tacrine: Elements of specificity for anti-Alzheimer's drugs targeting acetyl- and butyryl-cholinesterase. *Biochem. J.* **2013**, *453*, 393–399. [[CrossRef](#)] [[PubMed](#)]
43. Pohanka, M.; Karasova, J.Z.; Kuca, K.; Pikula, J.; Holas, O.; Korabecny, J.; Cabal, J. Colorimetric dipstick for assay of organophosphate pesticides and nerve agents represented by paraoxon, sarin and VX. *Talanta* **2010**, *81*, 621–624. [[CrossRef](#)] [[PubMed](#)]
44. Hostalkova, A.; Marikova, J.; Opletal, L.; Korabecny, J.; Hulcova, D.; Kunes, J.; Novakova, L.; Perez, D.I.; Jun, D.; Kucera, T.; et al. Isoquinoline Alkaloids from *Berberis vulgaris* as Potential Lead Compounds for the Treatment of Alzheimer's Disease. *J. Nat. Prod.* **2019**, *82*, 239–248. [[CrossRef](#)] [[PubMed](#)]
45. Cheung, J.; Rudolph, M.J.; Burshteyn, F.; Cassidy, M.S.; Gary, E.N.; Love, J.; Franklin, M.C.; Height, J.J. Structures of human acetylcholinesterase in complex with pharmacologically important ligands. *J. Med. Chem.* **2012**, *55*, 10282–10286. [[CrossRef](#)] [[PubMed](#)]
46. Pettersen, E.F.; Goddard, T.D.; Huang, C.C.; Couch, G.S.; Greenblatt, D.M.; Meng, E.C.; Ferrin, T.E. UCSF Chimera—a visualization system for exploratory research and analysis. *J. Comput. Chem.* **2004**, *25*, 1605–1612. [[CrossRef](#)] [[PubMed](#)]
47. Morris, G.M.; Huey, R.; Lindstrom, W.; Sanner, M.F.; Belew, R.K.; Goodsell, D.S.; Olson, A.J. AutoDock4 and AutoDockTools4: Automated docking with selective receptor flexibility. *J. Comput. Chem.* **2009**, *30*, 2785–2791. [[CrossRef](#)]
48. Panek, D.; Więckowska, A.; Wichur, T.; Bajda, M.; Godyń, J.; Jończyk, J.; Mika, K.; Janockova, J.; Soukup, O.; Knez, D.; et al. Design, synthesis and biological evaluation of new phthalimide and saccharin derivatives with alicyclic amines targeting cholinesterases, beta-secretase and amyloid beta aggregation. *Eur. J. Med. Chem.* **2017**, *125*, 676–695. [[CrossRef](#)]
49. Hepnarova, V.; Korabecny, J.; Matouskova, L.; Jost, P.; Muckova, L.; Hrabínova, M.; Vykoukalova, N.; Kerhartova, M.; Kucera, T.; Dolezal, R.; et al. The concept of hybrid molecules of tacrine and benzyl quinolone carboxylic acid (BQCA) as multifunctional agents for Alzheimer's disease. *Eur. J. Med. Chem.* **2018**, *150*, 292–306. [[CrossRef](#)]
50. Svobodova, B.; Mezeiova, E.; Hepnarova, V.; Hrabínova, M.; Muckova, L.; Koblíková, T.; Jun, D.; Soukup, O.; Jimeno, M.L.; Marco-Contelles, J.; et al. Exploring Structure-Activity Relationship in Tacrine-Squaramide Derivatives as Potent Cholinesterase Inhibitors. *Biomolecules* **2019**, *9*, 379. [[CrossRef](#)]




51. O'Boyle, N.M.; Banck, M.; James, C.A.; Morley, C.; Vandermeersch, T.; Hutchison, G.R. Open Babel: An open chemical toolbox. *J. Cheminformatics* **2011**, *3*, 33. [[CrossRef](#)]
52. Trott, O.; Olson, A.J. AutoDock Vina: Improving the speed and accuracy of docking with a new scoring function, efficient optimization and multithreading. *J. Comput. Chem.* **2010**, *31*, 455–461. [[CrossRef](#)] [[PubMed](#)]



© 2020 by the authors. Licensee MDPI, Basel, Switzerland. This article is an open access article distributed under the terms and conditions of the Creative Commons Attribution (CC BY) license (<http://creativecommons.org/licenses/by/4.0/>).

Article

Evaluation of the Adverse Effects of Chronic Exposure to Donepezil (An Acetylcholinesterase Inhibitor) in Adult Zebrafish by Behavioral and Biochemical Assessments

Gilbert Audira ^{1,2,†}, Nguyen Thi Ngoc Anh ^{2,†}, Bui Thi Ngoc Hieu ^{1,2}, Nemi Malhotra ³, Petrus Siregar ², Omar Villalobos ⁴ , Oliver B. Villaflores ⁵, Tzong-Rong Ger ^{3,6}, Jong-Chin Huang ⁷ , Kelvin H.-C. Chen ^{7,*} and Chung-Der Hsiao ^{1,3,6,*} 

¹ Department of Chemistry, Chung Yuan Christian University, Chung-Li 320314, Taiwan; gilbertaudira@yahoo.com (G.A.); hieubtn90@gmail.com (B.T.N.H.)

² Department of Bioscience Technology, Chung Yuan Christian University, Chung-Li 320314, Taiwan; nguyen021194@gmail.com (N.T.N.A.); siregar.petrus27@gmail.com (P.S.)

³ Department of Biomedical Engineering, Chung Yuan Christian University, Chung-Li 320314, Taiwan; nemi.malhotra@gmail.com (N.M.); sunbow@cycu.edu.tw (T.-R.G.)

⁴ Department of Pharmacy, Faculty of Pharmacy, University of Santo Tomas, Manila 1008, Philippines; oavillalobos@ust.edu.ph

⁵ Department of Biochemistry, Faculty of Pharmacy, University of Santo Tomas, Manila 1008, Philippines; obvillaflores@ust.edu.ph

⁶ Center of Nanotechnology, Chung Yuan Christian University, Chung-Li 320314, Taiwan

⁷ Department of Applied Chemistry, National Pingtung University, Pingtung 900391, Taiwan; hjc@mail.nptu.edu.tw

* Correspondence: kelvin@mail.nptu.edu.tw (K.H.-C.C.); cdhsiao@cycu.edu.tw (C.-D.H.)

† Equal contribution authors.

Received: 1 September 2020; Accepted: 17 September 2020; Published: 18 September 2020



Abstract: Donepezil (DPZ) is an acetylcholinesterase inhibitor used for the clinical treatment of mild cognitive impairment. However, DPZ has been reported to have adverse effects, including causing abnormal cardiac rhythm, insomnia, vomiting, and muscle cramps. However, the existence of these effects in subjects without Dementia is unknown. In this study, we use zebrafish to conduct a deeper analysis of the potential adverse effects of DPZ on the short-term memory and behaviors of normal zebrafish by performing multiple behavioral and biochemical assays. Adult zebrafish were exposed to 1 ppm and 2.5 ppm of DPZ. From the results, DPZ caused a slight improvement in the short-term memory of zebrafish and induced significant elevation in aggressiveness, while the novel tank and shoaling tests revealed anxiolytic-like behavior to be caused by DPZ. Furthermore, zebrafish circadian locomotor activity displayed a higher reduction of locomotion and abnormal movement orientation in both low- and high-dose groups, compared to the control group. Biomarker assays revealed that these alterations were associated with an elevation of oxytocin and a reduction of cortisol levels in the brain. Moreover, the significant increases in reactive oxygen species (ROS) and malondialdehyde (MDA) levels in muscle tissue suggest DPZ exposure induced muscle tissue oxidative stress and muscle weakness, which may underlie the locomotor activity impairment. In conclusion, we show, for the first time, that chronic waterborne exposure to DPZ can severely induce adverse effects on normal zebrafish in a dose-dependent manner. These unexpected adverse effects on behavioral alteration should be carefully addressed in future studies considering DPZ conducted on zebrafish or other animals.

Keywords: donepezil; acetylcholinesterase inhibitor; dementia; zebrafish; behavior

1. Introduction

According to 2019 WHO guidelines on “Risk reduction of cognitive decline and dementia”, 10 million new cases of dementia are reported annually and this figure is set to triple by 2050 [1]. Dementia is a progressive neurodegenerative disease where brain cell death happens over time, leading to the loss of memory and executive function. Many pharmacological strategies, in the form of medicines such as donepezil (DPZ), rivastigmine, and galantamine, as well as therapies, have been devised to ameliorate the symptoms and, in some instances, slow the progression of dementia. These medications boost the levels of chemical messengers involved in memory and judgment, whereas therapies help to cope and to manage patient behavior.

DPZ, sold with the trade name of Aricept, is a reversible inhibitor of the enzyme acetylcholinesterase (AChE) and is one of the most widely used therapeutics. Inhibition of AChE helps to enhance cholinergic function by increasing the cortical amount of acetylcholine. It has been shown to be helpful in treating the symptoms of Alzheimer’s disease (AD) or dementia, including sleep disturbances, aggression, and reduction in memory, as well as slowing the progression of neuronal loss, advancing cognitive symptoms, and postponing cognitive degeneration in patients [2,3]. In younger and older humans, several studies have shown that the percentages of rapid eye movement (REM) sleep and REM density were enhanced, while REM latency was reduced by donepezil [4]. Another study in humans also found that donepezil-treated AD patients were less threatening, had a lower level of behavioral disturbances, and needed fewer sedatives than those not on donepezil [5]. Furthermore, a prior study in patients with mild–moderate AD discovered that donepezil administration improved mood, ability to perform the activities of daily living (ADL), disturbing behavior, and social behavior, as well as memory after 3 months. The behavioral changes were found to occur in a dose-dependent manner [6]. Nevertheless, it is already known that cholinesterase inhibitors exhibit some side-effects with increased cholinergic activity in AD patients, such as loss of appetite and gastrointestinal distress, including diarrhea, nausea, vomiting, muscle and abdominal cramps, and anorexia [7,8]. Unfortunately, these side-effects can prevent patients from achieving an effective dose of the drug [9].

In a prior study, the potential effects on neurodegeneration and cognitive deficits of DPZ were studied in rats. DPZ was administered to male Wistar rats 15 days before a 192-IgG-saporin injection, which can cause a secretive depletion of basal forebrain cholinergic neurons, which is a key component of the cognitive deficits associated with aging and dementia. Later, rats were subjected to several behavioral tests to analyze their anxiety levels, spatial working memory, sociability test, social motivation, and discriminative competencies, followed later by biochemical tests. They observed increased hippocampal and neocortical caspase-3 activity and impaired working memory, spatial discrimination, and social novelty preference without affecting anxiety levels and fear conditioning. Thus, the study concluded that pre-treatment of DPZ has beneficial effects on behavioral activity induced by cholinergic depletion and diminishing hippocampal and neocortical neurodegeneration [10]. Next, the neuroprotective effect of DPZ was evaluated on neurotoxicity induced by amyloid-beta ($A\beta$) (1-40) in primary cultures of rat septal neurons highly susceptible to $A\beta$ toxicity. After $A\beta$ (1-40) was added to the medium, DPZ was found to reduce lactate dehydrogenase (LDH) in a dose-dependent manner, suggesting that DPZ applies a neuroprotective effect by dramatically reducing the amount of toxin from $A\beta$ fibrils in septal neuron cultures [11].

In current biomedicine research, zebrafish provide excellent experimental models to close the existing gap between *in vitro* and *in vivo* studies. As behavioral studies are important for a deeper understanding of the pathology and development of a neurological disease, zebrafish, as a model organism, provides an efficient alternative model platform for neurological and behavioral studies, as it shares similarities with the highly conserved nervous system structure and function of humans [12,13]. In a previous study in zebrafish, the effect of DPZ on zebrafish larvae was studied by vibrational startle response assay (VSRA). This assay was conducted to evaluate the habituation and escape response in zebrafish larvae. From the results, DPZ was found to be consistent with its acetylcholine receptor agonist role by significantly increasing the magnitude of startle response, area under the curve (AUC)

value, and reduced habituation to VSR [14,15]. In another prior study, zebrafish larvae were also used for behavior analysis, with the help of a series of acoustic stimuli. Administration of DPZ increased acoustic startle response and reduced habituation in larvae, similar to a study using a rodent model [14].

It is already well-known that donepezil can improve cognitive dysfunction by enhancing cholinergic function in humans and several animal models (including zebrafish), even though various side-effects are still observed in human patients with Alzheimer's disease. However, the effect of donepezil in enhancing cognition and intellectual function in normal-condition subjects remains unaddressed. Little is still known about its adverse effects on subjects without AD, especially in terms of behavior. In addition, considering its dose-dependent effects, a study to observe the different effects caused by the differences in DPZ concentration needs to be conducted. Thus, to further examine the positive and/or adverse effects of DPZ in subjects without neurodegenerative disorders and to further inspect its effects under different doses, we studied the effect of two concentrations of donepezil in normal adult zebrafish, particularly focused on their behavior. Moreover, to elucidate the possible mechanism that underlies its effect, biochemical assays were conducted. We hypothesized that chronic DPZ treatment would affect zebrafish behavior in the absence of neurodegeneration.

2. Experimental Methodology

2.1. Animal Husbandry

Wild-type AB strain zebrafish were raised and kept in standard laboratory conditions, according to the protocol described by Westerfield [16]. All procedures were approved by The Committee for Animal Experimentation of the Chung Yuan Christian University (Number: CYCU104024, Issue Date: 21 December 2015). Briefly, zebrafish were housed in a recirculating tank system on a 14:10 h light/dark cycle. A trapezoid tank with 34 cm at the top, 23 cm along the bottom, 19 cm along the diagonal side, 18 cm high, and 27 cm width filled with 8 L of water was used for holding the fish. Water quality was maintained at 28.5 °C (pH 7.2–7.6) with the conductivity of the system water kept between 300 and ~1500 μ S. The circulating water was constantly filtered by ultraviolet (UV) light. All fish used in this study were fed twice daily (09:00 and 17:00) with fresh brine shrimp and commercial dry food. For all experiments, around 5–6-month old adult zebrafish were used. All behavioral tests were done between 10:00 and 16:00, except for the circadian locomotor activity test.

2.2. Preparation and Exposure to Donepezil HCl

Donepezil hydrochloride (Donepezil HCl) was purchased from Sigma-Aldrich (St. Louis, MO, USA; CAT#D6821). Donepezil HCl was dissolved in 1% dimethyl sulfoxide (DMSO) to obtain a stock solution with a concentration of 1000 mg/L (ppm) and stored in the refrigerator (4–8 °C). For the first experiment, which was a T-maze test, zebrafish were randomly divided into 2 groups containing 18 animals each using the simple random allocation method to avoid experimental bias [17,18]. One of the groups served as control, while another group was exposed to 2.5 ppm of donepezil for 21 days. This initial experiment aimed to study whether donepezil at a relatively high concentration could improve the cognition of normal zebrafish or not. This particular concentration was used based on several prior studies, especially in rats, which found the positive effects of donepezil in a similar concentration on rat cognitive performance [19–23]. As no adverse or beneficial effects on cognitive performance in zebrafish were observed, the adverse effect of donepezil was further examined in other tests. In addition, another lower concentration was applied, in order to conduct a deeper study on its effect in zebrafish, especially on their behavior. In the following experiment, Zebrafish were randomly divided into 3 groups containing 30 animals each using the simple random allocation method [17,18]. In addition, this sample size determination was chosen as a statistical power analysis in the untreated group with a 90% confidence interval and a margin of error of 7 units showed that a sample of size 25 was needed [24]. The detail of *n* number calculation can be found in Table S1. One of the groups served as control, while other groups were exposed to 1 ppm and 2.5 ppm of donepezil, respectively,

for 21 days. Zebrafish behavior was observed at days 14 ± 1 (novel tank, mirror biting, predator avoidance, social interaction, and shoaling tests), 17 (color preference test), 19 (circadian locomotor activity test), and 21 (biochemical assay). All of the zebrafish in each group in every experiment were kept in a 4 L tank as, based on prior studies, this stocking density of zebrafish for the long-term helps to maintain low stress levels, with the assumption that all of the fish received equal amounts of the carrier [25–28]. Incubation water was changed every day and the donepezil concentration was maintained during incubation in all of the experiments. The schematic diagram of this experiment can be found in Figure S1.

2.3. T-maze Test (Short-Term Memory Test)

To observe the effects of donepezil on the memory of zebrafish, we used the T-maze test, referring to a previous publication reported by Ngoc Hieu et al. [29]. The T-Maze apparatus used in this study consisted of two deep-water arms and one straight long arm, which divided the inner space into a T-way intersection. The straight tunnel was separated with a white-color gate, dividing the start chamber and a novel arm, which branched into two short arms that led to deeper left/right chambers at a three-way junction. The apparatus included zones I, II (start chamber and novel arm), and III/IV (deep-water chambers) at each side of the T-way section. Based on the principle of the passive avoidance experiment [30], an electric stimulus was given in zone III (left arm) with mild electric shock (1–2 V, 0.3–0.5 mA.) In addition, for place preference conditioning in adult zebrafish [31], a green-cue was placed on one side of the wall in zone IV [32]. The camera for video recording (OPTO, CCD, China), NCH Debut Video software, and idTracker software [33] were used to observe the movement of the fish. First, the fish underwent habituation to minimize apparatus novelty stress [34]. In habitual group trials, 6 fish were placed in the starting chamber for 1 min before opening the gate, after which fish were allowed to explore the entire T-maze for 30 min. Before individual habituation trials, fish were placed into individual 600 mL plastic tanks to acclimate individually for 2 h. Afterward, each fish was placed in a starting chamber with its gate closed. After 30 s, the gate was opened and the fish was allowed to explore the T-maze for 5 min. Next, the fish was returned to the individual tank for 24 h prior to the start of training trials. For the training day, three training sessions were performed and a maximum of three electric shock times were given per session. In each session, fish were placed in a starting chamber for 30 s for acclimation. When fish swam into the left arm, they would immediately receive a mild electric shock. If it did not escape from the left arm in 20 s after receiving the electric shock, the fish would be retrained. Each training session ended when there was no entrance into the left arm within 5 min. Later, fish that completed three training sessions were stored in small plastic containers until the testing session, which consisted of the same protocol as the training trials, only without the electric shock. The testing session was based on time dependence, 24, 48, and 72 h after accomplishing the training trials. The latency of the first time fish crossed to the left arm in the habituation trial was recorded as the latency before training. The difference in the latency to enter the left arm of the apparatus (recorded for a maximum of 5 min) and the total number of electric shocks in training trials are important parameters for learning studies in zebrafish. Differences in the latency to enter the left arm between before training and testing were used as indices of memory retention. The difference in the time spent in the punish arm (left arm) and the time spent in the non-punish area between before training and testing were used as indices of the cognitive ability of zebrafish.

2.4. A Set of Behavioral Tests

Our battery of zebrafish behavioral tests consisted of novel tank, mirror biting, predator avoidance, social interaction, and shoaling tests. In these tests, a trapezoid test tank with 22 cm along the bottom, 28 cm at the top, 15.2 cm high, and 15.9 cm along the diagonal side was used during the experiment, which was filled with ~1.25 L of fish water, as described in the previous method [35]. Except for the novel tank test, after 5 to 10 min of fish acclimation in the tank, fish behaviors were recorded for a period of 5 min. In the novel tank test, video recording was started immediately after the fish

was put into the test tank for one minute, repeated with a 5 min interval until 30 min had passed. In the mirror biting test, a mirror was placed on one side of the test tank to observe their behaviors of biting the mirror, which indicated their level of aggressiveness. The 'biting' was defined as the movement of the fish when they traced their reflection as they swim quickly up and down or back and forth and was measured by counting the duration when the fish stayed in front of the mirror and contacted the mirror. Meanwhile, in the predator avoidance and social interaction tests, a transparent separator was placed in the middle of the tank to separate the test fish from a convict cichlid (*Amatitlania nigrofasciata*) or their conspecific, respectively. The conspecific was placed to study the social behavior of the tested fish by observing the number of interactions between the tested fish and the conspecific, while the convict cichlid in the predator avoidance test was used to stimulate the fear level of the tested fish, such that they could display predator avoidance behavior. In the shoaling test, fish in groups of three were placed into each tank and their behavior regarding shoal formation was observed after acclimation. All zebrafish behaviors were processed by trained observers blinded to the treatments. The difference of *n* number between some behavioral tests happened due to the death of the zebrafish, which was caused by an unidentified reason.

2.5. Circadian Locomotor Activity Test

The circadian locomotor activity test was conducted as described in our previous publication [36]. The dark/light cycle test apparatus consisted of six custom-made small fish tanks (20 × 10 × 5 cm) which were placed above a lightbox. For each tank, three fish were tested. For the light cycle, a light-emitting diode (LED) was used as a light source, while an infrared light-emitting diode (IR-LED) was used as a light source in the dark cycle. A 940 nm infrared camera with a magnifying lens was located above the experimental setup, in order to record the fish movements at 30 frames per second. The apparatus was placed inside an incubator to maintain the temperature. In this experiment, we recorded zebrafish locomotor activity for 1 min every hour. Several important behavioral endpoints—namely, average speed, average angular velocity, meandering, freezing, swimming, and rapid movement time ratios—were measured during the test.

2.6. Color Preferences Assay

The color preference assay was carried out in a 21 cm × 21 cm × 10 cm acrylic tank filled with 1.5 L of filtered water. Every tank consisted of four compartments, where each compartment was divided into two-color combinations among red, green, blue, and yellow colors. In total, there were six color combinations to determine the color preference of zebrafish. The color preference was recorded with a combination of an infrared (IR) camera and high-resolution HD camera and analyzed using idTracker software [33].

2.7. Estimation of Neurotransmitter Activity, Oxidative Stress Level, Antioxidant Enzyme Stress Hormone, and Neuropeptides in Brain Tissue

Six fish were randomly selected from each group for biochemical assays. For each group, six brains were divided into 3 samples (two brains per sample). Whole-brain tissue was homogenized on ice in 50 volumes (*v/w*) of PBS at pH 7.2 using a bullet blender tissue homogenizer (Next Advance, Inc., Troy, NY, USA). Later, samples were incubated on ice for 30 min before centrifuging at 12,000 g for 10 min. The crude homogenate was stored in 50 µL aliquots at −80 °C until their use in ELISA assays. Neurotransmitter levels of serotonin (5-HT), dopamine (DA), acetylcholine (ACh), acetylcholinesterase (AChE), melatonin, GABA (γ -aminobutyric acid), norepinephrine, oxytocin, and vasotocin were measured using target-specific ELISA kits purchased from a commercial company (ZGB-E1572, ZGB-E1573, ZGB-E1585, ZGB-E1637, ZGB-E1597, ZGB-E1574, ZGB-E1571, ZGB-E1668 and ZGB-E1673, Zgenebio Inc., Taipei, Taiwan). The levels of reactive oxygen species (ROS), superoxide dismutase (SOD), malondialdehyde (MDA), catalase (CAT), the stress hormone cortisol, and neuropeptide kisspeptin were measured using target-specific ELISA kits also purchased from a commercial company (ZGB-E1561,

ZGB-E1604, ZGB-E1592, ZGB-E1598, ZGB-E1575, and ZGB-E1696, Zgenebio Inc., Taipei, Taiwan). The target protein content or activity was analyzed according to the manufacturer's instructions.

2.8. Determination of ATP, Oxidative Stress Level and Antioxidant Enzyme Activity in Muscle Tissues

Six fish were randomly selected from each group for biochemical assays. For each group, the muscle was dissected from two fish and put together as one sample. Similar to the brain samples, muscle samples were homogenized. Later, the levels of reactive oxygen species (ROS), superoxide dismutase (SOD), malondialdehyde (MDA), catalase (CAT), and ATP were measured using target-specific ELISA kits purchased from a commercial company (ZGB-E1561, ZGB-E1604, ZGB-E1592, ZGB-E1598, and ZGB-E1580, Zgenebio Inc., Taipei, Taiwan). The target protein content or activity was analyzed according to the manufacturer's instructions.

2.9. Statistical Analysis

All data are presented either as mean \pm standard error of the mean (SEM) or median with interquartile range. Statistical analyses were conducted by either using a parametric test (*t*-test and ANOVA followed by least significant difference multiple comparison tests) or non-parametric tests (Mann–Whitney Test and Kruskal–Wallis tests followed by Dunn's multiple comparisons test) by trained analysts blind to the experimental conditions. The non-parametric tests were applied as behavioral data generally do not follow a normal distribution [37]. However, to confirm their non-normal distribution, as the prior study mentioned, testing for normal distribution was still conducted in the data, as calculated by non-parametric tests prior to the calculation. Normality tests included Anderson–Darling, D'Agostino and Pearson, Shapiro–Wilk, and Kolmogorov–Smirnov tests. The Prism software (GraphPad Software version 7, La Jolla, CA, USA) was used to perform the statistical tests and output the graphs.

3. Results

3.1. Effect of DPZ Exposure in Short-Term Memory in Zebrafish

DPZ, as an acetylcholinesterase inhibitor, has been reported to improve cognitive impairment and global function in patients with mild to moderately severe Alzheimer's disease [13,38]. First, we tested the impact of DPZ on short-term memory in healthy adult zebrafish using a T-maze test. A T-maze is an instrument that has been widely utilized to evaluate spatial learning and memory in rodents [39–41] and zebrafish [42,43] after exposure to chemical pollution [44,45] or pharmacological drugs [46–48]. Zebrafish learning and memory performance were tested after exposure to 2.5 ppm of DPZ for 21 days. The results showed that the DPZ-exposed group displayed no significant difference in both training (learning) latency and the total number of electric shocks received in training sessions, compared to the control fish, which indicated that DPZ exposure had no adverse effects on the learning process of adult zebrafish ($p = 0.0832$; $F(1, 136) = 3.046$; $p = 0.1374$; Figure 1A,B). Furthermore, freezing time also displayed no significant difference in before and after training between control and DPZ-exposed fish ($p = 0.0488$; $F(1, 136) = 3.951$; Figure 1C). On the testing day, DPZ-exposed fish showed no significant difference in terms of latency after training and time spent in the non-punish arm, compared to the control fish ($p = 0.1656$; $F(1, 136) = 1.944$; $p = 0.0666$; $F(1, 136) = 3.42$; Figure 1D,F). However, significantly reduced time spent in the punish-arm was observed in the DPZ-exposed fish in subsequent time points after the training, when compared to the control group ($p = 0.0063$; $F(1, 135) = 7.695$; Figure 1E). Taken together, these results demonstrate that chronic exposure to DPZ in normal adult zebrafish had no adverse or beneficial effects on their learning; however, a slight improvement, in terms of adult zebrafish short-term memory, was observed. As there was not any significant improvement in terms of cognitive performance displayed by the normal zebrafish after chronic exposure to 2.5 ppm DPZ, a lower concentration (1 ppm) of this compound was also used

in the following tests to observe the effect of both concentrations in normal zebrafish, especially in their behavior.

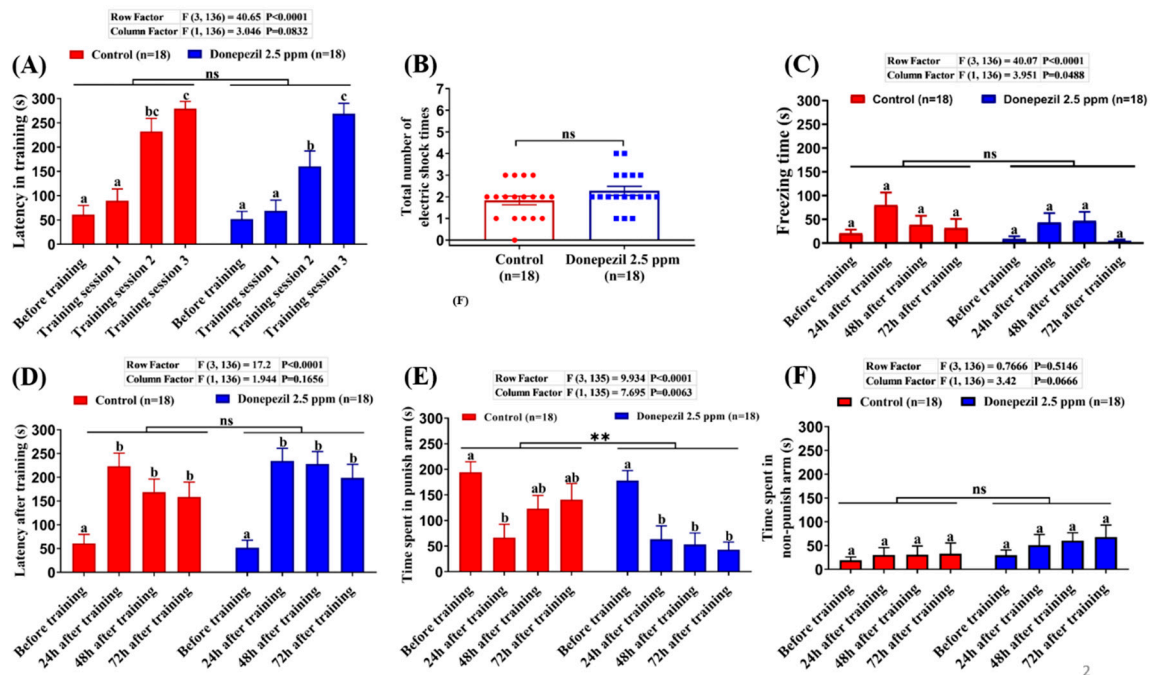


Figure 1. T-maze conditioning passive avoidance to test short-term memory of fish after 21 days exposure to 2.5 ppm of donepezil: (A) the latency of control and donepezil-exposed fish swimming into the punish chamber for each training session; (B) the total number of electric shocks given for successful training between control and donepezil-exposed fish; (C) the freezing time of control and donepezil-exposed fish at different time points before and after training; (D) the memory retention of control and donepezil-exposed fish at different time points before and after training; (E) the time spent in punish arm of control and donepezil-exposed fish at different time points before and after training; (F) the time spent in the non-punish area of control and donepezil-exposed fish at different time points before and after training. The data are expressed as the mean \pm standard error of the mean (SEM) values. Different letters (a, b, c) on the error bars represent the significant differences ($p < 0.05$); A and C–F were analyzed by two-way ANOVA with Tukey–HSD (Honestly Significant Difference) post hoc test; B was analyzed by unpaired t-test; $n = 18$, $** p < 0.01$.

3.2. Effects of DPZ in Novel Tank Test for Zebrafish

The novel tank test is a useful behavioral assay to measure fish anxiety when a fish is exposed to a novel environment. Normally, a zebrafish exhibits bottom-dwelling behavior when it is placed into a new environment and starts exploring the area after a few minutes of adaptation [49]. After chronic exposure for 14 days, DPZ-exposed zebrafish were observed for their locomotor activity and exploratory behavior in this test. From the results, it was found that zebrafish exposed to 1 ppm of DPZ showed no significant differences in average speed ($p = 0.251$; $F(2, 87) = 1.404$; Figure 2A) and freezing time movement ratio ($p = 0.0857$; $F(2, 87) = 2.528$; Figure 2B), compared to the control group, indicating that chronic exposure to DPZ in a low concentration had no significant effect on zebrafish locomotor activity during the test. In contrast, zebrafish treated with a higher concentration of DPZ (2.5 ppm) showed lower locomotor activity with a significantly high level of freezing time movement ratio (Figure 2B). Furthermore, DPZ-treated fish at both concentrations showed anxiolytic-like behavior based on significant alterations in all of the exploratory behavior endpoints after testing by Dunnett’s multiple comparisons test, which were higher time in the top duration ($p = 0.0394$; $F(2, 87) = 3.358$), the number of entries to the top ($p = 0.0021$; $F(2, 87) = 6.631$), total distance traveled in the top ($p = 0.0702$; $F(2, 87) = 2.739$), and lower latency to enter the top ($p = 0.0025$; $F(2, 87) = 6.418$) during the first

20 min of novel tank exposure (Figure 2C–F). The locomotion trajectories and behavioral changes in the novel tank test can be found in Figure 2J–L.

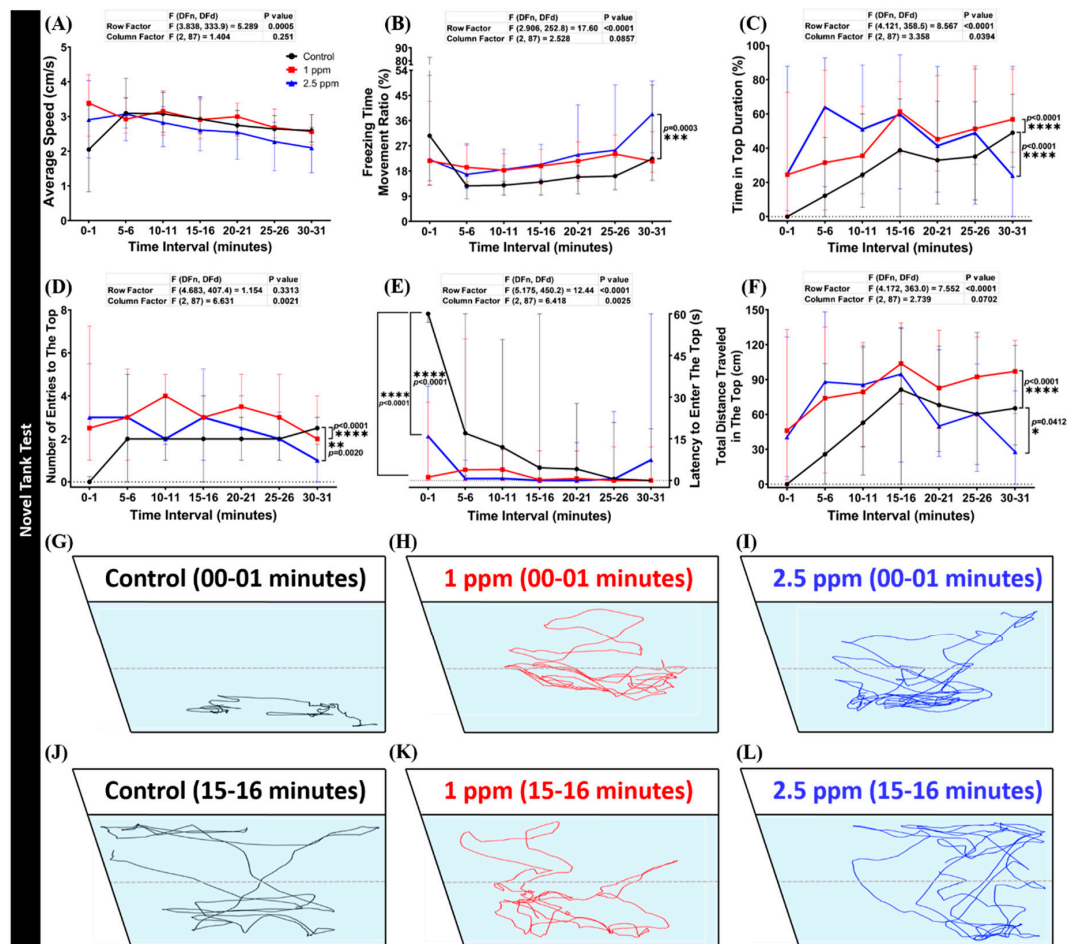


Figure 2. Behavior endpoints of control and donepezil-exposed zebrafish in novel tank test after 14 days of incubation: (A) average speed; (B) freezing time movement ratio; (C) time in top duration; (D) number of entries to the top; (E) latency to enter the top; and (F) total distance traveled in the top were analyzed. The swimming trajectories of (G,J) control; (H,K) 1 ppm Donepezil-exposed fish; and (I,L) 2.5 ppm Donepezil-exposed fish for novel tank test after 1 min and 15 min were recorded and compared. The black line represents control and the red line represented 1 ppm Donepezil-exposed fish, while the blue line represents 2.5 ppm Donepezil-exposed fish. The data are expressed as the median with interquartile range and were analyzed using a two-way repeated measure ANOVA with Geisser–Greenhouse correction. To observe the main column (donepezil) effect, Dunnett’s multiple comparison test was carried out; $n = 30$, * $p < 0.05$, ** $p < 0.01$, *** $p < 0.005$, **** $p < 0.001$.

3.3. Effects of DPZ in Aggressive Behavior of Zebrafish

The mirror biting test is a well-established fish paradigm which is commonly used for studying the social/aggressive behavior of adult zebrafish [50–52]. Unaltered mirror biting behaviors of the DPZ-exposed zebrafish were observed in the high concentration group ($p > 0.9999$; $p > 0.9999$; Figure 3A,B). On the other hand, the results showed that low concentration DPZ exposure induced aggressiveness in zebrafish, as indicated by a significantly higher mirror biting time percentage and longest duration in the mirror side than the control group ($p < 0.0001$; $p < 0.0001$; Figure 3A,B). Furthermore, both concentrations of DPZ affected the locomotion of zebrafish, as indicated by the hypoactivity-like behavior displayed by treated fish during the test. DPZ exposure led to a significant reduction of average speed and swimming time movement ratio, while the freezing

time movement ratio was significantly increased, compared to the control group (Figure S2A–C). In addition, regarding the rapid movement time ratio, no significant differences were found between the treated groups and the control group (Figure S2D). Taken together, these results indicate that DPZ led to a reduction of zebrafish locomotor activity and that a low dose of DPZ exposure induced a high aggressiveness level which was not observed in the high dose of DPZ. The locomotion trajectories and behavioral changes in the mirror biting test can be found in Figure 3C–E.

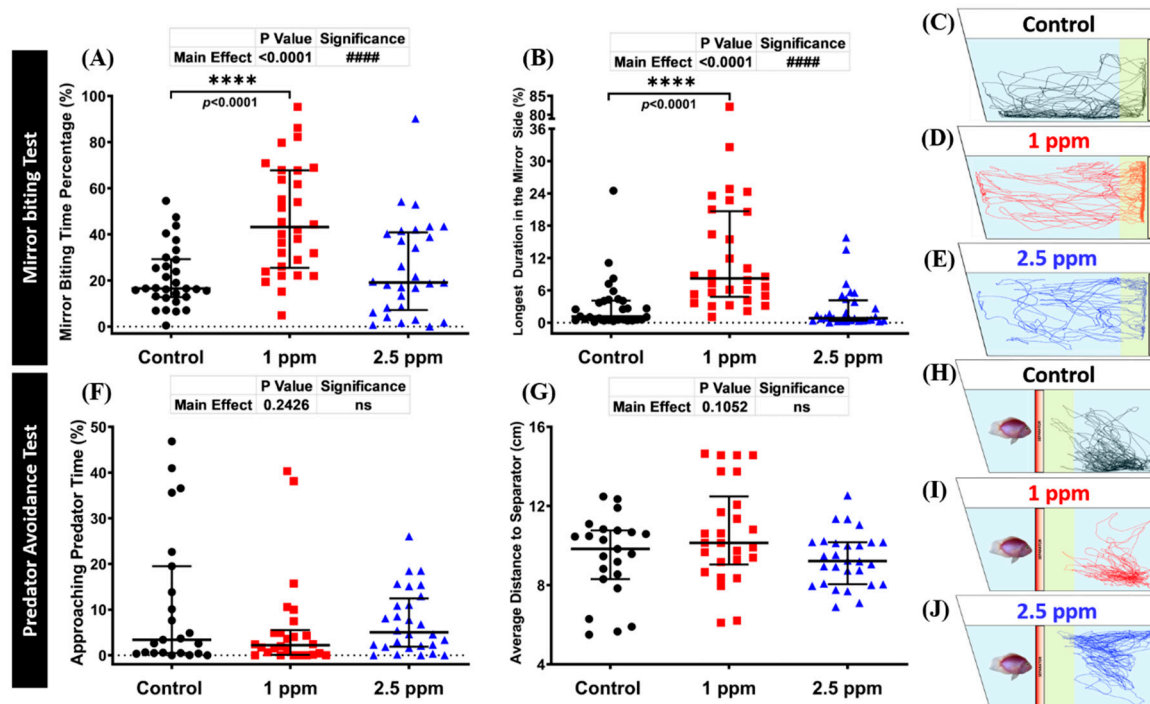


Figure 3. Mirror biting and predator avoidance behavior endpoint comparisons between the control, 1 ppm, and 2.5 ppm donepezil-exposed zebrafish groups after 14 days of exposure: (A) mirror biting time percentage and (B) longest duration in the mirror side were analyzed in the mirror biting. The swimming trajectories of (C) control, (D) 1 ppm Donepezil-exposed fish, and (E) 2.5 ppm Donepezil-exposed fish for the mirror biting test were recorded and compared ($n = 30$ for control and 1 ppm groups, $n = 29$ for 2.5 ppm group). (F) Approaching predator time and (G) average distance to the separator were measured in the predator avoidance test. The swimming trajectories of (H) control, (I) 1 ppm Donepezil-exposed fish, and (J) 2.5 ppm Donepezil-exposed fish for predator avoidance test were recorded and compared ($n = 23$ for the control group, $n = 26$ for 1 ppm group, $n = 28$ for 2.5 ppm group). The data are expressed as the median with interquartile range and were analyzed using the Kruskal–Wallis test followed by Dunn’s multiple comparisons test (####/**** $p < 0.001$, ns = not significant).

3.4. Effects of DPZ in Predator Avoidance Behavior of Zebrafish

Predator avoidance is an innate response of fish when they encounter their natural predators, in which they show high anxiety or even freezing behavior. In this test, we used convict cichlid (*Amatitlania nigrofasciata*) as a predator fish to induce the fear response of zebrafish. Six independent measurements in total were analyzed during the predator avoidance test, which were approaching predator time, average distance to the separator, average speed, freezing, swimming, and rapid movement time ratios. From the results, there was an indication that DPZ exposure did not alter the predator avoidance of zebrafish. This phenomenon was shown by no significant differences observed in approaching time percentage ($p = 0.4207$; $p > 0.9999$) and average distance to the separator ($p = 0.4337$; $p = 0.9999$) between treated and control groups (Figure 3F,G). Interestingly, while the locomotion activity of the high dose group was slightly decreased after 14 days of DPZ exposure, a low dose of DPZ showed more

pronounced hypo-activity behavior during the test. This alteration was supported by a decrement in average speed and swimming time movement ratio and increment in freezing time movement ratio observed in the low concentration group (Figure S2E–G). On the contrary, zebrafish exposed to 2.5 ppm DPZ only showed a reduction in rapid movement time ratio, while the other behavior endpoints were not found to be statistically different to the control group (Figure S2H). These results indicated that the locomotion of zebrafish was reduced in a dose-dependent manner and DPZ exposure did not alter the predator avoidance response in adult zebrafish. The locomotion trajectories and behavioral changes in the predator avoidance test can be found in Figure 3H–J.

3.5. Effects of DPZ Exposure in Social Interaction of Zebrafish

The social interaction test is a useful model to study zebrafish social phenotypes. In this consideration, we used a conspecific social interaction test to investigate whether DPZ exposure had any deleterious effect on zebrafish social performance. Normally, zebrafish display strong sociability when placed in a tank with conspecific fish. Interestingly, the results showed that exposure to 1 ppm of DPZ increased zebrafish sociability, as indicated by a significant increase in interaction time percentage ($p = 0.0152$), longest duration at separator side ($p = 0.0028$), and shorter average distance to the separator ($p = 0.0237$), compared to the control group (Figure 4A–C). On another hand, these phenomena were not observed in the high concentration group ($p = 0.3905$; $p = 0.7286$; $p = 0.3800$; Figure 4A–C). In addition, the average speed of zebrafish in both DPZ treatment groups was not significantly different from that of the control group ($p = 0.4711$; $p = 0.0900$; Figure 4D). Overall, these results indicate that DPZ exposure induced a slight increment in zebrafish sociability in a dose-dependent manner. The locomotion trajectories and behavioral changes in the social interaction test can be found in Figure 4E–G.

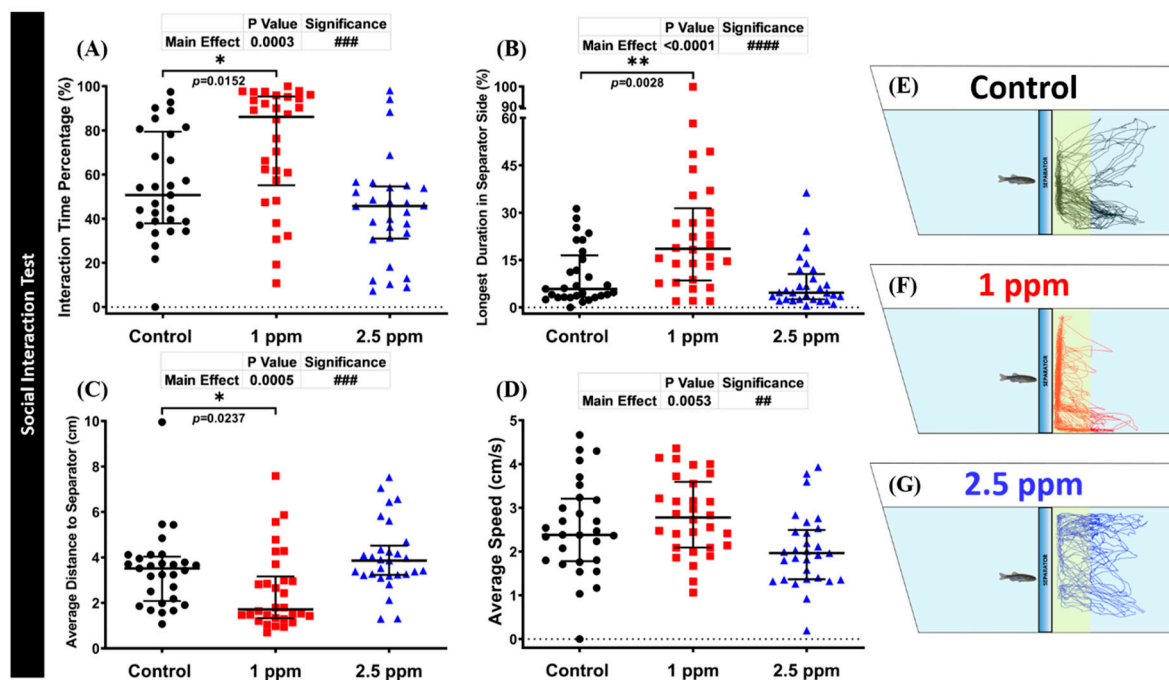


Figure 4. Social interaction behavior endpoint comparisons between the control group, 1 ppm, and 2.5 ppm donepezil-exposed zebrafish groups after 14 days of exposure: (A) interaction time percentage; (B) longest duration at separator side; (C) average distance to the separator; and (D) average speed were analyzed. The swimming trajectories of (E) control, (F) 1 ppm Donepezil-exposed fish, and (G) 2.5 ppm Donepezil-exposed fish for social interaction tests were recorded and compared. The data are expressed as the median with interquartile range and were analyzed using the Kruskal–Wallis test followed by Dunn’s multiple comparisons test ($n = 29$ for control and 2.5 ppm groups, $n = 30$ for 1 ppm group, * $p < 0.05$, ##/*** $p < 0.01$, #### $p < 0.001$, ##### $p < 0.0001$).

3.6. Effects of DPZ Exposure in Shoaling Formation of Zebrafish

The shoaling test is another social behavior test to assess the interaction of an animal group, as they move together in co-ordinated movements in order to reduce anxiety and the risk of being captured by predators. Generally, adult zebrafish display a stable shoal cohesion. When assessing shoaling behavior, the distance reduction from one individual to another is the most significant behavioral endpoint to evaluate group cohesion. Therefore, measuring average inter-fish distance and average nearest/farthest neighbor distances provides an objective and reproducible of group cohesion measurement [53]. From the results, the high concentration DPZ-exposed group displayed loosened shoaling formation behavior. This alteration was demonstrated by a significantly higher level of average inter-fish distance ($p = 0.0065$) and average nearest ($p = 0.0378$) and farthest neighbor distances ($p = 0.0046$) of this treated group than the control fish (Figure 5D–F). However, these behavior endpoints were observed to be at a similar level in the low concentration and control groups ($p > 0.9999$; $p = 0.5954$; $p = 0.8757$; $p = 0.3874$). Furthermore, after DPZ exposure in both concentrations, the locomotor activity of exposed fish showed no significant difference from the control group (Figure S2I). In addition, in agreement with other behavioral test results, DPZ also showed an anxiolytic effect in terms of zebrafish behavior. This phenomenon was supported by the high level of time in the top and average distance to the center of the tank (Figure S2J,K). Finally, these results demonstrated the potential anxiety-reducing effects of DPZ in zebrafish. The locomotion trajectories and behavioral changes in the shoaling test can be found in Figure 5D–F.

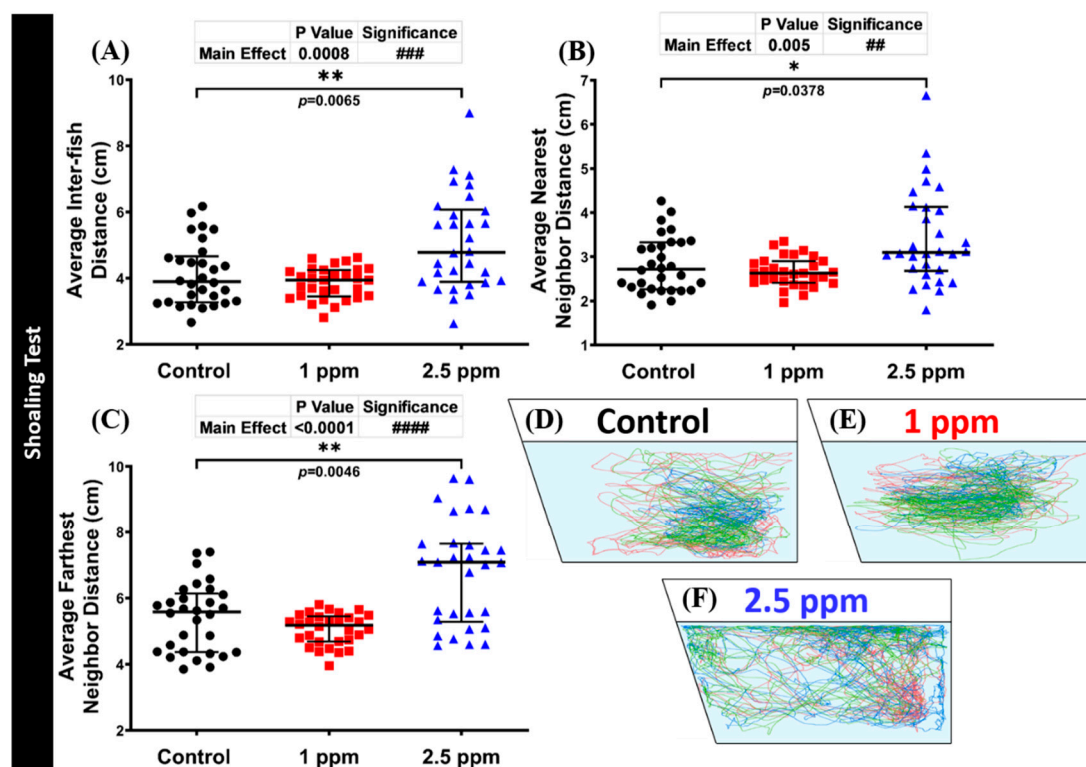


Figure 5. Shoaling behavior endpoint comparisons between the control group, 1 ppm, and 2.5 ppm donepezil-exposed zebrafish groups after 14 days of exposure: (A) average inter-fish distance; (B) average nearest neighbor distance; and (C) average farthest neighbor distance were analyzed. The swimming trajectories of (D) control, (E) 1 ppm Donepezil-exposed fish, and (F) 2.5 ppm Donepezil-exposed fish for shoaling tests were recorded and compared. Groups of three fish were tested for shoaling behavior. The data are expressed as the median with interquartile range and were analyzed using the Kruskal–Wallis test followed by Dunn’s multiple comparisons test ($n = 30$, * $p < 0.05$, ##/** $p < 0.01$, ### $p < 0.001$, #### $p < 0.0001$).

3.7. Effects of Donepezil Exposure in Circadian Locomotor Activity of Zebrafish

In a human physiological study, an increase in sleep efficiency and shortening in sleep latency were observed after DPZ administration in patients with Alzheimer's Type Dementia (ATD) [54]. Thus, it is intriguing to study the relationship between DPZ and circadian locomotor activity of zebrafish, which is closely related to its circadian rhythm, in the absence of neurodegeneration [55,56]. In this study, a circadian locomotor activity test was used to observe the chronic effects of DPZ exposure (19 days) on circadian locomotor activity patterns in normal adult zebrafish. Generally, as zebrafish is a typical diurnal fish species, it displays robust locomotion activity in the light cycle and sleep-like behavior in the dark cycle [36]. From the results, both treated groups displayed a decrement in their locomotor activity during the day and night cycles (Figure 6A), as indicated by the low level of average speed ($p < 0.0001$), swimming ($p = 0.0394$; $p = 0.030$; $p < 0.0001$; $p < 0.0001$), and rapid movement ratios ($p < 0.0001$), as well as the high level of freezing movement time ratio ($p < 0.0001$) (Figure 6B,E–H,K–M). In addition, regarding their movement orientation, the elevated level of meandering observed in both treated groups during light and dark cycles indicated a zigzag-like movement exhibited by the treated fish ($p < 0.0001$; Figure 6D,J). However, regarding their average angular velocity, both treated groups showed no significant difference to the control group in both cycles ($p = 0.0565$; $p > 0.9999$; $p = 0.7076$), except for a slight reduction in the 1 ppm group during the light cycle ($p = 0.0139$; Figure 6C,I). The P value from the main effects of each circadian locomotor activity endpoint can be found in Table S2.

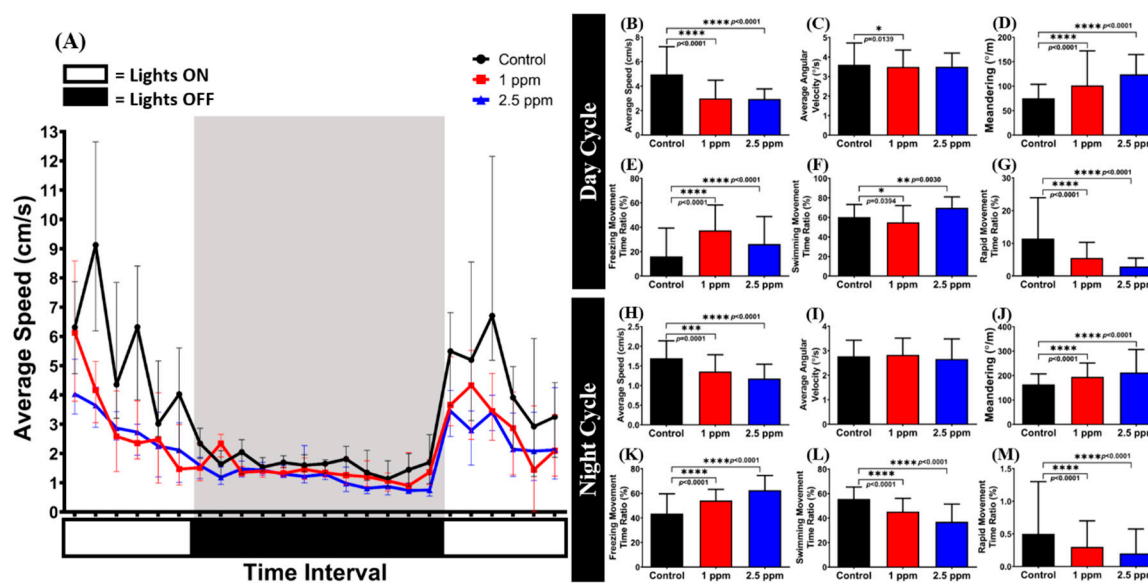


Figure 6. Evaluation of the circadian locomotor activity for control and chronic donepezil-exposed fish: (A) Circadian patterns of average speed; (B) average speed; (C) average angular velocity; (D) meandering; (E) freezing movement time ratio; (F) swimming movement time ratio; and (G) rapid movement ratio during the light cycle. (H) Average speed; (I) average angular velocity; (J) meandering; (K) freezing movement time ratio; (L) swimming movement time ratio; and (M) rapid movement ratio during the dark cycle. The data are expressed as the median with interquartile range and were analyzed using Kruskal–Wallis test followed by Dunn's multiple comparisons test (n control fish = 18; n donepezil-treated fish = 18; * $p < 0.05$, ** $p < 0.01$, *** $p < 0.001$, **** $p < 0.0001$).

3.8. Effects of DPZ Exposure in Color Preference of Zebrafish

Zebrafish have many specific photoreceptors in their cone cells to distinguish colors. Any adverse chemical effects targeting zebrafish-specific photoreceptors or neurotransmitter expression may cause changes in their color preference. The color preference tracking technique has been applied to evaluate neurodegenerative disorders, as an index for pre-clinical appraisal of drug efficacy, and behavioral

evaluation of toxicity. Moreover, color-based experiments have also been demonstrated to be associated with aversion, anxiety, or fear in the zebrafish [57]. Therefore, based on the well-known anxiolytic effect of DPZ, we suspected that DPZ might cause a slight difference in terms of zebrafish color preference. Thus, to verify this hypothesis, we performed a color preference test to investigate whether DPZ exposure affected zebrafish color preference. Generally, adult zebrafish have a clear color preference, ranked as follows: red > blue > green > yellow. Based on the results, both treatment groups did not show any significant changes, regarding their color preference ranking compared to the control group. However, the low concentration group displayed significant differences in the color choice index compared to the other groups, especially the control group. These differences were observed in the test with green–yellow, red–blue, red–yellow, and blue–yellow color combinations. In the green–yellow color combination, 1 ppm DPZ-exposed fish showed the lowest level of green color choice index among the three groups ($p < 0.0001$; $F(5, 138) = 46.03$; Figure 7B). Meanwhile, in the red–blue and red–yellow color combinations, 1 ppm DPZ-exposed fish showed a significantly higher choice index for red color than the other groups ($p < 0.0001$; $F(5, 138) = 189.3$; $p < 0.0001$; $F(5, 138) = 480.2$; Figure 7D,E). Furthermore, the most interesting results were observed in the blue–yellow color combination. In this color combination, even though the low concentration group showed a lower blue color choice index than the control, the high concentration group displayed the lowest choice index of blue color among these three groups ($p < 0.0001$; $F(5, 138) = 302.3$; Figure 7F). However, in the green–blue and green–red color combination groups, both DPZ-exposed groups displayed similar blue and red color choice indices, respectively, to control fish ($p < 0.0001$; $F(5, 138) = 24.09$; $p < 0.0001$; $F(5, 138) = 80.20$; Figure 7A,C). Taken together, zebrafish exposed to 2.5 ppm of DPZ did not show any significant difference regarding their color choice index in all of the color combinations, except in the blue–yellow combination (with a significantly low level of the blue color choice index), while 1 ppm of DPZ changed zebrafish color choice indices in several color combinations (Figure 7F).

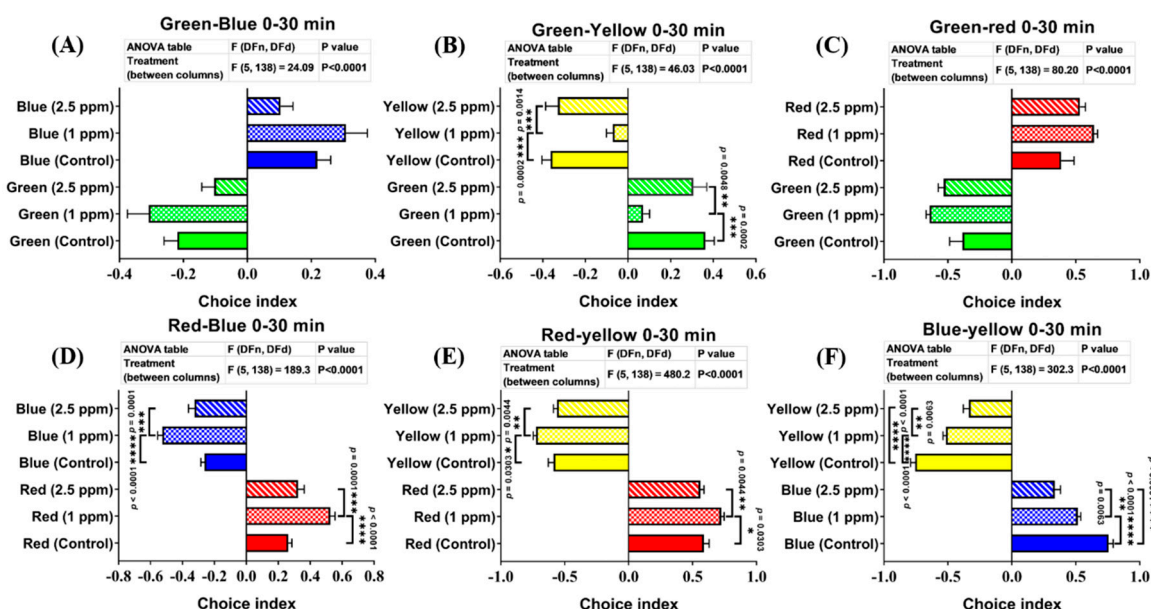


Figure 7. Comparison of the color preference behavior between control and donepezil-exposed fish after 17 days of donepezil exposure. The combinations of four colors were: (A) the green/blue test, (B) green/yellow test, (C) green/red test, (D) red/blue test, (E) red/yellow test, and (F) blue/yellow test. The data are expressed as the mean \pm SEM values and were analyzed by two-way ANOVA ($n = 24$; * $p < 0.05$, ** $p < 0.01$, *** $p < 0.001$, and **** $p < 0.0001$).

3.9. Effect of DPZ Exposure on Biomarker Expression in Zebrafish

In previous behavioral tests, DPZ exposure has been proven to induce adult zebrafish behavioral alterations in exploratory behavior, aggressiveness, social interaction, shoaling formation, and circadian locomotor activity, where these alterations might indicate an anxiolytic-like behavior. We examined the expression of biomarkers, in order to gain insight into the molecular mechanisms underlying the observed behavioral changes caused by DPZ exposure and to investigate the possible corresponding mechanisms controlling these behavioral alterations, by performing biochemical assays on some important biomarkers (Table 1). First, we tested the hypothesis that DPZ treatment reduces oxidative stress by evaluating several biomarkers of oxidative pathways in the brain and muscle by performing ELISA (Enzyme-linked immunosorbent assay) with target-specific antibodies. In brain tissues, DPZ exposure had no significant influence on reactive oxygen species (ROS), superoxide dismutase (SOD), and catalase (CAT) expression in the brain. However, DPZ treatment was found to elevate the lipid oxidation marker of the malondialdehyde (MDA) level ($p = 0.005$). In muscle tissues, DPZ exposure induced more robust biomarker changes, as shown by an elevation in ROS ($p = 0.0478$) and MDA ($p = 0.0086$) contents. Next, the determination of neurotransmitters was also performed in the brain tissues, in order to examine the possible mechanism underlying the alterations in behavioral responses of zebrafish after DPZ chronic exposure. By ELISA, the relative amounts of neurotransmitters or hormones such as cortisol, acetylcholine (ACh), acetylcholine esterase (AChE), serotonin (5-HT), norepinephrine, dopamine, γ -aminobutyric acid (GABA), kisspeptin, oxytocin, and vasotocin in the brain tissues of zebrafish could be precisely quantified and compared. From the results, it was shown that chronic DPZ exposure reduced the relative content of cortisol ($p = 0.0193$), while the oxytocin content was elevated in the brain ($p = 0.0184$). On another hand, other neurotransmitters or hormones displayed no significant differences when compared to the control group.

Table 1. Comparison of biochemical levels in brain and muscle tissue between control fish and donepezil-exposed fish by enzyme-linked immunosorbent assay (ELISA). Data are expressed as the mean ± SEM values and were analyzed by one-way ANOVA ($n = 3$; * $p < 0.05$, ** $p < 0.01$).

Biomarker	Control	1 ppm	2.5 ppm	Unit	Significance	p-Value
Brain						
Reactive Oxygen Species (ROS)	1.478 ± 0.220	1.696 ± 0.133	1.437 ± 0.108	U/μg of total protein	NO	0.812
Superoxide Dismutase (SOD)	0.324 ± 0.023	0.315 ± 0.028	0.294 ± 0.013	U/μg of total protein	NO	0.6533
Malondialdehyde (MDA)	0.010 ± 0.0003	0.009 ± 0.0004	0.008 ± 0.0002 (**)	nmol/μg of total protein	YES	0.0055
Cortisol	2.900 ± 0.190	2.485 ± 0.081	2.021 ± 0.168 (*)	pg/μg of total protein	YES	0.0193
Acetylcholine (ACh)	0.0315 ± 0.003	0.0398 ± 0.002	0.0372 ± 0.002	ng/μg of total protein	NO	0.0936
Acetylcholine esterase (AChE)	0.173 ± 0.021	0.183 ± 0.014	0.183 ± 0.005	nmol/μg of total protein	NO	0.5106
Serotonin (5-HT)	0.363 ± 0.012	0.372 ± 0.012	0.334 ± 0.008	ng/μg of total protein	NO	0.1437
Norepinephrine	0.011 ± 0.0006	0.010 ± 0.0004	0.011 ± 0.0006	ng/μg of total protein	NO	0.4131
Dopamine	0.175 ± 0.001	0.210 ± 0.011	0.199 ± 0.008	U/μg of total protein	NO	0.0716
γ-aminobutyric acid (GABA)	$1.05 \times 10^{-5} \pm 1.7 \times 10^{-7}$	$1.09 \times 10^{-5} \pm 6.6 \times 10^{-7}$	$9.90 \times 10^{-6} \pm 4.9 \times 10^{-7}$	μmol/μg of total protein	NO	0.4104
Melatonin	0.129 ± 0.005	0.133 ± 0.003	0.130 ± 0.009	pg/μg of total protein	NO	0.8793
Kisspeptin	0.798 ± 0.043	0.736 ± 0.010	0.746 ± 0.034	ng/μg of total protein	NO	0.4026
Oxytocin	0.045 ± 0.001	0.060 ± 0.002 (*)	0.048 ± 0.004	pg/μg of total protein	YES	0.0184
Vasotocin	2.603 ± 0.118	2.234 ± 0.146	2.216 ± 0.056	pg/μg of total protein	NO	0.0891
Muscle						
ROS	1.368 ± 0.141	1.479 ± 0.096	1.893 ± 0.120 (*)	U/μg of total protein	YES	0.0478
SOD	0.241 ± 0.022	0.237 ± 0.013	0.288 ± 0.012	U/μg of total protein	NO	0.1191
MDA	0.005 ± 0.0003	0.006 ± 0.0002	0.007 ± 0.0003 (**)	nmol/μg of total protein	YES	0.0086
Catalase	0.062 ± 0.003	0.061 ± 0.002	0.070 ± 0.004	U/μg of total protein	NO	0.1821
ATP	6.104 ± 0.476	6.045 ± 0.575	7.239 ± 0.224	nmol/μg of total protein	NO	0.1882

4. Discussion

Based on the findings regarding the side-effects of DPZ, regardless of its tolerability and evidence of its benefits on cognitive function, in the present study, we aimed to test the hypothesis that chronic exposure to DPZ leads to changes in behavior in healthy individuals using zebrafish as a model, as well as exploring the underlying biochemical processes affected. From the results, 2.5 ppm DPZ-exposed fish with no neurodegenerative disorder did not show any significant difference to control fish, in terms of cognitive performance. Interestingly, exposure to DPZ produced a slight improvement in the short-term memory of adult zebrafish, through the increased retention of adverse stimuli, as has been displayed in earlier studies on Alzheimer's disease patients [58,59]. It is already well-known that the efficacy of DPZ in cognitive improvement is related to the increase in ACh levels in the central nervous system through inhibiting AChE activity [60–62]. In addition, oxidative stress is one of the major factors contributing to neuronal degeneration in the brain implicated in neurobehavioral disorders [63–65]. As the main antioxidant enzymes, SOD and CAT play important roles in the defense system against oxidative stress [66]. In previous studies in mice, DPZ has been demonstrated to act as an antioxidant, an important aspect for neuroprotection, indicating its effective role in memory enhancement by decreasing biochemical markers of oxidative stress level, such as MDA [67,68]. Taken together, the assessment of ACh and AChE activities, as well as antioxidant enzyme level in the brain of zebrafish, is needed to understand the underlying mechanisms of the cognitive enhancement role of DPZ in normal zebrafish. In the present study, even though they did not reach a statistically significant level, ACh, and AChE levels tended to be slightly increased in the DPZ-treated groups, compared to the control group. Furthermore, we also found that the MDA level was significantly reduced in the brain of zebrafish exposed to 2.5 ppm DPZ, when compared to control fish. Thus, it was indicated that even the levels of ACh, AChE, and oxidative stress activities were not significantly altered after chronic exposure to donepezil; this condition is sufficient to enhance the retention of adverse stimuli in normal zebrafish, despite no significant difference occurring in their cognitive performance.

Next, DPZ was found to reduce zebrafish locomotor activity in a dose-dependent manner. This phenomenon was observed in most of our behavior assessments, including novel tank, mirror biting, predator avoidance, and circadian locomotor activity tests. Mostly, zebrafish displayed a higher reduction and variation of locomotor activity when exposed to the higher dose (2.5 ppm) of DPZ. This phenomenon may be related to the adverse effect of cholinesterase inhibitor drugs, as muscle cramps, weakness, and motor impairment are symptoms frequently associated with these drugs [69,70].

Another important finding in this study was a significant increase in the aggressiveness of zebrafish after exposure to low-dose donepezil. This finding was consistent with a previous publication in humans, reported by the Medicines Control Agency of the U.K., showing 41 cases of aggression or agitation in a total of 695 reports of a possible adverse drug reaction to DPZ [71]. Some patients became very paranoid and exhibited violent behaviors and, according to the manufacturer's report, 5% of patients became agitated (although only 1% of which showed physical aggression) after donepezil admission [72]. Next, during the novel tank and shoaling tests, anxiolytic-like behavior was observed in the DPZ-treated fish. In the novel tank test, this behavior was indicated by the longer duration spent in the top portion of the tank displayed by the DPZ-exposed fish, compared to the untreated fish. Normally, as displayed by the control group, zebrafish typically engage in the bottom area of the tank when first moved into a novel environment and start to explore the top area after a few minutes of acclimation. Therefore, more time spent in the upper part of the tank, as well as higher frequency to enter the upper area of the tank, indicate anxiolytic-like behavior in adult zebrafish [49,73]. Furthermore, loosened shoal formation in the treated group might also indicate an anxiolytic-like behavior, as previous studies have shown that anxious fish tend to swim closer together in tighter shoals, compared to non-anxious fish, when placed in a novel environment [73,74]. Taken together, even though the reduction in anxiety in humans may be the result of improvement in executive function, these results are in line with recent research that discovered the positive contribution of DPZ in moderation of anxiety in patients with mild neurocognitive impairment (MCI), where anxiety

symptoms were alleviated after 2 weeks of treatment with DPZ [75]. When studying anxiety, stress hormone levels can be used as a physiological endpoint to be paralleled with behavioral responses [76]. In this study, the biochemical assay showed decreased cortisol levels as well as slightly increased CAT levels in DPZ-exposed fish, compared to the control group. In zebrafish, cortisol is one of the physiological phenotypes which is used as a primary stress response hormone relevant to human stress physiology [77]. Excessive increases in cortisol level have been associated with hippocampal neuron dysfunction, as well as causing depression [78–80]. The alteration of stress hormone levels can also be valuable additions to parallel with behavioral observations in the study of anxiety [76]. Consistent with our findings, previous research demonstrated that chronic exposure to ethanol led to increased time spent in the upper zone with a trend towards reduced cortisol levels, indicating anxiolytic behavior in zebrafish [49]. In addition, therapies which can reduce cortisol levels also have a positive effect in treating Alzheimer’s disease (AD)-or depression-related symptoms, namely, stress, anxiety, and cognitive impairment [81–83]. Meanwhile, regarding the catalase result, a prior study discovered that CAT over-expression reduced anxiety in mice conducting the zero maze task [84]. Additionally, improved depression-like behavior associated with Alzheimer’s disease was shown to be dependent on CAT level increase induced by DPZ administration [85].

The social interaction test, another social interaction assay, showed a slightly increase in conspecific social interaction frequency in the low concentration DPZ group. In line with this result, disrupted shoaling was also displayed by the treated fish in the high concentration group. This set of results indicates that DPZ had noticeable effects on several measures used to determine zebrafish social behavior. Furthermore, these findings have been supported by a prior study which found that scopolamine-induced social behavior impairment in rats was clearly reversed by DPZ treatment [86]. Furthermore, another study found that patients with mild to moderate AD had improved social interaction, engagement, and interest after receiving treatment with DPZ [86–88].

Circadian rhythms of locomotor activity in zebrafish have been analyzed both in larvae and in adult fish, and are useful for studying the physiology of the adult zebrafish circadian system and the components of the system which are important for the generation and regulation of circadian rhythms of locomotor activity [89,90]. In addition, even though zebrafish locomotor activity was also measured in this test (as in the novel tank test), there was a fundamental difference that differentiated these tests from each other. In this test, the tested fish locomotor activity was measured after it was already acclimated in the environment while, in the novel tank test, its locomotor activity was observed when it was exposed to the new environment directly. From the results, it was shown that both concentrations of DPZ affected circadian locomotor activity, including an abnormal zigzag-like movement observed during both light and dark cycles. These abnormalities may be associated with central nervous system events affected by cholinesterase inhibition, such as sleep disorder; this symptom has mostly been reported in subjects treated with DPZ [91,92]. It has been shown that melatonin is an attractive candidate to mediate circadian processes, as the clock regulates its production (i.e., high-level signal during the night and low-level signal during the day) [93]. Moreover, melatonin has been reported to promote a sleep-like state in zebrafish [94] and to play a role in potentially linking circadian and homeostatic control of sleep [95]. In addition, cortisol has also demonstrated an important role in organizing the circadian system [80]. Cortisol peaks during daytime and an unusual increase in cortisol levels can be considered as risk factors of disease development [96]. Furthermore, even partial acute sleep loss can induce a higher cortisol level, compared to a normal sleep schedule [97]. In this study, based on the measured biochemical endpoints, we found a relationship between reduction of cortisol level and the abnormal circadian locomotor activity behavior of zebrafish after DPZ exposure. This result indicated that there was a possibility of DPZ having an effect in sleep disturbance, even in the absence of melatonin alteration. In a prior study, the potential effect of DPZ after its administration was discovered, as sleep efficiency was increased with shortened sleep latency in patients with Alzheimer’s Type Dementia (ATD) [54], having an adverse effect in a patient with night-time disturbance (NTD); thus, more research about the time of administration of DPZ is

necessary [98]. However, one has to keep in mind that, even though the daily rhythms of locomotor activity in adults and larvae zebrafish can be attributed to the circadian system, there are other ways to evaluate circadian rhythms in zebrafish besides locomotor activity, namely, hormone levels and sleep behaviors, such as sleep latency or sleep bouts/efficiency. These measurements are worth trying, in a future study, to confirm the effects of DPZ on sleep observed in the current study [55,56].

Next, the color preference test did not show any significant change in color discrimination sequence (ranking) in both concentrations of DPZ. However, in different color combinations, it was observed that treated zebrafish displayed the highest preference intensity for red color, which aligned with an earlier study which indicated the preference of zebrafish for certain colors (e.g., red) over other colors when tested in the place preference (PP) box and T-maze [99].

Beside cholinergic system analysis, other neurotransmitter assays are also necessary to validate the underlying mechanism in behavior response of zebrafish after donepezil exposure, as neurotransmitter modulation has been associated with all practically important physiological systems in the brain; thus, neurotransmitter alteration may affect several physiological behaviors that are controlled by them [100]. Dopamine and serotonin are two key neurotransmitters which regulate brain function and behavioral responses [101]. The relation of dopamine to locomotion, cognition, and even emotion has been reported before [102]; whereas serotonin has been demonstrated to be associated with aggressiveness, anxiety, as well as social interaction behavior [102,103]. Unfortunately, the relationship between unaltered dopamine level and decreased locomotor activity from donepezil exposure in zebrafish remains unknown; thus, further studies are needed to investigate the other effect linkages. However, we suggest that the decrease in locomotor activity was caused by muscle damage, considering the high level of MDA, as the status of this compound can provide an estimate of muscle stress [104]. Oxidative stress in muscle tissue was also indicated by the distinct production of ROS in the muscle of high concentration DPZ-exposed fish. In addition, the GABA receptor has been reported to modulate anxiety response, while norepinephrine (NE) plays an important role in mediating the responses related to fear and stress [105]. However, serotonin, GABA, and NE were not altered after donepezil exposure, suggesting the higher level of aggressiveness and anxiolytic behavior displayed by the exposed fish was not related to the alteration of these neurotransmitters. Furthermore, recent studies have also reported that the signaling of several neuropeptides, such as kisspeptin, is associated with some behavioral responses, including fear, anxiety, and mood [106]. In this study, the kisspeptin level of donepezil-exposed fish showed no significant difference, which may validate the similar predator avoidance behavior between treated fish and control fish. On the other hand, vasotocin, a nonapeptide hormone, has been demonstrated to reduce social interaction and shoaling behavior in zebrafish [107]. However, in this study, we could not find any related vasotocin alteration in social interaction and shoaling behavior after donepezil exposure. Nevertheless, oxytocin, another nonapeptide hormone, was significantly increased after exposure to 1 ppm donepezil for 14 days. This phenomenon might be related to the increased social interaction and increased aggressiveness of 1 ppm DPZ-exposed fish, as oxytocin has been demonstrated to reverse social interaction and aggression deficits in adult zebrafish induced by dizocilpine (MK-801) [108]. Moreover, it also acts as a crucial regulator in social interaction and the aggressive behavior of mammals [107]. Finally, it is intriguing that the chronic exposure effect of donepezil observed in the current experiment was different from the acute exposure effect of DPZ observed in the previous study by Giacomini et al., where 24 h incubation with DPZ in adult zebrafish yielded anxiogenic-like effects which were paralleled by analyses of AChE activity in the brain [109]. This difference is reasonable, as another prior study found that this drug induced changes in a number of neurotransmitters, such as dopamine, serotonin, and norepinephrine, in some specific regions including the rat dorsal hippocampus, in a time-dependent manner [110]. In addition, other studies are in progress to determine the pharmacological effects associated with acute treatment with this compound.

5. Conclusions

In summary, consistent with our hypothesis, the current study demonstrated the capability of donepezil in causing behavioral alterations in normal zebrafish; moreover, the outcomes showed significant variation with the dose of donepezil treatment, which is consistent with previous clinical studies (the overall results are summarized in Figure 8). The chemical composition of a substance plays a significant role in its toxicity mechanism inside an organism; therefore, the dissolution of concentration in the soluble form inside an organism must be understood specifically, in terms of particle-mediated toxicity. The side-effects of donepezil usually decrease after a few days or may be relieved by the maintenance of the present dose level, by omitting one or more doses, or by temporarily decreasing dosage [92,111]. In addition, even though donepezil treatment did not cause any significant difference in zebrafish cognitive performance, a slight improvement in adult zebrafish short-term memory was observed in the treated fish. However, the mechanisms underlying donepezil-associated responses in zebrafish behaviors still require further clarification. Therefore, further investigations of potential neuronal pathways are needed to understand more precisely the mechanisms underlying the behavioral responses observed.

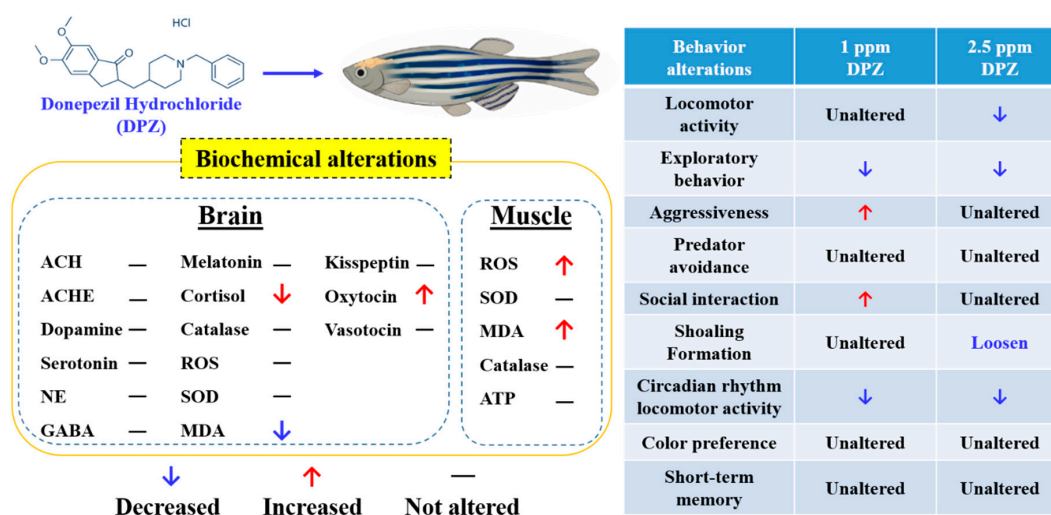


Figure 8. Summary of biochemical and behavioral changes in adult zebrafish after acute or chronic exposure to Donepezil. The behavioral alterations are summarized in the right panel and the biochemical alterations in brain and muscle tissues are summarized in the left panel.

Supplementary Materials: The following are available online at <http://www.mdpi.com/2218-273X/10/9/1340/s1>, Figure S1: Schematic diagram of the evaluation of the neurobehavioral toxicity of donepezil in normal adult zebrafish, Figure S2: Mirror biting, predator avoidance, and shoaling behavior endpoint comparisons between the control, 1 ppm, and 2.5 ppm donepezil-exposed zebrafish groups after 14 days of exposure, Table S1: The *n* number value calculated with 90% confidence interval and a margin of error of 7 units from each behavior test endpoint in control fish, Table S2: The *P* value from main effects of each circadian locomotor activity endpoint after Kruskal–Wallis test.

Author Contributions: Conceptualization, G.A., K.H.-C.C. and C.-D.H.; methodology, N.T.N.A. and B.T.N.H.; software and validation, N.M. and P.S.; formal analysis, G.A. and N.T.N.A.; investigation and resources, O.V. and O.B.V.; data curation, J.-C.H. and T.-R.G.; writing—original draft preparation, G.A., K.H.-C.C. and C.-D.H.; visualization, N.M.; supervision, K.H.-C.C. and C.-D.H.; project administration and funding acquisition, K.H.-C.C. and C.-D.H. All authors have read and agreed to the published version of the manuscript.

Funding: This study was funded by the grants sponsored by the Ministry of Science and Technology MOST 108-2313-B-033-001-MY3 and MOST 108-2622-B-033-001-CC2 to C.-D.H. and MOST 108-2113-M153-003 to K.H.-C.C.

Acknowledgments: We appreciate the Taiwan Zebrafish Core Facility at Academia Sinica (TZCAS) for providing AB strain zebrafish. We also appreciate the three anonymous reviewers and editors for their professional comments, which improved the quality of this paper.

Conflicts of Interest: The authors declare no conflict of interest. The funders had no role in the design of the study; in the collection, analyses, or interpretation of data; in the writing of the manuscript, or in the decision to publish the results.

References

1. World Health Organization. Risk reduction of cognitive decline and dementia: WHO guidelines. In *Risk Reduction of Cognitive Decline and Dementia: WHO Guidelines*; World Health Organization: Geneva, Switzerland, 2019; Available online: <https://apps.who.int/iris/bitstream/handle/10665/312180/9789241550543-eng.pdf?ua=1&ua=1&dom=prime&src=syn> (accessed on 28 August 2020).
2. Cummings, J.; Lai, T.J.; Hemrungsorn, S.; Mohandas, E.; Yun Kim, S.; Nair, G.; Dash, A. Role of donepezil in the management of neuropsychiatric symptoms in Alzheimer’s disease and dementia with lewy bodies. *CNS Neurosci. Ther.* **2016**, *22*, 159–166. [[CrossRef](#)]
3. Carrasco, M.M.; Agüera, L.; Gil, P.; Morínigo, A.; Leon, T. Safety and effectiveness of donepezil on behavioral symptoms in patients with Alzheimer disease. *Alzheimer Dis. Assoc. Disord.* **2011**, *25*, 333–340. [[CrossRef](#)]
4. Schredl, M.; Weber, B.; Leins, M.-L.; Heuser, I. Donepezil-induced REM sleep augmentation enhances memory performance in elderly, healthy persons. *Exp. Gerontol.* **2001**, *36*, 353–361. [[CrossRef](#)]
5. Cummings, J.L.; Donohue, J.A.; Brooks, R.L. The relationship between donepezil and behavioral disturbances in patients with Alzheimer’s disease. *Am. J. Geriatr. Psychiatry* **2000**, *8*, 134–140. [[CrossRef](#)]
6. Burt, T. Donepezil and related cholinesterase inhibitors as mood and behavioral controlling agents. *Curr. Psychiatry Rep.* **2000**, *2*, 473–478. [[CrossRef](#)] [[PubMed](#)]
7. De Leon-Casasola, O.A. *Cancer Pain: Pharmacologic, Interventional, and Palliative Approaches*; WB Saunders Company: Philadelphia, PA, USA, 2006.
8. Kauffman, T.L.; Barr, J.O.; Moran, M.L. *Geriatric Rehabilitation Manual*; Elsevier Health Sciences: Shanghai, China, 2007.
9. Jackson, S.; Ham, R.J.; Wilkinson, D. The safety and tolerability of donepezil in patients with Alzheimer’s disease. *Br. J. Clin. Pharmacol.* **2004**, *58*, 1–8. [[CrossRef](#)] [[PubMed](#)]
10. Cutuli, D.; De Bartolo, P.; Caporali, P.; Tartaglione, A.M.; Oddi, D.; D’Amato, F.R.; Nobili, A.; D’Amelio, M.; Petrosini, L. Neuroprotective effects of donepezil against cholinergic depletion. *Alzheimer’s Res. Ther.* **2013**, *5*, 50. [[CrossRef](#)] [[PubMed](#)]
11. Kimura, M.; Akasofu, S.; Ogura, H.; Sawada, K. Protective effect of donepezil against A β (1–40) neurotoxicity in rat septal neurons. *Brain Res.* **2005**, *1047*, 72–84. [[CrossRef](#)] [[PubMed](#)]
12. Martín-Jiménez, R.; Campanella, M.; Russell, C. New zebrafish models of neurodegeneration. *Curr. Neurol. Neurosci. Rep.* **2015**, *15*, 33. [[CrossRef](#)]
13. Kopp, R.; Legler, J.; Legradi, J. Alterations in locomotor activity of feeding zebrafish larvae as a consequence of exposure to different environmental factors. *Environ. Sci. Pollut. Res.* **2018**, *25*, 4085–4093. [[CrossRef](#)]
14. Best, J.D.; Berghmans, S.; Hunt, J.J.; Clarke, S.C.; Fleming, A.; Goldsmith, P.; Roach, A.G. Non-associative learning in larval zebrafish. *Neuropsychopharmacology* **2008**, *33*, 1206–1215. [[CrossRef](#)] [[PubMed](#)]
15. Faria, M.; Prats, E.; Novoa-Luna, K.A.; Bedrossiantz, J.; Gómez-Canela, C.; Gómez-Oliván, L.M.; Raldúa, D. Development of a vibrational startle response assay for screening environmental pollutants and drugs impairing predator avoidance. *Sci. Total. Environ.* **2019**, *650*, 87–96. [[CrossRef](#)] [[PubMed](#)]
16. Westerfield, M. *A Guide for the Laboratory Use of Zebrafish (Danio rerio)*; University of Oregon Press: Eugene, OR, USA, 2000.
17. De Abreu, M.S.; Giacomini, A.C.; dos Santos, B.E.; Genario, R.; Marchiori, N.I.; da Rosa, L.G.; Kalueff, A.V. Effects of lidocaine on adult zebrafish behavior and brain acetylcholinesterase following peripheral and systemic administration. *Neurosci. Lett.* **2019**, *692*, 181–186. [[CrossRef](#)]
18. Kim, J.; Shin, W. How to do random allocation (randomization). *Clin. Orthop. Surg.* **2014**, *6*, 103–109. [[CrossRef](#)]
19. Kotani, S.; Yamauchi, T.; Teramoto, T.; Ogura, H. Donepezil, an acetylcholinesterase inhibitor, enhances adult hippocampal neurogenesis. *Chem.-Biol. Interact.* **2008**, *175*, 227–230. [[CrossRef](#)] [[PubMed](#)]
20. Cutuli, D.; Foti, F.; Mandolesi, L.; De Bartolo, P.; Gelfo, F.; Federico, F.; Petrosini, L. Cognitive performances of cholinergically depleted rats following chronic donepezil administration. *J. Alzheimer’s Dis.* **2009**, *17*, 161–176. [[CrossRef](#)]

21. Lim, I.; Joung, H.-Y.; Yu, A.R.; Shim, I.; Kim, J.S. PET evidence of the effect of donepezil on cognitive performance in an animal model of chemobrain. *BioMed Res. Int.* **2016**, *2016*. [CrossRef]
22. Creeley, C.E.; Wozniak, D.F.; Nardi, A.; Farber, N.B.; Olney, J.W. Donepezil markedly potentiates memantine neurotoxicity in the adult rat brain. *Neurobiol. Aging* **2008**, *29*, 153–167. [CrossRef] [PubMed]
23. Jiang, L.; Wang, Y.; Su, L.; Ren, H.; Wang, C.; Chen, J.; Fu, X. Donepezil attenuates obesity-associated oxidative stress and central inflammation and improves memory deficit in mice fed a high-fat diet. *Dement. Geriatr. Cogn. Disord.* **2019**, *48*, 154–163. [CrossRef]
24. Sullivan, L. Power and sample size determination. Available online: https://sphweb.bumc.bu.edu/otlt/mph-modules/bs/bs704_power/bs704_power_print.html (accessed on 28 August 2020).
25. Rabbane, M.G.; Rahman, M.M.; Hossain, M.A. Effects of stocking density on growth of zebrafish (*Danio rerio*, Hamilton, 1822). *Bangladesh J. Zool.* **2016**, *44*, 209–218. [CrossRef]
26. Lidster, K.; Readman, G.D.; Prescott, M.J.; Owen, S.F. International survey on the use and welfare of zebrafish *Danio rerio* in research. *J. Fish Biol.* **2017**, *90*, 1891–1905. [CrossRef] [PubMed]
27. Aleström, P.; D’Angelo, L.; Midtlyng, P.J.; Schorderet, D.F.; Schulte-Merker, S.; Sohm, F.; Warner, S. Zebrafish: Housing and husbandry recommendations. *Lab. Anim.* **2019**. [CrossRef] [PubMed]
28. Castranova, D.; Lawton, A.; Lawrence, C.; Baumann, D.P.; Best, J.; Coscolla, J.; Doherty, A.; Ramos, J.; Hakkesteg, J.; Wang, C. The effect of stocking densities on reproductive performance in laboratory zebrafish (*Danio rerio*). *Zebrafish* **2011**, *8*, 141–146. [CrossRef] [PubMed]
29. Ngoc Hieu, B.T.; Ngoc Anh, N.T.; Audira, G.; Juniardi, S.; Liman, R.A.D.; Villaflores, O.B.; Lai, Y.-H.; Chen, J.-R.; Liang, S.-T.; Huang, J.-C. Development of a modified three-day t-maze protocol for evaluating learning and memory capacity of adult zebrafish. *Int. J. Mol. Sci.* **2020**, *21*, 1464. [CrossRef]
30. Aoki, R.; Tsuboi, T.; Okamoto, H. Y-maze avoidance: An automated and rapid associative learning paradigm in zebrafish. *Neurosci. Res.* **2015**, *91*, 69–72. [CrossRef]
31. Colwill, R.M.; Raymond, M.P.; Ferreira, L.; Escudero, H. Visual discrimination learning in zebrafish (*Danio rerio*). *Behav. Process.* **2005**, *70*, 19–31. [CrossRef]
32. Mueller, K.P.; Neuhauss, S.C. Automated visual choice discrimination learning in zebrafish (*Danio rerio*). *J. Integr. Neurosci.* **2012**, *11*, 73–85. [CrossRef]
33. Audira, G.; Sarasamma, S.; Chen, J.-R.; Juniardi, S.; Sampurna, B.; Liang, S.-T.; Lai, Y.-H.; Lin, G.-M.; Hsieh, M.-C.; Hsiao, C.-D. Zebrafish mutants carrying leptin (*lepa*) gene deficiency display obesity, anxiety, less aggression and fear, and circadian rhythm and color preference dysregulation. *Int. J. Mol. Sci.* **2018**, *19*, 4038. [CrossRef]
34. Braidia, D.; Ponzoni, L.; Martucci, R.; Sparatore, F.; Gotti, C.; Sala, M. Role of neuronal nicotinic acetylcholine receptors (nAChRs) on learning and memory in zebrafish. *Psychopharmacology* **2014**, *231*, 1975–1985. [CrossRef]
35. Audira, G.; Sampurna, B.; Juniardi, S.; Liang, S.-T.; Lai, Y.-H.; Hsiao, C.-D. A versatile setup for measuring multiple behavior endpoints in zebrafish. *Inventions* **2018**, *3*, 75. [CrossRef]
36. Audira, G.; Sampurna, B.P.; Juniardi, S.; Liang, S.-T.; Lai, Y.-H.; Han, L.; Hsiao, C.-D. Establishing simple image-based methods and a cost-effective instrument for toxicity assessment on circadian rhythm dysregulation in fish. *Biol. Open* **2019**, *8*. [CrossRef] [PubMed]
37. Adams, D.C.; Anthony, C.D. Using randomization techniques to analyse behavioural data. *Anim. Behav.* **1996**, *51*, 733–738. [CrossRef]
38. Audira, G.; Sampurna, B.P.; Juniardi, S.; Liang, S.-T.; Lai, Y.-H.; Hsiao, C.-D. A simple setup to perform 3D locomotion tracking in zebrafish by using a single camera. *Inventions* **2018**, *3*, 11. [CrossRef]
39. Itoh, J.; Nabeshima, T.; Kameyama, T. Utility of an elevated plus-maze for the evaluation of memory in mice: Effects of nootropics, scopolamine and electroconvulsive shock. *Psychopharmacology* **1990**, *101*, 27–33. [CrossRef] [PubMed]
40. Dudchenko, P.A. An overview of the tasks used to test working memory in rodents. *Neurosci. Biobehav. Rev.* **2004**, *28*, 699–709. [CrossRef] [PubMed]
41. Deacon, R.M.; Rawlins, J.N.P. T-maze alternation in the rodent. *Nat. Protoc.* **2006**, *1*, 7. [CrossRef] [PubMed]
42. Williams, F.E.; White, D.; Messer, W.S., Jr. A simple spatial alternation task for assessing memory function in zebrafish. *Behav. Process.* **2002**, *58*, 125–132. [CrossRef]
43. Darland, T.; Dowling, J.E. Behavioral screening for cocaine sensitivity in mutagenized zebrafish. *Proc. Natl. Acad. Sci. USA* **2001**, *98*, 11691–11696. [CrossRef]

44. Levin, E.D.; Pizarro, K.; Pang, W.G.; Harrison, J.; Ramsdell, J.S. Persisting behavioral consequences of prenatal domoic acid exposure in rats. *Neurotoxicology Teratol.* **2005**, *27*, 719–725. [[CrossRef](#)]
45. Mathangi, D.; Namasivayam, A. Effect of chronic cyanide intoxication on memory in albino rats. *Food Chem. Toxicol.* **2000**, *38*, 51–55. [[CrossRef](#)]
46. McGaugh, J.L.; Roozendaal, B. Drug enhancement of memory consolidation: Historical perspective and neurobiological implications. *Psychopharmacology* **2009**, *202*, 3–14. [[CrossRef](#)] [[PubMed](#)]
47. Takahashi, R.N.; Pamplona, F.A.; Fernandes, M.S. The cannabinoid antagonist SR141716A facilitates memory acquisition and consolidation in the mouse elevated T-maze. *Neurosci. Lett.* **2005**, *380*, 270–275. [[CrossRef](#)] [[PubMed](#)]
48. Graeff, F.; Viana, M.; Tomaz, C. The elevated T maze, a new experimental model of anxiety and memory: Effect of diazepam. *Braz. J. Med Biol. Res.* **1993**, *26*, 67–70. [[PubMed](#)]
49. Egan, R.J.; Bergner, C.L.; Hart, P.C.; Cachat, J.M.; Canavello, P.R.; Elegante, M.F.; Elkhayat, S.I.; Bartels, B.K.; Tien, A.K.; Tien, D.H. Understanding behavioral and physiological phenotypes of stress and anxiety in zebrafish. *Behav. Brain Res.* **2009**, *205*, 38–44. [[CrossRef](#)] [[PubMed](#)]
50. Pham, M.; Raymond, J.; Hester, J.; Kyzar, E.; Gaikwad, S.; Bruce, I.; Fryar, C.; Chanin, S.; Enriquez, J.; Bagawandoss, S. Assessing social behavior phenotypes in adult zebrafish: Shoaling, social preference, and mirror biting tests. In *Zebrafish Protocols for Neurobehavioral Research*; Springer: Berlin/Heidelberg, Germany, 2012; pp. 231–246.
51. Liu, Z.-H.; Li, Y.-W.; Hu, W.; Chen, Q.-L.; Shen, Y.-J. Mechanisms involved in tributyltin-enhanced aggressive behaviors and fear responses in male zebrafish. *Aquat. Toxicol.* **2020**, *220*, 105408. [[CrossRef](#)]
52. Cachat, J.; Kyzar, E.J.; Collins, C.; Gaikwad, S.; Green, J.; Roth, A.; El-Ounsi, M.; Davis, A.; Pham, M.; Landsman, S. Unique and potent effects of acute ibogaine on zebrafish: The developing utility of novel aquatic models for hallucinogenic drug research. *Behav. Brain Res.* **2013**, *236*, 258–269. [[CrossRef](#)] [[PubMed](#)]
53. Buske, C. *Zebrafish Shoaling Behavior: Its Development, Quantification, Neuro-Chemical Correlates, and Application in a Disease Model*; University of Toronto: Toronto, ON, Canada, 2013.
54. Mizuno, S.; Kameda, A.; Inagaki, T.; Horiguchi, J. Effects of donepezil on Alzheimer’s disease: The relationship between cognitive function and rapid eye movement sleep. *Psychiatry Clin. Neurosci.* **2004**, *58*, 660–665. [[CrossRef](#)]
55. Wolter, M.E.; Svoboda, K.R. Doing the locomotion: Insights and potential pitfalls associated with using locomotor activity as a readout of the circadian rhythm in larval zebrafish. *J. Neurosci. Methods* **2020**, *330*, 108465. [[CrossRef](#)]
56. Del Pozo, A.; Sánchez-Férez, J.A.; Sánchez-Vázquez, F.J. Circadian rhythms of self-feeding and locomotor activity in zebrafish (*Danio rerio*). *Chronobiol. Int.* **2011**, *28*, 39–47. [[CrossRef](#)]
57. Blaser, R.E.; Rosemberg, D.B. Measures of anxiety in zebrafish (*Danio rerio*): Dissociation of black/white preference and novel tank test. *PLoS ONE* **2012**, *7*, e36931. [[CrossRef](#)]
58. Burns, A.; Rossor, M.; Hecker, J.; Gauthier, S.; Petit, H.; Möller, H.-J.; Rogers, S.; Friedhoff, L. The Effects of Donepezil in Alzheimer’s Disease—Results from a Multinational Trial1. *Dement. Geriatr. Cogn. Disord.* **1999**, *10*, 237–244. [[CrossRef](#)] [[PubMed](#)]
59. Winblad, B.; Engedal, K.; Soininen, H.; Verhey, F.; Waldemar, G.; Wimo, A.; Wetterholm, A.-L.; Zhang, R.; Haglund, A.; Subbiah, P. A 1-year, randomized, placebo-controlled study of donepezil in patients with mild to moderate AD. *Neurology* **2001**, *57*, 489–495. [[CrossRef](#)] [[PubMed](#)]
60. Karvat, G.; Kimchi, T. Acetylcholine elevation relieves cognitive rigidity and social deficiency in a mouse model of autism. *Neuropsychopharmacology* **2014**, *39*, 831. [[CrossRef](#)] [[PubMed](#)]
61. Bryson, H.M.; Benfield, P. Donepezil. *Drugs Aging* **1997**, *10*, 234–239; discussion 240–231. [[CrossRef](#)]
62. Kosasa, T.; Kuriya, Y.; Matsui, K.; Yamanishi, Y. Effect of donepezil hydrochloride (E2020) on basal concentration of extracellular acetylcholine in the hippocampus of rats. *Eur. J. Pharmacol.* **1999**, *380*, 101–107. [[CrossRef](#)]
63. Hawkins, C.L.; Davies, M.J. Generation and propagation of radical reactions on proteins. *Biochim. Biophys. Acta (BBA)-Bioenerg.* **2001**, *1504*, 196–219. [[CrossRef](#)]
64. Keller, J.; Schmitt, F.; Scheff, S.; Ding, Q.; Chen, Q.; Butterfield, D.; Markesbery, W. Evidence of increased oxidative damage in subjects with mild cognitive impairment. *Neurology* **2005**, *64*, 1152–1156. [[CrossRef](#)]
65. Behl, C.; Skutella, T.; Frank, L.H.; Post, A.; Widmann, M.; Newton, C.J.; Holsboer, F. Neuroprotection against oxidative stress by estrogens: Structure-activity relationship. *Mol. Pharmacol.* **1997**, *51*, 535–541. [[CrossRef](#)]

66. Ighodaro, O.; Akinloye, O. First line defence antioxidants-superoxide dismutase (SOD), catalase (CAT) and glutathione peroxidase (GPX): Their fundamental role in the entire antioxidant defence grid. *Alex. J. Med.* **2018**, *54*, 287–293. [[CrossRef](#)]
67. Saxena, G.; Singh, S.P.; Agrawal, R.; Nath, C. Effect of donepezil and tacrine on oxidative stress in intracerebral streptozotocin-induced model of dementia in mice. *Eur. J. Pharmacol.* **2008**, *581*, 283–289. [[CrossRef](#)]
68. Munishamappa, V.; Vijayakumar, A.; Rajathilagam, T. Evaluation of the antioxidant activity of donepezil-in vitro study. *Natl. J. Physiol. Pharm. Pharmacol.* **2019**, *9*, 108–110. [[CrossRef](#)]
69. Folkesson, A.; Honoré, P.H.; Andersen, L.M.; Kristensen, P.; Bjerrum, O.J. Low dose of donepezil improves gabapentin analgesia in the rat spared nerve injury model of neuropathic pain: Single and multiple dosing studies. *J. Neural Transm.* **2010**, *117*, 1377–1385. [[CrossRef](#)] [[PubMed](#)]
70. Caldwell, J.E. Clinical limitations of acetylcholinesterase antagonists. *J. Crit. Care* **2009**, *24*, 21–28. [[CrossRef](#)]
71. Dunn, N.; Pearce, G.; Shakir, S. Adverse effects associated with the use of donepezil in general practice in England. *J. Psychopharmacol.* **2000**, *14*, 406–408. [[CrossRef](#)] [[PubMed](#)]
72. Bouman, W.P.; Pinner, G. Violent behavior associated with donepezil. *Am. J. Psychiatry* **1998**, *155*, 1626a–1626. [[CrossRef](#)]
73. Hamilton, T.J.; Morrill, A.; Lucas, K.; Gallup, J.; Harris, M.; Healey, M.; Pitman, T.; Schalomon, M.; Digweed, S.; Tresguerres, M. Establishing zebrafish as a model to study the anxiolytic effects of scopolamine. *Sci. Rep.* **2017**, *7*, 15081. [[CrossRef](#)]
74. Miller, N.; Gerlai, R. From schooling to shoaling: Patterns of collective motion in zebrafish (*Danio rerio*). *PLoS ONE* **2012**, *7*, e48865. [[CrossRef](#)] [[PubMed](#)]
75. Chu, C.-W.; Liang, C.-S.; Wan, F.-J. Adjunctive Donepezil for anxiety symptoms with poor response to paroxetine in a patient with probable mild cognitive impairment. *Clin. Neuropharmacol.* **2018**, *41*, 236–237. [[CrossRef](#)]
76. Alsop, D.; Vijayan, M. The zebrafish stress axis: Molecular fallout from the teleost-specific genome duplication event. *Gen. Comp. Endocrinol.* **2009**, *161*, 62–66. [[CrossRef](#)]
77. Barcellos, L.J.G.; Ritter, F.; Kreutz, L.C.; Quevedo, R.M.; da Silva, L.B.; Bedin, A.C.; Finco, J.; Cericato, L. Whole-body cortisol increases after direct and visual contact with a predator in zebrafish, *Danio rerio*. *Aquaculture* **2007**, *272*, 774–778. [[CrossRef](#)]
78. Brody, S.; Preut, R.; Schommer, K.; Schürmeyer, T.H. A randomized controlled trial of high dose ascorbic acid for reduction of blood pressure, cortisol, and subjective responses to psychological stress. *Psychopharmacology* **2002**, *159*, 319–324. [[CrossRef](#)] [[PubMed](#)]
79. Harris, T.; Borsanyi, S.; Messari, S.; Stanford, K.; Cleary, S.; Shiers, H.; Brown, G.; Herbert, J. Morning cortisol as a risk factor for subsequent major depressive disorder in adult women. *Br. J. Psychiatry* **2000**, *177*, 505–510. [[CrossRef](#)] [[PubMed](#)]
80. Herbert, J. Cortisol and depression: Three questions for psychiatry. *Psychol. Med.* **2013**, *43*, 449–469. [[CrossRef](#)] [[PubMed](#)]
81. Aboulafia-Brakha, T.; Suchecki, D.; Gouveia-Paulino, F.; Nitrini, R.; Ptak, R. Cognitive-behavioural group therapy improves a psychophysiological marker of stress in caregivers of patients with Alzheimer’s disease. *Aging Ment. Health* **2014**, *18*, 801–808. [[CrossRef](#)]
82. Field, T.; Hernandez-Reif, M.; Diego, M.; Schanberg, S.; Kuhn, C. Cortisol decreases and serotonin and dopamine increase following massage therapy. *Int. J. Neurosci.* **2005**, *115*, 1397–1413. [[CrossRef](#)]
83. Kaimal, G.; Ray, K.; Muniz, J. Reduction of cortisol levels and participants’ responses following art making. *Art Ther.* **2016**, *33*, 74–80. [[CrossRef](#)]
84. Olsen, R.H.; Johnson, L.A.; Zuloaga, D.G.; Limoli, C.L.; Raber, J. Enhanced hippocampus-dependent memory and reduced anxiety in mice over-expressing human catalase in mitochondria. *J. Neurochem.* **2013**, *125*, 303–313. [[CrossRef](#)]
85. Abdel-Salam, O.M.; Youness, E.R.; Morsy, F.A.; Mahfouz, M.M.; Kenawy, S.A. Study of the effect of antidepressant drugs and donepezil on aluminum-induced memory impairment and biochemical alterations in rats. *Comp. Clin. Pathol.* **2015**, *24*, 847–860. [[CrossRef](#)]
86. Riedel, G.; Kang, S.; Choi, D.; Platt, B. Scopolamine-induced deficits in social memory in mice: Reversal by donepezil. *Behav. Brain Res.* **2009**, *204*, 217–225. [[CrossRef](#)]
87. Boada-Rovira, M.; Brodaty, H.; Cras, P.; Baloyannis, S.; Emre, M.; Zhang, R.; Bahra, R. Efficacy and safety of donepezil in patients with Alzheimer’s disease. *Drugs Aging* **2004**, *21*, 43–53. [[CrossRef](#)]

88. Rockwood, K.; Graham, J.; Fay, S. Goal setting and attainment in Alzheimer’s disease patients treated with donepezil. *J. Neurol., Neurosurg. Psychiatry* **2002**, *73*, 500–507. [[CrossRef](#)] [[PubMed](#)]
89. López-Olmeda, J.F.; Madrid, J.A.; Sánchez-Vázquez, F.J. Light and temperature cycles as zeitgebers of zebrafish (*Danio rerio*) circadian activity rhythms. *Chronobiol. Int.* **2006**, *23*, 537–550. [[CrossRef](#)] [[PubMed](#)]
90. Hurd, M.W.; Debruyne, J.; Straume, M.; Cahill, G.M. Circadian rhythms of locomotor activity in zebrafish. *Physiol. Behav.* **1998**, *65*, 465–472. [[CrossRef](#)]
91. Inglis, F. The tolerability and safety of cholinesterase inhibitors in the treatment of dementia. *Int. J. Clin. Pract. Suppl.* **2002**, *127*, 45–63.
92. Mimica, N.; Presečki, P. Side effects of approved antidementives. *Psychiatr. Danub.* **2009**, *21*, 108–113. [[PubMed](#)]
93. Klein, D.C. Arylalkylamine N-acetyltransferase: “The Timezyme”. *J. Biol. Chem.* **2007**, *282*, 4233–4237. [[CrossRef](#)]
94. Zhdanova, I.V.; Wang, S.Y.; Leclair, O.U.; Danilova, N.P. Melatonin promotes sleep-like state in zebrafish. *Brain Res.* **2001**, *903*, 263–268. [[CrossRef](#)]
95. Gandhi, A.V.; Mosser, E.A.; Oikonomou, G.; Prober, D.A. Melatonin is required for the circadian regulation of sleep. *Neuron* **2015**, *85*, 1193–1199. [[CrossRef](#)]
96. Ziv, L.; Muto, A.; Schoonheim, P.J.; Meijnsing, S.H.; Strasser, D.; Ingraham, H.A.; Schaaf, M.J.; Yamamoto, K.R.; Baier, H. An affective disorder in zebrafish with mutation of the glucocorticoid receptor. *Mol. Psychiatry* **2013**, *18*, 681. [[CrossRef](#)]
97. Leproult, R.; Copinschi, G.; Buxton, O.; Van Cauter, E. Sleep loss results in an elevation of cortisol levels the next evening. *Sleep* **1997**, *20*, 865–870.
98. Agboton, C.; Mahdavian, S.; Singh, A.; Ghazvini, P.; Hill, A.; Sweet, R. Impact of nighttime donepezil administration on sleep in the older adult population: A retrospective study. *Ment. Health Clin.* **2014**, *4*, 257–259. [[CrossRef](#)]
99. Avdesh, A.; Martin-Iverson, M.T.; Mondal, A.; Chen, M.; Askraha, S.; Morgan, N.; Lardelli, M.; Groth, D.M.; Verdile, G.; Martins, R.N. Evaluation of color preference in zebrafish for learning and memory. *J. Alzheimer’s Dis.* **2012**, *28*, 459–469. [[CrossRef](#)]
100. Panula, P.; Sallinen, V.; Sundvik, M.; Kolehmainen, J.; Torkko, V.; Tiittula, A.; Moshnyakov, M.; Podlasz, P. Modulatory neurotransmitter systems and behavior: Towards zebrafish models of neurodegenerative diseases. *Zebrafish* **2006**, *3*, 235–247. [[CrossRef](#)] [[PubMed](#)]
101. Da Rocha, A.; Kist, L.; Almeida, E.; Silva, D.; Bonan, C.; Altenhofen, S.; Kaufmann Jr, C.; Bogo, M.; Barros, D.; Oliveira, S. Neurotoxicity in zebrafish exposed to carbon nanotubes: Effects on neurotransmitters levels and antioxidant system. *Comp. Biochem. Physiol. Part C: Toxicol. Pharmacol.* **2019**, *218*, 30–35. [[CrossRef](#)] [[PubMed](#)]
102. Rico, E.; Rosemberg, D.; Seibt, K.; Capiotti, K.; Da Silva, R.; Bonan, C. Zebrafish neurotransmitter systems as potential pharmacological and toxicological targets. *Neurotoxicology Teratol.* **2011**, *33*, 608–617. [[CrossRef](#)] [[PubMed](#)]
103. Parsey, R.V. Serotonin receptor imaging: Clinically useful? *J. Nucl. Med.* **2010**, *51*, 1495–1498. [[CrossRef](#)]
104. Brancaccio, P.; Lippi, G.; Maffulli, N. Biochemical markers of muscular damage. *Clin. Chem. Lab. Med.* **2010**, *48*, 757–767. [[CrossRef](#)] [[PubMed](#)]
105. Dell’Osso, B.; Buoli, M.; Baldwin, D.S.; Altamura, A.C. Serotonin norepinephrine reuptake inhibitors (SNRIs) in anxiety disorders: A comprehensive review of their clinical efficacy. *Hum. Psychopharmacol. Clin. Exp.* **2010**, *25*, 17–29. [[CrossRef](#)]
106. Comninou, A.N.; Dhillon, W.S. Emerging roles of kisspeptin in sexual and emotional brain processing. *Neuroendocrinology* **2018**, *106*, 195–202. [[CrossRef](#)]
107. Lindeyer, C.M.; Langen, E.M.; Swaney, W.T.; Reader, S.M. Nonapeptide influences on social behaviour: Effects of vasotocin and isotocin on shoaling and interaction in zebrafish. *Behaviour* **2015**, *152*, 897–915. [[CrossRef](#)]
108. Zimmermann, F.F.; Gaspary, K.V.; Siebel, A.M.; Bonan, C.D. Oxytocin reversed MK-801-induced social interaction and aggression deficits in zebrafish. *Behav. Brain Res.* **2016**, *311*, 368–374. [[CrossRef](#)] [[PubMed](#)]
109. Giacomini, A.; Bueno, B.; Marcon, L.; Scolari, N.; Genario, R.; Demin, K.; Kolesnikova, T.; Kalueff, A.; Abreu, M. An Acetylcholinesterase (Ache) Inhibitor Donepezil Increases Anxiety and Cortisol Levels in Adult Zebrafish. *J. Psychopharmacol.* **2020**. [[CrossRef](#)] [[PubMed](#)]








110. Shearman, E.; Rossi, S.; Szasz, B.; Juranyi, Z.; Fallon, S.; Pomara, N.; Sershen, H.; Lajtha, A. Changes in cerebral neurotransmitters and metabolites induced by acute donepezil and memantine administrations: A microdialysis study. *Brain Res. Bull.* **2006**, *69*, 204–213. [[CrossRef](#)] [[PubMed](#)]
111. Courtney, C.; Farrell, D.; Gray, R.; Hills, R.; Lynch, L.; Sellwood, E.; Edwards, S.; Hardyman, W.; Raftery, J.; Crome, P. Long-term donepezil treatment in 565 patients with Alzheimer’s disease (AD2000): Randomised double-blind trial. *Lancet (London, England)* **2004**, *363*, 2105–2115.



© 2020 by the authors. Licensee MDPI, Basel, Switzerland. This article is an open access article distributed under the terms and conditions of the Creative Commons Attribution (CC BY) license (<http://creativecommons.org/licenses/by/4.0/>).

Article

Postoperative Administration of the Acetylcholinesterase Inhibitor, Donepezil, Interferes with Bone Healing and Implant Osseointegration in a Rat Model

Faez Saleh Al-Hamed ¹, Ola M. Maria ¹, Jeff Phan ¹, Ahmed Al Subaie ^{1,2}, Qiman Gao ¹, Alaa Mansour ¹, Lina Abu Nada ¹, Imane Boukhatem ^{3,4}, Osama A. Elkashty ^{1,5}, Simon D. Tran ¹, Marie Lordkipanidzé ^{3,4}, Zahi Badran ^{1,6,7} and Faleh Tamimi ^{1,8,*}

- ¹ Faculty of Dentistry, McGill University, Montreal, QC H3A0C7, Canada; Faez.al-hamed@mail.mcgill.ca (F.S.A.-H.); ola.maria@mail.mcgill.ca (O.M.M.); jeff.phan@mail.mcgill.ca (J.P.); ahmed.alsubaie@mail.mcgill.ca (A.A.S.); qiman.gao@mail.mcgill.ca (Q.G.); alaa.mansour@mail.mcgill.ca (A.M.); lina.abunada@mail.mcgill.ca (L.A.N.); osama.elkashty@mail.mcgill.ca (O.A.E.); simon.tran@mcgill.ca (S.D.T.); zahi.badran@mcgill.ca (Z.B.)
- ² College of Dentistry, Imam Abdulrahman bin Faisal University, Dammam 34212, Saudi Arabia
- ³ Faculté de Pharmacie, Université de Montréal, Montréal, QC H3T 1J4, Canada; imane-bkm@hotmail.fr (I.B.); marie.lordkipanidze@umontreal.ca (M.L.)
- ⁴ Research Center, Montreal Heart Institute, Montreal, QC H1T 1C8, Canada
- ⁵ Faculty of Dentistry, Mansoura University, Mansoura 35516, Egypt
- ⁶ Department of Periodontology (CHU/Rmes Inserm U1229/UIC11), Faculty of Dental Surgery, University of Nantes, 44042 Nantes, France
- ⁷ College of Dental Medicine, University of Sharjah, Sharjah, P.O. Box 27272, UAE
- ⁸ College of Dental Medicine, Qatar University, Doha P.O. 2713, Qatar
- * Correspondence: faleh.tamimimarino@mcgill.ca; Tel.: +1-(514)-398-7203 (ext. 09654)

Received: 3 August 2020; Accepted: 10 September 2020; Published: 14 September 2020



Abstract: Donepezil is an acetylcholinesterase inhibitor commonly used to treat mild to moderate Alzheimer's disease. Its use has been associated with increased bone mass in humans and animals. However, the effect of postoperative administration of donepezil on bone healing remains unknown. Therefore, this study aimed to assess the impact of postoperative injection of donepezil on bone healing, titanium-implant osseointegration, and soft tissue healing. Twenty-two Sprague-Dawley rats were randomly assigned to receive a daily dose of either donepezil (0.6 mg/kg) or saline as a control. In each rat, a uni-cortical defect was created in the right tibia metaphysis and a custom-made titanium implant was placed in the left tibiae. After two weeks, rats were euthanized, and their bones were analysed by Micro-CT and histology. The healing of bone defect and implant osseointegration in the rats treated with donepezil were significantly reduced compared to the saline-treated rats. Histomorphometric analysis showed lower immune cell infiltration in bone defects treated with donepezil compared to the saline-treated defects. On the other hand, the healing time of soft tissue wounds was significantly shorter in donepezil-treated rats compared to the controls. In conclusion, short-term administration of donepezil hinders bone healing whereas enhancing soft tissue healing.

Keywords: acetylcholinesterase inhibitors; bone healing; osseointegration; donepezil; hemostasis

1. Introduction

Bone remodeling is a continuous process of bone resorption by osteoclasts followed by bone formation by osteoblasts [1]. It is regulated locally through direct interactions between osteoclasts,

osteoblasts, and immune cells, and centrally through three axes: the hypothalamic-pituitary-thyroid axis, the co-regulation of adipose tissue, bone tissue, and energy metabolism axis, and the IL-1 autonomic nervous system axis [2–7]. The latter two axes are mediated by both branches of the autonomic nervous system: the adrenergic and cholinergic branches. The adrenergic branch favors bone resorption, whereas the cholinergic branch favors bone formation [2].

The cholinergic system is regulated by the neurotransmitter, acetylcholine, an endogenous chemical that allows signal transmission between neurons [8]. Acetylcholine can activate nicotinic or muscarinic cholinergic receptors. The nicotinic receptors consist of α , β , γ , δ and ϵ subunits that form the ion channels. The muscarinic receptors are guanine nucleotide protein coupled receptors (m1, m2, m3, m4, and m5). Both muscarinic and nicotinic receptors are expressed on the membrane of bone cells and mesenchymal stem cells [9]. Among them, the nicotinic subtype- α 2 receptor and muscarinic-3 (m3) receptor affect bone remodeling [4,10]. Studies showed that knockout mice of nicotinic subtype- α 2 receptors are osteoporotic due to osteoclast upregulation [4], whereas m3 knockout mice are osteoporotic due to reduced osteoblast numbers and increased osteoclast numbers [10]. The stimulation of muscarinic receptors in vitro showed an increase in osteoblast proliferation [11]. In addition, the cholinergic system increases bone mass directly by inducing osteoclast apoptosis through the activation of the nicotinic receptors and indirectly by inhibiting the sympathetic nervous system signaling [4].

The hypothalamic cholinergic receptors are degraded in elderly patients (e.g., Alzheimer's disease (AD) patients) and thus may affect their bone health [12]. AD is the most common type of dementia affecting the elderly population and it is characterized by the neurodegeneration of the central nervous system (CNS). Acetylcholinesterase inhibitors (AChEIs) are a group of medications including Donepezil, Rivastigmine and Galantamine which are commonly used to treat mild to moderate cases of AD [13]. These drugs act as reversible acetylcholinesterase inhibitors that raise the concentration of acetylcholine at the neural synapses and result in improving patient's memory [14]. In addition, these medications have been found to stimulate muscarinic cholinergic pathways and thereby have beneficial effects on bone metabolism [15].

A considerable number of elderly patients including Alzheimer's patients are osteoporotic; they have reduced bone remodeling capacity and increased fracture risk [16]. Interestingly, the long-term use of AChEIs has been found to reduce the risk of hip fracture and enhance the outcomes of hip fracture surgeries in AD patients [17,18]. In addition, donepezil was found to reduce serum adrenaline level, a coagulation factor that affects hemostasis [15]. Hemostasis is required for bone and soft tissue regeneration and any disturbance in blood hemostasis may interfere with tissue healing. We hypothesized that cholinergic receptors can affect inflammation, coagulation, and bone formation, thus donepezil could affect bone healing by affecting hemostasis and inflammation. Therefore, we aimed to assess the effect of postoperative injection of donepezil on bone healing, soft tissue healing and hemostasis in a rat model. The use of acetylcholinesterase inhibitors by AD patients suffering from bone fractures has been associated with reduced risk of fracture non-union, improved bone quality, and fewer complications when compared to non-users [17]. Thus, understanding how postoperative administration of donepezil affects bone and soft tissue healing may have clinical implications in these patients.

2. Materials and Methods

This study was approved by McGill Animal Care and Use Committee (protocol # 2012–7269) in accordance with the Canadian Council for Animal Care guidelines.

2.1. Animals

A total of 30 healthy female (10–12 weeks-old) Sprague Dawley rats (Charles River Laboratories, Montreal, QC, Canada), weighing 200–250 g were purchased and housed (two animals per cage) in the Genome Animal Facility of McGill University. All animals were kept in a controlled environment at 22 °C and a humidity of 30–70% with 12-h light/dark cycles and were allowed to acclimatize to the new environment for two weeks prior to surgery. Water and a rodent diet were provided (ad libitum),

and rats were monitored daily by a veterinarian in the animal facility. Out of the 30 rats, eight rats were used for hemostasis assessment and 22 rats underwent surgery to assess bone healing and implant osseointegration. Eight rats of the rats that underwent bone surgeries, were used for soft tissue healing assessment.

2.2. Bone Healing Assessment

Twenty-two rats were used for bone healing assessment. Bilateral tibial bone defects were conducted as previously described [19]. A unicortical defect (1.5 mm \varnothing) was created in the left tibia, and a custom-made titanium implant (1.5 mm $\varnothing \times$ 2.0 mm depth, McMaster-CARR; Aurora, OH, USA) was inserted. In the right tibia, a unicortical defect (2.5 mm \varnothing) was created and was left empty. Postoperatively, the rats were divided randomly using a sealed envelope into two groups: the experimental group received daily subcutaneous injections of donepezil (0.6 mg/kg/day, Sigma-Aldrich) as described previously [15,20] and the control group received daily subcutaneous injections of saline (1 mL/kg/day). Rats were euthanized after two weeks using an overdose of CO₂, and their tibiae were collected and analysed using micro-CT and histology (Figure 1).

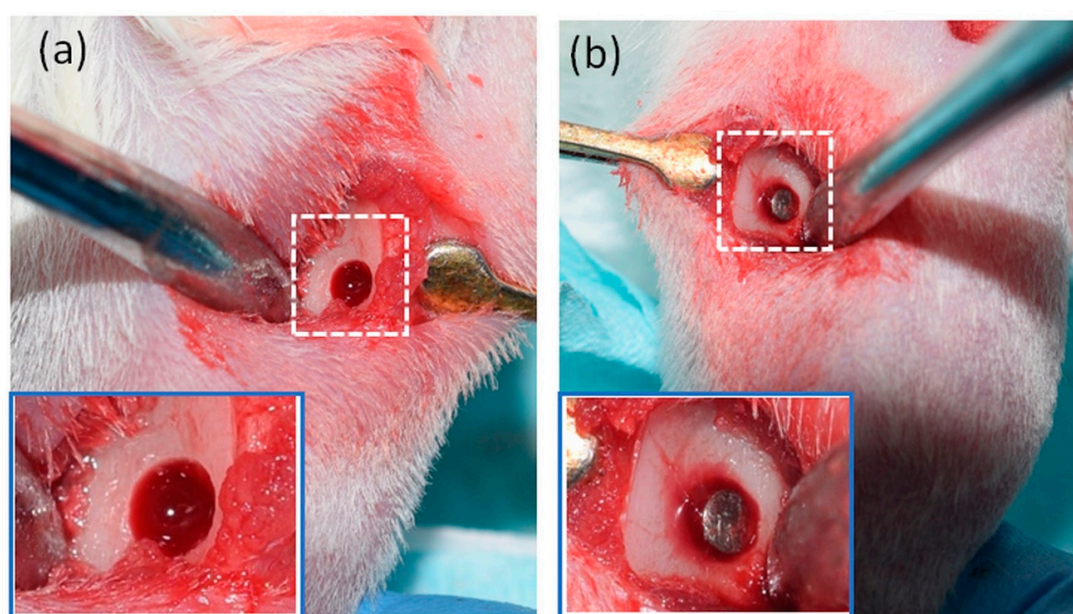


Figure 1. (a) A unicortical bone defect created in the lateral surface of the right tibial metaphysis. (b) A titanium implant placed in the lateral surface of the left tibial metaphysis.

Micro-computerized tomography (Micro-CT) analysis was conducted as described by Al Subaie et al., 2016 [19]. All tibiae with defects (n = 22) or titanium implants (n = 22) were scanned using a micro-CT (Sky-Scan1172; Bruker, Kontich, Belgium). Micro-CT image three-dimensional analysis was performed using the CTAn software (SkyScan 1172). The volume of interest of the bone samples was defined using a standardized algorithm as described in our previous studies [19,21,22]. Briefly, the volume of interest (VOI) was a cylinder that included the full diameter of the original defect (2.5 mm) and the thickness of the cortical bone surrounding the defect (Figure S1a,b). The cortical thickness was measured in coronal sections as shown in figure (Figure S1c). Bone architectures including the bone volume/tissue volume (BV/TV), the defect size, the trabecular thickness (Tb.Th), trabecular number (Tb.N), and trabecular separation (Tb.Sp)) were calculated within the VOI.

The peri-implant volume of interest (VOI) was determined as follows; first, the Ti implants were identified in 8-bit images by setting-up the greyscale index threshold ranging from 130 to 255. This threshold range was selected because it produced images that matched the real dimensions of the Ti implant as described in our previous study [19]. Second, using the “dilatation” tool of the CTAn

software, the region within 50 μm of the implant perimeter was excluded from the analysis because it presented substantial noise caused by metal artefacts. Third, the peri-implant VOI selected for analysis was determined to be 50 to 70 μm away from the implant surface. This was done by subtracting a VOI, expanding 50 μm away from the Ti-implant, from a second VOI expanding 70 μm away from the Ti-implant. Within the selected peri-implant VOI, the bone was determined from 8-bit images in which the lower threshold was set at a greyscale index of 6 and the upper threshold at greyscale index of 255 (Figure S1d–g). These thresholds were selected because they were found to accurately identify mineralized bone in previous studies [21].

Histology and histomorphometry analyses of bone defects were conducted as previously described [19]. The right tibiae defects were dehydrated in ascending concentrations of ethanol (70–100%) using the automated paraffin tissue processor (ASP300-Leica, Wetzlar, Germany) and cleared with Xylene. Samples were pre-infiltrated with Paraplast X-Tra wax at 58 °C and embedded in paraffin wax (EG1160-Leica, Toronto, ON, Canada) and cut into 5 μm thick sections using a microtome (RM2265-Leica, Richmond Hill, Ontario, Canada). Three horizontal sections were obtained from each defect. Sections were stained with Hematoxylin and eosin (H&E) and Toluidine Blue (TB) stains to assess the number of chronic inflammatory cells (macrophages and lymphocytes) and mast cells respectively. Von Kossa stain was used to measure the percentage of new bone formation. The average number of mast cells per each square millimeter (mm^2) were quantified using ZEN 2012 SP2 software (Zeiss, Jena, Germany) at a magnification of 40X. The chronic inflammatory cells were quantified using WEKA trainable segmentation plugin of the ImageJ software (Wayne Rasband; NIH, Bethesda, MD, USA) in which the region of interest in H&E stained sections were marked, followed by training the software in identifying the cells of interest by marking multiple immune cells. Thresholding adjustment was used to remove other types of cells, and finally a binary set-up was used to quantify the objects that represent the immune cells (Figure S2). Bone mineralization was assessed using ImageJ software by calculating the ratio of the new bone percentage divided by the total tissue area.

2.3. Soft Tissue Healing Assessment

Eight rats, underwent bone surgeries [saline recipient ($n = 4$) and donepezil recipient ($n = 4$)] as discussed above, were used for soft tissue assessment. In order to assess the effect of donepezil on wound healing, wounds in both legs were photographed on day 0, 2, 4, 8, 10, 12, and day 14. Wound healing was assessed using a modified scale based on wound color (red (necrotic), yellow, brown, or pink), surface regularity (regular or irregular), and wound edges (defined or ill-defined) [23]. The time required to heal was determined based on wound color and classified into two categories: healed (pink color) or non-healed (red, yellow, or brown color).

2.4. Platelet Function Testing

Eight rats that underwent bone surgeries as discussed above were used for platelet function assessment. At day 14 postoperatively, animals were sacrificed using intracardiac puncture, and their blood samples were collected in 3 mL Hirudin tubes (Mannheim, Germany). Whole blood platelet aggregation was assessed by impedance aggregometry (Multiplate[®] Analyzer, Roche Diagnostics International Ltd.). Briefly, hirudinized blood was diluted (1:1) with NaCl 0.9% prior to addition of the platelet agonist. The following agonists were used: adenosine diphosphate (ADP, 20 μM), arachnoid acid (AA, 0.5 mM), collagen (5 $\mu\text{g}/\text{mL}$), and protease-activated receptor 4 activating peptide (PAR4, 500 μM). Platelet aggregation was measured at 37 °C for 6 min and it was reported in arbitrary units (U) corresponding to the impedance area under the curve (AUC).

2.5. Assessment of Bleeding Time and Volume

The eight rats used for hemostasis assessment underwent sham surgeries; only the skin incision was done on both tibial bones of each rat. Afterwards, rats were randomly assigned to donepezil or saline treatments as discussed above. At day four postoperatively, bleeding time and volume were

measured using the tail transection technique. Prior to tail transection, a ruler was used to mark 2 mm of the tail where the transection was performed using blade #11. After tail transection, its bleeding end was placed immediately into a plastic tube containing 2mL saline and monitored visually to determine when cessation of bleeding occurred. To determine bleeding volume, the total volume was measured after subtracting the original volume of saline. After bleeding cessation, rats were euthanized as mentioned previously.

2.6. Blinding

The retrieved bone samples, blood samples, and wound photos were labeled in a blinded manner. Micro-CT, soft tissue healing, platelet function, and bleeding time analyses were performed by a researcher blinded to the group allocation.

2.7. Statistical Analysis

The effect of donepezil on bone formation and implant osseointegration was set to be the primary outcome, whereas its effect on soft tissue healing and hemostasis was set as secondary outcomes. Sample size for the bone healing experiment was calculated to achieve a power of 80% at a significance level of 5% to be able to reject the null hypothesis that donepezil has no effect on bone healing and implant osseointegration. 10% difference between study groups was considered to be clinically relevant, and a 12% potential standard deviation was assumed based on our previous study [24]. Accordingly, a total of 10 rats per group were determined to be sufficient. However, one rat was added to each group to compensate for 10% potential losses. For the soft tissue healing assessment, a total of eight wounds per group were determined to be sufficient as described in a previous study [25]. All results were presented as mean \pm SD. Normality of data was checked using Shapiro-Wilk test and all data were normally distributed. Student's t test was used to compare study groups for all parameters. A *p*-value of < 0.05 was considered statistically significant.

3. Results

3.1. Donepezil Hinders Bone Healing

Micro-CT analysis of the bone defects showed that Donepezil-treated rats presented lower values in terms of bone volume/tissue volume (BV/TV) ($14.7 \pm 7.5\%$ vs. $27.4 \pm 5.0\%$; $p = 0.003$), trabecular thickness (0.05 ± 0.01 mm vs. 0.10 ± 0.03 mm; $p = 0.001$), cortical thickness (0.6 ± 0.05 mm vs. 0.8 ± 0.06 mm; $p = 0.016$), and the percentage of newly formed bone ($16.0 \pm 9.3\%$ vs. $36.6 \pm 11.8\%$; $p = 0.002$) compared to saline-treated rats. The trabecular number (Tb.N) and trabecular separation (Tb.Sp) were comparable in both groups [Tb.N: donepezil ($5.3 \pm 1.01/\text{mm}$), saline ($5.1 \pm 1.01/\text{mm}$), Tb.Sp: donepezil ($0.13 \pm 0.03/\text{mm}$), saline ($0.12 \pm 0.03/\text{mm}$); $p \geq 0.05$] (Figures 2 and 3).

Histomorphometric analysis showed that donepezil-treated defects presented significantly lower chronic immune cell infiltration ($5.2 \cdot 10^3 \pm 0.9 \cdot 10^3$ vs. $7.3 \cdot 10^3 \pm 0.5 \cdot 10^3$ cell/mm², $p = 0.002$, $n = 14$) and comparable mast cell infiltration (34 ± 12 vs. 30 ± 12 cell/mm²; $p = 0.62$, $n = 14$) compared to saline-treated defects. The donepezil group showed a lower percentage of new bone formation compared to the saline group ($43 \pm 6\%$ vs. $52 \pm 4\%$; $p = 0.04$, $n = 12$) (Figure 4).

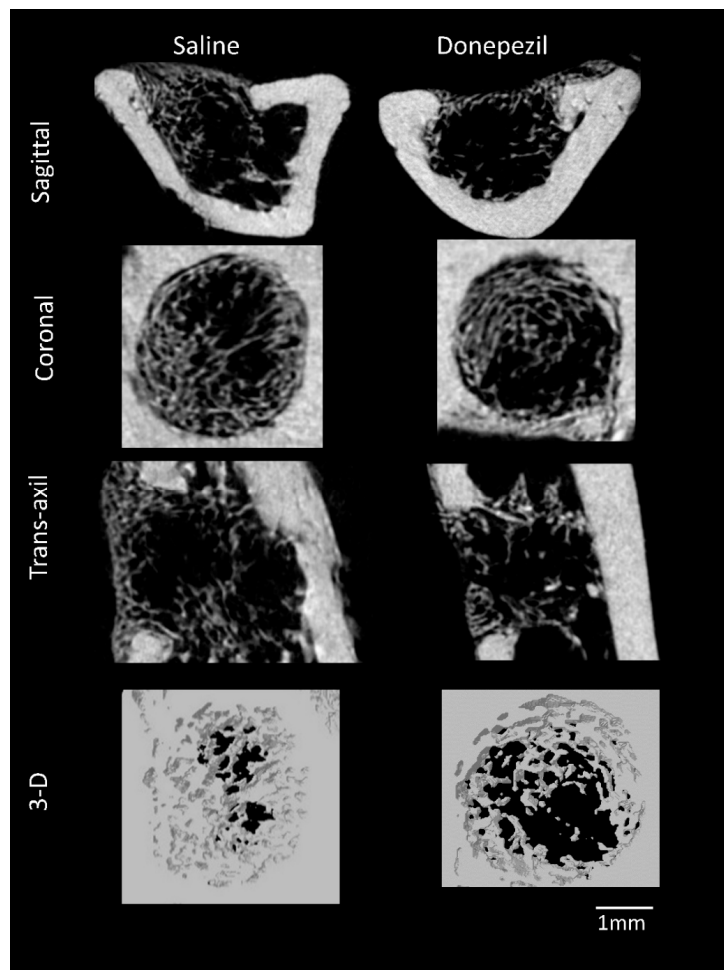


Figure 2. Sagittal, coronal, trans-axial, and 3-D μ -CT images of bone defects showing compromised bone healing in donepezil treated rats compared to saline treated rats.

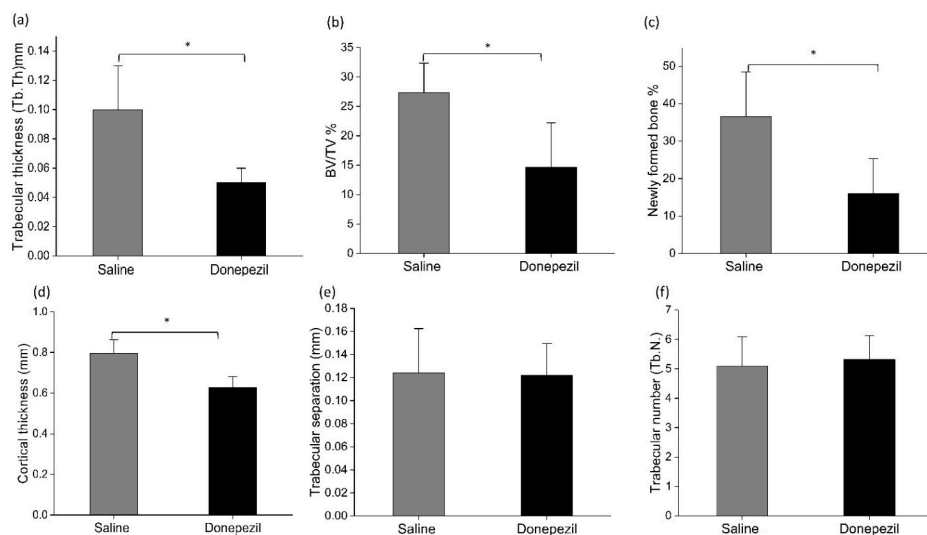


Figure 3. Micro-CT data analysis of bone defects in donepezil-treated rats compared to saline treated rats for the following parameters: trabecular thickness (Tb.Th), bone volume/tissue volume (BV/TV), percentage of new bone formation, cortical thickness, trabecular separation (Tb.Sp) and trabecular number (Tb.N). Statistical analysis was done using Student’s *t* test (*n* = 11 per each group). * indicates significant difference.

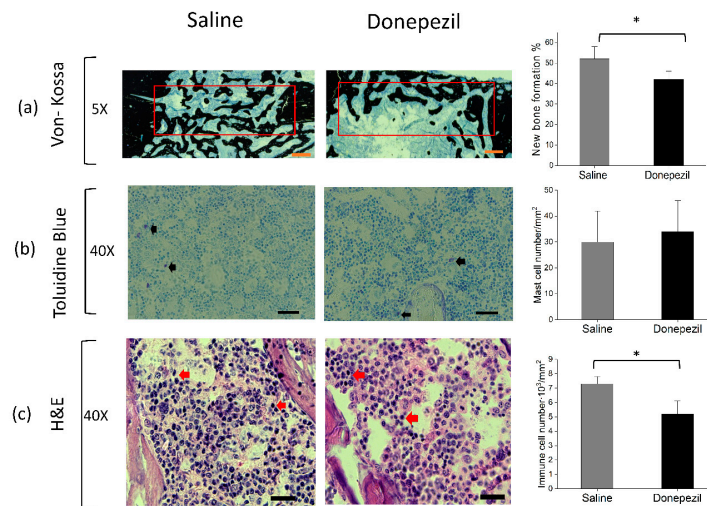


Figure 4. Histological analysis of bone defects. (a) Histological cross-sections stained with Von Kossa stain showing less mineralized newly formed bone in the donepezil group compared to the saline group (scale bar = 500 μ m). Red rectangles represent the region of interest. (b) Histological cross sections of bone samples stained with Toluidine blue showing mast cell infiltration in donepezil-treated rats compared to saline-treated rats (scale bar = 20 μ m). (c) Histological cross sections of bone samples stained with H & E showing chronic immune cells infiltration (lymphocytes & macrophages). Black and red arrows indicate the cells of interest. Bar charts represent the histomorphometric analyses. Data presented as mean \pm SD. Statistical analysis was done using Student’s *t* test. * indicates significant difference.

3.2. Donepezil Interferences with Titanium-Implant Osseointegration

Micro-CT analysis of peri-implant area revealed that Donepezil-treated rats presented lower values of bone-implant BV/TV ($32.8 \pm 10.7\%$ vs. $41.0 \pm 5.2\%$; $p = 0.03$) and trabecular number (25.7 ± 6.2 vs. $31.1 \pm 3.2\%$ [1/mm]; $p = 0.02$) compared to saline-treated rats (Figure 5).

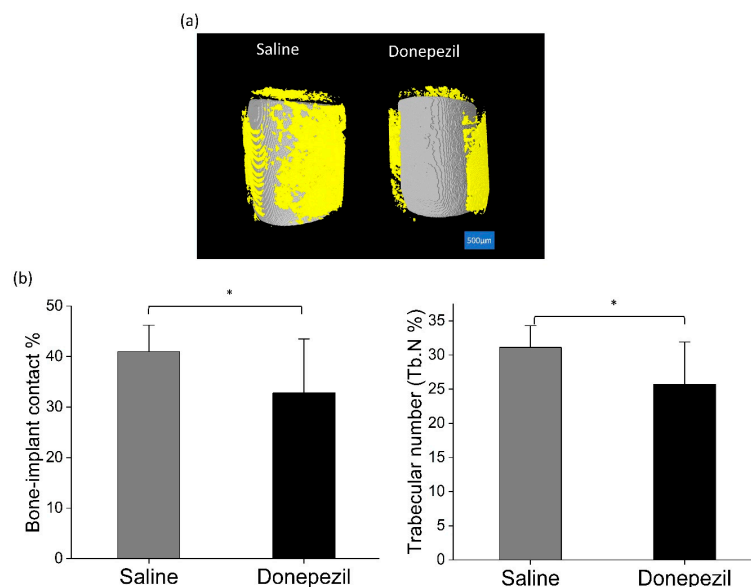


Figure 5. Micro-CT analysis of the implant. (a) 3-D μ -CT reconstructions of implants showing less bone (yellow) surrounding the implants (grey) in donepezil-treated rats compared to saline treated rats. Scale bar = 500 μ m. (b) μ -CT data analysis of bone-implant contact % and trabecular number %. Statistical analysis was done using Student’s *t* test ($n = 11$ per each group). * indicates significant difference.

3.3. The Role of Donepezil on Soft Tissue Healing

The average time required to heal was significantly shorter in donepezil-treated rats compared to the saline-treated ones (8.4 ± 2.9 days vs. 11.6 ± 1.7 days; $p = 0.02$) (Figure 6).

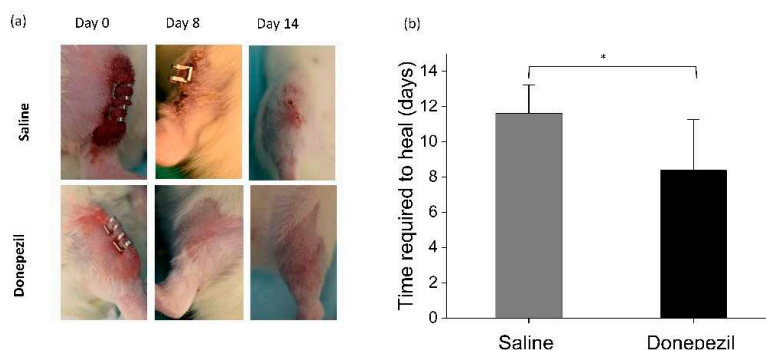


Figure 6. Time required to heal of skin wounds in donepezil and saline treated rats. (a) Photographs showing wound healing in donepezil and saline groups for day 0, 8, and day 14 postoperatively. (b) Bar-chart showing faster healing time of donepezil treated wounds compared to controls. * indicates significant difference.

3.4. The Role of Donepezil on Hemostasis and Platelet Function

Bleeding time in donepezil-treated rats was 230 ± 19 s compared to 250 ± 46 s in saline-treated rats ($p > 0.05$). In addition, bleeding volume was comparable between both groups (0.7 ± 0.4 vs. 0.7 ± 0.5 mL). Platelet aggregation responses to ADP (77 ± 20 U vs. 84 ± 11 U; $p = 0.68$), AA (56 ± 30 U vs. 41 ± 47 U; $p = 0.068$), collagen (94 ± 15 U vs. 103 ± 2 U; $p = 0.49$), and PAR4 activating peptide (67 ± 12 U vs. 72 ± 2 U; $p = 0.66$) in donepezil and saline-treated rats were comparable (Figure 7).

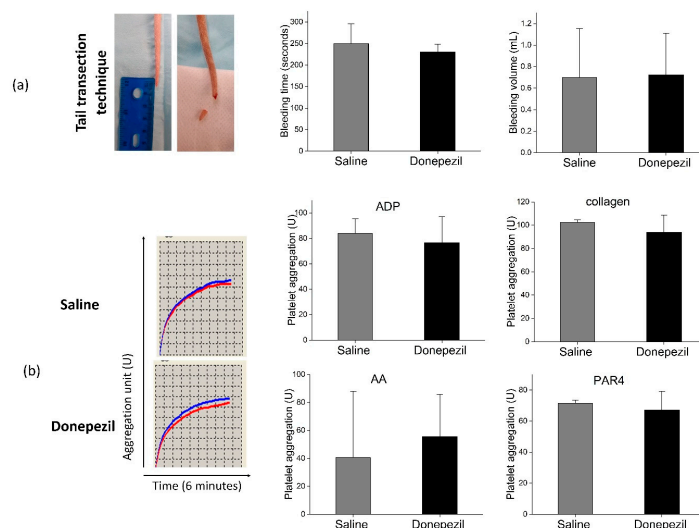


Figure 7. (a) Assessment of bleeding time and volume using tail transection technique. There was no significant difference between both groups ($p > 0.05$). (b) Platelet aggregation response to different agonists: adenosine diphosphate (ADP) ($20 \mu\text{M}$), arachnoid acid (AA) $500 \mu\text{M}$, collagen, and protease-activated receptor 4 (PAR4), assessed by five channel multi-plate analyzer in donepezil and saline groups. Platelet aggregation response represents the area under the curve. X axis represents the test duration (6 min), Y axis represents the aggregation unit (U). Red and blue lines represent both electrodes and the platelet aggregation response to adenosine diphosphate (ADP, $20 \mu\text{M}$) was shown as an example. There was no significant difference between both groups ($p \geq 0.05$). Statistical analysis was done using Student's *t* test ($n = 4$ rats per each group).

4. Discussion

An unexpected finding in this study was the fact that donepezil had opposing effects on skin healing and bone healing. These findings could be explained by differences between skin and bone healing in terms of the inflammatory processes, the cells involved, and the speed of the healing process.

During the early inflammatory phase of wound healing, immune cells and hematopoietic stem cells secrete pro-inflammatory cytokines such as interleukin-1 beta (IL-1 beta), interferon gamma (IFN γ), and tumor necrosis factor alpha (TNF α) [26–28]. TNF α and IFN γ have been found to enhance bone healing [29,30] and inhibit soft tissue healing [31,32]. Interestingly, donepezil is known to inhibit IFN γ and TNF α production [32–34]. This could partially explain why donepezil accelerated wound healing while it impaired bone healing.

Furthermore, donepezil may act differently on bone and skin cells [35,36]. Even though donepezil does not have a local direct effect on osteoprogenitor mesenchymal stem cell (MSCs) [37], acetylcholine could accelerate keratinocyte proliferation, migration, and viability [38]. This is mediated through the action of non-neuronal cholinergic receptors; muscarinic (M1 and M3) and $\alpha 7$ nicotinic receptors of keratinocytes [38,39]. Moreover, donepezil could further enhance skin wound healing through a feed-back loop, in which keratinocyte activation stimulates fibroblasts to release growth factors, which in turn stimulate keratinocyte proliferation [39,40].

Also, the healing time of bone defect lasts longer compared to skin wounds. Bone defects in rats take around 4–8 weeks to heal completely, and during this process, inflammation plays a predominant role during the first two weeks, while cell proliferation only kicks off in the second week. On the other hand, skin wounds have a short inflammatory phase and the proliferative phases kicks off as early as day three, when fibroblast starts to lay down the collagen matrix [41–44]. Given these differences in healing speed between skin and bone injuries, at the two-week time point of assessment in our study, bone healing would still have been under the influence of the inflammatory process, whereas skin healing would have been dominated by the proliferative stages of wound healing. This could also help explain why donepezil had opposite effects on skin healing and bone healing. Since donepezil is known to inhibit inflammation and stimulate cell proliferation, the two-week time point would have allowed us to perceive the positives effect on cell proliferation in skin healing but not in bone healing (Table S1).

The negative effect of donepezil on bone healing observed in our study could be seen to contradict the previous literature on the effect of donepezil on bone accrual. The use of donepezil has been associated with reduced risk of hip fracture and increased bone mass in animals, probably due to its effect on bone resorption during the remodeling process [15–18,45]. Furthermore, the use of AChEI was also associated with reduced risk of fracture complications in AD patients [45]. Thus, in the context of our results, we could hypothesize that the positive bone surgery outcomes associated with the long term use of AchEIs are probably due to better bone quality at the moment of the fracture compared to non-users [17], and this could outweigh the negative effects on bone healing. However, further studies investigating the effect of long-term donepezil administration on bone healing would be required to confirm this hypothesis.

Osseointegration and bone healing are similar processes that involve similar cells, cytokines and growth factors [46]. Therefore, drugs that reduce bone healing can also reduce osseointegration [47,48] and this is exactly what we observed herein. In our study, the bone-implant contact in the control group were comparable to previous studies [49,50]. However, donepezil decreased implant osseointegration compared to controls and this was similar to its effect on the healing of cortical bone defects. Those findings may have clinical implications in AD patients requiring orthopedic or maxillofacial surgeries particularly if they are requiring donepezil concurrently with the surgical procedure as donepezil interferes with the inflammatory phase of bone healing. Furthermore, bone implant contact is a well established indicator of mechanical stability of osseointegrated implants [51]. Thus, given its negative impact on osseointegration, donepezil would be expected to have also a detrimental effect on the mechanical stability of osseointegrated titanium implants. However additional mechanical studies would be required to confirm this.

Furthermore, Alzheimer's disease patients are at high risk of developing osteoporosis. Reports suggest the use of prophylactic anti-osteoporosis therapies in AD patient [52]. These therapies include bisphosphonate and Denosumab, a human monoclonal antibody, which are commonly used for preventing or treating osteoporosis. They act by reducing bone turnover, improve bone mineral density, and consequently could reduce fracture risk [53,54]. However, their long-term use may be associated with an increased fracture risk [55]. In terms of bone healing, *in vivo* studies showed that the use of antiosteoporotic medications, including bisphosphonates, denosumab, calcitonin, estrogen, and raloxifene, do not impair endochondral fracture healing but they may delay repair due to impaired remodeling. However, bisphosphonates and denosumab delay callus remodeling, they increase callus volume and this results in improved biomechanical properties [56,57]. In the context of AD, the use of antiresorptive medications, taken together with or without AChEIs may have an impact on bone healing process. However, there is no *in vivo* studies assessing the effect of such treatment combination, thus further studies are required.

Acetylcholinesterase inhibitors (AChEIs) induce cholinergic effects on bone. Donepezil, rivastigmine, and galantamine increase bone mass indirectly via inhibiting the sympathetic activity on bone and directly via activating nicotinic and muscarinic receptors on bone cells. However, pyridostigmine was not associated with significant changes on bone mass [4]. Donepezil, rivastigmine, and pyridostigmine bind to both nAChERs and mAChERs, whereas galantamine binds to mAChERs only. High nicotine concentration is inhibitory for bone healing [58]. Therefore, increased concentrations of such drugs may desensitize nAChRs and interfere with bone healing.

Donepezil was found to rapidly increase brain acetylcholine signals which are mediated by muscarinic receptors, although these signals were desensitized despite the continuous increase of brain Ach concentration [59]. In addition, an *in vivo* study showed that injection of 1 mg/kg/day donepezil upregulates mRNA expressions of the cortex muscarinic receptors (M3, M4, M5) and $\alpha 7$ nicotinic receptors. In the current study, the donepezil dose was 0.6 mg/kg/day and it has been found to induce cholinergic effects by our previous study [15]. However, it is still unclear whether higher levels of acetylcholine within the cortex may or may not trigger the upregulation of cholinergic receptors [60]. This may indicate other mechanisms in addition to the central effect of donepezil, in which donepezil affects bone healing.

To further understand the mechanism by which donepezil hinders bone healing, we measured the effect of donepezil on hemostasis via measuring bleeding time, bleeding volume, and platelet function. We expected that donepezil may reduce platelet aggregation and consequently increase bleeding time and result in a weak platelet clot formed at the injury site. However, in our study, both donepezil and saline-treated rats showed comparable results. This indicates that donepezil does not affect initial hemostasis and it affects bone healing by different mechanism independent of hemostasis.

Strengths, Limitations, and Future Directions

This study investigated the post-operative short-term effect of donepezil on bone using a well-established rat tibial bone defect model. This surgical model minimizes animal suffering while providing reliable and reproducible results regarding the assessment of the effect of medications on bone healing and implant osseointegration [61]. Nonetheless, future studies should be performed to further confirm our results in human patients and in more clinically relevant animal models such as bone fracture model or orthopedic osseointegrated devices.

One more limitation to be acknowledged was that the effect of donepezil on bone healing and osseointegration was assessed at a single time point, two weeks after surgery. At this time point, the control rats presented around 37% reduction in the volume of original defect. Thus, given the speed of bone healing in young rats, it is possible that at longer time points (i.e., four weeks), bone defects among controls would have completely heal, and thus hindering potential comparisons between groups. In addition, this period allows an accurate assessment of different medications on the inflammatory and proliferative phases of bone healing in terms of bone cells quantity and function [61].

However, further studies are required to study the long-term effect of donepezil on bone healing and implant osseointegration.

5. Conclusions

Short term postoperative administration of donepezil reduced bone defect healing and implant osseointegration in rats' tibiae, whereas it improved soft tissue healing. Donepezil administration did not affect hemostasis and platelet function.

Supplementary Materials: The following are available online at <http://www.mdpi.com/2218-273X/10/9/1318/s1>, Figure S1: The methodology used for bone defect and implant analyses, Figure S2: Validation of WEKA plugin in identifying chronic immune cell infiltration using ImageJ software, Table S1: The main differences between bone and skin wound healing.

Author Contributions: Conceptualization, F.S.A.-H., Z.B. and F.T.; Data Curation, I.B.; Formal Analysis, F.S.A.-H., O.M.M., J.P., A.M., L.A.N. and O.A.E.; Funding Acquisition, F.T.; Investigation, F.S.A.-H., A.A.S., Q.G., A.M., I.B. and M.L.; Methodology, F.S.A.-H., F.T. and Z.B.; Project Administration, F.T.; Supervision, Z.B. and F.T.; Visualization, F.S.A.-H.; Writing—Original Draft, F.S.A.-H.; Writing—Review and Editing, F.S.A.-H., O.M.M., J.P., O.A.E., S.D.T., M.L., Z.B. and F.T. All authors have read and agreed to the published version of the manuscript.

Funding: F.S.A.-H. was supported by scholarships from Al Awn Foundation for Development, Yemen, Fonds de Recherche Québec-Santé (FRQS: 257709), and Faculty of Dentistry, McGill University, and a grant from Alpha Omega Foundation of Canada. M.L. is a Fonds de recherche du Québec (FRQS) Research Scholar. M.L. received speaker fees from Bayer; has participated in industry-funded trials from Idorsia; has served on advisory boards for Servier; and has received in-kind and financial support for investigator-initiated grants from Leo Pharma, Roche Diagnostics and Aggreodyne, for unrelated work. The authors also acknowledge support from the Canada Research Chair Program, and Le Réseau de recherche en santé buccodentaire et osseuse (RSBO).

Conflicts of Interest: The authors declare no conflict of interest.

References

1. Hadjidakis, D.J.; Androulakis, I.I. Bone remodeling. *Ann. N. Y. Acad. Sci.* **2006**, *1092*, 385–396. [[CrossRef](#)]
2. Eimar, H.; Tamimi, I.; Murshed, M.; Tamimi, F. Cholinergic regulation of bone. *J. Musculoskelet. Neuronal. Interact.* **2013**, *13*, 124–132.
3. Shiratori, Y.T.; Kyumoto-Nakamura, A.; Kukita, N.; Uehara, J.; Zhang, K.; Koda, M.; Kamiya, T.; Badawy, E.; Tomoda, X.; Xu, T.; et al. IL-1 β induces pathologically activated osteoclasts bearing extremely high levels of resorbing activity: A possible pathological subpopulation of osteoclasts, accompanied by suppressed expression of kindlin-3 and talin-1. *J. Immunol.* **2018**, *200*, 218–228. [[CrossRef](#)]
4. Bajayo, A.; Bar, A.; Denes, A.; Bachar, M.; Kram, V.; Attar-Namdar, M.; Zallone, A.; Kovács, K.J.; Yirmiya, R.; Bab, I. Skeletal parasympathetic innervation communicates central IL-1 signals regulating bone mass accrual. *Proc. Natl. Acad. Sci. USA* **2012**, *109*, 15455–15460. [[CrossRef](#)] [[PubMed](#)]
5. Bassett, J.H.D.; Williams, G.R. Critical role of the hypothalamic–pituitary–thyroid axis in bone. *Bone* **2008**, *43*, 418–426. [[CrossRef](#)]
6. Takeda, S.; Elefteriou, F.; Levasseur, R.; Liu, X.; Zhao, L.; Parker, K.L.; Armstrong, D.; Ducy, P.; Karsenty, G. Leptin regulates bone formation via the sympathetic nervous system. *Cell* **2002**, *111*, 305–317. [[CrossRef](#)]
7. Feng, W.; Guo, J.; Li, M. RANKL-independent modulation of osteoclastogenesis. *J. Oral Biosci.* **2019**, *61*, 16–21. [[CrossRef](#)]
8. Berman, M.; Nachmansohn, D. On the formation of acetylcholine by choline acetylase in the nerve axon. *Fed. Proc.* **1946**, *5*, 122.
9. Carlson, A.B.; Kraus, G.P. *Physiology, Cholinergic Receptors*; StatPearls Publishing LLC.: Treasure Island, FL, USA, 2019.
10. Shi, Y.; Oury, F.; Yadav, V.K.; Wess, J.; Liu, X.S.; Guo, X.E.; Murshed, M.; Karsenty, G. Signaling through the m3 muscarinic receptor favors bone mass accrual by decreasing sympathetic activity. *Cell Metab.* **2010**, *11*, 231–238. [[CrossRef](#)]
11. Liu, P.S.; Chen, Y.Y.; Feng, C.K.; Lin, Y.H.; Yu, T.C. Muscarinic acetylcholine receptors present in human osteoblast and bone tissue. *Eur. J. Pharmacol.* **2011**, *650*, 34–40. [[CrossRef](#)]
12. Callen, D.; Black, S.E.; Gao, F.; Caldwell, C.; Szalai, J. Beyond the hippocampus: MRI volumetry confirms widespread limbic atrophy in AD. *Neurology* **2001**, *57*, 1669–1674. [[CrossRef](#)] [[PubMed](#)]

13. Collins, L.E.; Paul, N.E.; Abbas, S.F.; Leser, C.E.; Podurgiel, S.J.; Galtieri, D.J.; Chrobak, J.J.; Baqi, Y.; Müller, C.E.; Salamone, J.D. Oral tremor induced by galantamine in rats: A model of the parkinsonian side effects of cholinomimetics used to treat Alzheimer's disease. *Pharmacol. Biochem. Behav.* **2011**, *99*, 414–422. [[CrossRef](#)]
14. O'Brien, J.T.; Ballard, C.G. Drugs for Alzheimer's disease. *BMJ* **2001**, *323*, 123–124. [[CrossRef](#)] [[PubMed](#)]
15. Eimar, H.; Alebrahim, S.; Manickam, G.; Al-Subaie, A.; Abu-Nada, L.; Murshed, M.; Tamimi, F. Donepezil regulates energy metabolism and favors bone mass accrual. *Bone* **2016**, *84*, 131–138. [[CrossRef](#)] [[PubMed](#)]
16. Tamimi, F.; Ojea, T.; Sanchez-Siles, J.M.; Rojas, F.; Martín, I.; Gormaz, I.; Perez, A.; Dawid-Milner, M.S.; Méndez, L.; Tamimi, F. Acetylcholinesterase inhibitors and the risk of hip fracture in Alzheimer's disease patients: A case-control study. *J. Bone Miner. Res.* **2012**, *27*, 1518–1527. [[CrossRef](#)] [[PubMed](#)]
17. Eimar, H.; Lara, A.P.; Tamimi, I.; Sánchez, P.M.; Talavera, I.G.; Rojas-Tomba, F.; De La Oliva, T.G.; Tamimi, F. Acetylcholinesterase inhibitors and healing of hip fracture in Alzheimer's disease patients: A retrospective cohort study. *J. Musculoskelet. Neuronal Interact.* **2013**, *13*, 454–463.
18. Tamimi, I.; Nicolau, B.; Eimar, H.; Madathil, S.A.; Kezouh, A.; Karp, I.; Tamimi, F. Acetylcholinesterase inhibitors and the risk of osteoporotic fractures: Nested case-control study. *Osteoporos. Int.* **2018**, *29*, 849–857. [[CrossRef](#)]
19. Al-Subaie, A.E.; Laurenti, M.; Abdallah, M.N.; Tamimi, F.; Yaghoubi, F.; Eimar, H.; Makhoul, N.; Tamimi, F. Propranolol enhances bone healing and implant osseointegration in rats tibiae. *J. Clin. Periodontol.* **2016**, *43*, 1160–1170. [[CrossRef](#)]
20. Van Dam, D.; Abramowski, D.; Staufienbiel, M.; De Deyn, P.P. Symptomatic effect of donepezil, rivastigmine, galantamine and memantine on cognitive deficits in the APP23 model. *Psychopharmacology* **2005**, *180*, 177–190. [[CrossRef](#)]
21. Al Subaie, A.; Emami, E.; Tamimi, F.; Laurenti, M.; Eimar, H.; Abdallah, M.N.; Tamimi, F. Systemic administration of omeprazole interferes with bone healing and implant osseointegration: An in vivo study on rat tibiae. *J. Clin. Periodontol.* **2016**, *43*, 193–203. [[CrossRef](#)]
22. Alshahrani, N.S.; Abu Nada, L.; Garcia-Luna, J.L.R.; Al-Hamed, F.S.; Alamri, A.; Makhoul, N.M.; Tamimi, F. Ranitidine impairs bone healing and implant osseointegration in rats' tibiae. *J. Oral Maxillofac. Surg.* **2020**. [[CrossRef](#)]
23. Inbal, A.; Lubetsky, A.; Krapp, T.; Castel, D.; Shaish, A.; Dickneite, G.; Módis, L.; Muszbek, L.; Inbal, A. Impaired wound healing in factor XIII deficient mice. *Thromb. Haemost.* **2005**, *94*, 432–437. [[CrossRef](#)]
24. Al Subaie, A.; Eimar, H.; Abdallah, M.N.; Durand, R.; Feine, J.; Tamimi, F.; Emami, E. Anti-VEGFs hinder bone healing and implant osseointegration in rat tibiae. *J. Clin. Periodontol.* **2015**, *42*, 688–696. [[CrossRef](#)]
25. Gushiken, L.F.S.; Hussni, C.; Bastos, J.K.; Rozza, A.L.; Beserra, F.P.; Vieira, A.J.A.J.; Padovani, C.R.; Lemos, M.; Junior, M.P.; Da Silva, J.J.M.; et al. Skin wound healing potential and mechanisms of the hydroalcoholic extract of leaves and oleoresin of *copaifera langsdorffii* desf. kuntze in rats. *Evid. Based Complement. Altern. Med.* **2017**, *2017*, 1–16. [[CrossRef](#)]
26. Hoff, P.; Gaber, T.; Strehl, C.; Schmidt-Bleek, K.; Lang, A.; Huscher, D.; Burmester, G.R.; Schmidmaier, G.; Perka, C.; Duda, G.N.; et al. Immunological characterization of the early human fracture hematoma. *Immunol. Res.* **2016**, *64*, 1195–1206. [[CrossRef](#)]
27. Mirza, R.E.; Fang, M.M.; Ennis, W.J.; Koh, T.J. Blocking interleukin-1 β induces a healing-associated wound macrophage phenotype and improves healing in type 2 diabetes. *Diabetes* **2013**, *62*, 2579–2587. [[CrossRef](#)]
28. El-Jawhari, J.J.; Jones, E.; Giannoudis, P.V. The roles of immune cells in bone healing; what we know, do not know and future perspectives. *Injury* **2016**, *47*, 2399–2406. [[CrossRef](#)]
29. Glass, G.E.; Chan, J.K.; Freidin, A.; Feldmann, M.; Horwood, N.J.; Nanchahal, J. TNF-promotes fracture repair by augmenting the recruitment and differentiation of muscle-derived stromal cells. *Proc. Natl. Acad. Sci. USA* **2011**, *108*, 1585–1590. [[CrossRef](#)]
30. Takayanagi, H.; Ogasawara, K.; Hida, S.; Chiba, T.; Murata, S.; Sato, K.; Takaoka, A.; Yokochi, T.; Oda, H.; Tanaka, K.; et al. T-cell-mediated regulation of osteoclastogenesis by signalling cross-talk between RANKL and IFN- γ . *Nature* **2000**, *408*, 600–605. [[CrossRef](#)]
31. Ashcroft, G.S.; Jeong, M.J.; Ashworth, J.J.; Hardman, M.J.; Jin, W.; Moutsopoulos, N.; Wild, T.; McCartney-Francis, N.; Sim, D.; McGrady, G.; et al. Tumor necrosis factor-alpha (TNF- α) is a therapeutic target for impaired cutaneous wound healing. *Wound Repair Regen.* **2012**, *20*, 38–49. [[CrossRef](#)]

32. Laato, M.; Heino, J.; Gerdin, B.; Kahari, V.M.; Niinikoski, J. Interferon-gamma-induced inhibition of wound healing in vivo and in vitro. *Ann. Chir. Gynaecol.* **2001**, *215* (Suppl. 90), 19–23.
33. Sochocka, M.; Zaczynska, E.; Leszek, J.; Siemieniec, I.; Błach-Olszewska, Z. Effect of donepezil on innate antiviral immunity of human leukocytes. *J. Neurol. Sci.* **2008**, *273*, 75–80. [[CrossRef](#)] [[PubMed](#)]
34. Stamouli, E.; Piperi, C.; Katirtzoglou, E.; Siarkos, K.; Passa, M.; Maillis, A.; Papadimitriou, G.; Politis, A. P1-011: Donepezil treatment's late effects on cytokines release from lymphocytes of Alzheimer's disease patients. *Alzheimers Dement.* **2012**, *8*, P111. [[CrossRef](#)]
35. Kurzen, H.; Wessler, I.; Kirkpatrick, C.; Kawashima, K.; Grando, S. The non-neuronal cholinergic system of human skin. *Horm. Metab. Res.* **2007**, *39*, 125–135. [[CrossRef](#)] [[PubMed](#)]
36. Schlereth, T.; Birklein, F.; Haack, K.A.; Schiffmann, S.; Kilbinger, H.; Kirkpatrick, C.J.; Wessler, I. In vivorelease of non-neuronal acetylcholine from the human skin as measured by dermal microdialysis: Effect of botulinum toxin. *Br. J. Pharmacol.* **2006**, *147*, 183–187. [[CrossRef](#)]
37. Nachlinger, R.J.; Kauschke, V.; Trinkaus, K.; El Khassawna, T.; Heiss, C.; Lips, K.S. Application of donepezil increased collagen 1 expression in mesenchymal stroma cells of an ovine osteoporosis model. *J. Musculoskelet. Neuronal. Interact.* **2018**, *18*, 354–365.
38. Uberti, F.; Morsanuto, V.; Ghirlanda, S.; Ruga, S.; Clemente, N.; Boieri, C.; Boldorini, R.; Molinari, C. Highly diluted acetylcholine promotes wound repair in an in vivo model. *Adv. Wound Care* **2018**, *7*, 121–133. [[CrossRef](#)]
39. Uberti, F.; Bardelli, C.; Morsanuto, V.; Ghirlanda, S.; Cochis, A.; Molinari, C. Stimulation of the nonneuronal cholinergic system by highly diluted acetylcholine in keratinocytes. *Cells Tissues Organs* **2017**, *203*, 215–230. [[CrossRef](#)]
40. Sorg, H.; Hager, S.; Hauser, J.; Mirastschijski, U.; Tilkorn, D.J. Skin wound healing: An update on the current knowledge and concepts. *Eur. Surg. Res.* **2017**, *58*, 81–94. [[CrossRef](#)]
41. Marsell, R.; Einhorn, T. The biology of fracture healing. *Injury* **2011**, *42*, 551–555. [[CrossRef](#)]
42. Cañedo-Dorantes, L.; Cañedo-Ayala, M. Skin acute wound healing: A comprehensive review. *Int. J. Inflamm.* **2019**, *2019*, 3706315. [[CrossRef](#)] [[PubMed](#)]
43. Le, A.D.; Brown, J.J. Chapter 2—Wound healing: Repair biology and wound and scar treatment. In *Oral and Maxillofacial Surgery*; Bagheri, S.C., Bell, R.B., Khan, H.A., Eds.; W.B. Saunders: Saint Louis, MO, USA, 2012; pp. 6–10.
44. Bowden, L.; Byrne, H.M.; Maini, P.K.; Moulton, D.E. A morphoelastic model for dermal wound closure. *Biomech. Model. Mechanobiol.* **2015**, *15*, 663–681. [[CrossRef](#)] [[PubMed](#)]
45. Tamimi, I.; Madathil, S.; Kezouh, A.; Nicolau, B.; Karp, I.; Tamimi, F. Effect of acetylcholinesterase inhibitors on post-surgical complications and mortality following a hip fracture: A cohort study. *J. Musculoskelet. Neuronal. Interact.* **2017**, *17*, 69–77. [[PubMed](#)]
46. Berglundh, T.; Abrahamsson, I.; Lang, N.P.; Lindhe, J. De novo alveolar bone formation adjacent to endosseous implants. *Clin. Oral Implant. Res.* **2003**, *14*, 251–262. [[CrossRef](#)]
47. Davies, J. Understanding peri-implant endosseous healing. *J. Dent. Educ.* **2003**, *67*, 932–949. [[CrossRef](#)]
48. Mavrogenis, A.F.; Dimitriou, R.; Parvizi, J.; Babis, G.C. Biology of implant osseointegration. *J. Musculoskelet. Neuronal. Interact.* **2009**, *9*, 61–71.
49. Mair, B.; Tangl, S.; Feierfeil, J.; Skiba, D.; Watzek, G.; Gruber, R. Age-related efficacy of parathyroid hormone on osseointegration in the rat. *Clin. Oral Implant. Res.* **2009**, *20*, 400–405. [[CrossRef](#)]
50. Wong, M.; Eulenberger, J.; Schenk, R.; Hunziker, E. Effect of surface topology on the osseointegration of implant materials in trabecular bone. *J. Biomed. Mater. Res.* **1995**, *29*, 1567–1575. [[CrossRef](#)]
51. Daecke, W.; Veyel, K.; Wieloch, P.; Jung, M.; Lorenz, H.; Martini, A.K. Osseointegration and mechanical stability of pyrocarbon and titanium hand implants in a load-bearing in vivo model for small joint arthroplasty. *J. Hand Surg.* **2006**, *31*, 90–97. [[CrossRef](#)]
52. Tysiewicz-Dudek, M.; Pietraszkiewicz, F.; Drozdowska, B. Alzheimer's disease and osteoporosis: Common risk factors or one condition predisposing to the other? *Ortop. Traumatol. Rehabil.* **2008**, *10*, 315–323.
53. Tiihonen, M.; Taipale, H.; Tanskanen, A.; Tiihonen, J.; Hartikainen, S. Incidence and duration of cumulative bisphosphonate use among community-dwelling persons with or without alzheimer's disease. *J. Alzheimers Dis.* **2016**, *52*, 127–132. [[CrossRef](#)] [[PubMed](#)]
54. Zaheer, S.; LeBoff, M.; Lewiecki, E.M. Denosumab for the treatment of osteoporosis. *Expert Opin. Drug Metab. Toxicol.* **2015**, *11*, 461–470. [[CrossRef](#)] [[PubMed](#)]

55. Pedersen, A.B.; Heide-Jørgensen, U.; Sørensen, H.T.; Prieto-Alhambra, D.; Ehrenstein, V. Comparison of risk of osteoporotic fracture in denosumab vs alendronate treatment within 3 years of initiation. *JAMA Netw. Open* **2019**, *2*, e192416. [[CrossRef](#)] [[PubMed](#)]
56. Li, J.; Mori, S.; Kaji, Y.; Mashiba, T.; Kawanishi, J.; Norimatsu, H. Effect of bisphosphonate (incadronate) on fracture healing of long bones in rats. *J. Bone Miner. Res.* **1999**, *14*, 969–979. [[CrossRef](#)] [[PubMed](#)]
57. Hegde, V.; Jo, J.E.; Andreopoulou, P.; Lane, J.M. Effect of osteoporosis medications on fracture healing. *Osteoporos. Int.* **2016**, *27*, 861–871. [[CrossRef](#)]
58. Hollinger, J.O.; Schmitt, J.M.; Hwang, K.; Soleymani, P.; Buck, D. Impact of nicotine on bone healing. *J. Biomed. Mater. Res.* **1999**, *45*, 294–301. [[CrossRef](#)]
59. Basselin, M.; Nguyen, H.N.; Chang, L.; Bell, J.M.; Rapoport, S.I. Acute but not chronic donepezil increases muscarinic receptor-mediated signaling via arachidonic acid in unanesthetized rats. *J. Alzheimers Dis.* **2009**, *17*, 369–382. [[CrossRef](#)]
60. Chamoun, M.; Groleau, M.; Bhat, M.; Vaucher, E. Dose-dependent effect of donepezil administration on long-term enhancement of visually evoked potentials and cholinergic receptor overexpression in rat visual cortex. *J. Physiol.* **2016**, *110*, 65–74. [[CrossRef](#)]
61. Abu-Nada, L.; Al Subaie, A.; Mansour, A.; Wu, X.; Abdallah, M.-N.; Al-Waeli, H.; Ersheidat, A.; Stone, L.S.; Murshed, M.; Tamimi, F. The antidepressant drug, sertraline, hinders bone healing and osseointegration in rats' tibiae. *J. Clin. Periodontol.* **2018**, *45*, 1485–1497. [[CrossRef](#)]



© 2020 by the authors. Licensee MDPI, Basel, Switzerland. This article is an open access article distributed under the terms and conditions of the Creative Commons Attribution (CC BY) license (<http://creativecommons.org/licenses/by/4.0/>).

MDPI
St. Alban-Anlage 66
4052 Basel
Switzerland
Tel. +41 61 683 77 34
Fax +41 61 302 89 18
www.mdpi.com

Biomolecules Editorial Office
E-mail: biomolecules@mdpi.com
www.mdpi.com/journal/biomolecules



MDPI
St. Alban-Anlage 66
4052 Basel
Switzerland

Tel: +41 61 683 77 34
Fax: +41 61 302 89 18

www.mdpi.com



ISBN 978-3-0365-1797-1